



Universiteit
Leiden
The Netherlands

Trans-ruthenium(II) complexes for photoactivated cChemotherapy: from design to anticancer activity

Verbeet, W.

Citation

Verbeet, W. (2026, June 4). *Trans-ruthenium(II) complexes for photoactivated cChemotherapy: from design to anticancer activity*. Retrieved from <https://hdl.handle.net/1887/4304759>

Version: Publisher's Version

License: [Licence agreement concerning inclusion of doctoral thesis in the Institutional Repository of the University of Leiden](#)

Downloaded from: <https://hdl.handle.net/1887/4304759>

Note: To cite this publication please use the final published version (if applicable).

***Trans*-Ruthenium(II) Complexes for Photoactivated Chemotherapy From Design to Anticancer Activity**

Proefschrift

ter verkrijging van
de graad van doctor aan de Universiteit Leiden,
op gezag van rector magnificus prof.dr. S. de Rijcke,
volgens besluit van het college voor promoties
te verdedigen op donderdag 4 juni 2026
klokke 13:00 uur

door

Wessel Verbeet
geboren te Vlaardingen, Nederland
in 1992

Promotores:

Prof. dr. S. Bonnet

Prof. dr. E. Bouwman

Promotiecommissie:

Prof. dr. M. Ubbink

Prof. dr. A. Kros

Prof. dr. M. van de Stelt

Prof. dr. A.G. Quiroga (Universidad autónoma de Madrid)

Dr. E. Iengo (Università degli Studi di Trieste)

Printing: Ridderprint (www.ridderprint.nl)

Cover design: Joey Roberts (Ridderprint)

This work was financially supported by the Dutch Research Council (NWO) via a VICI grant (VI.C.182.011) to Prof. dr. S. Bonnet

Table of Contents

Chapter 1	7
Transition-Metal Complexes in Cancer Therapy: Mechanistic and Photochemical Perspectives	
Chapter 2	29
Simple and Efficient Method for Amination of Polypyridine N-oxides	
Chapter 3	55
Building a <i>Trans</i> Dissymmetric Ruthenium Complex for Sequential Ligand Photosubstitution	
Chapter 4	87
Dual Targeting of NAMPT and Tubulin with <i>Trans</i> Ruthenium-Based Photoactivated Chemotherapy Complexes	
Chapter 5	119
Targeting Heme Oxygenase 1 with Photoactivatable Ruthenium-Based Inhibitors	
Chapter 6	157
Summary, Discussion and Outlook	
Appendices	
Appendix I – General Methods	173
Appendix II – Supporting Information for Chapter 2	183
Appendix III – Supporting Information for Chapter 3	203
Appendix IV – Supporting Information for Chapter 4	239
Appendix V – Supporting Information for Chapter 5	267
Samenvatting	310
Curriculum Vitae	314
List of Publications	315
Acknowledgments	316

Chapter 1

Transition-Metal Complexes in Cancer Therapy: Mechanistic and Photochemical Perspectives

1.1 Anticancer drugs based on transition metals

1.1.1 Platinum chemotherapeutics

Transition metals including iron, zinc, copper, or manganese are essential in many biological processes. For example, iron is well-known for its crucial role in dioxygen transport in mammals, with a human body of 70 kg containing about 5 g of iron.^[1] It is therefore not surprising that a large amount of research has been dedicated to applying metal-containing compounds in modern medicine. In fact, a large number of inorganic compounds are currently in clinical use as imaging agents, diagnostics, or chemotherapeutics such as antibacterial, antibiotic, antiviral or antiparasitic drugs.^[2] In oncology, however, only a handful of “blockbuster” metallodrugs have been approved for anticancer therapy.

First recognized for its antiproliferation properties in 1965 by Barnett Rosenberg, Loretta van Camp and Thomas Krigas, *cis*-diamminedichloridoplatinum(II) (commonly referred to as cisplatin) is the most successful metallodrug for anticancer therapy (Figure 1.1).^[3] After its clinical introduction in 1978 for the treatment of testicular and ovarian cancers, cisplatin has become part of standard-of-care treatments against many types of cancer. Despite its success, patients treated with cisplatin experience severe side effects which arise from the toxicity of this compound to virtually every organ, but more particularly acute to the liver, heart and kidneys. Additionally, resistances of tumors first treated with cisplatin is often observed during relapse.^[4] These clinical limitations have led to an ever-evolving field of research targeted to the development of new platinum-based anticancer drugs.

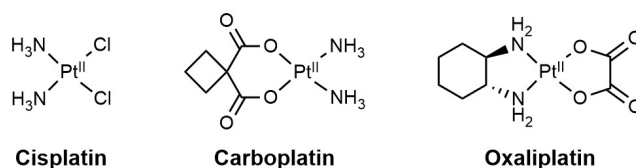


Figure 1.1 Selection of platinum-based metallodrugs for cancer treatment.

It is nowadays recognized that the curing power of cisplatin resides in its wide range of modes-of-action.^[4] However, the activity of cisplatin is often primarily attributed to the two reactive chloride ligands dissociating in intracellular conditions, thus “releasing” an activated platinum (Pt) center that can subsequently bind to biomolecules such as proteins or deoxyribonucleic acid (DNA). Dissociation of the chloride ligands is a thermal process that is non-specific to cancer cells, which causes systemic toxicity. The chelating ligand cyclobutane-dicarboxylate in carboplatin (Figure 1.1) was introduced as a protecting group preventing thermal hydrolysis. *In vitro*, carboplatin requires an esterase to lead to active cleavage of the bidentate chelating ligand, reducing the toxicity of the compound and allowing for use of higher doses of the chemotherapy agent. Long-term use of cisplatin or carboplatin, however, both results in drug resistance, which led to the development of oxaliplatin, which bears a chelating diamine ligand (Figure 1.1). While oxaliplatin produces a comparable therapeutic effect, this compound showed no cross-resistance with cisplatin

or carboplatin, suggesting it works via a different mode-of-action than cisplatin and carboplatin. Overall, despite the recognized efficacy of these three worldwide-approved Pt-based drugs and their presence in ~50% of chemotherapy regimens, their overall toxicity remains a medical challenge in anticancer therapy.

1.1.2 Mode-of-action

The undeniable clinical success of cisplatin, carboplatin and oxaliplatin for cancer treatment has led to in-depth investigation into the mode-of-action (MoA) of these chemotherapeutics. For these Pt-based drugs, the binding of Pt to guanine bases in DNA is usually proposed as their principal MoA, forming intra-strand and inter-strand crosslinks, ultimately leading to apoptosis.^[5] However, the reactivity of Pt towards sulfur, phosphorous and nitrogen-based ligands suggest interactions with biomolecules containing these elements that are not nuclear DNA. This hypothesis is consistent with the generally accepted idea that only 1-10% of cisplatin ends up in the nucleus.^[6] In addition to causing nuclear DNA damage, cisplatin affects many other subcellular processes, reducing proliferation. These effects include the formation of high levels of mitochondrial reactive-oxygen species, an increase of the endoplasmic reticulum (ER) stress, impairment of the function of the cytoskeleton and acidification of the cytoplasm.^[7-10] Apart from disrupting intracellular processes, cisplatin has also been shown to interact with the solid tumor microenvironment and to exhibit important immunomodulatory effects.^[11] The major histocompatibility complex class I (MHC-I) is a recognition factor present on the cell surface, which activates a T-cell mediated immune response. As this represents a way to evade the immune system, MHC-I is down-regulated in many cancer cells. Interestingly, up-regulation of MHC-I surface expression upon treatment with cisplatin has been reported to occur in several human lung carcinoma cell lines.^[12] This interaction with the cancer-immune interface highlights the capabilities of Pt-based chemotherapeutics to act as immunomodulators, as reviewed by Biasi et al. for cisplatin.^[13]

The broad range of biological processes within a tumor that are affected upon treatment with Pt-based metallodrugs can be viewed as a double-edged sword. On the one hand, such multi-targeting characteristics allow these drugs to be “universally applicable”, i.e., they can be used to treat many cancer types with a lower susceptibility to genetic mutations that would cancel the activity of drugs specifically targeting a certain mutation in a given tumor. On the other hand, severe side effects remain common for these “broad-spectrum” anticancer drugs such as pain, nausea, or damage to the hearing system, which limits the drug dose that can be given to patients, thereby limiting their therapeutic efficacy.

1.1.3 Ruthenium-based anticancer complexes

The limitations of Pt-based chemotherapeutics in the clinics has sparked the search for novel metallodrugs based on alternative transition metals, including for example gold, palladium, iron, or ruthenium.^[14,15] For ruthenium, a wide range of compounds have been described in the scientific literature as potential anti-tumor drugs, but only three of these

have made it to clinical trial. They can be divided into two types. On the one hand, photosensitizers, which require the action of light to deliver their cytotoxic load, which have been reviewed by McFarland et al.^[16] A lead compound in this class, TLD-1433 (Figure 1.2), is currently evaluated in a phase II clinical trial for the treatment of invasive bladder cancer. On the other hand, cytotoxic prodrugs that do not require any external trigger but are activated spontaneously upon entering the body or cancer cells. The latter family of compounds consists of a class of compounds similar to Pt-based drugs, which affect one or more cellular processes, resulting in anti-tumor and anti-metastatic activity that are as effective, or better, as Pt-based compounds.

The first clinically evaluated Ru compound, NAMI-A, was discovered by Mestroni and Alessio in the early 1990's following the preparation of ruthenium(III) complex, Na[*trans*-RuCl₄(dmsO-5)(imidazole)]. This complex was shown to have promising anti-tumor and anti-metastatic effects in a metastatic breast-cancer mice model.^[17] The imidazolium salt NAMI-A (Figure 1.2) was developed as a more stable and water-soluble analogue of this complex.^[18] Despite the promising pre-clinical results, the Phase I trial indicated severe side effects without a significant decrease in disease progression in several cancer types. In parallel, another class of structurally related anticancer ruthenium complexes were developed by Keppler and coworkers.^[19] Of this family of compounds, KP1019 was the first candidate that was clinically evaluated (Figure 1.2). Unlike for NAMI-A, the phase-I study of KP1019 revealed no serious side effects and it was found to stabilize the disease for up to ten weeks in five of the six patients included in the trial, who had been diagnosed with varying cancer types.^[20] Although good tolerability was shown for KP1019, the ending patent and sub-optimal solubility led to the development of the sodium salt analogue referred to as KP1339. This more soluble compound, commercially named BOLD-100, recently completed clinical phase II trial and has entered clinical phase III.

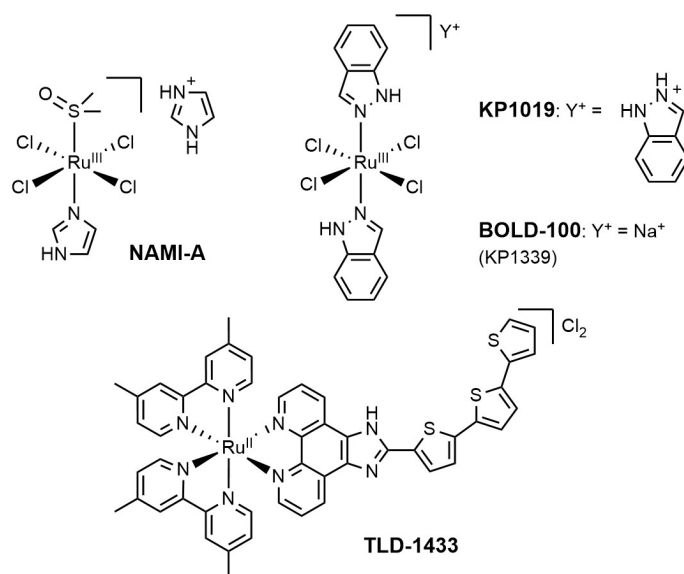


Figure 1.2 Selection of ruthenium-based metallodrugs for cancer treatment.

The Ru(III) coordination compounds NAMI-A and BOLD-100 are structurally related but exhibit distinct biological and pharmacological profiles. Compared to cisplatin, NAMI-A was found to be approximately 1000 times less cytotoxic in ovarian and breast cancer cell lines ($EC_{50} > 500 \mu\text{M}$).^[21] The observed association with cell membranes contrasts with the typical cellular internalization found for many other compounds; it might be an explanation for the strong antimetastatic effect of NAMI-A, while its cytotoxicity is usually considered as low to negligible.^[22] For KP1019 and its sodium salt analogue BOLD-100, slightly higher cytotoxicities were observed *in vitro* in several cancer cell lines ($EC_{50} \approx 100 \mu\text{M}$).^[23] Interestingly, BOLD-100 was shown to primarily induce ER stress in human patient-derived pancreatic ductal adenocarcinoma xenografts through inhibition of GRP78, a regulating chaperone protein of the unfolded protein response.^[24] This MoA is completely different from DNA damage, which makes it intrinsically different from approved platinum drugs and hence interesting for clinical investigation and use. On the other hand, it seems more and more clear that BOLD-100 shows several cytotoxic modes-of-action, similar to platinum compounds. Clinically evaluated Ru compounds such as BOLD-100 contain only monodentate ligands and hence exhibit comparatively fast ligand-exchange reactions in physiological conditions. These thermal activation processes in living cells produce several metal-based species that can interact with biomolecules, thus resulting in a potentially large number of bioinorganic interactions. These interactions complicate mechanistic investigations, but they also offer several routes to harm cancer cells with diverse genetic backgrounds.

The anticancer efficacy of both NAMI-A and BOLD-100 is limited compared to that of approved chemotherapy agents; they are hence not ideal for application in monotherapy.

However, their low systemic toxicity opens promising opportunities for combination therapy. The latest clinical trials involving this ruthenium complex all consist of a combination therapy with other anticancer drugs. For example, a combination of NAMI-A and gemcitabine (a nucleoside analog) in non-small cell lung cancer patients after first line treatment was evaluated in a phase I/II study.^[25] Unfortunately, the combination was found to be only moderately tolerated and less active than gemcitabine alone. For BOLD-100, on the other hand, synergistic effects were demonstrated in established preclinical models when combined with various anticancer therapies.^[26] Therefore, a combination of BOLD-100 with the folinic acid, fluorouracil, and oxaliplatin (Figure 1.3, FOLFOX) regimen was recently evaluated in patients with advanced biliary duct or gastric cancer.^[27,28] This phase II study concluded that the BOLD-100 + FOLFOX combination was well-tolerated and more effective than the FOLFLOX treatment alone. These studies highlight the importance of investigating drug combinations, which increases the efficacy of the so-called combination therapy, especially for anticancer metallodrugs.

1.2 Combination therapy

Chemotherapy is the main modality for cancer treatment. Conventional, small-molecule chemotherapeutics can be subdivided into four classes based on their mode of action. Firstly, anti-microtubule agents based on taxanes such as paclitaxel or vinca alkaloids like vinblastine, interact with tubulin to disrupt the function of microtubules and inhibit mitosis.^[29] Secondly, the topoisomerase (Top) inhibitors cause DNA damage by blocking DNA unwinding enzymes. Top inhibitors include camptothecin analogues, anthracyclines such as doxorubicin and semisynthetic natural product derivatives such as etoposide.^[30] Alkylating agents are another important class of anticancer drugs, which reduce tumor growth by inducing DNA damage through chemical modification (e.g. cyclophosphamide, temozolomide), intercalation (anthracyclines such as doxorubicin) or crosslinking (e.g. Pt-based metallodrugs) of nucleotides.^[31–33] The last class involves antimetabolites including 5-fluorouracil and gemcitabine, that disrupt DNA transcription/translation by displacing natural nucleosides.^[34]

Although countless small molecular chemotherapeutics have been developed for the treatment of cancer, single agent therapies generally result in time-limited remission due to drug resistances as discussed above for platinum drugs. Therefore, most chemotherapy regimens used to date consist of a combination of two or more drugs. The combined drugs generally exhibit different individual mode of actions and the combination is thus expected to be less vulnerable to oncogenic resistance. The POMP regime (Figure 1.3 A), combining antimetabolite 6-mercaptopurine (**P**urinethol), anti-microtubule agent Vincristine (**O**ncovin[®]), antimetabolite **M**ethotrexate and immunosuppressor **P**rednisone, was one of the first combination chemotherapies for the treatment of adult acute leukemia.^[35]

Although the mode-of-action remains largely unknown, the POMP therapy combines antimetabolites and an anti-microtubule agent, which results in an efficacy increase compared to monotherapies of the individual components. To date, POMP is still used for maintenance therapy in adult acute lymphoblastic leukemia.^[36] For the treatment of metastatic colorectal cancer, the FOLFOX (**F**olinic acid, **5-F**luorouracil and **O**xaliplatin) regime combines antimetabolites with Pt-based chemotherapeutics (Figure 1.3 B).^[37] Despite being the standard-of-care, a reduced therapeutic effect of the FOLFOX regimen is regularly observed and has been related to oxaliplatin resistance.^[38] These chemotherapeutic regimes highlight the clinical potential of combinatorial therapy for the treatment of cancer, while also emphasizing that they are not almighty.

Besides circumventing drug resistance, the combinatorial cancer-therapy approach may result in additional benefits for patients. To achieve a certain therapeutic effect, the dose needed of a synergistic drug combination is usually intrinsically lower than for monotherapy to realize the same effect. Furthermore, the lower dose of the more potent combination increases the selectivity towards cancerous cells, which in turn reduces side effects. With the ever-increasing understanding of biological processes in oncology, which enables development of highly selective anticancer drugs, targeting two or more specific cellular mechanisms can be achieved nowadays. The combination Ibrutinib and Venetoclax (Figure 1.3 C) for the treatment of chronic lymphocytic leukemia (CLL), is a highly successful example of such a synergy. Ibrutinib is a Burton's tyrosine kinase (BTK) inhibitor that blocks the B cell receptor pathway and is used for the treatment of lymphocytic cancers.^[39] When BTK inhibition fails, Bcl-2 inhibitor Venetoclax is used as an alternative therapy.^[40] Blocking Bcl-2 prevents this apoptosis-regulatory protein from promoting cancer-cell survival.^[41] As Ibrutinib-resistant cells were shown to express high levels of Bcl-2, combining Ibrutinib with Venetoclax synergistically suppressed *in vitro* proliferation of Ibrutinib-resistant lymphoma cells. Recently, the effectivity of this combination therapy was translated into a clinical setting, with a phase II trial showing no relapse in 75% of CLL patients with a 3-year overall survival of 96%.^[42]

While the results of the Ibrutinib/Venetoclax combination are encouraging, rational design of drug combination remains challenging as it requires extensive understanding of the involved cellular mechanisms and of their interactions.^[43] High-throughput screening (HTS) has shown promising results in identifying relevant drug combinations.^[44] HTS can, however, only be utilized for initial drug selection as large scale screening in *in vivo* using animal-tumor models is financially unviable and unethical. Alternatively, predicting synergistic drug combinations with computational methods is expected to become more prevalent with the rapidly expanding field of artificial intelligence and application of machine learning in health sciences.^[45]

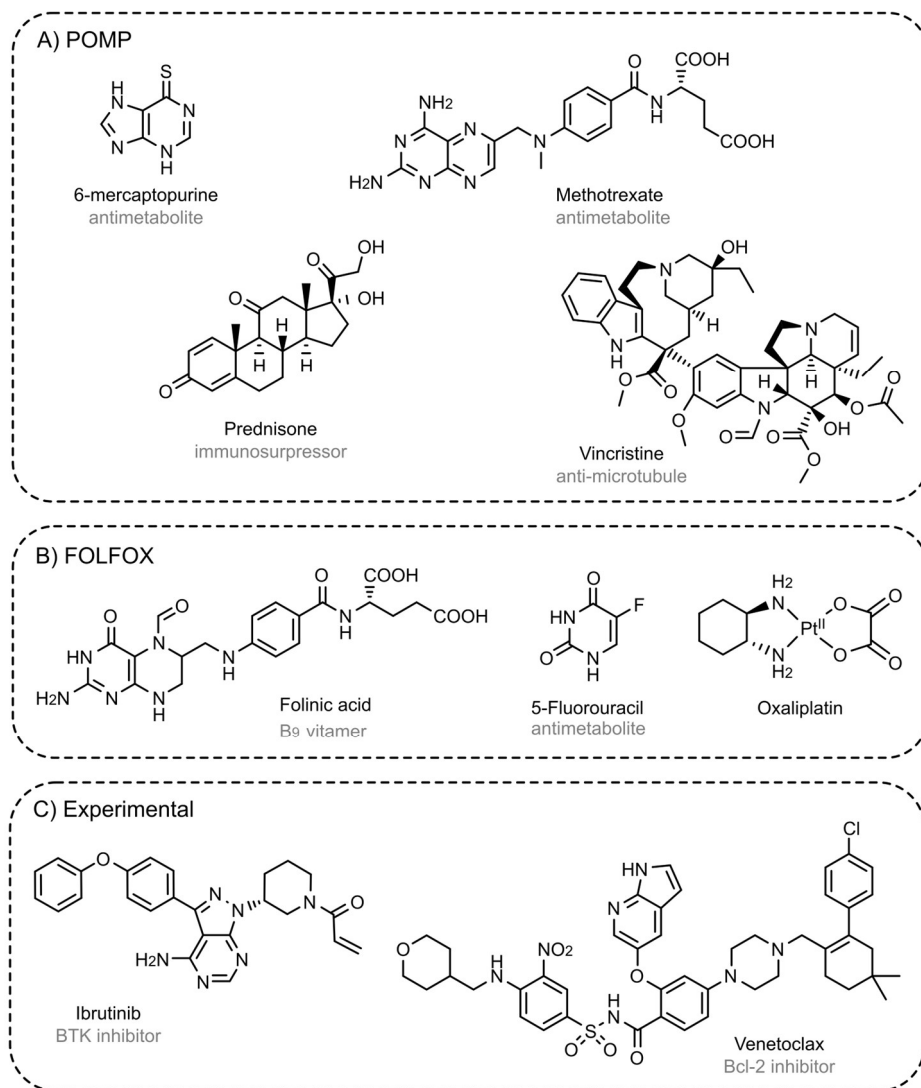


Figure 1.3 Examples of approved and experimental chemotherapy regimens for cancer treatment. A) The POMP regime was the first clinically used combination therapy for adult acute leukemia. B) The FOLFOX regime is the current first-line treatment for advanced colorectal cancer. C) Experimental combination of Ibrutinib and Venetoclax that successfully completed phase II clinical trial for the treatment of chronic lymphocytic leukemia.

1.3 Ruthenium(II)-based prodrugs for phototherapy

1.3.1 Activation by light

The activation of a prodrug with light irradiation is an excellent way to gain spatiotemporal control of the cytotoxic action of a chemical compound in the body. For cancer treatment, phototherapeutic polypyridyl-ruthenium(II) complexes can be divided into two categories: those for photodynamic therapy (PDT) and those for photoactivated chemotherapy (PACT). These two strategies have been extensively reviewed.^[16,46,47] In PDT, light-induced excitation of a photosensitizer results in formation of reactive oxygen species (ROS) including $O_2^{\bullet-}$, H_2O_2 and/or OH^{\bullet} (PDT type I), or of singlet oxygen (1O_2 , PDT type II). While the cytotoxicity of a PDT compound such as TLD-1433 arises from the oxidation of biomolecules induced by massive ROS generation,^[16] PACT operates through a different mechanism. Light activation of a PACT compound triggers a photosubstitution reaction, thus dissociating a ligand from the first coordination sphere of the metal center. This photocleavage reaction produces cytotoxicity either via the action of the released ligand, or via the action of the ruthenium-based photoproduct, or via both. The highly tunable photophysical and photochemical properties of polypyridyl-ruthenium complexes therefore offers remarkable opportunities for Ru-based PACT, which are described in more detail below.

1.3.2 Photochemistry of polypyridyl-ruthenium(II) complexes

Upon irradiation of a Ru(II)-polypyridyl complex with ultraviolet or visible light, a triplet excited state is populated through intersystem crossing from the initially generated singlet excited state (Figure 1.4). Depending on the electronical properties of the complex, these triplet excited states can have an intra-ligand (IL), intra-ligand charge transfer (ILCT) or metal-to-ligand charge transfer (MLCT) character. In PACT compounds, a metal-centered (3MC) state must be accessible to be thermally populated through internal conversion of the 3MLCT state, leading to elongation of the ruthenium–ligand bond and facilitating ligand dissociation. If the 3MLCT – 3MC energy barrier cannot be overcome thermally, other photophysical/photochemical processes may occur such as phosphorescence, electron transfer (PDT type I) or energy transfer (PDT type II). Importantly, the energies of the different excited states of Ru(II)-polypyridyl complexes are strongly dependent on the electronical features of the ligands and the geometrical constraints in the metal complex. These properties allow for exquisite tunability of the photochemistry of Ru(II)-polypyridyl complexes through modification of their molecular structure. So far, ligand photosubstitution from Ru(II)-polypyridyl complexes has been reported for a variety of ligands including pyridine, pyrazine, imidazole, nitriles, primary amine, thioether and sulfoxide (Figure 1.5).

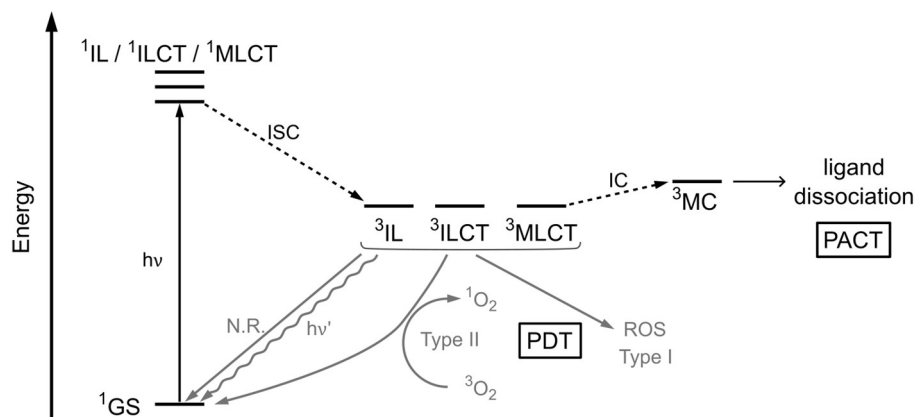


Figure 1.4 Jablonski energy diagram of the photophysical processes involved upon excitation of ruthenium(II)-polypyridyl complexes. When the complex is excited from the ground state (1GS) to the first singlet excited state, which can be of metal-to-ligand-charge-transfer (1MLCT), intra-ligand (1IL) or intra-ligand charge transfer (1ILCT) character, intersystem crossing (ISC) occurs to populate a triplet excited state (3IL , 3ILCT or 3MLCT). Relaxation from this triplet state to the 1GS can occur thermally (i.e. non-radiative decay, N.R.) or be accompanied by phosphorescent emission, electron transfer to form radical-based oxygen species (ROS; PDT type I), or energy transfer to form singlet oxygen (1O_2 ; PDT type II). However, a triplet metal-centered state (3MC) can be populated through internal conversion from the 3MLCT if the associated energy barrier can overcome thermally, which subsequently leads to ligand dissociation.

For PACT compounds, ligand dissociation should only occur upon excitation, while the Ru-ligand bond should be thermally stable in the dark. Furthermore, the photosubstitution quantum yield (ϕ_{ps}), i.e., the fraction of absorbed photons that lead to a photoreaction, is an important parameter for PACT compounds. Etchenique and coworkers reported a series of *cis*-[Ru(bpy)₂(L)(ACN)]²⁺ complexes [**1a**]²⁺ – [**1d**]²⁺, where bpy = 2,2'-bipyridine, ACN = acetonitrile, and L = ACN, triphenylphosphine (PPh₃), trimethylphosphine (PMe₃) or NH₃, and investigated their stability and ϕ_{ps} (Figure 1.5).^[48] While all complexes exhibited relatively high ϕ_{ps} between 0.34 and 0.46 upon blue light (405 nm) irradiation in aqueous solution, only the PMe₃-containing complex was shown to be thermally stable in the dark, underlining the importance of the spectator ligands in fine-tuning the properties of PACT compounds. Using this scaffold, photorelease of neurotransmitter γ -aminobutyric acid (GABA) or Janus kinase inhibitor Ruxolitinib was achieved from complex [**2a**]⁺ and [**2b**]²⁺, respectively.^[49,50] The Glazer group investigated the influence of steric and electronic effects in a series of [Ru(tpy)(NN)(Py)]²⁺ complexes on the stability of the compounds and ϕ_{ps} of pyridine (Py) photodissociation (tpy = 2,2':6',2''-terpyridine and NN = bpy [**3a**]²⁺; 6,6'-dimethyl-2,2'-bipyridine (dmbpy) [**3b**]²⁺; 2,9-dimethyl-1,10-phenanthroline (dmphen) [**3c**]²⁺; 2,2'-biquinoline(biq) [**3d**]²⁺.^[51] These results showed an increase in ϕ_{ps} upon increasing steric bulk around the metal center, unfortunately at the cost of thermal stability in aqueous solution. For [**3d**]²⁺, the increased aromatic surface of the biq ligand resulted in a

bathochromic shift of 60 nm of the $^1\text{MLCT}$ absorbance band compared to bpy-containing complex **[3a]** $^{2+}$.

Red-shifting of the activation wavelength is important for PACT compounds, due to the deeper penetration of lower-energy light in biological tissues.^[52] Furthermore, the cytotoxicity of complexes in HL-60 cells were also evaluated and indicated that biq-containing complex **[3d]** $^{2+}$ was the most toxic, both before and after photoactivation. These results underline the importance of the molecular design of PACT compounds on not only their photochemical, but also their biological properties. When the Ru(II)-complex is intended as a photocage for a photolabile and biologically active ligand, the Ru(II)-photoproduct should be biologically inert such as for compounds **[4]**, **[5]** $^{2+}$ and **[6]** $^{2+}$ shown in Figure 1.5.^[53–55] In the case of a toxic Ru(II) photoproduct, like compounds **[7]** $^{2+}$, **[8]** $^{2+}$ and **[9]** $^{2+}$, the dissociating ligand is typically a biologically inert spectator ligand (for example, dmso in **[8]** $^{2+}$).^[56–59] Combination of these two approaches may lead to synergy of the toxicity of the released ligand and that of the Ru(II)-photoproduct, resulting in a more potent PACT compound. For example, red-light photoactivation of compound **[10]** $^{2+}$ was recently shown to result in synergy between released STF31, a nicotinamide phosphoribosyl transferase (NAMPT) inhibitor, and the $[\text{Ru}(\text{tpy})(\text{biq})(\text{OH}_2)]^{2+}$ photoproduct in hypoxic glioblastoma cells (U87MG).^[60] Another approach was reported by Turro et al., who combined PDT and PACT by incorporating dimethylbenzo[*i*]dipyrido[3,2-*a*:2',3'-*c*]phenazine (Me_2dppn) in compound $[\text{Ru}(\text{tpy})(\text{Me}_2\text{dppn})(\text{L})]^{2+}$ (**[11]** $^{2+}$), where L is a pyridyl-based cytochrome P450 3A4 inhibitor.^[61] With a ϕ_{ps} of 0.024 in acetonitrile and $^1\text{O}_2$ generation quantum yield of 0.59 in methanol, the cytotoxicity (EC_{50}) of compound **[4]** upon blue light irradiation increased from $>25 \mu\text{M}$ to $2.8 \mu\text{M}$ in human prostate cancer cells (DU-145). These results indicate the potential of such dual-action compounds that can generate both PDT and PACT action in cancer cells.

While most PACT compounds reported to date contain a single photolabile ligand coordinated to a Ru(II)-based photocage, a few examples have been reported wherein two photolabile ligands are bound to a single Ru(II) complex. The photorelease of two protease inhibitors from complex **[12]** $^{2+}$ was one of the first examples reported, although it delivered two molecules of one drug.^[62] In such complexes the second photosubstitution process has a much lower quantum yield than the first one, so that the second light-induced delivery only occurs at very high light doses. Photosubstitution of symmetrical bidentate ligands such as dithioethers in complex **[7]** $^{2+}$ has been studied, indicating a two-step substitution mechanism. Alternatively, dissymmetric bidentate N,S ligands such as 2-methylthiomethylpyridine (mtmp) were also photosubstituted upon blue light irradiation from tris-heteroleptic complex **[13]** $^{2+}$, resulting in a cytotoxic bis-aqua Ru-based photoproduct.^[63] A detailed computational study on the photorelease of mtmp from **[13]** $^{2+}$ revealed the mechanism of the photoreaction, indicating the involvement of multiple excited states depending on the first released functionality, either the thioether or

pyridine.^[64] These results underline the differences in photoreactivity of different bidentate ligands and the possible high selectivity of photosubstitution reactions in tris-heteroleptic ruthenium(II) complexes.

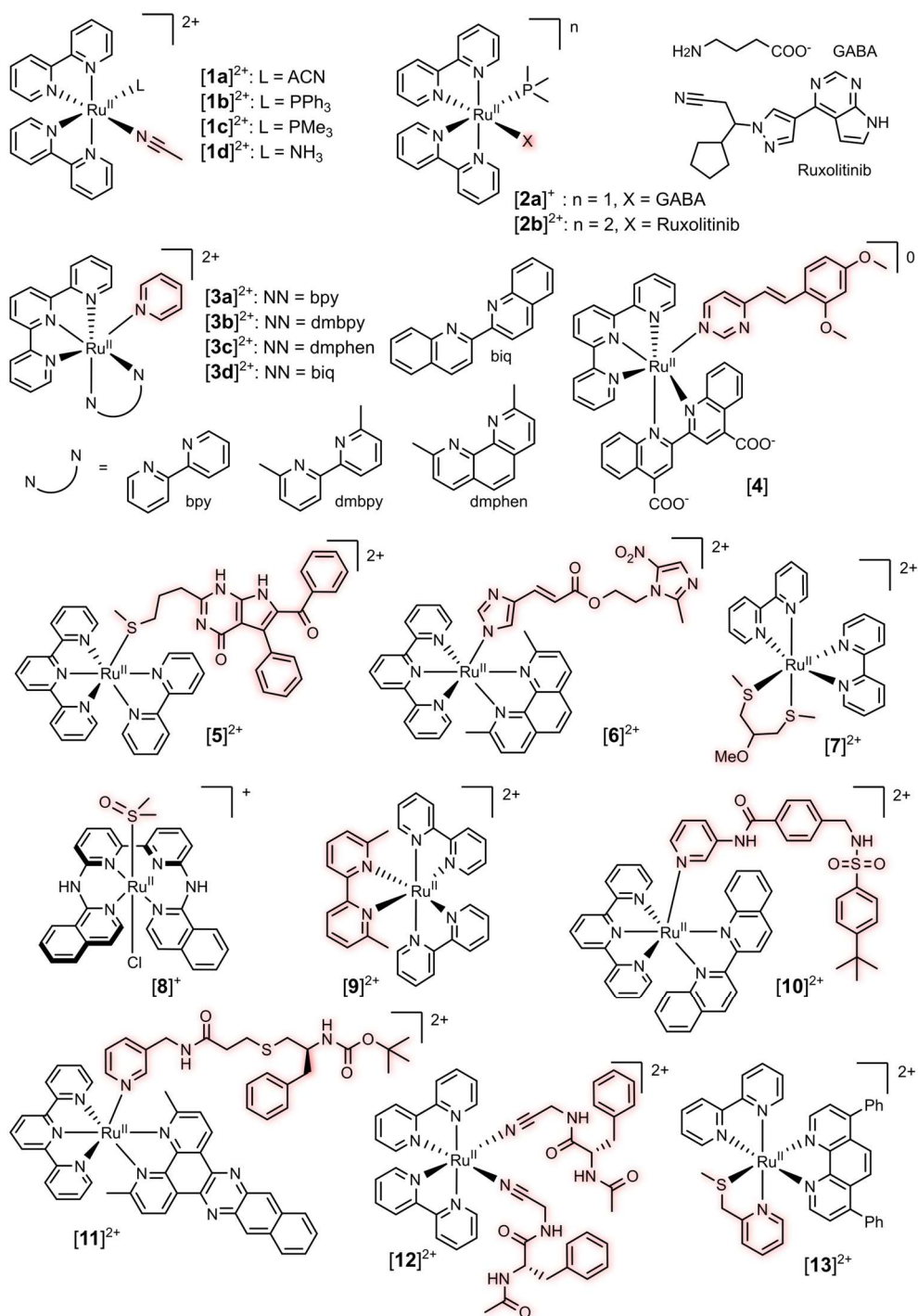


Figure 1.5 Selection of polypyridyl-ruthenium(II) based PACT compounds with the photolabile ligands highlighted in red. See text for details and references.

1.4 Coordination isomerism in metal-based chemotherapeutics

1.4.1 *Cis* versus *trans* platinum(II) complexes

While cisplatin and its derivatives are widely used in the clinic, its *trans* isomer, *trans*-[PtCl₂(NH₃)₂] (also called transplatin) is deemed clinically ineffective.^[65] From a chemical point of view, the two isomers exhibit distinct differences in reactivity towards hydrolysis of the chloride ligands (Figure 1.6). While the exchange of the first Cl⁻ ligand by H₂O from *trans*-complex occurs relatively fast compared to the *cis*-isomer, the second hydrolysis step occurs much slower due to the H₂O in *trans* position. The accepted order of the *trans* effect is Cl⁻ > NH₃ > OH⁻ > H₂O.^[66] In contrast, both chlorido ligands in the *cis*-isomer are *trans* to the amine ligands, ensuring similar exchange rates. The varying exchange rates of transplatin also leads to potential deactivation by coordination to thiol-containing moieties such as human serum albumin and glutathione, which may contribute to the reduced antitumoral activity of this complex.^[67] Furthermore, for d⁸ square-planar platinum complexes different isomers also affect DNA binding modes of the platinum complexes and therefore their cytotoxicities. While cisplatin predominantly forms 1,2-GG intra- and interstrand crosslinked adducts with DNA, transplatin crosslinks 1,3-GG intrastand and 1,1-GC interstrand.^[68] However, the slower ligand exchanges rates prevent the conversion of monofunctional to bifunctional adducts, which may account for the observed decrease in interstrand crosslinks induced by transplatin, compared with cisplatin.

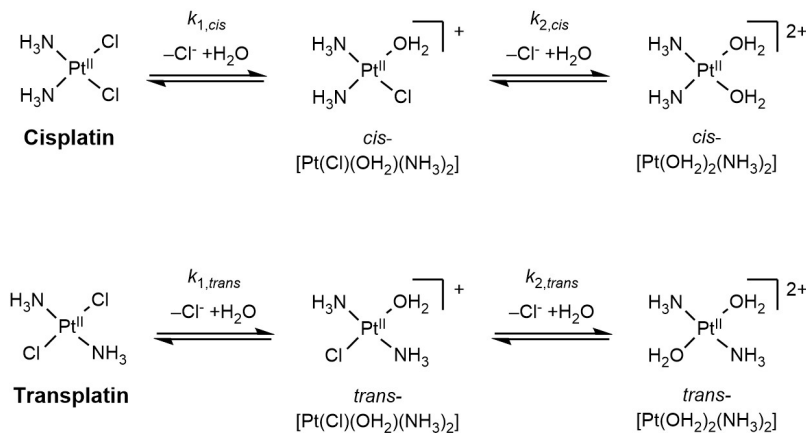


Figure 1.6 Proposed scheme for the hydrolysis of cisplatin and transplatin.

Although transplatin exhibits no clinically relevant anticancer activity, similar cytotoxicity to that of cisplatin can be achieved with *trans*-platinum(II) complexes by incorporation of various ligands to modulate numerous pharmacokinetic properties of the resulting complex, including lipophilicity, hydrolysis kinetics and mode-of-action.^[69–72] Substitution of one or both NH₃ ligands with a planar, heterocyclic amine ligand such as in compound **14** and **15** (Figure 1.7), enhances their toxicity compared to the “parent” transplatin, while they exhibit no cross resistance with cisplatin or oxaliplatin.^[69,73] However, these complexes are

poorly water soluble and suffer from high levels binding to serum proteins due to increased hydrolysis reactivity induced by the planar amine ligands. Replacing the chloride with carboxylate ligands has been shown to significantly reduce the undesirable reactivity of these compounds.^[74] Additionally, *in vitro* evaluation of complexes **16–18** suggested production of DNA-protein crosslinked adducts, a striking difference in mode-of-action compared to cisplatin which predominately yields DNA-DNA crosslinked adducts.^[75] In order to further mitigate the reactivity of the Pt(II)-complex while maintaining its toxicity, Fabra et al. reported two Pt(II) complexes containing one acetate ligand in *trans* position to either chloride (complex **19**) or acetate (complex **20**; Figure 1.7).^[76] While both complexes were shown to be sufficiently stable in DMSO or in a 1:1 (v/v) mixture of DMSO and 0.9% (w/w) NaCl aqueous solution, complex **20** was much more reactive towards *N*-acetyl-methionine, a frequently used model to investigate the role of biological S-donor molecules in Pt(II) drug-protein binding. On the other hand, complex **19** showed higher anticancer activity and selectivity against multiple human cancer cell lines. Further investigation of the cellular uptake mechanism of both complexes also suggested that **20** is taken up actively while **19** enters the cell passively. With no cross-resistance observed for cisplatin and oxaliplatin, both complexes likely induce anticancer activity through non-DNA-associated mechanisms. These studies emphasize how the geometric isomerism of a complex can lead to distinct differences in chemical and biological effects, offering ample possibilities in the development of more effective anticancer therapeutics based on transition metals.

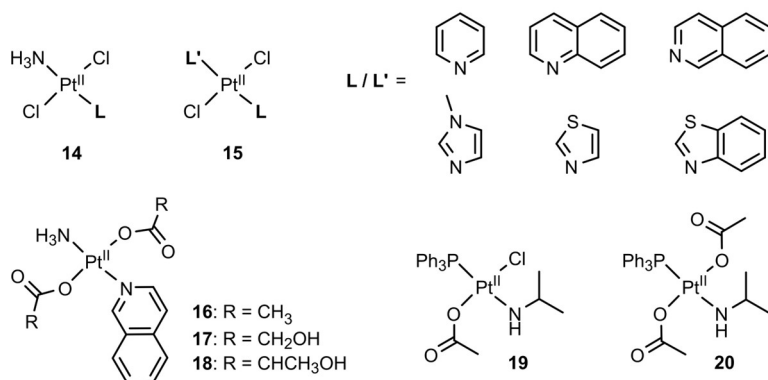


Figure 1.7 Selection of *trans*-platinum(II) complexes. See text for details and references.

1.4.2 Ruthenium(II) polypyridyl complexes

The octahedral geometry of ruthenium(II)-polypyridyl complexes provides ample opportunity for using the *trans* effect to influence the kinetics of ligand substitution processes. For example, the substitution of H₂O by acetonitrile (ACN) from [Ru(tpy)(4,4'-(X)₂-bpy)(H₂O)]²⁺, where X is H, CH₃, OCH₃, NH₂, N(CH₃)₂, has been shown to be dependent on the electron-donating character of substituent X.^[77] Because of their effect on ligand substitution kinetics, and similar to Pt(II) compounds, *trans*-Ru(II)-polypyridyl complexes

might also exhibit different cytotoxic profiles than their *cis*-isomers. For example, the Glazer group reported a study on the cytotoxicity of *cis*-[Ru(bpy)₂Cl₂] and *trans*-[Ru(qpy)Cl₂] (qpy = 2,2':6',2'':6'',2''':6''',2''''-quaterpyridine) in human leukemia (HL-60) and lung cancer (A549) cell lines.^[78] Although both ruthenium complexes could not match the toxicity of cisplatin, the *trans*-Ru(II) complexes was about 10 times more toxic than the *cis*-derivative. Interestingly, the *trans*-complex also exhibited a 49-fold increase in cellular accumulation than the *cis* analogue in these cancer cell lines. It was therefore hypothesized that the slower exchange rate of the Cl⁻ ligand in the *trans* complex prevents interaction with media or non-essential biomolecules, while facilitating its cytotoxic behavior. These results underline the importance of geometric conformation when fine-tuning the pharmacological properties of ruthenium(II)-polypyridyl complexes for anticancer therapy.

1.4.3 Photoactivated *trans*-ruthenium complexes

While *trans* effects on the reactivity of metal complexes in the ground state are well studied, reports on such effects in the excited state are quite rare. This is unfortunate, as *trans* effects could potentially be used to tune the photochemical and phototherapeutic properties of PACT compounds. The Etchenique group reported on the photo-isomerization of [Ru(bpy)₂(PMe₃)(H₂O)]²⁺ from the *cis* to *trans* isomer with 405 nm light, and the reverse reaction with 532 nm light. Distinct differences in photochemical properties were observed with different irradiation wavelengths. Firstly, the MLCT absorbance band of the *trans* isomer exhibited a bathochromic shift with a higher absorptivity than that of the *cis* isomer. In addition, conversion from the *trans* to the *cis* isomer at elevated temperature was observed in absence of light, indicating thermal instability of the former. Interestingly, green (532 nm) light irradiation of the imidazole (ImH) derivative *trans*-[Ru(bpy)₂(PMe₃)(ImH)]²⁺ resulted in photosubstitution of the ImH ligand in aqueous solution with much higher quantum yield than the *cis* isomer (0.23 and 0.10, respectively). Although these compounds were mainly investigated for their photochemical properties, these observations emphasize the importance of conformation on the photoreactivity of ruthenium complexes.

Similar to cisplatin and transplatin, therapeutic application of photoactivated ruthenium(II) complexes may be significantly influenced by their conformation. For example, from *trans*-[Ru(biqbpy)(Amet)₂]²⁺ a single κS coordinated *N*-acetyl-methionine (Amet) ligand can be readily substituted by H₂O upon green light irradiation.^[79] From the resulting mono-aqua complex [Ru(biqbpy)(Amet)(H₂O)]²⁺, however, photosubstitution of the second Amet ligand does not occur in the reported conditions. Furthermore, [Ru(biqbpy)(Amet)(H₂O)]²⁺ was also shown to be less cytotoxic than the bis-aqua complex [Ru(biqbpy)(H₂O)₂]²⁺ in several human cancer cells lines. Since minor molecular changes of the formula of a ruthenium polypyridyl complex, such as a *trans* vs. *cis* conformation can significantly influence the photochemical and biological properties of the complex, we foresee that *trans* effects in the

excited state may also take place and could potentially be utilized for improved PACT compounds.

1.5 Aim and outline of this thesis

The aim of this thesis is to advance the understanding of wavelength-dependent photosubstitution reactions in *trans*-ruthenium(II) polypyridyl complexes and to explore their application in the development of dual-targeting PACT compounds. In particular, this work focuses on photoactive ruthenium(II) complexes designed to enable the controlled release of two distinct cytotoxic agents. To address these objectives, the research is structured along two complementary lines. The first research line involves the synthetic and photochemical investigation of *trans*-Ru(II)-based photocages, together with *in vitro* studies assessing their ability to sequentially photorelease a pyridine-based nicotinamide phosphoribosyltransferase (NAMPT) inhibitor and a thioether-based microtubule polymerization inhibitor. The second research line focusses on the synthesis and evaluation of *trans*-Ru(II)-based photocages targeting heme oxygenase-1 (HO-1), either through functionalization of the tetrapyridyl ligand or via coordination of an organic imidazole-based HO-1 inhibitor to the metal center.

In Chapter 2, the development of a novel methodology is reported for mono- or di-amination of polypyridine *N*-oxides. The approach combines activation with tosyl chloride and nucleophilic substitution using potassium phthalimide, followed by hydrolysis to afford the aminated product. This work establishes access to aminopyridine building blocks that are relevant for the synthesis of coordination complexes, including the PACT compounds investigated in subsequent chapters.

In Chapter 3, a study is reported focusing on the design, synthesis and photochemical investigation of a series of *trans*-ruthenium(II) complexes based on the tetrapyridyl scaffold di([2,2'-bipyridin]-6-yl)amine HL and its *N*-methylated analogue MeL. The $[\text{Ru}(\text{HL})(\text{X})(\text{Y})]^{2+}$ and $[\text{Ru}(\text{MeL})(\text{X})(\text{Y})]^{2+}$ complexes are designed, with methyl(2-thioethanol) (MTE), ACN or pyridine coordinated to the two *trans* axial positions. The synthesis and characterization of the symmetric complexes ($X = Y$) and *trans*-dissymmetric complex ($X \neq Y$) is reported, and their photosubstitution behavior is examined under irradiation with visible light of different wavelengths. In particular, the differences in ligand photosubstitution kinetics are compared and the potential influence of *trans* effects in the excited state evaluated. These results provide a foundation for the development of the photoactive ruthenium(II)-based complexes investigated in this thesis.

Chapter 4 investigates the applicability of the *trans*-ruthenium(II) photocages developed in Chapter 3 for dual-targeting PACT. Here, a pyridine-based NAMPT inhibitor called STF31, and the thioether-based microtubule polymerization inhibitor MTI are coordinated to the tetrapyridyl-ruthenium(II) scaffold, providing two symmetric complexes and one

dissymmetric complex. The photochemical characteristics of these complexes are investigated under different irradiation conditions, and their capacity for sequential photorelease of the inhibitors is assessed. Furthermore, the phototoxicities of caged inhibitors are evaluated *in vitro* in human skin melanoma, lung adenocarcinoma and glioblastoma cancer cell lines in both normoxia (21% O₂) and hypoxia (<1% O₂). This study explores the potential dual-targeting PACT compounds based on the photorelease of multiple anticancer agents.

In Chapter 5, two synthetic approaches are explored for the development of PACT compounds designed to release a Ru(II)-based inhibitor of HO-1 upon photoactivation. The first approach focuses on the functionalization of the tetrapyrridyl ligand HL with carboxylic acid substituents using cross-coupling or pyridyl C–H functionalization methodologies. After coordination, the resulting Ru(II)-complexes are intended to mimic heme, the enzymatic substrate of HO-1, and as a result inhibit HO-1. The second approach involves the preparation of a series of *trans*-Ru(II) tetrapyrridyl complexes incorporating QC82, a known organic imidazole-based HO-1 inhibitor, leading to dissymmetric photocages bearing additional monodentate pyridyl-type ligands. The photochemical behavior of these complexes is investigated under visible light irradiation, and their capacity to generate ruthenium–aqua species is examined. Furthermore, computational docking studies and preliminary *in vitro* evaluations are employed to assess the potential of the photoactivated products as Ru(II)-based HO-1 inhibitors.

The findings of the research presented in this thesis are summarized and discussed in Chapter 6, which also contains an outlook on dual-targeting photoactivated prodrugs based on ruthenium and its implementation in modern combination therapy.

1.6 References

- (1) Maret, W. *IJMS* **2016**, *17* (1), 66.
- (2) Orvig, C.; Abrams, M. J. *Chem. Rev.* **1999**, *99* (9), 2201–2204.
- (3) Rosenberg, B.; Van Camp, L.; Krigas, T. *Nature* **1965**, *205* (4972), 698–699.
- (4) Romani, A. M. P. *Biochemical Pharmacology* **2022**, *206*, 115323.
- (5) Yimit, A.; Adebali, O.; Sancar, A.; Jiang, Y. *Nat Commun* **2019**, *10* (1), 309.
- (6) Raudenska, M.; Balvan, J.; Fojtu, M.; Gumulec, J.; Masarik, M. *Metallomics* **2019**, *11* (7), 1182–1199.
- (7) Kleih, M.; Böpplé, K.; Dong, M.; Gaißler, A.; Heine, S.; Olayioye, M. A.; Aulitzky, W. E.; Essmann, F. *Cell Death Dis* **2019**, *10* (11), 851.
- (8) Mandic, A.; Hansson, J.; Linder, S.; Shoshan, M. C. *Journal of Biological Chemistry* **2003**, *278* (11), 9100–9106.
- (9) Raudenska, M.; Kratochvilova, M.; Vicar, T.; Gumulec, J.; Balvan, J.; Polanska, H.; Pribyl, J.; Masarik, M. *Sci Rep* **2019**, *9* (1), 1660.

- (10) Shirmanova, M. V.; Druzhkova, I. N.; Lukina, M. M.; Dudenkova, V. V.; Ignatova, N. I.; Snopova, L. B.; Shcheslavskiy, V. I.; Belousov, V. V.; Zagaynova, E. V. *Sci Rep* **2017**, *7* (1), 8911.
- (11) Englinger, B.; Pirker, C.; Heffeter, P.; Terenzi, A.; Kowol, C. R.; Keppler, B. K.; Berger, W. *Chem. Rev.* **2019**, *119* (2), 1519–1624.
- (12) Gameiro, S. R.; Caballero, J. A.; Hodge, J. W. *Cancer Biotherapy and Radiopharmaceuticals* **2012**, *27* (1), 23–35.
- (13) De Biasi, A. R.; Villena-Vargas, J.; Adusumilli, P. S. *Clinical Cancer Research* **2014**, *20* (21), 5384–5391.
- (14) Gamberi, T.; Chiappetta, G.; Fiaschi, T.; Modesti, A.; Sorbi, F.; Magherini, F. *Medicinal Research Reviews* **2022**, *42* (3), 1111–1146.
- (15) Ferraro, M. G.; Piccolo, M.; Misso, G.; Santamaria, R.; Irace, C. *Pharmaceutics* **2022**, *14* (5), 954.
- (16) Monro, S.; Colón, K. L.; Yin, H.; Roque, J.; Konda, P.; Gujar, S.; Thummel, R. P.; Lilje, L.; Cameron, C. G.; McFarland, S. A. *Chem. Rev.* **2019**, *119* (2), 797–828.
- (17) Sava, G.; Pacor, S.; Mestroni, G.; Alessio, E. *Clin Exp Metast* **1992**, *10* (4).
- (18) Rademaker-Lakhai, J. M.; Van Den Bongard, D.; Pluim, D.; Beijnen, J. H.; Schellens, J. H. M. *Clinical Cancer Research* **2004**, *10* (11), 3717–3727.
- (19) Meier-Menches, S. M.; Gerner, C.; Berger, W.; Hartinger, C. G.; Keppler, B. K. *Chem. Soc. Rev.* **2018**, *47* (3), 909–928.
- (20) Hartinger, C. G.; Jakupec, M. A.; Zorbas-Seifried, S.; Groessl, M.; Egger, A.; Berger, W.; Zorbas, H.; Dyson, P. J.; Keppler, B. K. *Chemistry & Biodiversity* **2008**, *5* (10), 2140–2155.
- (21) Pluim, D.; Van Waardenburg, R. C. A. M.; Beijnen, J. H.; Schellens, J. H. M. *Cancer Chemother Pharmacol* **2004**, *54* (1), 71–78.
- (22) Aitken, J. B.; Antony, S.; Weekley, C. M.; Lai, B.; Spiccia, L.; Harris, H. H. *Metallomics* **2012**, *4* (10), 1051.
- (23) Heffeter, P.; Böck, K.; Atil, B.; Reza Hoda, M. A.; Körner, W.; Bartel, C.; Jungwirth, U.; Keppler, B. K.; Micksche, M.; Berger, W.; Koellensperger, G. *J Biol Inorg Chem* **2010**, *15* (5), 737–748.
- (24) Gifford, J. B.; Huang, W.; Zeleniak, A. E.; Hindoyan, A.; Wu, H.; Donahue, T. R.; Hill, R. *Molecular Cancer Therapeutics* **2016**, *15* (5), 1043–1052.
- (25) Leijen, S.; Burgers, S. A.; Baas, P.; Pluim, D.; Tibben, M.; Van Werkhoven, E.; Alessio, E.; Sava, G.; Beijnen, J. H.; Schellens, J. H. M. *Invest New Drugs* **2015**, *33* (1), 201–214.
- (26) Baier, D.; Mendrina, T.; Schoenhacker-Alte, B.; Pirker, C.; Mohr, T.; Rusz, M.; Regner, B.; Schaier, M.; Sgarlato, N.; Raynal, N. J. -M.; Nowikovskiy, K.; Schmidt, W. M.; Heffeter, P.; Meier-Menches, S. M.; Koellensperger, G.; Keppler, B. K.; Berger, W. *Advanced Science* **2023**, *10* (32), 2301939.
- (27) O’Kane, G. M.; Spratlin, J. L.; Oh, D.-Y.; Rha, S. Y.; Elimova, E.; Kavan, P.; Choi, M. K.; Goodwin, R. A.; Kim, S. T.; Koo, D.-H.; Halani, K.; McAllister, E. R.; Jones, M.; Snow, M.; Lemmerick, Y.; Spera, G.; Pankovich, J. *JCO* **2023**, *41*, 4098–4098.
- (28) O’Kane, G. M.; Oh, D.-Y.; Spratlin, J.; Rha, S. Y.; Elimova, E.; Kavan, P.; Goodwin, R. A.; Cha, Y.; Kim, S. T.; McAllister, E. R.; Jones, M.; Snow, M.; Lemmerick, Y.; Spera, G.; Pankovich, J. *JCO* **2024**, *42*, 4115–4115.
- (29) Jordan, M. A.; Wilson, L. *Nat Rev Cancer* **2004**, *4* (4), 253–265.
- (30) Liang, X.; Wu, Q.; Luan, S.; Yin, Z.; He, C.; Yin, L.; Zou, Y.; Yuan, Z.; Li, L.; Song, X.; He, M.; Lv, C.; Zhang, W. *European Journal of Medicinal Chemistry* **2019**, *171*, 129–168.
- (31) Fu, D.; Calvo, J. A.; Samson, L. D. *Nat Rev Cancer* **2012**, *12* (2), 104–120.

- (32) Mattioli, R.; Ilari, A.; Colotti, B.; Mosca, L.; Fazi, F.; Colotti, G. *Molecular Aspects of Medicine* **2023**, *93*, 101205.
- (33) Rottenberg, S.; Disler, C.; Perego, P. *Nat Rev Cancer* **2021**, *21* (1), 37–50.
- (34) Longley, D. B.; Harkin, D. P.; Johnston, P. G. *Nat Rev Cancer* **2003**, *3* (5), 330–338.
- (35) Rodriguez, V.; Hart, J. S.; Freireich, E. J.; Bodey, G. P.; McCredie, K. B.; Whitecar, J. P.; Coltman, C. A. *Cancer* **1973**, *32* (1), 69–75.
- (36) Samra, B.; Jabbour, E.; Ravandi, F.; Kantarjian, H.; Short, N. J. *J Hematol Oncol* **2020**, *13* (1), 70.
- (37) Gustavsson, B.; Carlsson, G.; Machover, D.; Petrelli, N.; Roth, A.; Schmoll, H.-J.; Tveit, K.-M.; Gibson, F. *Clinical Colorectal Cancer* **2015**, *14* (1), 1–10.
- (38) Nagourney, R. A.; Evans, S.; Tran, P. H.; Nagourney, A. J.; Sugarbaker, P. H. *European Journal of Surgical Oncology* **2021**, *47* (4), 738–742.
- (39) Wen, T.; Wang, J.; Shi, Y.; Qian, H.; Liu, P. *Leukemia* **2021**, *35* (2), 312–332.
- (40) Eyre, T. A.; Walter, H. S.; Iyengar, S.; Follows, G.; Cross, M.; Fox, C. P.; Hodson, A.; Coats, J.; Narat, S.; Morley, N.; Dyer, M. J. S.; Collins, G. P. *Haematologica* **2019**, *104* (2), e68–e71.
- (41) Kapoor, I.; Bodo, J.; Hill, B. T.; Hsi, E. D.; Almasan, A. *Cell Death Dis* **2020**, *11* (11), 941.
- (42) Jain, N.; Keating, M.; Thompson, P.; Ferrajoli, A.; Burger, J. A.; Borthakur, G.; Takahashi, K.; Estrov, Z.; Sasaki, K.; Fowler, N.; Kadia, T.; Konopleva, M.; Alvarado, Y.; Yilmaz, M.; DiNardo, C.; Bose, P.; Ohanian, M.; Pemmaraju, N.; Jabbour, E.; Kanagal-Shamanna, R.; Patel, K.; Wang, W.; Jorgensen, J.; Wang, S. A.; Garg, N.; Wang, X.; Wei, C.; Cruz, N.; Ayala, A.; Plunkett, W.; Kantarjian, H.; Gandhi, V.; Wierda, W. G. *JAMA Oncol* **2021**, *7* (8), 1213.
- (43) Jin, H.; Wang, L.; Bernards, R. *Nat Rev Drug Discov* **2023**, *22* (3), 213–234.
- (44) Jaaks, P.; Coker, E. A.; Vis, D. J.; Edwards, O.; Carpenter, E. F.; Leto, S. M.; Dwane, L.; Sassi, F.; Lightfoot, H.; Barthorpe, S.; Van Der Meer, D.; Yang, W.; Beck, A.; Mironenko, T.; Hall, C.; Hall, J.; Mali, I.; Richardson, L.; Tolley, C.; Morris, J.; Thomas, F.; Lleshi, E.; Aben, N.; Benes, C. H.; Bertotti, A.; Trusolino, L.; Wessels, L.; Garnett, M. J. *Nature* **2022**, *603* (7899), 166–173.
- (45) Fan, K.; Cheng, L.; Li, L. *Briefings in Bioinformatics* **2021**, *22* (6), bbab271.
- (46) Bonnet, S. *J. Am. Chem. Soc.* **2023**, *145* (43), 23397–23415.
- (47) Chen, Y.; Bai, L.; Zhang, P.; Zhao, H.; Zhou, Q. *Molecules* **2021**, *26* (18), 5679.
- (48) Rafic, E.; Slep, L. D.; Etchenique, R. *Pure and Applied Chemistry* **2023**, *95* (8), 879–889.
- (49) Filevich, O.; Etchenique, R. *Photochem Photobiol Sci* **2013**, *12* (9), 1565–1570.
- (50) Rafic, E.; Ma, C.; Shih, B. B.; Miller, H.; Yuste, R.; Palomero, T.; Etchenique, R. *J. Am. Chem. Soc.* **2024**, *146* (19), 13317–13325.
- (51) Havrylyuk, D.; Stevens, K.; Parkin, S.; Glazer, E. C. *Inorg. Chem.* **2020**, *59* (2), 1006–1013.
- (52) Fan, W.; Huang, P.; Chen, X. *Chem. Soc. Rev.* **2016**, *45* (23), 6488–6519.
- (53) Havrylyuk, D.; Hachey, A. C.; Fenton, A.; Heidary, D. K.; Glazer, E. C. *Nat. Commun.* **2022**, *13* (1), 3636.
- (54) Van Rixel, V. H. S.; Ramu, V.; Auyeung, A. B.; Beztsinna, N.; Leger, D. Y.; Lameijer, L. N.; Hilt, S. T.; Le Dévédec, S. E.; Yildiz, T.; Betancourt, T.; Gildner, M. B.; Hudnall, T. W.; Sol, V.; Liagre, B.; Kornienko, A.; Bonnet, S. *J. Am. Chem. Soc.* **2019**, *141* (46), 18444–18454.
- (55) Giacomazzo, G. E.; Conti, L.; Fagorzi, C.; Pagliai, M.; Andreini, C.; Guerri, A.; Perito, B.; Mengoni, A.; Valtancoli, B.; Giorgi, C. *Inorg. Chem.* **2023**, *62* (20), 7716–7727.
- (56) Meijer, M. S.; Bonnet, S. *Inorg. Chem.* **2019**, *58* (17), 11689–11698.
- (57) Van Rixel, V. H. S.; Moolenaar, G. F.; Siegler, M. A.; Messori, L.; Bonnet, S. *Dalton Trans.* **2018**, *47* (2), 507–516.

- (58) Azar, D. F.; Audi, H.; Farhat, S.; El-Sibai, M.; Abi-Habib, R. J.; Khnayzer, R. S. *Dalton Trans.* **2017**, 46 (35), 11529–11532.
- (59) Hakkennes, M. L. A.; Meijer, M. S.; Menzel, J. P.; Goetz, A.-C.; Van Duijn, R.; Siegler, M. A.; Buda, F.; Bonnet, S. *J. Am. Chem. Soc.* **2023**, 145 (24), 13420–13434.
- (60) Abyar, S.; Huang, L.; Husiev, Y.; Bretin, L.; Chau, B.; Ramu, V.; Wildeman, J. H.; Belfor, K.; Wijaya, L. S.; Van Der Noord, V. E.; Harms, A. C.; Siegler, M. A.; Le Dévédec, S. E.; Bonnet, S. *J. Med. Chem.* **2024**, 67 (13), 11086–11102.
- (61) Toupin, N.; Steinke, S. J.; Nadella, S.; Li, A.; Rohrabough, T. N.; Samuels, E. R.; Turro, C.; Sevrioukova, I. F.; Kodanko, J. J. *J. Am. Chem. Soc.* **2021**, 143 (24), 9191–9205.
- (62) Respondek, T.; Garner, R. N.; Herroon, M. K.; Podgorski, I.; Turro, C.; Kodanko, J. J. *J. Am. Chem. Soc.* **2011**, 133 (43), 17164–17167.
- (63) Cuello-Garibo, J.-A.; Meijer, M. S.; Bonnet, S. *Chem. Commun.* **2017**, 53 (50), 6768–6771.
- (64) Belletto, D.; Ponte, F.; Mazzone, G.; Sicilia, E. *Dalton Trans.* **2024**, 53 (19), 8243–8253.
- (65) Kishimoto, T.; Yoshikawa, Y.; Yoshikawa, K.; Komeda, S. *IJMS* **2019**, 21 (1), 34.
- (66) Appleton, T. G.; Bailey, A. J.; Barnham, K. J.; Hall, J. R. *Inorg. Chem.* **1992**, 31 (14), 3077–3082.
- (67) Pérez, J. M.; Kelland, L. R.; Montero, E. I.; Boxall, F. E.; Fuertes, M. A.; Alonso, C.; Navarro-Ranninger, C. *Mol Pharmacol* **2003**, 63 (4), 933–944.
- (68) Bernal-Méndez, E.; Boudvillain, M.; González-Vílchez, F.; Leng, M. *Biochemistry* **1997**, 36 (24), 7281–7287.
- (69) Aris, S. M.; Farrell, N. P. *Eur J Inorg Chem* **2009**, 2009 (10), 1293–1302.
- (70) Quiroga, A. G. *Journal of Inorganic Biochemistry* **2012**, 114, 106–112.
- (71) Johnstone, T. C.; Suntharalingam, K.; Lippard, S. J. *Chem. Rev.* **2016**, 116 (5), 3436–3486.
- (72) Kalinowska-Lis, U.; Ochocki, J.; Matlawska-Wasowska, K. *Coordination Chemistry Reviews* **2008**, 252 (12–14), 1328–1345.
- (73) Farrell, N.; Ha, T. T. B.; Souchard, J. P.; Wimmer, F. L.; Cros, S.; Johnson, N. P. *J. Med. Chem.* **1989**, 32 (10), 2240–2241.
- (74) Benedetti, B. T.; Quintal, S.; Farrell, N. P. *Dalton Trans.* **2011**, 40 (41), 10983.
- (75) Menon, V.; Katner, S. J.; Lee, D. E.; Peterson, E. J.; Koblinski, J. E.; Farrell, N. P. *Journal of Inorganic Biochemistry* **2024**, 252, 112475.
- (76) Fabra, D.; Mendrina, T.; Matesanz, A. I.; Medrano, Á.; Pitek, R.; Poetsch, I.; Berger, W.; Heffeter, P.; Quiroga, A. G. *Inorg. Chem. Front.* **2025**, 12, 6191-6203
- (77) Mecchia Ortiz, J. H.; Peyrot, A. M.; Fagalde, F.; Katz, N. E. *Inorganic Chemistry Communications* **2018**, 98, 44–47.
- (78) Wachter, E.; Zamora, A.; Heidary, D. K.; Ruiz, J.; Glazer, E. C. *Chem. Commun.* **2016**, 52 (66), 10121–10124.
- (79) Van Rixel, V. H. S.; Siewert, B.; Hopkins, S. L.; Askes, S. H. C.; Busemann, A.; Siegler, M. A.; Bonnet, S. *Chem. Sci.* **2016**, 7 (8), 4922–4929.

Chapter 2

Simple and efficient method for amination of polypyridine N-oxides

Abstract: Herein we report a simple synthetic route towards both known and novel aminated polypyridyl ligands. The use of tosyl chloride in combination with potassium phthalimide followed by hydrolysis allows for chemo-selective ortho-amination of (poly)pyridyl mono-N-oxides with good to excellent yield. The reactions are scalable and reproducible while using inexpensive, commercially available reagents.

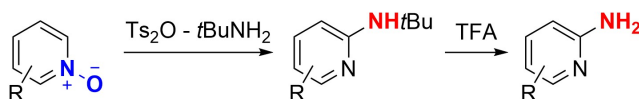
This work has been published as a full paper: W. Verbeet, Y. Husiev, S. Bonnet, *Eur. J. Org. Chem.* 2024, 27, e202400054

2.1 Introduction

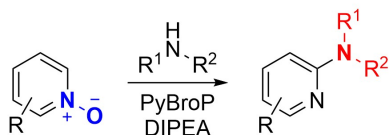
Nitrogen heterocycles form an important class of chemicals used in a wide variety of scientific disciplines such as medicinal chemistry, photochemistry, or catalysis.^[1] Polypyridyl derivatives, in particular, are in high demand as they form the core of many functional molecules. Therefore, the development of simple and efficient functionalization methods remains of high interest in chemistry. Among the wide range of preparative reactions available for the functionalization of polypyridine compounds, amination reactions are of particular interest, as amine-functionalized polypyridyl compounds have shown fascinating applications in drug discovery or catalysis. Fier *et al.* discussed the importance of 2-aminopyridines as pharmacophores and gave an excellent overview of their preparation using conventional methods such as the Chichibabin reaction.^[2] More recently, Chen and Li demonstrated the application of 2-aminopyridines in the synthesis of various imidazo[1,2-*a*]pyridines as key intermediates in the synthesis of e.g. aldehyde dehydrogenase inhibitors.^[3,4]

Although great progress has been made towards the direct C–H activation of N-heterocycles, the reported procedures are generally limited by a poor regioselectivity, a narrow functional-group tolerance, and/or the use of harsh conditions and special equipment (*e.g.*, for reactions in liquid ammonia).^[5] The challenges of selective functionalization mainly arise from the electron deficiency of N-heterocycles and their tendency to coordinate to metal ions. Conversely, pyridines and quinolines can be more easily functionalized *ortho* to the nitrogen atom of the heterocycle from their corresponding *N*-oxides, which have enhanced electrophilic character of the C2 carbon.^[6] The conversion of pyridine *N*-oxides into their 2-amino-pyridyl analogues was already reported in the 1960's by Abramovitch.^[7] As reported by Yin *et al.*, these reactions typically utilize an *N*-O activator such as acetic anhydride (Ac₂O), tosyl anhydride (Ts₂O) or tosyl chloride (TsCl), to make the *ortho*-C2 more reactive towards an amine-based nucleophile (Scheme 2.1A).^[8] However, competing side-reactions between the two reagents are relatively common, which significantly lowers preparative yields, and complicates both the product isolation and the general applicability of this method notably at multi-gram scales.^[8] One way to minimize the formation of side-products is to use phosphonium salts as activating agent, such as bromo-tris(1-pyrrolidinyl)phosphonium hexafluoridophosphate (PyBroP), which are less reactive towards nucleophilic amines (Scheme 2.1B).^[9] Despite all efforts made to improve the selective amination of pyridines, these methods are still focused on single pyridines.^[10,11] For example, the preparation of [2,2'-bipyridine]-6,6'-diamine, which is widely used in synthesis of polypyridine ligands, has only been reported using harsh reaction conditions and/or multi-step synthesis routes.^[12–14] To our knowledge, amination procedures of polypyridine *N*-oxides using mild conditions and without extensive isolation have not been reported yet (Scheme 2.1C).

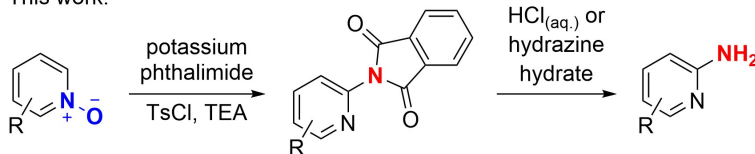
A. Yin et al. (2007)



B. Londregan, Jennings & Wei (2010)

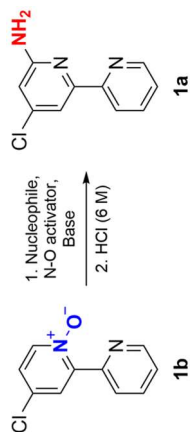


This work:

**Scheme 2.1** Current methods towards 2-aminopyridines.

2.2 Results and Discussion

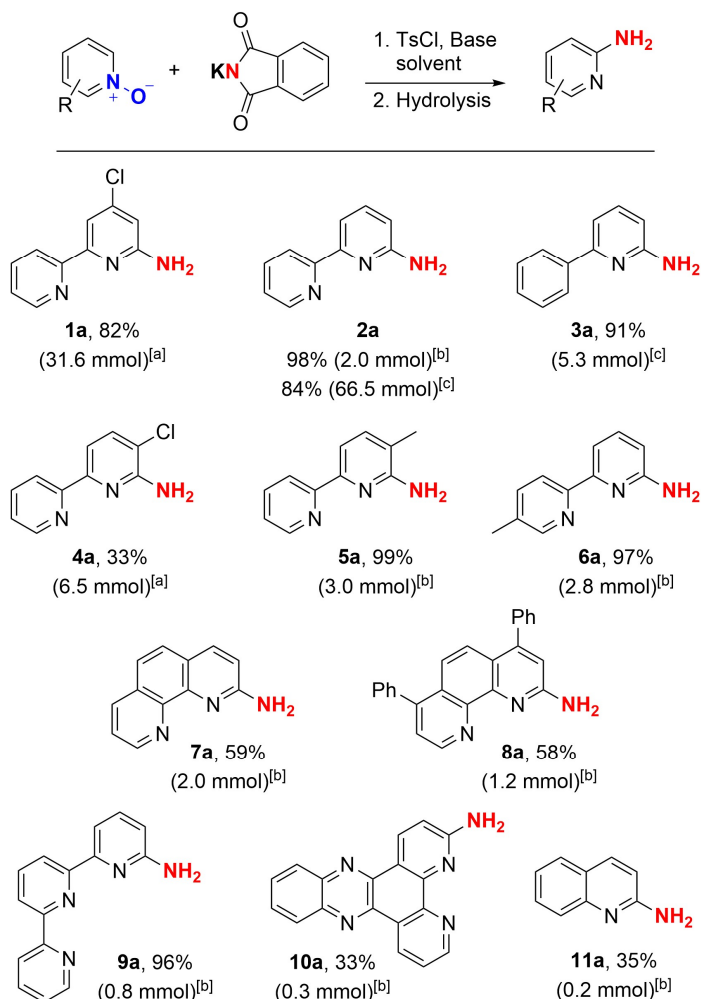
To investigate the synthesis of 4-chloro-2,2'-bipyridine-6-amine **1a** from the corresponding *N*-oxide **1b**, we screened a selection of previously reported reagents (Scheme 2.1 & Table 2.1). The procedure described by Yin was chosen as a starting point, since it reported good yields for mono-aminated products starting from 4-chloro-pyridine-1-oxide and 2,2'-bipyridine-1-oxide (between 71 and 81%) using Ts_2O and *tert*-butyl amine (NH_2tBu).^[8] Unfortunately, application of these conditions on **1b** resulted in a low yield (Table 2.1, entry 1), also when the reaction was performed at a larger scale (entry 2). This is likely related to a side reaction between Ts_2O and NH_2tBu , as we observed significant amounts of the resulting *N*-(*t*Bu)-tosylamide. The use of PyBroP as a milder activator resulted in less side-products but not in increased yields (Table 2.1 entry 3 & 4). Therefore, we investigated the use of other amine sources as nucleophiles.

Table 2.1 Screening of reaction conditions for *ortho*-amination of 4-chloro-[2,2'-bipyridine]-1-oxide.

Entry ^[a]	Nucleophile (eq.)	N-O activator (eq.)	Base (eq)	Conc. (M)	Scale ^[b] (mmol)	Yield (%) ^[c]
1	NH ₂ tBu	6.0	2.5	-	0.20	23
2	NH ₂ tBu	6.0	2.5	-	0.20	16
3	NH ₂ tBu	1.3	3.0	DIPEA	0.25	26
4	NH ₂ tBu	1.8	2.5	DIPEA	0.25	5
5	Saccharin	1.2	1.2	DIPEA	0.32	40
6	HMDS	4.0	1.2	DIPEA	0.32	18
7	PHT	1.2	1.2	DIPEA	0.32	94
8	PHT	1.2	1.2	DIPEA	0.32	82

^[a] All reactions were performed in dichloromethane (DCM) at RT. Entries 1-2 were performed in trifluorotoluene (PhCF₃). ^[b] Scale represents the amount of starting *N*-oxide. ^[c] Isolated yield. DIPEA = diisopropylethylamine.

While using bis(trimethylsilyl)amine (HMDS) (Table 2.1, entry 6) did not result in an increased yield, Gabriel-type reagents saccharin (Table 2.1, entry 5) and phthalimide (PHT; Table 2.1, entry 7) provided a major breakthrough. Although saccharin and phthalimide are chemically relatively similar, the reaction yields dramatically increased from 40% with saccharin to 94% when phthalimide was used as nucleophile. Moreover, the latter reaction conditions allowed for 80-fold upscaling (Table 2.1, entry 8) without major reduction of the yield or formation of side-products, illustrating the excellent potential of this methodology. After establishing a working procedure (Method A), we applied it to a variety of polyaryl *N*-oxides (Scheme 2.2).

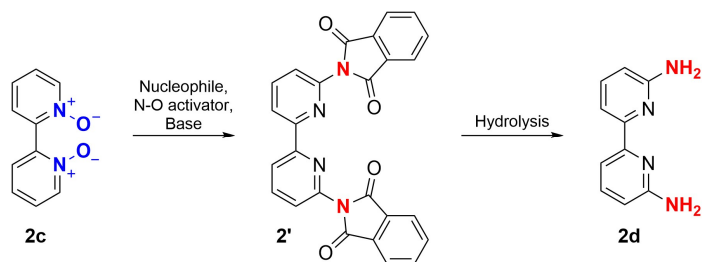


Scheme 2.2 Scope of mono-amination of polyaryl *N*-oxide. ^[a] PHT (1.2 eq), TsCl (1.2 eq) DIPEA (2.0 eq) in DCM (0.4 M) at RT for 24 h; hydrolysis with HCl (6.0 M) at 80 °C for 6 h (Method A). ^[b] KPHT (2.0 eq), TsCl (2.0 eq), TEA (2.0 eq) in DCM (0.2 M) at RT for 24 h; hydrolysis with hydrazine hydrate (5.0

eq) at 80 °C for 6 h (Method B). ^[c] KPHT (2.5 eq), TsCl (2.5 eq), TEA (2.5 eq) in ACN (0.05 M); hydrolysis with hydrazine hydrate (5.0 eq) at 80 °C for 24 h (Method C). Yields refer to the isolated product in percentage and amount in parentheses.

Interestingly, changing the position of the chloro substituent from para to meta relative to the *N*-oxide (**1a** and **4a**), resulted in a lower yield of 33%. Since complete consumption of the corresponding starting *N*-oxide towards **4a** was observed, we hypothesize that the lower yield might be due to isolation challenges. To circumvent the need of acid neutralization after hydrolysis of the phthalimide intermediate, hydrazine hydrate was used instead of hydrochloric acid. Additionally, the use of potassium phthalimide (KPHT) omits the need for deprotonation of the nucleophile, reducing the amount of base needed in the reaction (Method B). This leads to an overall higher concentration of the reaction mixture and facilitates unambiguous product isolation. With these conditions we were able to obtain various aminated products in good to excellent yields, including derivatives of methyl-2,2'-bipyridine (**5a**, **6a**), phenanthroline (**7a**, **8a**, **10a**), terpyridine (**9a**) and quinoline (**11a**). Changing the solvent to acetonitrile to ensure solubilization of the reagents when more equivalents were used (Method C), enabled the synthesis of **2a** and **3a** in excellent yield, on a notably large scale for **2a** (>11 g). For this reaction, most polar aprotic solvents could be used as long as *i*) there was no reactivity towards the reagents (e.g., DMF and DMSO did not work well), and *ii*) the solubility of the substrate and reagent were sufficient.

To further study the scope of this reaction, we decided to investigate the possibility of conducting two aminations in the same molecule. For this study 2,2'-bipyridine-1,1'-dioxide **2c** was chosen as a substrate, with the aim to synthesize the corresponding diamino product **2d** (Table 2.2). Since double amination of a substrate comes with new challenges, related to reactivity and solubility, an additional optimization study was performed (Table 2.2, Table S1).

Table 2.2 Optimization of reaction conditions towards the synthesis of [2,2'-bipyridine]-6,6'-diamine.

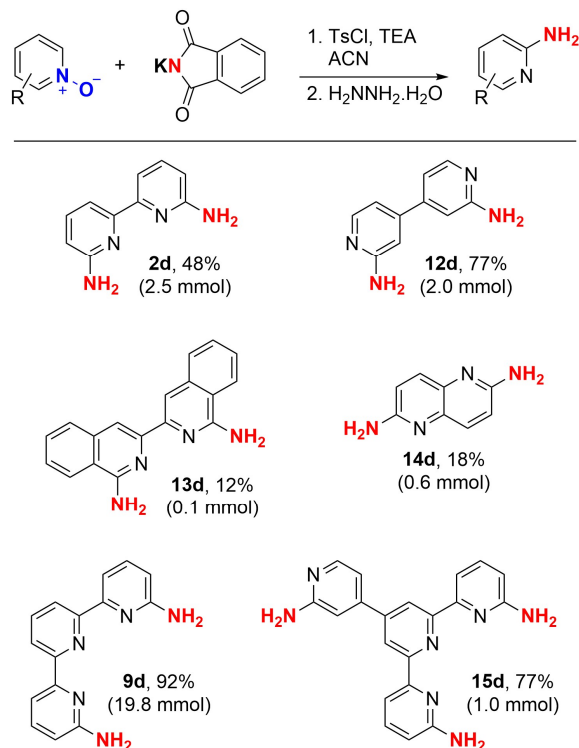
Entry ^[a]	Nucleophile (eq.)	N-O activator ^[b] (eq.)	Base (eq)	Solvent	Yield (%)
1	PHT	2.5	DIPEA	ACN	34
2	PHT	2.5	DBU	ACN	0
3	PHT	2.5	Pyridine	ACN	0
4	PHT	2.5	DIPEA	PhCN	14
5	PHT	2.5	DIPEA	Acetone	20
6	PHT	3.0	TEA	ACN	39
7	KPHT	3.0	DIPEA	ACN	40
8	PHT	3.0	DIPEA	ACN	35 ^[c]
9	KPHT	5.0	K ₂ CO ₃	ACN ^[d]	42
10	PHT	5.0	Cs ₂ CO ₃	ACN ^[d]	22
11	KPHT	5.0	TEA	ACN ^[d]	51
12	KPHT	5.0	TEA	ACN ^[d]	>99 ^[e]

^[a] All reactions were conducted in one-pot with 100 mg (0.53 mmol) of **2c** at 0.1 M in a sealed glass tubes at RT for 48 h, followed by hydrolysis with HCl (6 M) at 80 °C for 6 h. The final mixtures were analyzed using quantitative ¹H-NMR, using 1,3,5-trimethoxybenzene as internal standard.^[15] ^[b] TsCl was used as N-O activator during all reactions. ^[c] The first reaction step was performed at 50 °C. ^[d] The reaction was performed at 0.05 M. ^[e] Hydrazine hydrate (5 eq.) was used for the hydrolysis.

The main problem to be solved for the di-amination reactions is the poor solubility of di-*N*-oxides in the organic aprotic solvents that were used for the mono-amination reactions. Polar solvents like DMF and DMSO were found to be unsuitable for this transformation, due to their reactivity towards TsCl.^[16,17] Of the solvents investigated, acetonitrile seemed to be most suitable (entry 1, 4, 5). When other bases than TEA and DIPEA were used such as 1,8-diazabicyclo(5.4.0)undec-7-ene (DBU; entry 2) or pyridine (entry 3), no product formation

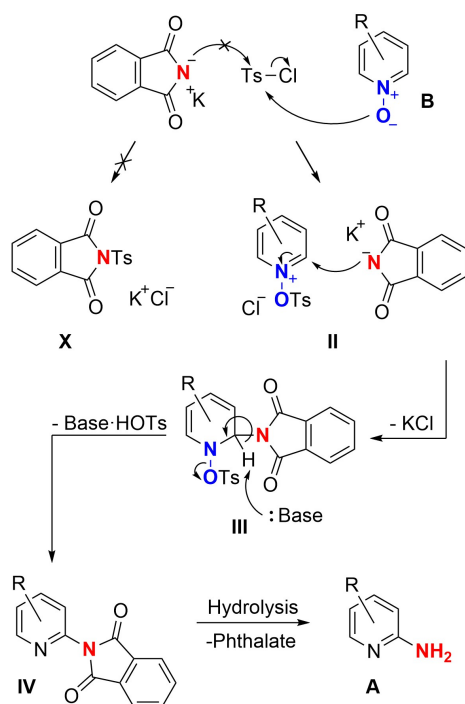
was observed. However, the use of K_2CO_3 (entry 9) or Cs_2CO_3 (entry 10) resulted in a decent yield. Performing the reaction under mild heating (50 °C) during the first step, did not lead to an increase in yield (entry 8). A significant increase of product formation was observed when a higher dilution and an excess of reagents was used (entry 1 *versus* 11). Subsequently, changing from HCl (entry 11) to hydrazine hydrate (entry 12) as hydrolysis agent increased the yield to quantitative. As we observed poor solubility of intermediate **2'** in both organic solvents and water, **2'** could be simply isolated before hydrolysis by filtration. Additionally, lowering the amount of hydrolysis reagent we managed to generate conditions in which the target product precipitated from the final reaction mixture, enabling its isolation and purification by simple filtration.

Altogether, the optimized procedure is very simple to perform and was applied on a series of polypyridyl substrates (Scheme 3). While it was optimized towards **2d**, this methodology also allowed for the preparation of its *para* isomer **12d** with a good yield. Additionally, this procedure also allowed for the synthesis of biisoquinoline **13d** and naphthyridine **14d** albeit with a lower yield. Strikingly, the reaction conditions allow for the synthesis towards terpyridine derivative **9d** with an excellent yield at a 20 mmol scale. This is particularly interesting since the synthesis of this compound has only been reported using liquid ammonia under high pressure.^[18] As demonstrated by the preparation of compound **15d**, the procedure allows for multiple amination reactions within a substrate.



Scheme 2.3 Scope of double amination of polypyridyl di-*N*-oxides. All reactions were performed at room temperature with KPHT (2.5 eq), TsCl (2.5 eq), TEA (2.5 eq) in ACN (0.05 M); hydrolysis with hydrazine hydrate (5.0 eq) at 80 °C for 24 hours (Method C). Yields refer to the isolated product in percentage and amount in parentheses.

The mechanism of the reaction is assumed to be similar to that discussed in previous reports (Scheme 2.4).^[8] In short, a nucleophilic attack of starting *N*-oxide **B** towards TsCl results in the formation of pyridinium-tosylate **II**. The *N*-tosylate withdraws electron density from the pyridine and allows for a nucleophilic substitution by a phthalate anion on the C2 position of the pyridyl ring while between the activator and the nucleophile. This advantage is due to the use of TsCl as activator and KPHT as nucleophile, which releases tosylic acid (Scheme 2.4, **III**). The formed phthalate intermediate **IV** is then hydrolyzed to produce the target amine product **A**. The phthalate intermediate **2e** (**IV**, R = 2,2'-pyridyl) towards product **2a** has been characterized. The main difference of our conditions compared to previous work is the prevention of a side-reaction taking place, as side-product **X** can only form at elevated temperatures.^[19]



Scheme 2.4 Proposed reaction mechanism.

2.3 Conclusion

In summary, we have developed an efficient and facile procedure for mono- and di-amination of (poly)pyridine *N*-oxides in an operationally simple manner with high selectivity and good to excellent yields. While the substrate examples reported here are primarily focused on the preparation of polyaminopyridyl building blocks for ligands to be used in coordination complexes, the scope might be extended to pharmaceutical compounds. Especially the possibility to prepare diaminopolypyridyl compounds with ease in a two-step procedure makes this a useful methodology. Further exploration of the substrate scope is currently ongoing. Several of the amino-bipyridines reported here have been used in other parts of this thesis, i.e. **2a** in Chapters 3, 4 and 5 while **1a**, **4a**, **5a** and **6a** have been used in Chapter 5.

2.4 Experimental

2.4.1 General

All reagents and solvents were purchased from commercial suppliers (Fluorochem, Sigma-Aldrich, BLDPharm, VWR, TCI) and used without further purification unless noted otherwise.

Anhydrous and oxygen-free solvents were obtained using common distillation, drying (activated 4 Å molecular sieves) and degassing (freeze-pump-thaw method) procedures. The reactions were carried under air at room temperature (RT) unless stated otherwise. The standard Schlenk technique was used for the reactions that were carried out under an inert atmosphere. TLCs were performed using either Supelco analytical silica gel on Al foils with fluorescence indicator 254 nm or Supelco analytical aluminium oxide 60 with fluorescence indicator 254 nm. Column chromatography was carried on silica gel (40-63 μm) or on activated neutral aluminium oxide (Brockmann Grade I) from VWR Chemicals and driven by pressurized air; the columns were packed using slurry method. NMR spectra were recorded on Bruker Avance 300, 400 or 500 MHz and the FIDs were treated with MestReNova software. The chemical shifts are given relative to the residual signal of the solvent (CDCl₃: δ (¹H) = 7.26 ppm, δ (¹³C) = 77.16 ppm; DMSO-*d*₆: δ (¹H) = 2.50 ppm; δ (¹³C) = 39.52 ppm; D₂O: δ (¹H) = 4.79 ppm), or relative to an external standard (TMS: δ (¹H) = 0 ppm, δ (¹³C) = 0 ppm).^[20] The mass spectra were recorded on Shimadzu LCMS-2020 (ESI-Q). All the *N*-oxides were prepared according to procedures modified from literature.

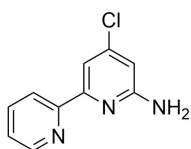
2.4.2 Amination procedures

Method A: Phthalimide (1.2 eq), DIPEA (2 eq) and the respective *N*-oxide (1 eq) were dissolved in DCM (0.4 M by *N*-oxide) and cooled to 0 °C. TsCl (1.2 eq) was added portionwise and the mixture was allowed to stir overnight at RT. Once the reaction was completed according to thin layer chromatography, the solvent was evaporated *in vacuo*. The remaining residue was redissolved in 6 M HCl and stirred at 80 °C for 6 h. The resulting solution was neutralized with a saturated aqueous solution of NaHCO₃, extracted with EtOAc or DCM and dried with MgSO₄. Activated charcoal (1 g per 2.5 mmol of N-O) was added and the mixture was refluxed for 20 min. Hot filtration and evaporation of the solvent yielded the target compound.

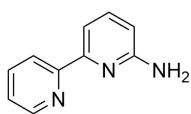
Method B: Potassium phthalimide (2 eq), TEA (2.0 eq), and the respective *N*-oxide (1 eq) were dissolved in DCM (0.2 M by *N*-oxide) and cooled to 0 °C. TsCl (2 eq) was added portionwise and the mixture was allowed to stir overnight at RT. Once the reaction was complete according to thin layer chromatography, the solvent was evaporated *in vacuo*. The remaining residue was redissolved in aq. 80% hydrazine hydrate solution (5 eq per N-O group, d = 1.02 g/ml), diluted with H₂O (0.2 M by *N*-oxide) and stirred at 80 °C for 6 h. After completion of the reaction, the mixture was extracted with CHCl₃. The combined organic phase was washed with 1 M NaOH, dried with MgSO₄ and filtered. Evaporation of the solvent yielded the target product.

Method C: Potassium phthalimide (2.5 eq per N-O group), TEA (2.5 eq per N-O group) and respective *N*-oxide (1 eq) were mixed with acetonitrile (0.05 M by *N*-oxide) in a round-bottom flask equipped with a CaCl₂ drying tube, followed by careful addition of solid TsCl

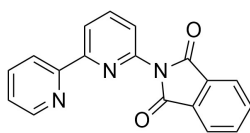
(2.5 eq per N-O group). The obtained mixture was stirred at RT for 24 h until thin layer chromatography indicated reaction completion. The resulting suspension was diluted twice with water, filtered, and the precipitate was washed with plenty of water. The obtained powder was air-dried, then mixed with aq. 80% hydrazine hydrate solution (5 eq per N-O group, $d = 1.02$ g/ml) diluted with H₂O (0.2 M by N-oxide), and the mixture was stirred at 80 °C for another 24 h. The resulting suspension was diluted twice with water, filtered, and the precipitate was washed with plenty of water. Drying *in vacuo* afforded the target product.



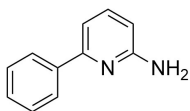
4-chloro-2,2'-bipyridin-6-amine, 1a: Method A yielded the product as an off-white powder (6.50 g, 31.6 mmol, 82%). ¹H NMR (400 MHz, CDCl₃) δ 8.65 (ddd, $J = 4.8, 1.8, 0.9$ Hz, 1H), 8.25 (dt, $J = 8.0, 1.1$ Hz, 1H), 7.81 – 7.74 (m, 2H), 7.29 (ddd, $J = 7.5, 4.8, 1.2$ Hz, 1H), 6.53 (d, $J = 1.6$ Hz, 1H), 4.60 (s, 2H). ¹³C{¹H} NMR (101 MHz, CDCl₃) δ 158.84, 156.06, 153.33, 149.29, 146.08, 136.96, 124.02, 121.30, 112.29, 108.27. ESI-MS: exact m/z calculated for [C₁₀H₈ClN₃ + H]⁺: 206.1, found: 206.2.



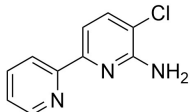
2,2'-bipyridin-6-amine, 2a: Method B (341 mg, 2.0 mmol, 98%) and Method C (11.40 g, 66.5 mmol, 84%) yielded a light-yellow powder. TLC (CHCl₃/MeOH = 8/1: product $R_f = 0.55$; UV lamp). Analysis was consistent with previous reports.^[21] ¹H NMR (500 MHz, CDCl₃) δ 8.66 (ddd, $J = 4.8, 1.8, 0.9$ Hz, 1H), 8.30 – 8.23 (m, 1H), 7.78 (td, $J = 7.8, 1.8$ Hz, 1H), 7.70 (dd, $J = 7.6, 0.9$ Hz, 1H), 7.58 (dd, $J = 8.1, 7.5$ Hz, 1H), 7.27 (ddd, $J = 7.5, 4.8, 1.2$ Hz, 1H), 6.56 (dd, $J = 8.1, 0.8$ Hz, 1H), 4.67 (s, 2H). ¹³C{¹H} NMR (126 MHz, CDCl₃) δ 158.01, 156.12, 154.27, 149.34, 138.98, 136.92, 123.58, 121.15, 111.70, 109.26. ESI-MS: exact m/z calculated for [C₁₀H₉N₃ + H]⁺: 172.1, found: 172.0.



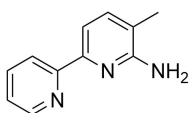
2,2'-bipyridin-6-phthalamide, 2e: Prior to the hydrolysis step in method B, the target compound by precipitation from acetonitrile and H₂O as a white powder. ¹H NMR (400 MHz, CDCl₃) δ 8.68 (ddd, $J = 4.9, 1.8, 0.9$ Hz, 1H), 8.48 (dd, $J = 7.9, 1.0$ Hz, 1H), 8.42 (dt, $J = 8.0, 1.1$ Hz, 1H), 8.06 – 7.95 (m, 3H), 7.87 – 7.75 (m, 3H), 7.46 (dd, $J = 7.9, 0.9$ Hz, 1H), 7.32 (ddd, $J = 7.5, 4.8, 1.2$ Hz, 1H). ¹³C{¹H} NMR (101 MHz, CDCl₃) δ 166.88, 156.46, 155.34, 149.28, 145.67, 139.29, 137.17, 134.72, 132.00, 124.22, 124.10, 121.84, 121.81, 120.69. ESI-MS: exact m/z calculated for [C₁₈H₁₂N₃O₂ + H]⁺: 302.1, found: 302.1.



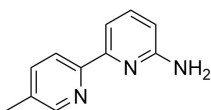
6-phenylpyridin-2-amine, 3a: Method C yielded a light-yellow powder (0.91 g, 5.3 mmol, 91%). TLC (CHCl₃/MeOH = 12/1: product *R*_f = 0.63; UV lamp). Analysis was consistent with previous reports.^[22] ¹H NMR (400 MHz, CDCl₃) δ 7.98 – 7.89 (m, 2H), 7.54 – 7.49 (m, 1H), 7.47 – 7.42 (m, 2H), 7.41 – 7.35 (m, 1H), 7.09 (dd, *J* = 7.5, 0.8 Hz, 1H), 6.48 (dd, *J* = 8.1, 0.8 Hz, 1H), 4.66 (s, 2H). ¹³C{¹H} NMR (101 MHz, CDCl₃) δ 158.15, 155.85, 139.33, 138.70, 128.79, 128.67, 126.90, 111.03, 107.34. ESI-MS: exact *m/z* calculated for [C₁₁H₁₀N₂ + H]⁺: 171.1, found: 171.0; exact *m/z* calculated for [C₁₁H₁₀N₂ + ACN + H]⁺: 212.1, found: 212.1.



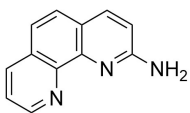
5-chloro-2,2'-bipyridin-6-amine, 4a: Method A yielded the product as an off-white powder (1.34 g, 6.5 mmol, 33%). ¹H NMR (300 MHz, CDCl₃) δ 8.65 (ddd, *J* = 4.8, 1.8, 0.9 Hz, 1H), 8.24 (dt, *J* = 8.0, 1.1 Hz, 1H), 7.77 (ddd, *J* = 8.0, 7.5, 1.8 Hz, 1H), 7.71 (d, *J* = 8.1 Hz, 1H), 7.61 (d, *J* = 8.1 Hz, 1H), 7.27 (ddd, *J* = 7.5, 4.8, 1.2 Hz, 1H), 4.94 (s, 2H). ¹³C{¹H} NMR (101 MHz, CDCl₃) δ 155.62, 154.18, 153.01, 149.25, 137.72, 136.90, 123.62, 121.03, 115.44, 112.51. ESI-MS: exact *m/z* calculated for [C₁₀H₈ClN₃ + H]⁺: 206.1, found: 206.2.



5-methyl-2,2'-bipyridin-6-amine, 5a: Method B yielded the product as a white powder (0.56 g, 3.0 mmol, 99%). ¹H NMR (400 MHz, CDCl₃) δ 8.64 (ddd, *J* = 4.8, 1.9, 0.9 Hz, 1H), 8.24 (dt, *J* = 8.0, 1.2 Hz, 1H), 7.75 (td, *J* = 7.7, 1.8 Hz, 1H), 7.67 (d, *J* = 7.5 Hz, 1H), 7.41 (d, *J* = 7.5 Hz, 1H), 7.24 (ddd, *J* = 7.5, 4.8, 1.2 Hz, 1H), 4.48 (s, 2H), 2.19 (s, 3H). ¹³C{¹H} NMR (101 MHz, CDCl₃) δ 156.74, 156.68, 152.49, 149.21, 138.77, 136.81, 123.11, 120.85, 117.29, 112.18, 17.20. ESI-MS: exact *m/z* calculated for [C₁₁H₁₁N₃ + H]⁺: 186.1, found: 186.3.

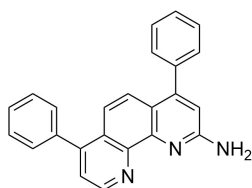


5'-methyl-2,2'-bipyridin-6-amine, 6a: Method B yielded the product as a white powder (0.51 g, 2.8 mmol, 97%). ¹H NMR (400 MHz, CDCl₃) δ 8.48 (d, *J* = 2.2 Hz, 1H), 8.14 (d, *J* = 8.0 Hz, 1H), 7.67 (dd, *J* = 7.5, 0.8 Hz, 1H), 7.60 – 7.52 (m, 2H), 6.52 (dd, *J* = 8.1, 0.9 Hz, 1H), 4.52 (s, 2H), 2.37 (s, 3H). ¹³C{¹H} NMR (101 MHz, CDCl₃) δ 158.08, 154.75, 153.90, 149.70, 138.70, 137.38, 133.09, 120.61, 111.38, 108.69, 18.44. ESI-MS: exact *m/z* calculated for [C₁₁H₁₁N₃ + H]⁺: 186.1, found: 186.3



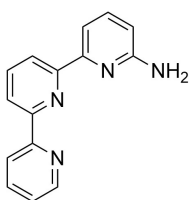
1,10-phenanthrolin-2-amine, 7a: After performing method B, isolation by column chromatography (alumina, gradient from 0 to 10% MeOH in DCM with 0.5% triethylamine) yielded the product as an off-white powder (208 mg, 1.1 mmol, 59%). Analysis was consistent with previous reports.^[23] ¹H NMR (400 MHz, CDCl₃) δ 9.09 (dd, *J* = 4.3, 1.8 Hz, 1H), 8.17 (dd, *J* = 8.1, 1.8 Hz, 1H), 7.97 (d, *J* = 8.6 Hz, 1H), 7.64 (d, *J* = 8.6 Hz, 1H), 7.56 – 7.49 (m, 2H), 6.89 (d, *J* = 8.6 Hz, 1H), 5.13 (s, 2H). ¹³C{¹H} NMR (101 MHz, CDCl₃) δ 157.89, 149.64, 145.83, 145.16, 138.20, 136.08, 129.35,

126.58, 122.90, 122.54, 122.00, 112.03. ESI-MS: exact m/z calculated for $[C_{12}H_9N_3 + H]^+$: 196.1, found: 196.2.



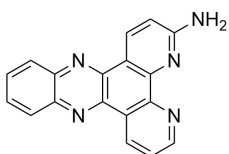
4,7-diphenyl-1,10-phenanthroline-2-amine, 8a: After performing method B, isolation by column chromatography (alumina, gradient from 0 to 10% MeOH in DCM with 0.5% triethylamine) yielded the product as a yellow powder (233 mg, 0.7 mmol, 58%).

1H NMR (400 MHz, $CDCl_3$) δ 9.14 (d, $J = 4.5$ Hz, 1H), 7.65 (d, $J = 9.3$ Hz, 1H), 7.57 (d, $J = 9.3$ Hz, 1H), 7.53 – 7.46 (m, 11H), 6.88 (s, 1H), 5.41 (s, 2H). $^{13}C\{^1H\}$ NMR (101 MHz, $CDCl_3$) δ 157.17, 150.88, 149.17, 148.44, 146.03, 145.36, 138.42, 138.24, 129.78, 129.52, 128.65, 128.54, 128.46, 127.20, 124.24, 123.15, 121.18, 119.61, 112.41. ESI-MS: exact m/z calculated for $[C_{24}H_{17}N_3 + H]^+$: 348.2, found: 348.2.



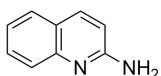
2,2':6',2''-terpyridin-6-amine, 9a: Method B yielded the product as an off-white powder (192 mg, 0.8 mmol, 96%). Analysis was consistent with previous reports.^[24]

1H NMR (400 MHz, $CDCl_3$) δ 8.69 (ddd, $J = 4.8, 1.8, 0.9$ Hz, 1H), 8.62 (dt, $J = 8.0, 1.1$ Hz, 1H), 8.41 (dd, $J = 7.8, 1.1$ Hz, 1H), 8.35 (dd, $J = 7.9, 1.1$ Hz, 1H), 7.98 (dd, $J = 7.5, 0.8$ Hz, 1H), 7.92 (t, $J = 7.8$ Hz, 1H), 7.85 (td, $J = 7.7, 1.8$ Hz, 1H), 7.61 (t, $J = 7.8$ Hz, 1H), 7.32 (ddd, $J = 7.5, 4.8, 1.2$ Hz, 1H), 6.57 (dd, $J = 8.1, 0.8$ Hz, 1H), 4.51 (s, 2H). $^{13}C\{^1H\}$ NMR (101 MHz, $CDCl_3$) δ 158.08, 156.52, 155.74, 155.34, 154.84, 149.21, 138.68, 137.85, 136.97, 123.81, 121.36, 120.96, 120.75, 111.83, 109.05. ESI-MS: exact m/z calculated for $[C_{15}H_{12}N_4 + H]^+$: 249.1, found: 249.2



dipyrido[3,2-a:2',3'-c]phenazin-3-amine, 10a: Method B yielded the product as a brown powder (93 mg, 0.3 mmol, 93%). 1H NMR (400 MHz, $CDCl_3$) δ 9.63 (dd, $J = 8.1, 1.8$ Hz, 1H), 9.33 (d, $J = 8.7$ Hz, 1H), 9.23 (dd, $J = 4.5, 1.9$ Hz, 1H), 8.32 – 8.25 (m, 2H), 7.90 – 7.81 (m, 2H), 7.74 (dd, $J = 8.1, 4.5$ Hz, 1H), 6.99 (d, $J = 8.7$ Hz, 1H), 5.29

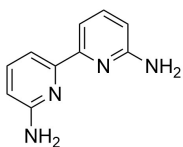
(s, 2H). $^{13}C\{^1H\}$ NMR (101 MHz, $CDCl_3$) δ 160.02, 152.34, 148.40, 148.27, 142.77, 141.86, 141.71, 140.24, 135.86, 133.95, 130.47, 129.65, 129.58, 129.31, 127.89, 123.76, 119.98, 111.56. ESI-MS: exact m/z calculated for $[C_{18}H_{11}N_5 + H]^+$: 298.1, found: 298.1.



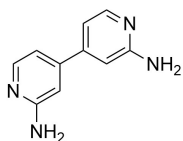
Quinoline-2-amine, 11a: Method B yielded an off-white powder (34 mg, 0.24 mmol, 35%). Analysis was consistent with previous reports.^[25]

1H NMR (400 MHz, $CDCl_3$) δ 7.89 (dd, $J = 8.8, 0.8$ Hz, 1H), 7.67 (dq, $J = 8.4, 0.9$ Hz, 1H), 7.63 (dd, $J = 7.9, 1.5$ Hz, 1H), 7.56 (ddd, $J = 8.4, 6.9, 1.5$ Hz, 1H), 7.27 (ddd, $J = 8.0, 6.9, 1.2$ Hz, 1H), 6.73 (d, $J = 8.8$ Hz, 1H), 4.94 (s, 2H). $^{13}C\{^1H\}$ NMR (101 MHz, $CDCl_3$) δ 156.93,

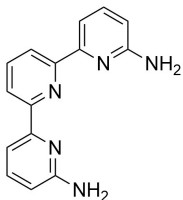
147.31, 138.46, 130.07, 127.67, 125.81, 123.66, 122.97, 111.85. ESI-MS: exact m/z calculated for $[C_9H_8N_2 + H]^+$: 145.1, found: 145.2.



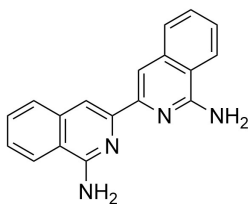
2,2'-bipyridine-6,6'-diamine, 2d: Method C yielded a light-yellow crystals (0.47 g, 2.5 mmol, 48%). Analysis was consistent with previous reports.^[26] TLC ($CHCl_3/MeOH = 8/1$: product $R_f = 0.63$; UV lamp). 1H NMR (500 MHz, $DMSO-d_6$) δ 7.48 – 7.38 (m, 4H), 6.43 (dd, $J = 7.8, 1.3$ Hz, 2H), 5.88 (s, 4H). $^{13}C\{^1H\}$ NMR (101 MHz, $DMSO-d_6$) δ 159.04, 154.11, 137.58, 108.67, 108.11. ESI-MS: exact m/z calculated for $[C_{10}H_{10}N_4 + H]^+$: 187.1, found: 187.2.



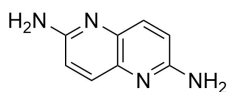
4,4'-bipyridine-2,2'-diamine, 12d: Method C yielded a light-beige powder (0.38 g, 2.0 mmol, 77%). Analysis was consistent with previous reports.^[27] 1H NMR (500 MHz, $DMSO-d_6$) δ 7.97 (dd, $J = 5.3, 0.7$ Hz, 2H), 6.68 (dd, $J = 5.3, 1.6$ Hz, 2H), 6.64 (dd, $J = 1.7, 0.8$ Hz, 2H), 6.05 (s, 4H). $^{13}C\{^1H\}$ NMR (75 MHz, $DMSO-d_6$) δ 160.50, 148.68, 146.71, 109.50, 104.80. ESI-MS: exact m/z calculated for $[C_{10}H_{10}N_4 + ACN + H]^+$: 228.1, found: 228.1.



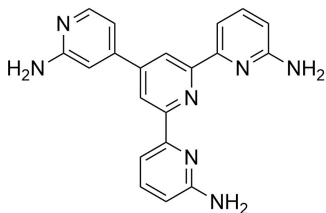
2,2':6',2''-terpyridine-6,6''-diamine, 9d: Method C yielded a white powder (5.21 g, 19.8 mmol, 92%). TLC ($CHCl_3/MeOH = 2/1$: product $R_f = 0.75$; UV lamp). 1H NMR (300 MHz, $DMSO-d_6$) δ 8.23 (d, $J = 7.8$ Hz, 2H), 7.97 (t, $J = 7.8$ Hz, 1H), 7.72 (dd, $J = 7.4, 0.9$ Hz, 2H), 7.55 (t, $J = 7.8$ Hz, 2H), 6.53 (dd, $J = 8.1, 0.9$ Hz, 2H), 6.05 (s, 4H). $^{13}C\{^1H\}$ NMR (75 MHz, $DMSO-d_6$) δ 159.34, 155.23, 153.48, 137.96, 137.59, 119.66, 108.89, 108.79. ESI-MS: exact m/z calculated for $[C_{15}H_{13}N_5 + H]^+$: 264.1, found: 264.2; exact m/z calculated for $[2C_{15}H_{13}N_5 + Na]^+$: 549.2, found: 549.2.



[3,3'-bis-isoquinoline]-1,1'-diamine, 13d: Method C with isolation by column chromatography (silica, gradient from 10% to 50% MeOH in $CHCl_3$ with 0.2% TEA) yielded a yellow powder (0.04 g, 0.14 mmol, 12%). TLC ($CHCl_3/MeOH = 8/1$: product $R_f = 0.10$; UV lamp). 1H NMR (500 MHz, $DMSO-d_6$) δ 8.73 – 8.17 (m, 6H), 8.02 (d, $J = 5.5$ Hz, 2H), 7.98 – 7.81 (m, 4H), 7.79 – 7.61 (m, 2H). ^{13}C NMR (126 MHz, $DMSO-d_6$) δ 155.87, 137.34, 132.97, 127.84, 125.07, 117.52, 107.38. ESI-MS: exact m/z calculated for $[C_{18}H_{14}N_4 + H]^+$: 287.1; found: 287.2.

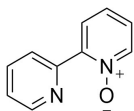


1,5-naphthyridine-2,6-diamine, 14d: Method C yielded a brown powder (0.09 g, 0.6 mmol, 18%). TLC (CHCl₃/MeOH = 1/1: product R_f = 0.68; UV lamp). ¹H NMR (300 MHz, DMSO-*d*₆) δ 7.52 (d, J = 8.9 Hz, 2H), 6.79 (d, J = 8.9 Hz, 2H), 6.06 (s, 4H). ¹³C{¹H} NMR (75 MHz, DMSO-*d*₆) δ 155.35, 137.66, 134.74, 114.42. ESI-MS: exact m/z calculated for [C₈H₈N₄ + H]⁺: 161.1, found: 161.1.

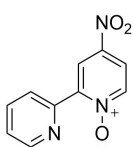


4'-(2-aminopyridin-4-yl)-[2,2':6',2''-terpyridine]-6,6''-diamine, 15d: Method C yielded a yellow powder (0.36 g, 1.01 mmol, 77%). ¹H NMR (400 MHz, DMSO-*d*₆) δ 8.46 (s, 2H), 8.09 (d, J = 5.3 Hz, 1H), 7.77 (dd, J = 7.4, 0.9 Hz, 2H), 7.63 – 7.54 (m, 2H), 6.93 – 6.77 (m, 2H), 6.56 (dd, J = 8.2, 0.8 Hz, 2H), 6.21 (s, 2H), 6.13 (s, 4H). ¹³C NMR (101 MHz, DMSO-*d*₆) δ 160.64, 159.45, 156.22, 153.10, 149.04, 147.68, 146.57, 138.05, 116.95, 109.68, 109.16, 109.12, 105.20. ESI-MS: exact m/z calculated for [C₂₀H₁₇N₇+H]⁺: 356.2; found: 356.2.

2.4.3 Precursor synthesis

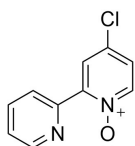


2,2'-bipyridine-1-oxide, 2b: A solution of 2,2'-bipyridine (10.00 g, 63.4 mmol, 1 eq) in TFA (43 ml) was stirred at 0 °C for 10 min. Then the aqueous H₂O₂ (6.0 ml, 35%, d = 1.13 g/ml, 69.7 mmol, 1.1 eq) was added dropwise to the mixture over 15 min at 0 °C followed by stirring at RT for 24 h. After reaction completion, TFA was distilled out under vacuum and the remaining crude was poured in ice and neutralized with 6 M NaOH. The resulting solution was extracted with CHCl₃ (4 x 50 mL), the combined organic phases were dried over Na₂SO₄ and concentrated *in vacuo* to afford final product as white powder (10.73 g, 62.3 mmol, 98%). TLC (Hexane/EtOAc = 4/1: starting material R_f = 0.35, product R_f = 0.08; CHCl₃/MeOH = 4/1: product R_f = 0.65; UV lamp). Analysis was consistent with previous reports.^[28,29] ¹H NMR (500 MHz, CDCl₃) δ 8.89 (dt, J = 8.0, 1.1 Hz, 1H), 8.72 (ddd, J = 4.9, 1.9, 1.0 Hz, 1H), 8.31 (dd, J = 6.6, 1.3 Hz, 1H), 8.17 (dd, J = 8.1, 2.2 Hz, 1H), 7.83 (td, J = 7.8, 1.8 Hz, 1H), 7.40 – 7.31 (m, 2H), 7.26 (td, J = 7.0, 2.2 Hz, 1H). ¹³C{¹H} NMR (126 MHz, CDCl₃) δ 149.68, 149.44, 147.40, 140.82, 136.47, 128.04, 125.91, 125.68, 125.40, 124.43. ESI-MS: exact m/z calculated for [C₁₀H₈N₂O – e]⁺: 172.1, found: 172.1

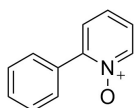


4-nitro-2,2'-bipyridine-1-oxide, 1c: A mixture of 2,2'-bipyridine 1-oxide **2b** (34.40 g, 0.2 mol, 1 eq) and KNO₃ (152.00 g, 1.5 mol, 7.5 eq) in concentrated H₂SO₄ (267 ml) was stirred at 80 °C. After 45 h, the mixture was allowed to cool to RT, poured onto ice and neutralized with 6 M NaOH to pH = 9. The formed precipitate was collected by filtration, washed with cold water and dried *in vacuo*. The resulting crude was redissolved in DCM, filtered and concentrated *in vacuo*. Recrystallization from DCM/hexane (2/1) at -20 °C overnight yielded the product as a yellow crystalline solid (11.10 g, 51.1 mmol, 26%). Analysis was consistent with previous

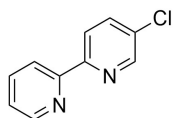
reports.^[30,31] ^1H NMR (500 MHz, $\text{DMSO-}d_6$) δ 8.89 (dd, $J = 3.4, 0.5$ Hz, 1H), 8.82 (ddd, $J = 4.7, 1.8, 1.0$ Hz, 1H), 8.77 (dt, $J = 8.1, 1.1$ Hz, 1H), 8.58 (dd, $J = 7.2, 0.5$ Hz, 1H), 8.23 (dd, $J = 7.2, 3.4$ Hz, 1H), 8.02 (ddd, $J = 8.1, 7.6, 1.8$ Hz, 1H), 7.58 (ddd, $J = 7.6, 4.7, 1.1$ Hz, 1H). $^{13}\text{C}\{^1\text{H}\}$ NMR (126 MHz, $\text{DMSO-}d_6$) δ 149.85, 147.52, 146.84, 142.44, 142.19, 136.93, 125.48, 124.65, 121.60, 119.86. ESI-MS: exact m/z calculated for $[\text{C}_{10}\text{H}_7\text{N}_3\text{O}_3 + \text{H}]^+$: 218.1, found: 218.2.



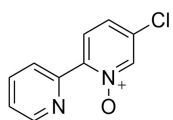
4-chloro-2,2'-bipyridine-1-oxide, 1b: Acetyl chloride (54.2 ml, $d = 1.10$ g/ml, 0.8 mol, 15 eq) was dropwise added to solid 4-nitro-2,2'-bipyridine-1-oxide **1c** (11.00 g, 50.6 mmol, 1 eq) and stirred at 50 °C. After 1 h, excess acetyl chloride was removed under vacuum. To the residue ice water (100 ml) was added and the mixture was neutralized with aqueous saturated Na_2CO_3 solution. The resulting mixture was extracted with CHCl_3 (5 x 100 ml) and the combined organic phase was dried over MgSO_4 . After filtration and evaporation of the solvent, the crude was recrystallized from acetone yielding the product as a faint yellow solid (10.32 g, 49.9 mmol, 99%). Analysis was consistent with previous reports.^[31,32] ^1H NMR (300 MHz, CDCl_3) δ 8.96 (dt, $J = 8.1, 1.1$ Hz, 1H), 8.72 (ddd, $J = 4.8, 1.9, 1.0$ Hz, 1H), 8.27 – 8.17 (m, 2H), 7.83 (ddd, $J = 8.1, 7.5, 1.8$ Hz, 1H), 7.37 (ddd, $J = 7.6, 4.8, 1.2$ Hz, 1H), 7.23 (dd, $J = 7.0, 3.1$ Hz, 1H). $^{13}\text{C}\{^1\text{H}\}$ NMR (101 MHz, CDCl_3) δ 149.56, 148.53, 147.92, 141.55, 136.59, 132.02, 127.78, 125.60, 125.49, 124.91. ESI-MS: exact m/z calculated for $[\text{C}_{10}\text{H}_7\text{ClN}_2\text{O} + \text{H}]^+$: 207.0, found: 207.4.



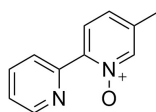
2-phenylpyridine-1-oxide, 3b: *m*-CPBA (11.83 g (77%), 52.8 mmol, 1.4 eq) was added as a solid to a solution of 2-phenylpyridine (5.5 ml, $d = 1.09$ g/ml, 37.7 mmol, 1 eq) in DCM (189 ml) and the resulting mixture was stirred for 24 h at RT. Upon reaction completion the organic phase was washed with 1 M NaOH (3 x 50 ml), dried over Na_2SO_4 and concentrated *in vacuo* to afford final product as white powder (5.87 g, 34.3 mmol, 91%). TLC (Hexane/EtOAc = 4/1: starting material $R_f = 0.66$, product $R_f = 0$; $\text{CHCl}_3/\text{MeOH} = 8/1$: product $R_f = 0.64$; UV lamp). Analysis was consistent with previous report.^[33] ^1H NMR (500 MHz, CDCl_3) δ 8.38 (ddd, $J = 6.5, 1.3, 0.6$ Hz, 1H), 7.85 – 7.77 (m, 2H), 7.53 – 7.41 (m, 4H), 7.34 (td, $J = 7.7, 1.3$ Hz, 1H), 7.25 (ddd, $J = 7.5, 6.5, 2.1$ Hz, 1H). $^{13}\text{C}\{^1\text{H}\}$ NMR (126 MHz, CDCl_3) δ 149.58, 140.72, 132.57, 129.87, 129.45, 128.48, 127.64, 126.46, 124.71. ESI-MS: exact m/z calculated for $[\text{C}_{11}\text{H}_9\text{NO} + \text{H}]^+$: 172.1, found: 172.0.



5-chloro-2,2'-bipyridine, 4c: 2-tributylstannylpyridine (8.1 ml, $d = 1.14$ g/ml, 25.0 mmol, 1 eq) was added to a solution of 2-bromo-5-chloropyridine (5.29 g, 27.5 mmol, 1.1 eq) in anhydrous toluene (83 ml) and degassed by bubbling N_2 through the mixture. After 1 h, $Pd(PPh_3)_4$ (2.89 g, 2.50 mmol, 0.1 eq) was added and the reaction mixture was refluxed for 3 days under N_2 atmosphere. The reaction mixture was cooled to RT, filtered to remove any solids and concentrated *in vacuo*. Aqueous 1 M HCl (100 ml) was added to the residue, which was washed with DCM (100 ml) and neutralized with solid $NaHCO_3$. The product was extracted from the aqueous phase with DCM (3 x 100 ml). The combined organic phase was dried over $MgSO_4$, filtered and concentrated under vacuum. Purification of the crude by column chromatography on alumina (petroleum ether/EtOAc = 98/2) provided the product as an off-white solid (3.98 g, 21.0 mmol, 83 %). TLC (alumina, petroleum ether/EtOAc = 98/2: product $R_f = 0.51$; UV lamp). Analysis was consistent with previous reports.^[34,35] 1H NMR (300 MHz, $CDCl_3$) δ 8.68 – 8.63 (m, 1H), 8.61 (dd, $J = 2.5, 0.7$ Hz, 1H), 8.39 – 8.36 (m, 1H), 8.36 – 8.33 (m, 1H), 7.84 – 7.75 (m, 2H), 7.30 (ddd, $J = 7.4, 4.8, 1.2$ Hz, 1H). $^{13}C\{^1H\}$ NMR (75 MHz, $CDCl_3$) δ 155.25, 154.44, 149.35, 148.13, 137.11, 136.74, 132.37, 124.05, 121.96, 121.13. ESI-MS: exact m/z calculated for $[C_{10}H_7ClN_2 + H]^+$: 191.0, found: 191.2.

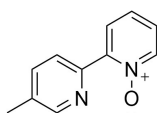


5-chloro-2,2'-bipyridine-1-oxide, 4b: A solution of 5-chloro-2,2'-bipyridine **4c** (3.80 g, 19.9 mmol, 1 eq) in TFA (15 ml) was cooled to $0^\circ C$ and hydrogen peroxide (35 % aq., 2.6 ml, $d = 1.11$ g/ml, 30 mmol, 1.5 eq) was added dropwise. After the addition, the reaction mixture was allowed to stir overnight at RT. Excess TFA was removed by vacuum distillation and the remaining residue was poured onto ice. The mixture was neutralized with 6 M NaOH (aq.) and extracted with $CHCl_3$ (6 x 50 ml). The combined organic phase was dried with $MgSO_4$ and filtered. Evaporation of the solvent yield the product as a white crystalline solid (3.90 g, 18.9 mmol, 95%). 1H NMR (300 MHz, $CDCl_3$) δ 8.88 (dt, $J = 8.1, 1.1$ Hz, 1H), 8.71 (ddd, $J = 4.8, 1.8, 0.9$ Hz, 1H), 8.35 (dd, $J = 2.0, 0.5$ Hz, 1H), 8.19 (d, $J = 8.8$ Hz, 1H), 7.83 (ddd, $J = 8.1, 7.5, 1.8$ Hz, 1H), 7.39 – 7.31 (m, 2H). $^{13}C\{^1H\}$ NMR (101 MHz, $CDCl_3$) δ 149.57, 148.82, 146.13, 139.86, 136.54, 132.60, 127.87, 126.87, 125.45, 124.65. ESI-MS: exact m/z calculated for $[C_{10}H_7ClN_2O + H]^+$: 207.0, found: 207.2.



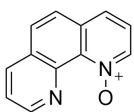
5-methyl-2,2'-bipyridine-1-oxide, 5b: A solution of 5-methyl-2,2'-bipyridine (1.70 g, 10 mmol, 1 eq) in TFA (7.7 ml) was cooled to $0^\circ C$ and H_2O_2 (35 % aq., 1.3 ml; $d = 1.11$ g/ml, 15 mmol, 1.5 eq) was added dropwise. After the addition, the reaction mixture was allowed to stir overnight at RT. Excess TFA was removed by vacuum distillation and the remaining residue was poured onto ice. The mixture was neutralized with 6 M NaOH (aq.) and extracted with $CHCl_3$ (6 x 50 ml). The combined organic phase was dried with $MgSO_4$, filtered and concentrated *in vacuo*. Isolation by column chromatography (silica, acetone/hexane = 2/5 with 0.5 % of

triethylamine) yielded the product as an off-white crystalline solid (0.64 g, 3.4 mmol, 34%). TLC (Silica; acetone/hexane = 2/5: product R_f = 0.5; UV lamp). Analysis was consistent with previous reports.^[31] ^1H NMR (400 MHz, CDCl_3) δ 8.85 (dt, J = 8.1, 1.1 Hz, 1H), 8.66 (ddd, J = 4.8, 1.9, 0.9 Hz, 1H), 8.13 (dt, J = 1.7, 0.8 Hz, 1H), 8.03 (d, J = 8.2 Hz, 1H), 7.80 – 7.73 (m, 1H), 7.30 – 7.26 (m, 1H), 7.14 (ddd, J = 8.3, 1.8, 0.9 Hz, 1H), 2.30 (t, J = 0.8 Hz, 3H). $^{13}\text{C}\{^1\text{H}\}$ NMR (101 MHz, CDCl_3) δ 149.80, 149.32, 144.67, 140.40, 136.26, 136.08, 127.30, 127.22, 125.41, 124.04, 18.12. ESI-MS: exact m/z calculated for $[\text{C}_{11}\text{H}_{10}\text{N}_2\text{O} + \text{H}]^+$: 187.1, found: 186.9.



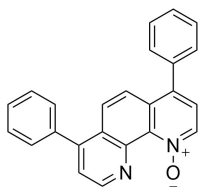
5'-methyl-2,2'-bipyridine-1-oxide, 6b: A solution of 5-methyl-2,2'-bipyridine (1.70 g, 10 mmol, 1 eq) in TFA (7.7 ml) was cooled to 0 °C and H_2O_2 (35 % aq., 1.3 ml, d = 1.11 g/ml, 15 mmol, 1.5 eq) was added dropwise. After the addition, the reaction mixture was allowed to stir overnight at

RT. Excess TFA was removed by vacuum distillation and the remaining residue was poured onto ice. The mixture was neutralized with 6 M NaOH (aq.) and extracted with CHCl_3 (6 x 50 ml). The combined organic phase was dried with MgSO_4 , filtered and concentrated *in vacuo*. Isolation by column chromatography (silica, acetone/hexane = 2/5 with 0.5 % of triethylamine) yielded the product as an off-white crystalline solid (0.55 g, 3.0 mmol, 30%). TLC (Silica; acetone/hexane = 2/5: product R_f = 0.45; UV lamp). Analysis was consistent with previous reports.^[31] ^1H NMR (400 MHz, CDCl_3) δ 8.77 (dd, J = 8.2, 0.8 Hz, 1H), 8.51 (dt, J = 2.3, 0.8 Hz, 1H), 8.26 (dd, J = 6.5, 1.4 Hz, 1H), 8.13 (dd, J = 8.1, 2.1 Hz, 1H), 7.60 (ddd, J = 8.2, 2.3, 0.8 Hz, 1H), 7.34 – 7.28 (m, 1H), 7.21 (ddd, J = 7.5, 6.5, 2.2 Hz, 1H), 2.36 (s, 3H). $^{13}\text{C}\{^1\text{H}\}$ NMR (101 MHz, CDCl_3) δ 149.93, 147.50, 146.99, 140.71, 136.71, 134.31, 127.66, 125.76, 124.97, 18.51. ESI-MS: exact m/z calculated for $[\text{C}_{11}\text{H}_{10}\text{N}_2\text{O} + \text{H}]^+$: 187.1, found: 187.0.

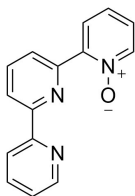


1,10-phenanthroline-1-oxide, 7b: A solution of 1,10-phenanthroline (510 mg, 2.8 mmol, 1 eq) in TFA (2.1 ml) was cooled to 0 °C and H_2O_2 (35% aq., 0.4 ml, d = 1.11 g/ml, 4.2 mmol, 1.5 eq) was added dropwise. After the addition, the reaction mixture was allowed to stir overnight at RT. The resulting

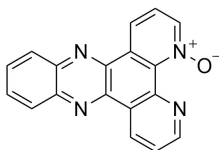
mixture was poured onto ice and neutralized with 6 M NaOH (aq.) to pH 9. The mixture extracted with CHCl_3 (4 x 50 ml) and the combined organic phase was dried with MgSO_4 , filtered. Evaporation of the solvent *in vacuo* yielded the product as an off-white crystalline solid (427 mg, 2.2 mmol, 77%). Analysis was consistent with previous reports.^[36] ^1H NMR (400 MHz, CDCl_3) δ 9.27 (dd, J = 4.3, 1.9 Hz, 1H), 8.70 (dd, J = 6.3, 1.2 Hz, 1H), 8.19 (dd, J = 8.1, 1.9 Hz, 1H), 7.75 (d, J = 8.8 Hz, 1H), 7.69 (dd, J = 8.6, 1.7 Hz, 2H), 7.62 (dd, J = 8.1, 4.4 Hz, 1H), 7.41 (dd, J = 8.1, 6.3 Hz, 1H). $^{13}\text{C}\{^1\text{H}\}$ NMR (101 MHz, CDCl_3) δ 150.05, 142.69, 140.83, 138.41, 135.91, 133.34, 129.10, 128.95, 126.55, 124.53, 123.20, 122.89. ESI-MS: exact m/z calculated for $[\text{C}_{12}\text{H}_8\text{N}_2\text{O} + \text{H}]^+$: 197.1, found: 197.1.



4,7-diphenyl-1,10-phenanthroline-1-oxide, 8b: A solution of 4,7-diphenyl-1,10-phenanthroline (501 mg, 1.5 mmol, 1 eq) in TFA (1.2 ml) was cooled to 0 °C and H₂O₂ (35% aq., 0.2 ml, d = 1.11 g/ml, 2.2 mmol, 1.5 eq) was added dropwise. After the addition, the reaction mixture was allowed to stir overnight at RT. The resulting mixture was poured onto ice and neutralized with 6 M NaOH (aq.) to pH 9. The mixture extracted with CHCl₃ (4 x 50 ml) and the combined organic phase was dried with MgSO₄ and filtered. Evaporation of the solvent *in vacuo* yielded the product as a yellow crystalline solid (519 mg, 1.5 mmol, 99%). ¹H NMR (400 MHz, CDCl₃) δ 9.31 (d, *J* = 4.5 Hz, 1H), 8.79 (d, *J* = 6.5 Hz, 1H), 7.84 (d, *J* = 9.5 Hz, 1H), 7.74 (d, *J* = 9.5 Hz, 1H), 7.59 (d, *J* = 4.5 Hz, 1H), 7.55 – 7.44 (m, 10H), 7.42 (d, *J* = 6.5 Hz, 1H). ¹³C{¹H} NMR (101 MHz, CDCl₃) δ 149.12, 148.17, 143.36, 140.07, 138.71, 137.88, 137.54, 136.96, 130.82, 129.88, 129.84, 128.93, 128.82, 128.76, 128.68, 126.96, 126.53, 124.36, 123.93, 123.72. ESI-MS: exact *m/z* calculated for [C₂₄H₁₆N₂O + H]⁺: 349.1, found: 349.6

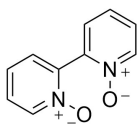


2,2':6',2''-terpyridine-1-oxide, 9b: To a solution of 2,2':6',2''-terpyridine (517 mg, 2.1 mmol, 1 eq) in DCM (21 ml) was slowly added *m*-CPBA (526 mg (77%), 2.4 mmol, 1.1 eq). After the addition, the reaction mixture was allowed to stir overnight at RT. The resulting mixture was quenched with Na₂CO₃ (20 ml, sat. aq.) and extracted with DCM (3 x 50 mL). The combined organic phase was dried with MgSO₄, filtered and concentrated *in vacuo*. Isolation by column chromatography (silica, acetone/hexane = 1/1 with 0.5 % of triethylamine) yielded the product as a white solid (297 mg, 1.2 mmol, 54%). Analysis was consistent with previous reports.^[37] ¹H NMR (400 MHz, CDCl₃) δ 8.99 (dd, *J* = 8.0, 1.0 Hz, 1H), 8.70 (ddd, *J* = 4.7, 1.8, 0.9 Hz, 1H), 8.51 – 8.46 (m, 2H), 8.38 (ddd, *J* = 8.0, 2.2, 0.6 Hz, 1H), 8.34 (ddd, *J* = 6.5, 1.3, 0.6 Hz, 1H), 7.97 (t, *J* = 7.9 Hz, 1H), 7.83 (ddd, *J* = 8.0, 7.4, 1.8 Hz, 1H), 7.40 (ddd, *J* = 8.0, 7.4, 1.3 Hz, 1H), 7.35 – 7.27 (m, 2H). ¹³C{¹H} NMR (101 MHz, CDCl₃) δ 155.98, 155.80, 149.35, 148.88, 147.61, 140.93, 137.49, 137.02, 128.15, 125.76, 125.58, 125.30, 124.03, 121.76, 121.20. ESI-MS: exact *m/z* calculated for [C₁₅H₁₂N₃O + H]⁺: 250.1, found: 250.1.

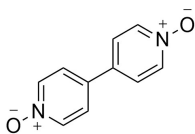


dipyrido[3,2-a:2',3'-c]phenazine-4-oxide, 10b: A solution of dipyrido[3,2-a:2',3'-c]phenazine (300 mg, 1.1 mmol, 1 eq) in TFA (0.8 ml) was cooled to 0 °C and H₂O₂ (35% aq., 0.14 ml, d = 1.11 g/ml, 1.6 mmol, 1.5 eq) was added dropwise. After the addition, the reaction mixture was allowed to stir overnight at RT. The resulting mixture was poured onto ice and neutralized with 6 M NaOH (aq.) to pH 9. The mixture extracted with CHCl₃ (6 x 50 ml) and the combined organic phase was dried with MgSO₄ and filtered. Evaporation of the solvent *in vacuo* yielded the product as a red powder (154 mg, 0.5 mmol, 49%). ¹H NMR (400 MHz, CDCl₃) δ 9.66 (dd, *J* = 8.1, 1.9 Hz, 1H), 9.33 (dd, *J* = 4.4, 1.9 Hz, 1H), 9.24 (dd, *J* = 8.2, 1.3 Hz, 1H), 8.79 (dd, *J* = 6.4, 1.3 Hz, 1H), 8.35 – 8.28 (m, 2H), 7.98 – 7.89

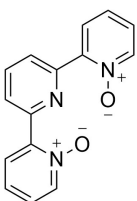
(m, 2H), 7.79 (dd, $J = 8.1, 4.4$ Hz, 1H), 7.60 (dd, $J = 8.2, 6.4$ Hz, 1H). $^{13}\text{C}\{^1\text{H}\}$ NMR (101 MHz, CDCl_3) δ 151.51, 144.81, 143.91, 143.22, 142.79, 141.04, 139.73, 133.57, 132.50, 131.57, 131.24, 129.80, 129.68, 127.38, 126.00, 124.30, 124.00, 121.87. ESI-MS: exact m/z calculated for $[\text{C}_{18}\text{H}_{10}\text{N}_4\text{O} + \text{H}]^+$: 299.1, found: 299.2.



2,2'-bipyridine-1,1'-dioxide, 2c: 2,2'-bipyridine (5.10 g, 32.3 mmol, 1 eq) was firstly dissolved in EtOAc (160 ml) at RT and then solid *m*-CPBA (17.35 g (77%), 77.0 mmol, 2.4 eq) was slowly added inside. The obtained mixture was stirred for 24 h at RT until reaction completion. The resulting suspension was stirred at 80 °C for 30 min followed by hot filtration of white precipitate. The solid on a filter was washed with EtOAc (30 ml) and pentane (30 ml), dried under air flow for 10 min and then transferred to round-bottomed flask. Drying *in vacuo* afforded target compound as white powder (5.60 g, 29.8 mmol, 92%). Analysis was consistent with previous reports.^[11,12] ^1H NMR (500 MHz, CDCl_3) δ 8.38 – 8.32 (m, 2H), 7.73 – 7.67 (m, 2H), 7.40 – 7.31 (m, 4H). $^{13}\text{C}\{^1\text{H}\}$ NMR (126 MHz, CDCl_3) δ 141.98, 140.42, 130.07, 128.92, 127.52. ^1H NMR (500 MHz, D_2O) δ 8.51 – 8.45 (m, 2H), 7.85 (ddd, $J = 8.4, 7.4, 1.2$ Hz, 2H), 7.76 (dtd, $J = 6.9, 3.6, 2.1$ Hz, 4H). $^{13}\text{C}\{^1\text{H}\}$ NMR (126 MHz, D_2O) δ 141.86, 139.79, 131.56, 128.94, 128.53. ESI-MS: exact m/z calculated for $[\text{C}_{10}\text{H}_8\text{N}_2\text{O}_2 + \text{H}]^+$: 189.1, found: 189.1.

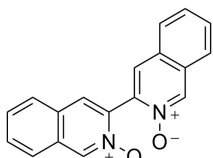


4,4'-bipyridine-1,1'-dioxide, 12c: To a solution of 4,4'-bipyridine (1.00 g, 6.4 mmol, 1 eq) in glacial acetic acid (8 ml) was dropwise added H_2O_2 (0.9 ml (35%), $d = 1.13$ g/ml, 19.2 mmol, 3 eq) and the mixture was heated to 80 °C. After 7.5 h, another 3 equivalents of hydrogen peroxide were added and the reaction was refluxed for 18 h. Once completed, the mixture was concentrated *in vacuo*. Crystallization from H_2O /acetone = 1/20 yielded the product as a white crystalline solid (1.07 g, 5.7 mmol, 89%). Analysis was consistent with previous reports.^[13] ^1H NMR (300 MHz, D_2O) δ 8.40 – 8.35 (m, 4H), 7.94 – 7.89 (m, 4H). $^{13}\text{C}\{^1\text{H}\}$ NMR (75 MHz, D_2O) δ 139.44, 138.04, 124.76. ESI-MS: exact m/z calculated for $[\text{C}_{10}\text{H}_8\text{N}_2\text{O}_2 + \text{H}]^+$: 189.1, found: 189.2.

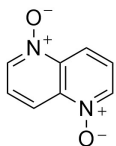


2,2':6',2''-terpyridine-1,1''-dioxide, 9c: 2,2':6',2''-terpyridine (5.00 g, 20.8 mmol, 1 eq) and *m*-CPBA (11.62 g (70%), 47.1 mmol, 2.3 eq) were dissolved in DCM (214 ml) and stirred at RT for 24 h. The resulting suspension was quenched with saturated aqueous Na_2CO_3 (40 ml) and concentrated *in vacuo*. The obtained residue was then crushed to powder and refluxed for 15 min in CHCl_3 (250 ml) with a few spoons of anhydrous Na_2SO_4 . The precipitate was then filtered, washed with hot CHCl_3 (2 x 250 ml) and the filtrate was concentrated *in vacuo* to afford target product as white powder (5.50 g, 20.7 mmol, 100%). Analysis was consistent with previous reports.^[14] TLC ($\text{CHCl}_3/\text{MeOH} = 8/1$: product $R_f = 0.51$; UV lamp). ^1H NMR (500 MHz, CDCl_3) δ 8.94 (d, $J = 8.0$ Hz, 2H), 8.33 (ddd, $J = 6.5, 1.3, 0.6$ Hz,

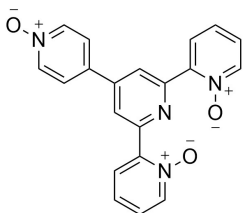
2H), 8.19 (ddd, $J = 8.0, 2.2, 0.6$ Hz, 2H), 7.97 (t, $J = 8.0$ Hz, 1H), 7.37 (ddd, $J = 8.0, 7.5, 1.3$ Hz, 2H), 7.29 (ddd, $J = 7.5, 6.5, 2.2$ Hz, 2H). $^{13}\text{C}\{^1\text{H}\}$ NMR (126 MHz, CDCl_3) δ 149.51, 147.31, 140.88, 136.78, 128.09, 126.20, 125.76, 125.50. ESI-MS: exact m/z calculated for $[\text{C}_{15}\text{H}_{11}\text{N}_3\text{O}_2 + \text{H}]^+$: 266.1, found: 266.1.



[3,3'-biisoquinoline] 2,2'-dioxide, 13c: 3,3'-biisoquinoline (0.50 g, 1.95 mmol, 1 eq) and *m*-CPBA (1.20 g (70%), 4.88 mmol, 2.5 eq) were dissolved in ACN (20 mL) and stirred at RT for 24 h. Upon reaction completion the mixture was quenched with saturated aqueous Na_2CO_3 (10 mL) and concentrated *in vacuo*. The obtained residue was then crushed to powder and refluxed for 15 min in ACN (150 mL) with a few spoons of anhydrous Na_2SO_4 . The precipitate was then filtered, washed with hot ACN (2 x 50 mL) and the filtrate was concentrated *in vacuo* to afford target product as light-yellow powder (0.35 g, 1.21 mmol, 62%). ^1H NMR (400 MHz, $\text{DMSO}-d_6$) δ 9.10 (s, 2H), 8.29 (s, 2H), 7.98 (ddd, $J = 10.7, 8.1, 1.2$ Hz, 4H), 7.74 (ddd, $J = 8.3, 7.0, 1.3$ Hz, 2H), 7.68 (ddd, $J = 8.2, 7.0, 1.4$ Hz, 2H). ^{13}C NMR (101 MHz, $\text{DMSO}-d_6$) δ 140.83, 135.21, 129.85, 128.64, 127.51, 126.98, 126.58, 124.65. ESI-MS: exact m/z calculated for $[\text{C}_{18}\text{H}_{12}\text{N}_2\text{O}_2 + \text{H}]^+$: 289.1; found: 289.1; exact m/z calculated for $[2 \cdot \text{C}_{18}\text{H}_{12}\text{N}_2\text{O}_2 + \text{Na}]^+$: 599.2; found: 599.3.



1,5-naphthyridine-1,5-dioxide, 14c: 1,5-naphthyridine (2.00 g, 14.6 mmol, 1 eq) and *m*-CPBA (7.58 g (77%), 33.8 mmol, 2.3 eq) were mixed in DCM (146 ml) and stirred at RT for 24 h. The resulting suspension was quenched with saturated aqueous Na_2CO_3 (20 ml) and concentrated *in vacuo*. The obtained residue was then crushed to powder and refluxed for 15 min in CHCl_3 (500 ml) with a few spoons of anhydrous Na_2SO_4 . The precipitate was then filtered, washed with hot CHCl_3 (2 x 500 ml) and the filtrate was concentrated *in vacuo* to afford target product as light-yellow crystals (1.38 g, 8.3 mmol, 57%). ^1H NMR (500 MHz, D_2O) δ 8.87 (d, $J = 6.2$ Hz, 2H), 8.77 – 8.67 (m, 2H), 7.93 (dd, $J = 9.1, 6.1$ Hz, 2H). ^1H NMR (500 MHz, $\text{DMSO}-d_6$) δ 8.72 (dt, $J = 6.2, 0.6$ Hz, 2H), 8.29 (dt, $J = 8.8, 0.5$ Hz, 2H), 7.69 (dd, $J = 8.8, 6.0$ Hz, 2H). $^{13}\text{C}\{^1\text{H}\}$ NMR (126 MHz, $\text{DMSO}-d_6$) δ 137.45, 124.89, 116.11. ESI-MS: exact m/z calculated for $[\text{C}_8\text{H}_6\text{N}_2\text{O}_2 + \text{MeOH} + \text{H}]^+$: 195.1, found: 195.1.



4'-(1-oxidopyridin-4-yl)-[2,2':6',2''-terpyridine] 1,1''-dioxide, 15c: 4'-(pyridin-4-yl)-2,2':6',2''-terpyridine (0.50 g, 1.61 mmol, 1 eq) and *m*-CPBA (1.39 g (70%), 5.64 mmol, 3.5 eq) were dissolved in ACN (16 mL) and stirred at RT for 24 h. Upon reaction completion the mixture was quenched with saturated aqueous Na_2CO_3 (10 mL) and concentrated *in vacuo*. The obtained residue was then crushed to powder and refluxed for 15 min in CHCl_3 (150 mL) with a few spoons of anhydrous Na_2SO_4 . The precipitate was then filtered, washed with hot CHCl_3 (2 x 50 mL) and the filtrate was

concentrated in vacuo to afford target product as light-yellow powder (0.47 g, 1.31 mmol, 81%). ^1H NMR (400 MHz, CDCl_3) δ 9.31 (s, 2H), 8.40–8.33 (m, 2H), 8.31–8.25 (m, 4H), 7.78–7.72 (m, 2H), 7.43 (td, $J = 7.8, 1.3$ Hz, 2H), 7.35 (ddd, $J = 7.5, 6.4, 2.2$ Hz, 2H). ^{13}C NMR (101 MHz, CDCl_3) δ 150.47, 146.62, 144.19, 141.00, 139.82, 135.16, 128.15, 126.11, 125.96, 124.45, 123.03. ESI-MS: exact m/z calculated for $[\text{C}_{20}\text{H}_{14}\text{N}_4\text{O}_3+\text{H}]^+$: 359.1; found: 359.2; exact m/z calculated for $[\text{C}_{20}\text{H}_{14}\text{N}_4\text{O}_3+\text{Na}]^+$: 381.1; found: 381.1.

2.5 References

- [1] Gourdon, L.; Cariou, K.; Gasser, G. *Chem. Soc. Rev.* **2022**, *51* (3), 1167–1195.
- [2] Fier, P. S.; Kim, S.; Cohen, R. D. *J. Am. Chem. Soc.* **2020**, *142* (19), 8614–8618.
- [3] Chen, W.; Li, Z. *J. Org. Chem.* **2022**, *87* (1), 76–84.
- [4] Quattrini, L.; Gelardi, E. L. M.; Coviello, V.; Sartini, S.; Ferraris, D. M.; Mori, M.; Nakano, I.; Garavaglia, S.; La Motta, C. *J. Med. Chem.* **2020**, *63* (9), 4603–4616.
- [5] Murakami, K.; Yamada, S.; Kaneda, T.; Itami, K. *Chem. Rev.* **2017**, *117* (13), 9302–9332.
- [6] Wang, D.; Désaubry, L.; Li, G.; Huang, M.; Zheng, S. *Adv. Synth. Catal.* **2021**, *363* (1), 2–39.
- [7] Abramovitch, R. A.; Singer, G. M. *J. Am. Chem. Soc.* **1969**, *91* (20), 5672–5673.
- [8] Yin, J.; Xiang, B.; Huffman, M. A.; Raab, C. E.; Davies, I. W. *J. Org. Chem.* **2007**, *72* (12), 4554–4557.
- [9] Londregan, A. T.; Jennings, S.; Wei, L. *Org. Lett.* **2010**, *12* (22), 5254–5257.
- [10] Xiong, H.; Hoye, A. T. *Synlett* **2022**, *33* (04), 371–375.
- [11] Farrell, R. P.; Silva Elipe, M. V.; Bartberger, M. D.; Tedrow, J. S.; Vounatsos, F. *Org. Lett.* **2013**, *15* (1), 168–171.
- [12] Thibault, M.; Luska, K.; Schlaf, M. *Synthesis* **2007**, *2007* (5), 791–793.
- [13] Ihara, T.; Shirasaka, Y.; Sato, Y.; Kitamura, Y.; Okada, K.; Tazaki, M.; Jyo, A. *HETEROCYCLES* **2005**, *65* (2), 293.
- [14] Kremer, C.; Schnakenburg, G.; Lützen, A. *Beilstein J. Org. Chem.* **2014**, *10*, 814–824.
- [15] Pauli, G. F.; Jaki, B. U.; Lankin, D. C. *J. Nat. Prod.* **2005**, *68* (1), 133–149.
- [16] Ulery, H. E. *J. Org. Chem.* **1965**, *30* (7), 2464–2465.
- [17] Zhang, L.; Wu, Y.; Wang, N.; Gao, X.; Yan, Z.; Xu, B.; Liu, N.; Wang, B.; Xing, Y. *Eur. J. Org. Chem.* **2021**, *2021* (9), 1446–1451.
- [18] Taylor, R. A.; Law, D. J.; Sunley, G. J.; White, A. J. P.; Britovsek, G. J. P. *Angew. Chem. Int. Ed.* **2009**, *48* (32), 5900–5903.
- [19] Houmam, A.; Hamed, E. M. *Chem. Commun.* **2012**, *48* (92), 11328.
- [20] Fulmer, G. R.; Miller, A. J. M.; Sherden, N. H.; Gottlieb, H. E.; Nudelman, A.; Stoltz, B. M.; Bercaw, J. E.; Goldberg, K. I. *Organometallics* **2010**, *29* (9), 2176–2179.
- [21] Den Boer, D.; Konovalov, A. I.; Siegler, M. A.; Hetterscheid, D. G. H. *Inorg. Chem.* **2023**, *62* (14), 5303–5314.
- [22] Bollenbach, M.; Nemska, S.; Wagner, P.; Camelin, G.; Daubeuf, F.; Obrecht, A.; Villa, P.; Rognan, D.; Bihel, F.; Bourguignon, J.-J.; Schmitt, M.; Frossard, N. *Molecules* **2021**, *26* (2), 391.
- [23] Engel, Y.; Dahan, A.; Rozenshine-Kemelmakher, E.; Gozin, M. *J. Org. Chem.* **2007**, *72* (7), 2318–2328.
- [24] Petersen, A. R.; Taylor, R. A.; Vicente-Hernández, I.; Mallender, P. R.; Olley, H.; White, A. J. P.; Britovsek, G. J. P. *J. Am. Chem. Soc.* **2014**, *136* (40), 14089–14099.
- [25] Yin, J.; Xiang, B.; Huffman, M. A.; Raab, C. E.; Davies, I. W. *J. Org. Chem.* **2007**, *72* (12), 4554–4557.
- [26] Yamada, M.; Kimura, M.; Nishizawa, M.; Kuroda, S.; Shimao, I. *BCSJ* **1991**, *64* (6), 1821–1827.
- [27] Kelly, T. R.; Lee, Y.-J.; Mears, R. J. *J. Org. Chem.* **1997**, *62* (9), 2774–2781.

- (28) Homberg, L.; Roller, A.; Hultsch, K. C. *Org. Lett.* **2019**, *21* (9), 3142–3147.
- (29) Joachim Demnitz, F. W.; D’heni, M. B. *Organic Preparations and Procedures International* **1998**, *30* (4), 467–469.
- (30) Zalas, M.; Gierczyk, B.; Klein, M.; Siuzdak, K.; Pędziński, T.; Łuczak, T. *Polyhedron* **2014**, *67*, 381–387.
- (31) Zucker, S. P.; Wossidlo, F.; Weber, M.; Lentz, D.; Tzschucke, C. C. *J. Org. Chem.* **2017**, *82* (11), 5616–5635.
- (32) Murray, J. I.; Spivey, A. C. *Adv. Synth. Catal.* **2015**, *357* (18), 3825–3830.
- (33) Roudesly, F.; Veiros, L. F.; Oble, J.; Poli, G. *Org. Lett.* **2018**, *20* (8), 2346–2350.
- (34) Boulay, A.; Deraeve, C.; Vander Elst, L.; Leygue, N.; Maury, O.; Laurent, S.; Muller, R. N.; Mestre-Voegtli, B.; Picard, C. *Inorg. Chem.* **2015**, *54* (4), 1414–1425.
- (35) Lehr, M.; Paschelke, T.; Bendt, V.; Petersen, A.; Pietsch, L.; Harders, P.; McConnell, A. J. *Eur. J. Org. Chem.* **2021**, *2021* (19), 2728–2735.
- (36) Klenner, M. A.; Pascali, G.; Zhang, B.; Sia, T. R.; Spare, L. K.; Krause-Heuer, A. M.; Aldrich-Wright, J. R.; Greguric, I.; Guastella, A. J.; Massi, M.; Fraser, B. H. *Chem. Eur. J.* **2017**, *23* (27), 6499–6503.
- (37) Lewis, F. W.; Harwood, L. M.; Hudson, M. J.; Drew, M. G. B.; Sypula, M.; Modolo, G.; Whittaker, D.; Sharrad, C. A.; Videva, V.; Hubscher-Bruder, V.; Arnaud-Neu, F. *Dalton Trans.* **2012**, *41* (30), 9209.
- (38) Zhou, Q.; Reekie, T. A.; Abbassi, R. H.; Indurthi Venkata, D.; Font, J. S.; Ryan, R. M.; Munoz, L.; Kassiou, M. *Bioorganic & Medicinal Chemistry* **2018**, *26* (22), 5852–5869.
- (39) Palav, A.; Misal, B.; Ernolla, A.; Parab, V.; Waske, P.; Khandekar, D.; Chaudhary, V.; Chaturbhuj, G. *Org. Process Res. Dev.* **2019**, *23* (2), 244–251.
- (40) He, Y.; Huang, Y.-R.; Li, Y.-L.; Li, H.-H.; Chen, Z.-R.; Jiang, R. *Inorg. Chem.* **2019**, *58* (20), 13862–13880.
- (41) Thummel, R. P.; Jahng, Y. *J. Org. Chem.* **1985**, *50* (19), 3635–3636.

Chapter 3

Building a *Trans* Dissymmetric Ruthenium(II) Complex for Sequential Ligand Photosubstitution

Abstract: In pursuit of better understanding the photochemistry of *trans* ruthenium(II) complexes, a series of *trans*-complexes $[\text{Ru}(\text{HL})(\text{X})(\text{Y})](\text{PF}_6)_2$ has been studied, where X = Y is methyl(2-thioethanol) (MTE; **[1a]**(PF₆)₂), acetonitrile (ACN; **[2a]**(PF₆)₂), or pyridine (Py; **[3a]**(PF₆)₂) based on the planar tetrapyridyl ligand HL (di([2,2'-bipyridin]-6-yl)amine) as well as its *N*-methyl analogue MeL $[\text{Ru}(\text{MeL})(\text{X})(\text{Y})](\text{PF}_6)_2$ (**[1b]**(PF₆)₂–**[3b]**(PF₆)₂). While the compounds are thermally stable in the dark, in all complexes irradiation with blue or green light induced photosubstitution of the axial ligands. Red light photosubstitution of both ligands was only observed for **[3a]**²⁺ and **[3b]**²⁺. Using this knowledge it was possible to photochemically prepare the dissymmetric complex $[\text{Ru}(\text{MeL})(\text{Py})(\text{MTE})](\text{PF}_6)_2$ (**[4b]**(PF₆)₂). Strikingly, sequential release was observed for this complex of Py with red light, followed by MTE with green light, providing the first example of selective, wavelength-dependent photosubstitution in a dissymmetric *trans*-ruthenium(II) complex. The kinetics of all photosubstitution reactions was determined, thus providing the first quantitative analysis of *trans* effects in excited, triplet states of ruthenium complexes.

This work from W. Verbeet, A. Jiao, M.A. Siegler, S. Bonnet, will be submitted for publication. *Manuscript in preparation.*

3.1 Introduction

Light allows for exquisite control over the ligand exchange reactivity in ruthenium(II)-based complexes. This principle has been used for diverse applications, ranging from photocatalysis to photomedicine. The tunable triplet excited states of polypyridyl ruthenium complexes can indeed be steered towards a variety of light-induced photophysical and photochemical processes, such as phosphorescence, energy transfer, electron transfer, ligand isomerization, or ligand photosubstitution.^[1–3] The latter has been employed to trigger the photorelease of cytotoxic inhibitors in an anticancer treatment modality called photo-activated chemotherapy (PACT).^[4] Typically, polypyridine ligands in ruthenium-based PACT compounds are often combinations of tridentate 2,2':6',2'-terpyridine (tpy) and/or bidentate 2,2'-bipyridine (bpy) ligands. In the $[\text{Ru}(\text{tpy})(\text{bpy})(\text{L})]^{2+}$ photocage for example, the monodentate position in the first coordination sphere allows for the incorporation of photolabile ligands such as pyridine,^[5] pyrimidine,^[6] nitrile,^[7] amine,^[8] or thioether.^[9] Other ruthenium-based photocages have been extensively studied, such as those based on the *cis*- $[\text{Ru}(\text{bpy})_2(\text{L}_2)]^{2+}$ architecture, where L is a N- or S-based bidentate chelate.^[10–13] The photochemistry of the analogous complexes *cis*- $[\text{Ru}(\text{bpy})_2(\text{L}')(\text{L}'')]^{2+}$, where L' and L'' are N- or P-based monodentate ligands such as pyridines, nitriles, imidazoles or phosphines, has been thoroughly studied both experimentally and theoretically. Typically, the first photosubstitution is efficient but the second is much slower (e.g., when L' = L'' = pyridine) or does not take place at all (e.g., when L' = amine and L'' = phosphine).^[14–18]

Much less information is available on the photoreactivity of *trans* ruthenium(II) complexes. *Cis* complexes are usually more stable thermally, while *trans*- and *cis*- $[\text{Ru}(\text{bpy})_2(\text{X})(\text{Y})]^{2+}$ complexes do show *cis*-to-*trans* isomerization upon light irradiation, leading to complex mixtures and difficult kinetic analysis. *Trans* ruthenium complexes are, however, of particular relevance due to the central role of a classical concept in coordination chemistry called the *trans* effect. Due to the centrosymmetric nature of the d orbitals, monodentate ligands situated in *trans* position in the coordination sphere of a metal complex, share the *trans* lobes of the same d orbital(s). As a consequence, the bond distance and the kinetics of ligand substitution of any given ligand in the coordination sphere of the metal ion are usually strongly influenced by the ligand in *trans* position. These two concepts are called the *trans* influence and *trans* effect, respectively. Basically, ligands with a strong *trans* effect facilitate substitution of the ligand *trans* to them. Coordination chemists have tabulated the *trans* effect of classical monodentate ligands and established a *trans* effect series, from ethylene, CN^- , or CO on the side of the ligands that labilise their *trans* ligands particularly well, to OH^- , OH_2 , and F^- that are very bad at it.^[19]

The *trans* effect has been well described for ground-state metal complexes, and has important applications such as the industrial production of the approved anticancer drug cisplatin, without traces of its inactive isomer.^[20] Several teams have focused their efforts on understanding the specific biochemical properties of *trans* complexes, in particular for cancer treatment.^[21,22] However, little is known on what the *trans* effect series becomes when a metal complex is excited with light. In other words, what is the influence of *trans* effects on the photoreactivity of photolabile ruthenium complexes, and what is the effect of excitation of a ruthenium complex on the *trans* effect of a given monodentate ligand?

This question can be illustrated by two examples reported by the Etchenique group. In a series of *cis*-[Ru(bpy)₂(L)(ACN)]²⁺ complexes, where L is NH₃, PPh₃ (triphenylphosphine), PMe₃ (trimethylphosphine) or ACN, variation of L primarily affected the Ru–N(bpy) bond distance *trans* to L, indicating a *trans* influence.^[23] However, both the Ru–N(ACN) bond length and ACN photosubstitution quantum yield were largely independent of L, demonstrating the expected absence of a *trans* effect or *trans* influence in the *cis*-complex. In another study, photosubstitution of imidazole (ImH) was shown to occur more efficiently from *trans*-[Ru(bpy)₂(PMe₃)(ImH)]²⁺ than from its *cis* isomer under green light irradiation with quantum yields of 0.23 and 0.10, respectively. The latter example illustrates the stronger *trans* effect of phosphines compared to that of pyridines.^[24] However, thorough understanding of *trans* effects in photosubstitution reactions is currently lacking due the limited data available on the photosubstitution of ruthenium(II) complexes with *trans* geometries.

To fill this knowledge gap, we focused here on the rigid tetrapyridyl ligands di([2,2'-bipyridin]-6-yl)amine (HL), and its *N*-methylated analogue (MeL). When coordinated to a metal center in octahedral geometry, these ligands leave only two *trans* positions in the coordination sphere (Figure 3.1). Although photosubstitution of methyl(2-thioethanol) (MTE) from tetrapyridyl complexes *trans*-[Ru(H₂bapbpy)(MTE)₂]²⁺ (H₂bapbpy = 6,6'-bis(2-aminopyridinyl)-2,2'-bipyridine) and *trans*-[Ru(H₂biqbpy)(MTE)₂]²⁺ (H₂biqbpy = 6,6'-bis(2-aminoisoquinolyl)-2,2'-bipyridine) have been reported, only a single MTE ligand was released upon blue light irradiation (Figure 3.1a).^[25] To investigate the possibility to photorelease two monodentate ligands upon irradiation with longer wavelengths, we prepared a series of new symmetric bis-thioether complexes [Ru(HL)(L')(L'')](PF₆)₂ where L' = L'' = MTE ([**1a**](PF₆)₂), and their acetonitrile (ACN; [**2a**](PF₆)₂) and pyridine (Py; [**3a**](PF₆)₂) analogues. The *N*-methyl derivatives [Ru(MeL)(L')(L'')](PF₆)₂ ([**1b**](PF₆)₂ – [**3b**](PF₆)₂) were prepared as well to investigate the influence of the electron density of the tetrapyridyl ligand on the photosubstitution reactivity. All complexes were found to be photolabile using visible light irradiation; the kinetics of all photosubstitution reactions were quantified under blue, green, or red light, to investigate the effect of *trans* ligands were on the photoreactivity of the complex at different wavelengths. Only the bis-pyridine complexes appeared to be photolabile in red light, which allowed us to prepare photochemically the

dissymmetric complex $[\text{Ru}(\text{MeL})(\text{L}')(\text{L}'')](\text{PF}_6)_2$ (**[4b]** $(\text{PF}_6)_2$) containing two different axial ligands, i.e., $\text{L}' = \text{MTE}$ and $\text{L}'' = \text{Py}$. The photolability of the thioether vs. pyridine ligand of this dissymmetric complex was also quantified upon irradiation with blue, green or red light. Based in the analysis of the *trans* effects of the ligands MTE, Py, ACN, and OH_2 in the excited state of all metal complexes **[1b]** $^{2+}$ – **[4b]** $^{2+}$, we were able to realize the sequential photosubstitution of Py first, followed by MTE, using consecutive irradiation with red and green light, respectively, thus showing exquisite control over the photoreactivity of the complex.

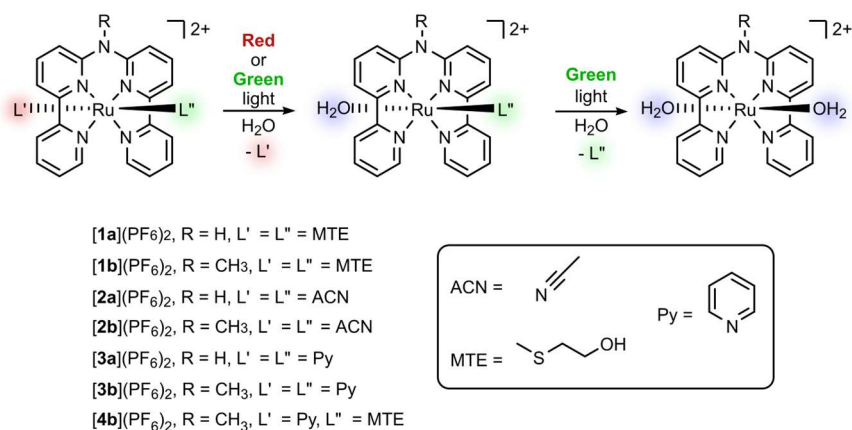
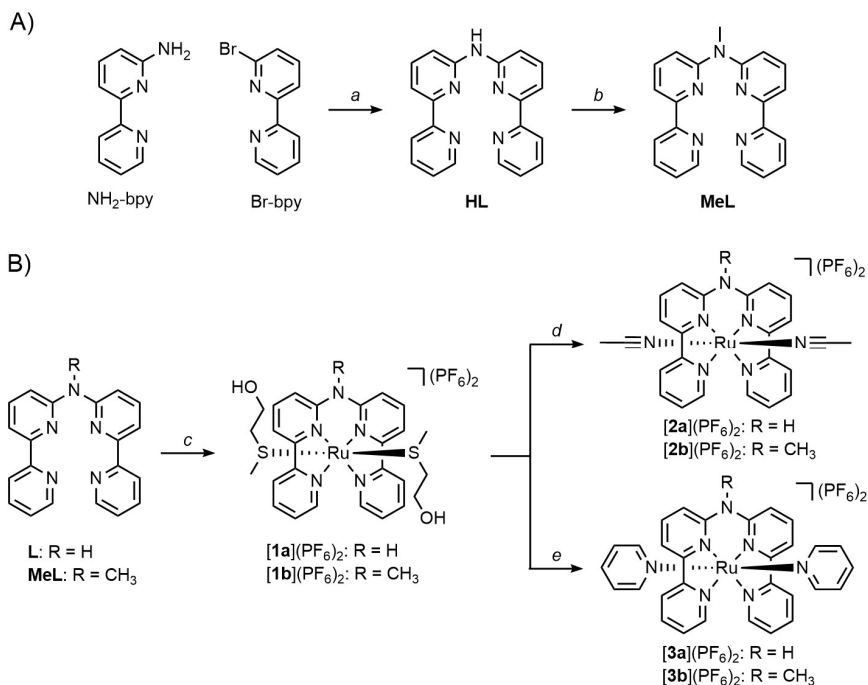


Figure 3.1 Schematic overview of sequential photosubstitution of axial ligands X and Y from *trans*-tetrapyridyl ruthenium(II) complexes presented in this study.

3.2 Results

3.2.1 Synthesis

Ligand HL was synthesized via a modified Buchwald-Hartwig coupling between (2,2'-bipyridine)-6-amine ($\text{NH}_2\text{-bpy}$) and (2,2'-bipyridine)-6-bromide (Br-bpy) using 1,3-bis(diphenylphosphino)propane (dppp) instead of 2,2'-bis(diphenylphosphino)-1,1'-binaphthyl (BINAP) as previously reported (Scheme 3.1).^[26] Subsequently, the amine-bridge in HL was methylated with methyl iodide in presence of an excess of potassium hydroxide in DMSO, providing the MeL ligand in good yield. Complexes **[1a]** $(\text{PF}_6)_2$ and **[1b]** $(\text{PF}_6)_2$ were synthesized in good to excellent yield by reacting the tetrapyridyl ligands HL or MeL, respectively, with $[\text{Ru}(\text{DMSO})_4\text{Cl}_2]$ dissolved in MTE.

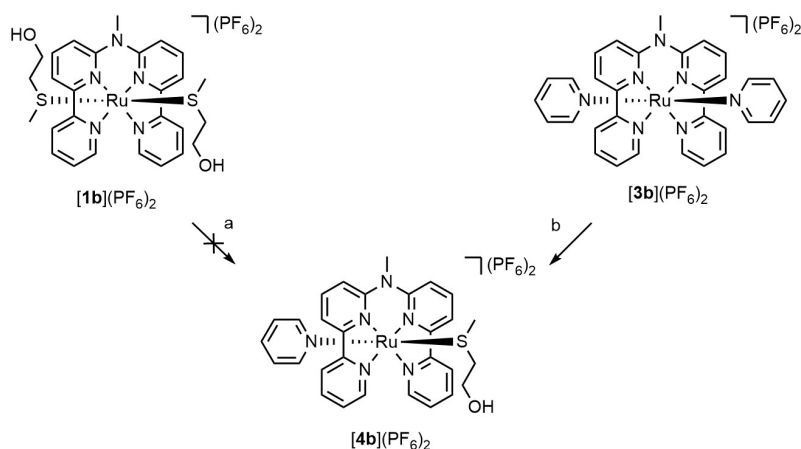


Scheme 3.1 Overview of synthetic routes. A) Synthesis of ligand HL and MeL; a) Pd(dba)₃, dppp, NaOtBu in toluene, 80 °C, 18 h, 85%; b) MeI, KOH in DMSO, RT, 3 hr, 95%. B) Synthesis of complexes [1a,b](PF₆)₂ – [3a,b](PF₆)₂; c) i) Ru(DMSO)₄Cl₂ in 2-(methylthio)ethanol, N₂, 150 °C, 3 days for [1a](PF₆)₂, 2 days for [1b](PF₆)₂; ii) KPF₆ (aq.), 71% for [1a](PF₆)₂, 90% for [1b](PF₆)₂; d) i) ACN, reflux, 5 days for [2a](PF₆)₂, 2 days for [2b](PF₆)₂; ii) KPF₆ (aq.), 79% for [2a](PF₆)₂, 46% for [2b](PF₆)₂; e) i) Pyridine, N₂, 115 °C, 1 day for [3a](PF₆)₂, 2 day for [3b](PF₆)₂; ii) KPF₆ (aq.), 93% for [3a](PF₆)₂, 77% for [3b](PF₆)₂.

From the thioether complexes, the corresponding acetonitrile ([2a,b](PF₆)₂) and pyridine ([3a,b](PF₆)₂) analogues were synthesized by refluxing [1a,b](PF₆)₂ in the desired monodentate ligand as solvent. While all other complexes were pure after washing the precipitate, [2b](PF₆)₂ had to be purified by silica gel chromatography. Characterization of all new compounds was performed using NMR spectroscopy, mass spectrometry, elemental analysis, and UV-Vis absorption spectroscopy (see Experimental part and Appendix III).

Since [4b](PF₆)₂ contains both MTE and pyridine as axial ligands *trans* to each other, the synthesis could theoretically be performed either by reacting the bis-MTE complex [1b](PF₆)₂ with free pyridine, or by reacting the bis-pyridine complex [3b](PF₆)₂ with free MTE. However, initial attempts to perform these reactions under thermal conditions resulted in a mixture of the three possible complexes with [1b](PF₆)₂ and [3b](PF₆)₂ as major thermodynamic products. The reactions were also performed at room temperature by irradiation with 650 nm light (Scheme 3.2), as photosubstitution of thioether or pyridyl ligands from ruthenium (II) polypyridyl complexes has been reported extensively.^[27–29] In

such conditions, $[\mathbf{4b}](\text{PF}_6)_2$ could not be generated by light irradiation of $[\mathbf{1b}](\text{PF}_6)_2$ in an acetone solution containing an excess (> 5 equivalents) of free pyridine because it was essentially photochemically unreactive at such high wavelengths. However, the photoreaction starting from $[\mathbf{3b}](\text{PF}_6)_2$ in presence of 10 equivalents of free MTE, provided $[\mathbf{4b}](\text{PF}_6)_2$ with a good yield (63%) after isolation by column chromatography. Characterization using NMR spectroscopy, mass spectrometry and elemental analysis confirmed the successful preparation of the dissymmetric complex $[\mathbf{4b}](\text{PF}_6)_2$.



Scheme 3.2 Schematic overview towards the synthesis of $[\mathbf{4b}](\text{PF}_6)_2$ via red light (650 nm) irradiation. a) Pyridine in acetone, N_2 , 25 °C, 1 h; b) 2-(methylthio)ethanol in acetone, N_2 , 25 °C, 1 h, 63%.

3.2.2 Crystal structures

Single crystals of $[\mathbf{1a}](\text{PF}_6)_2$, $[\mathbf{1b}](\text{PF}_6)_2 \cdot \text{TPPO}$ (TPPO = triphenylphosphine oxide), $[\mathbf{2b}](\text{PF}_6)_2$, $[\mathbf{3b}](\text{PF}_6)_2$ and $[\mathbf{4b}](\text{PF}_6)_2$ suitable for X-ray diffraction were obtained via vapor diffusion of diethyl ether into a solution of the complex in acetone, or a THF/acetone mixture (Figure 3.2 and Table 3.1). For $[\mathbf{1b}](\text{PF}_6)_2$, TPPO was added to the complex solution in acetone, and ended up as solvate in the crystal structure. While $[\mathbf{1b}]^{2+}$ is an analogue of $[\mathbf{1a}]^{2+}$, differences between the crystal structures of the two complexes were observed. Firstly, a larger difference between the Ru-N1 and the Ru-N2 distances was found in $[\mathbf{1a}]^{2+}$, compared to $[\mathbf{1b}]^{2+}$ (Ru-N1 – Ru-N2 = ~ 0.20 Å and ~ 0.07 Å, respectively), showing the more open geometry of the NH-bridged analogue. Also, a difference of ~ 0.1 Å in Ru-S distances was observed in $[\mathbf{1a}]^{2+}$, while both Ru-S distances are near identical in $[\mathbf{1b}]^{2+}$. Furthermore, a larger $\text{N1}'\text{-Ru-N2}$ bond angle was observed for $[\mathbf{1a}]^{2+}$ than in $[\mathbf{1b}]^{2+}$ (176° and 172° , respectively), with a torsion angle of the coordinated pyridyl N-atoms ($\text{N1-N2-N2}'\text{-N1}'$) larger for $[\mathbf{1a}]^{2+}$ than for $[\mathbf{1b}]^{2+}$ (-5.6° and 2.4° , respectively). In other words, the methyl group in MeL ligand prevents the helical “twisting” of the tetrapyrrolyl ligand upon coordination to ruthenium. However, $[\mathbf{1a}]^{2+}$ and $[\mathbf{1b}]^{2+}$ are far more planar compared to the previously reported $[\text{Ru}(\text{H}_2\text{bapbpy})(\text{MTE})_2]^{2+}$ and $[\text{Ru}(\text{H}_2\text{bapbpy})(\text{MTE})_2]^{2+}$ in which the tetrapyrrolyl ligand to a helical conformation around the metal center.^[25] The τ_4 value, a

structural distortion parameter indicative for a square-planar geometry when $\tau_4 = 0$, is lower for $[\mathbf{1a}]^{2+}$ (0.05) than for $[\mathbf{1b}]^{2+}$ (0.11). However, for both $[\mathbf{1a}]^{2+}$ and $[\mathbf{1b}]^{2+}$ a similar distortion of the octahedral geometry was observed, with values for the octahedral distortion parameter (Σ) of 68° and 67° , respectively. These results indicate that the subtle modification of **HL** by methylation of the bridging N-atom affects the binding of the tetrapyrridyl ligand.

Between the symmetrical methylated complexes $[\mathbf{1b}]^{2+}$, $[\mathbf{2b}]^{2+}$ and $[\mathbf{3b}]^{2+}$, small differences in the bond lengths between the polypyridyl ligand and ruthenium center were observed. The Ru-N bond lengths for the MeL pyridyl N-atoms are comparable, with Ru-N1 = ~ 2.096 Å and Ru-N2 = ~ 2.020 Å. However, variations in the metal-axial ligand bond lengths were observed among the complexes. The Ru-S bonds in $[\mathbf{1b}]^{2+}$ measured approximately 2.370 Å, reflecting the larger van der Waals radius of sulfur atoms. In contrast, shorter Ru-N distances were found in $[\mathbf{2b}]^{2+}$ (~ 2.026 Å) compared to the slightly longer Ru-N distances found in the bis-pyridine compound $[\mathbf{3b}]^{2+}$ (~ 2.106 Å). These results are similar to those reported earlier for polypyridyl complexes bearing thioether, acetonitrile and pyridine ligands.^[30–32] Interestingly, similar bond lengths were observed for the dissymmetric complex $[\mathbf{4b}]^{2+}$, with Ru-S1 = ~ 2.363 Å and Ru-N4 = ~ 2.110 Å, suggesting no significant *trans*-influence in the ground state of the dissymmetric complex. The axial ligands also do not affect the square planar geometry of the MeL ligand, with τ_4 values around 0.11 for all four molecules. A slightly lower octahedral distortion was observed for $[\mathbf{3b}]^{2+}$ ($\Sigma = 56^\circ$) than for $[\mathbf{1b}]^{2+}$, $[\mathbf{2b}]^{2+}$ and $[\mathbf{4b}]^{2+}$ ($\Sigma = 67^\circ$, 61° and 66° , respectively), which we attribute mostly to packing effects. The torsion angle between coordinating pyridyl nitrogen atoms in **HL** (N1-N2-N2'-N1') was twice larger in $[\mathbf{1a}]^{2+}$ (-5.6°) than in the MeL analogue $[\mathbf{1b}]^{2+}$ (2.1°). While no torsion was observed for acetonitrile complex $[\mathbf{2b}]^{2+}$, angles of 3.5° and 1.0° were found for $[\mathbf{3b}]^{2+}$ and $[\mathbf{4b}]^{2+}$, respectively. Interestingly, the MeL containing complexes $[\mathbf{1b}](\text{PF}_6)_2$ – $[\mathbf{4b}](\text{PF}_6)_2$ all appear to appear to be coordinated in a “saddle-shape” geometry, while the HL containing complex $[\mathbf{1a}](\text{PF}_6)_2$ has a more helical geometry.

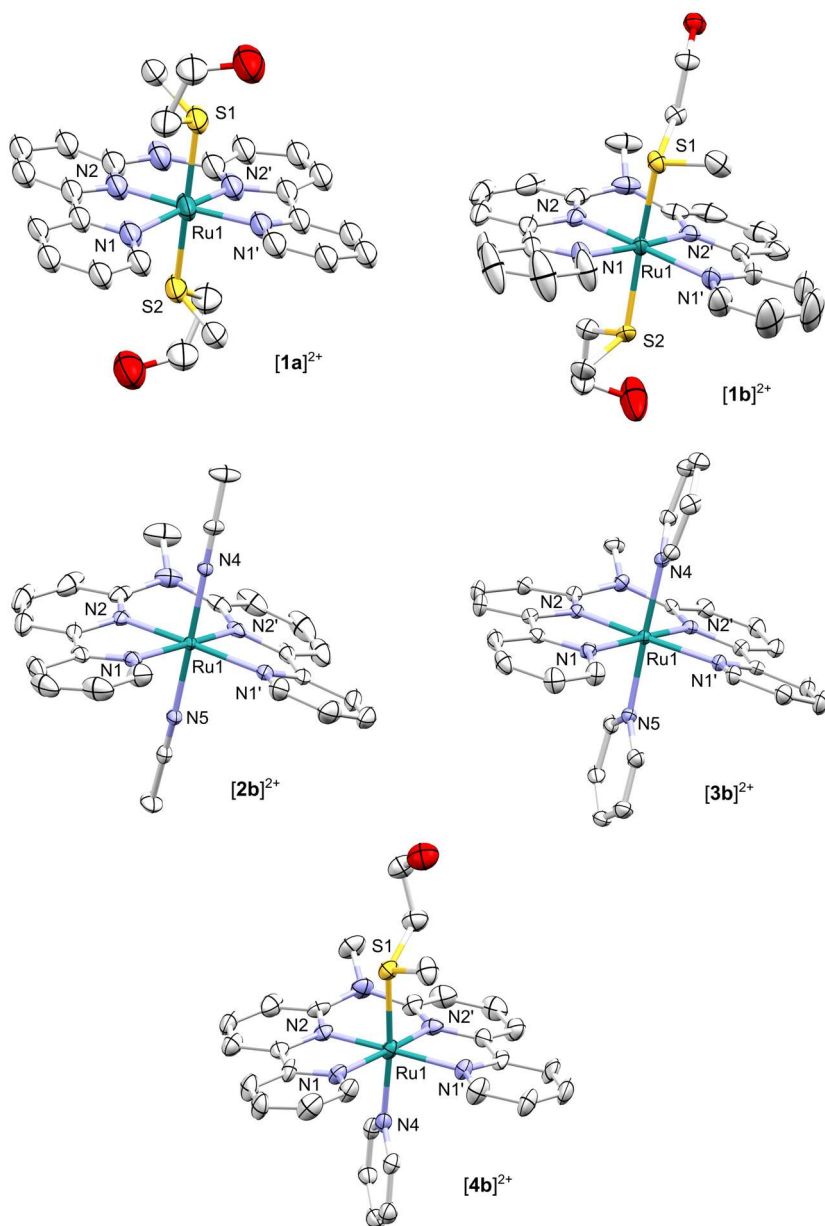


Figure 3.2 Displacement ellipsoid plots (50% probability level) in the crystal structures of complexes $[1a](PF_6)_2$, $[1b](PF_6)_2(TPPO)$, $[2b](PF_6)_2$, $[3b](PF_6)_2$ and $[4b](PF_6)_2$. For clarity, hydrogen atoms, counterions and lattice solvent molecules have been omitted.

Table 3.1 Selected bond distances (Å) and bond angles (°) for complexes **[1a]**(PF₆)₂, **[1b]**(PF₆)₂•TPPO, **[2b]**(PF₆)₂, **[3b]**(PF₆)₂ and **[4b]**(PF₆)₂.

	[1a] (PF ₆) ₂	[1b] (PF ₆) ₂	[2b] (PF ₆) ₂	[3b] (PF ₆) ₂	[4b] (PF ₆) ₂
Ru1-N1	2.141	2.096(3)	2.096	2.095(3)	2.121(7)
Ru1-N2	1.886	2.026(3)	2.020	2.015(3)	2.020(7)
Ru1-N1'	2.174	2.100(2)	2.098	2.095(3)	2.119(7)
Ru1-N2'	1.984	2.023(2)	2.020	2.017(3)	2.028(7)
Ru1-S1	2.432	2.372(1)	-	-	2.363(3)
Ru1-S2	2.324	2.369(7)	-	-	-
Ru1-N4	-	-	2.024	2.109(3)	2.110(9)
Ru1-N5	-	-	2.029	2.104(3)	-
N1-Ru1-N2'	176.7	172.9(1)	171.8	172.0(1)	172.8(3)
N1'-R1-N2	176.4	172.1(1)	171.8	173.7(1)	172.2(3)
S1-Ru1-S2	177.3	173.9(2)	-	-	-
N4-Ru1-N5	-	-	178.3	178.2(1)	-
N4-Ru1-S4	-	-	-	-	173.9(3)
Torsion angle (°) N1-N2-N2'-N1'	5.6	2.4(1)	0.0(1)	3.5(2)	1.0(3)
τ ₄ ^a	0.05	0.11(9)	0.12	0.10(1)	0.11(3)
Σ ^b (°)	68	67(5)	61	56(5)	66(5)

^a The coordination angles N1-Ru1-N2' (α) and N1'-Ru-N2 (β) were used to calculate τ₄.^[33]

$$\tau_4 = \frac{360 - (\alpha + \beta)}{141}$$

^b Octahedral distortion parameter Σ was calculated using all *cis* bond angles in the primary coordination sphere.^[34] $\Sigma = \sum_{i=1}^{12} |\phi_i - 90|$

3.2.3 Photochemistry

To investigate the thermal stability of the complexes, the UV-Vis absorbance in 1/5 acetone/H₂O solutions of the complexes vs. time was monitored over time. Compounds **[1a,b]**(PF₆)₂ – **[3a,b]**(PF₆)₂ and **[4b]**(PF₆)₂ were found to be thermally stable for at least 2 h in solution in the dark at 298 K (Appendix III.2.2). The photochemical reactivity of the symmetric complexes was then investigated by monitoring the ¹H-NMR spectra of **[1a,b]**(PF₆)₂ – **[2a,b]**(PF₆)₂ in 1/5 acetone-d₆/D₂O and **[3a,b]**(PF₆)₂ in 1/3 acetone-d₆/D₂O at 298 K upon irradiation with white or green (530 nm) light. As shown in Figure 3.3 for **[3b]**²⁺ upon green (505 nm) light irradiation for 90 min, the characteristic signals of free pyridine at 8.38, 7.72 and 7.31 ppm appeared. Additionally, the doublet at 9.74 ppm corresponding to a C-H aromatic proton of MeL was initially replaced by a doublet at 9.67 ppm for the

intermediate $[7b]^{2+}$ (Scheme 3.3), which then converted to a doublet at 9.82 ppm corresponding to the final bis-aqua photoproduct $[8b]^{2+}$. Similar reactivity was observed for the two other symmetric complexes in these conditions, with signals appearing for free MTE at 3.60 ppm (triplet), free acetonitrile at 1.93 ppm (singlet), and free pyridine at 8.38 ppm (multiplet) upon irradiation of $[1a,b]^{2+}$, $[2a,b]^{2+}$, or $[3a,b]^{2+}$, respectively. These results indicate that $[1a,b]^{2+}$ – $[3a,b]^{2+}$ undergo two-step photosubstitution of the axial ligands in presence of water, during which intermediates $[5a,b]^{2+}$ – $[7a,b]^{2+}$ are formed first, where one axial ligand is replaced by a H_2O molecule, before photosubstitution of the second non-aqua ligand takes place (Scheme 3.3).

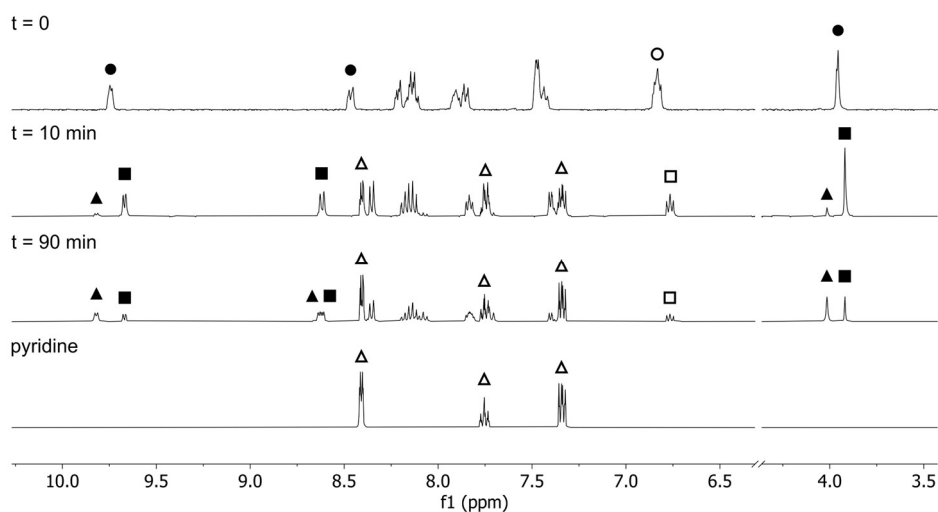
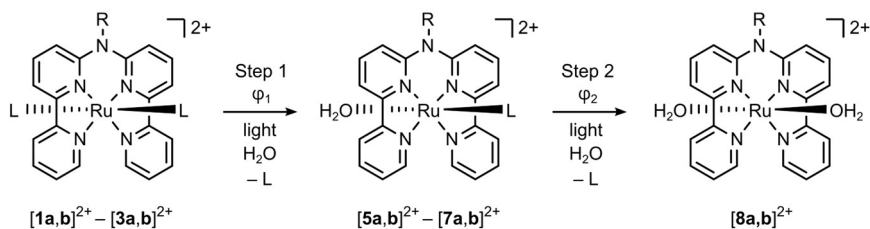


Figure 3.3 Time-evolution of the 1H -NMR spectra evolution of $[3b](PF_6)_2$ (● for MeL protons, ○ for coordinated pyridine) in 1/3 acetone- d_6/D_2O at 298 K upon irradiation with green light (530 nm for 90 minutes). Symbols indicate mono-aqua intermediate $[7b]^{2+}$ (■ for MeL protons, □ for coordinated pyridine), bis-aqua photoproduct $[8b]^{2+}$ (▲), and free pyridine (Δ).

To be able to quantify the kinetics of Steps 1 and 2 in Scheme 3.3 and to evaluate how changing the nature of the axial ligands and methylating the bridging amine of the tetrapyrrolyl ligand affects the light absorption properties of the complexes, the UV-Vis absorption spectra of complexes $[1a,b]^{2+}$ – $[3a,b]^{2+}$ were first recorded in 1/5 acetone/water. Typical 1MLCT absorption bands culminating between 430 and 485 nm were observed, which are quintessential for polypyridyl ruthenium(II) complexes containing two thioether, nitrile, or pyridine ligands (Table 3.2).



Scheme 3.3 Schematic representation of photosubstitution of axial ligands L in $[1\mathbf{a},\mathbf{b}]^{2+} - [3\mathbf{a},\mathbf{b}]^{2+}$ in presence of H_2O ; φ_1 and φ_2 are the photosubstitution quantum yields of Step 1 and Step 2, respectively. $[1\mathbf{a}]^{2+} - [8\mathbf{a}]^{2+}$: R = H; $[1\mathbf{b}]^{2+} - [8\mathbf{b}]^{2+}$: R = Me; $[1\mathbf{a},\mathbf{b}]^{2+}$, $[5\mathbf{a},\mathbf{b}]^{2+}$: L = MTE; $[2\mathbf{a},\mathbf{b}]^{2+}$, $[6\mathbf{a},\mathbf{b}]^{2+}$: L = acetonitrile; $[3\mathbf{a},\mathbf{b}]^{2+}$, $[7\mathbf{a},\mathbf{b}]^{2+}$: L = pyridine.

A bathochromic shift was observed of the $^1\text{MLCT}$ bands of $[3\mathbf{a},\mathbf{b}]^{2+}$ (~ 486 nm) compared to $[1\mathbf{a},\mathbf{b}]^{2+}$ and $[2\mathbf{a},\mathbf{b}]^{2+}$ (~ 443 nm and ~ 432 nm, respectively). Clearly, the pyridine ligands in $[3\mathbf{a},\mathbf{b}]^{2+}$ stabilize the $^1\text{MLCT}$ states of the complexes, compared to thioether or nitrile ligands in $[1\mathbf{a},\mathbf{b}]^{2+}$ and $[2\mathbf{a},\mathbf{b}]^{2+}$. For the **MeL** containing analogues $[1\mathbf{b}]^{2+} - [2\mathbf{b}]^{2+}$, a slight bathochromic shift of the absorption maximum λ_{max} of the $^1\text{MLCT}$ bands was observed, compared to **HL** complexes $[1\mathbf{a}]^{2+} - [2\mathbf{a}]^{2+}$. In contrast, identical $^1\text{MLCT}$ absorption maxima were found for $[3\mathbf{a}]^{2+}$ and $[3\mathbf{b}]^{2+}$. A more obvious difference between the **HL** and **MeL** complexes can be observed when comparing the absorption of red light, with ϵ at 625 nm being lower for the methylated compounds $[1\mathbf{b}]^{2+} - [3\mathbf{b}]^{2+}$ than for the **HL** complexes $[1\mathbf{a}]^{2+} - [3\mathbf{a}]^{2+}$.

To evaluate the photoreactivity of the complexes, time evolution of the UV-Vis spectra of solutions of $[1\mathbf{a},\mathbf{b}]^{2+} - [3\mathbf{a},\mathbf{b}]^{2+}$ in a 1/5 acetone/water mixture were recorded upon irradiation with blue (435 nm), green (505 nm) or red light (625 nm). Similar to previous reports and as observed by $^1\text{H-NMR}$, upon irradiation with 435 nm and 505 nm light all complexes showed distinct two-step photoreactions characterized by bathochromic shifts of the $^1\text{MLCT}$ band.^[29] Strikingly, upon red light irradiation photosubstitution was only observed for the pyridine complexes $[3\mathbf{a}]^{2+}$ and $[3\mathbf{b}]^{2+}$. The molar absorption coefficients of these complexes at 625 nm was not significantly higher than those of the other complexes, hence the observed red-light reactivity of the bis-pyridine complexes must be related to differences in excited state properties.

Global fitting of the time-evolution of the absorbance data provided the fitted spectra of the mono-aqua intermediate species $[5\mathbf{a},\mathbf{b}]^{2+} - [7\mathbf{a},\mathbf{b}]^{2+}$ and of the bis-aqua final photoproduct $[8\mathbf{a},\mathbf{b}]^{2+}$ (Appendix III.2.2). These fitted spectra indicated that the degree of bathochromic shifting depends on the ligands that are photosubstituted: while both substitution steps resulted in a shift of the $^1\text{MLCT}$ band between 20 and 40 nm for MTE in $[1\mathbf{a}]^{2+}$ and ACN in $[2\mathbf{a}]^{2+}$ respectively, substitution of the axial pyridine ligands in $[3\mathbf{a}]^{2+}$ only resulted in a shift of 10 nm.

Global fitting of the time-evolution UV-Vis absorbance data also provided their kinetic reaction profiles (Table 3.2 and Appendix III.2.2). The kinetic curves of the intermediates $[5a,b]^{2+} - [7a,b]^{2+}$ during irradiation of complexes $[1a,b]^{2+} - [3a,b]^{2+}$ are shown in Figure 3.4. For blue and green light irradiation these traces can be separated into two domains. In the first domain, a positive slope relates to the formation of mono-aqua intermediate $[5a,b]^{2+} - [7a,b]^{2+}$ where one axial ligand of the starting complex has been photosubstituted by water. In the second domain, the slope is negative and relates to the decay rate of $[5a,b]^{2+} - [7a,b]^{2+}$ to the final products $[8a,b]^{2+}$ through photosubstitution of the second axial ligand. When comparing the kinetic curves, key differences between the different complexes were observed (Figure 3.4). Firstly, the acetonitrile complexes behaved in a different manner than the thioether and pyridine compounds. In $[2a]^{2+}$ and $[2b]^{2+}$, photosubstitution of the second ligand begun before completion of the first photosubstitution step, pointing to the higher photoreactivity of intermediates $[5a]^{2+}$ and $[5b]^{2+}$, compared to all other mono-aqua intermediates. With the thioether and pyridine complexes, photosubstitution of the first axial ligand took place first and go to completion, before the second ligand started to be photosubstituted. Secondly, the photosubstitution rates were dependent on the irradiation wavelength, breaking Kasha's rule which states that "polyatomic molecular entities react with appreciable yield only from the lowest excited state of a given multiplicity". Unlike at shorter wavelength, under red light irradiation the Py complexes $[3a,b]^{2+}$ showed a single photosubstitution step characterized by a slower rate than upon blue or green light irradiation (Figure 3.4 E and F). Although less distinct, differences were also observed between the MTE complexes $[1a,b]^{2+}$ and Py complexes $[3a,b]^{2+}$ when comparing blue (435 nm) vs. green (505 nm) light irradiation. Upon blue light irradiation, the similar slopes observed for the initial formation of $[5a,b]^{2+}$ and $[7a,b]^{2+}$ (green and red lines, respectively, in Figure 3.4 A–D) indicate that the rates of the first photosubstitution steps were neither influenced by the nature of the leaving ligand nor by the N-methylation of the tetrapyrridyl ligand. However, the rates of the second step were significantly lower for the **MeL** complexes, while the Py complex $[3b]^{2+}$ reacted faster than its MTE analogue $[1b]^{2+}$ (Figure 3.2 A and B). In contrast, upon green light irradiation rates of the first step were influenced only by the nature of the leaving ligand, with release of MTE ligands in $[1a,b]^{2+}$ being slower than release of the Py ligands in $[3a,b]^{2+}$ (Figure 3.2 C and D), while methylation of the N bridge did not change the rates much. This effect was reversed for the rates of the second step: methylation of the tetrapyridine ligand resulted in lower rates, without much difference between MTE and Py complexes.

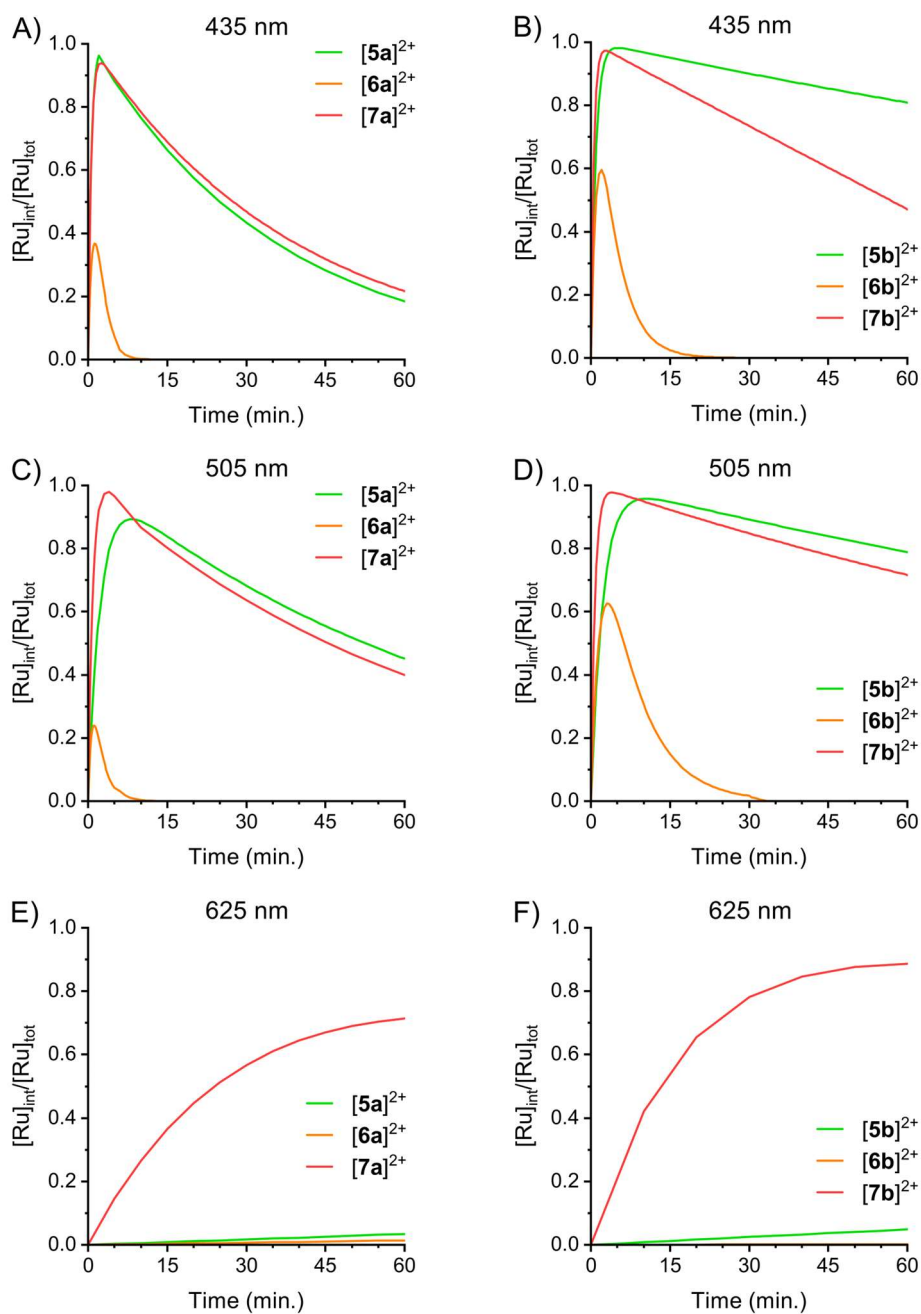


Figure 3.4 Kinetic curves obtained with global fitting of the absorbance spectra of $[\mathbf{1a,b}](\text{PF}_6)_2 - [\mathbf{3a,b}](\text{PF}_6)_2$ in 1/5 acetone/water at 298 K irradiated with blue (435 nm; A, B), green (505 nm; C, D), or red (625 nm) light, following the fraction of the intermediate species $[\mathbf{5a,b}]^{2+} - [\mathbf{7a,b}]^{2+}$ ($[\text{Ru}]_{\text{int}}$) over the total ruthenium concentration ($[\text{Ru}]_{\text{tot}}$).

From these global fitted data and used photon fluxes it was also possible to calculate the photosubstitution quantum yields φ_1 and φ_2 for both steps of all complexes $[\mathbf{1a,b}]^{2+} - [\mathbf{3a,b}]^{2+}$ (see Appendix III and Table 3.2). The QYs of the first photosubstitution step (φ_1) were found to be generally 2 orders of magnitude higher than the QY of the second step (φ_2). A notable exception was $[\mathbf{2a}]^{2+}$, for which φ_2 was higher than φ_1 upon irradiation with either blue or green light. Irradiation with red light, which resulted in photoreactivity only for the Py complexes $[\mathbf{3a}]^{2+}$ and $[\mathbf{3b}]^{2+}$, gave $\varphi_{1,625}$ values of 0.0073 and 0.015, respectively. When comparing complexes containing **HL**, $[\mathbf{1a}]^{2+} - [\mathbf{3a}]^{2+}$, with the ones containing **MeL**, $[\mathbf{1b}]^{2+} - [\mathbf{3b}]^{2+}$, we noticed that the former compound showed QYs within the same order of magnitude with blue (435 nm) or green (505 nm) light. Surprisingly, the photoreactivity of the **MeL** complexes was much more dependent on the irradiation wavelength. For example, $\varphi_{1,435}$ and $\varphi_{1,505}$ are near-identical for $[\mathbf{1a}]^{2+}$ (between 0.017 and 0.014, respectively), while the QYs for $[\mathbf{1b}]^{2+}$ differed 5-fold ($\varphi_{1,435} = 0.079$ and $\varphi_{1,505} = 0.015$).

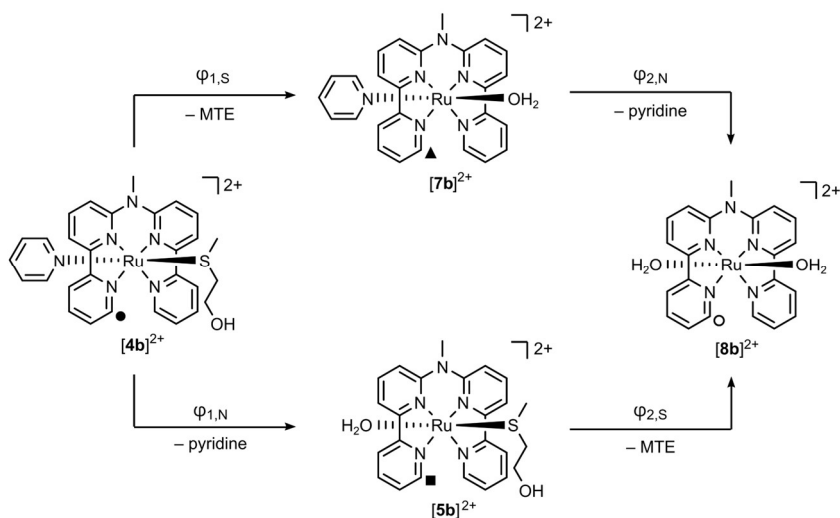
Table 3.2 Photochemical properties of **[1a,b](PF₆)₂** – **[3a,b](PF₆)₂** in 1/5 acetone/water at 298 K including maximum absorption wavelength (λ_{\max} , in nm), molar extinction coefficient at the absorption maximum (ϵ_{\max} , in M⁻¹cm⁻¹), molar extinction coefficient at irradiation wavelength for each step ($\epsilon_1(\lambda_i)$, $\epsilon_2(\lambda_i)$, in M⁻¹cm⁻¹) photosubstitution quantum yields (φ_1 , φ_2) and photoreactivity at irradiation wavelength (ζ_1 , ζ_2 , in M⁻¹cm⁻¹).^a

		[1a]²⁺	[1b]²⁺	[2a]²⁺	[2b]²⁺	[3a]²⁺	[3b]²⁺
	λ_{\max} (nm) (ϵ_{\max}) ^b	439 (5300)	447 (6250)	429 (6990)	434 (6490)	486 (7200)	485 (6870)
435 nm	$\epsilon_1(\lambda_i)$ ^b	5190	5450	6630	6480	3060	1960
	$\epsilon_2(\lambda_i)$ ^c	4100	3800	4300	2600	3000	2400
	φ_1 (ζ_1)	0.017 (91)	0.079 (430)	0.032 (210)	0.034 (220)	0.018 (54)	0.19 (372)
	φ_2 (ζ_2)	0.00031 (1.3)	0.00029 (1.1)	0.041 (180)	0.020 (52)	0.00027 (0.82)	0.00083 (2.0)
505 nm	$\epsilon_1(\lambda_i)$ ^b	1340	1190	1150	693	4140	4410
	$\epsilon_2(\lambda_i)$ ^c	2500	2800	2000	1500	7000	5900
	φ_1 (ζ_1)	0.014 (18)	0.015 (18)	0.023 (27)	0.062 (43)	0.019 (77)	0.025 (110)
	φ_2 (ζ_2)	0.00023 (0.58)	0.00014 (0.39)	0.031 (63)	0.0098 (19)	0.00018 (0.54)	0.00019 (1.1)
625 nm	$\epsilon_1(\lambda_i)$ ^b	226	36.3	82.6	6.03	82	42.2
	$\epsilon_2(\lambda_i)$ ^c	520	140	290	6.4	460	440
	φ_1 (ζ_1)	0.00004 (0.009)	0.00035 (0.013)	0.00004 (0.0033)	0.00010 (0.0006)	0.0073 (0.60)	0.015 (0.65)
	φ_2 (ζ_2)	n.d. (<0.0052)	n.d. (<0.0013)	n.d. (<0.0029)	n.d. (<0.00008)	0.00016 (0.012)	0.00005 (0.02)

^a $\zeta_i = \epsilon(\lambda_i) \times \varphi_i$. ^b Molar extinction coefficient determined experimentally. ^c Molar extinction coefficient determined by global fitting.

For the dissymmetric complex **[4b]²⁺**, the presence of two different monodentate ligands in axial positions, pyridine and an MTE, generates two possible intermediates **[7b]²⁺** and **[5b]²⁺** through via photosubstitution of either MTE ($\varphi_{1,S}$) or pyridine ($\varphi_{1,N}$), respectively (Scheme 3.4). The secondary photosubstitution, which can take place on each intermediate, leads to final bis-aqua complex **[8b]²⁺**, by substitution of pyridine from **[7b]²⁺** ($\varphi_{2,N}$) or MTE from

[5b]²⁺ ($\varphi_{2,S}$). For this complex there are hence 4 different photosubstitution reactions that may take place simultaneously upon light irradiation.



Scheme 3.4 Schematic overview of the possible photosubstitution pathways of **[4b]²⁺**.

To investigate possible four photoreactions, a solution of **[4b](PF₆)₂** in 1/5 acetone-*d*₆/D₂O was initially monitored by ¹H-NMR upon irradiation, first using red light (650 nm) followed by green light (530 nm, Figure 3.5). Photorelease of axial ligands clearly took place, as indicated by the multiplet emerging at 8.39 ppm for free pyridine, the triplet appearing at 2.54 ppm for free MTE, and the disappearance of the doublet at 9.65 ppm of the starting reagent **[4b]²⁺**. The time-evolution of the ratios of the integrals of the peaks corresponding to **[4b]²⁺** (9.5 - 9.8 ppm), free pyridine (8.2 - 8.4 ppm), and free MTE (2.5 - 3.2 ppm), divided by the integral of all ruthenium species, are presented in Figure 3.5B. These integral ratios indicated that after 6 h red light irradiation approximately half of **[4b]²⁺** had been converted: about half of the pyridine had been released while only 10% of MTE had been substituted. Subsequent irradiation with green light (530 nm) completed the conversion of **[4b]²⁺** by releasing of the residual pyridine within 1 h, while release of the remaining MTE required about 5 h irradiation at this wavelength and intensity. Clearly, red light irradiation of **[4b]²⁺** released primarily the pyridine ligand, while release of the thioether was slower and required more extensive green light irradiation. Etchenique et al. have reported selective photosubstitution of nitrogen-based ligands in *cis* ruthenium complexes containing also phosphine ligands that did not participate in the photosubstitution reactivity.^[35] However, selective photosubstitution of pyridine in a ruthenium polypyridine complex containing two different photolabile ligands is, to our knowledge, unreported.

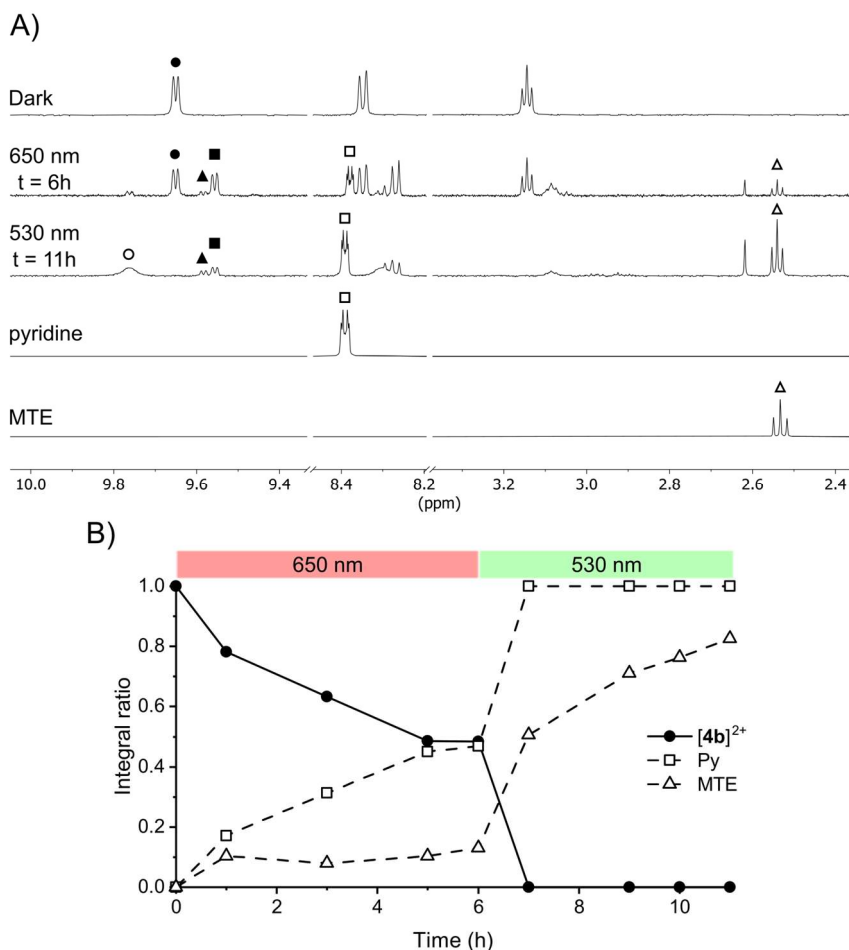


Figure 3.5 Sequential photosubstitution reactions of compound $[4b]^{2+}$ followed by $^1\text{H-NMR}$. A) $^1\text{H-NMR}$ spectra of $[4b](\text{PF}_6)_2$ (2.50 mM) measured in 1/5 acetone- $d_6/\text{D}_2\text{O}$ before irradiation (dark), following 6 h irradiation with 650 nm light ($\sim 335 \text{ mW/cm}^2$), and finally following by a second step of 5 h irradiation with 530 nm light ($\sim 150 \text{ mW/cm}^2$). B) Time evolution of the $^1\text{H-NMR}$ integral ratios. As depicted in Scheme 3.4, the symbols indicate $[4b]^{2+}$ (●), intermediates $[5b]^{2+}$ (■) and $[7b]^{2+}$ (▲), photoproduct $[8b]^{2+}$ (○) free pyridine (Py, □) and free 2-(methylthio)ethanol (MTE, Δ).

The kinetics of the four photosubstitution reactions were investigated by recording the time evolution of the absorbance spectra of a solution of $[4b](\text{PF}_6)_2$ in 1/5 acetone/ H_2O at 298 K upon light irradiation with blue (435 nm), green (505 nm) or red light (625 nm). The spectra are shown in Figure 3.6. In all cases, the $^1\text{MCLT}$ band of the complex at 459 nm showed a bathochromic shift upon light irradiation. Interestingly, two isosbestic points at 414 nm and 470 nm were only observed upon red light irradiation, indicating the existence of a single photoreaction only when using low-energy light (Figure 3.6C). With blue or green light, clearly several photosubstitution reactions occurred simultaneously as indicated by the

absence of isosbestic points. However, when a solution first irradiated for 6 h with red light was subjected to a second irradiation using green light, another bathochromic shift with a single isosbestic point at 501 nm was also observed, indicating a second one-step photosubstitution reaction (Figure 3.6D). Since the UV-Vis absorbance spectra of $[5b]^{2+}$ and $[7b]^{2+}$ were obtained through global-fitting of the UV-Vis absorbance data from $[1b]^{2+}$ and $[3b]^{2+}$, respectively, the kinetics of the individual photoreactions starting from $[4b]^{2+}$ were deconvoluted through targeted-fitting (see Appendix I for details). Besides having an influence on the photosubstitution rates, the irradiation wavelength also influenced the ratio between the intermediates $[5b]^{2+}$ and $[7b]^{2+}$ present during the experiment (insets in Figure 3.6A-D). While a ratio of ~ 2 was found using green light irradiation, blue light irradiation resulted in an intermediate ratio of 10, confirming that in these *trans* complexes the photoreactivity strongly depended on the irradiation wavelength.

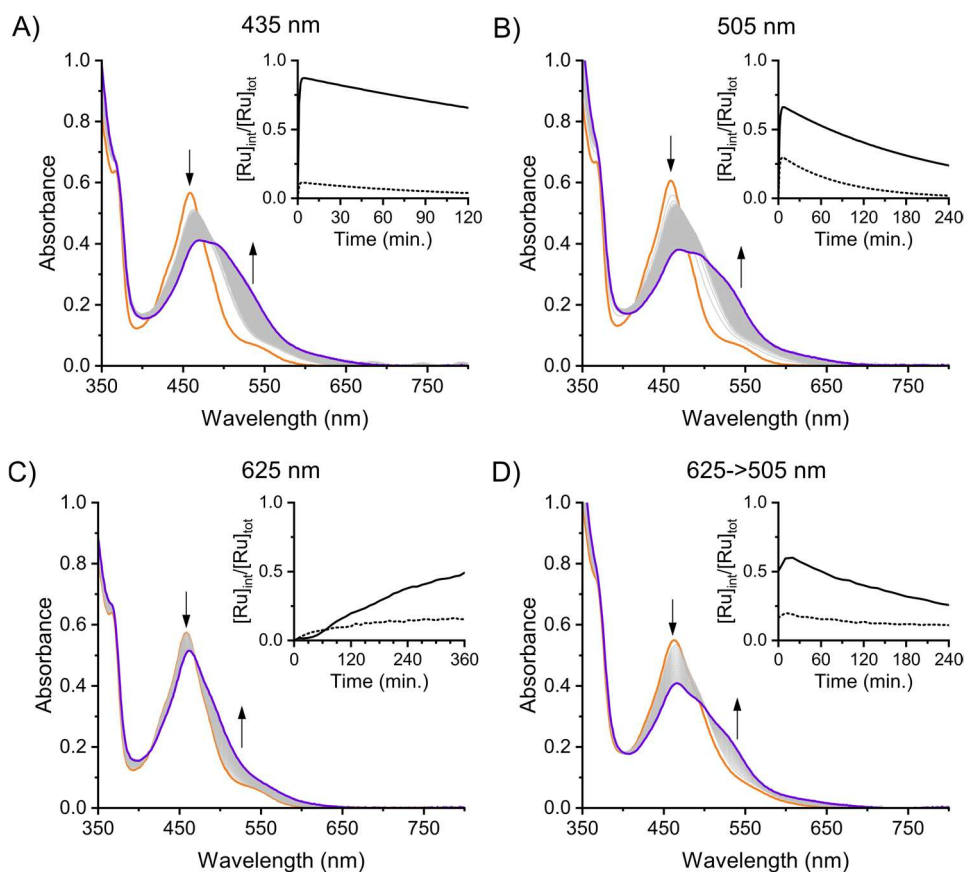


Figure 3.6 Time-evolution of the absorbance spectrum of a solution of $[4b](PF_6)_2$ in 1/5 acetone/water at 298 K irradiated with blue (435 nm, photon flux = 3.29×10^{-7} mol. s^{-1} ; A), green (505 nm, photon flux = 2.00×10^{-7} mol. s^{-1} ; B) or red (625 nm, photon flux = 4.24×10^{-7} mol. s^{-1} ; C) light. In (D), the solution was irradiated first with red (625 nm) light for 6 h, then with green (505 nm) light after a 6 h period of

irradiation with red (625 nm) light. Inset depicts the evolution of the fraction of the two intermediates $[5b]^{2+}$ (solid line) and $[7b]^{2+}$ (dotted line) over the total ruthenium concentration $[Ru]_{tot}$ during irradiation.

To quantitatively analyze the kinetics of the photoreactivity of $[4b](PF_6)_2$, the quantum yields of the four individual photosubstitution reactions were calculated using the targeted fitted data. The results are shown in Table 3.3. Most importantly, under blue light irradiation the photosubstitution of MTE ($\varphi_{1,S}$) proceeded with a quantum yield of 0.0017 while the quantum yield for pyridine substitution ($\varphi_{1,N}$) was almost one order of magnitude higher, i.e., 0.013. Similar differences in QY were also observed upon irradiation with green or red light. This selectivity towards Py substitution is in accordance with the preferred formation of intermediate $[5b]^{2+}$ observed in the 1H -NMR experiments under light irradiation (as shown in Figure 3.5 and 3.6). Although $\varphi_{1,N}$ was mostly independent from the irradiation wavelength, distinct differences in QY were observed for $\varphi_{1,S}$: a much lower value (0.0017) was found upon 435 nm irradiation than for 505 nm irradiation (0.0085). Photosubstitution of the second ligand ($\varphi_{2,S}$ or $\varphi_{2,N}$) showed much lower QYs than that of the first ligand ($\varphi_{1,S}$ or $\varphi_{1,N}$), similar as observed for symmetrical complexes $[1b]^{2+}$ and $[3b]^{2+}$. For example, upon blue light irradiation $\varphi_{2,N}$ was 0.00074 and $\varphi_{2,S}$ was 0.000048, compared with 0.0017 and 0.013 for $\varphi_{1,S}$ and $\varphi_{1,N}$, respectively. Overall, these data highlighted a highly ligand-dependent and wavelength-dependent photosubstitution quantum efficiency for this complex as well.

Table 3.3 Photosubstitution properties for Steps 1 and 2 of $[4b](PF_6)_2$ in 1/5 acetone/water at 298 K upon irradiation with blue (435 nm), green (505 nm) or red (625 nm) light including molar extinction coefficient ($\epsilon(\lambda_{irr})$, in $M^{-1}cm^{-1}$), photosubstitution quantum yield (φ_i) and photoreactivity (ζ_i , in $M^{-1}cm^{-1}$) at irradiation wavelength.^a

		$\varphi_{1,S}^b$ ($[4b]^{2+} \rightarrow [7b]^{2+}$)	$\varphi_{1,N}^b$ ($[4b]^{2+} \rightarrow [5b]^{2+}$)	$\varphi_{2,N}^c$ ($[7b]^{2+} \rightarrow [8b]^{2+}$)	$\varphi_{2,S}^c$ ($[5b]^{2+} \rightarrow [8b]^{2+}$)
435 nm	$\epsilon(\lambda_i)$	4540	4540	3800	2400
	φ_i	0.0017	0.013	0.00074	0.000048
	ζ_i	(7.9)	(61)	(1.7)	(0.18)
505 nm	$\epsilon(\lambda_i)$	1700	1700	2800	5900
	φ_i	0.0085	0.019	0.00035	0.00030
	ζ_i	(14)	(32)	(2.0)	(0.84)
625 nm	$\epsilon(\lambda_i)$	3.26	3.26	140	440
	φ_i	0.0033	0.014	0.000030	0.000037
	ζ_i	(0.011)	(0.046)	(0.013)	(0.005)

^a $\zeta_i = \epsilon(\lambda_i) \times \varphi_i$. ^b Molar extinction coefficient determined experimentally. ^c Molar extinction coefficient determined by global fitting.

3.3 Discussion

The reactivity of ruthenium compounds towards photosubstitution is dependent on many electronic and structural aspects of a ruthenium(II) polypyridyl complex including the efficiency of absorbance of irradiation, steric repulsion towards the leaving ligand and stabilization of excited states. Of all the complexes reported here, only **[3b]**²⁺, **[4b]**²⁺ and to some extent **[3a]**²⁺ were shown to undergo significant ligand photosubstitution upon red light (625 nm) irradiation even though their red-light absorbance was relatively low ($\epsilon_{600-700} < 200 \text{ M}^{-1}\text{cm}^{-1}$). In contrast, photosubstitution was not detected for previously reported *trans* bis-pyridine ruthenium(II) complexes such as $[\text{Ru}(\text{qtpy})(\text{Py})_2]^{2+}$ (qtpy = 2,2':6',2'':6'',2''':6''',2''''-quaterpyridine) upon irradiation with blue light (470 nm) in water for 9 hours.^[36] The red light photoreactivity of **[3b]**²⁺, **[4b]**²⁺ and **[3a]**²⁺ must therefore be primarily induced by the tetrapyridyl ligands HL and MeL. Still, the presence of Py is of importance since MTE and ACN show minimal red light photoreactivity. Although Py is not causing the photoreactivity, it is the most labile for photosubstitution upon red light irradiation. The main difference between the qtpy and MeL complexes is that qtpy only generates 5-membered rings upon coordination to Ru, while MeL also generates a 6-membered ring involving the bridging amine. The difference in structure appears to have major consequences on the stability of the MLCT states, although such consequences should be confirmed by an extensive computational study. Whatever the reason, the ability to undergo photosubstitution reactions under red light irradiation is a strong advantage of complexes containing the MeL ligand, notably in the field of photoactivated chemotherapy where red light reactivity is often considered as prerequisite for clinical applications.

This being said, it is also interesting to discuss the wavelength dependence of pyridine vs. thioether photosubstitution, notably in **[4b]**²⁺. The distinct photolability of Py and thioethers has been qualitatively observed in the *cis*- $[\text{Ru}(\text{bpy})_2(\text{mtmp})]^{2+}$, where the bidentate N,S-ligand 2-methylthiomethylpyridine (mtmp) was photosubstituted upon blue light irradiation.^[37] While a sequential two-step process was clearly observed, a detailed photosubstitution mechanism was not reported and in particular it remained unclear if the thioether or pyridine was photosubstituted first. In this complex, the chelating nature of mtmp also forced a *cis* geometry of both ligands, while in **[4b]**²⁺ they are *trans*. This new geometry, in combination with the availability of kinetic data for **[1b]**²⁺, **[3b]**²⁺, and **[4b]**²⁺, allowed us to investigate for the first time *trans* effects in the excited state of metal compounds (Table 3.3).

Table 3.3 Substitution photoreactivities (ζ in $M^{-1}cm^{-1}$) of pyridine and MTE depending on the *trans* ligand upon irradiation with blue, green or red light.

		<i>trans to</i>		
Ligand		Pyridine	MTE	OH ₂
435 nm	Pyridine	372	61	2.0
	MTE	7.9	430	1.1
505 nm	Pyridine	110	32	1.1
	MTE	14	18	0.39
625 nm	Pyridine	0.65	0.046	0.02
	MTE	0.011	0.00035	<0.0013

According to our new, quantitative data, the *trans* effect in the excited state appears to be dependent on the wavelength of the light used for excitation. Under green light irradiation, the Py *trans* to MTE is almost four-fold less reactive towards photosubstitution compared to Py *trans* to Py ($\zeta_{1,N} = 32$ in **[4b]**²⁺ and $\zeta_1 = 110$ in **[3b]**²⁺, respectively). This difference increases to 14-fold when irradiated with red light ($\zeta_{1,N} = 0.046$ in **[4b]**²⁺ and $\zeta_1 = 0.65$ in **[3b]**²⁺), clearly indicating irradiation wavelength dependency. As the substitution reaction only occurs upon irradiation, the difference in reactivity is expected to originate from the properties of the excited states. This is supported by the near identical bond distances between the Ru(II) center and the axial ligands observed in the crystal structures of **[4b]**(PF₆)₂, **[1b]**(PF₆)₂ and **[3b]**(PF₆)₂, showing no significant *trans*-influence in the ground state. However, excitation of polypyridyl ruthenium(II) complexes leads, after intersystem crossing, to population of a triplet Metal-to-Ligand Charge Transfer excited state (³MLCT). In this state, the polypyridyl ligand acquires a radical anion character while the metal center is formally oxidized to Ru(III), which increases interaction with σ - and π -donating ligands, while reducing the ability of the metal center to back-donate electron density into empty π^* orbitals.^[38] Thioethers are slightly σ - and π -donating ligands while pyridine is a strong σ -donating and good π -accepting ligand. In the ³MLCT state of complex **[4b]**²⁺, elongation of the Ru-Py bond is to be expected, increasing the ³MLCT state energy. This results in a decrease in the energy gap between the ³MLCT state and the triplet Metal-Centered excited state (³MC), which is the more readily thermally accessible through intersystem crossing leading to ligand dissociation. However, compared to the symmetric bis-Py complex **[3b]**²⁺, π -donation from MTE to the metal center in **[4b]**²⁺ stabilizes the ³MLCT state by enabling π -back-donation to Py. Consistent with this interpretation, Py photosubstitution occurs more efficiently in **[3b]**²⁺ than in **[4b]**²⁺.

Although ϕ_{PS} measurements at different wavelengths are rarely reported, the photosubstitution reactivity of ruthenium compounds is generally independent on excitation wavelength. For example, photosubstitution of the thioether ligand from $[\text{Ru}(\text{tpy})(\text{bpy})(\text{R-SCH}_3)]^{2+}$ has been reported with a quantum yield of 0.0055 with blue (445 nm) light and 0.0038 with green (530 nm) light in acetonitrile.^[9] However, wavelength-dependent ϕ_{PS} for the photosubstitution of L from $[\text{Ru}(\text{NH}_3)_5(\text{L})]^{2+}$ (where L is N-methylpyrazinium, isonicotinamide, pyrazine or 4-acetylpyridine) has been observed in aqueous solution.^[39] For chromium complexes this wavelength-dependent effect on photosubstitution and excited-state dynamics has been revealed through transient absorbance spectroscopy.^[40,41] A more recent, detailed study on the photophysics of a series of binuclear d^8d^8 di-isocyanide complexes with either Rh(I) or Ir(I), revealed specific relaxation cascades depending on the excitation wavelength.^[42] For the symmetrical complexes reported here, excitation-wavelength dependency was only observed for **MeL** complexes $[\mathbf{1b}]^{2+}$ – $[\mathbf{3b}]^{2+}$, with increasing ϕ_{PS} between 2- and 6-fold upon blue light irradiation compared to green or red light depending on the axial ligands. While the available data does not provide clear evidence for a specific photophysical mechanism, the correlation between ϕ_{PS} and excitation wavelength suggests more efficient population of the ^3MC state from higher MLCT_n states, leading to more efficient photosubstitution (Figure 3.7). Since this effect is not observed for the **HL** complexes $[\mathbf{1a}]^{2+}$ – $[\mathbf{3a}]^{2+}$, the **MeL** ligand possibly stabilizes MLCT states through its increased electron-donating character and rigidity, allowing for direct population of the ^3MC state from higher $^3\text{MLCT}_n$ states. While this photophysical mechanism remains a hypothesis, time-resolved spectroscopy combined with density-functional theory might provide more insight.

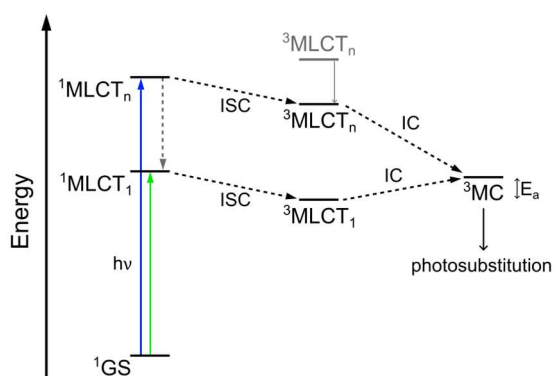


Figure 3.7 Proposed Jablonski diagram for the excited state energy levels that are involved during photosubstitution of axial ligands from the **MeL** containing complexes $[\mathbf{1b}]^{2+}$ – $[\mathbf{3b}]^{2+}$. Upon green light irradiation, the energetically lowest singlet Metal-to-Ligand-Charge-Transfer state ($^1\text{MLCT}_1$) is populated that, after intersystem crossing (ISC), converts to the $^3\text{MLCT}_1$ state and finally the dissociative triplet Metal-Centered state (^3MC) via internal conversion (IC). Excitation with blue light to higher $^1\text{MLCT}_n$ states however, can lead to population of $^3\text{MLCT}_n$ states that are accessible and can

directly convert to the ^3MC state. As the IC from $^3\text{MLCT}_1$ to the ^3MC occurs thermally, an energy barrier (E_a) has to be overcome. This is not the case from the $^3\text{MLCT}_n$ states as the conversion is energetically favorable, which leads to more efficient photosubstitution.

3.4 Conclusion

In this work, we successfully synthesized a series of *trans* ruthenium(II) complexes based on the tetrapyrrolyl ligand **HL** ($[\mathbf{1a}]^{2+} - [\mathbf{3a}]^{2+}$) and its *N*-methyl analogue **MeL** ($[\mathbf{1b}]^{2+} - [\mathbf{3b}]^{2+}$). This ligand occupies the basal plane of an octahedron, leaving two *trans* axial positions for the coordination of monodentate ligands L' and L'' such as thioethers (MTE), acetonitrile (ACN), and pyridine (Py), resulting in symmetrical complexes $[\mathbf{1a,b}]^{2+} - [\mathbf{3a,b}]^{2+}$ ($L'=L''$). Additionally, dissymmetric complex $[\mathbf{4b}]^{2+}$ containing both MTE and Py as axial ligands ($L' \neq L''$), was prepared by red light irradiation (650 nm) of $[\mathbf{3b}]^{2+}$ in presence of MTE. The crystal structure of $[\mathbf{4b}]^{2+}$ did not reveal significant differences in bond distances, angles or geometrical distortion compared to symmetric complexes $[\mathbf{1b}]^{2+}$ and $[\mathbf{3b}]^{2+}$, suggesting the absence of a *trans* influence in the ground state. The photochemical properties of the complexes were characterized by UV-Vis absorbance and $^1\text{H-NMR}$ spectrometry, which revealed significant differences in photoreactivity. For the ACN complexes $[\mathbf{2a,b}]^{2+}$, both substitution reactions occurred with similar rates when irradiated with blue (435 nm) or green (505 nm) light in 1/5 acetone/ H_2O . In contrast, substitution of the second MTE in $[\mathbf{1a,b}]^{2+}$ and pyridine in $[\mathbf{3a,b}]^{2+}$ occurred much less efficient than the first one in the same conditions. For the symmetrical complexes, red light (625 nm) irradiation only resulted in photosubstitution of the axial ligands in bis-Py complexes $[\mathbf{3a,b}]^{2+}$. Interestingly, the **MeL** containing complexes $[\mathbf{1-3b}]^{2+}$ showed higher photosubstitution quantum yields upon blue light irradiation than for green or red light, indicating excitation-wavelength dependency of the quantum efficiency of the photoreaction.

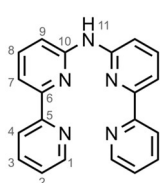
Visible-light induced photosubstitution of both MTE and Py ligands in $[\mathbf{4b}]^{2+}$, was shown to proceed to the bis-aqua photoproduct $[\mathbf{8b}]^{2+}$ via the formation of intermediates $[\mathbf{5b}]^{2+}$ ($L'=\text{MTE}; L''=\text{OH}_2$) as well as $[\mathbf{7b}]^{2+}$ ($L'=\text{OH}_2; L''=\text{Py}$). Targeted fitting of the time-evolution UV-Vis absorbance data, allowed for the determination of the photosubstitution quantum yields of each individual step. While photosubstitution of both ligands was observed with blue or green light, the kinetic data revealed selectivity towards Py over MTE substitution from $[\mathbf{4b}]^{2+}$, depending on the irradiation wavelength. Strikingly, red light (625 nm) irradiation resulted in a 4-fold increase in Py photosubstitution quantum yield. The wavelength-dependent photosubstitution selectivity of $[\mathbf{4b}]^{2+}$ enabled for sequential release of pyridine with red light, followed by MTE release with green light. These first-in-class results open unprecedented opportunities in the field of photoactivated chemotherapy, where two inhibitors based on thioether and pyridine may be released sequentially using light of different color.

3.5 Experimental

3.5.1 General information

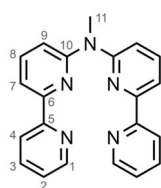
Unless otherwise noted, all reagents and solvents were purchased from commercial suppliers (Fluorochem, Sigma-Aldrich, BLDPharm, VWR, TCI) and used without further purification. [2,2'-bipyridine]-6-amine was synthesized according to the procedure reported in Chapter 2.^[43] Anhydrous and oxygen-free solvents were obtained using common distillation, drying (activated 4 Å molecular sieves) and degassing (freeze-pump-thaw method) procedures. The reactions were carried under air unless stated otherwise. The standard Schlenk technique was used for the reactions that were carried out under nitrogen atmosphere. Filters used were Whatman® regenerated cellulose membrane filters, RC60 Membrane circles, diam. 47 mm, pore size 1 µm. TLCs were performed using either Supelco analytical silica gel on Al foils with fluorescence indicator 254 nm or Supelco analytical aluminum oxide 60 with fluorescence indicator 254 nm. Column chromatography was carried on silica gel (40-63 µm) or on activated neutral aluminum oxide (Brockmann Grade I) from VWR Chemicals. The microwave tubes (product number: 351521) were purchased from Biotage (Uppsala, Sweden) and heated using Thermo Scientific™ Reacti-block™ T-1 (9 holes; dimensions: 17mm diameter × 45 mm deep). All synthesized ruthenium complexes were stored at room temperature and protected from light. NMR spectra were recorded on Bruker Avance 300, 400 or 500 MHz and the FIDs were treated with MestReNova software. The chemical shifts are given relative to the residual signal of the solvent (Acetone-d₆: δ (¹H) = 2.05 ppm, δ (¹³C) = 29.84 ppm; CDCl₃: δ (¹H) = 7.26 ppm, δ (¹³C) = 77.16 ppm; DMSO-d₆: δ (¹H) = 2.50 ppm, δ (¹³C) = 39.52 ppm), or relative to an external standard (TMS: δ (¹H) = 0 ppm, δ (¹³C) = 0 ppm). The mass spectra were recorded in methanol (UPLC grade) with 1% (v/v) of formic acid on a Shimadzu LCMS-2020 (ESI-Q). The high-resolution mass spectra (HRMS) were recorded on a Thermo Finnigan LTQ Orbitrap.

3.5.2 Synthesis



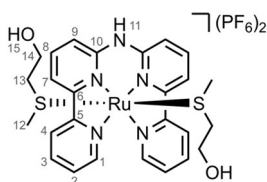
di([2,2'-bipyridin]-6-yl)amine, HL: In a 250 mL two-necked flask was transferred 6-bromo-2,2'-bipyridine (3.32 g, 14.02 mmol, 1.0 eq), [2,2'-bipyridine]-6-amine (2.42 g, 14.02 mmol, 1.0 eq), palladium bis(dibenzylideneacetone) (660 mg, 1.121 mmol, 0.08 eq), 1,3-bis(diphenylphosphino)propane (469 mg, 1.121 mmol, 0.08 eq) and sodium tert-butoxide (1.905 g, 19.63 mmol, 1.4 eq). The flask was purged with nitrogen by cycling three times between vacuum and nitrogen. After 140 mL of toluene, the mixture was stirred at 80 °C and the reaction progress was followed by TLC (Alumina; 1 : 1 EtOAc : toluene). Once the amine and bromide starting materials were both consumed (after 22 h), the mixture was allowed to cool to RT. 50 mL of H₂O was added and stirred for 1 hour. The layers were separated and the aqueous phase was extracted with DCM (3 x 200

mL). The combined organic layers were washed with brine (200 mL), dried with MgSO₄ and concentrated in vacuo. The resulting crude was purified by column chromatography (Alumina; 10 – 40% EtOAc : toluene) yielding the target compound as an off-white powder (4.33 g, 13.3 mmol, 95%). Analysis was consistent with previous reports.^[26] ¹H NMR (400 MHz, DMSO-d₆) δ 9.91 (s, 1H, H¹¹), 8.69 (ddd, *J* = 4.8, 1.8, 0.9 Hz, 2H, H¹), 8.38 (dt, *J* = 7.9, 1.1 Hz, 2H, H⁴), 8.01 – 7.96 (m, 2H, H³), 7.95 – 7.85 (m, 6H, H⁷, H⁸, H⁹), 7.45 (ddd, *J* = 7.5, 4.7, 1.2 Hz, 2H, H²). ¹³C{¹H} NMR (101 MHz, DMSO-d₆) δ 155.47 (C⁵), 153.86 (C¹⁰), 153.43 (C⁶), 149.29 (C¹), 138.74 (C⁷, C⁸, C⁹), 137.28 (C³), 124.00 (C²), 120.38 (C⁴), 112.84 (C⁷, C⁸, C⁹), 112.32 (C⁷, C⁸, C⁹). ESI-MS: exact *m/z* calculated for [C₂₀H₁₅N₅ + H⁺]⁺: 326.1 *m/z*, found: 326.2 *m/z*.



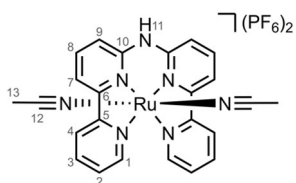
N-bis([2,2'-bipyridin]-6-yl)-N-methylamine, MeL: Potassium hydroxide (3.45 g, 61.5 mmol, 10 eq) was added to a solution of di([2,2'-bipyridin]-6-yl)amine **L** (2.0 g, 6.15 mmol, 1.0 eq) in 60 mL DMSO and the mixture was stirred at RT. After 1.5 hours, iodomethane (2.3 mL, *d* = 0.461 g/mL, 7.38 mmol, 1.2 eq) was added and stirred for another 2 hours. The reaction was

quenched with 150 mL H₂O and extracted with toluene (5 x 150 mL). The combined organic phase was dried with MgSO₄ and concentrated in vacuo. Purified by flash column chromatography (Alumina; 10 – 50% EtOAc : Toluene + 0.5% Et₃N) yielded the product as an off-white powder (1.78 g, 5.26 mmol, 85%). Analysis was consistent with previous reports.^[44] ¹H NMR (400 MHz, DMSO-d₆) δ 8.68 (ddd, *J* = 4.8, 1.8, 0.9 Hz, 2H, H¹), 8.31 (dt, *J* = 8.0, 1.1 Hz, 2H, H⁴), 8.00 (dd, *J* = 7.5, 0.8 Hz, 2H, H⁷), 7.94 (td, *J* = 7.7, 1.8 Hz, 2H, H³), 7.86 (dd, *J* = 8.3, 7.5 Hz, 2H, H⁸), 7.46 – 7.39 (m, 4H, H², H⁹), 3.75 (s, 3H, H¹¹). ¹³C{¹H} NMR (101 MHz, DMSO-d₆) δ 156.48 (C¹⁰), 155.29 (C⁵), 153.47 (C⁶), 149.25 (C¹), 138.59 (C⁸), 137.30 (C³), 124.08 (C²), 120.38 (C⁴), 114.59 (C⁹), 113.67 (C⁷), 35.67 (C¹¹). ESI-MS: exact *m/z* calculated for [C₂₁H₁₇N₅ + H⁺]⁺: 340.2 *m/z*, found: 340.2 *m/z*.



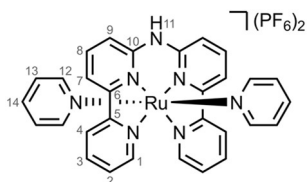
[Ru(L)(MTE)₂](PF₆)₂, [1a](PF₆)₂: To a 50 mL two-necked flask was added **L** (100 mg, 0.31 mmol, 1 eq), Ru(DMSO)₄Cl₂ (150 mg, 0.31 mmol, 1 eq) and the flask was purged with nitrogen by cycling three times between vacuum and nitrogen. After addition of 2-(methylthio)ethanol (8.0 mL, *d* = 1.06 g/mL, 92 mmol), the mixture was stirred at 150 °C while monitoring the reaction progress by TLC (SiO₂; acetone : H₂O : aq. saturated KPF₆, 10 : 1 : 1). After 72 hours, the mixture was cooled to RT and precipitated in a 100 mL half saturated aqueous KPF₆ solution. The precipitate was filtered over a membrane filter and washed with a minimal amount of half saturated aqueous KPF₆ followed by diethyl ether. Drying under high vacuum yielded the product as a

brown powder (196 mg, 0.22 mmol, 71%). Brown/red single crystals suitable for X-ray diffraction were obtained using vapor diffusion of diethyl ether into a solution of **[1a]**(PF₆)₂ in 1:1 THF/acetone. ¹H NMR (500 MHz, Acetone-*d*₆) δ 11.38 (s, 1H, H¹¹), 9.92 (ddd, *J* = 5.7, 1.4, 0.7 Hz, 2H, H¹), 8.96 (dt, *J* = 8.2, 1.1 Hz, 2H, H⁴), 8.63 (dd, *J* = 7.9, 0.9 Hz, 2H, H⁷), 8.45 (ddd, *J* = 8.1, 7.5, 1.4 Hz, 2H, H³), 8.38 (dd, *J* = 8.4, 7.7 Hz, 2H, H⁸), 8.07 (ddd, *J* = 7.4, 5.7, 1.4 Hz, 2H, H²), 7.83 (dd, *J* = 8.4, 1.0 Hz, 2H, H⁹), 3.75 (t, *J* = 5.2 Hz, 2H, H¹⁵), 3.28 (q, *J* = 5.6 Hz, 4H, H¹⁴), 1.77 (t, *J* = 5.8 Hz, 4H, H¹³), 1.34 (s, 6H, H¹²). ¹³C{H} NMR (126 MHz, Acetone-*d*₆) δ 158.35 (C¹⁰), 156.04 (C⁵), 154.69 (C¹), 150.27 (C⁶), 139.87 (C³), 138.94 (C⁸), 128.36 (C²), 125.40 (C⁴), 118.91 (C⁷), 117.45 (C⁹), 59.00 (C¹⁴), 37.91 (C¹³), 16.00 (C¹²). ESI-MS: exact *m/z* calculated for [C₂₆H₃₁N₅O₂RuS₂]²⁺: 305.6 *m/z*, found: 305.3 *m/z*. Elemental analysis (%) for compound **[1a]**(PF₆)₂ (C₂₆H₃₁F₁₂N₅O₂P₂RuS₂), calculated C, 34.67; H, 3.47; N, 7.78; found C, 34.28; H, 3.41; N, 7.63. UV-Vis (1/5 H₂O/acetone): λ_{max} (ε): 440 nm (5.1 × 10³ M⁻¹cm⁻¹).



[Ru(L)(ACN)₂](PF₆)₂, [2a](PF₆)₂: A solution of **[1a]**(PF₆)₂ (61 mg, 0.068 mmol, 1 eq) in ACN (6.5 mL, 0.10 M) was stirred at 80 °C under N₂. The conversion was monitored by TLC (SiO₂; acetone : H₂O : aq. saturated KPF₆, 10 : 1 : 1). After 5 days, the mixture was cooled to RT and precipitated in a 60 mL half

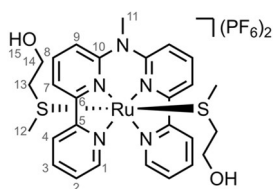
saturated aqueous KPF₆ solution. The precipitate was filtered over a membrane filter and washed with a minimal amount of half saturated aqueous KPF₆ followed by diethyl ether. Drying under high vacuum yielded the product as a brown powder (43 mg, 0.054 mmol, 79%). ¹H NMR (500 MHz, Acetone-*d*₆) δ 11.30 (s, 1H, H¹¹), 9.88 (d, *J* = 5.6 Hz, 2H, H¹), 8.89 (d, *J* = 8.0 Hz, 2H, H⁴), 8.55 (d, *J* = 8.0 Hz, 2H, H⁷), 8.42 (td, *J* = 7.8, 1.4 Hz, 2H, H³), 8.34 (t, *J* = 8.0 Hz, 2H, H⁸), 8.02 (ddd, *J* = 7.3, 5.5, 1.4 Hz, 2H, H²), 7.79 (dd, *J* = 8.4, 0.9 Hz, 2H, H⁹), 1.98 (s, 6H, H¹³). ¹³C{H} NMR (126 MHz, Acetone-*d*₆) δ 158.74 (C¹⁰), 156.75 (C⁵), 154.55 (C¹), 150.63 (C⁶), 139.62 (C³), 138.94 (C⁸), 127.58 (C²), 125.71 (C¹²), 124.52 (C⁴), 117.80 (C⁷), 116.66 (C⁹), 3.28 (C¹³). ESI-MS: exact *m/z* calculated for [C₂₄H₂₁N₇Ru]²⁺: 254.5 *m/z*, found: 254.2 *m/z* and [C₂₄H₂₁N₇Ru - H]⁺: 508.1 *m/z*, found: 508.0 *m/z*. Elemental analysis (%) for compound **[2a]**(PF₆)₂ (C₂₄H₂₁F₁₂N₇P₂Ru), calculated C, 36.10; H, 2.65; N, 12.28; found C, 35.18; H, 2.68; N, 11.91. UV-Vis (1/5 H₂O/acetone): λ_{max} (ε): 429 nm (7.0 × 10³ M⁻¹cm⁻¹).



[Ru(L)(Py)₂](PF₆)₂, [3a](PF₆)₂: A solution of **[1a]**(PF₆)₂ (55 mg, 0.061 mmol, 1 eq) in pyridine (6.0 mL, 0.10 M) was stirred at 115 °C under N₂. The conversion was monitored by TLC (SiO₂; acetone : H₂O : aq. saturated KPF₆, 10 : 1 : 1). After 24 hours, the mixture was cooled to RT and precipitated in a 60 mL half

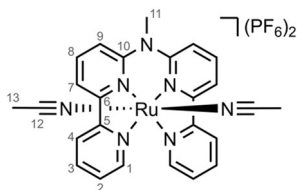
saturated aqueous KPF₆ solution. The precipitate was filtered over a membrane filter and washed with a minimal amount of half saturated aqueous KPF₆ followed by diethyl ether. Drying under high vacuum yielded the product as a red powder (50 mg, 0.054 mmol, 93%).

^1H NMR (500 MHz, DMSO- d_6) δ 12.35 (s, 1H, H¹¹), 9.97 (d, J = 6.2 Hz, 2H, H¹), 8.75 (d, J = 8.1 Hz, 2H, H⁴), 8.45 (d, J = 7.7 Hz, 2H, H⁷), 8.30 – 8.22 (m, 4H, H³, H⁸), 8.02 (ddd, J = 7.2, 5.6, 1.3 Hz, 2H, H²), 7.85 (d, J = 8.4 Hz, 2H, H⁹), 7.59 – 7.52 (m, 6H, H¹², H¹⁴), 7.02 (dd, J = 8.1, 6.0 Hz, 4H, H¹³). $^{13}\text{C}\{^1\text{H}\}$ NMR (126 MHz, DMSO- d_6) δ 156.85 (C¹⁰), 154.77 (C⁵), 153.32 (C¹), 151.85 (C¹²), 148.47 (C⁶), 138.32 (C³), 137.57 (C¹⁴), 137.03 (C⁸), 127.35 (C²), 125.76 (C¹³), 123.71 (C⁴), 117.39 (C⁷), 116.61 (C⁹). ESI-MS: exact m/z calculated for $[\text{C}_{30}\text{H}_{25}\text{N}_7\text{Ru}]^{2+}$: 292.6 m/z , found: 292.5 m/z and $[\text{C}_{30}\text{H}_{25}\text{N}_7\text{Ru} - \text{H}^+]$: 584.1 m/z , found: 584.2 m/z . Elemental analysis (%) for compound **[3a]**(PF₆)₂ (C₃₀H₂₅F₁₂N₇P₂Ru), calculated C, 41.20; H, 2.88; N, 11.21; found C, 40.64; H, 2.91; N, 11.03. UV-Vis (1/5 H₂O/acetone): λ_{max} (ϵ): 486 nm ($7.0 \times 10^3 \text{ M}^{-1}\text{cm}^{-1}$).



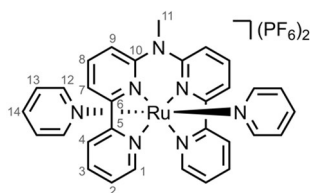
[Ru(MeL)(MTE)₂](PF₆)₂, [1b](PF₆)₂: To a 100 mL two-necked flask was added **MeL** (337 mg, 1 mmol, 1 eq), Ru(DMSO)₄Cl₂ (480 mg, 1 mmol, 1 eq) and the flask was purged with nitrogen by cycling three times between vacuum and nitrogen. After addition of 2-(methylthio)ethanol (2.2 mL, $d = 1.06 \text{ g/mL}$, 25 mmol, 25 eq) and

methanol (20 mL), the mixture was stirred at 150 °C while monitoring the reaction progress by TLC (SiO₂; acetone : H₂O : aq. saturated KPF₆, 10 : 1 : 1). After 48 hours, the mixture was cooled to RT and precipitated in a 100 mL half saturated aqueous KPF₆ solution. The precipitate was filtered over a membrane filter and washed with a minimal amount of half saturated aqueous KPF₆ followed by diethyl ether. Drying under high vacuum yielded the product as a brown-orange powder (823 mg, 0.90 mmol, 90%). Pale orange needle-shaped single crystals suitable for X-ray diffraction were obtained using vapor diffusion of diethyl ether into a solution of **[1b]**(PF₆)₂ in acetone containing 5 molar equivalents of triphenylphosphine oxide. ^1H NMR (400 MHz, Acetone- d_6) δ 9.85 (ddd, J = 5.7, 1.6, 0.8 Hz, 2H, C¹), 8.92 (dt, J = 8.1, 1.1 Hz, 2H, C⁴), 8.66 (dd, J = 7.9, 0.9 Hz, 2H, H⁷), 8.47 – 8.37 (m, 4H, H³, H⁸), 8.08 – 7.99 (m, 4H, H², H⁹), 4.22 (s, 3H, H¹¹), 3.75 (t, J = 5.2 Hz, 2H, H¹⁵), 3.27 (q, J = 5.5 Hz, 4H, H¹⁴), 1.80 (t, J = 5.8 Hz, 4H, H¹³), 1.36 (s, 6H, H¹²). $^{13}\text{C}\{^1\text{H}\}$ NMR (101 MHz, Acetone- d_6) δ 158.56 (C¹⁰), 156.80 (C⁵), 156.26 (C⁶), 154.60 (C¹), 140.10 (C³), 139.18 (C⁸), 128.49 (C²), 125.61 (C⁴), 119.52 (C⁷), 119.10 (C⁹), 59.09 (C¹⁴), 44.85 (C¹¹), 38.29 (C¹³), 16.38 (C¹²). ESI-MS: exact m/z calculated for $[\text{C}_{27}\text{H}_{33}\text{N}_5\text{O}_2\text{RuS}_2]^{2+}$: 312.6 m/z , found: 312.1 m/z . Elemental analysis (%) for compound **[1b]**(PF₆)₂ (C₂₇H₃₃F₁₂N₅O₂P₂RuS₂), calculated C, 35.45; H, 3.64; N, 7.66; found C, 35.30; H, 3.68; N, 7.61. UV-Vis (1/5 H₂O/acetone): λ_{max} (ϵ): 447 nm ($6.5 \times 10^3 \text{ M}^{-1}\text{cm}^{-1}$).



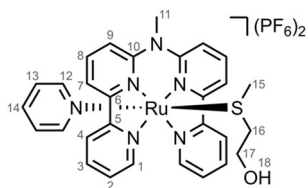
[Ru(MeL)(ACN)₂](PF₆)₂, [2b](PF₆)₂: **[1b]**(PF₆)₂ (120 mg, 0.13 mmol, 1 eq) was added to an 8 mL microwave tube. The tube was sealed with a crimp cap and purged with nitrogen by cycling three times between vacuum and nitrogen. After addition of acetonitrile (1.31 mL, $d = 0.786 \text{ g/mL}$, 25.0 mmol,

190 eq), the mixture was stirred at 80 °C while monitoring the reaction progress by TLC (SiO₂; acetone : H₂O : aq. saturated KPF₆, 8 : 1 : 1). After 48 hours, the mixture was cooled to RT and precipitated in a 100 mL half saturated aqueous KPF₆ solution. The precipitate was filtered over a membrane filter and washed with a minimal amount of half saturated aqueous KPF₆ followed by diethyl ether. Drying under high vacuum resulted the crude product. Further purification by column chromatography (SiO₂; acetone : H₂O : aq. saturated KPF₆, 8 : 1 : 1) yielded the pure product as an orange-brown powder (49 mg, 0.06 mmol, 46%). Orange single crystals suitable for X-ray diffraction were obtained using vapor diffusion of diethyl ether into a solution of **[2b]**(PF₆)₂ in acetone. ¹H NMR (400 MHz, Acetone-*d*₆) δ 9.81 (ddd, *J* = 5.6, 1.5, 0.7, 2H, H¹), 8.85 (dt, *J* = 8.2, 1.0 Hz, 2H, H⁴), 8.57 (dd, *J* = 7.9, 0.9 Hz, 2H, H⁷), 8.44 – 8.34 (m, 4H, H³, H⁸), 8.05 – 7.94 (m, 4H, H², H⁹), 4.19 (s, 3H, H¹¹), 1.99 (s, 6H, H¹³). ¹³C{¹H} NMR (101 MHz, Acetone-*d*₆) δ 158.95 (C¹⁰), 157.38 (C⁵), 156.57 (C⁶), 154.48 (C¹), 139.86 (C³), 139.24 (C⁸), 127.72 (C²), 125.59 (C¹²), 124.79 (C⁴), 118.49 (C⁷), 118.23 (C⁹), 44.75 (C¹¹), 3.24 (C¹³). ESI-MS: exact *m/z* calculated for [C₂₅H₂₃N₇Ru]²⁺: 261.5 *m/z*, found: 261.2 *m/z* and [C₂₅H₂₃N₇Ru + PF₆]⁺: 668.1 *m/z*, found: 668.0 *m/z*. Elemental analysis (%) for compound **[2b]**(PF₆)₂ (C₂₅H₂₃F₁₂N₇P₂Ru), calculated C, 36.96; H, 2.85; N, 12.07; found C, 36.78; H, 2.86; N, 11.97. UV-Vis (1/5 H₂O/acetone): λ_{max} (ε): 434 nm (6.5 × 10³ M⁻¹cm⁻¹).



[Ru(MeL)(Py)₂](PF₆)₂, **[3b]**(PF₆)₂: **[1b]**(PF₆)₂ (250 mg, 0.273 mmol, 1 eq) was added to an 8 mL microwave tube. The tube was sealed with a crimp cap and with nitrogen by cycling three times between vacuum and nitrogen. After addition of pyridine (2.75 mL, *d* = 0.982 g/mL, 34.2 mmol, 125 eq), the mixture was stirred at 115 °C while monitoring the reaction progress by TLC (SiO₂; acetone : H₂O : aq. saturated KPF₆, 10 : 1 : 1). After 48 hours, the mixture was cooled to RT and precipitated in a 250 mL half saturated aqueous KPF₆ solution. The precipitate was filtered over a membrane filter and washed with a minimal amount of half saturated aqueous KPF₆ followed by diethyl ether. Drying under high vacuum yielded the product as a red powder (188 mg, 0.21 mmol, 77%). Red needle-shaped single crystals suitable for X-ray diffraction were obtained using vapor diffusion of diethyl ether into a solution of **[3b]**(PF₆)₂ in acetone. ¹H NMR (400 MHz, Acetone-*d*₆) δ 10.06 (d, *J* = 5.6 Hz, 2H, H¹), 8.73 (d, *J* = 8.1 Hz, 2H, H⁴), 8.48 (d, *J* = 7.7 Hz, 2H, H⁷), 8.32 (dt, *J* = 10.6, 7.8 Hz, 4H, H³, H⁸), 8.10 – 8.03 (m, 4H, H², H⁹), 7.78 – 7.73 (m, 4H, H¹²), 7.63 (dd, *J* = 8.5, 7.0 Hz, 2H, H¹⁴), 7.02 (t, *J* = 6.9 Hz, 4H, H¹³), 4.15 (s, 3H, H¹¹). ¹³C{¹H} NMR (101 MHz, Acetone-*d*₆) δ 158.65 (C¹⁰), 157.18 (C⁵), 156.11 (C⁶), 154.17 (C¹), 153.07 (C¹²), 139.67 (C³), 138.49 (C⁸), 138.45 (C¹⁴), 128.65 (C²), 126.53 (C¹³), 125.11 (C⁴), 119.17 (C⁷), 119.13 (C⁹), 44.27 (C¹¹). ESI-MS: exact *m/z* calculated for [C₃₁H₂₇N₇Ru]²⁺: 299.6 *m/z*, found: 299.5 *m/z* and [C₃₁H₂₇N₇Ru + PF₆]⁺: 744.1 *m/z*, found: 744.1 *m/z*. Elemental analysis (%) for compound **[3b]**(PF₆)₂ (C₃₁H₂₇F₁₂N₇P₂Ru), calculated C,

41.90; H, 3.06; N, 11.03; found C, 41.58; H, 3.04; N, 10.97. UV-Vis (1/5 H₂O/acetone): λ_{\max} (ϵ): 485 nm ($7.1 \times 10^3 \text{ M}^{-1}\text{cm}^{-1}$).



[Ru(MeL)(Py)(MTE)](PF₆)₂, [4b](PF₆)₂: [3b](PF₆)₂ (148 mg, 0.17 mmol, 1 eq) in 50 mL acetone and 17 mL of a 100 mM solution of 2-(methylthio)ethanol (1.7 mmol, 10 eq) in acetone were added under nitrogen to a 140 mL double-walled photoreactor with water cooling (see Figure I.1).

Acetone was added to a total volume of 125 mL and the reaction mixture was irradiated with a 650 nm LED lamp at RT while monitoring the reaction progress by TLC (SiO₂; acetone : H₂O : aq. saturated KPF₆, 10 : 1 : 1). After 1 hour, the mixture was concentrated *in vacuo* and precipitated in diethyl ether. The precipitate was filtered over a membrane filter and washed with diethyl ether. The mixture was purified by column chromatography (SiO₂; acetone : H₂O : aq. saturated KPF₆, 8 : 1 : 1). The product containing fractions were combined and concentrated, followed by precipitation in 100 mL half saturated aqueous KPF₆. After filtration over a membrane filter, the product was washed with a minimal amount of water followed by diethyl ether. Drying under high vacuum yielded the product as an orange powder (95 mg, 0.10 mmol, 63%). Red/brown needle-shaped single crystals suitable for X-ray diffraction were obtained using vapor diffusion of diethyl ether into a solution of **[4b](PF₆)₂** in acetone/THF (1:1). ¹H NMR (400 MHz, Acetone-*d*₆) δ 10.05 (ddd, *J* = 5.6, 1.5, 0.8 Hz, 2H, H¹), 8.70 (dt, *J* = 8.1, 1.2 Hz, 2H, H⁴), 8.46 (dd, *J* = 7.8, 0.9 Hz, 2H, H⁷), 8.31 – 8.31 (m, 4H, H³, H⁸), 8.13 – 8.04 (m, 4H, H², H⁹), 7.73 – 7.68 (m, 2H, H¹²), 7.60 (tt, *J* = 7.6, 1.5 Hz, 1H, H¹⁴), 6.99 (dd, *J* = 7.6, 6.6 Hz, 2H, H¹³), 4.27 (s, 3H, H¹¹), 3.80 (t, *J* = 5.2 Hz, 1H, H¹⁸), 3.37 (td, *J* = 5.8, 4.9 Hz, 2H, H¹⁷), 1.59 (s, 3H, H¹⁵). ¹³C{¹H} NMR (101 MHz, Acetone-*d*₆) δ 158.47 (C¹⁰), 156.90 (C⁵), 156.20 (C⁶), 154.38 (C¹), 151.82 (C¹²), 139.89 (C³), 139.22 (C¹⁴), 138.94 (C⁸), 128.69 (C²), 126.82 (C¹³), 125.09 (C⁴), 119.32 (C⁹), 119.17 (C⁷), 59.32 (C¹⁷), 44.44 (C¹¹), 39.77 (C¹⁶), 17.85 (C¹⁵). ESI-HRMS: exact *m/z* calculated for [C₂₉H₃₀N₆ORuS]²⁺: 306.0621 *m/z*, found: 306.0617 *m/z*. Elemental analysis (%) for compound **[4b](PF₆)₂** (C₂₉H₃₀F₁₂N₇OP₂RuS), calculated C, 38.63; H, 3.35; N, 9.32; found C, 38.53; H, 3.34; N, 9.30. UV-Vis (1/5 H₂O/acetone): λ_{\max} (ϵ): 459 nm ($7.3 \times 10^3 \text{ M}^{-1}\text{cm}^{-1}$).

3.5.3 Single crystal X-ray crystallography

Detailed crystallographic data are provided in appendix III.1.

3.5.4 Photochemistry

Molar absorption coefficient determination

Molar absorption coefficients were determined as described in appendix I.2.1. Results for the compounds reported in this chapter are provided in appendix III.2.1.

Photosubstitution quantum yield measurements

Photon fluxes of all LEDs were determined using ferrioxalate actinometry and is described in detail in appendix I.2.2. The photosubstitution quantum yields were determined as described in appendix I.2.3.

Photosubstitution followed by $^1\text{H-NMR}$

The $^1\text{H-NMR}$ photosubstitution experiments were performed as described in appendix I.2.6. Results for the compounds reported in this chapter are provided in appendix III.2.3.

3.6 References

- (1) Papish, E. T.; Oladipupo, O. E. *Current Opinion in Chemical Biology* **2022**, *68*, 102143.
- (2) Campagna, S.; Puntoriero, F.; Nastasi, F.; Bergamini, G.; Balzani, V. Photochemistry and Photophysics of Coordination Compounds: Ruthenium. In *Photochemistry and Photophysics of Coordination Compounds I*; Balzani, V., Campagna, S., Eds.; Topics in Current Chemistry; Springer Berlin Heidelberg: Berlin, Heidelberg, 2007; Vol. 280, 117–214.
- (3) White, J. K.; Schmehl, R. H.; Turro, C. *Inorganica Chimica Acta* **2017**, *454*, 7–20.
- (4) Bonnet, S. *J. Am. Chem. Soc.* **2023**, *145* (43), 23397–23415.
- (5) L. N. Lameijer, D. Ernst, S. L. Hopkins, M. S. Meijer, S. H. C. Askes, S. E. Le Dévédec, S. Bonnet, *Angew. Chem. Int. Ed.* **2017**, *56*, 11549–11553.
- (6) D. Havrylyuk, A. C. Hachey, A. Fenton, D. K. Heidary, E. C. Glazer, *Nat. Commun.* **2022**, *13*, 3636.
- (7) Respondek, T.; Sharma, R.; Herroon, M. K.; Garner, R. N.; Knoll, J. D.; Cueny, E.; Turro, C.; Podgorski, I.; Kodanko, J. J. *ChemMedChem* **2014**, *9* (6), 1306–1315.
- (8) Filevich, O.; Etchenique, R. *Photochem Photobiol Sci* **2013**, *12* (9), 1565–1570.
- (9) Van Rixel, V. H. S.; Ramu, V.; Auyeung, A. B.; Beztsinna, N.; Leger, D. Y.; Lameijer, L. N.; Hilt, S. T.; Le Dévédec, S. E.; Yildiz, T.; Betancourt, T.; Gildner, M. B.; Hudnall, T. W.; Sol, V.; Liagre, B.; Kornienko, A.; Bonnet, S. *J. Am. Chem. Soc.* **2019**, *141* (46), 18444–18454.
- (10) Hakkennes, M. L. A.; Meijer, M. S.; Menzel, J. P.; Goetz, A.-C.; Van Duijn, R.; Siegler, M. A.; Buda, F.; Bonnet, S. *J. Am. Chem. Soc.* **2023**, *145* (24), 13420–13434.
- (11) Collin, J.-P.; Jouvenot, D.; Koizumi, M.; Sauvage, J.-P. *Inorganica Chimica Acta* **2007**, *360* (3), 923–930.
- (12) Garner, R. N.; Joyce, L. E.; Turro, C. *Inorg. Chem.* **2011**, *50* (10), 4384–4391.
- (13) Meijer, M. S.; Bonnet, S. *Inorg. Chem.* **2019**, *58* (17), 11689–11698.
- (14) Pinnick, D. V.; Durham, B. *Inorg. Chem.* **1984**, *23* (10), 1440–1445.
- (15) Liu, Y.; Turner, D. B.; Singh, T. N.; Angeles-Boza, A. M.; Chouai, A.; Dunbar, K. R.; Turro, C. *J. Am. Chem. Soc.* **2009**, *131* (1), 26–27.
- (16) Zayat, L.; Calero, C.; Alborés, P.; Baraldo, L.; Etchenique, R. *J. Am. Chem. Soc.* **2003**, *125* (4), 882–883.
- (17) Awada, A.; Loiseau, F.; Jouvenot, D. *Eur J Inorg Chem* **2021**, *2021* (44), 4539–4542.
- (18) Ballester, F. J.; Hernández-García, A.; Santana, M. D.; Bautista, D.; Ashoo, P.; Ortega-Forte, E.; Barone, G.; Ruiz, J. *Inorg. Chem.* **2024**, *63* (14), 6202–6216.
- (19) Coe, B. J.; Glenwright, S. J. *Coordination Chemistry Reviews* **2000**, *203* (1), 5–80.
- (20) Wilson, J. J.; Lippard, S. J. *Chem. Rev.* **2014**, *114* (8), 4470–4495.

- (21) Quiroga, A. G. *Journal of Inorganic Biochemistry* **2012**, *114*, 106–112.
- (22) Aris, S. M.; Farrell, N. P. *Eur J Inorg Chem* **2009**, *2009* (10), 1293–1302.
- (23) Rafic, E.; Slep, L. D.; Etchenique, R. *Pure and Applied Chemistry* **2023**, *95* (8), 879–889.
- (24) Rojas Pérez, Y.; Slep, L. D.; Etchenique, R. *Inorg. Chem.* **2019**, *58* (17), 11606–11613.
- (25) Van Rixel, V. H. S.; Moolenaar, G. F.; Siegler, M. A.; Messori, L.; Bonnet, S. *Dalton Trans.* **2018**, *47* (2), 507–516.
- (26) Den Boer, D.; Konovalov, A. I.; Siegler, M. A.; Hetterscheid, D. G. H. *Inorg. Chem.* **2023**, *62* (14), 5303–5314.
- (27) Havrylyuk, D.; Stevens, K.; Parkin, S.; Glazer, E. C. *Inorg. Chem.* **2020**, *59* (2), 1006–1013.
- (28) Van Rixel, V. H. S.; Ramu, V.; Auyeung, A. B.; Beztsinna, N.; Leger, D. Y.; Lameijer, L. N.; Hilt, S. T.; Le Dévédec, S. E.; Yildiz, T.; Betancourt, T.; Gildner, M. B.; Hudnall, T. W.; Sol, V.; Liagre, B.; Kornienko, A.; Bonnet, S. *J. Am. Chem. Soc.* **2019**, *141* (46), 18444–18454.
- (29) Meijer, M. S.; Bonnet, S. *Inorg. Chem.* **2019**, *58* (17), 11689–11698.
- (30) Bahreman, A.; Limburg, B.; Siegler, M. A.; Bouwman, E.; Bonnet, S. *Inorg. Chem.* **2013**, *52* (16), 9456–9469.
- (31) Johnson, B. A.; Agarwala, H.; White, T. A.; Mijangos, E.; Maji, S.; Ott, S. *Chemistry A European J* **2016**, *22* (42), 14870–14880.
- (32) Knoll, J. D.; Albani, B. A.; Durr, C. B.; Turro, C. J. *J. Phys. Chem. A* **2014**, *118* (45), 10603–10610.
- (33) Yang, L.; Powell, D. R.; Houser, R. P. *Dalton Trans.* **2007**, *9*, 955–964.
- (34) Marchivie, M.; Guionneau, P.; Létard, J.-F.; Chasseau, D. *Acta Crystallogr B Struct Sci* **2005**, *61* (1), 25–28.
- (35) Rafic, E.; Slep, L. D.; Etchenique, R. *Pure and Applied Chemistry* **2023**, *95* (8), 879–889.
- (36) Havrylyuk, D.; Deshpande, M.; Parkin, S.; Glazer, E. C. *Chem. Commun.*, **2018**, *54*, 12487–12490.
- (37) Cuello-Garibo, J.-A.; Meijer, M. S.; Bonnet, S. *Chem. Commun.* **2017**, *53* (50), 6768–6771.
- (38) Steinke, S. J.; Piechota, E. J.; Loftus, L. M.; Turro, C. J. *J. Am. Chem. Soc.* **2022**, *144* (44), 20177–20182.
- (39) Malouf, G.; Ford, P. C. *J. Am. Chem. Soc.* **1977**, *99* (22), 7213–7221.
- (40) Shaw, L. E.; Langford, C. H. *Inorg. Chem.* **2000**, *39* (3), 541–546.
- (41) Vichova, J.; Hartl, F.; Vlcek, A. *J. Am. Chem. Soc.* **1992**, *114* (27), 10903–10910.
- (42) Pižl, M.; Hunter, B. M.; Sazanovich, I. V.; Towrie, M.; Gray, H. B.; Zálíš, S.; Vlček, A. *Inorg. Chem.* **2022**, *61* (6), 2745–2759.
- (43) Verbeet, W.; Husiev, Y.; Bonnet, S. *Eur J Org Chem* **2024**, *27* (14), e202400054.
- (44) Zhou, X.-Q.; Xiao, M.; Ramu, V.; Hilgendorf, J.; Li, X.; Papadopoulou, P.; Siegler, M. A.; Kros, A.; Sun, W.; Bonnet, S. *J. Am. Chem. Soc.* **2020**, *142* (23), 10383–10399.

Chapter 4

Dual targeting of NAMPT and tubulin with *trans* ruthenium-based photoactivated chemotherapy complexes

Abstract: Here, a series of *trans*-tetrapyridyl ruthenium(II) complexes $[\text{Ru}(\text{MeL})(\text{L}')(\text{L}'')]^{2+}$ is reported, where MeL = di([2,2'-bipyrid]-6-yl)-N-methylamine, from which the axial ligand L' and L'' can be photosubstituted upon irradiation with visible light. Two identical or different axial ligands were considered, i.e. the nicotinamide phosphoribosyl transferase (NAMPT) inhibitor STF31 and/or microtubule polymerization inhibitor MTI were incorporated, resulting in three complexes: $[\text{Ru}(\text{MeL})(\text{STF31})_2]^{2+}$ ($[\mathbf{1}]^{2+}$), $[\text{Ru}(\text{MeL})(\text{MTI})_2]^{2+}$ ($[\mathbf{2}]^{2+}$), and $[\text{Ru}(\text{MeL})(\text{STF31})(\text{MTI})]^{2+}$ ($[\mathbf{3}]^{2+}$). Distinct differences in photoreactivity were observed for $[\mathbf{1}]^{2+}$ – $[\mathbf{3}]^{2+}$ upon irradiation with blue, green or red light in aqueous solution. Strikingly, red light irradiation resulted in selective photosubstitution of STF31 from the dissymmetric complex $[\mathbf{3}]^{2+}$, which allowed for wavelength-dependent sequential release of both inhibitors: red light released STF31, followed by blue light released MTI. *In vitro* evaluation of a STF31:MTI co-treatment in a 1:1 molar ratio in skin melanoma (A375), lung adenocarcinoma (A549) and glioblastoma (U87MG and U251) cell lines in normoxia (21% O₂) and hypoxia (>1% O₂) revealed a synergistic effect and EC₅₀ < 2.0 μM. The three complexes $[\mathbf{1}]^{2+}$ – $[\mathbf{3}]^{2+}$ were also evaluated in the same cell lines. While for $[\mathbf{2}]^{2+}$ minimal photocytotoxicity was found when activated with green or red light, photoactivation of $[\mathbf{1}]^{2+}$ and $[\mathbf{3}]^{2+}$ resulted in an increased toxicity up to 33-fold. Strikingly, synergistic cell killing of the 1:1 mixture of free drugs STF31:MTI was also observed when $[\mathbf{3}]^{2+}$ was activated with green light, while the photocytotoxicity of this complex was found to be O₂-independent. The exceptional photochemical and *in vitro* properties of $[\mathbf{3}]^{2+}$ underline the potential of such dual-targeting PACT compounds for the treatment of hypoxic tumors.

This work will be published as a full paper: W. Verbeet, S. K. Götzfried, A. Kornienko, S. Bonnet, *manuscript in preparation*

4.1 Introduction

The main challenges for chemotherapy treatment of human malignancies arises from systemic toxicity in patients due to off-targets, as well as from the development of drug resistance. To avoid these issues as much as possible, the simultaneous use of two or more chemotherapeutic agents, often referred to as “combination chemotherapy”, has become the standard-of-care in clinical cancer treatment.¹ Since the first successful application of combination therapy in the mid-1960’s against acute lymphoblastic leukemia, the concept has been applied in most clinical treatments.² Combination therapy generally leads to an enhanced therapeutic effect through synergy, reaching a higher antitumor activity while lowering the individual dose of each component of the combination, thereby reducing side-effects, compared to high-dose monotherapy. Though the experience of oncologists with combination therapy keeps progressing, the ability to rationally design a synergistic combination of drugs remains a challenge, due to the limited comprehension of fundamental cellular processes in cancer and of the mode-of-action of many anticancer drugs.³ High-throughput or computational library screening are therefore often needed to elucidate potential combination candidates.⁴ With the recent developments in artificial intelligence, machine learning methods are gaining popularity to predict potential drug synergies through computational modelling.⁵ Nonetheless, combination therapies may still suffer from deleterious side-effects or efficacy issues resulting from one of the components not reaching the targeted location at the same time as the other one, thereby drastically limiting their synergy.⁶ In some cases, liposomal or nanoparticle-based formulations can improve the bioavailability of the drug mixtures and ensure the simultaneous delivery of two or more drugs.⁷ However, nano-formulations are not as chemically homogenous as molecular drugs, and do not penetrate cells via the same mechanisms as the drugs they contain. Binary molecular prodrugs have also been proposed, in which two biologically active moieties are connected molecularly by a labile linker that is sensitive to the cancer-associated microenvironment such as the lower pH, the presence of high oxidative stress, or the overexpression of specific enzymes.^{8,9} However, side-effects might occur due to non-specific cleavage of the linker, which motivates the use of light for the controlled release of two active pharmaceutical components from a single prodrug.

For single-component therapies, light-activated prodrugs are frequently utilized to increase the tumor selectivity and minimize interaction with off-targets before the (pro)drug reaches its target. An example of this strategy is found in ruthenium-based photoactivated chemotherapy (PACT), in which a ruthenium-based “caged” prodrug dissociates upon visible-light irradiation, thus releasing a biologically active species.¹⁰ While the potential of PACT has been demonstrated *in vitro* by numerous groups,^{11–13} and more recently *in vivo*,^{14,15} this strategy is generally focuses on the light-induced release of a single chemotherapeutic agent. The integration of the PACT concept with the idea of combination

therapy could lead to a new jump in the antitumor efficacy of these molecules, for example to address the challenging targets of hypoxic tumors. In such an approach, enhanced potency can be achieved between two drugs attached to a single ruthenium photocage. This strategy may result in increased photocytotoxicity compared to traditional PACT compounds that release only a single active agent. Secondly, constructing the linkage of two bioactive components in a single PACT prodrug ensures that both components of the combination therapy would reach the tumor in an equimolar ratio at the target location. Last but not least, the photochemical properties of a ruthenium-based prodrug can be tuned in a way that allows for selective release of one component before releasing the second one using specific excitation wavelengths. Such wavelength-dependent behavior may afford favorable treatment options if sequential release of the two components in time would be advantageous.

In Chapter 3, the sequential photosubstitution was reported of two biologically benign compounds pyridine (Py) and methyl(2-thioethanol) (MTE) from *trans* tetrapyriddy-ruthenium complex $[\text{Ru}(\text{MeL})(\text{Py})(\text{MTE})](\text{PF}_6)_2$ (MeL = di([2,2'-bipyrid]-6-yl)-N-methylamine). To further explore the applicability of such a photoreactive system for PACT, the incorporation of two biologically active photolabile ligands based on pyridine and thioether functionalities into a single ruthenium-based photocage is reported here (Figure 4.1). Specifically, 4-(((4-(tert-butyl)phenyl)sulfonamido)methyl)-N-(pyridin-3-yl)benzamide (STF31) and 6-benzoyl-2-(3-(methylthio)propyl)-5-phenyl-1,7-dihydro-4H-pyrrolo[2,3-d]pyrimidin-4-one (MTI) were employed as *trans* ligands coordinated at the ruthenium center. The rigidin-analogue MTI inhibits tubulin polymerization while STF31 is a known inhibitor of nicotinamide phosphoribosyl transferase (NAMPT) and glucose transporter 1 (GLUT1).^{16,17} Of note, both have been photocaged with ruthenium agent for anticancer PACT treatment, but they have never been combined.^{15,18,19} In this work, the complexes *trans*- $[\text{Ru}(\text{MeL})(\text{STF31})_2](\text{X})_2$ (**[1]**(X)₂) and *trans*- $[\text{Ru}(\text{MeL})(\text{MTI})_2](\text{X})_2$ (**[2]**(X)₂) were first prepared, followed by the synthesis of the dissymmetric *trans*- $[\text{Ru}(\text{MeL})(\text{STF31})(\text{MTI})](\text{X})_2$ (**[3]**(X)₂), where X = hexafluorophosphate (PF₆) or chloride (Cl). The photochemical and photobiological properties of these complexes were compared *in vitro* to demonstrate the potential of dual-targeted PACT in cancer treatment.

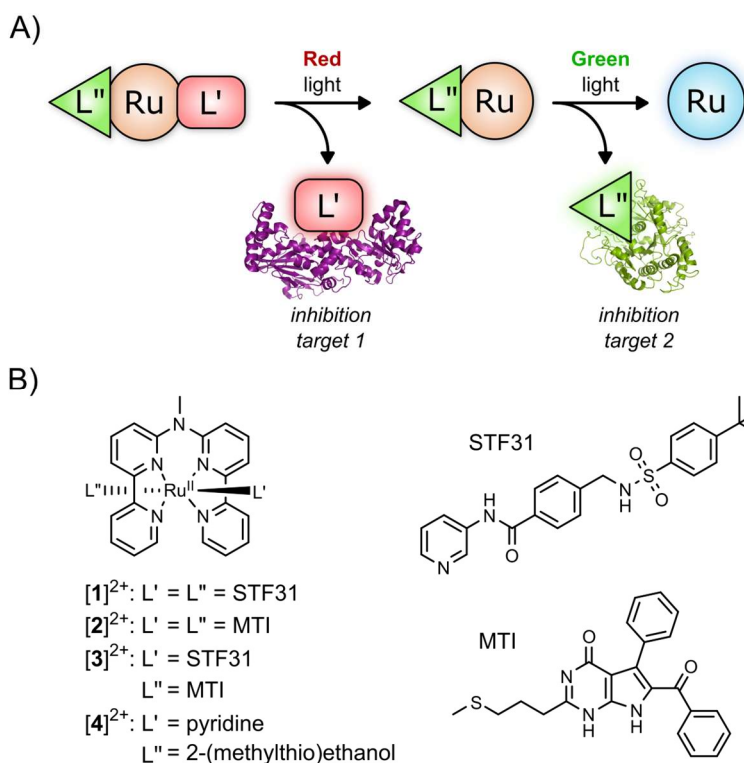


Figure 4.1 A) Schematic overview of multi-targeted photoactivated chemotherapy concept. B) Chemical structures of the compounds presented in this work.

4.2 Results

4.2.1 Synthesis

Following the synthesis of MeL as reported in Chapter 3, the corresponding dichloride-ruthenium precursor **5** was prepared with a good yield through refluxing MeL and [Ru(1,5-cyclooctadiene)Cl₂] in *o*-dichlorobenzene (Figure 4.2). Compounds [1](PF₆)₂ and [2](PF₆)₂ were synthesized thermally from **5** in presence of an excess of STF31 or MTI, respectively. To ensure dissociation of the coordinated chloride ions in **5**, water (10-20% v/v) was added to the reaction mixture, which facilitated ligand exchange. Compound [3](PF₆) was prepared by red-light induced photosubstitution of one of the STF31 ligands in [1](PF₆)₂ in presence of 3 molar equivalents of MTI in acetone. The hexafluorophosphate (PF₆) salts of [1]²⁺ – [3]²⁺ were finally converted into their corresponding chloride salts by anion exchange chromatography. All compounds were characterized with NMR spectroscopy, mass spectrometry, elemental analysis and UV-Vis spectroscopy (see Appendix IV.4).

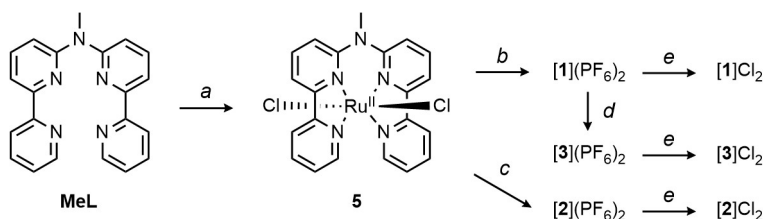


Figure 4.2 Overview of synthetic routes. a) $[\text{Ru}(1,5\text{-cyclooctadiene})\text{Cl}_2]$, *o*-dichlorobenzene, N_2 , 180 °C, 48 h, 86%; b) i) STF31, methanol with 10% H_2O , 80 °C, 48 h; ii) KPF_6 (sat. aq.), 61%; c) i) MTI, ethylene glycol with 20% H_2O , ii) KPF_6 (sat. aq.), 24%; d) i) MTI, light irradiation at 650 nm, 1:5 THF:acetone, 25 °C, 1.5 h; ii) KPF_6 (sat. aq.), 28%; e) anion exchange resin from PF_6^- to Cl^- in MeOH, $\geq 95\%$.

4.2.2 Photochemistry

Since PACT photocages act as prodrugs that only become active upon irradiation, these compounds must first be shown to be stable in absence of light. Therefore, the UV-Vis absorbance spectra of $[\mathbf{1}](\text{PF}_6)_2 - [\mathbf{3}](\text{PF}_6)_2$ in 1:1 H_2O :acetone were monitored in the dark at 298 K. All complexes were found to be thermally stable for at least 12 h (Appendix IV.1.2), and exhibited a metal-to-ligand charge transfer ($^1\text{MLCT}$) absorption band between 449 and 489 nm with molar absorptivities between 6500 and 8300 $\text{M}^{-1}\text{cm}^{-1}$ (Table 4.1 and figure IV.1).

The $^1\text{H-NMR}$ spectra of $[\mathbf{1}](\text{PF}_6)_2 - [\mathbf{3}](\text{PF}_6)_2$ in 1:5 D_2O :acetone- d_6 were monitored upon blue (450 nm), green (530 nm) or red (650 nm) light irradiation to identify the photochemical reactivity of the complexes. For $[\mathbf{1}]^{2+}$ irradiated with green light (Figure 4.3 A), the doublet at 10.00 ppm corresponding to a C–H signal of the tetrapyrridyl ligand was replaced by a doublet at 9.87 ppm within 15 min irradiation. During this period, two doublets at 8.87 and 8.76 ppm appeared corresponding a 1:1 ratio of free STF31 and coordinated STF31, indicating the formation of aqua/STF31 intermediate $[\mathbf{6}]^{2+}$. After 180 min of green light irradiation, the doublets at 8.76 and 9.87 ppm were replaced by a broad peak at 9.95 ppm while the signals for free STF31 increased further. Similar results were obtained when a solution containing $[\mathbf{2}]^{2+}$ was irradiated with green light (Figure IV.9), showing the release of MTI with the temporary presence of aqua/MTI intermediate $[\mathbf{7}]^{2+}$. When a solution $[\mathbf{3}]^{2+}$ was irradiated with red light, a shoulder peak adjacent to the doublet at 9.89 ppm and a doublet at 9.72 ppm appeared (Figure 4.3 B). In addition, a doublet at 8.87 ppm and multiplet at 7.16 ppm appeared, corresponding to free STF31 and MTI in a ratio around 72:28 after 510 min of red light irradiation. At this time point the other peaks can be assigned to the same intermediates $[\mathbf{6}]^{2+}$ and $[\mathbf{7}]^{2+}$ observed during photoreactions of $[\mathbf{1}]^{2+}$ and $[\mathbf{2}]^{2+}$. For example, the doublet at 8.76 ppm corresponds to the aqua/STF31 intermediate $[\mathbf{6}]^{2+}$ and the doublet at 8.64 ppm corresponds to the aqua/MTI intermediate $[\mathbf{7}]^{2+}$. After irradiation with red light, the solution of $[\mathbf{3}]^{2+}$ was irradiated with blue light, which resulted in increased intensities of the signals corresponding to free STF31 and free MTI, together with the appearance of broad signals for the final ruthenium bis-aqua

photoproduct $[8]^{2+}$ (for example at 9.95 ppm). The integrals of the free STF31 and free MTI peaks revealed, after blue light irradiation for 180 min, a 1:1 ratio between both photoreleased inhibitors. According to these results, red light irradiation released primarily STF31, while further blue light irradiation released the remaining STF31 as well as all MTI ligands.

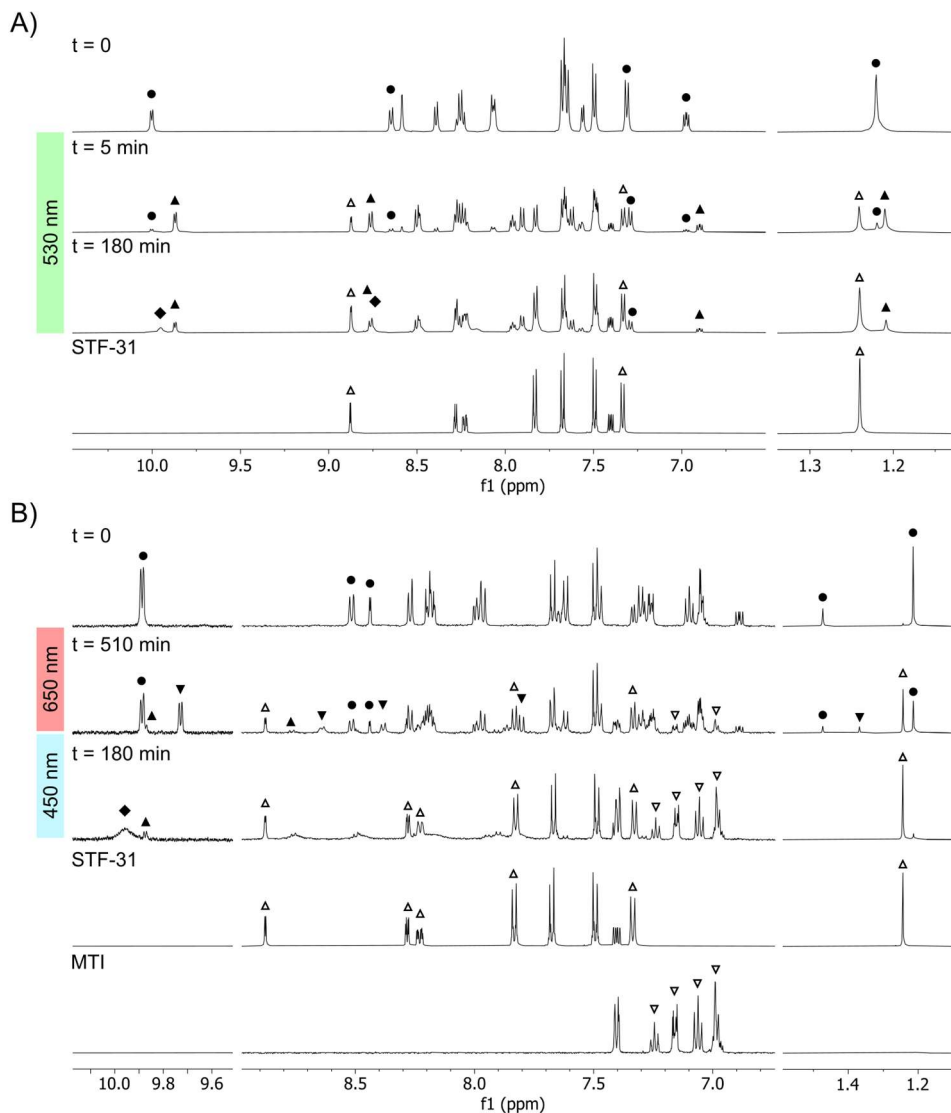


Figure 4.3 Time-evolution of the $^1\text{H-NMR}$ spectra of $[1](\text{PF}_6)_2$ upon irradiation with green light (180 min) (A) and $[3](\text{PF}_6)_2$ irradiated first with red light (510 min) followed by blue light (180 min) (B). Spectra were measured in 1:5 $\text{D}_2\text{O}:\text{acetone-}d_6$ at 298K. Symbols indicate starting compound (\bullet), intermediates $[6]^{2+}$ (\blacktriangle) or $[7]^{2+}$ (\blacktriangledown), STF-31 (\triangle), MTI (∇) or photoproduct $[8]^{2+}$ (\blacklozenge).

As observed during the light irradiated NMR experiments, the reaction from $[1]^{2+}$ – $[3]^{2+}$ to bis-aqua photoproduct $[8]^{2+}$ occurs through a sequential two-step photosubstitution route *via* the formation of a mono-aqua intermediate (Figure 4.4). In the case of $[1]^{2+}$ and $[2]^{2+}$, with identical axial ligands, the photoreaction proceeds *via* a single intermediate ($[6]^{2+}$ for $[1]^{2+}$, $[7]^{2+}$ for $[2]^{2+}$). For complex $[3]^{2+}$, however, the different axial ligands result in the possible formation of both intermediates $[6]^{2+}$ or $[7]^{2+}$ depending on which ligand is initially photosubstituted (Figure 4.4). As photosubstitution of the second ligand in either of the intermediates yields product $[8]^{2+}$, the overall two-step photoreaction of the dissymmetric complex occurred through a parallel pathways involving four different photosubstitution reactions.

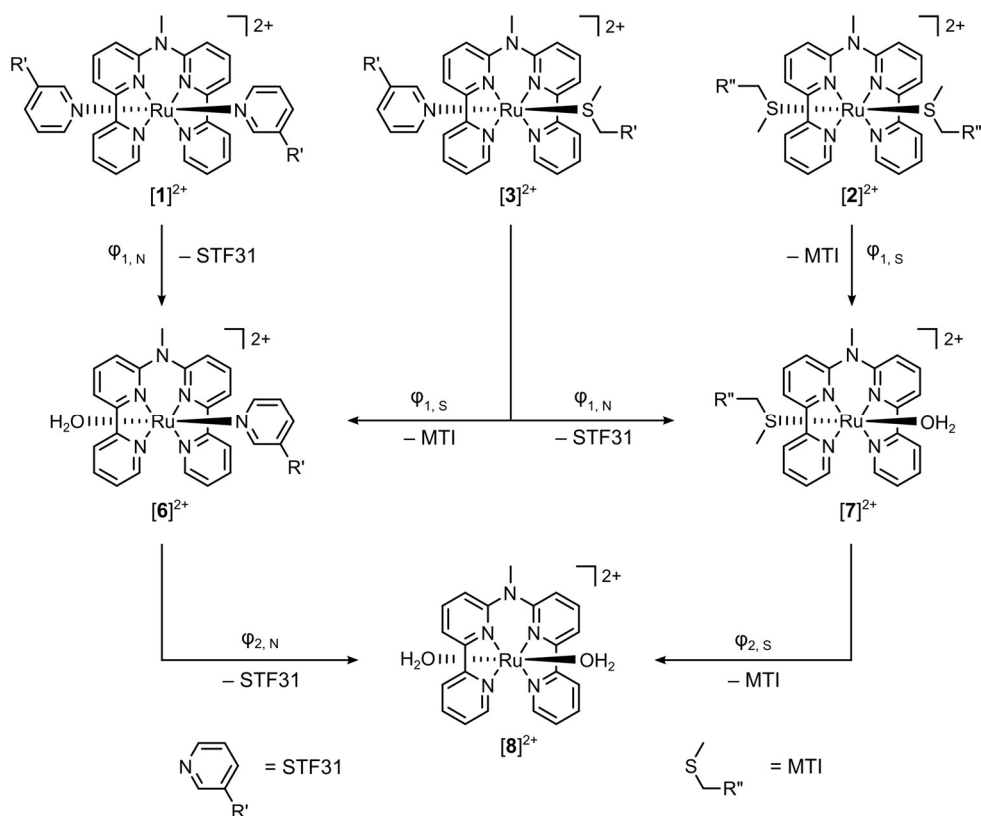


Figure 4.4 Schematic overview of the four possible photosubstitution pathways when irradiating $[1]^{2+}$ – $[3]^{2+}$ in H_2O depending on the symmetry of the complex. In the case of a symmetric complexes (i.e. $[1]^{2+}$ or $[2]^{2+}$), the photosubstitution of the axial ligands will proceed through a two-step sequential mechanism with specific quantum yields $\phi_{1,x}$ and $\phi_{2,x}$ ($X = \text{N}$ for STF31 and $X = \text{S}$ for MTI), resulting in bis-aqua product $[8]^{2+}$. For complex $[3]^{2+}$, both intermediates $[6]^{2+}$ and $[7]^{2+}$ can be formed depending which ligand is photosubstituted first. The resulting two parallel 2-step mechanisms also yield $[8]^{2+}$.

To further investigate the photosubstitution kinetics, the UV-Vis absorbance spectra of $[1](PF_6)_2 - [3](PF_6)_2$ in 1:1 acetone:H₂O were recorded during irradiation with blue (435 nm), green (505 nm) or red light (625 nm), which are shown in Figure 4.5 and Appendix IV.1.2. The reaction profiles of $[1]^{2+}$ and $[2]^{2+}$ (insets in Figure 4.5) were obtained *via* global fitting of the kinetic data using R package TIMP with Glotaran, which also provided the absorbance spectra of intermediates $[6]^{2+}$ and $[7]^{2+}$.²⁰ The spectra of $[6]^{2+}$ and $[7]^{2+}$ were then used for targeted fitting of the kinetic data of $[3]^{2+}$. This methodology provided the necessary information to calculate the photosubstitution quantum yield of all reactions involved in both the two-step sequential mechanisms for $[1]^{2+} - [2]^{2+}$ and the two parallel two-step mechanisms for $[3]^{2+}$. The photosubstitution quantum yields were calculated and are reported in Table 4.1.

The pyridine-bound complexes $[1]^{2+}$ and $[3]^{2+}$ respond to red light in spite of their low absorbance at 625 nm (molar absorptivity $\epsilon_{1,625} = 3.2$ and $120 \text{ M}^{-1} \text{ cm}^{-1}$, respectively), but the UV-Vis absorbance of a solution of the bis-thioether compound did not change upon red light irradiation (Figure 4.5 D). All compounds showed photoreactivity upon blue or green light irradiation (see Appendix IV.1.2 for time-evolution absorbance spectra upon blue light irradiation), with kinetics that corresponded to a two-step reaction: a fast initial ligand exchange yield a mono-aqua intermediate ($[6]^{2+}$ and/or $[7]^{2+}$) followed by a second, slower process forming photoproduct $[8]^{2+}$. Their data were well-fitted using a sequential model as proposed in Figure 4.4. For all complexes, the photosubstitution quantum yields of the first step (ϕ_1) were found to be 2 to 3 orders of magnitude higher than those of the second step (ϕ_2). While for bis-thioether complex $[2]^{2+}$ $\phi_{1,s}$ and $\phi_{2,s}$ were nearly identical upon blue or green light irradiation (~ 0.013 for $\phi_{1,s}$ and ~ 0.00006 for $\phi_{2,s}$), no significant photosubstitution was observed when red light was used ($\phi_{1,s} < 0.00010$ and $\phi_{2,s} < 0.00001$). However, the photosubstitution quantum efficiencies for the bis-pyridine complex $[1]^{2+}$ were similar when irradiated with blue, green or red light, both for the first ($\phi_{1,N}$ values of 0.012, 0.0078 and 0.014, respectively) and second photosubstitution ($\phi_{2,N}$ values of 0.00007, 0.00007 and 0.00010, respectively). In a way, this complex seemed to obey Kasha–Vavilov rule, stating that the outcome of a photoreaction is independent of irradiation wavelength.²¹ By contrast, for the dissymmetric complex $[3]^{2+}$ the photosubstitution quantum yields were dependent on irradiation wavelength. Especially the ratio between $\phi_{1,s}:\phi_{1,N}$ ($\phi_{1,s}$ relates to MTI substitution and $\phi_{1,N}$ to STF31 substitution) deviated strongly when irradiated with blue ($\phi_{1,s}:\phi_{1,N} = 0.0042:0.012 = 0.35$), green ($\phi_{1,s}:\phi_{1,N} = 0.0017:0.015 = 0.11$) or red light ($\phi_{1,s}:\phi_{1,N} = 0.00005:0.00029 = 0.17$). The higher quantum yields observed for STF31 photosubstitution compared to MTI from $[3]^{2+}$, suggested that the excited states leading to the dissociation of STF31 were populated more efficiently under certain excitation wavelengths. Quenching of the excited state by oxygen

seems to be insignificant, as no singlet oxygen generation was observed for $[1](PF_6)_2 - [3](PF_6)_2$, with quantum yields (ϕ_Δ) of <0.01 in acetonitrile.

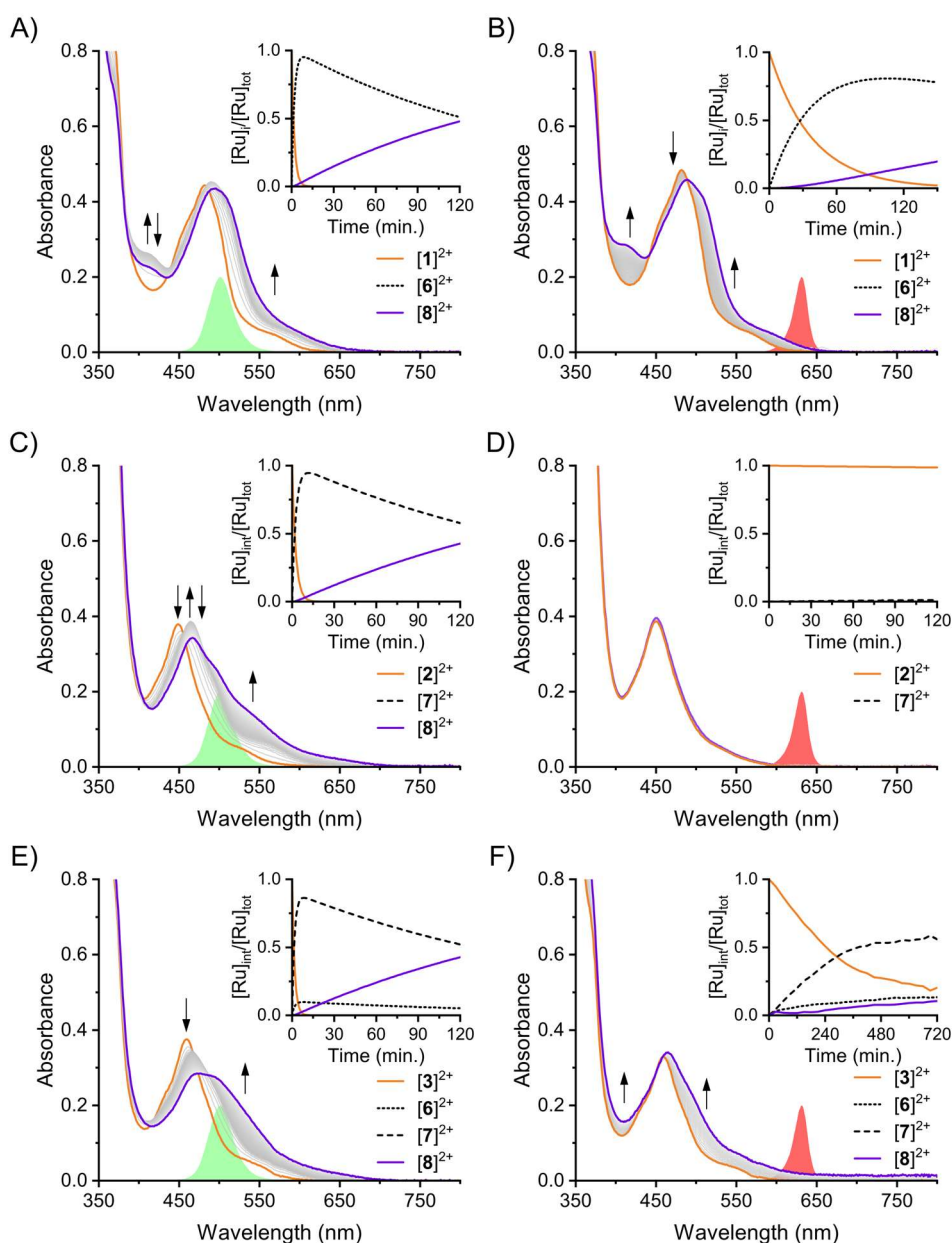


Figure 4.5 Time-evolution of the UV-Vis absorbance spectra of $[1](PF_6)_2$ at 59 μM (A, B), $[2](PF_6)_2$ at 61 μM (C, D) and $[3](PF_6)_2$ at 56 μM (E, F) in 1:1 acetone/H₂O at 298 K upon irradiation with green light (A, C, E; 505 nm, photon flux = 2.27×10^{-7} mol.s⁻¹) or red light (B, D, F; 625 nm, photon flux = 4.32×10^{-7} mol.s⁻¹). Arrows indicate changes in the spectra (from orange to purple). Inserts depict the time-

evolution of the fraction of starting reactant (orange line), intermediates (dotted black line for $[6]^{2+}$, dashed black line for $[7]^{2+}$) or photoproduct $[8]^{2+}$ (purple line).

Table 4.1 Photochemical properties of $[1](PF_6)_2$, $[2](PF_6)_2$ and $[3](PF_6)_2$ in 1:1 acetone:H₂O at 298 K including maximum absorption wavelength (λ_{max} , in nm), molar absorptivity (ϵ_{max} , in M⁻¹cm⁻¹), photosubstitution quantum yield (ϕ_i) for each step with the corresponding photosubstitution reactivity (ζ_i) and molar absorptivity at the irradiation wavelength (ϵ_i) and singlet oxygen generation quantum yield (ϕ_Δ).^a

		$[1]^{2+}$	$[2]^{2+}$	$[3]^{2+}$	
λ_{max} (nm)		484	449	459	
$(\epsilon_{max})^b$		(8300)	(6500)	(6500)	
		$\phi_{i,N}$	$\phi_{i,S}$	$\phi_{i,N}$	$\phi_{i,S}$
435 nm	ϵ_1^b	2600	5100	4100	4100
	ϕ_1	0.012 ^d	0.013 ^e	0.012 ^d	0.0042 ^e
	(ζ_1)	(32)	(69)	(49)	(18)
	ϵ_2^c	4000	5100	4000	5100
	ϕ_2	0.00007 ^f	0.00004 ^g	0.00031 ^f	0.00006 ^g
	(ζ_2)	(0.26)	(0.21)	(1.2)	(0.23)
505 nm	ϵ_1^b	5500	1200	1700	1700
	ϕ_1	0.0078 ^d	0.014 ^e	0.015 ^d	0.0017 ^e
	(ζ_1)	(43)	(18)	(25)	(2.8)
	ϵ_2^c	7300	3700	7300	3700
	ϕ_2	0.00007 ^f	0.00008 ^g	0.00044 ^f	0.00009 ^g
	(ζ_2)	(0.55)	(0.28)	(1.6)	(0.66)
625 nm	ϵ_1^b	3.2	20	120	120
	ϕ_1	0.014 ^d	<0.00010 ^e	0.00029 ^d	0.00005 ^e
	(ζ_1)	(0.46)	(<0.0020)	(0.034)	(0.0063)
	ϵ_2^c	360	260	360	260
	ϕ_2	0.00010 ^f	<0.00001 ^g	0.00007 ^f	0.00002 ^g
	(ζ_2)	(0.035)	(<0.0026)	(0.025)	(0.0052)
ϕ_Δ^h		<0.01	<0.01	<0.01	

^a $\zeta_i = \epsilon_i \times \phi_i$. ^b Molar extinction coefficient determined experimentally. ^c Molar extinction coefficient determined by global fitting. ^d Quantum yield ($\phi_{1,N}$) and photoreactivity ($\zeta_{1,N}$). ^e Quantum yield ($\phi_{1,S}$) and photoreactivity ($\zeta_{1,S}$). ^f Quantum yield ($\phi_{2,N}$) and photoreactivity ($\zeta_{2,N}$). ^g Quantum yield ($\phi_{2,S}$) and photoreactivity ($\zeta_{2,S}$). ^h determined by ¹O₂ phosphorescence ($\lambda_{em} = 1275$ nm) in aerated acetonitrile at 298 K. Excitation wavelength (λ_{irr}) = 450 nm.

As revealed by the kinetic modeling of the UV-Vis data upon red-light irradiation of $[3]^{2+}$, the initial photosubstitution reaction primarily led to the formation of MTI-bound intermediate $[7]^{2+}$ (Figure 4.5 F). Importantly, the difference in quantum yields for the formation of STF31-bound $[6]^{2+}$ (photosubstitution of MTI) and MTI-bound $[7]^{2+}$ (photosubstitution of STF31) was dependent on the excitation wavelength (Table 4.1). For red light, the quantum yield for the formation of towards $[7]^{2+}$ ($\phi_{1,N}$) was six times higher than for the formation of $[6]^{2+}$ ($\phi_{1,S}$). It was therefore hypothesized that it may be possible to sequentially release STF31 first, and MTI second, by subsequent irradiation with red and blue light. Indeed, as shown in Figure 4.3 B, the $^1\text{H-NMR}$ irradiation experiment for $[3]^{2+}$ (1.38×10^{-3} M) in 5:1 acetone- D_6 : D_2O demonstrated the selective release of the two inhibitors after first using red light (650 nm), followed by blue light (450 nm). After identification of the $^1\text{H-NMR}$ signals of free STF31 (8.9 ppm) and free MTI (7.0 ppm), the relative concentrations of the released inhibitor was determined by calculating the integral ratios, which demonstrate sequential release (Figure 4.6 A). To further investigate sequential release of the axial ligand, a similar irradiation experiment (first 625 nm, then 435 nm light) was conducted while monitoring the UV-Vis absorbance of a solution of $[3]^{2+}$ (5.62×10^{-7} M) in 1:1 H_2O :acetone. Targeted fitting of the time-evolution UV-Vis absorbance spectra provided relative concentrations of the ruthenium-based components during the photoreaction (Figure 4.6 B). During the first irradiation step in the UV-Vis setup, $[3]^{2+}$ was mainly converted into $[7]^{2+}$ (releasing STF31) with red light while the second irradiation step resulted in the formation of $[8]^{2+}$. Although the conditions of the NMR and UV-Vis experiments differ in solvent, light sources, concentration of $[3]^{2+}$ and overall irradiation setup, the results of both experiments indicated selective photosubstitution of STF31 upon red light irradiation, followed by complete release of the inhibitors and the formation of $[8]^{2+}$ upon blue light irradiation. These results highlight the robustness of the sequential photosubstitution reaction from $[3]^{2+}$ and exceptional wavelength-dependent control of photorelease.

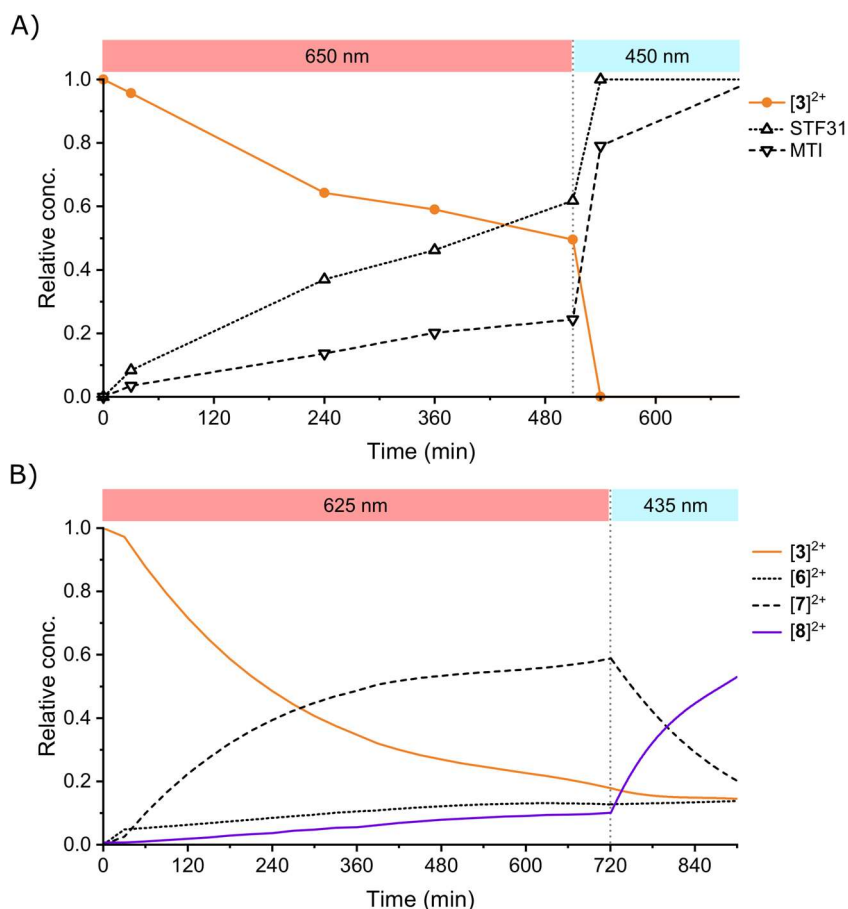


Figure 4.6 Sequential release of STF-31 and MTI from $[3](PF_6)_2$ upon irradiation with red light followed by blue light. A) Relative concentration profile of $[3]^{2+}$, STF-31 and MTI followed by 1H -NMR upon irradiation with 650 nm ($t = 0 - 510$ min) followed by 450 nm ($t = 510 - 690$ min) at 298 K. Starting concentration of $[3]^{2+} = 1.38 \times 10^{-3}$ M in 5:1 acetone- D_6 : D_2O . The relative concentration profile was derived from the integral ratios (9.9 ppm for $[3]^{2+}$; 8.9 ppm for STF31; 7.0 ppm for MTI). B) Relative concentration profile of $[3]^{2+}$, $[6]^{2+}$, $[7]^{2+}$ and $[8]^{2+}$ followed by UV-Vis absorbance upon irradiation with 625 nm ($t = 0 - 720$ min; photon flux = 4.32×10^{-7} mol. s^{-1}) followed by 435 nm ($t = 720 - 900$ min; photon flux = 2.27×10^{-7} mol. s^{-1}) at 298 K. Starting concentration of $[3]^{2+} = 5.62 \times 10^{-7}$ M in 1:1 acetone: H_2O . Relative concentration profile was derived from the time-evolution of the UV-Vis spectrum of the solution for which the method described in Appendix I.2.3 (Equation I.8).

4.2.3 Cytotoxicity and cellular uptake

Considering the well-characterized photoreactivity of all three complexes under different irradiation conditions, we investigated the consequence of these photoreactions *in vitro*. As $[3]^{2+}$ can photorelease STF31 and MTI in a 1:1 ratio upon full activation, the cytotoxicity of the ruthenium PACT compounds $[1]Cl_2 - [3]Cl_2$ was evaluated together with that of a 1:1 combination of free STF31 and free MTI. All *in vitro* experiments were realized under

normoxic (21% O₂) and hypoxic conditions (1% O₂) in human skin melanoma (A375), lung (A549) and glioblastoma (U87MG and U251) cancer cell lines. The dissymmetric ruthenium compound [Ru(MeL)(Py)(MTE)]Cl₂ ([4]Cl₂, see Chapter 3) was added to this study to investigate the effect of only the ruthenium cage in the same conditions, assuming that free pyridine and free MTE had negligible biological effects. In all cases, the chloride salts of the compounds were used, because of their increased solubility in aqueous solution. To evaluate the light dose needed to ensure full activation in the cell irradiation setup, a mock irradiation experiment was realized for both wavelengths used in this study (see Appendix IV.1.5). The necessary light doses were 30.8 J/cm² for green light (520 nm) and 115 J/cm² for red light (630 nm; Figure IV.10). The cytotoxicity of the compounds was then determined as described in Appendix I.3. In short: the different cell lines were treated with either prodrug or the 1:1 free drug mixture and incubated in the dark for 24 h. The medium was then replaced by drug-free medium, and the cells were irradiated with green light (530 nm, 30.8 J/cm²), red light (630 nm, 115 J/cm²), or kept in the dark. The cells were further incubated in the dark for 48 h, and at t = 96 h the cell viability assessed using the MTT metabolic activity assay and compared to the untreated control. From the resulting dose-response curves, the metabolic activity inhibition effective concentrations (EC₅₀ in μM) were determined (Figure 4.7 and Tables IV.2, IV.3).

For all cell lines, the ruthenium cage [4]Cl₂ was found to be non-cytotoxic (EC₅₀ > 100 μM) both in the dark and after light irradiation (Table IV.2). Therefore, no cytotoxic effect originating from the ruthenium cage (or pyridine or MTE) is expected. On the other hand, the free inhibitors did induce a significant effect on cell proliferation: STF31 was highly cytotoxic for A375, A549 and U251 (EC₅₀ < 5 μM), but less for U87MG (EC₅₀ > 18 μM). Additionally, STF31 appeared to be more potent under normoxia than in hypoxia. This result is possibly related to upregulation of NAMPT expression induced by hypoxia-inducible factor 1α (HIF1α).²² The microtubule inhibitor MTI showed a similar cytotoxic effect on all cell lines (EC₅₀ < 7 μM), although with some contrasting differences. In A375, MTI was found to be almost eight times more cytotoxic under normoxia than in hypoxia (EC₅₀ = 0.26 μM vs. 1.97 μM respectively), while the reverse was observed in A549 (EC₅₀ = 6.21 μM vs. 0.91 μM respectively). Furthermore, the 1:1 combination of STF31 and MTI was shown to be highly cytotoxic to all cell lines (EC₅₀ < 1.3 μM). Strikingly, cotreatment with STF31 and MTI was found to be more cytotoxic in all cell lines, except in A375 cells under normoxia, compared to treatment with one of the drugs. These results suggest a potential synergistic effect of MTI and STF-31 on the reduction of cell viability, independent of oxygen concentration.

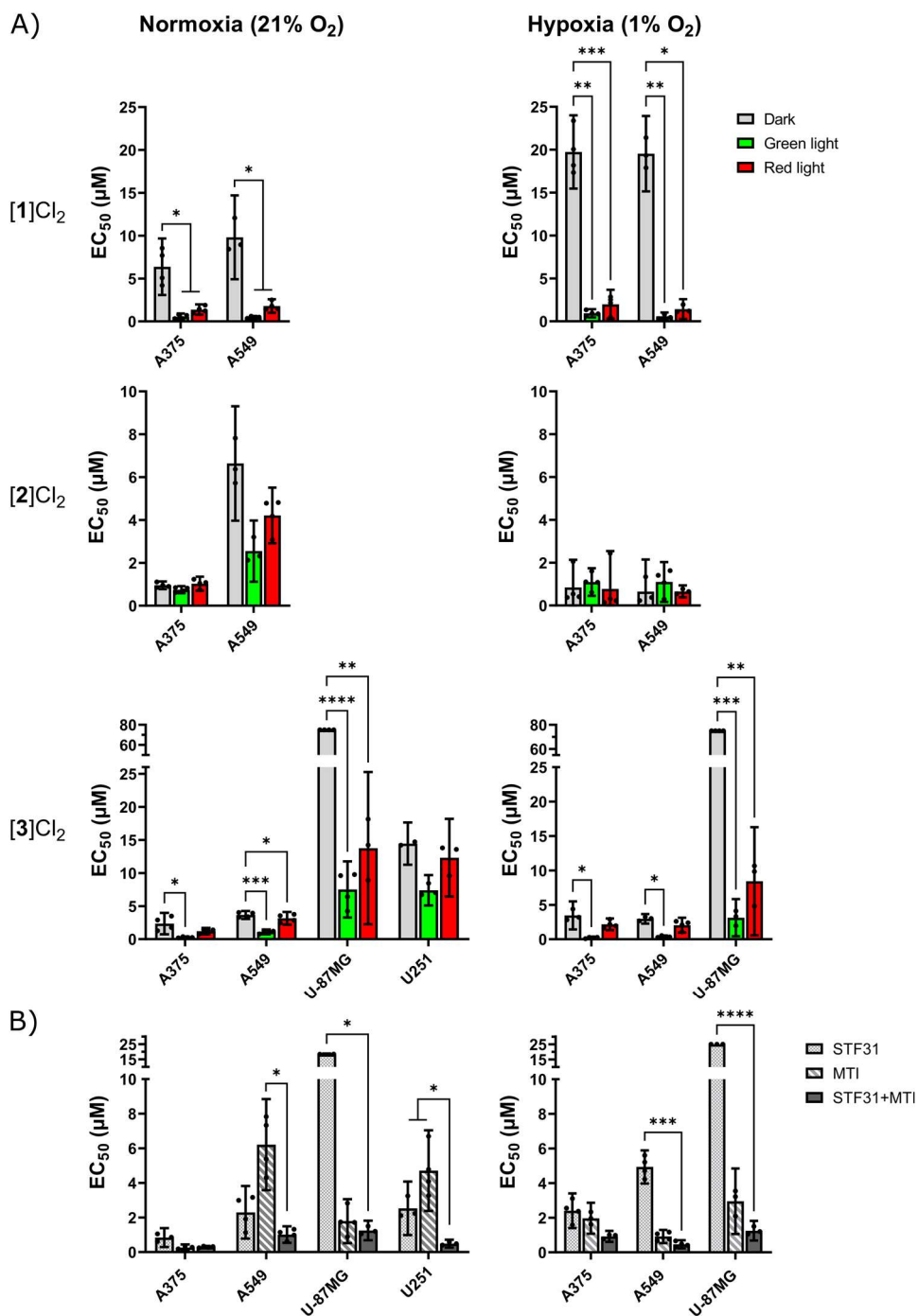


Figure 4.7 Metabolic activity inhibition effective concentrations (EC₅₀ in μM) in A375, A549, U87MG and U251 human cancer cell lines incubated in normoxic (21% O₂) or hypoxic (1% O₂) conditions. A) EC₅₀ for [1]Cl₂, [2]Cl₂ and [3]Cl₂ in the dark and upon irradiation with green light (520 nm, 30.8

J/cm²) and red light (630 nm, 115 J/cm²). B) EC₅₀ for STF31, MTI and STF31 + MTI (1:1 molar ratio). Experiments were performed in biological quadruplicate; error bars indicate 95% confidence intervals (in μM). * = $p \leq 0.05$, ** = $p \leq 0.01$, *** = $p \leq 0.001$, **** = $p \leq 0.0001$, ns = Not Significant has been omitted for clarity. See Table IV.1 and IV.2 for all EC₅₀ values.

The symmetric ruthenium-caged MTI-releasing compound [2]Cl₂ showed high cytotoxicity, comparable to free MTI, in both A375 and A549 cells under normoxic and hypoxic conditions (EC_{50, dark} < 7 μM). However, no significant differences were observed between irradiated and non-irradiated cells, suggesting thermal release of the MTI inhibitor in cell media. This result was in great contrast to those obtained with the symmetric STF31-releasing compound [1]Cl₂, which was much less cytotoxic in the dark and in normoxia in A375 and A549 cell lines, and became far more cytotoxic after irradiation with both red and green light (EC₅₀ < 2 μM and < 0.6 μM , respectively). Under hypoxia, the photoactivation of [1]Cl₂ had even stronger effects, characterized by a lower dark toxicity (EC_{50, dark} > 19 μM) while maintaining a similar cytotoxicity after irradiation, compared to normoxic conditions. This resulted in an increase of the photoindices under hypoxia for [1]Cl₂ with both red light and green light. For red light, the PI values went from 4.6 and 5.5 for A375 and A549 cells under normoxia to 10 and 14 under hypoxia, respectively. For green light, they increased from 12 and 22 for A375 and A549 under normoxia to 21 and 33 under hypoxia, respectively. As note, these PI values were considerably higher than the ones found for the previously reported ruthenium-caged STF-31 compound [Ru(tpy)(biq)(STF-31)]Cl₂ (tpy = 2,2',6',2''-terpyridine, biq = 2,2'-bisisoquinoline) which were 2.6 and 2.4 for A549 cells in normoxia and hypoxia, respectively.¹⁹ It is unclear at this stage if these much improved PI values for [1]Cl₂ are due to the double amount of STF-31 molecules released by the ruthenium cage, to the different nature of the ruthenium cage, to the different lipophilicity and/or cellular localization of the caged prodrug, or to several of these factors at the same time.

For the dissymmetric compound [3]Cl₂, a relatively high toxicity was found in the dark (EC_{50, dark} < 4 μM) across both A375 and A549 cell lines under normoxic and hypoxic conditions. Nonetheless, green light activation resulted in a significantly increased cytotoxicity (EC_{50, 520nm} < 1 μM). It should be noted that like for [1]Cl₂ the green light-induced photoindexes in A375 and A549 cells under hypoxia increased two-fold compared to normoxia (8.7 and 3.3 under normoxia, and 16 and 8.1 under hypoxia, respectively). The sensitivity of the U87MG and U251 cells towards [3]Cl₂ differed notably despite both being glioblastoma cell lines. In U251 cells, [3]Cl₂ exhibited measurable dark cytotoxicity under normoxic conditions ((EC_{50, dark} = 14 μM). In contrast, no dark toxicity was detected in U87MG cells (EC_{50, dark} > 75 μM), either in normoxic or hypoxic conditions. Upon irradiation with green or red light, no significant change was observed for [3]Cl₂ in U251 cells. By comparison, pronounced phototoxicity was observed in U87MG cells under normoxia, with EC₅₀ values of 7.51 μM under green light (PI > 10) and 13.8 μM under red light (PI > 5.5). This light-induced cytotoxicity was further enhanced under hypoxic conditions, yielding EC₅₀ values of 3.13 μM

under green light (PI > 24) and 8.44 μM under red light (PI > 9). Notably, this behavior is unusual, as most ruthenium-based PACT compounds reported up to now exhibit either similar or strongly reduced photoindices under hypoxia relative to normoxia.

To investigate the potential synergistic effect exerted by STF31 and MTI in the 1:1 mixture or for the green light-activated complex **[3]**²⁺, the CompuSyn software was used to calculate the combination indexes (CI) based on the Chou-Talalay method (see experimental section 4.5 for details).²³ With this method, CI values are determined for each drug combination as a function of the fraction of affected cells (F_a), thereby allowing evaluation of drug interactions across different effect levels. The CI values can be used to define the nature of the combination effect: an additive effect is indicated by CI = 1, synergism by CI < 1, and antagonism by CI > 1. In Figure 4.7, the Chou-Talalay plots are shown for treatment of A375, A549, U87MG and U251 in normoxia or hypoxia with 1:1 STF31:MTI or green light-activated **[3]**²⁺ at a light dose where it is fully activated and has released both inhibitors.

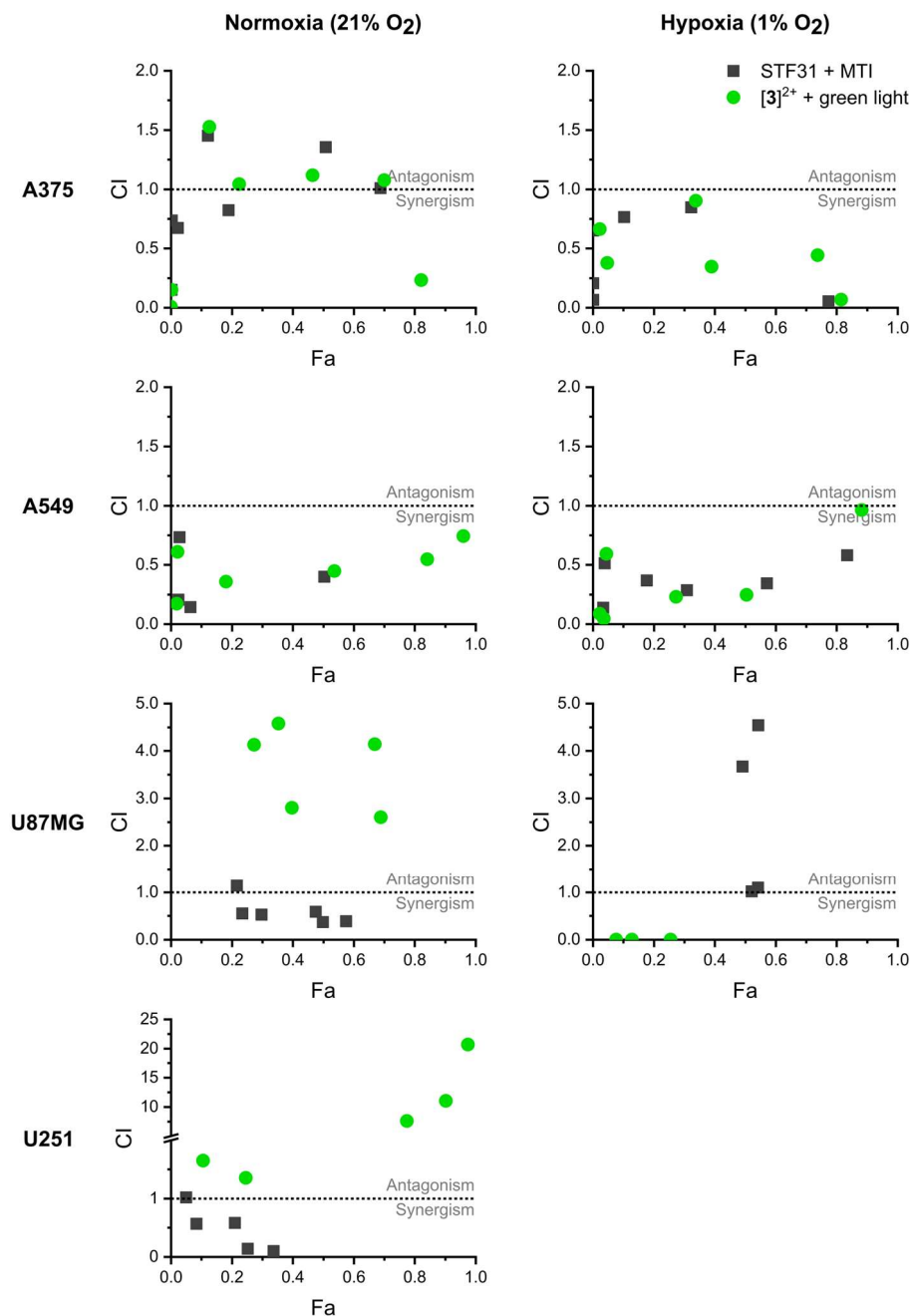


Figure 4.7 Chou-Talalay plots for combination treatment with STF31:MTI mixtures (1:1 molar ratio; grey squares), or [3]²⁺ after green light activation (green circles) in A375, A549, U87MG and U251 under normoxic (21% O₂) or hypoxia (1% O₂). The y-axis indicates the combination index (CI) at an observed effect upon treatment generating an effect F_a on the x-axis.

For the A375 and A549 cells, the data points for both STF31:MTI and photoactivated [3]²⁺ were comparable, pointing to similar CI values, indicating that the effect of co-treatment with a 1:1 mixture of both free drugs was retained when both inhibitors were released by green light activation of [3]²⁺. For A375 cells in normoxia, the data points were spread around CI = 1, suggesting an additive effect. However, CI values clearly below 1 were observed in hypoxic cells, indicative for synergy in such conditions. The CI values were all well-below 1 in A549 cells in both normoxia and hypoxia, indicating a strong synergistic effect independent of the oxygen concentration for these cells. In glioblastoma cells, larger differences between the CI values of STF31:MTI and photoactivated [3]²⁺ were observed. While synergy was observed for STF31:MTI mixtures in normoxic U87MG cells, photo-releasing these inhibitors from [3]²⁺ resulted in an antagonistic effect in the same conditions. These differences were more pronounced in U251 cells. Strikingly, however, in hypoxic U87MG cells this difference was completely reversed, leading to strong synergism for light-activated [3]²⁺ while the combined mixture of free inhibitors worked antagonistically. Although only speculations can be made at this stage, these contrasting results between the photo-released mixture and the combination of free inhibitors in the glioblastoma cell lines may be related to differences in cellular uptake mechanisms and/or intracellular localization. Further studies will be needed to investigate the cell line-dependent effects on the drug-drug interactions and may provide a better understanding of the cellular pathways that are involved upon the combined inhibition of tubulin polymerization and NAMPT inhibition.

Cellular uptake has a crucial influence on the therapeutic efficacy of a drug, and it is expected to play an important role on the efficacy of ruthenium-based PACT prodrugs as well. Therefore, the intracellular ruthenium content of A375, U87MG and U251 cells incubated with [1]Cl₂ – [3]Cl₂ in the dark and under normoxia or hypoxia for 24 h was quantified by ICPMS. This uptake was compared to the molar amount of added compound, to investigate potential differences in cellular accumulation of the three compounds. To ensure a number of live cells sufficient for analysis, the compounds were incubated at concentrations below their EC₅₀ (see Figure 4.8 for details). As note, comparison of these results can therefore only be done qualitatively as different concentrations were used for the different compounds. As shown in Figure 4.8 A, the ruthenium uptake efficiency in A375 cells after incubation with [1]Cl₂ was thrice lower in hypoxia compared to normoxia (6% vs. 19%, respectively). This result indicates a significant effect of the oxygen concentration on the accumulation of [1]²⁺ and suggest potentially reduced efficacy against hypoxic tumors. In contrast, incubation with [2]²⁺ resulted in minimal uptake (<1.5%) regardless of the oxygen concentration. Accumulation of [3]²⁺ was observed in A375 independent from oxygen concentration, with uptake efficiencies of 2.7% in normoxia and 2.5% in hypoxia (Figure 4.8 B). Furthermore, in normoxia the uptake of [3]²⁺ was found to be more efficient by the U87MG and U251 glioblastoma cells (8% and 11%, respectively). In hypoxia, uptake

of $[3]^{2+}$ by U87MG was similarly efficient as in normoxia (7% and 8%, respectively). While slight differences are observed between the different cell lines, the cellular uptake efficiency of $[3]^{2+}$ was generally independent of the oxygen concentration. Unfortunately, the uptake of free drugs STF31 and MTI could not be determined with the tools available in our laboratories.

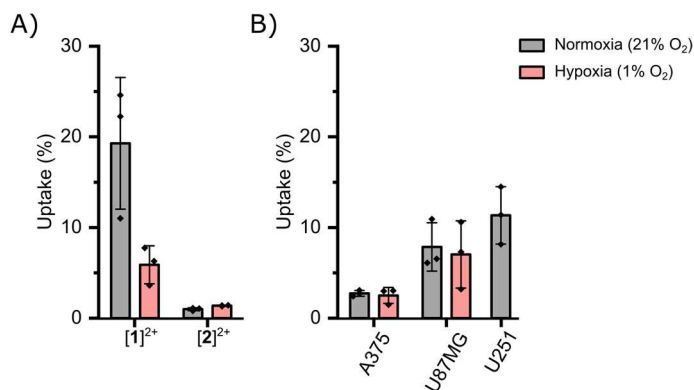


Figure 4.8 Cellular ruthenium uptake efficiency (percentage uptake per million cells of the administered dose) in different human cancer cells under normoxic and hypoxic conditions as determined by ICP-MS. A) Ruthenium uptake of A375 cells incubated with $[1]Cl_2$ (2 μ M) or $[2]Cl_2$ (0.5 μ M) for 24 h in the dark. B) Ruthenium uptake of A375, U87MG or U251 human cancer cell lines incubated with $[3]Cl_2$ (1 μ M for A375, 5 μ M for U87MG NX, 10 μ M for U87MG HX and U251) for 24 h in the dark. Boxes are the mean of three biologically independent experiments, and error bars depict standard deviation (in μ M). See Table IV.4 for exact values.

4.3 Discussion

While the red-light molar absorptivity of the complexes reported here are low ($>200 \text{ M}^{-1}\text{cm}^{-1}$ at 625 nm), only $[2](PF_6)_2$ was not reactive upon irradiation at this wavelength. $[1](PF_6)_2$ and $[3](PF_6)_2$ demonstrate the interesting red-light sensitive photocaging properties of the new $[Ru(MeL)(L)_2]^{2+}$ scaffold. Furthermore, the photosubstitution quantum yields with blue (435 nm) and green (505 nm) light for $[1](PF_6)_2$ and $[2](PF_6)_2$ are within the same order of magnitude (~ 0.01 for the first step and 0.00006 for the second). Although the available data do not allow for a definitive explanation for the lack of red-light photoreactivity observed for the bis-thioether complex $[2](PF_6)_2$, this behavior is likely related to thermal or emissive relaxation pathways from the excited state.

The quantum yield for STF31 photosubstitution were comparable for $[3]^{2+}$ and $[1]^{2+}$ upon blue light irradiation (0.012 for both complexes) and remained of the same order of magnitude under green light (0.015 for $[3]^{2+}$ versus 0.0078 for $[1]^{2+}$). In contrast, upon red light irradiation, STF31 photosubstitution was significantly more efficient for $[1]^{2+}$ than for $[3]^{2+}$, with quantum yields of 0.014 and 0.00029, respectively. For MTI, the

photosubstitution reaction occurred significantly less efficient for $[3]^{2+}$ than $[2]^{2+}$. These results suggest that the thioether-based MTI and the pyridine-based STF31 ligands coordinated in *trans*-position in $[3]^{2+}$ affect the photoreactivity of the complex, similar to the excited state *trans*-effects for *trans*-[Ru(MeL)(pyridine)(MTE)] $^{2+}$ discussed in Chapter 3. Nonetheless, the more efficient photoreaction for STF31 substitution compared to MTI from $[3]^{2+}$ makes it possible to selectively release STF31 upon red light irradiation.

As demonstrated for $[1]^{2+}$, incorporation of two equivalents of the same inhibitors on a PACT complex can increase its overall cytotoxicity and potency. It allows for doubling of the amount of delivered inhibitor, while probably also significantly changing the lipophilicity of the complex. This approach has been pioneered by the Turro group who reported ruthenium cages featuring two or more equivalents of 5-cyanouracil (5CNU) that were released upon white-light activation.^{24,25} Yet, the *in vitro* cytotoxicity after irradiation of these compounds did not reach the same level as free 5CNU, making the authors suggest that only a single 5CNU ligand was released in these conditions. This difference with our results highlights the importance of an optimization of the light irradiation conditions in relation to the photoreactivity of a given photocage. On the other hand, the cytotoxic effect of a PACT compound releasing two equivalents of an inhibitor per ruthenium center could be in principle also reached by doubling the dose of a “traditional” PACT compound bearing a single inhibitor per ruthenium center. However, increasing the dose of such a “singular” PACT compound to reach the same effect as a double PACT compound also increase the chance of undesirable side-effects. Nonetheless, if the Ru cage is biologically inactive, the added value of a double PACT compound such as $[1]^{2+}$ or $[2]^{2+}$ is limited, while the applicability of such compounds for the treatment of various cancer types is not guaranteed and the possibility of drug resistances often observed for monotherapies remains. The phototoxicity of the dissymmetric complex $[3]^{2+}$ in the different cell lines reported here clearly demonstrated, however, the advantages of dual-targeting PACT. Even if synergy between the two different photoreleased ligands did not occur in every cancer cell type, the overall effect of the treatment was surprisingly better, compared with the individual monotherapies.²⁶ Furthermore, releasing two different inhibitors from a single PACT compound (such as $[3]^{2+}$) can be advantageous compared to co-treatment with two free inhibitors, or the combination of two PACT compound each releasing one inhibitor. The use of two PACT compounds simultaneously clearly comes with the same spatiotemporal challenge as with mixtures of free chemotherapeutic drugs: both PACT compounds should reach the cells at the same time to be able to generate synergies following simultaneous light activation. Therefore, a single PACT compound releasing two different inhibitors, appears as the more powerful approach.

Even though the synergy between biologically active compounds can be rationalized in some cases, most synergistic effects remain challenging to explain due to the complexity of

cancer cell biology. The synergistic combination of STF31 and MTI investigated here is also difficult to explain rationally, although a number of reports in the literature provide indicative evidence that both inhibitors might act synergistically. A study by Harkcom et al. showed that increasing levels of intracellular NAD⁺ blocked the microtubule disassembly by microtubule depolymerizing agents such as colchicine, vinblastine and nocodazole, reducing the cytotoxicity of the drugs.²⁷ This NAD⁺-dependent drug resistance was mediated by the activation of mitochondrial sirtuin-3 (SIRT3), a protein involved in metabolic regulation and mitigation of oxidative stress within the cancer cell. The NAD⁺-SIRT3 mediated regulation of microtubule dynamics was observed in multiple human cancer cell lines (MCF-7, HEK293T and HeLa), suggesting a cellular pathway that is conserved between different cancer types. As also suggested by the authors, the combination of a microtubule depolymerizing agent (such as MTI) and an inhibitor of the NAD⁺ synthesis (such as NAMPT inhibitor STF31) might lead to a synergistic effect on cancer cell proliferation, which is corroborated by our observations. Besides the synergy between STF31 and MTI observed under normoxia, a stronger cytotoxic effect after photoactivation of **[3]**²⁺ was observed in hypoxia compared to normoxia. This O₂-dependent effect was rather unexpected as PACT compounds, and chemotherapeutics in general, usually become less cytotoxic with decreasing oxygen concentration.²⁸ The persisting synergistic effect between STF31 and MTI photoreleased from **[3]**²⁺ at low oxygen concentrations may be related to mitochondrial dysfunction. In hypoxia, perinuclear localization of mitochondria is known to activate of HIF-1 α , the main transcription factor responsible for the hypoxia response.²⁹ This mitochondrial clustering around the nucleus is driven by the dynein motor system, facilitating the retrograde mitochondrial movement along the microtubules. Consequently, inhibition of microtubule polymerization (by inhibitors such as MTI) diminishes perinuclear mitochondrial localization. On the other hand, NAMPT inhibition has been shown to cause mitochondrial dysfunction.³⁰ Therefore, the combined inhibition of NAMPT and microtubule polymerization might exert negative effects on downstream mechanisms that are crucial for cell survival in hypoxia. With the current available data, this analysis only remains a hypothesis. However, the potency of photoactivated release of STF31 and MTI from **[3]**²⁺ in hypoxia, highlights the strong potential of *trans* complexes for dual-targeting PACT.

4.4 Conclusion

In this study, the successful synthesis of three novel ruthenium-based PACT compounds was demonstrated based on the *trans*-[Ru(MeL)(L')(L'')]²⁺ scaffold where the axial ligands L' and L'' were either identical or different protein inhibitors. Symmetric compounds **[1]**²⁺ and **[2]**²⁺ featured two equivalents of pyridine-based NAMPT inhibitor STF31 or two thioether-based tubulin polymerization inhibitor MTI, respectively. The preparation of the dissymmetric compound **[3]**²⁺, with L' = STF31 and L'' = MTI, was achieved by a red light-induced

photosubstitution reaction starting from $[1]^{2+}$ in the presence of 3 eq. MTI. In all three cases, photosubstitution of the axial ligands was demonstrated with $^1\text{H-NMR}$ and UV-Vis spectroscopy, and the photosubstitution quantum yields upon blue, green or red light irradiation were determined. Distinct differences in photoreactivity between the compounds were observed, with $[2]^{2+}$ being the only compound not reactive upon red-light irradiation. Moreover, the characteristic reactivity of the axial ligands in $[3]^{2+}$ allowed for selective photosubstitution first of STF31 upon red light irradiation, followed by MTI upon blue light irradiation. Compound $[3]^{2+}$ is the first compound allowing for controlled release of two different inhibitors by varying the irradiation wavelength, highlighting the potential of such *trans* complexes for PACT.

While no significant photoindexes were observed for the bis-MTI compound $[2]^{2+}$, the bis-(STF31) analogue $[1]^{2+}$ and the dissymmetric analogue bearing 1 eq. of each inhibitor, $[3]^{2+}$, became significantly more cytotoxic after green or red light activation in skin melanoma (A375) and lung cancer (A549) cells, both under normoxia and hypoxia. Independent on oxygen concentration, $[3]^{2+}$ showed no toxicity in the dark in U87MG glioblastoma cells ($\text{EC}_{50} > 75 \mu\text{M}$), while green or red light activation increased its toxicity significantly. Strikingly, $[3]^{2+}$ appeared to be more potent in hypoxic conditions than in normoxic conditions, with photoindexes increasing up to 3-fold. These exceptional results also indicate an oxygen-independent synergistic effect on cell viability upon photorelease of STF31 and MTI from $[3]^{2+}$. Though *in vivo* validation and further mechanistic investigation will be needed to assess NAMPT and microtubule inhibition, the exceptional *in vitro* properties of $[3]^{2+}$ under hypoxia underlines the high potential of such dual-targeting, *trans* PACT compounds for the treatment of hypoxic tumors.

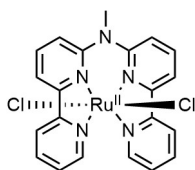
4.5 Experimental

4.5.1 General information

Unless otherwise noted, all reagents and solvents were purchased from commercial suppliers (Fluorochem, Sigma-Aldrich, BLDPharm, VWR, TCI) and used without further purification. Compounds MeL and $[4](\text{PF}_6)_2$ were synthesized according to the procedure reported in Chapter 3. STF-31 was prepared by Yurii Husiev as previously reported.¹⁹ MTI was provided by Alexander Kornienko and prepared as previously reported.¹⁶ Anhydrous and oxygen-free solvents were obtained using common drying (activated 4 Å molecular sieves) and degassing (freeze-pump-thaw method) procedures. The reactions were carried under air unless stated otherwise. Standard Schlenk techniques were used for the reactions that were carried out under an inert atmosphere. Filters used were Whatman® regenerated cellulose membrane filters, RC60 Membrane circles, diam. 47 mm, pore size 1 μm. TLCs were performed using either Supelco analytical silica gel on aluminium foils with fluorescence indicator 254 nm or Supelco analytical aluminum oxide 60 with fluorescence

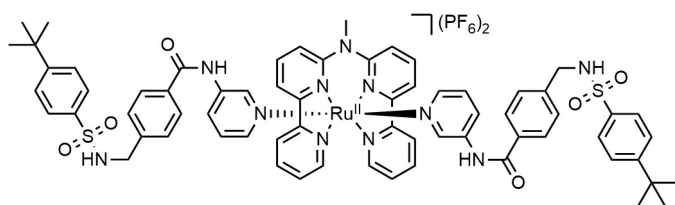
indicator 254 nm. Column chromatography was carried on silica gel (40-63 μm) or on activated neutral aluminum oxide (Brockmann Grade I) from VWR Chemicals. The microwave tubes (product number: 351521) were purchased from Biotage (Uppsala, Sweden) and heated using Thermo Scientific™ Reacti-block™ T-1 (9 holes; dimensions: 17mm diameter \times 45 mm deep). Size exclusion chromatography was performed using Cytiva Sephadex LH-20 (3 \times 60 cm) as stationary phase. Anion exchange from hexafluorophosphate (PF_6) salts to the corresponding chloride salts was performed using DOWEX® 22 resin (3 \times 11 cm) in methanol. Prior to the initial use, the resin was allowed to swell overnight in methanol. Additionally, the column was flushed with one column volume of 1 M HCl in methanol and washed with methanol until neutral pH. A 1 M HCl in methanol flush and methanol wash until neutral pH was done before every use to regenerate the resin. All synthesized ruthenium complexes were stored at room temperature and protected from light. NMR spectra were recorded on Bruker Avance 400 or 500 MHz and the FIDs were treated with MestReNova software. The chemical shifts are given relative to the residual signal of the solvent (Acetone- d_6 : δ (^1H) = 2.05 ppm, δ (^{13}C) = 29.84 ppm; CDCl_3 : δ (^1H) = 7.26 ppm, δ (^{13}C) = 77.16 ppm; DMSO- d_6 : δ (^1H) = 2.50 ppm, δ (^{13}C) = 39.52 ppm), or relative to an external standard (TMS: δ (^1H) = 0 ppm, δ (^{13}C) = 0 ppm). The mass spectra (ESI-MS) were recorded in methanol (UPLC grade) with 1% (v/v) of formic acid on a Shimadzu LCMS-2020 (ESI-Q). High-resolution mass spectra (HRMS) were recorded on Thermo Finnigan LTQ Orbitrap.

4.5.2 Synthesis



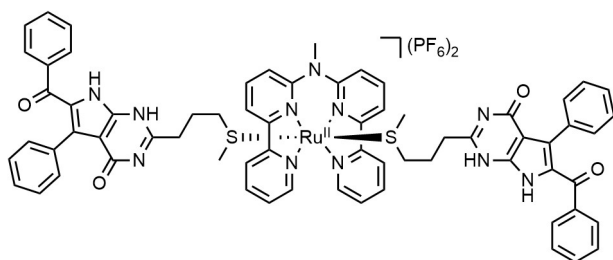
$[\text{Ru}(\text{MeL})\text{Cl}_2]$, **5**: A microwave tube was charged with N-([2,2'-bipyridin]-6-yl)-N-methyl-[2,2'-bipyridin]-6-amine **MeL** (400 mg, 1.18 mmol, 1.0 eq), dichloro(1,5-cyclooctadiene)ruthenium(II) (335 mg, 1.19 mmol, 1.01 eq), *o*-dichlorobenzene (4.7 mL) and a stirring bar. The tube was sealed with a septum containing crimp cap and the vessel

was purged with N_2 for 15 min. Once purged, the mixture was stirred at 180 $^\circ\text{C}$. After 48 h, the reaction mixture was allowed to cool to RT and the product precipitated upon addition of diethyl ether (100 mL). The precipitate was filtered over a membrane filter and washed with diethyl ether, toluene and pentane. Drying under high vacuum yielded the product as dark green powder (519 mg, 1.01 mmol, 86%). ^1H -NMR (400 MHz, DMSO- d_6) δ 9.64 (dd, J = 5.8, 1.5 Hz, 2H), 8.67 (dd, J = 8.2, 1.4 Hz, 2H), 8.38 (dd, J = 7.9, 0.9 Hz, 2H), 8.06 (td, J = 7.8, 1.4 Hz, 2H), 7.96 (t, J = 8.1 Hz, 2H), 7.73 (ddd, J = 7.2, 5.6, 1.3 Hz, 2H), 7.56 (dd, J = 8.5, 0.9 Hz, 2H), 3.96 (s, 3H). $^{13}\text{C}\{\text{H}\}$ NMR (101 MHz, DMSO- d_6) δ 159.05, 158.33, 154.64, 153.54, 135.61, 133.21, 124.71, 122.11, 116.33, 114.25, 43.83. ESI-MS: exact m/z calculated for $[\text{C}_{21}\text{H}_{17}\text{N}_5\text{RuCl} + \text{CH}_3\text{OH}]^{2+}$: 508.1 m/z , found: 507.1 m/z .



$[\text{Ru}(\text{MeL})(\text{STF31})_2](\text{PF}_6)_2$, **[1]**(PF₆)₂: In a microwave tube **5** (101 mg, 0.20 mmol, 1.0 eq) was dissolved in water (0.5 mL), and purged with

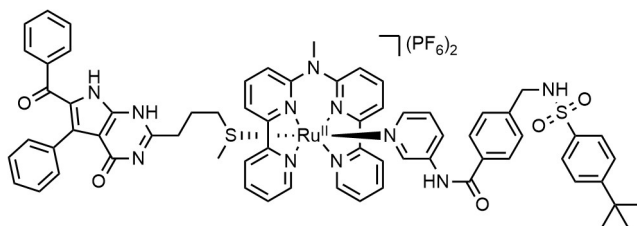
N₂ for 15 min. After stirring at 80 °C for 1 h, the solution was cooled to RT and STF31 (252 mg, 0.59 mmol, 3.0 eq) in methanol (4.5 mL) was added. The resulting mixture was stirred 80 °C and the solution changed color from black to dark red. The conversion was monitored with TLC (SiO₂, 10% methanol half-saturated with KPF₆ in DCM). After 48 h, the reaction was completed and the reaction mixture was allowed to cool to RT. The product was precipitated by addition of half-saturated aqueous KPF₆ solution, the suspension was filtered over a membrane filter and washed with minimal amount of water (5 mL) followed by diethyl ether (100 mL). The crude product was purified by size exclusion chromatography (LH-20 in acetone). The product-containing fractions were combined and concentrated *in vacuo*. After precipitation in diethyl ether and filtration over a membrane filter, drying under high vacuum yielded the product as red powder (188 mg, 0.12 mmol, 61%). ¹H-NMR (400 MHz, Acetone-*d*₆) δ 10.15 – 10.11 (m, 2H), 9.51 (s, 2H), 8.78 – 8.71 (m, 4H), 8.48 (dd, *J* = 7.9, 0.9 Hz, 2H), 8.36 – 8.29 (m, 4H), 8.16 (dd, *J* = 8.7, 0.9 Hz, 2H), 8.10 (ddd, *J* = 7.4, 5.7, 1.3 Hz, 2H), 7.78 – 7.70 (m, 12H), 7.62 – 7.57 (m, 4H), 7.42 (d, *J* = 8.3 Hz, 4H), 7.09 – 7.01 (m, 4H), 4.35 (s, 3H), 4.19 (d, *J* = 6.5 Hz, 4H), 1.33 (s, 18H). ¹³C{H} NMR (101 MHz, Acetone-*d*₆) δ 206.18, 166.38, 158.74, 157.27, 156.62, 156.20, 154.08, 147.94, 144.73, 143.66, 139.60, 138.42, 138.20, 133.54, 128.76, 128.63, 128.56, 128.43, 127.61, 126.88, 126.23, 124.98, 119.29, 118.95, 47.10, 44.92, 31.32. ESI-MS: exact *m/z* calculated for [C₆₇H₆₇N₁₁O₆S₂Ru]²⁺: 643.7 *m/z*, found: 643.9 *m/z*. Elemental analysis (%) for compound **[1]**(PF₆)₂ (C₆₇H₆₇F₁₂N₁₁O₆P₂RuS₂), calculated C, 51.01; H, 4.28; N, 9.77; found C, 50.91; H, 4.17; N, 9.66. UV-Vis (1/1 acetone/H₂O): λ_{max} (ε) = 484 nm (8.3 × 10³ M⁻¹cm⁻¹).



$[\text{Ru}(\text{MeL})(\text{MTI})_2](\text{PF}_6)_2$, **[2]**(PF₆)₂: In a microwave tube **5** (75 mg, 0.15 mmol, 1.0 eq) was dissolved in water (1.0 mL), and purged with N₂ for 15 min. After stirring at 80 °C for 30 min, the solution was cooled to RT and MTI (125 mg, 0.31 mmol, 2.1

eq) in ethylene glycol (3.9 mL) was added. The resulting mixture was stirred at 120 °C and changed color from black to dark red. The conversion was monitored with TLC (SiO₂, 15% methanol half-saturated with KPF₆ in DCM). After 18 h, the reaction was completed and the mixture was allowed to cool to RT. The mixture was precipitated in half-saturated aqueous

KPF₆ solution, filtered over a membrane filter and washed with minimal amount of water (1 mL) followed by diethyl ether (50 mL). The crude product was purified by size-exclusion chromatography (LH-20 in acetone). The product-containing fractions were combined and concentrated *in vacuo*. After precipitation in diethyl ether and filtration over a membrane filter, drying under high vacuum yielded the product as pale brown powder (57 mg, 0.037 mmol, 24%). ¹H-NMR (500 MHz, Acetone-*d*₆) δ 11.33 (s, 2H), 10.45 (s, 2H), 9.79 (dd, *J* = 5.5, 1.3 Hz, 2H), 8.80 – 8.76 (m, 2H), 8.52 (dd, *J* = 8.0, 0.9 Hz, 2H), 8.31 (td, *J* = 7.8, 1.4 Hz, 2H), 8.26 (dd, *J* = 8.6, 7.7 Hz, 2H), 7.94 (ddd, *J* = 7.3, 5.6, 1.4 Hz, 2H), 7.85 (dd, *J* = 8.6, 0.9 Hz, 2H), 7.54 (dd, *J* = 8.3, 1.3 Hz, 4H), 7.36 – 7.31 (m, 7H), 7.17 – 7.12 (m, 5H), 7.11 – 7.05 (m, 7H), 4.12 (s, 3H), 2.47 (t, *J* = 6.5 Hz, 4H), 1.79 (t, *J* = 7.1 Hz, 4H), 1.70 (q, *J* = 6.9 Hz, 4H), 1.36 (s, 6H). ¹³C{H} NMR (126 MHz, Acetone-*d*₆) δ 158.60, 158.33, 156.69, 155.99, 154.50, 140.11, 139.26, 138.48, 133.49, 132.76, 132.41, 130.25, 128.58, 128.46, 127.92, 125.62, 119.52, 118.86, 44.83, 34.20, 32.59, 23.54, 15.40. ESI-MS: exact *m/z* calculated for [C₆₇H₅₉N₁₁O₄S₂Ru]²⁺: 623.7 *m/z*, found: 623.8 *m/z*. Elemental analysis (%) for compound [2](PF₆)₂ (C₆₇H₅₉F₁₂N₁₁O₄P₂RuS₂), calculated C, 52.34; H, 3.87; N, 10.02; found C, 51.82; H, 4.04; N, 9.89. UV-Vis (1/1 acetone/H₂O): λ_{max} (ε) = 449 nm (6.5 × 10³ M⁻¹cm⁻¹).



[Ru(MeL)(STF31)(MTI)](PF₆)₂, [3](PF₆)₂: [1](PF₆)₂ (101 mg, 0.06 mmol, 1 eq) in acetone (50 mL) and MTI (78.4 mg, 0.19 mmol, 3 eq) in tetrahydrofuran (25 mL) were added under nitrogen

to a 140 mL double-walled photoreactor with water cooling (see Figure I.1 and Appendix I for details). Acetone was added to a total volume of 125 mL and the reaction mixture was irradiated with a 650 nm LED lamp at RT while monitoring the reaction progress with TLC (SiO₂, 10% methanol half saturated with KPF₆ in DCM). After 1.5 h, the mixture was concentrated *in vacuo* and the product precipitated upon addition of diethyl ether. The precipitate was filtered over a membrane filter and washed with diethyl ether (50 mL). The crude product was purified by column chromatography (SiO₂, 10% methanol half saturated with KPF₆ in DCM). The product-containing fractions were combined and concentrated, followed by precipitation in half-saturated aqueous KPF₆ (100 mL). After filtration over a membrane filter, the product was washed with a minimal amount of water (1 mL) followed by diethyl ether (50 mL). Drying under high vacuum yielded the product as a brown/red powder (28 mg, 0.018 mmol, 28%). ¹H-NMR (500 MHz, Acetone-*d*₆) δ 11.35 (s, 1H), 10.53 (s, 1H), 10.01 (d, *J* = 5.6 Hz, 2H), 9.47 (s, 1H), 8.71 – 8.62 (m, 3H), 8.41 (d, *J* = 7.8 Hz, 2H), 8.28 (td, *J* = 7.8, 2.7 Hz, 4H), 8.07 (d, *J* = 8.5 Hz, 2H), 8.05 – 8.01 (m, 2H), 7.80 – 7.73 (m, 2H), 7.69 (d, *J* = 8.1 Hz, 2H), 7.63 – 7.56 (m, 3H), 7.56 – 7.50 (m, 2H), 7.45 (d, *J* = 5.6 Hz, 1H), 7.41 (d, *J* = 8.3 Hz, 2H), 7.32 (dq, *J* = 5.9, 3.9, 2.9 Hz, 3H), 7.14 (t, *J* = 7.6 Hz, 2H), 7.10 – 7.01 (m,

4H), 6.96 (dd, $J = 8.4, 5.7$ Hz, 1H), 4.28 (s, 3H), 4.19 (d, $J = 6.6$ Hz, 2H), 2.58 (t, $J = 6.7$ Hz, 2H), 1.84 – 1.75 (m, 2H), 1.58 (s, 3H), 1.33 (s, 9H). ^{13}C -NMR (126 MHz, Acetone- d_6) δ 166.35, 159.59, 158.77, 158.42, 156.89, 156.16, 154.24, 150.42, 146.52, 143.78, 143.08, 139.86, 138.98, 138.54, 133.51, 133.46, 132.68, 132.41, 130.19, 129.01, 128.67, 128.63, 128.54, 128.42, 127.86, 127.62, 126.89, 126.56, 125.12, 119.24, 119.13, 47.09, 44.63, 35.71, 32.85, 31.33, 23.94, 16.87. ESI-HRMS: exact m/z calculated for $[\text{C}_{67}\text{H}_{63}\text{N}_{11}\text{O}_5\text{S}_2\text{Ru}]^{2+}$: 633.6752 m/z , found: 633.6750 m/z . Elemental analysis (%) for compound **[3]**(PF₆)₂ (C₆₇H₆₃F₁₂N₁₁O₅P₂RuS₂), calculated C, 51.67; H, 4.28; N, 9.89; found C, 50.64; H, 4.50; N, 8.95. UV-Vis (1/1 acetone/H₂O): λ_{max} (ϵ) = 459 nm ($6.5 \times 10^3 \text{ M}^{-1}\text{cm}^{-1}$).

Anion exchange: The ruthenium complex of interest as hexafluorophosphate salt was dissolved in a minimum amount of acetone, and diluted with an equal amount of methanol. The solution was brought onto an anion exchange column and eluted with methanol. After collection of the colored fractions and concentration *in vacuo*, the product was precipitated in diethyl ether. Filtration over a membrane filter and drying under high vacuum provided the chloride salt of the product as a red powder. Anion exchange typically proceeded with a yield of around 95%.

[Ru(MeL)(STF31)₂]Cl₂, **[1]**Cl₂

^1H -NMR (400 MHz, MeOD) δ 9.90 (d, $J = 5.6$ Hz, 2H), 8.64 (d, $J = 8.1$ Hz, 2H), 8.50 (d, $J = 2.3$ Hz, 2H), 8.38 (d, $J = 7.8$ Hz, 2H), 8.24 (dt, $J = 11.2, 7.6$ Hz, 4H), 8.06 – 7.98 (m, 4H), 7.76 – 7.70 (m, 4H), 7.69 – 7.64 (m, 4H), 7.61 (ddd, $J = 8.5, 2.3, 1.2$ Hz, 2H), 7.57 – 7.53 (m, 4H), 7.40 (d, $J = 5.5$ Hz, 2H), 7.35 (d, $J = 8.1$ Hz, 4H), 6.95 (dd, $J = 8.4, 5.6$ Hz, 2H), 4.15 (s, 3H), 4.11 (s, 4H), 1.32 (s, 18H). $^{13}\text{C}\{^1\text{H}\}$ NMR (101 MHz, MeOD) δ 168.01, 159.17, 157.68, 157.47, 156.52, 154.23, 148.05, 144.83, 143.90, 139.87, 139.06, 138.80, 138.62, 133.90, 128.92, 128.76, 127.87, 127.16, 126.35, 125.37, 119.36, 119.27, 47.27, 44.49, 31.46. ESI-MS: exact m/z calculated for $[\text{C}_{67}\text{H}_{67}\text{N}_{11}\text{O}_6\text{S}_2\text{Ru}]^{2+}$: 643.7 m/z , found: 643.8 m/z . Elemental analysis (%) for compound **[1]**Cl₂ (C₆₇H₆₇Cl₂N₁₁O₆RuS₂), calculated C, 59.24; H, 4.97; N, 11.34; found C, 59.31; H, 4.92; N, 11.24.

[Ru(MeL)(MTI)₂]Cl₂, **[2]**Cl₂:

^1H NMR (600 MHz, MeOD) δ 9.54 (dt, $J = 5.7, 1.1$ Hz, 2H), 8.57 (dd, $J = 8.1, 1.3$ Hz, 2H), 8.32 – 8.28 (m, 2H), 8.17 (td, $J = 7.8, 1.3$ Hz, 2H), 8.12 – 8.08 (m, 2H), 7.84 (ddd, $J = 7.2, 5.5, 1.3$ Hz, 2H), 7.59 (d, $J = 8.5$ Hz, 2H), 7.57 – 7.55 (m, 4H), 7.36 – 7.31 (m, 6H), 7.16 – 7.10 (m, 10H), 3.90 (s, 3H), 2.44 – 2.37 (m, 4H), 1.69 – 1.61 (m, 4H), 1.54 (t, $J = 7.0$ Hz, 4H), 1.20 (s, 6H). $^{13}\text{C}\{^1\text{H}\}$ NMR (151 MHz, MeOD) δ 190.39, 161.54, 158.58, 158.53, 156.97, 156.08, 154.59, 151.01, 140.36, 139.66, 138.59, 133.72, 133.35, 132.63, 130.74, 129.42, 129.03, 128.93, 128.65, 128.53, 128.46, 125.80, 119.70, 118.71, 106.04, 44.67, 34.33, 32.06, 23.08, 15.37. ESI-MS: exact m/z calculated for $[\text{C}_{67}\text{H}_{59}\text{N}_{11}\text{O}_4\text{S}_2\text{Ru}]^{2+}$: 623.7 m/z , found: 623.8 m/z .

[Ru(MeL)(STF31)(MTI)]Cl₂, [3]Cl₂:

¹H-NMR (500 MHz, MeOD) δ 9.78 (d, *J* = 5.7 Hz, 2H), 8.47 (d, *J* = 8.1 Hz, 2H), 8.42 (d, *J* = 2.4 Hz, 1H), 8.22 (d, *J* = 7.8 Hz, 2H), 8.16 (q, *J* = 8.2 Hz, 4H), 7.95 (t, *J* = 6.7 Hz, 2H), 7.89 (d, *J* = 8.5 Hz, 2H), 7.73 (d, *J* = 8.3 Hz, 2H), 7.64 (d, *J* = 8.1 Hz, 2H), 7.55 (dd, *J* = 7.8, 4.4 Hz, 5H), 7.49 (d, *J* = 8.3 Hz, 1H), 7.33 (dt, *J* = 11.5, 7.8 Hz, 5H), 7.22 (d, *J* = 5.6 Hz, 1H), 7.16 – 7.07 (m, 6H), 6.86 (dd, *J* = 8.4, 5.6 Hz, 1H), 4.11 (d, *J* = 3.4 Hz, 5H), 2.52 (t, *J* = 6.2 Hz, 2H), 1.84 (s, 2H), 1.75 (s, 2H), 1.45 (s, 3H), 1.32 (s, 10H). ¹³C{H} NMR (126 MHz, MeOD) δ 168.06, 161.56, 158.76, 157.26, 156.47, 154.37, 146.72, 144.10, 143.22, 140.17, 139.40, 138.98, 138.68, 133.81, 133.75, 133.68, 133.31, 132.61, 130.63, 129.36, 128.93, 128.73, 128.50, 127.88, 127.17, 126.67, 125.33, 119.38, 119.21, 47.26, 44.39, 36.12, 32.47, 31.47, 17.03. ESI-MS: exact *m/z* calculated for [C₆₇H₆₃N₁₁O₅S₂Ru]²⁺: 633.7 *m/z*, found: 633.8 *m/z*. Elemental analysis (%) for compound [3]Cl₂ (C₆₇H₆₃Cl₂N₁₁O₅RuS₂), calculated C, 59.24; H, 4.97; N, 11.34; found C, 59.94; H, 4.66; N, 11.32.

[Ru(MeL)(Py)(MTE)]Cl₂, [4]Cl₂:

¹H-NMR (400 MHz, MeOD) δ 9.85 (dd, *J* = 6.1, 1.2 Hz, 2H), 8.58 (d, *J* = 7.8 Hz, 2H), 8.34 (dd, *J* = 7.9, 1.0 Hz, 2H), 8.31 – 8.21 (m, 4H), 8.02 (ddd, *J* = 7.3, 5.6, 1.4 Hz, 2H), 7.97 (dd, *J* = 8.5, 1.0 Hz, 2H), 7.53 (tt, *J* = 7.7, 1.5 Hz, 1H), 7.48 (dt, *J* = 5.1, 1.5 Hz, 2H), 6.95 – 6.87 (m, 2H), 4.14 (s, 3H), 1.90 (t, *J* = 5.7 Hz, 2H), 1.46 (s, 3H). ¹³C{H} NMR (101 MHz, MeOD) δ 158.91, 157.40, 156.56, 154.54, 151.90, 140.19, 139.36, 128.91, 127.07, 125.36, 119.44, 119.29, 58.98, 44.23, 40.29, 17.71. ESI-HRMS: exact *m/z* calculated for [C₂₉H₃₀N₆O₁S₁Ru]²⁺: 306.0617 *m/z*, found: 306.0619 *m/z*. Elemental analysis (%) for compound [4]Cl₂ (C₂₉H₃₀Cl₂N₆ORuS), calculated C, 51.03; H, 4.43; N, 12.31; found C, 49.99; H, 4.70; N, 11.94.

4.5.3 Photochemistry

Photosubstitution followed by ¹H-NMR

The ¹H-NMR photosubstitution experiments were performed as described in appendix I.2.5. Results for the compounds reported in this chapter are provided in appendix IV.2.3.

Molar absorption coefficient determination

Molar absorption coefficients were determined as described in appendix I.2.1. Results for the compounds reported in this chapter are provided in appendix IV.1.1.

Photosubstitution quantum yield measurements

Photon fluxes of all LEDs were determined using ferrioxalate actinometry and is described in detail in appendix I. The photosubstitution quantum yields were determined as described in appendix I, and the results are reported in appendix IV.1.2.

Singlet oxygen generation quantum yield measurements

The emission spectra were recorded, and the corresponding singlet oxygen generation quantum yields determined as described in appendix I.2.4. The emission spectra and data are reported in appendix IV.1.3.

UV-Vis absorbance evolution in OptiMEM media (“mock irradiation”)

To model what happens in cell culture conditions, compounds [1]Cl₂, [2]Cl₂ or [3]Cl₂ were dissolved in DMSO and further diluted with OptiMEM complete (OptiMEM supplemented with 2.5% v/v fetal calf serum, 0.1% v/v penicillin/streptomycin, and 1.0% v/v Glutamine-S) to a final concentration of 5.0×10^{-5} M with 0.14% DMSO. The compound solution were transferred to a 96-well plate (flat base; Sarstedt; v = 200 μ L per well) and irradiated at different time intervals with green light (520 ± 35 nm; 17.1 mW/cm²; t = 0, 2.5, 5, 7.5, 10, 12.5, 15, 20, 25 and 30 minutes) or red light (630 ± 24 nm; 31.3 mW/cm²; t = 0, 5, 10, 15, 20, 25, 30, 40, 50 and 60 minutes). The absorbance between 300 and 800 nm was measured by a M1000 Tecan reader. Averaging the absorbance of a technical triplicate and baseline subtraction provided the resulting spectra reported in appendix IV.5.

4.5.4 Cell viability assay

Experimental details of cell culturing, cytotoxicity and cell irradiation are described in appendix I.3. The results are reported in detail in appendix IV.2.

4.5.5 Combination index calculations

The combination indexes were calculated based on the method by Chou and Talalay using the CompuSyn software (free download after registration; www.combosyn.com).²³ The method is based on the median-effect equation derived from the mass-action law principle, as shown equation 4.1:

$$\frac{f_a}{f_u} = \left(\frac{D}{D_m} \right)^m \quad (4.1)$$

where f_a is the affected fraction (metabolic activity inhibition compared to untreated wells), f_u is the unaffected fraction ($f_u = 1 - f_a$), D is the dose of the drug (in μ M), D_m is the median-effect dose (in μ M), and m is the slope of the dose-response curve. Because evaluated mixture of STF31:MTI was kept at a 1:1 ratio, the CI values can be calculated for each effect according equation 4.2:

$$CI = (D_{mix})_{f_a} \cdot \left(\frac{1}{(D_{STF31})_{f_a}} + \frac{1}{(D_{MTI})_{f_a}} \right) \quad (4.2)$$

where $(D_{mix})_{f_a}$ is the dose (in μ M) of the mixture (STF-31:MTI, or of green light-activated [3]²⁺) to achieve an effect f_a and $(D_x)_{f_a}$ is the dose (in μ M) of a single drug x (STF-31 or MTI) to achieve the same effect f_a .

4.5.6 Cellular uptake

Materials and instrumentation

65% Nitric acid (Suprapur, Merck) was used in the sample digestion process, while diluted 1% nitric acid (v/v) was employed as a carrying solution throughout the ICP measurements. For preparation of calibration and internal standards National Institute of Standards and Technology (NIST)-traceable 1000 mg/L elemental standards were used (TraceCERT, Fluka). Approximately 18 M Ω cm⁻¹ water (Milli-Q) was employed in all sample preparation and analysis steps. Calibration standards were prepared in a Secuflow fume hood (SCALA) to prevent contamination by atmospheric particulates. The standard samples and measurement samples were analyzed for trace elements using the NexION 2000 (PerkinElmer) ICP-MS instrument equipped with a concentric glass nebulizer and Peltier-cooled glass spray chamber. An SC2 DX autosampler (PerkinElmer) was connected to the ICP-MS for sample introduction. Syngistix software for ICP-MS (v.2.5, PerkinElmer) was used for all data recording and processing. Five trace elemental calibration standards for ICP-MS analysis were prepared using NIST-traceable 1000 mg/L Ru standards: 0, 1, 5, 20, and 100 μ g/L. Samples were analyzed without dilution in the original delivery containers to minimize the possibility of contamination. Here, 10 μ g/L Rh and In were used as internal standards. To check the calibration, samples were analyzed with a blank measurement and a repeat measurement of one of the calibration standards. For the calibration curve, the accepted correlation coefficient (Cor.Coeff) was to be found higher than 0.999.

Determination of cellular ruthenium content

Cellular ruthenium content in A375 (normoxic and hypoxic), U87MG (normoxic and hypoxic) and U251 (normoxic) cells was determined by ICP-MS. The cells were seeded (density = 175 \times 10³ cells/well for A375 and U251; 200 \times 10³ cells/well for U87MG) in OptiMEM complete media (1 mL) in 12-well transparent plates (Sarstedt, #83.3921.500) at t = 0 h and incubated at 37°C. After 24h, 1 mL of the compound solution was added (final concentrations: [1]Cl₂ = 2 μ M; [2]Cl₂ = 0.5 μ M; [3]Cl₂ = 1 μ M for A375, 5 μ M for U87MG NX, 10 μ M for U87MG HX and U251). At t = 72 h, the medium was aspirated and the well washed with 1 mL PBS. After trypsinization of the cells (1 mL for 1 min), OptiMEM complete (900 μ L) was added and the cell suspension was transferred to a 1.5 mL Eppendorf tube. Trypan blue (10 μ L) and the cell suspension (10 μ L) were mixed, and the cells were counted using a BioRad TC20™ automated cell counter. The cell suspension was centrifuged (5 min at 1 \times 10⁵ rpm), the supernatant removed, and the pellet was washed twice with PBS (2 \times 1 mL). To digest the cells, the cell pellet was dissolved in 65% nitric acid (500 μ L), transferred to glass test tube covered with a marble and incubated in an oven at 95 °C overnight. The resulting solution was transferred to a 15 mL corning tube (Sarstedt) and diluted with MilliQ water to a total volume of 10 mL (~3.2% HNO₃). The Ru content was analyzed by ICPMS. The amount of ruthenium taken up by cells was calculated and is reported in Table IV.3. The reported values are the mean with standard deviation of three individual experiments.

4.6 References

- (1) Mokhtari, R. B.; Homayouni, T. S.; Baluch, N.; Morgatskaya, E.; Kumar, S.; Das, B.; Yeger, H. *Oncotarget* **2017**, *8*, 38022.
- (2) Al-Lazikani, B.; Banerji, U.; Workman, P. *Nat Biotechnol* **2012**, *30*, 679.
- (3) Nair, N. U.; Greninger, P.; Zhang, X.; Friedman, A. A.; Amzallag, A.; Cortez, E.; Sahu, A. D.; Lee, J. S.; Dastur, A.; Egan, R. K.; Murchie, E.; Ceribelli, M.; Crowther, G. S.; Beck, E.; McClanaghan, J.; Klump-Thomas, C.; Boisvert, J. L.; Damon, L. J.; Wilson, K. M.; Ho, J.; Tam, A.; McKnight, C.; Michael, S.; Itkin, Z.; Garnett, M. J.; Engelman, J. A.; Haber, D. A.; Thomas, C. J.; Ruppin, E.; Benes, C. H. *Nat Commun* **2023**, *14*, 3830.
- (4) Jaaks, P.; Coker, E. A.; Vis, D. J.; Edwards, O.; Carpenter, E. F.; Leto, S. M.; Dwane, L.; Sassi, F.; Lightfoot, H.; Barthorpe, S.; Van Der Meer, D.; Yang, W.; Beck, A.; Mironenko, T.; Hall, C.; Hall, J.; Mali, I.; Richardson, L.; Tolley, C.; Morris, J.; Thomas, F.; Lleshi, E.; Aben, N.; Benes, C. H.; Bertotti, A.; Trusolino, L.; Wessels, L.; Garnett, M. J. *Nature* **2022**, *603*, 166.
- (5) Fan, K.; Cheng, L.; Li, L. *Briefings in Bioinformatics* **2021**, *22*, bbab271.
- (6) Qu, C.-P.; Sun, G.-X.; Yang, S.-Q.; Tian, J.; Si, J.-G.; Wang, Y.-F. *Medicine* **2017**, *96*, e5797.
- (7) Wu, D.; Pusuluri, A.; Vogus, D.; Krishnan, V.; Shields, C. W.; Kim, J.; Razmi, A.; Mitragotri, S. *Journal of Controlled Release* **2020**, *323*, 36.
- (8) Jangili, P.; Won, M.; Kim, S. J.; Chun, J.; Shim, I.; Kang, C.; Ren, W. X.; Kim, J. S. *ACS Appl. Bio Mater.* **2019**, *2*, 3532.
- (9) Sharma, A.; Chun, J.; Ji, M. S.; Lee, S.; Kang, C.; Kim, J. S. *ACS Appl. Bio Mater.* **2021**, *4*, 2026.
- (10) Bonnet, S. J. *Am. Chem. Soc.* **2023**, *145*, 23397.
- (11) Havrylyuk, D.; Hachey, A. C.; Fenton, A.; Heidary, D. K.; Glazer, E. C. *Nat. Commun.* **2022**, *13*, 3636.
- (12) Respondek, T.; Garner, R. N.; Herroon, M. K.; Podgorski, I.; Turro, C.; Kodanko, J. J. *Am. Chem. Soc.* **2011**, *133*, 17164.
- (13) Filevich, O.; Ethenique, R. *Photochem Photobiol Sci* **2013**, *12*, 1565.
- (14) He, G.; He, M.; Wang, R.; Li, X.; Hu, H.; Wang, D.; Wang, Z.; Lu, Y.; Xu, N.; Du, J.; Fan, J.; Peng, X.; Sun, W. *Angew Chem Int Ed* **2023**, *62*, e202218768.
- (15) Bretin, L.; Husiev, Y.; Ramu, V.; Zhang, L.; Hakkennes, M.; Abyar, S.; Johns, A. C.; Le Dévédec, S. E.; Betancourt, T.; Kornienko, A.; Bonnet, S. *Angew Chem Int Ed* **2024**, *63*, e202316425.
- (16) Medellin, D. C.; Zhou, Q.; Scott, R.; Hill, R. M.; Frail, S. K.; Dasari, R.; Ontiveros, S. J.; Pelly, S. C.; Van Otterlo, W. A. L.; Betancourt, T.; Shuster, C. B.; Hamel, E.; Bai, R.; LaBarbera, D. V.; Rogelj, S.; Frolova, L. V.; Kornienko, A. J. *Med. Chem.* **2016**, *59*, 480.
- (17) Kraus, D.; Reckenbeil, J.; Veit, N.; Kuerpig, S.; Meisenheimer, M.; Beier, I.; Stark, H.; Winter, J.; Probstmeier, R. *Cell Oncol.* **2018**, *41*, 485.
- (18) Van Rixel, V. H. S.; Ramu, V.; Auyeung, A. B.; Beztsinna, N.; Leger, D. Y.; Lameijer, L. N.; Hilt, S. T.; Le Dévédec, S. E.; Yildiz, T.; Betancourt, T.; Gildner, M. B.; Hudnall, T. W.; Sol, V.; Liagre, B.; Kornienko, A.; Bonnet, S. J. *Am. Chem. Soc.* **2019**, *141*, 18444.
- (19) Lameijer, L. N.; Ernst, D.; Hopkins, S. L.; Meijer, M. S.; Askes, S. H. C.; Le Dévédec, S. E.; Bonnet, S. *Angew. Chem. Int. Ed.* **2017**, *56*, 11549.
- (20) Snellenburg, J. J.; Laptinok, S. P.; Seger, R.; Mullen, K. M.; Stokkum, I. H. M. V. *J. Stat. Soft.* **2012**, *49*.
- (21) *The IUPAC Compendium of Chemical Terminology: The Gold Book*; Gold, V., Ed.; 4th ed.; International Union of Pure and Applied Chemistry (IUPAC): Research Triangle Park, NC, **2019**.
- (22) Bae, S.-K.; Kim, S.-R.; Kim, J. G.; Kim, J. Y.; Koo, T. H.; Jang, H.-O.; Yun, I.; Yoo, M.-A.; Bae, M.-K. *FEBS Letters* **2006**, *580*, 4105.
- (23) Chou, T.-C.; Talalay, P. *Advances in Enzyme Regulation* **1984**, *22*, 27.
- (24) Garner, R. N.; Gallucci, J. C.; Dunbar, K. R.; Turro, C. *Inorg. Chem.* **2011**, *50*, 9213.
- (25) Sgambellone, M. A.; David, A.; Garner, R. N.; Dunbar, K. R.; Turro, C. J. *Am. Chem. Soc.* **2013**, *135*, 11274.

- (26) Doroshow, J. H.; Simon, R. M. *Cell* **2017**, *171*, 1476.
- (27) Harkcom, W. T.; Ghosh, A. K.; Sung, M. S.; Matov, A.; Brown, K. D.; Giannakakou, P.; Jaffrey, S. R. *Proc. Natl. Acad. Sci. U.S.A.* **2014**, *111*.
- (28) Jing, X.; Yang, F.; Shao, C.; Wei, K.; Xie, M.; Shen, H.; Shu, Y. *Mol Cancer* **2019**, *18*, 157.
- (29) Al-Mehdi, A.-B.; Pastukh, V. M.; Swiger, B. M.; Reed, D. J.; Patel, M. R.; Bardwell, G. C.; Pastukh, V. V.; Alexeyev, M. F.; Gillespie, M. N. *Sci. Signal.* **2012**, *5*.
- (30) Sharma, P.; Xu, J.; Williams, K.; Easley, M.; Elder, J. B.; Lonser, R.; Lang, F. F.; Lapalombella, R.; Sampath, D.; Puduvalli, V. K. *Neuro-Oncology* **2022**, *24*, 229.

Chapter 5

Targeting Heme Oxygenase 1 with photoactivatable ruthenium-based inhibitors

Abstract: By degrading heme into biliverdin, iron(II) ions, and carbon monoxide, Heme Oxygenase 1 (HO-1) plays a crucial role in the cellular stress response and maintenance of cellular homeostasis. Overexpression of HO-1 is observed in various cancers, promoting tumor growth, invasiveness, chemoresistance, and poor prognosis. Inhibiting HO-1 can re-sensitize resistant cancer cells, making it a target for anti-cancer therapy. However, many inhibitors cause side effects due to poor selectivity, as hemoproteins are present in nearly every tissue. Herein, two strategies are reported for development of photoactivatable ruthenium(II)-based HO-1 inhibitors. The first strategy involves modification of the tetrapyrridyl ligand di([2,2'-bipyridin]-6-yl)amine (HL) with propyl carboxylic acid groups through sp^2 - sp^3 Suzuki-Miyaura cross-coupling or pyridylic C-H functionalization reactions. Upon coordination, the resulting ruthenium(II) complexes may mimic heme and as a result inhibit HO-1. For the second strategy, complexes based on $[\text{Ru}(\text{MeL})(\text{X})(\text{Y})]^{2+}$ were prepared, with MeL being an *N*-methylated analogue of HL and X = QC82, a known HO-1 inhibitor coordinated through imidazole. For **[24]**²⁺, where X = Y = QC82, green or red light induced photosubstitution of a single axial ligand was relatively inefficient with a quantum yield of ~ 0.00035 . Strikingly, for dissymmetric complexes **[25]**²⁺ (Y = STF31, a NAMPT inhibitor) and **[26]**²⁺ (Y = pyridine) selective photosubstitution of the pyridyl ligand was observed with quantum yields of 0.012. Docking of $[\text{Ru}(\text{MeL})(\text{QC82})]^{2+}$, a model for the aqua-photoproduct $[\text{Ru}(\text{MeL})(\text{QC82})(\text{H}_2\text{O})]^{2+}$, with HO-1 using the program MetalDock suggested a similar binding mode as heme. While *in vitro* photocytotoxicity was observed for **[24]**²⁺ and **[25]**²⁺ in skin melanoma cells, the current data do not provide evidence for HO-1 inhibition. Nonetheless, these results provide a foundation for developing photoactivatable ruthenium-based HO-1 inhibitors.

This work will be published as a full paper: W. Verbeet, M.L.N. Hakkennes, S. Bonnet, *manuscript in preparation*.

5.1 Introduction

Heme Oxygenase 1 (HO-1) is the main enzyme responsible for the catabolism of free heme and it is critical for maintaining cellular homeostasis. By catalyzing the degradation of heme into biliverdin, carbon monoxide (CO) and iron(II) ion (Fe^{2+}), the enzymatic activity of HO-1 mitigates the cytotoxic effects of free heme while also generating biologically active products.¹ Biliverdin is rapidly converted into bilirubin, a potent antioxidant. CO is an important signaling molecule that can activate a wide range of cytoprotective pathways, including anti-inflammation, anti-apoptosis and angiogenesis.² The pro-oxidative Fe^{2+} ions released in the cytosol are readily sequestered by ferritin, a globular protein responsible for iron storage. Unlike the two other isoforms of the enzyme (HO-2 and HO-3), the expression of HO-1 is upregulated in response to various stimuli, including its substrate heme, oxidative stress and hypoxia, highlighting its cytoprotective role.

Although HO-1 is crucial for mitigating cellular stress, its overexpression has been observed in various cancer types and has been linked with tumor growth, angiogenesis, invasiveness, resistance to therapy and poor prognosis.³ Furthermore, the induction of HO-1 expression by treatment with chemo,^{4,5} radio,⁶ and photodynamic^{7,8} therapeutics has been widely reported and generally reduces the efficacy of the therapy. Chemoresistance can be diminished by inhibition of HO-1 re-sensitizing the cancer cells towards a given treatment, as demonstrated for doxorubicin in breast adenocarcinoma.⁵ HO-1 is therefore an emerging target in anti-cancer therapy. HO-1 was shown to be inhibited by either metalloporphyrins (MPs) or organic inhibitors. As structural analogs of heme, MPs consist of a protoporphyrin (PP) chelating a metal ion such as zinc (ZnPP), tin (SnPP) and manganese (MnPP).⁹ Although MPs are competitive HO-1 inhibitors and have proven their clinical significance, side effects are common as the close resemblance between MPs and heme can lead to upregulation of HO-1 upon treatment with MPs. Alternatively, organic inhibitors have been reported such as azalanstat. They typically act as non-competitive inhibitors by coordinating their imidazole moiety to the iron center of the heme substrate, thereby preventing degradation of the substrate by the enzyme.¹⁰ Despite significant advancements in potency (μM) and selectivity (vs. HO-2 and HO-3) of the inhibitors that have been achieved by medicinal chemistry efforts, selective nanomolar HO-1 inhibitors have yet to be identified. The ubiquitous expression of HO-1 and hemoproteins means that the doses required for current inhibitors can affect normal cellular functions, causing significant side effects. Consequently, novel therapeutic strategies must be developed to inhibit HO-1 activity, and confirm it as a viable target for anti-cancer therapy.

Since the poor selectivity and off-target effects are the main challenges in HO-1 inhibition, the use of external stimuli to locally activate the inhibitor could present a viable solution. By employing light as a trigger, ruthenium-based, photoactivated chemotherapy (PACT)

has been demonstrated to be a promising strategy for cancer treatment. In PACT, a chemotherapeutic drug is modified to become inactive (and non-toxic) in the dark, but to recover its biological activity after irradiation with visible light.^{11–13} One typical design for PACT compounds consists in “photocaging” a biologically active organic inhibitor by conjugating it to a non-toxic but photocleavable ruthenium polypyridyl complex. In this work we envisioned an alternative strategy where the ruthenium fragment is the inhibitor, and the ligand bound to it is the photocleavable protecting group. We hence designed a tetrapyridyl ruthenium(II) complex that closely resembles the heme substrate of HO-1 and thereby may serve as HO-1 inhibitor (Figure 5.1). The two axial coordination sites of the octahedral complex are occupied by photolabile ligands that will prevent, in the dark, interaction of the ruthenium-based prodrug with HO-1. To simplify the study, these axial ligands were chosen to be biologically inactive and be photosubstituted, upon light irradiation, by solvent molecules (e.g., H₂O) that can be readily exchanged for the heme-binding His25 residue in the enzymatic pocket of HO-1, thereby ensuring enzyme inhibition. The slower kinetics for ligand exchange of ruthenium(II) compared to iron(II) should result in competitive inhibition of HO-1 and a near covalent binding mode of the ruthenium-based inhibitor.

In this chapter two strategies are described for the development of a ruthenium-based HO-1 inhibitors (Figure 5.1). In the first strategy (Figure 5.1b), modification is proposed of the tetrapyridyl ligand di([2,2'-bipyridin]-6-yl)amine (HL) with propyl carboxylic acid (–C₂H₄COOH) groups, that will result in a ruthenium(II) complex that may mimic the structure of the heme group.¹⁴ To maximize close interaction between the ruthenium complex and the catalytic pocket of the enzyme, the –C₂H₄COOH substituents will be located, like in heme, on the “same” side of the ligand. Furthermore, coordination of two biologically inactive but photolabile ligands at the two axial positions of the octahedron will prevent inhibition of HO-1 by the metal complex in the dark. The second strategy investigated here consisted in coordinating 1-(adamantan-1-yl)-2-(1*H*-imidazol-1-yl)ethanone (QC82), a synthetically available and known HO-1 inhibitor, to a [Ru^{II}(MeL)]²⁺ moiety.¹⁵ In this approach, the imidazole of QC82 remains strongly bound to the ruthenium center even under light irradiation, thereby providing a ruthenium complex that may inhibit HO-1 due to its resemblance to the heme bound to QC82 in the catalytic pocket of HO-1 (Figure 5.1c). Here as well a photolabile but inactive pyridine ligand is coordinated in *trans* position to QC82 to prevent inhibition of the protein by the prodrug in the dark, thereby yielding a PACT complex that potentially generates an active inhibitor for HO-1 upon light irradiation. If one of these strategies works, it would become possible to replace the biologically inactive photolabile ligands by biologically active analogues, to generate synergistic effects between the HO-1 inhibiting metal complex and the photoreleased cytotoxic axial ligand (Figure 5.1a). Since cancer cells are generally in an up-regulated metabolic state, combining HO-1 inhibitors with an

inhibitor targeting a metabolic pathway may lead to synergies. In this study, we envision the use of 4-[[[4-(2-methyl-2-propanyl)phenyl]sulfonyl]amino)methyl]-N-(3-pyridinyl)benzamide (STF31) for that purpose. STF31 was reported as an inhibitor of both glucose transporter 1 (GLUT1) and nicotinamide phosphoribosyltransferase (NAMPT), which is the rate-limiting enzyme in the NAD salvage pathway. STF31 is too cytotoxic to be used as a drug in the free form, but it has been reported as powerful motif for ruthenium-based PACT as it binds strongly to ruthenium(II) via its non-hindered pyridine ring, and can be released by light irradiation.¹⁶ In this chapter, we also describe the results of our efforts towards the second strategy where light irradiation generates both a ruthenium-based inhibitor specifically designed to target HO-1, and STF31.

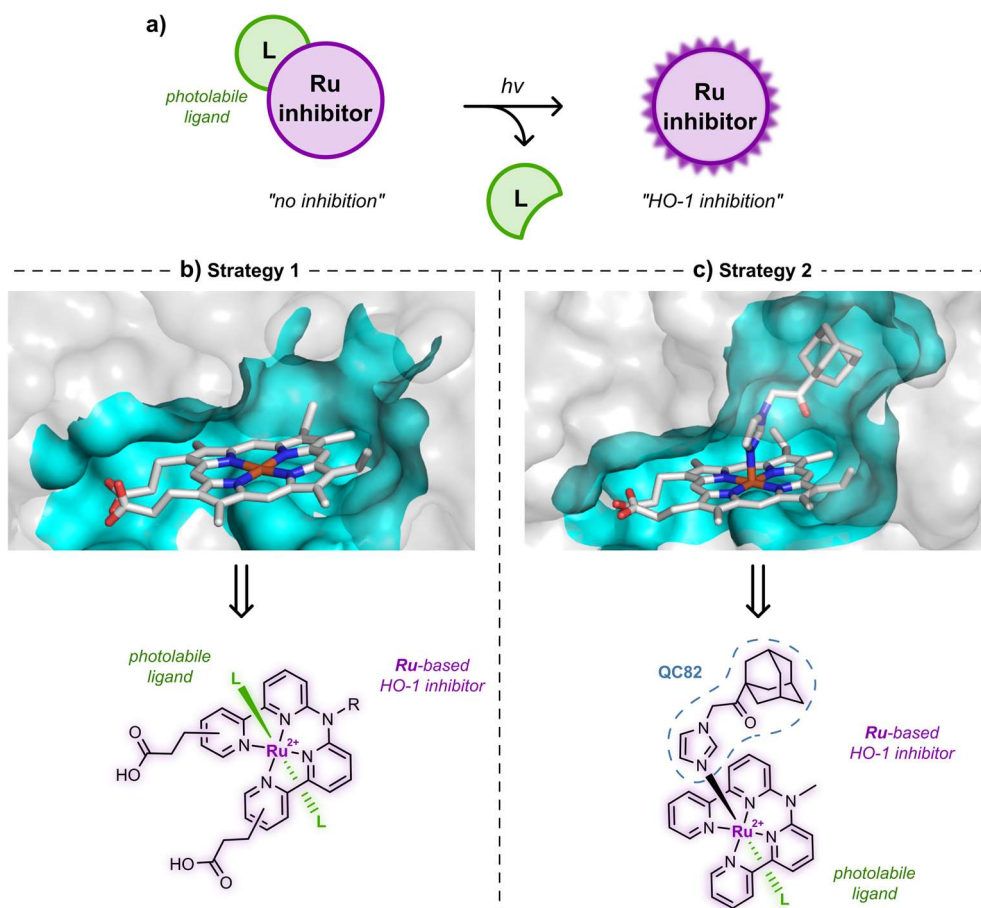


Figure 5.1 Two strategies towards the design of photoactivated ruthenium(II)-based inhibitors targeting Heme Oxygenase-1 (a). In strategy 1 (b), a planar tetrapyrridyl ligand bound to ruthenium is functionalized with propionic acid side chains to result in a ruthenium complex that mimics the heme substrate of the protein (as shown in the crystal structure of the heme binding pocket of HO-1; PDB 1N3U). In strategy 2 (c), a ruthenium tetrapyrridyl fragment remains bound to the known organic

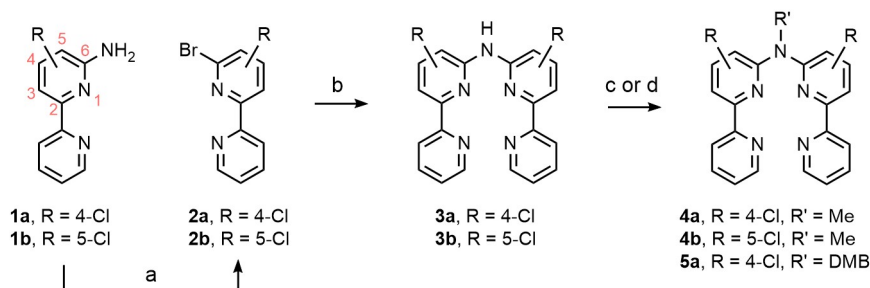
inhibitor QC82 to mimic the heme substrate bound to an HO-1 inhibitor (as shown in the crystal structure; PDB 3CZY). In both cases, the remaining axial position(s) is(are) used to bind a photocleavable protecting group **L** (green) that can be photosubstituted to trigger HO-1 inhibition by the ruthenium-based inhibitor (purple).

5.2 Results & discussion

5.2.1 Strategy 1: Functionalization of the tetrapyrridyl ligand HL

To facilitate the functionalization of the tetrapyrridyl ligand HL and mimic the structure of protoporphyrin IX (heme without and iron center), reactive moieties are needed that allow for introducing carboxylic acid-terminated alkyl groups. Importantly, these reactive moieties should not interfere with the synthesis of the HL scaffold. Incorporation of chloro-substituents in ortho or meta position with respect to the amine bridge of HL was first envisioned, since these substituents have been reported as substrates in numerous sp^2 - sp^3 cross-coupling reactions.¹⁷⁻¹⁹

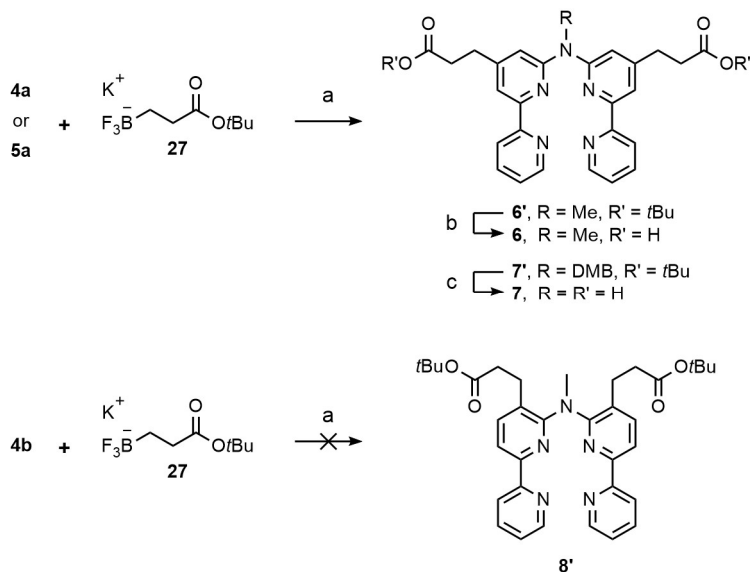
Following the synthesis of **1a** and **1b** as reported in Chapter 2, the corresponding bromo-derivatives **2a** and **2b** were prepared through a Sandmeyer-type reaction in moderate to good yields (Scheme 5.1). Subsequently, a palladium-catalyzed Buchwald-Hartwig coupling between the amino- and bromo-bipyridine yielded the corresponding dichloro-tetrapyridine compounds **3a** and **3b**. As the acidic proton of the resulting bridging amine may interfere with the substitution of the chloro-substituents, **3a** and **3b** were *N*-methylated in presence of iodomethane under basic conditions to provide **4a** and **4b**. To investigate the potential effect of the *N*-methyl capping on the inhibitory properties of the final inhibitor, the protecting group 2,4-dimethoxybenzyl (DMB), was also installed on one of the isomers (**3a**) to provide **5a**.



Scheme 5.1 a) NaNO_2 , Br_2 in HBr (48%, aq.), -5°C – rt., 1.5 h, 60% for **2a**, 71% for **2b**; b) $\text{Pd}_2(\text{DBA})_3$, dppp, NaOtBu in toluene, 80°C , 5 days, 82% for **3a**, 50% for **3b**; c) *i.* KOH in DMSO, rt., 1 h; *ii.* MeI, rt., 2 h, 89% for **4a**, 89% for **4b**; d) *i.* NaH in DMF, rt., 1.5 h; *ii.* DMB-Br, rt., 18 h, 99% for **5a**.

With the dichloro-substrates **4a**, **4b** and **5a** in hand, various reaction conditions were screened for the cross-coupling of the sp^2 C atoms of the chloride-functionalized pyridyl groups with alkyl (sp^3) chains (Scheme 5.2). Initial attempts involving various phosphine-

palladium based catalysts, were unsuccessful. This result is not surprising, as reports specifically aimed towards functionalization of heteroaryl halides through sp^2 - sp^3 cross-coupling reactions are relatively rare compared to reports on sp^2 - sp^2 cross-coupling reactions. Furthermore, we need to perform cross-coupling not once but twice per molecule of substrate, highlighting the necessity for optimal reaction conditions. The use of potassium trifluoroborate salt **27** was therefore envisioned as substrate in a palladium-catalyzed Suzuki-Miyaura cross-coupling reaction. As extensively reported on by Molander, alkyltrifluoroborates have emerged as an excellent alternative for alkylboronic acids and alkylboronate esters as coupling partners in this reaction.²⁰ These alkyltrifluoroborates function as protected boronic acids due to the strong fluorine-boron bond and tetrasubstituted character of the boron center; they are deprotected *in situ* during the cross-coupling reaction. While these conditions did provide **6'** and **7'** in low yields, a relatively high molar percentage (>60 mol%) of Pd-catalyst was needed which led to Pd contamination of the isolated products.¹⁷ This contamination was likely due to the coordinative character of the tetrapyridyl substrate. Therefore, 2,4,6-trimercaptotriazine-functionalized silica (Silia-DMT) was used as a Pd-scavenger after the coupling step, which provided **6'** and **7'** with yields of 62% and 67%, respectively (Scheme 5.2). Subsequent hydrolysis under basic or acidic conditions yielded the di-carboxylic acid compounds **6** and **7**.



Scheme 5.2 a) *i.* potassium (3-(tert-butoxy)-3-oxopropyl)trifluoroborate **27**, Pd(OAc)₂, XPhos, K₂CO₃ in toluene/H₂O, 80 °C, 2–3 days; *ii.* Silica-DMT in toluene, rt., 2–3 h, 62% for **6'**, 67% for **7'**. b) NaOH in DCM/methanol, rt., 16 h, 25%. c) TFA/DCM, 40 °C, 2 h, 34%.

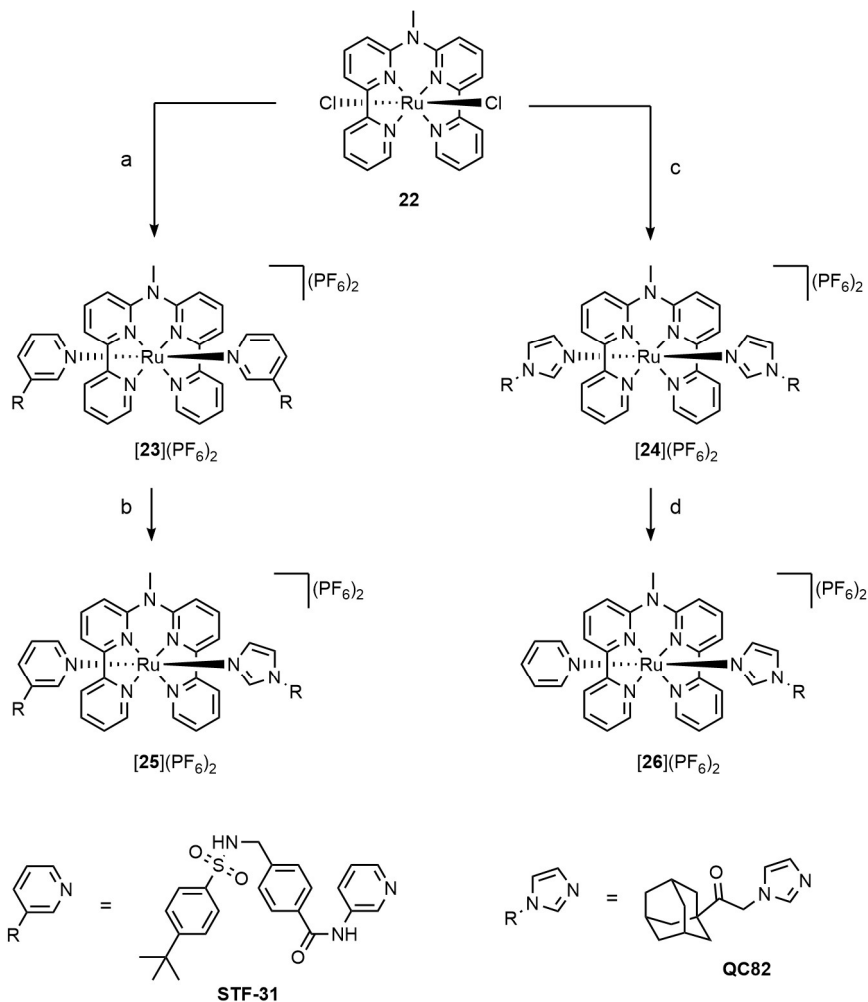
The methodology, however, did not result in a substitution reaction for substrate **4b**, which is probably a consequence of the sterically hindered character of the *ortho* position of the

chlorine on the pyridyl ring with respect to the amine bridge, combined with the coordinative character of the substrate. Since the Suzuki-Miyaura cross-coupling was only successful for the functionalization of the *para* position of the pyridyl N atom and *meta* to the bridging amine, an alternative synthetic route was needed for the functionalization of the C5 position (**4b**). For this strategy to succeed, several aspects were considered. Firstly, the use of transition metal catalysts was avoided to prevent coordinative quenching of the catalyst by the substrate. Secondly, halogens or other highly reactive moieties were avoided as leaving groups since they could lead to undesired side reactions during the synthetic route towards the target compound. Therefore, the use of methyl groups on the pyridine rings was considered since C-H functionalization through lithiation and/or deprotonation of benzylic positions has been extensively reported.²¹ The use of a strong base to deprotonate the methyl groups, combined with the addition of a suitable carbon-based electrophile, would yield the C5-functionalized product. In the end, the alternative synthetic route depicted in Scheme 5.3 was conceived and realized.

Following this new scheme, the asymmetric 5-methyl-2,2'-bipyridine **11** was prepared in good yield from **10** via a classical Kröhnke pyridine synthesis in presence of methacrolein and ammonium acetate. Oxidation of **11** with hydrogen peroxide in trifluoroacetic acid resulted in a 1:1 mixture of pyridyl *N*-oxides **12** and **13** which could be efficiently isolated by column chromatography. Using the method as described in Chapter 2, amination of **12** and **13** provided **16a** and **17a** in excellent yields. As described above, **17b** could be prepared from **17a** via a Sandmeyer-type reaction, which allowed to form the tetrapyridyl backbone **18** in good yield by a palladium-catalyzed Buchwald-Hartwig amination between **17a** and **17b**. To prepare the isomer **19**, an alternative approach was successfully developed consisting in preparing the bromo-derivative **16b** via formation of pyridinium salt **15** and a Kröhnke pyridine synthesis, which can be realized in large scale. The Buchwald-Hartwig amination between **16a** and **16b** finally provided isomer **19**, which was *N*-methylated to yield **20**. As a proof-of-principle that this strategy was successful, *in situ* deprotonation of the methyl substituents on the pyridines of **20** by lithium diisopropylamine (LDA) followed by the addition of ethyl bromoacetate, effectively resulted in the formation of **21** in good yield (67%).

Overall, coordination of ligand **21** to ruthenium(II) and investigation of the photobiological properties of such ruthenium-based HO-1 inhibitor candidates, as shown for strategy 1 in Figure 5.1, could not be realized due to lack of time. However, the developed approach for methyl group functionalization depicted in Scheme 5.3 was shown to be more versatile and more successful than the sp^2 - sp^3 cross-coupling approach shown in Scheme 5.1 and 5.2. It has the potential to provide a range of tetrapyridyl compounds bearing alkylcarboxylic groups of various lengths in different positions on the central coordinating ligand, which could afford a family of ruthenium-based HO-1 inhibitor candidates.

and **[24]**(PF₆)₂ bearing either two STF31 or two QC82 axial ligands were prepared by first heating a solution of precursor **22** in H₂O to hydrolyze the ruthenium-chloride bonds, and then adding a methanolic solution containing 3.0 or 2.1 equivalents of the desired inhibitor, respectively. The complexes **[23]**(PF₆)₂ and **[24]**(PF₆)₂ were obtained in an isolated yield of 61% and 98%, respectively (Scheme 5.4).



Scheme 5.4 a) *i.* H₂O, 80 °C, 1 h; *ii.* STF31 in methanol, 80 °C, 48 h; *iii.* KPF₆ (aq.), 61%. b) *i.* QC82 in ethylene glycol, 100 °C, 18 h; *ii.* KPF₆ (aq.), 35%. c) *i.* H₂O, 80 °C, 1h; *ii.* QC82 in methanol, 80 °C, 18 h; *iii.* KPF₆ (aq.), 98%. d) *i.* Pyridine in acetone, 650 nm, rt., 6 h; *ii.* KPF₆ (aq.), 29%.

The synthesis of the dissymmetric complexes **[25]**(PF₆)₂ and **[26]**(PF₆)₂ was initially attempted photochemically by irradiation of **[23]**(PF₆)₂ and **[24]**(PF₆)₂ with 650 nm light, a procedure similar to that reported in Chapter 4. While the photoreaction did yield **[26]**(PF₆)₂ when **[24]**(PF₆)₂ was irradiated in presence of 10 equivalents of pyridine, the reaction time

had to be increased to 6 h compared to 1.5 h reported in Chapter 4. Even though the longer irradiation time and larger excess of ligand does not necessarily pose a problem for $[\mathbf{26}](\text{PF}_6)_2$, this procedure was deemed inefficient for the preparation of $[\mathbf{25}](\text{PF}_6)_2$ as it would be difficult to scale-up. Ultimately, the preparation of $[\mathbf{25}](\text{PF}_6)_2$ was performed by heating the bis-STF31 complex $[\mathbf{23}](\text{PF}_6)_2$ with 1.0 equivalent of QC82 in ethylene glycol. After purification of the dissymmetric complex by column chromatography, $[\mathbf{25}](\text{PF}_6)_2$ was isolated with in a yield of 35%. All complexes $[\mathbf{23}](\text{PF}_6)_2 - [\mathbf{26}](\text{PF}_6)_2$ were reprecipitated from an aqueous potassium hexafluorophosphate (KPF_6) solution to ensure isolation as PF_6 salts. For the biological studies, compounds $[\mathbf{24}](\text{PF}_6)_2 - [\mathbf{26}](\text{PF}_6)_2$ were converted into their chloride salts by anion exchange chromatography to increase their solubility in aqueous solvents.

5.2.2.2 Crystal structures

Single crystals of $[\mathbf{24}]\text{Cl}_2$ and $[\mathbf{26}](\text{PF}_6)_2$ suitable for X-ray diffraction were obtained via vapor diffusion of diethyl ether into a solution of the complex in methanol and THF, respectively (Figure 5.2). While $[\mathbf{24}]^{2+}$ in the crystal structure was found to be symmetric along the axial plane, the bond lengths between the two coordinated imidazole N atoms and the ruthenium center were not identical ($\text{Ru1-N3} = 2.120 \text{ \AA}$ and $\text{Ru1-N3}' = 2.090 \text{ \AA}$, respectively, Table 5.1). The same observation was made for the dissymmetric complex $[\mathbf{26}]^{2+}$, in which the distance of the imidazole N atom to the metal ($\text{Ru1-N3} = 2.088 \text{ \AA}$) was found to be slightly shorter than the distance of the pyridine N atom to the metal ($\text{Ru1-N4} = 2.108 \text{ \AA}$). Since both $[\mathbf{24}]^{2+}$ and $[\mathbf{26}]^{2+}$ contain the tetradentate MeL ligand, the structural parameter (τ_4) can provide an indication on the geometric nature of the coordination center. For a tetrahedral geometry the τ_4 is close to 1, while a square planar geometry correlates with a τ_4 close to 0. For $[\mathbf{24}]^{2+}$ and $[\mathbf{26}]^{2+}$ the structural parameter (τ_4) was found to be similar (0.10 and 0.11, respectively), while the torsion angle between the coordinated pyridyl N-atoms ($\text{N1-N2-N2'-N1}'$) was slightly larger for $[\mathbf{24}]^{2+}$ than for $[\mathbf{26}]^{2+}$ (5.3° and 1.5° , respectively). Furthermore, the octahedral geometry distortion parameter (Σ) was nearly identical for both $[\mathbf{24}]^{2+}$ and $[\mathbf{26}]^{2+}$ ($\Sigma = 55^\circ$ and 56° , respectively). These results indicate that the axial ligand in $[\mathbf{26}]^{2+}$ has only a minimal impact on the distortion of the metal center's first coordination sphere, in contrast to the imidazole-based QC82 ligand in $[\mathbf{24}]^{2+}$. The observed distortions are similar to those reported previously of analogous iron(II), cobalt(II) and copper(II) complexes.^{22–25}

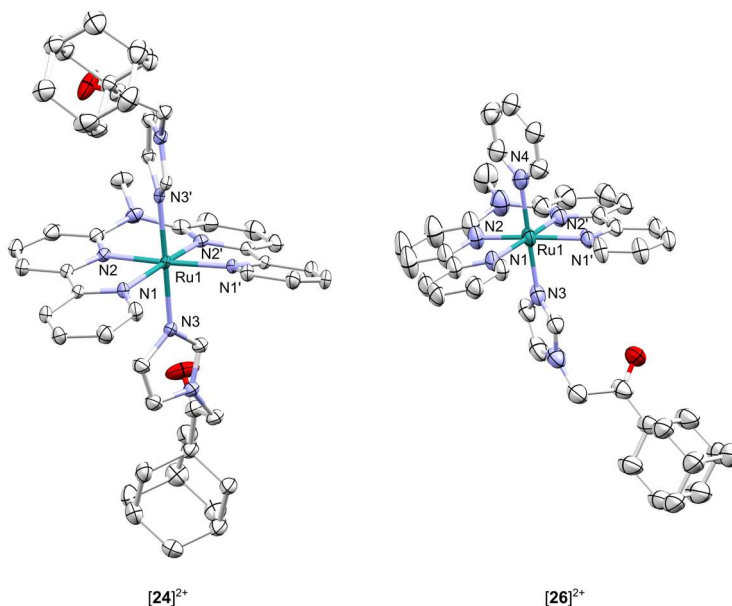


Figure 5.2 Displacement ellipsoid plots (50% probability level) of the cationic part of the crystal structure **[24]**Cl₂·(MeOH)₂ and **[26]**(PF₆)₂. Counter-ions, hydrogen atoms and solvent molecules have been omitted for clarity.

Table 5.1 Selected bond distances (Å) and bond angles (°) in the crystal structures of **[24]**Cl₂·(MeOH)₂ and **[26]**(PF₆)₂.

	[24] Cl ₂	[26] (PF ₆) ₂		[24] Cl ₂	[26] (PF ₆) ₂
Ru1–N1	2.090(2)	2.101(3)	N1–Ru1–N2'	171.9(1)	173.0(1)
Ru1–N1'	2.089(2)	2.099(3)	N1'–Ru1–N2	174.1(1)	172.0(1)
Ru1–N2	2.009(2)	2.009(4)	N3–Ru1–N3'	178.8(1)	-
Ru1–N2'	2.004(2)	2.022(3)	N3–Ru1–N4	-	177.4(3)
Ru1–N3	2.120(2)	2.088(4)	Torsion angle (°) N1–N2–N2'–N1'	5.3(1)	1.5(2)
Ru1–N3'	2.090(2)	-	τ ₄ ^a	0.10(9)	0.11(1)
Ru1–N4	-	2.108(8)	Σ ^b (°)	55(5)	56(5)

^a The coordination angles N1–Ru1–N2' (α) and N1'–Ru1–N2 (β) were used to calculate τ₄.²⁶

$$\tau_4 = \frac{360 - (\alpha + \beta)}{141}$$

^b Octahedral distortion parameter Σ was calculated using all *cis* bond angles in the primary coordination sphere.²⁷ $\Sigma = \sum_{i=1}^{12} |\phi_i - 90|$

5.2.2.3 Photochemical characterization

Since for PACT compounds ligand exchange should only occur upon light irradiation, the thermal stability of the complexes was investigated by monitoring the UV-Vis absorbance

vs. time. In absence of light, $[\mathbf{24}](\text{PF}_6)_2 - [\mathbf{26}](\text{PF}_6)_2$ were found to be thermally stable for at least 16 h in 1/1 $\text{H}_2\text{O}/\text{acetone}$ at 298 K (Appendix V.2.2). To identify the photochemical reactivity of the complexes, the ^1H -NMR spectra of $[\mathbf{24}](\text{PF}_6)_2 - [\mathbf{26}](\text{PF}_6)_2$ in 1/1 $\text{D}_2\text{O}/\text{acetone-d}_6$ were monitored upon irradiation with deep red (650 nm) light. For $[\mathbf{24}]^{2+}$, the triplet at 6.72 ppm corresponding to the imidazole C-H of coordinated QC82 was replaced by a triplet at 6.69 ppm while a multiplet integrating for a single proton at 6.90 ppm corresponding to free QC82 appeared, indicating photodissociation of a single QC82 ligand (Figure 5.3). When a solution of $[\mathbf{26}](\text{PF}_6)_2$ was irradiated with 650 nm, the appearance of a distinctive multiplet for free pyridine at 8.44 ppm was observed while the doublet for the HL ligand in $[\mathbf{26}]^{2+}$ at 8.50 ppm decreased (Figure 5.4). Furthermore, irradiation of a solution containing $[\mathbf{25}](\text{PF}_6)_2$ resulted in the replacement of the doublet at 9.79 ppm by a doublet at 9.72 ppm while the characteristic singlet for the *t*-butyl group in free STF31 appeared at 1.13 ppm (Figure 5.5).

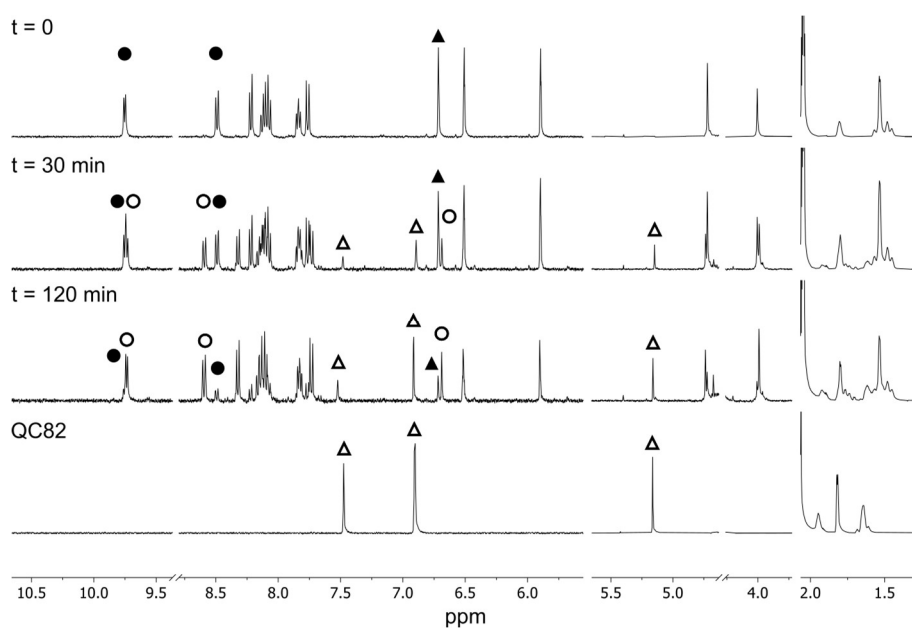


Figure 5.3 Time-evolution of the ^1H -NMR spectrum of $[\mathbf{24}](\text{PF}_6)_2$ (●) in 1/1 $\text{D}_2\text{O}/\text{acetone-d}_6$ upon irradiation with 650 nm light for 120 minutes at 298 K. Symbols indicate the ruthenium photoproduct (○), coordinated QC82 (▲) and free QC82 (△).

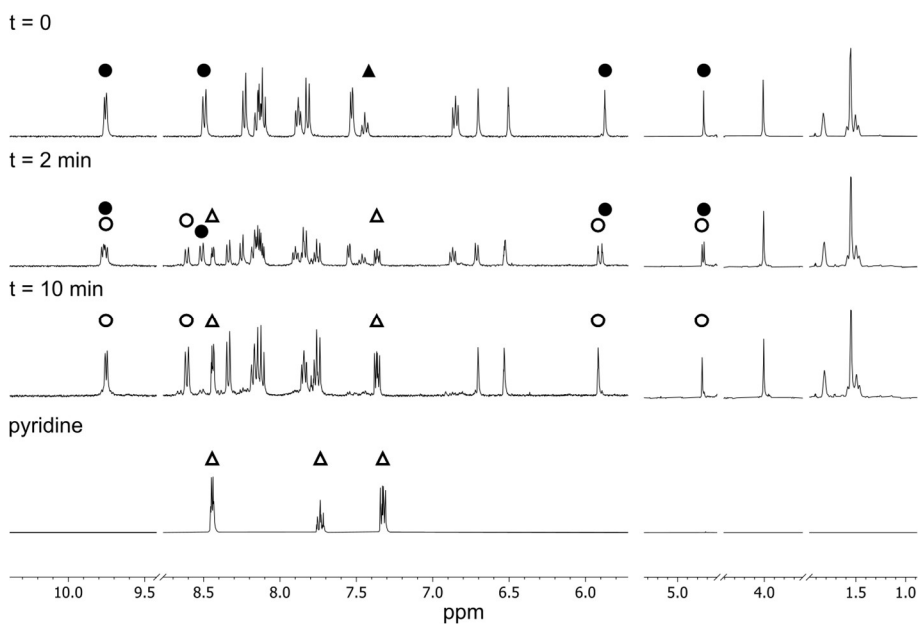


Figure 5.4 Time-evolution of the ^1H -NMR spectrum of $[\mathbf{26}](\text{PF}_6)_2$ (●) in 1/1 D_2O /acetone- d_6 upon irradiation with 650 nm light for 10 minutes at 298 K. Symbols indicate the ruthenium photoproduct (○) and free pyridine (Δ).

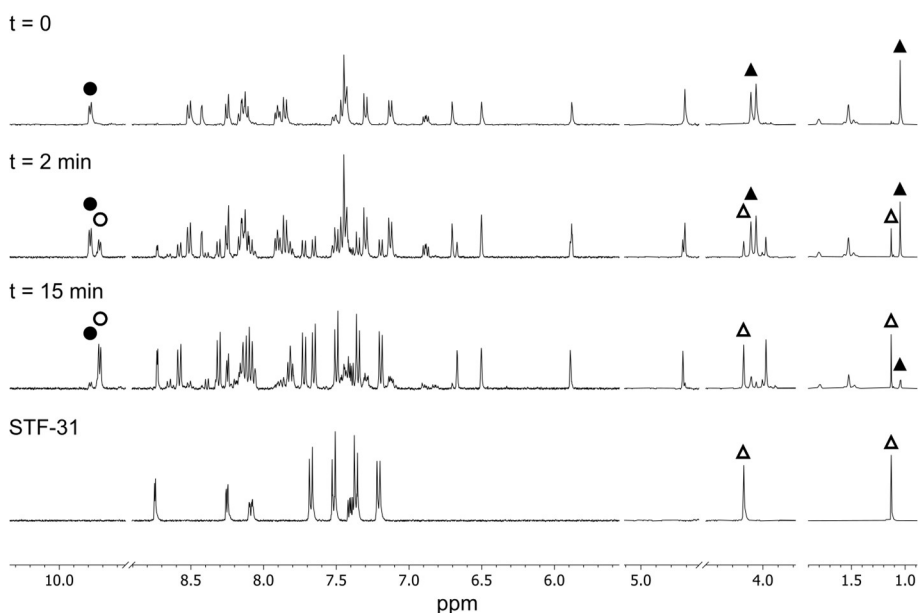


Figure 5.5 Time-evolution of the ^1H -NMR spectrum of $[\mathbf{25}](\text{PF}_6)_2$ (●) in 1/1 D_2O /acetone- d_6 upon irradiation with 650 nm light for 10 minutes at 298 K. Symbols indicate the ruthenium photoproduct (○), coordinated STF31 (▲) and free STF31 (Δ).

In all cases, the photosubstitution of a single axial ligand was observed in such conditions. While red-light irradiation of $[24]^{2+}$ induced the release of a single QC82 ligand, selective release of the pyridyl moiety was observed for $[25]^{2+}$ and $[26]^{2+}$ irradiated in the same conditions. Additionally, the irradiation time needed for the complete photosubstitution of a single ligand was significantly longer for $[24]^{2+}$ than for $[25]^{2+}$ and $[26]^{2+}$ (>120 min vs. 10–20 min, respectively). This indicates a strong difference in reaction kinetics when an imidazole vs. pyridine ligand is photolabilized *trans* to an imidazole.

The kinetics of the photosubstitution reactions observed in the $^1\text{H-NMR}$ experiments were investigated by monitoring the evolution of the UV-Vis absorbance spectra upon irradiation of a solution of each complex in 1/1 $\text{H}_2\text{O}/\text{acetone}$ (Figure 5.6). When irradiated with either 505 nm or 625 nm, distinct changes in the absorbance spectra were observed for all complexes. The spectrum of $[24]^{2+}$ exhibited a hypsochromic shift of the $^1\text{MLCT}$ band while for $[25]^{2+}$ and $[26]^{2+}$ a bathochromic shift was observed. Plotting the relative concentrations of the starting complex and photoproduct ($[\text{Ru}_i]/[\text{Ru}_{\text{tot}}]$) vs. time, demonstrates faster photosubstitution kinetics for $[25]^{2+}$ and $[26]^{2+}$ than for $[24]^{2+}$ (figure 5.6 insets), as already noticed in the $^1\text{H-NMR}$ studies. For the dissymmetric pyridyl/imidazole analogues $[25]^{2+}$ and $[26]^{2+}$, the overall absorption spectra were found to be similar, with $^1\text{MLCT}$ bands at 510 nm and 503 nm, respectively (Table 5.2). In comparison, the $^1\text{MLCT}$ absorption band of bis-imidazole complex $[24]^{2+}$ is at a significant higher wavelength of 530 nm, with molar absorptivity at these wavelengths of $\sim 7.8 \times 10^3 \text{ M}^{-1}\text{cm}^{-1}$ for all complexes. Quantification of the photosubstitution kinetics for $[24]^{2+}$ – $[26]^{2+}$ was realized by global fitting of the UV-Vis data to enable calculation of the photosubstitution quantum yields (ϕ_{PS} , Table 5.2). The ϕ_{PS} values for $[24]^{2+}$ were determined to be 0.00042 and 0.00031 when irradiated with either green ($\phi_{\text{PS}, 505}$) or red ($\phi_{\text{PS}, 625}$) light, respectively. In contrast, photosubstitution of the pyridyl moieties from $[25]^{2+}$ and $[26]^{2+}$ occurred with a 20- to 40-fold higher quantum efficiency of around 0.010 and 0.016, respectively, similar to many reported PACT compounds.

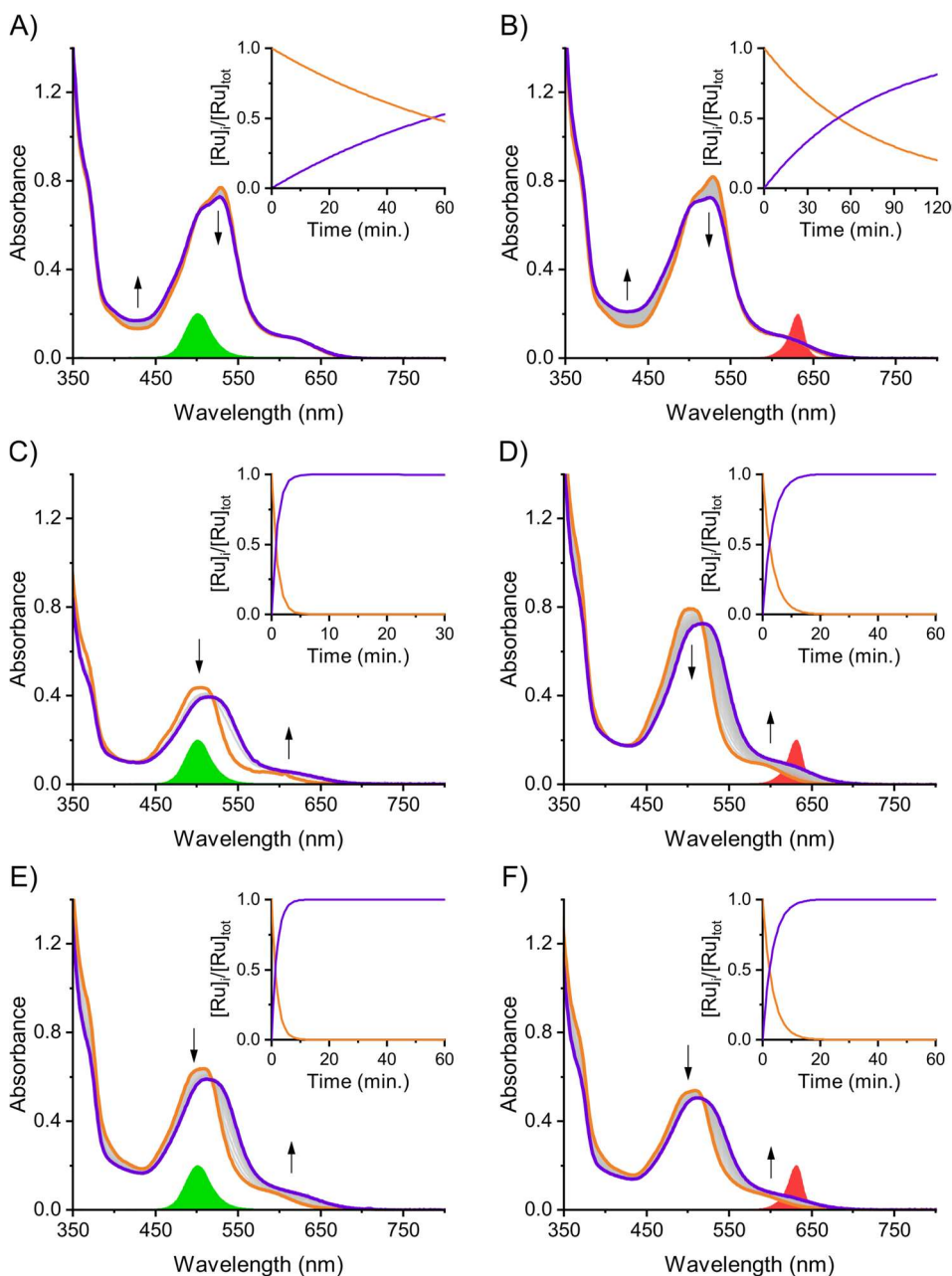


Figure 5.6 Time-evolution of the UV-Vis absorbance spectra of [24](PF₆)₂ at 100 μM (A, B), [26](PF₆)₂ at 56 μM (C) or 100 μM (D) and [25](PF₆)₂ at 84 μM (E, F) in 1/1 acetone/H₂O at 298 K upon irradiation with green (A, C, E; 505 nm at $2.09 \times 10^{-7} \text{ mol}\cdot\text{s}^{-1}$) or red light (B, D, F; 625 nm at $4.32 \times 10^{-7} \text{ mol}\cdot\text{s}^{-1}$). Insets depict relative concentration ratio $[Ru]_i/[Ru]_{tot}$ over time of starting reactant (orange line) and photoproduct (purple line). The green and red bands represent irradiance spectra of the light sources.

All complexes were found to be weakly emissive in acetonitrile at room temperature under air with phosphorescence quantum yields (ϕ_p) of 0.0010 for $[24]^{2+}$ and 0.0003 for $[25]^{2+}$ and $[26]^{2+}$ (table 5.2). Interestingly, the emission wavelength for $[24]^{2+}$ ($\lambda_{em} = 695$ nm) was observed around ~ 30 nm higher than for $[25]^{2+}$ and $[26]^{2+}$ ($\lambda_{em} = 666$ nm and 668 nm, respectively). Furthermore, singlet oxygen generation under the same condition was only observed for $[24]^{2+}$ with a low quantum yield (ϕ_Δ) of 0.07. Overall, these results suggest a considerable effect of the pyridyl ligand in $[25]^{2+}$ and $[26]^{2+}$ compared to the bis-imidazole analogue $[24]^{2+}$ on the excited states of the complexes. Especially the bathochromic shift of the absorption and emission maximum wavelengths, together with the lower ϕ_{PS} value for $[24]^{2+}$ indicate stabilization of the 1MLCT and 3MLCT excited states, which increases the 3MLCT – 3MC energy gap, resulting in higher ϕ_p and ϕ_Δ . The 3MLCT stabilization can be explained by the stronger π donating character of imidazole-based ligands compared to pyridines, which increases the energy of the t_{2g} orbital levels in the octahedral ruthenium complex without affecting the MeL-based π^* orbital energy.

Table 5.2 Photochemical properties of $[24](PF_6)_2$, $[25](PF_6)_2$ and $[26](PF_6)_2$ in 1/1 acetone/H₂O at 298 K including maximum absorption wavelength (λ_{max} , in nm), molar absorptivity (ϵ_{max} , in $M^{-1}cm^{-1}$), molar absorptivity at excitation wavelength ($\epsilon_{\lambda_{irr}}$, in $M^{-1}cm^{-1}$), photosubstitution quantum yield (ϕ_{PS}) with the corresponding photosubstitution reactivity ($\zeta_{PS} = \epsilon(\lambda_{irr}) \times \phi_{PS}$, in $M^{-1}cm^{-1}$), singlet oxygen quantum yield (ϕ_Δ) and emission quantum yield (ϕ_p).

	$[24]^{2+}$	$[25]^{2+}$	$[26]^{2+}$	
λ_{max} (nm)	530	510	503	
$(\epsilon_{max} (M^{-1}cm^{-1}))$	(8.00×10^3)	(7.37×10^3)	(7.42×10^3)	
505 nm	ϵ at λ_{irr} ($M^{-1}cm^{-1}$)	6.98×10^3	7.34×10^3	7.41×10^3
	$\phi_{PS, 505}$	0.00042	0.011	0.014
	$\zeta_{PS, 505}$ ($M^{-1}cm^{-1}$)	3.0	79	102
625 nm	ϵ at λ_{irr} ($M^{-1}cm^{-1}$)	8.88×10^2	3.79×10^3	3.27×10^2
	$\phi_{PS, 625}$	0.00031	0.0088	0.017
	$\zeta_{PS, 625}$	0.28	3.3	5.6
ϕ_p^a	0.0010	0.0003	0.0003	
$(\lambda_{em} (nm))$	(695)	(668)	(666)	
ϕ_Δ^a	0.07	<0.01	<0.01	

^a in aerated acetonitrile at 298 K. Excitation wavelength (λ_{irr}) = 450 nm.

Selective photosubstitution of a pyridine ligand was also reported in Chapter 3 for a *trans*-thioether/pyridine ruthenium complex. Therein, it was proposed that stronger π -donating ligands such as thioethers, increasing the bond length of a π -accepting

trans-ligand in the excited state, making it more prone for photosubstitution. Since a *N*-methyl-imidazole ligand such as QC82 has similar π -donating capabilities as thioether ligands, the selective photosubstitution of pyridine in $[26]^{2+}$ and STF31 in $[25]^{2+}$ is, retrospectively, logical.

5.2.2.4 *In silico* docking of photoproduct

To investigate whether the photoproduct of an irradiated solution of $[24]^{2+}$, $[25]^{2+}$ or $[26]^{2+}$, i.e., $[\text{Ru}(\text{MeL})(\text{QC82})]^{2+}$, may serve as a potential inhibitor of HO-1, a docking study was performed using the MetalDock software developed in our group.²⁸ A model was prepared from the crystal structure of $[26]^{2+}$ from which the pyridyl ligand was removed; this model was docked into the HO-1 protein (PDB: 3CZY) with a $20 \times 20 \times 20 \text{ \AA}$ box size centered around the active site. Of the ten best poses generated by MetalDock, two poses of the $[\text{Ru}(\text{MeL})(\text{QC82})]^{2+}$ were found in which the ruthenium center interacted with either the Met34 or Asp140 residues. Interestingly, in the remaining eight generated poses interaction between the metal center of $[\text{Ru}(\text{MeL})(\text{QC82})]^{2+}$ and the His25 residue was observed, as shown in Figure 5.7, which is reminiscent to the binding mode of heme. These results suggested that $[24]^{2+}$, $[25]^{2+}$ or $[26]^{2+}$ may indeed act as a competitive, covalent inhibitor of HO-1 after photoactivation.

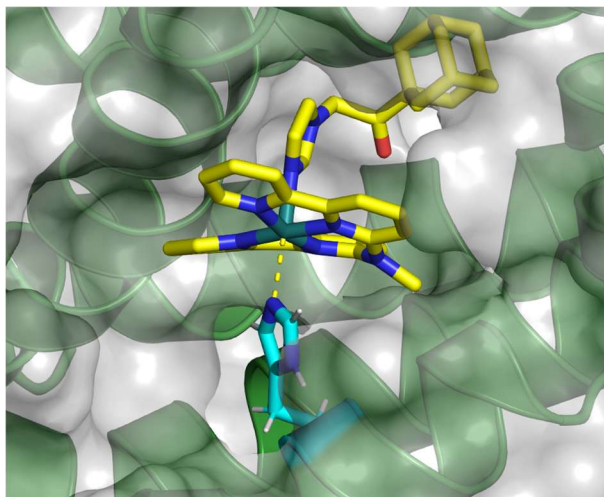


Figure 5.7 Docking with MetalDock of the $[\text{Ru}(\text{MeL})(\text{QC82})]^{2+}$ photoproduct with HO-1 (PDB: 3CZY) interacting with the His25 residue (cyan). Color code: Ru (turquoise), O (red), N (blue) and C (yellow). The grey area indicates the van der Waals surface of the protein.

5.2.2.5 Cytotoxicity

The *in vitro* cytotoxic properties of $[24]^{2+}$ – $[26]^{2+}$ were investigated in the dark and after red light activation ($\lambda = 630 \text{ nm}$) in human skin melanoma cancer cell line (A375) under

normoxic (21% O₂) and hypoxic (1% O₂) conditions (Table 5.3 and Figure V.6). The A375 cell line was chosen as a model since the influence of HO-1 on cell proliferation has been previously studied for this cell line, while these cancer cells are also commonly used to study PACT compounds in our group.²⁹ In all cases the chloride salts of the complexes were used, which have increased solubility in water. To evaluate the light dose needed for the photoactivation of the complexes [25]²⁺ and [26]²⁺ in the irradiation setup, a mock irradiation experiment was realized. The light dose necessary to photoactivate 60% to 70% of [25]²⁺ and [26]²⁺ was found to be 58 J/cm², which corresponds to 30 min irradiation time in our conditions (31.3 mW/cm², Appendix V.2.4). Since all three complexes contain HO-1 inhibitor QC82 and/or NAMPT inhibitor STF31, the cytotoxicity of both free inhibitors was also evaluated in this study. As simultaneous NAMPT and HO-1 inhibition could lead to a synergistic effect on cell viability, the simultaneous co-treatment with [26]²⁺ and STF31 (1 molar equivalent) was also included in this study.

For bis-QC82 complex [24]²⁺, significant cytotoxicity was observed under normoxic conditions in the dark, which was minimally affected by photoactivation (EC_{50, dark} = 9.8 μM and EC_{50, light} = 6.9 μM). The low photo-index can be interpreted as a consequence of the low photosubstitution ($\phi_{PS, 625} = 0.00031$) and ¹O₂ ($\phi_{\Delta} = 0.067$) quantum yields observed for this complex, combined with a light-dose that is too low for significant photoactivation. Under hypoxic conditions, however, the cytotoxicity of [24]²⁺ was found to be very low (EC_{50, dark} = 83 μM and EC_{50, light} = 62 μM). This oxygen dependence of the cytotoxicity of [24]²⁺ could be related to HO-1 overexpression in hypoxia or to the generally observed resistance of hypoxic cells to chemotherapy.

Interestingly, free HO-1 inhibitor **QC82** and its ruthenium mono-conjugate [26]²⁺ were both found to be non-cytotoxic (EC₅₀ > 100 μM) with or without light irradiation and independent on oxygen concentration. The combination of [26]²⁺ with STF31 resulted in a similar cytotoxicity compared to free STF31 alone in both normoxia and hypoxia, indicating the absence of synergy in these experimental conditions. The differences in cytotoxicity between [24]²⁺, [26]²⁺ and free QC82 may be explained by variation in cellular uptake related to the hydrophilicity of the compounds. Further studies are necessary to determine the biological mechanism of cytotoxicity for [24]Cl₂.

Table 5.3 Metabolic activity inhibition effective concentrations (EC₅₀ in μM) and 95% confidence interval (CI) determined by MTT assay for [23]Cl₂ – [26]Cl₂, [26]Cl₂ + STF31 (1:1 molar ratio), QC82 and STF31 in A375 cell line incubated in normoxic (21% O₂) and hypoxic (1% O₂) conditions.^{a, b}

	Light dose (J/cm ²)	Normoxia			Hypoxia		
		EC ₅₀ (μM)	±CI	PI	EC ₅₀ (μM)	±CI	PI
[23]Cl ₂ ^c	0	6.4	+1.8 -1.5	4.6	20	+6.3 -4.3	10
	115	1.4	+0.30 -0.24		2.0	+0.50 -0.42	
[24]Cl ₂	0	9.8	+15 -5.2	1.4	83	+65 -30	1.3
	58	6.9	+5.6 -3.3		62	+19 -15	
[25]Cl ₂	0	5.1	+1.7 -1.3	3.9	13	+3.2 -2.2	6.8
	58	1.3	+0.24 -0.21		1.9	+0.39 -0.33	
[26]Cl ₂	0	>100	-	-	>100	-	-
	58	>100	-		>100	-	
[26]Cl ₂ + STF31	0	0.61	+0.30 -0.21	0.92	2.4	+0.87 -0.62	1.5
	58	0.66	+0.44 -0.26		1.6	+0.47 -0.38	
QC82	0	>100	-	-	>100	-	-
STF31	0	0.83	+0.27 -0.21	-	2.3	+0.84 -0.64	-

^a PI = Photoindex, defined as EC_{50,dark}/EC_{50,light}. ^b Irradiation conditions: 630 nm, 31.3 mW/cm², 30 min. ^c As reported in Chapter 4 with irradiation conditions: 630 nm, 31.3 mW/cm², 60 min.

None of the complexes showed increased cytotoxicity upon photoactivation except for [25]²⁺, which exhibited a similar EC₅₀ value upon red-light activation compared to free STF31 in normoxia (1.3 μM and 0.83 μM, respectively) corresponding to a photoindex of 3.9. Strikingly, the photoindex increased to 6.8 in hypoxia while the EC₅₀ value upon photoactivation only slightly increased to 1.9 μM. The higher PI is a consequence of the lower dark toxicity in hypoxia vs. normoxia. Although ruthenium-based STF31 photocages have been previously reported, the increased photoindex for [25]²⁺ in hypoxia is unexpected and might be valuable for further studies.¹⁶

Although some of the complexes reported here were found to decrease the proliferation of A375 cells, neither a clear biological proof of HO-1 inhibition nor a synergy between the “designed” HO-1 inhibitor and the NAMPT inhibitor STF31 can be claimed with the currently available data. This absence of clear-cut effect might be due to multiple reasons, notably by the complexity of the HO-1 enzymatic system. Even though heme oxygenase is present in nearly every cell, basal HO-1 expression levels can vary greatly between cancer types and result in an inhomogeneous effect of inhibition in different cell lines.³⁰ Furthermore, the absence of a cytotoxic effect upon incubation with QC82 or its ruthenium analogue [26]²⁺ is unexpected, as QC82 has a reported low micromolar inhibitory activity (IC₅₀ = 3.0 μM) on the enzyme isolated from rat spleen.³¹ However, a large difference between inhibitory activity (IC₅₀) and *in vitro* cytotoxicity (EC₅₀) has been observed for other organic imidazole-based HO-1 inhibitors, such as 1-{4-[(4-bromobenzyl)oxy]phenyl}-2-(1H-imidazol-1-yl)ethanol (VP13/47). While VP13/47 has been reported to have an IC₅₀ value of 0.95 μM, the cell viability of non-small-cell lung cancer cells (A549) was only reduced by 35% and 23% after 24 and 48 h, respectively, after treatment with 10 μM VP13/47.³² Interestingly, a 4-fold increase of reactive oxygen species was observed after 3 h of treatment, highlighting intricate role of HO-1 to reduce oxidative stress and maintain cellular homeostasis. Although no cytotoxic or synergistic effect related to HO-1 inhibition was observed for complexes reported here, replacing the QC82 moiety by other, more potent imidazole-based HO-1 inhibitors such as VP13/47, could improve the photocytotoxicity of our ruthenium-based PACT compound.

5.3 Conclusion

In this work, we report two strategies towards the development of ruthenium-based HO-1 inhibitor candidates that are activated by visible light. In the first part, the synthesis of three tetrapyrridyl-based compounds functionalized with propionic carboxylic acid moieties was achieved. These ligands can be used to make photoactivatable ruthenium-based complexes that mimic heme upon photosubstitution of one or both axial ligands. The late-stage functionalization of methyl groups on the tetrapyrridyl core was shown to be more efficient and versatile than performing sp²-sp³ cross-coupling on chloropyridine rings, likely due to deactivation of the cross-coupling palladium catalyst by coordination of the tetradentate substrate.

In the second part of this chapter, the synthesis and photochemical characterization of three ruthenium-based conjugates of HO-1 inhibitor QC82 were reported. The complexes were based on the [Ru(MeL)(QC82)(X)]²⁺ scaffold where the *trans*-ligand X=pyridine, STF31, or QC82 can be photosubstituted for a solvent molecule. Our design, which was corroborated by *in silico* docking, hypothesized that the activated ruthenium complex [Ru(MeL)(QC82)(OH₂)]²⁺ may inhibit HO-1. MetalDock showed that a clear interaction may occur between the metal center and the His25 residue of HO-1, which is similar to the heme-

HO-1 interaction. For the dissymmetric complexes $[25]^{2+}$ and $[26]^{2+}$, where X was either STF31 (NAMPT inhibitor) or pyridine respectively, selective release of the pyridyl moiety upon green and red light irradiation was observed, with photosubstitution quantum yields of approximately 1 percent. For bis-(QC82) complex $[24]^{2+}$, photosubstitution of a single QC82 ligand occurred at much slower rates in the same conditions due to the π -donating character of imidazole-based ligands, which stabilized the $^3\text{MLCT}$ state. For $[25](\text{PF}_6)_2$ and $[26](\text{PF}_6)_2$, however, the stronger π -donating character of imidazole compared to pyridine leads to a *trans*-effect in the excited state originating from the imidazole-based ligand, resulting in the selective photosubstitution of pyridine. *In vitro*, neither the published organic HO-1 inhibitor QC82, nor the newly designed ruthenium-based photoactivated HO-1 inhibitor candidate $[24]^{2+}$ showed any cytotoxic effect. There is hence no current evidence that HO-1 inhibition takes place in A375 skin melanoma cells or not, nor whether HO-1 inhibition (e.g., using QC82) can harm them. In these cells $[25]^{2+}$ showed the best PACT properties upon photoactivation, with similar $\text{EC}_{50,\text{light}}$ values as free STF31 in both normoxia and hypoxia, resulting in photoindices of 3.9 and 6.8, respectively. However, here as well, the absence of synergistic effect between the toxicity of added or photoreleased STF31 and that of the $[\text{Ru}(\text{MeL})(\text{QC82})(\text{OH}_2)]^{2+}$ fragment, shed doubt on whether HO-1 inhibition occurs at all. Evaluation of HO-1 inhibition by these compounds using the recombinant isolated enzyme, in combination with determining HO-1 expression levels in various cancer cell lines, will provide more insight on these two important questions.

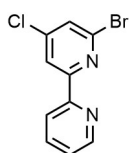
5.4 Experimental

5.4.1 General

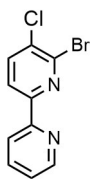
Unless otherwise noted, all reagents and solvents were purchased from commercial suppliers (Fluorochem, Sigma-Aldrich, BLDPharm, VWR, TCI) and used without further purification. STF31 and QC82 were prepared by Yurii Husiev as previously reported.^{15,16} Compounds **1a**, **1b**, **12**, **13**, **16a** and **17a** were prepared as reported in Chapter 2. Compounds **22** and $[23](\text{PF}_6)_2$ were prepared as reported in Chapter 4. Anhydrous and oxygen-free solvents were obtained using common distillation, drying (activated 4 Å molecular sieves) and degassing (freeze-pump-thaw method) procedures. The reactions were carried under air unless stated otherwise. The standard Schlenk technique was used for the reactions that were carried out under an inert atmosphere. Filters used were Whatman® regenerated cellulose membrane filters, RC60 Membrane circles, diam. 47 mm, pore size 1 μm . TLCs were performed using either Supelco analytical silica gel on Al foils with fluorescence indicator 254 nm or Supelco analytical aluminum oxide 60 with fluorescence indicator 254 nm. Column chromatography was carried on silica gel (40-63 μm) or on activated neutral aluminum oxide (Brockmann Grade I) from VWR Chemicals. 2,4,6-trimercaptotriazine-functionalized silica (SiliCycle SilliaMetS-DMT) was purchased from Screening Devices BV. Size exclusion chromatography was performed using Cytiva Sephadex

LH-20 (3 × 60 cm) as stationary phase. Anion exchange from hexafluorophosphate (PF₆) salts to the corresponding chloride salts was performed using DOWEX® 22 resin (3 × 11 cm) in methanol. Prior to the initial use, the resin was allowed to swell overnight in methanol. Additionally, the column was flushed with one column volume of 1 M HCl in methanol and wash with methanol until neutral pH. A 1.0 M HCl in methanol flush was done before every use to regenerate the resin. The microwave tubes (product number: 351521) were purchased from Biotage (Uppsala, Sweden) and heated using Thermo Scientific™ Reacti-block™ T-1 (9 holes; dimensions: 17mm diameter × 45 mm deep). All synthesized ruthenium complexes were stored at room temperature and protected from light. NMR spectra were recorded on Bruker Avance 300, 400 or 500 MHz and the FIDs were treated with MestReNova software. The chemical shifts are given relative to the residual signal of the solvent (Acetone-d₆: δ (¹H) = 2.05 ppm, δ (¹³C) = 29.84 ppm; Benzene-d₆: δ (¹H) = 7.16 ppm, δ (¹³C) = 128.06 ppm; CDCl₃: δ (¹H) = 7.26 ppm, δ (¹³C) = 77.16 ppm; DMSO-d₆: δ (¹H) = 2.50 ppm, δ (¹³C) = 39.52 ppm); Methanol-d₄: δ (¹H) = 3.31 ppm, δ (¹³C) = 49.00 ppm, or relative to an external standard (TMS: δ (¹H) = 0 ppm, δ (¹³C) = 0 ppm). The mass spectra (ESI-MS) were recorded in methanol (UPLC grade) with 1% (v/v) of formic acid on a Shimadzu LCMS-2020 (ESI-Q). The high-resolution mass spectra (HRMS) were recorded on a Thermo Finnigan LTQ Orbitrap.

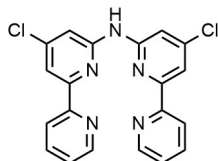
5.4.2 Synthesis



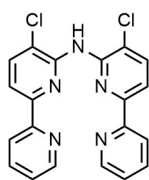
6-bromo-4-chloro-2,2'-bipyridine, 2a: A flask was charged with 4-chloro-[2,2'-bipyridin]-6-amine **1a** (3.00 g, 14.6 mmol, 1.0 eq) dissolved in hydrobromic acid (48% aq., 29 mL) and cooled to -5 °C in a brine ice bath. After portionwise addition of bromine (2.25 mL, $d = 3.102$ g/mL, 43.8 mmol, 3.0 eq) followed by sodium nitrite (2.52 mg, 36.5 mmol, 2.5 eq) in H₂O (50 mL), the mixture was stirred at RT for 1.5 h. The reaction was neutralized by addition of sodium hydroxide (1.0 M, aq.) and extracted with DCM (3 × 200 mL). The combined organic phase was washed with brine (200 mL), dried with MgSO₄, filtered and concentrated in vacuo. Purification of the resulting crude by column chromatography (silica, 30% acetone in hexane) yielded the desired product as a white solid (2.33 g, 8.75 mmol, 60%). ¹H-NMR (400 MHz, CDCl₃) δ 8.67 (ddd, $J = 5.0, 1.8, 1.0$ Hz, 1H), 8.42 (d, $J = 1.7$ Hz, 1H), 8.39 (dt, $J = 8.0, 1.1$ Hz, 1H), 7.83 (td, $J = 7.8, 1.8$ Hz, 1H), 7.51 (d, $J = 1.7$ Hz, 1H), 7.35 (ddd, $J = 7.5, 4.8, 1.1$ Hz, 1H). ¹³C{H} NMR (101 MHz, CDCl₃) δ 158.22, 153.49, 149.45, 146.53, 141.83, 137.29, 127.64, 124.95, 121.89, 120.56. ESI-MS: exact m/z calculated for [C₁₀H₆BrClN₂ + H⁺]⁺: 270.9 m/z , found 271.1 m/z .



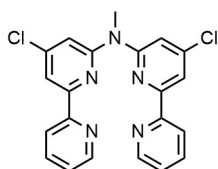
6-bromo-5-chloro-2,2'-bipyridine, 2b: A flask was charged with 5-chloro-[2,2'-bipyridyl]-6-amine **1b** (700 mg, 3.40 mmol, 1.0 eq) dissolved in hydrobromic acid (48% aq., 6.8 mL) and cooled to $-5\text{ }^{\circ}\text{C}$ in a brine ice bath. After portionwise addition of bromine (0.53 mL, $d = 3.102\text{ g/mL}$, 10.2 mmol, 3.0 eq) followed by sodium nitrite (587 mg, 8.51 mmol, 2.5 eq) in H_2O (11 mL), the mixture was stirred at RT for 1.5 h. The reaction was neutralized with by addition of sodium hydroxide (1.0 M, aq.) and extracted with DCM ($3 \times 30\text{ mL}$). The combined organic phase was washed with brine (30 mL), dried with MgSO_4 , filtered and concentrated *in vacuo*. The resulting crude was dissolved in EtOAc (50 mL) with activated charcoal (1.0 g) and reflux for 30 min. Filtration over celite and evaporation of the solvent *in vacuo* yielded the desired product as a white solid (652 mg, 2.41 mmol, 71%). $^1\text{H-NMR}$ (850 MHz, CDCl_3) δ 8.66 (ddd, $J = 4.7, 1.8, 1.0\text{ Hz}$, 1H), 8.38 (dt, $J = 7.9, 1.1\text{ Hz}$, 1H), 8.35 (d, $J = 8.2\text{ Hz}$, 1H), 7.84 (d, $J = 8.2\text{ Hz}$, 1H), 7.82 (ddd, $J = 7.9, 7.4, 1.8\text{ Hz}$, 1H), 7.34 (ddd, $J = 7.4, 4.7, 1.2\text{ Hz}$, 1H). $^{13}\text{C}\{\text{H}\}\text{NMR}$ (214 MHz, CDCl_3) δ 155.06, 153.83, 149.44, 140.92, 139.02, 137.25, 133.35, 124.58, 124.57, 121.59, 120.87, 120.86. ESI-MS: exact m/z calculated for $[\text{C}_{10}\text{H}_6\text{BrClN}_2 + \text{H}^+]^+$: 270.9 m/z , found 270.9 m/z .



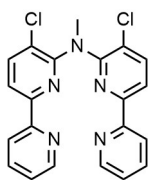
Bis(4-chloro-[2,2'-bipyridin]-6-yl)amine, 3a: An oven-dried two-necked flask fitted with a condenser and N_2 inlet was charged with 6-bromo-4-chloro-2,2'-bipyridine **2a** (3.00 g, 11.1 mmol, 1.0 eq), tris(dibenzylideneacetone)dipalladium (408 mg, 0.44 mmol, 0.04 eq), 1,3 bis(diphenylphosphino)propane (367 mg, 0.89 mmol, 0.08 eq) and sodium tert-butoxide (1.50 g, 15.6 mmol, 1.4 eq). The flask was purged with N_2 , toluene (60 mL) was added and the mixture was stirred. After 10 min, 4-chloro-[2,2'-bipyridin]-6-amine **1a** (2.30 g, 11.1 mmol, 1.0 eq) dissolved in toluene (50 mL) was added and the resulting mixture was stirred at $80\text{ }^{\circ}\text{C}$. Once the amine and bromide starting materials were both consumed (after 5 days as determined by TLC (alumina; 1/1 EtOAc/toluene)), the mixture was allowed to cool to RT and H_2O (100 mL) was added. After stirring for 1 hour, the phases were separated, and the aqueous phase was extracted with DCM ($4 \times 100\text{ mL}$). The combined organic phase was dried with MgSO_4 , filtered and the filtrate concentrated *in vacuo*. Purification of the resulting crude by column chromatography (alumina; 10 – 40% EtOAc in toluene) yielded the desired compound as an off-white solid (3.58 g, 9.13 mmol, 82%). $^1\text{H-NMR}$ (850 MHz, $\text{DMSO-}d_6$) δ 10.31 (s, 1H), 8.68 (d, $J = 4.6\text{ Hz}$, 2H), 8.27 (dt, $J = 7.9, 1.1\text{ Hz}$, 2H), 7.99 (td, $J = 7.6, 1.8\text{ Hz}$, 2H), 7.97 – 7.94 (m, 2H), 7.89 (d, $J = 1.8\text{ Hz}$, 2H), 7.48 (ddd, $J = 7.4, 4.6, 1.1\text{ Hz}$, 2H). $^{13}\text{C}\{\text{H}\}\text{NMR}$ (214 MHz, $\text{DMSO-}d_6$) δ 155.05, 154.29, 153.91, 149.44, 149.43, 144.51, 137.37, 124.73, 120.52, 113.05, 111.55. ESI-MS: exact m/z calculated for $[\text{C}_{20}\text{H}_{13}\text{Cl}_2\text{N}_5 + \text{H}^+]^+$: 394.1 m/z , found 394.1 m/z .



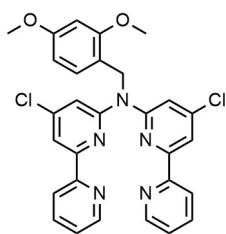
Bis(5-chloro-[2,2'-bipyridin]-6-yl)amine, 3b: An oven-dried two-necked flask fitted with a condenser and N₂ inlet was charged with 6-bromo-5-chloro-2,2'-bipyridine **2b** (600 mg, 2.23 mmol, 1.0 eq), tris(dibenzylideneacetone)dipalladium (82.0 mg, 89 μmol, 0.04 eq), 1,3-bis(diphenylphosphino)propane (73.0 mg, 0.18 mmol, 0.08 eq) and sodium tert-butoxide (300 mg, 3.12 mmol, 1.4 eq). The flask was purged with N₂, toluene (10 mL) was added and the mixture was stirred. After 10 min, 5-chloro-[2,2' bipyridyl]-6-amine **1b** (458 mg, 2.23 mmol, 1.0 eq) dissolved in toluene (10 mL) was added and the resulting mixture was stirred at 80 °C. Once the amine and bromide starting materials were both consumed (after 5 days as determined by TLC (alumina; 1/1 EtOAc/toluene)), the mixture was allowed to cool to RT and 2,4,6-trimercaptotriazine-functionalized silica (SilliaMetS-DMT, 2.30 g, 0.59 mmol/g, 1.36 mmol, 0.64 eq) was added. After stirring for 3 h, the mixture was filtered and the filtrate concentrated *in vacuo*. Purification of the resulting crude by column chromatography (alumina; 10 – 40% EtOAc in toluene) yielded the desired compound as an off-white solid (436 mg, 1.11 mmol, 50%). ¹H-NMR (500 MHz, DMSO-*d*₆) δ 9.12 (s, 1H), 8.66 (ddd, *J* = 4.8, 1.8, 0.9 Hz, 2H), 8.09 – 8.06 (m, 6H), 7.84 (ddd, *J* = 8.0, 7.5, 1.8 Hz, 2H), 7.41 (ddd, *J* = 7.5, 4.8, 1.2 Hz, 2H). ¹³C{H} NMR (126 MHz, DMSO-*d*₆) δ 154.27, 152.11, 150.15, 149.35, 139.06, 137.28, 124.28, 121.65, 120.39, 115.84. ESI-MS: exact *m/z* calculated for [C₂₀H₁₃Cl₂N₅ + H⁺]⁺: 394.1 *m/z*, found 394.2 *m/z*.



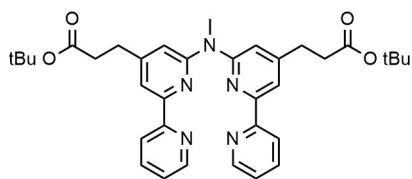
Bis(4-chloro-[2,2'-bipyridin]-6-yl)-N-methylamine, 4a: Under N₂, **3a** (2.50 g, 6.34 mmol, 1 eq) was dissolved in DMSO (63.4 mL). Potassium hydroxide (3.56 g, 63.4 mmol, 10 eq) was added and the mixture was allowed to stir at RT for 1 h followed by the addition of iodomethane (0.48 mL, 1.06 mmol, 1.2 eq). After 2 h, reaction completion was confirmed by TLC (Alumina; 1/4 EtOAc/toluene) and the reaction was quenched by adding H₂O (250 mL). The aqueous mixture was extracted with EtOAc (5 × 200 mL) and the combined organic phase was washed with brine (200 mL) followed by drying with MgSO₄. Filtration and evaporation of the solvent yielded the desired product as a white solid (2.59 g, 6.34 mmol, 89%). ¹H-NMR (300 MHz, DMSO-*d*₆) δ 8.71 (d, *J* = 4.8 Hz, 2H), 8.27 (d, *J* = 7.9 Hz, 2H), 8.04 – 7.93 (m, 4H), 7.64 (d, *J* = 1.6 Hz, 2H), 7.54 – 7.46 (m, 2H), 3.75 (s, 3H). ¹H-NMR (400 MHz, Benzene-*d*₆) δ 8.57 (d, *J* = 1.6 Hz, 2H), 8.49 (dt, *J* = 4.8, 1.4 Hz, 2H), 8.38 (dt, *J* = 8.0, 1.2 Hz, 2H), 7.21 (td, *J* = 7.7, 1.8 Hz, 2H), 6.68 (ddd, *J* = 7.5, 4.8, 1.2 Hz, 2H), 3.30 (s, 3H). ¹³C{H} NMR (101 MHz, Benzene-*d*₆) δ 157.25, 155.90, 155.36, 149.51, 145.82, 136.66, 124.14, 121.13, 115.39, 114.32, 35.62. ESI-MS: exact *m/z* calculated for [C₂₁H₁₅Cl₂N₅ + H⁺]⁺: 408.1 *m/z*, found 408.1 *m/z*.



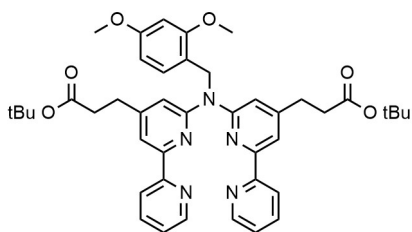
Bis(5-chloro-[2,2'-bipyridin]-6-yl)-N-methylamine, 4b: Under N_2 , **3b** (350 mg, 0.89 mmol, 1 eq) was dissolved in DMSO (8.9 mL). Potassium hydroxide (498 mg, 8.8 mmol, 10 eq) was added and the mixture was allowed to stir at RT for 1 h followed by the addition of iodomethane (67 μ L, 1.06 mmol, 1.2 eq). After 2 h, reaction completion was confirmed by TLC (Alumina; 1/4 EtOAc/toluene) and the reaction was quenched by adding H_2O (50 mL). The aqueous mixture was extracted with EtOAc (5×50 mL) and the combined organic phase was washed with brine (50 mL) followed by drying with $MgSO_4$. Filtration and evaporation of the solvent yielded the crude product. Purification by column chromatography (silica; 20% EtOAc in toluene with a few drops of Et_3N) yield the product as a white solid (1.07 g, 2.91 mmol, 89%). 1H -NMR (500 MHz, $DMSO-d_6$) δ 8.69 (ddd, $J = 4.8, 1.8, 0.9$ Hz, 2H), 8.16 – 8.10 (m, 4H), 8.04 (d, $J = 8.2$ Hz, 2H), 7.90 (td, $J = 7.7, 1.8$ Hz, 2H), 7.45 (ddd, $J = 7.5, 4.8, 1.2$ Hz, 2H), 3.60 (s, 3H). $^{13}C\{H\}$ NMR (126 MHz, $DMSO-d_6$) δ 154.55, 154.07, 152.07, 149.40, 140.19, 137.46, 124.39, 123.83, 120.45, 117.03, 37.73. ESI-MS: exact m/z calculated for $[C_{21}H_{15}Cl_2N_5 + H^+]^+$: 408.1 m/z , found 408.2 m/z .



Bis(4-chloro-[2,2'-bipyridin]-6-yl)-N-(2,4-dimethoxybenzyl)amine, 5a: Under N_2 , **3a** (500 mg, 1.27 mmol, 1.0 eq) was dissolved in dimethylformamide (5.1 mL). The solution was cool to $0^\circ C$ and sodium hydride (60% dispersion in mineral oil, 65.9 mg, 1.65 mmol, 1.3 eq) was added. After stirring for 1.5 h at RT, 3,4-dimethoxybenzyl bromide (265 μ L, $d = 1.438$ g/mL, 1.65 mmol, 1.3 eq) was added and the mixture was stirred for 18 h. The completion of the reaction was confirmed by TLC (alumina, 1/10 EtOAc/toluene) and unreacted sodium hydride was quenched by addition of ethanol (25 mL). After concentrating *in vacuo*, H_2O (50 mL) was added and the mixture was extracted with DCM (5×50 mL). The combined organic phase was washed with brine (50 mL), dried with $MgSO_4$, filtered and concentrated *in vacuo* to obtain the crude product. Purification by column chromatography (alumina, 1 – 10% EtOAc/toluene) yielded the desired product as an off-white solid (687 mg, 1.26 mmol, 99%). 1H -NMR (400 MHz, $DMSO-d_6$) δ 8.69 (ddd, $J = 4.8, 1.9, 0.9$ Hz, 2H), 8.24 (dt, $J = 8.0, 1.1$ Hz, 2H), 8.00 (d, $J = 1.6$ Hz, 2H), 7.95 (td, $J = 7.7, 1.8$ Hz, 2H), 7.59 (d, $J = 1.6$ Hz, 2H), 7.48 (ddd, $J = 7.5, 4.8, 1.2$ Hz, 2H), 7.18 (d, $J = 2.1$ Hz, 1H), 6.96 (dd, $J = 8.3, 2.0$ Hz, 1H), 6.85 (d, $J = 8.3$ Hz, 1H), 5.55 (s, 2H), 3.66 (s, 3H), 3.63 (s, 3H). $^{13}C\{H\}$ NMR (101 MHz, $DMSO-d_6$) δ 156.58, 154.94, 153.78, 149.47, 148.63, 147.74, 144.73, 137.55, 130.71, 124.86, 120.64, 119.22, 114.55, 114.17, 111.73, 111.38, 55.36, 55.30, 50.62. ESI-MS: exact m/z calculated for $[C_{29}H_{24}Cl_2N_5O_2 + H^+ + MeOH]^+$: 544.2 m/z , found 544.2 m/z .

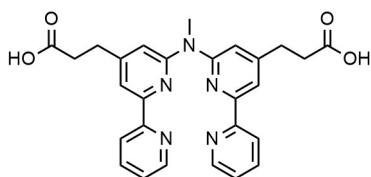


6': Three separate pressure vials were charged with **4a** (204 mg, 0.50 mmol, 1.0 eq), potassium (3-(tert-butoxy)-3-oxopropyl)trifluoroborate **27** (260 mg, 1.10 mmol, 2.2 eq), palladium acetate (45 mg, 0.20 mmol, 0.4 eq), XPhos (191 mg, 0.40 mmol, 0.8 eq) and potassium carbonate (415 mg, 3.00 mmol, 6.0 eq). The vials were sealed with crimp caps and brought under N₂ by three vacuum-N₂ cycles. Degassed toluene (4.6 mL) and H₂O (0.46 mL) was added and the mixture was stirred at 80 °C for 2 days while monitoring the reaction progress by TLC (silica, 1/4 EtOAc/Toluene). Once all starting materials were consumed, the mixtures were allowed to cool to RT and combined. Toluene (50 mL) and 2,4,6-trimercaptotriazine-functionalized silica (SilliaMetS-DMT, 4.80 g, 0.59 mmol/g, 2.83 mmol, 4.7 eq) were added. After stirring for 3 hours, the mixture was filtered and the filtrate concentrated *in vacuo* to obtain the crude product. Isolation by column chromatography (silica, 10 – 50% EtOAc in toluene) yielded the desired product as a yellow solid (533 mg, 0.90 mmol, 62%). ¹H-NMR (300 MHz, DMSO-*d*₆) δ 8.67 (ddd, *J* = 4.8, 1.8, 0.9 Hz, 2H), 8.31 (dt, *J* = 7.9, 1.1 Hz, 2H), 7.96 – 7.88 (m, 4H), 7.43 (ddd, *J* = 7.5, 4.8, 1.2 Hz, 2H), 7.29 (d, *J* = 1.3 Hz, 2H), 3.73 (s, 3H), 2.90 (t, *J* = 7.2 Hz, 4H), 2.61 (t, *J* = 7.3 Hz, 4H), 1.32 (s, 18H). ¹³C{H} NMR (75 MHz, DMSO-*d*₆) δ 171.28, 156.70, 155.32, 153.27, 151.98, 149.15, 137.17, 124.01, 120.46, 114.17, 114.04, 79.86, 35.68, 35.08, 30.13, 27.65. ESI-MS: exact *m/z* calculated for [C₃₅H₄₁N₅O₄ + H]⁺: 596.3 *m/z*, found 596.4 *m/z*.

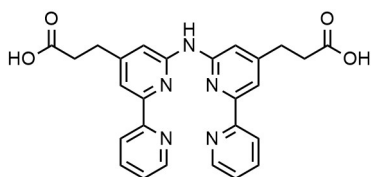


7': A pressure vials was charged with **5a** (300 mg, 0.55 mmol, 1.0 eq), potassium (3-(tert-butoxy)-3-oxopropyl)trifluoroborate **27** (286 mg, 1.21 mmol, 2.2 eq), palladium acetate (50 mg, 0.22 mmol, 0.4 eq), XPhos (210 mg, 0.44 mmol, 0.8 eq) and potassium carbonate (457 mg, 3.31 mmol, 6.0 eq). The vial was sealed with a crimp cap and brought under N₂ by three vacuum-N₂ cycles. Degassed toluene (5.0 mL) and H₂O (0.50 mL) was added and the mixture was stirred at 80 °C for 3 days while monitoring the reaction progress by TLC (silica, 1/4 EtOAc/Toluene). Once all starting materials were consumed, the mixture was allowed to cool to RT. Toluene (15 mL) and 2,4,6-trimercaptotriazine-functionalized silica (SilliaMetS-DMT, 2.80 g, 0.59 mmol/g, 1.65 mmol, 7.5 eq) were added. After stirring for 2 h, the mixture was filtered and the filtrate concentrated *in vacuo* to obtain the crude product. Isolation by column chromatography (silica, 5 – 10% EtOAc in toluene) yielded the desired product as a yellow solid (268 mg, 0.37 mmol, 67%). ¹H-NMR (400 MHz, DMSO-*d*₆) δ 8.66 (ddd, *J* = 4.8, 1.8, 0.9 Hz, 2H), 8.30 (dt, *J* = 7.9, 1.1 Hz, 2H), 7.95 – 7.87 (m, 4H), 7.42 (ddd, *J* = 7.6, 4.7, 1.2 Hz, 2H), 7.26 (d, *J* = 1.2 Hz, 2H), 7.25 – 7.13 (m, 6H), 6.98 (dd, *J* = 8.2, 2.0 Hz, 1H), 6.80 (d, *J* = 8.3 Hz, 1H), 5.55 (s, 2H), 3.62 (d, *J* = 18.5 Hz, 6H), 2.87 (t, *J* = 7.2 Hz, 4H), 2.58 (t, *J* = 7.2 Hz, 4H), 1.30 (s, 17H). ¹³C{H}

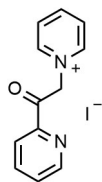
NMR (101 MHz, DMSO- d_6) δ 171.26, 156.15, 155.27, 153.46, 152.09, 149.19, 148.49, 147.52, 137.20, 132.07, 128.91, 128.22, 125.33, 124.05, 120.41, 119.47, 114.40, 114.29, 111.59, 79.83, 55.35, 55.16, 34.99, 30.06, 27.62. ESI-MS: exact m/z calculated for $[C_{43}H_{49}N_5O_6 + H^+]^+$: 735.4 m/z , found 735.2 m/z .



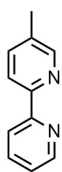
6: To a solution of **6'** (520 mg, 0.87 mmol, 1.0 eq) in DCM (16 mL) was added sodium hydroxide (209 mg, 5.24 mmol, 6.0 eq) in methanol (1.7 mL). The mixture was stirred for 16 h at RT. Once complete conversion was confirmed by TLC (alumina, 30% acetone in hexane), the mixture was concentrated *in vacuo* and H₂O (40 mL) was added. After washing the aqueous phase with EtOAc (2 × 20 mL), the solution was neutralized with HCl (1.0 M, aq.) and the extracted with EtOAc (4 × 100 mL). The combined organic phase was dried with MgSO₄ and filtered. Evaporation of the solvent *in vacuo* yield the desired product as a yellow solid (106 mg, 0.22 mmol, 25%). ¹H-NMR (500 MHz, DMSO- d_6) δ 12.19 (s, 2H), 8.68 (ddd, J = 4.8, 1.8, 0.9 Hz, 2H), 8.31 (dt, J = 8.0, 1.1 Hz, 2H), 7.95 – 7.88 (m, 4H), 7.44 (ddd, J = 7.5, 4.8, 1.2 Hz, 2H), 7.32 (d, J = 1.3 Hz, 2H), 3.73 (s, 3H), 2.91 (t, J = 7.4 Hz, 4H), 2.64 (t, J = 7.5 Hz, 4H). ¹³C{H} NMR (126 MHz, DMSO- d_6) δ 173.51, 156.68, 155.34, 153.25, 152.26, 149.13, 137.21, 124.00, 120.51, 114.26, 113.95, 35.70, 34.05, 30.07. ESI-MS: exact m/z calculated for $[C_{27}H_{25}N_5O_4 + H^+]^+$: 484.2 m/z , found 484.2 m/z .



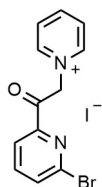
7: In a flask fitted with a condenser, Bis(4-tBuOProp)-N-DMB-L **7'** (250 mg, 0.34 mmol, 1.0 eq) was dissolved in DCM (4.3 mL) and trifluoroacetic acid (4.3 mL). After stirring at 40 °C for 2 h, the mixture was concentrated *in vacuo* and H₂O was added (25 mL). Sodium hydroxide (1.0 M, aq.) was added until pH ~4 and the aqueous solution was washed with DCM (2 × 30 mL). After freeze-drying of the aqueous phase, the crude was purified by size-exclusion chromatography (LH-20 in methanol) which yielded the desired product as an off-white solid (55 mg, 0.12 mmol, 34%). ¹H-NMR (400 MHz, DMSO- d_6) δ 12.35 (s, 2H), 8.61 (d, J = 4.3 Hz, 2H), 8.49 (d, J = 8.0 Hz, 2H), 8.03 (td, J = 7.6, 2.2 Hz, 4H), 7.61 – 7.48 (m, 4H), 3.00 (t, J = 7.2 Hz, 4H), 2.73 (t, J = 7.3 Hz, 4H). ¹³C{H} NMR (126 MHz, DMSO- d_6) δ 173.28, 158.44, 158.18, 149.27, 137.96, 125.23, 121.64, 118.02, 115.66, 113.51, 33.32, 30.20. ESI-MS: exact m/z calculated for $[C_{26}H_{23}N_5O_4 + Na^+]^+$: 492.2 m/z , found 493.4 m/z .



1-(2-pyridacyl)pyridinium iodide, 10: This compound was synthesized according to an adapted literature procedure.³³ In a 250 mL flask fitted with a condenser and calcium chloride drying tube, 2-acetylpyridine **9** (12.1 g, 100 mmol, 1.0 eq) and iodine (28.4 g, 112 mmol, 1.12 eq) were dissolved in pyridine (121 mL, 1.50 mol, 15 eq). The resulting mixture was stirred at 90 °C for 1.5 h during which a precipitate formed. The mixture was cooled to 0 °C and filtered. The collected precipitate was dissolved in ethanol (50 mL) containing activated charcoal (4.0 g) and refluxed. After 2 h, the mixture was filtered while hot and the resulting filtrate was concentrated *in vacuo*. Recrystallization from ethanol yielded the desired product as a yellow crystalline powder (9.06 g, 27.7 mmol, 28%). Analysis was consistent with previous reports.³³ ¹H-NMR (400 MHz, CDCl₃) δ 9.02 (d, *J* = 6.0 Hz, 2H), 8.88 (d, *J* = 5.4 Hz, 1H), 8.74 (t, *J* = 7.8 Hz, 1H), 8.29 (t, *J* = 7.0 Hz, 2H), 8.14 (td, *J* = 7.7, 1.7 Hz, 1H), 8.08 (d, *J* = 7.7 Hz, 1H), 7.84 (ddd, *J* = 7.1, 4.8, 1.3 Hz, 1H), 6.52 (s, 2H). ¹³C{H} NMR (101 MHz, CDCl₃) δ 191.50, 150.46, 149.59, 146.36, 146.32, 138.18, 129.17, 127.73, 122.06, 66.68. ESI-MS: exact *m/z* calculated for [C₁₂H₁₁N₂O - I]⁺: 199.1 *m/z*, found 199.0 *m/z*.

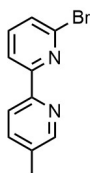


5-methyl-2,2'-bipyridine, 11: This compound was synthesized according to an adapted literature procedure.³³ To a solution containing ammonium acetate (16.2 g, 210 mmol, 6.0 eq) and methacrolein (3.19 mL, *d* = 0.847 g/mL, 38.5 mmol, 1.1 eq) in formamide (350 mL) was added pyridium salt **10** (11.4 g, 35.0 mmol, 1.0 eq). The mixture was stirred overnight at 80 °C during which the solution turned orange and a white precipitate formed. After the reaction was completed as shown by TLC (silica, 5% MeOH in DCM), the mixture was allowed to cool to RT and extracted with diethyl ether (3 × 150 mL). The combined organic phase was washed with brine (150 mL), dried with MgSO₄, filtered and concentrated *in vacuo*. Purification by column chromatography (silica, 5% MeOH in DCM) yielded the desired product as a colorless oil (4.55 g, 26.7 mmol, 76%). Analysis was consistent with previous reports.³³ ¹H-NMR (300 MHz, CDCl₃) δ 8.66 (ddd, *J* = 4.8, 1.8, 0.9 Hz, 1H), 8.50 (dt, *J* = 2.3, 0.8 Hz, 1H), 8.36 (dt, *J* = 8.0, 1.1 Hz, 1H), 8.28 (dd, *J* = 8.1, 0.9 Hz, 1H), 7.79 (td, *J* = 7.8, 1.8 Hz, 1H), 7.62 (ddd, *J* = 8.0, 2.3, 0.8 Hz, 1H), 7.27 (ddd, *J* = 7.7, 4.8, 1.2 Hz, 1H), 2.38 (s, 3H). ¹³C{H} NMR (75 MHz, CDCl₃) δ 156.42, 153.76, 149.74, 149.22, 137.54, 136.94, 133.50, 123.46, 120.88, 120.69, 18.44. ESI-MS: exact *m/z* calculated for [C₁₁H₁₀N₂ + H]⁺: 171.1 *m/z*, found 171.0 *m/z*.

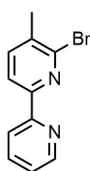


1-(6-bromo-2-pyridacyl)pyridinium iodide, 15: This compound was synthesized according to an adapted literature procedure.³⁴ In a 100 mL flask fitted with a condenser and calcium chloride drying tube, 2-acetyl-6-bromopyridine **14** (5.00 g, 25.0 mmol, 1.0 eq) and iodine (7.11 g, 28.0 mmol, 1.12 eq) were dissolved in pyridine (30.2 mL, 375 mmol, 15 eq). The resulting mixture was stirred at 90 °C for 1.5 h during which a precipitate formed. The mixture was cooled to 0 °C and

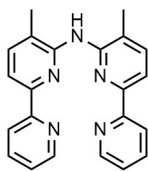
filtered. The collected precipitate was dispersed in chloroform (30 mL), sonicated and filtered. After repeating this process twice, drying under high vacuum yielded the desired product as a yellow crystalline powder (7.41 g, 18.3 mmol, 73%). Analysis was consistent with previous reports.³⁴ $^1\text{H-NMR}$ (300 MHz, $\text{DMSO-}d_6$) δ 8.98 (d, $J = 5.2$ Hz, 2H), 8.74 (t, $J = 7.8$ Hz, 1H), 8.29 (t, $J = 7.0$ Hz, 2H), 8.10 (s, 3H), 6.46 (s, 2H). $^{13}\text{C}\{^1\text{H}\}$ NMR (75 MHz, $\text{DMSO-}d_6$) δ 189.97, 151.37, 146.42, 146.29, 141.35, 140.81, 133.49, 127.74, 121.53, 66.47. ESI-MS: exact m/z calculated for $[\text{C}_{12}\text{H}_{10}\text{BrN}_2\text{O} - \text{I}^-]^+$: 277.0 m/z , found 276.9 m/z .



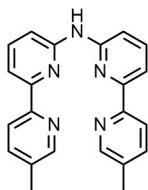
6'-bromide-5-methyl-2,2'-bipyridine, 16b: This compound was synthesized according to an adapted literature procedure.³⁴ To a solution containing ammonium acetate (20.8 g, 270 mmol, 15 eq) and methacrolein (1.64 mL, $d = 0.847$ g/mL, 19.8 mmol, 1.1 eq) in formamide (45 mL) was added pyridinium salt **15** (7.29 g, 18.0 mmol, 1.1 eq). The mixture was stirred at 90 °C for 2 h during which the solution turned orange and a white precipitate formed. The reaction mixture was allowed to cool to RT and extracted with DCM (4×150 mL). The combined organic phase was washed with H_2O (150 mL), dried with MgSO_4 , filtered and concentrated *in vacuo*. Purification by column chromatography (Alumina; 1/1 DCM/hexane; $R_f = 0.52$) yielded the desired product as a white solid (2.07 g, 8.31 mmol, 46%). Analysis was consistent with previous reports.³⁴ $^1\text{H-NMR}$ (400 MHz, CDCl_3) δ 8.48 (d, $J = 2.2$ Hz, 1H), 8.33 (dd, $J = 7.7, 0.9$ Hz, 1H), 8.29 (d, $J = 8.0$ Hz, 1H), 7.68 – 7.59 (m, 2H), 7.45 (dd, $J = 7.9, 0.9$ Hz, 1H), 2.39 (s, 3H). $^{13}\text{C}\{^1\text{H}\}$ NMR (101 MHz, CDCl_3) δ 157.65, 152.11, 149.84, 141.66, 139.31, 137.63, 134.27, 127.72, 121.16, 119.51, 18.56. ESI-MS: exact m/z calculated for $[\text{C}_{11}\text{H}_9\text{BrN}_2 + \text{H}^+]$: 251.0 m/z , found 250.8 m/z .



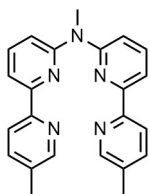
6-bromide-5-methyl-2,2'-bipyridine, 17b: A flask was charged with 5-methyl-[2,2'-bipyridyl]-6-amine **17a** (100 mg, 0.54 mmol, 1.0 eq) dissolved in hydrobromic acid (48% aq., 1.1 mL) and cooled to -5 °C in a brine ice bath. After portionwise addition of bromine (0.08 mL, $d = 3.102$ g/mL, 1.62 mmol, 3.0 eq) followed by sodium nitrite (93.0 mg, 1.35 mmol, 2.5 eq) in H_2O (4 mL), the mixture was stirred at RT for 1.5 h. The reaction was neutralized with by addition of sodium hydroxide (1.0 M, aq.) and extracted with DCM (3×30 mL). The combined organic phase was washed with brine (50 mL), dried with MgSO_4 , filtered and concentrated *in vacuo*. Purification by column chromatography (silica, 30% acetone in hexane) yielded the desired product as an off-white solid (97 mg, 0.39 mmol, 72%). $^1\text{H-NMR}$ (400 MHz, CDCl_3) δ 8.64 (ddd, $J = 4.8, 1.9, 1.0$ Hz, 1H), 8.37 (dt, $J = 8.0, 1.1$ Hz, 1H), 8.27 (d, $J = 7.7$ Hz, 1H), 7.80 (td, $J = 7.7, 1.8$ Hz, 1H), 7.63 (dd, $J = 7.8, 0.9$ Hz, 1H), 7.30 (ddd, $J = 7.5, 4.8, 1.2$ Hz, 1H), 2.44 (s, 3H). $^{13}\text{C}\{^1\text{H}\}$ NMR (101 MHz, CDCl_3) δ 154.82, 154.76, 149.26, 144.20, 139.72, 137.11, 135.30, 124.06, 121.34, 119.99, 22.10. ESI-MS: exact m/z calculated for $[\text{C}_{11}\text{H}_9\text{BrN}_2 + \text{H}^+]$: 249.0 m/z , found 248.9 m/z .



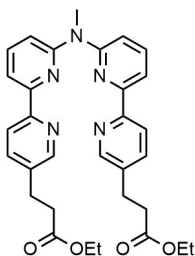
Bis(5-methyl-[2,2'-bipyridin]-6-yl)amine, 18: An oven-dried pressure vial was charged with 6-bromo-5-methyl-2,2'-bipyridine **17b** (50.0 mg, 0.20 mmol, 1.0 eq), 5-methyl-[2,2' bipyridyl]-6-amine **17a** (37.0 mg, 0.20 mmol, 1.0 eq), tris(dibenzylideneacetone)dipalladium (7.35 mg, 8.0 μ mol, 0.04 eq), 1,3-bis(diphenylphosphino)propane (6.62 mg, 16 μ mol, 0.08 eq) and sodium tert-butoxide (27.0 mg, 0.28 mmol, 1.4 eq). The vial was sealed with a crimp cap and purged with nitrogen by cycling three times between vacuum and nitrogen. After addition of toluene (2.0 mL), the mixture was stirred at 80 °C and the reaction progress was followed by TLC (Alumina; 40% EtOAc in toluene). Once the amine and bromide starting materials were both consumed (after 24 h), the mixture was allowed to cool to RT. The mixture was concentrated *in vacuo* and the resulting crude purified by column chromatography (alumina; 10 – 30% EtOAc in toluene) yielding the target compound as a yellow powder (58.3 g, 0.16 mmol, 82%). $^1\text{H-NMR}$ (400 MHz, $\text{DMSO-}d_6$) δ 8.63 (ddd, $J = 4.8, 1.8, 0.9$ Hz, 2H), 8.42 (s, 1H), 8.05 (dt, $J = 8.1, 1.1$ Hz, 2H), 7.98 (d, $J = 7.6$ Hz, 2H), 7.82 (td, $J = 7.7, 1.8$ Hz, 2H), 7.73 (dd, $J = 7.7, 0.9$ Hz, 2H), 7.35 (ddd, $J = 7.5, 4.7, 1.2$ Hz, 2H), 2.25 (s, 6H). $^{13}\text{C}\{\text{H}\}$ NMR (101 MHz, $\text{DMSO-}d_6$) δ 155.45, 153.60, 151.04, 149.15, 139.35, 137.04, 124.59, 123.57, 119.79, 114.29, 17.77. ESI-MS: exact m/z calculated for $[\text{C}_{22}\text{H}_{19}\text{N}_5 + \text{H}]^+$: 354.2 m/z , found 354.0 m/z .



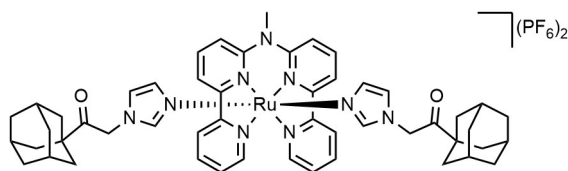
Bis(5'-methyl-[2,2'-bipyridin]-6-yl)amine, 19: In a 250 mL two-necked flask was transferred 6-bromo-5'-methyl-2,2'-bipyridine **16b** (1.10 g, 5.94 mmol, 1.0 eq), 5'-methyl-[2,2' bipyridyl]-6-amine **16a** (1.48 g, 5.94 mmol, 1.0 eq), palladium bis(dibenzylideneacetone) (273 mg, 0.475 mmol, 0.08 eq), 1,3-bis(diphenylphosphino)propane (196 mg, 0.475 mmol, 0.08 eq) and sodium tert-butoxide (799 mg, 8.31 mmol, 1.4 eq). The flask was purged with nitrogen by cycling three times between vacuum and nitrogen. After addition of toluene (59 mL), the mixture was stirred at 80 °C and the reaction progress was followed by TLC (Alumina; 1/1 EtOAc/Toluene). Once the amine and bromide starting materials were both consumed (after 22 h), the mixture was allowed to cool to RT. The mixture was concentrated *in vacuo* and the resulting crude purified by column chromatography (Alumina; 10 – 40% EtOAc in toluene) yielding the target compound as an off-white powder (1.48 g, 4.20 mmol, 70%). $^1\text{H-NMR}$ (400 MHz, $\text{DMSO-}d_6$) δ 9.84 (s, 1H), 8.56 – 8.49 (m, 2H), 8.27 (dd, $J = 7.9, 0.8$ Hz, 2H), 7.91 – 7.84 (m, 6H), 7.79 (ddd, $J = 8.2, 2.3, 0.9$ Hz, 2H), 2.37 (s, 6H). $^{13}\text{C}\{\text{H}\}$ NMR (101 MHz, $\text{DMSO-}d_6$) δ 153.82, 153.54, 153.01, 149.54, 138.63, 137.53, 133.36, 119.89, 112.44, 111.89, 17.85. ESI-MS: exact m/z calculated for $[\text{C}_{22}\text{H}_{19}\text{N}_5 + \text{H}]^+$: 354.2 m/z , found 354.2 m/z .



Bis(5'-methyl-[2,2'-bipyridin]-6-yl)-N-methylamine, 20: In a two-necked flask, **19** (1.20 g, 3.40 mmol, 1.0 eq) was dissolved in DMSO (34 mL) under N_2 . Potassium hydroxide (1.90 g, 34.0 mmol, 10 eq) was added and the mixture was allowed to stir at RT for 1 h followed by the addition of iodomethane (0.26 mL, 4.07 mmol, 1.2 eq). After 2 h, reaction completion was confirmed by TLC (Alumina; 1/5 EtOAc/toluene; $R_{f\text{starting material}} = 0.35$, $R_{f\text{product}} = 0.65$) and the reaction was quenched by adding H_2O (100 mL). The aqueous mixture was extracted with toluene (5×100 mL) and the combined organic phase was dried with $MgSO_4$. Filtration and evaporation of the solvent yielded the crude product. Purification by column chromatography (Alumina; 10 – 50% EtOAc in toluene with a few drops of Et_3N) yield the product as a white solid (1.07 g, 2.91 mmol, 89%). 1H -NMR (400 MHz, $DMSO-d_6$) δ 8.51 (dt, $J = 2.4, 0.9$ Hz, 2H), 8.20 (dd, $J = 7.9, 0.8$ Hz, 2H), 7.96 (dd, $J = 7.5, 0.8$ Hz, 2H), 7.82 (dd, $J = 8.2, 7.5$ Hz, 2H), 7.74 (ddd, $J = 8.1, 2.3, 0.8$ Hz, 2H), 7.37 (dd, $J = 8.2, 0.8$ Hz, 2H), 3.73 (s, 3H), 2.35 (s, 6H). $^{13}C\{H\}$ NMR (101 MHz, $DMSO-d_6$) δ 156.43, 153.62, 152.85, 149.51, 138.47, 137.55, 133.46, 119.89, 114.18, 113.29, 35.62, 17.86. ESI-MS: exact m/z calculated for $[C_{23}H_{21}N_5 + H]^+$: 368.2 m/z , found 368.2 m/z .

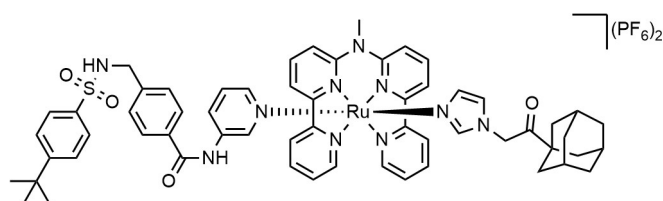


21: A two-neck flask was charged with diisopropylamine (41 μ L, $d = 0.71$ g/mL, 0.29 mmol, 2.1 eq) and dry THF (2 mL) under N_2 . The solution was cool to -78 $^\circ$ C in an acetone/dry ice bath and *n*-butyl lithium in hexane (170 μ L, 1.6 M, 0.27 mmol, 2.0 eq) was added. After stirring for 1 h at -78 $^\circ$ C, a solution of **20** (50 mg, 0.14 mmol, 1.0 eq) in dry THF (2 mL) was added dropwise. The resulting mixture was stirred at -78 $^\circ$ C for 30 min, allowed to slowly warm up to RT for 1 h and stirred at RT for an additional 30 min. After cooling the mixture back to -78 $^\circ$ C, ethyl bromoacetate (90 μ L, $d = 1.501$ g/mL, 0.82 mmol, 6 eq) in dry THF (1 mL) was added dropwise and the resulting mixture was allowed to reach RT. After stirring for 18 h, H_2O (5 mL) was added and extracted with $CHCl_3$ (3×15 mL). The combined organic phase was washed with brine (15 mL), dried with $MgSO_4$, filtered and concentrated *in vacuo*. Purification by column chromatography (alumina, $CHCl_3 + 0.05\%$ triethylamine) yielded the desired product as an off-white solid (49 mg, 0.091 mmol, 67%). 1H -NMR (400 MHz, $CDCl_3$) δ 8.53 (d, $J = 1.5$ Hz, 2H), 8.31 (dd, $J = 8.1, 0.8$ Hz, 2H), 8.00 – 7.95 (m, 2H), 7.71 – 7.62 (m, 4H), 7.28 (dd, $J = 8.3, 0.8$ Hz, 2H), 4.14 (q, $J = 7.1$ Hz, 4H), 3.82 (s, 3H), 3.01 (t, $J = 7.6$ Hz, 4H), 2.67 (t, $J = 7.6$ Hz, 4H), 1.27 – 1.23 (m, 9H). $^{13}C\{H\}$ NMR (101 MHz, $CDCl_3$) δ 172.54, 157.18, 154.78, 154.39, 149.22, 138.10, 136.87, 136.01, 120.92, 114.38, 113.87, 60.79, 36.03, 35.59, 28.12, 14.35. ESI-MS: exact m/z calculated for $[C_{31}H_{33}N_5O_4 + H]^+$: 540.3 m/z , found 540.3 m/z .



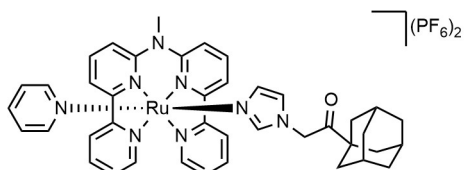
[Ru(MeL)(QC82)](PF₆)₂, [24](PF₆)₂: **22** (150 mg, 0.29 mmol, 1.0 eq) was transferred into a microwave tube and dissolved in H₂O (0.6 mL). The tube was sealed, purged with N₂ for

15 min. After stirring at 80 °C for 1 h, the solution was cooled to RT and QC82 (125 mg, 0.62 mmol, 2.1 eq) dissolved in methanol (5.3 mL) was added. After stirring at 80 °C for 18 h, the mixture was cooled to RT and precipitated in half-saturated aqueous KPF₆ solution. The precipitate was filtered over a membrane filter and washed of the filtrate with H₂O (2 mL) followed by diethyl ether (50 mL). Drying under high vacuum yielded the product as purple powder (352 mg, 0.29 mmol, 98%). ¹H-NMR (400 MHz, Acetone-*d*₆) δ 9.98 (ddd, *J* = 5.6, 1.5, 0.7 Hz, 2H), 8.69 (dt, *J* = 8.0, 1.1 Hz, 2H), 8.41 (dd, *J* = 7.9, 0.9 Hz, 2H), 8.30 – 8.17 (m, 4H), 7.99 – 7.89 (m, 4H), 6.94 (t, *J* = 1.4 Hz, 2H), 6.69 (t, *J* = 1.6 Hz, 2H), 6.06 (t, *J* = 1.5 Hz, 2H), 4.89 (s, 4H), 4.18 (s, 3H), 1.93 (q, *J* = 3.2 Hz, 6H), 1.74 – 1.57 (m, 24H). ¹³C{H} NMR (101 MHz, Acetone-*d*₆) δ 206.92, 158.99, 157.68, 156.06, 154.12, 138.74, 137.21, 128.57, 127.78, 124.49, 123.20, 118.48, 117.98, 52.45, 45.93, 44.41, 38.25, 36.89, 28.57. ESI-MS: exact *m/z* calculated for [C₅₁H₅₇N₉O₂Ru]²⁺: 464.7 *m/z*, found 464.6 *m/z*. Elemental analysis (%) for compound **[24](PF₆)₂** (C₅₁H₅₇F₁₂N₉O₂P₂Ru), calculated C, 50.25; H, 4.71; N, 10.34; found C, 50.21; H, 4.75; N, 10.40. UV-Vis (1/1 acetone/H₂O): λ_{max} (ε) = 530 nm (8.61 × 10³ M⁻¹cm⁻¹).



[Ru(Mebbpya)(QC82)(STF31)](PF₆)₂, [25](PF₆)₂: **[23](PF₆)₂** (120 mg, 0.08 mmol, 1.0 eq) and QC82 (18.6 mg, 0.08 mmol, 1.0 eq) were dissolved in ethylene glycol (5 mL) in a microwave tube. The tube was sealed and purged with N₂ by three freeze-pump-thaw cycles. After stirring at 100 °C for 18 h, the solution was allowed to cool to RT. Methanol (5 mL) was added and the mixture precipitated by dropwise addition into diethyl ether (100 mL). The precipitate was filtered over a membrane filter, washed with diethyl ether, and extracted from the filter with acetone. After evaporation of the solvent *in vacuo*, the resulting crude was purified by column chromatography (SiO₂) and eluted with 1:1 THF:Acetone containing 0.5% saturated aqueous KPF₆. The product-containing fractions were combined, concentrated *in vacuo* and precipitated in half saturated aqueous KPF₆ solution. The precipitate was filtered over a membrane filter and washed of the filtrate with H₂O followed by diethyl ether. Drying under high vacuum yielded the product as a red-brown powder (37 mg, 0.027 mmol, 35%). ¹H-NMR (850 MHz, Acetone-*d*₆) δ 10.04 (dd, *J* = 5.0, 0.8 Hz, 2H), 9.50 (s, 1H), 8.72 (td, *J* = 7.0, 1.6 Hz, 3H), 8.46 (d, *J* = 7.3 Hz, 2H), 8.30 (td, *J* = 7.7, 1.4 Hz, 2H), 8.27

(dd, $J = 8.5, 7.6$ Hz, 2H), 8.04 (dd, $J = 8.6, 0.9$ Hz, 2H), 8.02 (ddd, $J = 7.3, 5.5, 1.3$ Hz, 2H), 7.77 – 7.75 (m, 2H), 7.70 (d, $J = 7.7$ Hz, 4H), 7.59 (dd, $J = 8.5, 1.9$ Hz, 2H), 7.40 (d, $J = 8.4$ Hz, 2H), 7.05 – 7.00 (m, 2H), 6.93 (t, $J = 1.4$ Hz, 1H), 6.68 (t, $J = 1.6$ Hz, 1H), 6.03 (t, $J = 1.6$ Hz, 1H), 4.88 (s, 2H), 4.25 (s, 3H), 4.20 – 4.17 (m, 2H), 1.94 (d, $J = 3.2$ Hz, 3H), 1.73 – 1.68 (m, 9H), 1.64 – 1.60 (m, 4H), 1.33 (s, 9H). $^{13}\text{C}\{\text{H}\}$ NMR (214 MHz, Acetone- d_6) δ 165.46, 165.39, 158.01, 156.61, 155.87, 155.85, 155.28, 153.21, 153.14, 147.12, 144.13, 144.05, 142.71, 139.82, 138.30, 138.23, 137.19, 136.98, 132.75, 127.73, 127.51, 127.34, 126.73, 125.99, 125.18, 123.90, 122.50, 117.89, 117.70, 51.63, 46.22, 46.12, 45.04, 43.78, 37.35, 36.00, 30.44, 27.69, 27.66. ESI-MS: exact m/z calculated for $[\text{C}_{59}\text{H}_{62}\text{N}_{10}\text{O}_4\text{RuS}]^{2+}$: 554.2 m/z , found 554.3 m/z . Elemental analysis (%) for compound **[25]**(PF₆)₂ (C₅₉H₆₂F₁₂N₁₀O₄P₂Ru), calculated C, 50.68; H, 4.47; N, 10.02; found C, 50.66; H, 4.52; N, 10.04. UV-Vis (1/1 acetone/H₂O): λ_{max} (ϵ) = 510 nm (7.77×10^3 M⁻¹cm⁻¹).



[Ru(MeL)(QC82)(Py)](PF₆)₂, **[26]**(PF₆)₂:
[24](PF₆)₂ (150 mg, 0.12 mmol, 1 eq) in acetone (50 mL) and 10 mL of a 125 mM pyridine solution in acetone (1.23 mmol, 10 eq) were added under nitrogen to a 140 mL

double-walled photoreactor equipped with water-cooling (see Figure I.1). Acetone was added until the total reaction volume was 125 mL and the reaction mixture was irradiated with a 650 nm LED lamp at RT while monitoring the reaction progress by TLC (silica; 10% half saturated KPF₆ in MeOH/DCM). After 6 h, the reaction was concentrated *in vacuo* and precipitated in diethyl ether. The precipitate was filtered over a membrane filter and washed with diethyl ether. The resulting crude product was purified by column chromatography (silica; 10% half saturated KPF₆ in MeOH/DCM). The product-containing fraction were combined and concentrated, followed by precipitation in 100 mL half saturated aqueous KPF₆. After filtration over a membrane filter, the precipitate was washed with a minimal amount of water followed by diethyl ether. Drying under high vacuum yield the product as a red-brown powder (38 mg, 0.036 mmol, 29%). Red needle-shaped single crystals suitable for X-ray diffraction were obtained by vapor diffusion of diethyl ether into a solution of **[26]**(PF₆)₂ in THF. ^1H -NMR (400 MHz, Acetone- d_6) δ 10.02 (dt, $J = 5.5, 1.4$ Hz, 2H), 8.73 (dt, $J = 8.2, 1.1$ Hz, 2H), 8.46 (dd, $J = 7.9, 0.9$ Hz, 2H), 8.34 – 8.25 (m, 4H), 8.04 – 7.98 (m, 4H), 7.79 – 7.74 (m, 2H), 7.65 – 7.58 (m, 1H), 7.01 (dd, $J = 7.6, 6.5$ Hz, 2H), 6.96 – 6.93 (m, 1H), 6.70 (t, $J = 1.5$ Hz, 1H), 6.05 (t, $J = 1.5$ Hz, 1H), 4.89 (s, 2H), 4.16 (s, 3H), 1.94 (s, 3H), 1.74 – 1.58 (m, 14H). $^{13}\text{C}\{\text{H}\}$ NMR (101 MHz, Acetone- d_6) δ 158.83, 156.39, 154.11, 153.05, 139.23, 138.08, 137.87, 128.51, 128.19, 126.39, 124.84, 123.37, 118.85, 118.52, 52.53, 38.25, 36.88, 28.55. ESI-MS: exact m/z calculated for $[\text{C}_{41}\text{H}_{42}\text{N}_8\text{ORu}]^{2+}$: 382.1 m/z , found 382.2 m/z . Elemental analysis (%) for compound **[26]**(PF₆)₂ (C₄₁H₄₂F₁₂N₈OP₂Ru), calculated C, 46.73; H, 40.2; N, 10.63; found C, 46.32; H, 4.25; N, 10.85. UV-Vis (1/1 acetone/H₂O): λ_{max} (ϵ) = 503 nm (7.88×10^3 M⁻¹cm⁻¹).

Anion exchange: The ruthenium complex as PF₆-salt (~25 mg) was dissolved in a minimal amount acetone and diluted with equal amount of methanol (total volume of ~5 mL). The solution was brought onto a prepared anion exchange column (see paragraph 5.4.1 for details) and eluted with methanol. After collection of the colored fraction and concentration *in vacuo*, the product-containing methanolic solution was dropwise added into diethyl ether. The formed precipitate was collected by filtration over a membrane filter. Drying the collected precipitate under high vacuum, provided the chloride salt of the product as a red powder. Anion exchange typically proceeded with a yield of around 95%.

[Ru(MeL)(QC82)₂]Cl₂, [24]Cl₂: Purple needle-shaped single crystals suitable for X-ray diffraction were obtained by vapor diffusion of diethyl ether into a solution of [24]Cl₂ in methanol. ¹H-NMR (400 MHz, MeOD) δ 9.78 (dt, *J* = 5.4, 1.3 Hz, 2H), 8.60 (dt, *J* = 8.1, 1.1 Hz, 2H), 8.32 (dd, *J* = 7.9, 0.9 Hz, 2H), 8.23 – 8.09 (m, 4H), 7.89 (ddd, *J* = 7.3, 5.6, 1.3 Hz, 2H), 7.81 (dd, *J* = 8.5, 0.9 Hz, 2H), 6.68 (t, *J* = 1.4 Hz, 2H), 6.56 (t, *J* = 1.6 Hz, 2H), 5.89 (t, *J* = 1.5 Hz, 2H), 4.05 (s, 3H), 1.97 (s, 6H), 1.79 – 1.64 (m, 24H). ¹³C{H} NMR (MHz, MeOD) δ 201.67, 159.57, 158.26, 156.42, 154.23, 140.86, 138.91, 137.49, 128.77, 127.86, 124.80, 123.23, 118.76, 117.86, 63.38, 38.71, 37.33, 29.18. ESI-MS: exact *m/z* calculated for [C₅₁H₅₇N₉O₂Ru]²⁺: 464.7 *m/z*, found 464.7 *m/z*. Elemental analysis (%) for compound [24]Cl₂ (C₅₁H₅₇Cl₂N₉O₂Ru), calculated C, 61.25; H, 5.75; N, 12.61; found C, 60.77; H, 5.97; N, 12.58.

[Ru(MeL)(QC82)(STF31)]Cl₂, [25]Cl₂: ¹H-NMR (400 MHz, MeOD) δ 9.83 (dd, *J* = 5.8, 1.5 Hz, 2H), 8.67 – 8.59 (m, 2H), 8.46 (d, *J* = 2.3 Hz, 1H), 8.37 (d, *J* = 7.8 Hz, 2H), 8.27 – 8.14 (m, 4H), 7.95 (ddd, *J* = 7.3, 5.5, 1.3 Hz, 2H), 7.90 (d, *J* = 8.5 Hz, 2H), 7.76 – 7.70 (m, 2H), 7.68 – 7.63 (m, 2H), 7.61 (ddd, *J* = 8.4, 2.3, 1.1 Hz, 1H), 7.57 – 7.52 (m, 2H), 7.39 (d, *J* = 4.9 Hz, 1H), 7.34 (d, *J* = 8.1 Hz, 2H), 6.94 (dd, *J* = 8.4, 5.6 Hz, 1H), 6.70 (d, *J* = 1.4 Hz, 1H), 6.56 (t, *J* = 1.6 Hz, 1H), 5.88 (t, *J* = 1.5 Hz, 1H), 4.79 (s, 2H), 4.10 (s, 2H), 4.08 (s, 3H), 3.35 (s, 2H), 1.97 (s, 3H), 1.81 – 1.63 (m, 13H), 1.32 (s, 9H). ¹³C NMR (101 MHz, MeOD) δ 208.22, 168.01, 159.38, 157.98, 157.47, 156.49, 154.19, 148.06, 145.05, 143.86, 141.02, 139.40, 139.07, 138.47, 138.19, 133.94, 128.92, 128.73, 128.65, 128.36, 127.87, 127.16, 126.18, 125.14, 123.44, 119.11, 118.51, 52.73, 47.27, 46.49, 44.34, 38.74, 37.32, 35.97, 31.46, 29.17. ESI-HRMS: exact *m/z* calculated for [C₅₉H₆₂N₁₀O₄RuS]²⁺: 554.1862 *m/z*, found 554.1861 *m/z*. Elemental analysis (%) for compound [25]Cl₂ (C₅₉H₆₂Cl₂N₁₀O₄Ru), calculated C, 60.09; H, 5.30; N, 11.88; found C, 59.60; H, 5.16; N, 11.88.

[Ru(MeL)(QC82)(Py)]Cl₂, [26]Cl₂: ¹H-NMR (101 MHz, MeOD) δ 9.79 (d, *J* = 5.0 Hz, 2H), 8.63 (d, *J* = 8.3 Hz, 2H), 8.36 (dd, *J* = 7.9, 0.9 Hz, 2H), 8.25 – 8.16 (m, 4H), 7.94 (ddd, *J* = 7.4, 5.7, 1.3 Hz, 2H), 7.87 (dd, *J* = 8.6, 1.0 Hz, 2H), 7.54 (ddt, *J* = 15.9, 6.7, 1.5 Hz, 3H), 6.99 – 6.91 (m, 2H), 6.68 (t, *J* = 1.4 Hz, 1H), 6.56 (t, *J* = 1.6 Hz, 1H), 5.86 (s, 1H), 4.79 (s, 2H), 4.02 (s, 3H), 1.97 (d, *J* = 3.6 Hz, 5H), 1.80 – 1.63 (m, 15H). ¹³C{H} NMR (101 MHz, MeOD) δ 159.33, 157.97, 156.46, 154.23, 153.07, 141.05, 139.44, 138.32, 138.22, 128.66, 128.34, 126.62, 125.16,

123.46, 119.16, 118.43, 52.74, 44.11, 38.75, 37.32, 29.18. ESI-HRMS: exact m/z calculated for $[\text{C}_{41}\text{H}_{42}\text{N}_8\text{ORu}]^{2+}$: 382.1257 m/z , found 382.1261 m/z . Elemental analysis (%) for compound **[26]**Cl₂ ($\text{C}_{41}\text{H}_{42}\text{Cl}_2\text{N}_8\text{ORu}$), calculated C, 58.99; H, 5.07; N, 13.42; found C, 58.43; H, 5.35; N, 13.22.

5.4.3 Photochemistry

Photosubstitution followed by ¹H-NMR

The ¹H-NMR photosubstitution experiments were performed as described in appendix I.2.5.

Molar absorption coefficient determination

Molar absorption coefficients were determined as described in appendix I.2.1. Results for the compounds reported in this chapter are provided in appendix V.2.1.

Photosubstitution quantum yield measurements

Photon fluxes of all LEDs were determined using ferrioxalate actinometry and is described in detail in appendix I.2.2. The photosubstitution quantum yields were determined as described in appendix I.2.3, and the results are reported in appendix V.2.2.

Phosphorescence and singlet oxygen generation quantum yield measurements

The emission spectra were recorded, and the corresponding phosphorescence and singlet oxygen generation quantum yields determined as described in appendix I.2.4. The emission spectra and data are reported in appendix V.2.3.

Mock irradiation in OptiMEM media using 96-well plates

Compounds **[25]**Cl₂ and **[26]**Cl₂ were dissolved in DMSO in the dark and further diluted with OptiMEM complete (OptiMEM supplemented with 2.5% v/v fetal calf serum, 0.1% v/v penicillin/streptomycin, and 1.0% v/v Glutamine-S) to a final concentration of 5.0×10^{-5} M with 0.14% DMSO. The compound solutions were transferred to a 96-well plate ($v = 200 \mu\text{L}$ per well) and irradiated at different time intervals with red light ($630 \pm 4 \text{ nm}$; 31.3 mW/cm^2 ; $t = 0, 5, 10, 15, 20, 25, 30, 40, 50$ and 60 min). The absorption spectra between 300 and 800 nm were measured by a M1000 Tecan reader. Averaging the absorbance of a technical triplicate and baseline subtraction provided the resulting spectra. The time-evolution UV-Vis absorbance spectra are provided in appendix V.2.4.

5.4.4 Cell viability assay

Experimental details of cell culturing, cytotoxicity assay and *in vitro* irradiation are described in appendix I.3. The cell viability curves are reported in appendix V.3

5.5 References

- (1) Abraham, N. G.; Kappas, A. *Pharmacol Rev* **2008**, *60* (1), 79–127.
- (2) Motterlini, R.; Foresti, R. *American Journal of Physiology-Cell Physiology* **2017**, *312* (3), C302–C313.
- (3) Nitti, M.; Ivaldo, C.; Traverso, N.; Furfaro, A. L. *Antioxidants* **2021**, *10* (5), 789.
- (4) Abe, K.; Ikeda, S.; Nara, M.; Kitadate, A.; Tagawa, H.; Takahashi, N. *Cancer Medicine* **2023**, *12* (8), 9709–9722.
- (5) Tan, Q.; Wang, H.; Hu, Y.; Hu, M.; Li, X.; Aodengqimuge; Ma, Y.; Wei, C.; Song, L. *Cancer Science* **2015**, *106* (8), 1023–1032.
- (6) Shi, L.; Fang, J. *J Exp Clin Cancer Res* **2008**, *27* (1), 13.
- (7) Nowis, D.; Legat, M.; Grzela, T.; Niderla, J.; Wilczek, E.; Wilczynski, G. M.; Głodkowska, E.; Mrówka, P.; Issat, T.; Dulak, J.; Józkwicz, A.; Waś, H.; Adamek, M.; Wrzosek, A.; Nazarewski, S.; Makowski, M.; Stokłosa, T.; Jakóbiśiak, M.; Gołab, J. *Oncogene* **2006**, *25* (24), 3365–3374.
- (8) Takahashi, T.; Misawa, S.; Suzuki, S.; Saeki, N.; Shinoda, Y.; Tsuneoka, Y.; Akimoto, J.; Fujiwara, Y. *Photodiagnosis and Photodynamic Therapy* **2020**, *32*, 102009.
- (9) Schulz, S.; Wong, R. J.; Vreman, H. J.; Stevenson, D. K. *Front. Pharmacol.* **2012**, *3*, 68.
- (10) Salerno, L.; Floresta, G.; Ciaffaglione, V.; Gentile, D.; Margani, F.; Turnaturi, R.; Rescifina, A.; Pittalà, V. *European Journal of Medicinal Chemistry* **2019**, *167*, 439–453.
- (11) Bonnet, S. *J. Am. Chem. Soc.* **2023**, *145* (43), 23397–23415.
- (12) White, J. K.; Schmehl, R. H.; Turro, C. *Inorganica Chimica Acta* **2017**, *454*, 7–20.
- (13) Chen, Y.; Bai, L.; Zhang, P.; Zhao, H.; Zhou, Q. *Molecules* **2021**, *26* (18), 5679.
- (14) Zheng, S.; Reintjens, N. R. M.; Siegler, M. A.; Roubeau, O.; Bouwman, E.; Rudavskiy, A.; Havenith, R. W. A.; Bonnet, S. *Chemistry A European J* **2016**, *22* (1), 331–339.
- (15) Rahman, M. N.; Vlahakis, J. Z.; Szarek, W. A.; Nakatsu, K.; Jia, Z. *J. Med. Chem.* **2008**, *51* (19), 5943–5952.
- (16) Lameijer, L. N.; Ernst, D.; Hopkins, S. L.; Meijer, M. S.; Askes, S. H. C.; Le Dévédec, S. E.; Bonnet, S. *Angew. Chem. Int. Ed.* **2017**, *56* (38), 11549–11553.
- (17) Dreher, S. D.; Lim, S.-E.; Sandrock, D. L.; Molander, G. A. *J. Org. Chem.* **2009**, *74* (10), 3626–3631.
- (18) Liu, Z.; Dong, N.; Xu, M.; Sun, Z.; Tu, T. *J. Org. Chem.* **2013**, *78* (15), 7436–7444.
- (19) Zhang, Y.; Du, P.; Ji, Y.; Wang, S.; Zhu, Y.; Liu, Z.; He, Y.; Peng, Q.; Feng, Z. *Chem* **2023**, *9* (12), 3623–3636.
- (20) Molander, G. A. *J. Org. Chem.* **2015**, *80* (16), 7837–7848.
- (21) Wong, J. Y. F.; Barker, G. *Tetrahedron* **2020**, *76* (50), 131704.
- (22) Hernández, E. M.; Zheng, S.; Shepherd, H. J.; Yufit, D. S.; Ridier, K.; Bedoui, S.; Nicolazzi, W.; Velázquez, V.; Bonnet, S.; Molnár, G.; Bousseksou, A. CCDC 1547458: Experimental Crystal Structure Determination, 2017.
- (23) Schnidrig, Stephan; Bachmann, Cyril; Müller, Peter; Weder, Nicola; Spingler, Bernhard; Joliat-Wick, Evelyne; Mosberger, Mathias; Windisch, Johannes; Alberto, Roger; Probst, Benjamin. CCDC 1480797: Experimental Crystal Structure Determination.
- (24) Schnidrig, Stephan; Bachmann, Cyril; Müller, Peter; Weder, Nicola; Spingler, Bernhard; Joliat-Wick, Evelyne; Mosberger, Mathias; Windisch, Johannes; Alberto, Roger; Probst, Benjamin. CCDC 1480798: Experimental Crystal Structure Determination.
- (25) Boer, Daan den; Konovalov, Andrey I.; Siegler, Maxime A.; Hetterscheid, Dennis G. H. CCDC 2026077: Experimental Crystal Structure Determination.
- (26) Yang, L.; Powell, D. R.; Houser, R. P. *Dalton Trans.* **2007**, No. 9, 955–964.
- (27) Marchivie, M.; Guionneau, P.; Létard, J.-F.; Chasseau, D. *Acta Crystallogr B Struct Sci* **2005**, *61* (1), 25–28.
- (28) Hakkennes, M. L. A.; Buda, F.; Bonnet, S. *J. Chem. Inf. Model.* **2023**, *63* (24), 7816–7825.

- (29) Liu, L.; Wu, Y.; Bian, C.; Nisar, M. F.; Wang, M.; Hu, X.; Diao, Q.; Nian, W.; Wang, E.; Xu, W.; Zhong, J. L. *Cell Commun Signal* **2019**, *17* (1), 3.
- (30) Fallica, A. N.; Sorrenti, V.; D'Amico, A. G.; Salerno, L.; Romeo, G.; Intagliata, S.; Consoli, V.; Floresta, G.; Rescifina, A.; D'Agata, V.; Vanella, L.; Pittalà, V. *J. Med. Chem.* **2021**, *64* (18), 13373–13393.
- (31) Salerno, L.; Amata, E.; Romeo, G.; Marrazzo, A.; Prezzavento, O.; Floresta, G.; Sorrenti, V.; Barbagallo, I.; Rescifina, A.; Pittalà, V. *European Journal of Medicinal Chemistry* **2018**, *148*, 54–62.
- (32) Spampinato, M.; Sferrazzo, G.; Pittalà, V.; Di Rosa, M.; Vanella, L.; Salerno, L.; Sorrenti, V.; Carota, G.; Parrinello, N.; Raffaele, M.; Tibullo, D.; Li Volti, G.; Barbagallo, I. *Mol Biol Rep* **2020**, *47* (3), 1949–1964.
- (33) Chung, C. W. Y.; Toy, P. H. *J. Comb. Chem.* **2007**, *9* (1), 115–120.
- (34) Charbonnière, L. J.; Weibel, N.; Ziesel, R. F. *Synthesis* **2002**, *2002* (08), 1101–1109.

Chapter 6

Summary, discussion, and outlook

6.1 Summary

Metalloodrugs play a crucial role in modern cancer treatment, with platinum(II)-based drugs being used in about half of all chemotherapeutic regimes prescribed to cancer patients worldwide. Despite their broad application, Pt(II)-drugs suffer from several limitations including systemic toxicity and resistance. The numerous limitations of Pt-drugs have therefore sparked the search for chemotherapeutics based on alternative transition metals, including gold, palladium, iron, or ruthenium. **Chapter 1** provides a general overview of the clinical application of Pt-based and Ru-based anticancer drugs and describes the recent progress made in the development of photoactivated chemotherapy (PACT).

Since polypyridyl ligands are key building blocks in many transition metal-based therapeutics, the necessity for efficient and simple functionalization methods for polypyridyl ligands is high, with synthetic methods evolving constantly. As part of this development, a new synthetic route towards *ortho*-amino-polypyridines is reported in **Chapter 2**. Starting from pyridine *N*-oxides, the described reaction conditions allow for functionalization with one to three amine substituents of various polypyridine derivatives, including bipyridine, phenanthroline, terpyridine, quinoline, and isoquinoline. The simplicity, efficiency and selectivity of this method also allow for easy upscaling, as exemplified by the high-yielding preparation of 2,2'-bipyridine-6-amine at a >66 mmol scale.

The study reported in **Chapter 3** was aimed at investigating the possibility to sequentially photosubstitute two monodentate ligands from a single *trans*-ruthenium(II) polypyridyl complex upon two-color light irradiation. To do so, a series of symmetric complexes was synthesized based on the *trans*-[Ru(RL)(X)(Y)]²⁺ scaffold, where RL is HL (di([2,2'-bipyridin]-6-yl)amine) or MeL (di([2,2'-bipyridin]-6-yl)-*N*-methyl-amine), and with identical axial ligands where X=Y=MTE (methyl(2-thioethanol), ACN (acetonitrile) or Py (pyridine). While all complexes were stable in absence of light, irradiation with blue (435 nm), green (505 nm) or red (625 nm) light resulted in significant differences in photosubstitution kinetics depending on the nature of the axial ligands. Additionally, the photosubstitution quantum yields for several complexes appeared to be wavelength dependent, affording one of a few descriptions of anti-kasha behavior in ruthenium-based photosubstitution reactions. These observations encouraged us to synthesize the dissymmetric complex [Ru(MeL)(Py)(MTE)]²⁺, which was achieved by red light irradiation of [Ru(MeL)(Py)₂]²⁺ in presence of free MTE. Strikingly, selective photosubstitution of the Py ligand took place under red light irradiation of this complex, which allowed for developing a protocol that sequentially substituted first Py with red light followed by MTE using subsequent green light irradiation. These results provided the first example of selective, wavelength-dependent photosubstitution in ruthenium polypyridyl complexes. They also allowed for providing the first quantitative analysis of *trans* effects in the excited triplet states in ruthenium complexes.

Applying the results of **Chapter 3**, the concept of dual-targeting PACT was investigated in **Chapter 4**. To do so, pyridine-based nicotinamide phosphoribosyltransferase inhibitor STF31 and thioether-based microtubule polymerization inhibitor MTI were incorporated in the dissymmetric scaffold reported in **Chapter 3**. The corresponding dissymmetric complexes $[\text{Ru}(\text{MeL})(\text{STF31})(\text{MTI})]^{2+}$ and the symmetric analogues $[\text{Ru}(\text{MeL})(\text{STF31})_2]^{2+}$ and $[\text{Ru}(\text{MeL})(\text{MTI})_2]^{2+}$ were synthesized and characterized. They exhibited distinct photoreactivity upon irradiation with blue, green, or red light in aqueous solution. Importantly, the wavelength-dependent sequential release of both ligands observed in **Chapter 3** was retained in the dissymmetric $[\text{Ru}(\text{MeL})(\text{STF31})(\text{MTI})]^{2+}$ complex: releasing STF31 first was possible using red light, followed by MTI using blue light. *In vitro* evaluation of the bis-MTI complex in several human cancer cell lines under both normoxia and hypoxia showed strong dark toxicity but little additional toxicity when activated with green or red light. However, the toxicity of the bis-STF31 and STF31-MTI complexes increased up to 33-fold upon photoactivation with green light. Co-treatment of cells with an equimolar STF31:MTI mixture of both free inhibitors in the same *in vitro* conditions revealed a synergistic effect between the two inhibitors. Strikingly, this synergistic effect was also observed upon green-light activation of the $[\text{Ru}(\text{MeL})(\text{STF31})(\text{MTI})]^{2+}$ complex; this observation was independent from the O_2 concentration. The exceptional photochemical and *in vitro* properties of the dissymmetric complex $[\text{Ru}(\text{MeL})(\text{STF31})(\text{MTI})]^{2+}$ underline the potential of such dual-targeting PACT compounds, especially for the treatment of hypoxic tumors.

For many PACT compounds reported in the literature, the ruthenium fragment mainly functions as a photocleavable protective group to prevent interaction between an organic cytotoxic inhibitor and its protein target.¹ While this approach has shown great promise in killing cancer cells, it neglects the potential of the photoreleased ruthenium photocage as a potential biologically-active moiety, besides the photoreleased cytotoxic ligand. Although few studies have reported interaction between the ruthenium complexes and nucleic acids, no rationally designed photoactivatable Ru(II)-based protein inhibitors have been reported to date.² In **Chapter 5**, two strategies are reported for the design and development of novel PACT compounds targeting Heme Oxygenase 1 (HO-1). The first strategy focused on the modification of the tetrapyrrolyl ligand di([2,2'-bipyridin]-6-yl)amine (HL) with propyl carboxylic acid groups through cross-coupling or pyridylic C-H functionalization reactions. Upon coordination, the resulting ruthenium(II) complex mimics the natural HO-1 substrate, i.e., heme and as a result inhibit HO-1 after photorelease of the two monodentate, axial ligands. In the second strategy a series of complexes is reported based on $[\text{Ru}(\text{MeL})(\text{QC82})(\text{X})]^{2+}$ where QC82 is a known imidazole-based organic inhibitor of HO-1, and X is QC82, pyridine or STF31. While photosubstitution reactions were observed in all complexes upon irradiation with green or red light, a single QC82 ligand remained coordinated in the Ru-photoproduct. To evaluate the HO-1 inhibiting potential of this

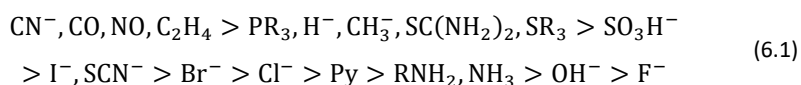
ruthenium-containing photoproduct, *in silico* docking studies of $[\text{Ru}(\text{MeL})(\text{QC82})]^{2+}$ with HO-1 were performed, which suggested a binding mode similar to that of heme. Although the complexes $[\text{Ru}(\text{MeL})(\text{QC82})_2]^{2+}$ and $[\text{Ru}(\text{MeL})(\text{QC82})(\text{STF31})]^{2+}$ showed significant *in vitro* cytotoxicity in human skin melanoma cancer cells, with the currently available data it was impossible to conclude that this cytotoxicity was a consequence of (or related to) HO-1 inhibition. These results do, however, provide a foundation for future development of photoactivatable ruthenium-based HO-1 inhibitors.

6.2 Discussion

6.2.1 Observation of *trans* effects in excited ruthenium(II) complexes

In coordination chemistry the ability of a ligand to labilize the metal-ligand bond in *trans* position, which is called the “*trans* effect”, is a widely reported yet poorly understood kinetic phenomenon. Its thermodynamic counterpart, called the *trans* influence, characterizes an elongation of a metal-ligand bond distance in the ground state due to the influence of the *trans* ligand. Both effects are frequently described for square planar complexes containing a d^8 metal center (e.g., Pt(II)) and less for octahedral complexes with a metal center either in d^0 or d^6 electron configuration, such as Ru(II).^{3,4} Despite the many reports and decades of research, a conclusive and universal understanding of the underlying mechanisms of the *trans* effect remains to be described.

The preparation of cisplatin often serves as the textbook example of this kinetic effect, where addition of ammonia to tetrachloroplatinate(II) ($[\text{PtCl}_4]^{2-}$) results in the formation of cisplatin (*cis*- $[\text{PtCl}_2(\text{NH}_3)_2]$). This reaction proceeds through the $[\text{PtCl}_3(\text{NH}_2)]^-$ monosubstituted intermediate, which proceeds forming the final product cisplatin as shown in Figure 6.1A, due to the stronger *trans* effect of Cl^- compared to NH_3 . A large number of experimental investigations exploring the effect of the *trans*-ligand on the substitution kinetics of square-planar Pt(II) complexes have led to the following order of ligands with decreasing *trans*-effect:⁵



To explain the relative order of *trans*-directing ligands, the reaction mechanism needs to be known. In the case of square-planar Pt(II) complexes, substitution usually occurs through an associative mechanism with the formation of a trigonal bipyramidal transition state as shown in Figure 6.1. Computational studies have confirmed that the *trans*-effect strength correlates with the electronic nature of the *trans* ligand T through both electron donation and back-donation.⁵⁻⁷ In more detail, σ -donor ligands tend to destabilize the ground state GS (Figure 6.1B) while π -acceptor ligands stabilize the transition state TS (Figure 6.1C).

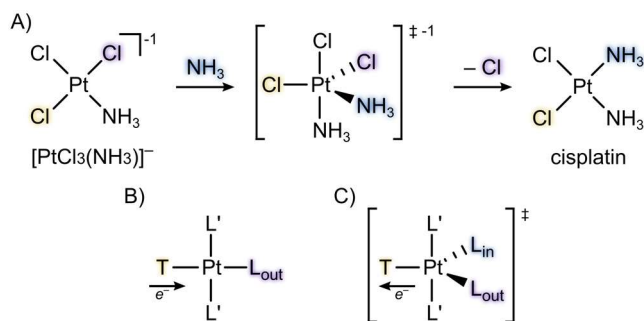


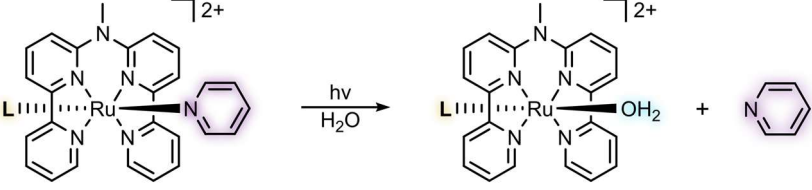
Figure 6.1 The substitution reaction (A) of chloride by ammonia from $[\text{PtCl}_3(\text{NH}_3)]^-$ forming cisplatin. Schematic representation (B, C) of how the *trans* ligand T can affect the substitution of L_{out} in square-planar Pt(II) complexes. T can either destabilize the ground state GS through electron donation (B) or stabilize the transition state TS through electron withdrawal (C), where L' are spectator ligands, L_{out} is the ligand to be substituted (outgoing) and L_{in} is the substituting ligand (incoming).

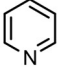
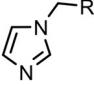
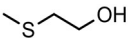
The structures and substitution reactions of octahedral complexes are geometrically more complicated than of square planar complexes, in the sense that more isomers may exist both for the reagent and the product. Therefore, the *trans* effect in octahedral complexes has been less studied systematically in the literature. Importantly, ligand substitution in octahedral complexes generally occurs dissociatively rather than associatively as in square planar complexes. The difference in substitution mechanism makes that the *trans* effect and *trans* influence often correlate in octahedral complexes. Although trends have been observed in numerous studies, many exceptions are known and dependent on the metal center, its electron configuration as well as the involved ligands.⁴ However, a more recent computational study using conceptual density functional theory has provided a quantitative scale of *trans* effect strength by monitoring differences in electron density of d^6 octahedral complexes.⁸ Although the scope of investigated ligands is rather small, the computational results closely matched the experimental ones, indicating that *trans* effects are primarily regulated by the electron-donating properties of the *trans* ligand.

The work presented in this PhD thesis involves the photochemical characterization of multiple Ru(II)-tetrapyrrolyl complexes containing two photolabile, monodentate ligands in *trans* positions. These monodentate ligands include derivatives of pyridine, thioether, water and N-methyl-imidazole. As observed in the crystal structures of several of these complexes, reported in **Chapter 3** and **Chapter 5**, the ligand-Ru(II) bond lengths are not significantly different upon varying the *trans* ligands, indicating the absence of significant *trans* influence in the ground state of these molecules. Furthermore, at the investigated temperatures these *trans*-Ru(II) polypyridyl complexes only underwent ligand substitution when irradiated with light, limiting the possibilities to study their ground state *trans* effects. However, detailed quantitative analysis of the photosubstitution kinetics reported in this

thesis provides new insights into *trans* effects in the excited states of ruthenium compounds (Table 6.1).

Table 6.1 Quantum yield $\phi_{\lambda_{\text{irr}}}$ and photoreactivity $\zeta_{\lambda_{\text{irr}}}$ ($\zeta_{\lambda_{\text{irr}}} = \phi_{\lambda_{\text{irr}}} \times \epsilon_{\lambda_{\text{irr}}}$) for the photosubstitution of pyridine from $[\text{Ru}(\text{MeL})(\text{L})(\text{Py})]^{2+}$ with different *trans* ligands **L** in aqueous solution.



L =				OH_2
ϕ_{505}	0.025	0.014	0.019	0.00019
ζ_{505}	110	100	32	1.1
ϕ_{625}	0.015	0.017	0.014	0.00005
ζ_{625}	0.65	5.6	0.046	0.020

Differences in reaction kinetics between photoactive compounds are generally evaluated by comparing their efficiency to generate a specific excited state or reaction product, i.e., by comparing their photosubstitution quantum yields. Comparing photochemical kinetics based on quantum yields is in many cases preferred as it ignores differences in light absorption properties. Also, this habit is driven by the common assumption that Kasha's rule is valid, which states that once the excited state is obtained the probability to obtain a molecule of photoproduct does not depend too much on the irradiation wavelength, and hence that only quantum yields matter. When examining the photosubstitution kinetics of pyridine from $[\text{Ru}(\text{MeL})(\text{L})(\text{Py})]^{2+}$ as shown in Table 6.1, we found that quantum yields for its photosubstitution with red light were highly similar for complexes with different *trans* ligands **L** = pyridine (Py), N-methyl-imidazole (NMI) or MTE; only for **L** = water a significant drop of the quantum yield was observed. For green light, the measured differences were slightly more significant and suggested a decreasing kinetic *trans*-effect in the order $\text{Py} > \text{MTE} > \text{NMI} \gg \text{H}_2\text{O}$.

On the other hand, we found that the photosubstitution quantum yield depended on the irradiation wavelength and hence did not really obey Kasha's rule. In addition, the generation of an excited state through light absorption is a crucial step during any photoreaction, so that the kinetics utterly depend on the absorption of a complex as well. It would hence be more realistic, when comparing photosubstitution kinetics, to compare instead of quantum yields $\phi_{\lambda_{\text{irr}}}$ the photochemical reactivities $\zeta_{\lambda_{\text{irr}}}$, which is defined as the product of the (dimensionless) quantum yield $\phi_{\lambda_{\text{irr}}}$ and the molar absorptivity

$\epsilon_{\lambda \text{ irr}}$ (in $\text{M}^{-1} \text{cm}^{-1}$). When comparing the photochemical reactivities of $[\text{Ru}(\text{MeL})(\text{L})(\text{Py})]^{2+}$, the trends at both wavelengths were different from those observed for quantum yields (Table 6.1). Under green light irradiation ζ_{505} decreased in the order $\text{NMI} > \text{Py} > \text{MTE} \gg \text{H}_2\text{O}$. The differences in ζ_{625} values were way larger than those of the ϕ_{625} values, highlighting the very different red light absorption of the different molecules. Overall, a *trans* N-methylimidazole ligand seems to be the best to labilize a pyridine ligand on this type of ruthenium complexes using red light, both because it increases the photosubstitution quantum yield and because it increases the molar absorption coefficient in this domain of the spectrum. These results emphasize the difficulty of predicting the kinetics of photosubstitution reactions for *trans*-Ru(II) polypyridyl complexes, because one needs to understand not only the distribution and nature of the excited states of the reagent, its light absorption properties, but also the mechanism of the reaction.

Since the photolability of pyridine in $[\text{Ru}(\text{MeL})(\text{L})(\text{Py})]^{2+}$ appears to depend on the *trans*-ligand L, the electronic nature of the *trans*-ligand likely affects the energies of the excited states involved in photosubstitution. To qualitatively evaluate these effects, the energies of the frontier molecular orbitals (FMOs) of Py, NMI, MTE and H_2O were calculated with density functional theory (DFT) at the BLYP/def2-svp level using ORCA 6.1 (Figure 6.2).⁹ All ligands act as σ donors with an decreasing σ -donating strength following the order $\text{MTE} > \text{Py} \sim \text{NMI} \gg \text{H}_2\text{O}$. The order follows the decreasing energy level of their highest occupied σ molecular orbital (HOMO): assuming that the empty metal-based d-orbitals on ruthenium are high in energy, they will interact more strongly with monodentate ligands that have a higher HOMO (if symmetry allows). In addition, Py and NMI contain an aromatic system and a low-lying lowest unoccupied molecular orbital (LUMO) with an anti-bonding π^* character that can interact with filled d-orbitals of the metal center (back-bonding). However, the additional mesomeric N-donor atom in NMI increases the electron density of the π system and thereby the energy of its π^* LUMO, thus making it a worse π -acceptor than Py. Similarly, the higher HOMO-2 of π character of NMI also increase its π -donating abilities compared with Py. In contrast, the coordinating sulfur atom in MTE is sp^3 hybridized and has an anti-bonding LUMO orbital of σ^* character that could accept electrons from the metal via a π -like overlap, but this interaction is energetically unfavorable as the LUMO is relatively high in energy. While one S-based electron pair acts as a σ donor (HOMO) in a "side-on" binding mode, the second electron pair is located in a low-lying occupied π orbital (HOMO-2), resulting in weak π -donation to the metal center. Finally, H_2O has the lowest σ donating properties and little to no π -accepting properties. According to this analysis Py is an average σ -donating and the best π -acceptor ligand in the series, NMI an equally good σ -donor but less π -accepting ligand, while MTE is the strongest σ -donor and a weak

σ^* -acceptor and π -donor, and finally H₂O is the weakest σ -donating ligand with no π -accepting or π -donating properties.

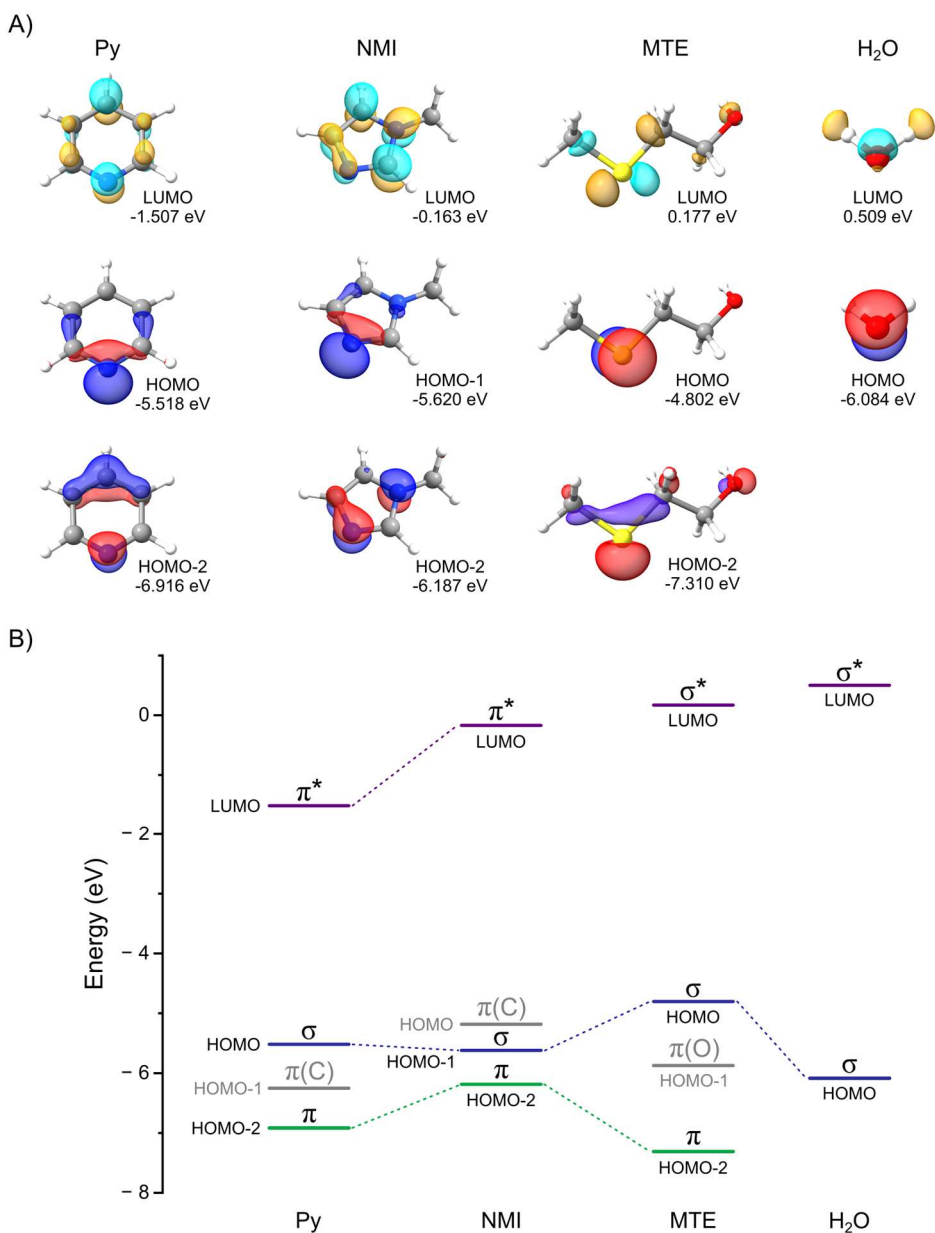


Figure 6.2: Comparison between the frontier molecular orbitals (A) and corresponding energies (B) of Py, NMI, MTE, and water. Calculated with density functional theory using the Becke-Lee-Yang-Parr (BLYP) functional with def2-svp basis set in the ORCA 6.1 software package.⁹

This qualitative orbital analysis highlights the fundamental differences in electronic character of the different monodentate ligands in this series, but it does not allow us to fully rationalize the *trans* effects in the triplet excited state. If we assume that green light quantum yields offer the best measure of this photo-*trans* effect, then the decrease in *trans*-effect in $[\text{Ru}(\text{MeL})(\text{L})(\text{Py})]^{2+}$ complexes follows $\text{Py} > \text{MTE} > \text{NMI} \gg \text{H}_2\text{O}$, which more or less follows the ligand-field strength of the *trans* ligand in the traditional spectrochemical series.¹⁰ If we focus on red light and compare ζ_{625} values, then the *trans* effect decreases following $\text{NMI} > \text{Py} > \text{MTE} \gg \text{H}_2\text{O}$, which does not follow the spectrochemical series notably due to the effect of the *trans* ligand on the absorption spectrum of the complex. While the FMO analysis provides qualitative insight into the electronic nature of the ligands, it must be noted that these FMOs will likely differ upon coordination to a metal center. In fact, the properties of the free *trans* ligands cannot be used to directly predict their effect on the dynamics of the excited state of the metal complex, which depends on the spectator ligands, on the geometry and sterics of the Ru(II) complex, on the solvent, and finally, on the irradiation wavelength.

The observed increase in photosubstitution kinetics with stronger donating ligands in *trans* position is consistent with trends reported by others. For example in the ground state albeit with a different mechanism, the rate of H_2O substitution by acetonitrile was reported to increase with increasing electron-donating strength of substituent X in $[\text{Ru}(\text{tpy})(4,4'\text{-X}_2\text{bpy})(\text{H}_2\text{O})]^{2+}$ complexes, with $\text{tpy} = 2,2':6',2''\text{-terpyridine}$, $4,4'\text{-X}_2\text{bpy} = 4,4'\text{-bis-substituted } 2,2'\text{-bipyridine}$ and substituent $\text{X} = \text{H}, \text{CH}_3, \text{OCH}_3, \text{NH}_2$ and $\text{N}(\text{CH}_3)_2$.¹¹ Similarly, the photosubstitution quantum yield of acetonitrile in aqueous solution increased with the electron-donating ability of R in $[\text{Ru}(\text{R-phtpy})(\text{acac})(\text{MeCN})]^+$, where $\text{acac} = \text{acetylacetonate}$ and $\text{R-phtpy} = 4'\text{-(4-R-phenyl)-2,2':6',2''-terpyridine}$ with $\text{R} = \text{N}(\text{ethyl})_2, \text{N}(\text{CH}_3)_2, \text{OCH}_3, \text{CH}_3, \text{H},$ or NO_2 .¹² This effect on the photosubstitution of acetonitrile in aqueous solution was also reported by the Turro group for $[\text{Ru}(\text{tpy})(4,4'\text{-X}_2\text{bpy})(\text{L})]^{2+}$, where $\text{X} = \text{H}, \text{CH}_3, \text{OCH}_3,$ or $t\text{-C}(\text{CH}_3)_3$ and $\text{L} = \text{acetonitrile}$.¹³ However, for the pyridine analogues of these complexes ($\text{L} = \text{pyridine}$), photosubstitution in aqueous solution occurred very inefficiently when irradiated with green light (500 nm; $\phi < 0.0001$), pointing to the very band *trans* effect of the *trans* pyridine ring of the bpy chelate in this family of complexes. Interestingly, both the acetonitrile and pyridine complexes showed an increasing energy gap between the $^3\text{MLCT}$ and ^3MC states upon increasing donating strength of the bidentate ligand. This observation led to the controversial conclusion that the photo-release of acetonitrile must occur directly from the $^3\text{MLCT}$ state, without thermal promotion to the ^3MC state. Together with our findings, these contradicting reports indicate that the mechanism of photosubstitution may be strongly depend on the nature of the released ligand; they also highlight the complex photochemistry behind photosubstitution reactions. In absence of a full mechanistic understanding of photosubstitution, providing a concluding interpretation of experimental trends in excited state *trans* effects remains challenging.

More elaborate computational approaches may be needed, such as the dynamic model described recently by our group.¹⁴

6.2.2 Determining the (photo)toxicity of dual-targeting ruthenium(II) complexes

One of the important aspects for ruthenium(II) complexes to be effective as a PACT compound is the difference in cytotoxicity of the intact complex in the dark and the combined cytotoxicity of the photoproducts released by light activation. Several complexes reported in **Chapter 4** and **Chapter 5** can release two biologically active ligands and therefore, an intermediate is formed during light activation. Although the light-dose needed to ensure a photo-stationary state *in vitro* was determined, formation of this intermediate is unavoidable and may give rise to unexpected biological effects. For example, in **Chapter 5** the intermediate $[\text{Ru}(\text{MeL})(\text{QC82})(\text{H}_2\text{O})]^{2+}$ obtained upon release of STF31 from $[\text{Ru}(\text{MeL})(\text{QC82})(\text{STF31})]^{2+}$ was found to be a promising inhibitor for HO-1 (according to *in silico* results). In **Chapter 4**, the Ru-MTI intermediate $[\text{Ru}(\text{MeL})(\text{MTI})(\text{H}_2\text{O})]^{2+}$ obtained after release of STF31 from $[\text{Ru}(\text{MeL})(\text{STF31})(\text{MTI})]^{2+}$ may also interact with biological off-targets, either related to the ligand that remains coordinated or via the free coordination site on the Ru(II) center. While the biological effects of such reactive species are not expected, they could be beneficial for eradicating cancer cells.

Clinically evaluated Ru(II)-based anticancer drug BOLD-100 owes its success to multiple modes-of-action due to thermal ligand exchange with biomolecules, resulting in a potentially large number of bioinorganic interactions that make resistance mechanisms difficult to evolve. A similar mechanism could occur for the bis-aqua complexes or mono-aqua complexes obtained from light-activated $[\text{Ru}(\text{MeL})(\text{QC82})(\text{STF31})]^{2+}$ or $[\text{Ru}(\text{MeL})(\text{STF31})(\text{MTI})]^{2+}$, although the results obtained so far do not suggest such behavior. To evaluate such potential behaviour of the complexes presented here, $[\text{Ru}(\text{MeL})(\text{Py})(\text{MTE})]^{2+}$ was incorporated in the cytotoxicity evaluation reported in **Chapter 4**. The lack of toxicity observed for this model complex with or without light irradiation could, however, be due to its hydrophilicity, which predicts lower cellular uptake compared with the complexes bound to more hydrophobic inhibitors STF31 and MTI.

Alternatively, drug-ruthenium conjugates may interact with biomolecules prior to activation. Such unexpected behavior was encountered in a study reported by Toupin et al., in which a Ru(II)-caged inhibitor of cytochrome P450 3A4 was investigated.¹⁵ Surprisingly, the Ru(II)-inhibitor conjugate exhibited a stronger inhibitory effect than the free inhibitor. Crystal structure analysis of the enzyme bound to the Ru(II)-inhibitor complex showed that the conjugate interacted with a hydrophobic pocket close to the catalytic site of the enzyme. This unexpected binding mode was different from that of the parent organic inhibitor, which exemplifies how unexpected the interaction between Ru(II)-based complexes and proteins can be.

While the complexes reported here have been shown to reduce cancer cell proliferation after light activation, the presented data do not provide evidence for inhibition of the targeted proteins. *In vitro* inhibition assays for NAMPT and microtubule polymerization are commercially available, but a lack of time prevented verification of the expected inhibition properties.^{16,17} Proving inhibition of HO-1, however, remains more challenging because no commercial *in vitro* assays are available, and the published chemical assay could not be reproduced in our labs. Therefore, biological evaluation of HO-1 inhibition may be preferred and is typically performed by monitoring the enzyme's activity from isolated animal samples such as microsomal extracts from rat spleen.¹⁸

6.3 Outlook

The results reported in this thesis provide a proof-of-concept for dual-targeting PACT compounds from which two different biologically active ligands can be released sequentially. To further develop this strategy and rationally design new compounds, the exact photochemical mechanisms need to be elucidated with a focus on understanding *trans* effects in the excited state of coordination compounds. Combination of time-resolved spectroscopic techniques with time-dependent density functional theory (TD-DFT) could greatly advance the understanding of these complex systems. A likely first step would be to compare lifetimes of the different triplet excited states and to determine their electronic nature (i.e., whether they are MLCT or MC states). Besides further characterization of the complexes reported in this thesis, extending the series based on $[\text{Ru}(\text{MeL})(\text{L})(\text{Py})]^{2+}$ with other monodentate ligands L following the ligand FMO analysis should provide valuable insights (Figure 6.3). Firstly, incorporating pyridyl ligands containing electron-withdrawing substituents could provide insight into the effect of increasing π -accepting character on the photosubstitution kinetics of Py in $[\text{Ru}(\text{MeL})(\text{L})(\text{Py})]^{2+}$. For example, the LUMO energy of 4-(trifluoromethyl)pyridine is lower than that of Py, making it a better π -acceptor while maintaining a similar energy gap between HOMO and HOMO-2 of the ligand. On the other hand, pyridyl ligands containing electron-donating substituents such as 4-(methoxy)pyridine, result in increased σ -donation and π -donation similar to that of NMI, as shown in Figure 6.2. In **Chapter 3**, the preparation and photochemical characterization of acetonitrile-containing symmetric complex $[\text{Ru}(\text{MeL})(\text{ACN})_2]^{2+}$ is described. While this complex appeared to be too reactive for the preparation of a dissymmetric complex, further efforts could provide highly photoreactive complexes with strong *trans* effects due to the low-lying HOMO orbitals of ACN. Similar to the FMOs of MTE, trimethylphosphine (PMe_3) is a relatively strong σ -donor due to the high-lying HOMO orbital while the high-lying LUMO makes π back-donation from the Ru(II) center unlikely. The steric bulk of PMe_3 also makes it an interesting candidate to investigate the role of sterics on excited-state *trans* effects. Lastly, use of primary amines such as n-butylamine that are primarily σ -donors could

provide insight in the effects of ligands that coordinate to Ru(II) without the participation of π -orbitals. Importantly, the non-conventional photochemical synthetic route towards the dissymmetric complexes reported in this thesis is far from straightforward and difficult to upscale. Further optimization will be required to synthetically access novel dissymmetric ruthenium compounds bearing various monodentate ligands beyond those reported in this thesis.

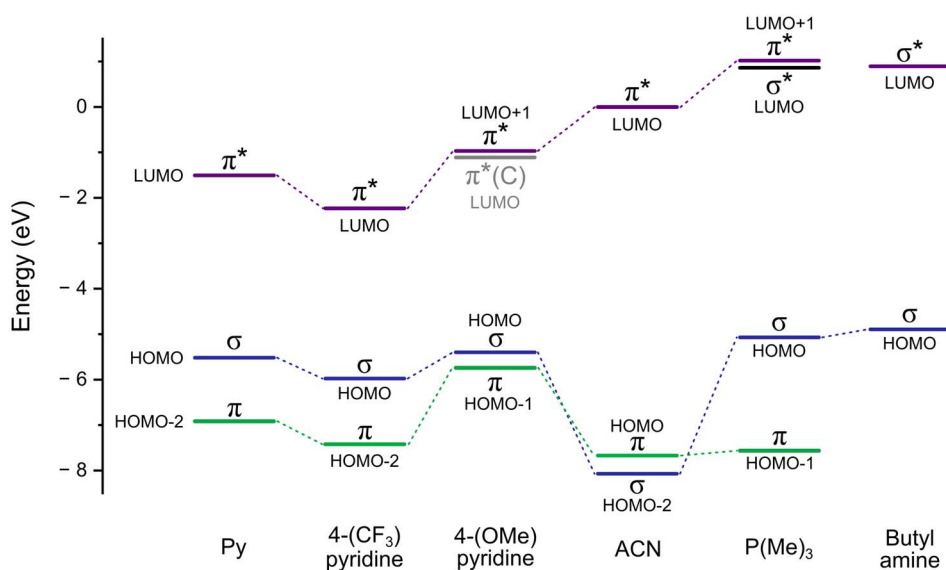


Figure 6.3 Comparison of the frontier molecular orbital energies of Py, 4-(trifluoromethyl)pyridine, 4-(methoxy)pyridine, ACN, trimethylphosphine and 1-butylamine. Calculated with density functional theory using the Becke-Lee-Yang-Parr (BLYP) functional with def2-svp basis set in the ORCA software package.⁹

To further improve the anticancer efficacy of dual-targeting PACT compounds, several aspects can be considered (Figure 6.4). Firstly, the STF31/MTI combination reported in **Chapter 4** was found to work synergistically, while synergism had not been reported for this combination before. Incorporating a combination that is known to induce synergy could therefore induce an even stronger inhibitory effect on cancer cell proliferation after photo-activation.¹⁹ Secondly, the dissymmetric complex $[\text{Ru}(\text{MeL})(\text{STF31})(\text{MTI})]^{2+}$ releases the two biologically active ligands, but also a Ru(II)-based photoproduct for which no significant cytotoxicity was observed. Increasing the toxicity of this Ru(II)-based photoproduct could therefore add another dimension to the anticancer properties of the overall complex. A possible strategy to increase its toxicity could be to extend the aromatic π surface of the tetrapyrrolyl ligand, which has been shown to result in Ru(II) complexes with PDT characteristics and DNA-binding properties.^{20,21} Since several precursors of such extended polypyridyl ligands have been reported in **Chapter 2**, the preparation of such

complexes might be relatively straightforward. Alternatively, covalently linking a third drug to the bridging nitrogen in the tetrapyrridyl ligand could also lead to a toxic, Ru-based photoproduct. Apart from phototoxicity of the compounds, high accumulation in a specific tissue, cell type or organelle is a desirable characteristic in anticancer therapeutic compounds. Combining a targeting moiety into the dual-targeting PACT strategy would therefore be of great interest as it has been shown to benefit PACT.²² In the molecule shown in Figure 6.4, both drug 2 or drug 3 could be tumor-targeting fragments. The vast range of design possibilities makes the multifunctional ruthenium platform presented in this thesis a promising and tunable scaffold for bioinorganic applications in oncology.

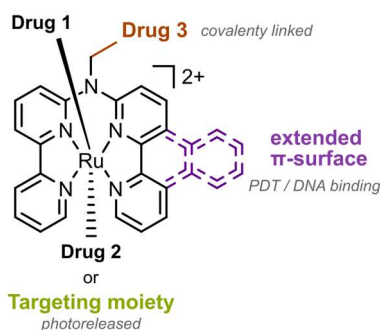


Figure 6.4 General design strategy towards the next generation of dual-targeting PACT compounds.

6.4 References

- (1) Bonnet, S. *J. Am. Chem. Soc.* **2023**, *145* (43), 23397–23415.
- (2) Papish, E. T.; Oladipupo, O. E. *Current Opinion in Chemical Biology* **2022**, *68*, 102143.
- (3) Quagliano, J. V.; Schubert, Leo. *Chem. Rev.* **1952**, *50* (2), 201–260.
- (4) Coe, B. J.; Glenwright, S. J. *Coordination Chemistry Reviews* **2000**, *203* (1), 5–80.
- (5) Chval, Z.; Sip, M.; Burda, J. V. *J Comput Chem* **2008**, *29* (14), 2370–2381.
- (6) Pinter, B.; Van Speybroeck, V.; Waroquier, M.; Geerlings, P.; De Proft, F. *Phys. Chem. Chem. Phys.* **2013**, *15* (40), 17354.
- (7) Santos-Jr, C. V.; Da Silva, G. M. B.; Dias, R. P.; Moura, R. T.; Da Silva, J. C. S. *Advcd Theory and Sims* **2024**, *7* (5), 2301148.
- (8) Guégan, F.; Tognetti, V.; Joubert, L.; Chermette, H.; Luneau, D.; Morell, C. *Phys. Chem. Chem. Phys.* **2016**, *18* (2), 982–990.
- (9) Neese, F. *WIREs Comput Mol Sci* **2025**, *15* (2), e70019.
- (10) Ishii, T.; Tsuboi, S.; Sakane, G.; Yamashita, M.; Breedlove, B. K. *Dalton Trans.* **2009**, No. 4, 680–687.
- (11) Mecchia Ortiz, J. H.; Peyrot, A. M.; Fagalde, F.; Katz, N. E. *Inorganic Chemistry Communications* **2018**, *98*, 44–47.
- (12) Mudrak, V.; Lacroix, P. G.; Labra-Vázquez, P.; Tassé, M.; Mallet-Ladeira, S.; Malfant, I. *Dalton Trans.* **2025**, *54* (22), 9021–9031.
- (13) Dunbar, M. N.; Steinke, S. J.; Piechota, E. J.; Turro, C. J. *Phys. Chem. A* **2024**, *128* (3), 599–610.
- (14) Hakkennes, M. L. A.; Regeni, I.; Husiev, Y.; Andreeva, V. D.; Siegler, M. A.; Buda, F.; Bonnet, S. *J. Am. Chem. Soc.* **2025**, *147* (39), 35767–35787.

- (15) Toupin, N.; Steinke, S. J.; Nadella, S.; Li, A.; Rohrbaugh, T. N.; Samuels, E. R.; Turro, C.; Sevrioukova, I. F.; Kodanko, J. J. *J. Am. Chem. Soc.* **2021**, *143* (24), 9191–9205.
- (16) Bretin, L.; Husiev, Y.; Ramu, V.; Zhang, L.; Hakkennes, M.; Abyar, S.; Johns, A. C.; Le Dévédec, S. E.; Betancourt, T.; Kornienko, A.; Bonnet, S. *Angew Chem Int Ed* **2024**, *63* (5), e202316425.
- (17) Wang, X.; Xu, T.-Y.; Liu, X.-Z.; Zhang, S.-L.; Wang, P.; Li, Z.-Y.; Guan, Y.-F.; Wang, S.-N.; Dong, G.-Q.; Zhuo, S.; Le, Y.-Y.; Sheng, C.-Q.; Miao, C.-Y. *Sci Rep* **2015**, *5* (1), 12657.
- (18) Virzi, N. F.; Alvarez-Lorenzo, C.; Concheiro, A.; Consoli, V.; Salerno, L.; Vanella, L.; Pittalà, V.; Diaz-Rodriguez, P. *International Journal of Pharmaceutics* **2025**, *668*, 124997.
- (19) You, T.; Wang, L.; Wang, J.; Xu, D.; Xu, X.; Li, N.; Li, M. J.; Wang, H.; Dong, X. *Sci Data* **2025**, *12* (1), 1284.
- (20) Toupin, N. P.; Nadella, S.; Steinke, S. J.; Turro, C.; Kodanko, J. J. *Inorg. Chem.* **2020**, *59* (6), 3919–3933.
- (21) Brabec, V.; Kasparkova, J. *Coordination Chemistry Reviews* **2018**, *376*, 75–94.
- (22) Zhang, L.; Wang, P.; Zhou, X.-Q.; Bretin, L.; Zeng, X.; Husiev, Y.; Polanco, E. A.; Zhao, G.; Wijaya, L. S.; Biver, T.; Le Dévédec, S. E.; Sun, W.; Bonnet, S. *J. Am. Chem. Soc.* **2023**, *145* (27), 14963–14980.

Appendix I: General methods

I.1 Photoreactor for synthesis of dissymmetric complexes

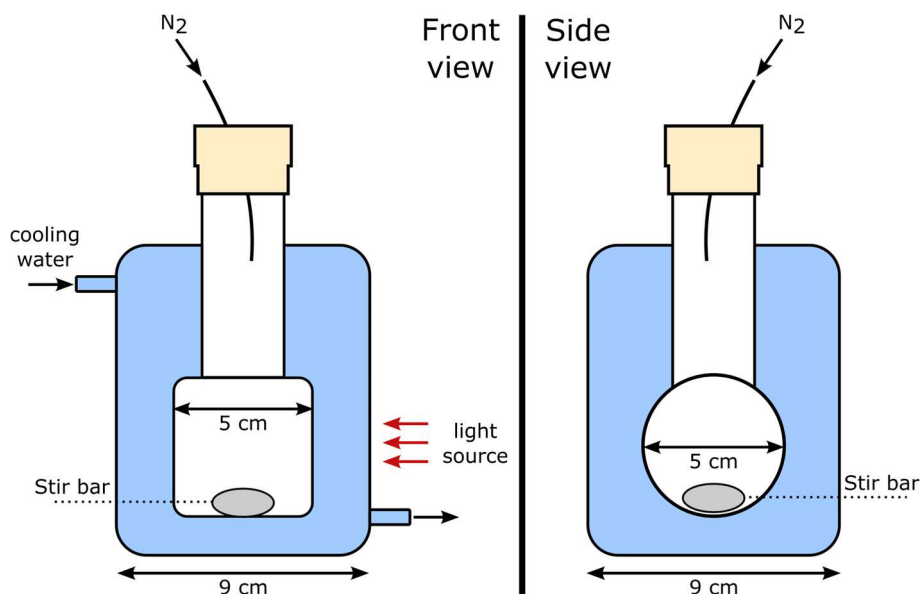


Figure I.1 Schematic representation of water-cooled photoreactor.

I.2 Photochemistry

I.2.1 Determination of molar extinction coefficients

The molar extinction coefficients (ϵ) of the reported compounds were determined according to the following procedure. Three stock samples of the compound were prepared with a known mass. Following dissolution in the same solvent used for absorbance experiments, the UV-Vis absorbance spectra between 200 and 800 nm were measured for 5 dilutions of each stock solution at 25 °C. Linear regression of the maximum absorbance at the ¹MLCT band of every measurement provided the molar extinction coefficient according to the Lambert-Beer law.

I.2.2 Actinometry

According to standard protocol, ferrioxalate actinometry was used to determine the photon flux (in mol/s) of the blue ($\lambda_{\text{irr}} = 435 \text{ nm}$) and green ($\lambda_{\text{irr}} = 505 \text{ nm}$) LEDs used in this work.^{1,2} In short, the cuvette used for the photoreactions was charged freshly prepared solution of $\text{K}_3\text{Fe}(\text{C}_2\text{O}_4)_3 \cdot 3 \text{H}_2\text{O}$ (3 mL, 150 mM in 50 mM H_2SO_4). The solution was stirred for 2 minutes at 25 °C to ensure thermal stability, followed by irradiation (vertical beam, pathlength = 3

cm) for a given time. A portion of the irradiated sample (2 mL) was transferred to a 10 mL volumetric flask containing an aqueous solution of 1,10-phenanthroline (4 mL, 5.55 mM) and 1 ml of a solution of glacial acetic acid (1.76 M), sodium hydroxide (0.71 mM) and sodium sulfate (0.53 mM). After filling the volumetric flask to 10 mL, the absorbance spectrum of the resulting ferrous tris-1,10-phenanthroline $[\text{Fe}(\text{phen})_3]^{2+}$ solution was measured by UV-Vis spectroscopy. With the absorbance at 510 nm and the molar absorption coefficient ($\epsilon = 11500 \text{ M}^{-1}\text{cm}^{-1}$) for $[\text{Fe}(\text{phen})_3]^{2+}$ in water, the amount of formed Fe^{2+} after irradiation of a given time ($d[\text{Fe}^{2+}]/dt$) could be calculated. This slope (as visualized in Figure I.2) was then used to calculate the photon flux (ϕ) of the respective LEDs with equation I.1:

$$\phi = \frac{d[\text{Fe}^{2+}]}{dt(1-10^{-A_{\text{ref}}})\varphi_{\text{ref}}} \quad (\text{I.1})$$

in which $(1-10^{-A_{\text{ref}}})$ is the photon absorption probability of the solution and φ_{ref} is the reference quantum yield at the irradiated wavelength of the ferrioxalate actinometer to generate Fe^{2+} .¹ Since the length of the vertical irradiation beam pathway is 3 cm, A_{ref} equals $A'_{\text{ref}} \times 3$ where A'_{ref} is the absorbance of the non-irradiated actinometer $\text{K}_3\text{Fe}(\text{C}_2\text{O}_4)_3 \cdot 3\text{H}_2\text{O}$ (150 mM in 50 mM H_2SO_4) at the irradiation wavelength of the LED, measured in a cuvette with a 1 cm pathlength. Using equation II.1, ϕ was 307.6 nmol/s for the 435 nm LED ($I = 13.5 \text{ mW/cm}^2$) and 25.8 nmol/s for the 505 nm LED ($I = 12.0 \text{ mW/cm}^2$).

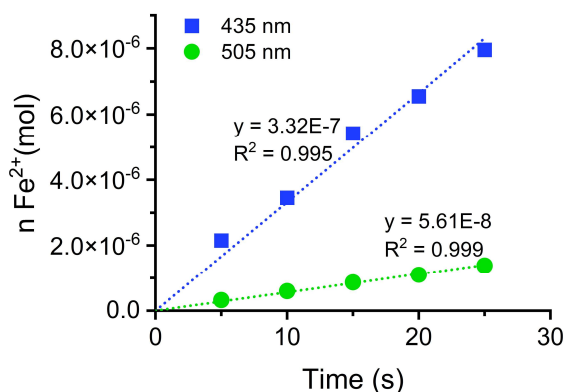


Figure I.2 Plot of Fe^{2+} evolution from ferrioxalate actinometer when irradiated with the LEDs used within the photoirradiation setup.

Since the ferrioxalate actinometer has a quantum yield below 1% when irradiated with $\lambda_{\text{irr}} > 570 \text{ nm}$, it is not suitable for determining the photon flux of a light source with a maximum output at higher wavelength. Therefore, the photon flux of the red LED ($\lambda_{\text{irr}} = 625 \text{ nm}$) (ϕ_{625}) used was determined indirectly using equation I.2:

$$\phi_{625} = \frac{\phi_{\text{ref}} \times E_{\text{ref}}}{E_{625}} \times \frac{I_{625}}{I_{\text{ref}}} \quad (1.2)$$

in which ϕ_{ref} is the photon flux of a reference LED in mol per second, E_{ref}/E_{625} is the photon energy of the reference or 625 nm LED in Joule and I_{ref}/I_{625} is the irradiance of the used LEDs in mW per cm². Using equation 1.2, ϕ_{625} was 423.5 nmol/s for the 625 nm LED ($I = 11.3$ mW/cm²). The emission spectra of the LEDs (used in UV-Vis absorbance measurements) and lamps (used in ¹H-NMR photosubstitution experiments and preparation of dissymmetric complexes) are shown in Figure I.3.

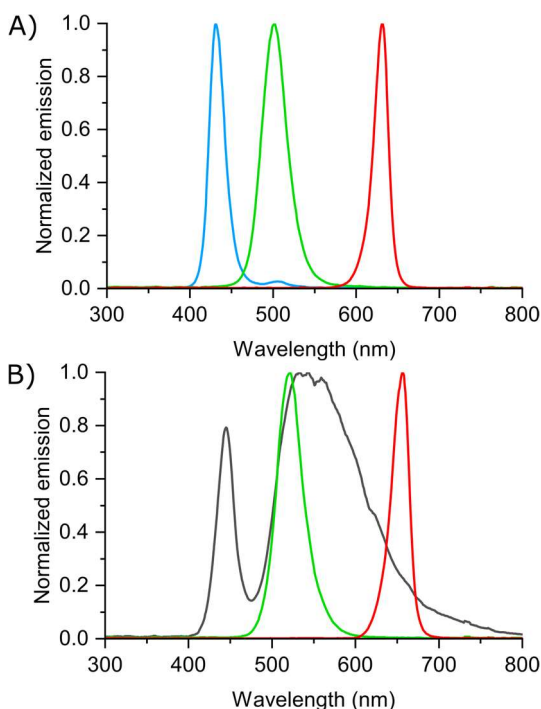


Figure I.3 Normalized emission spectra of used LEDs (A; 435 nm in blue, 505 nm in green, 625 nm in red; obtained from Mouser Electronics) and lamps (B; white in grey, 530 nm in green, 650 nm in red; obtained from HepatoChem).

I.2.3 Photosubstitution quantum yield

For symmetric complexes: The photosubstitution reactions of the symmetric complexes reported in this work all follow a sequential two-step mechanism according to the general equation $R \rightarrow I \rightarrow P$, in which a reagent R is converted into a photoproduct P through intermediate I . Therefore, global fitting of the time-dependent evolution of the UV-Vis absorption spectra with a sequential first-order kinetic model using the Glotaran software package was performed as previously described by Meijer and Bonnet.^{3,4} This approach provided the fitted UV-Vis absorption spectra of all species as well as the time-evolution of

the relative concentrations. Using the known molar extinction coefficients of **R** (ϵ_R), the molar extinction coefficients of **I** (ϵ_I) and **P** (ϵ_P) were calculated. From the known starting concentration of **R**, the time-evolution of the relative concentrations and the molar extinction coefficient of all species, the time evolutions of n_R , n_I and n_P were derived. The average absorbance between two consecutive UV-Vis measurements ($(A_{\lambda,irr})_{avg}$ at t_i and t_{i+1} , at the irradiation wavelength λ_{irr} was then calculated according to equation II.3:

$$(A_{\lambda,irr})_{avg} = \frac{(A_{\lambda,irr})_i + (A_{\lambda,irr})_{i+1}}{2} \quad (I.3)$$

According to equation I.4, the number of moles of photons absorbed by the reagent between two consecutive UV-Vis measurements ($\Delta t = t_{i+1} - t_i$) $q_{i,R}$ was calculated. Here $\phi_{\lambda,irr}$ is the photon flux at the irradiation wavelength (λ_{irr}) and $(1 - 10^{-3(A_{\lambda,irr})_{avg}})$ is the photon absorption probability. Because the sample was irradiated from the top of the UV-Vis cuvette (vertical beam, pathlength = 3 cm), the photon absorption probability is obtained by multiplying $(A_{\lambda,irr})_{avg}$ by 3.

$$q_{i,R} = \left(\frac{A_R}{(A_{\lambda,irr})_{avg}} \right)_i \times (1 - 10^{-3(A_{\lambda,irr})_{avg}}) \times \phi_{\lambda,irr} \times \Delta t \quad (I.4)$$

The total number of moles of photons absorbed by the **R** at time t since $t = 0$, $Q_{i,R}(t)$, was calculated according I.5.

$$Q_{i,R}(t) = \sum_{i=0}^t q_{i,R} \quad (I.5)$$

When plotting n_R vs. $Q_{i,R}$, the slope provided the quantum yield of the first photosubstitution step ϕ_1 . Similarly, the resulting slope of plotting n_P vs. $Q_{i,R}$ provided the quantum yield of the second step ϕ_2 .

For dissymmetric complexes: As the dissymmetric complexes follow a “branched” sequential first-order pathway that can be described by the equation $\mathbf{R} \rightarrow \mathbf{I}' + \mathbf{I}'' \rightarrow \mathbf{P}$, fitting to a general sequential model can only provide overall reaction rates. Therefore, targeted fitting was used to describe the system more accurately and provided the time-evolution of the relative concentrations for all species with the irradiation wavelength λ_{irr} being 435 nm and 505 nm. Since the molar extinction coefficients of **I'**, **I''** and **P** were calculated from the symmetric complexes, the time-evolution of n_R , $n_{I'}$, $n_{I''}$ and n_P could be readily derived. Subsequently, the total number of photons absorbed by **R**, **I'** and **I''** at time t since $t = 0$ was calculated. The resulting slope of plotting $n_{I'}$ vs. $Q_{i,R}$ and $n_{I''}$ vs. $Q_{i,R}$ provided the quantum yield of the first steps $\phi_{R \rightarrow I'}$ and $\phi_{R \rightarrow I''}$. The slopes of the plotting n_P vs. $Q_{i,I'}$ and n_P vs. $Q_{i,I''}$ provided the quantum yield of the second steps $\phi_{R \rightarrow I'}$ and $\phi_{R \rightarrow I''}$.

Since the photosubstitution experiments with 625 nm irradiation generally show significantly less spectral difference, targeted fitting does not provide satisfactorily results.

Therefore, the time-evolution of the relative concentrations for all species were calculated using simultaneous equation matrix method (equation 1.8).⁵ Importantly, the molar extinction coefficients of the individual species should not be identical at the selected wavelengths.

$$A_{\lambda}(t) = \varepsilon_{R,\lambda}C_R + \varepsilon_{I',\lambda}C_{I'} + \varepsilon_{I'',\lambda}C_{I''} + \varepsilon_{P,\lambda}C_P \quad (1.6)$$

$$\begin{bmatrix} A_1 \\ A_2 \\ A_3 \\ A_4 \end{bmatrix}_t = \begin{bmatrix} \varepsilon_{R,1} & \varepsilon_{I',1} & \varepsilon_{I'',1} & \varepsilon_{P,1} \\ \varepsilon_{R,2} & \varepsilon_{I',2} & \varepsilon_{I'',2} & \varepsilon_{P,2} \\ \varepsilon_{R,3} & \varepsilon_{I',3} & \varepsilon_{I'',3} & \varepsilon_{P,3} \\ \varepsilon_{R,4} & \varepsilon_{I',4} & \varepsilon_{I'',4} & \varepsilon_{P,4} \end{bmatrix}_t \times \begin{bmatrix} C_R \\ C_{I'} \\ C_{I''} \\ C_P \end{bmatrix}_t \quad (1.7)$$

$$\begin{bmatrix} C_R \\ C_{I'} \\ C_{I''} \\ C_P \end{bmatrix}_t = \begin{bmatrix} \varepsilon_{R,1} & \varepsilon_{I',1} & \varepsilon_{I'',1} & \varepsilon_{P,1} \\ \varepsilon_{R,2} & \varepsilon_{I',2} & \varepsilon_{I'',2} & \varepsilon_{P,2} \\ \varepsilon_{R,3} & \varepsilon_{I',3} & \varepsilon_{I'',3} & \varepsilon_{P,3} \\ \varepsilon_{R,4} & \varepsilon_{I',4} & \varepsilon_{I'',4} & \varepsilon_{P,4} \end{bmatrix}_t^{-1} \times \begin{bmatrix} A_1 \\ A_2 \\ A_3 \\ A_4 \end{bmatrix}_t \quad (1.8)$$

1.2.4 Phosphorescence and singlet oxygen generation quantum yield

The quantum yields of phosphorescence and singlet oxygen generation were determined using a custom-built setup and experimental procedure as previously reported.⁶⁻⁸ The compounds were dissolved in aerated acetonitrile (3 mL) and transferred into a fluorescence cuvette (Helma Analytics, light path 1 × 1 cm). The absorbance spectra at 268 K were recorded using Agilent Cary 60 UV-Vis spectrometer. Emission spectroscopy was performed at 298 K by irradiating the sample using 450 nm fiber-coupled laser (LRD-0450, Laserglow) set to 80 mW at the cuvette as determined with a power meter (PM100USB, Thorlabs). The phosphorescence of the complexes was recorded between 530 nm to 900 nm using a UV-Vis spectrometer (Avantes 2048L Starline), with an acquisition time of 100 ms. The phosphorescence of singlet oxygen (around 1275 nm) was recorded between 1200 nm to 1350 nm using a NIR spectrometer (Avantes NIR256-1.7TEC, detector set at -12 °C), with an acquisition time of 10 s. For phosphorescence quantum yield (ϕ_p) determination, [Ru(bpy)₃]Cl₂ was used as reference ($\phi_p = 0.018$ in aerated acetonitrile).⁹ For singlet oxygen generation quantum yield (ϕ_{Δ}) determination, perinaphthenone was used as a reference ($\phi_p = 0.98 \pm 0.07$ in aerated acetonitrile) and [Ru(bpy)₃]Cl₂ as validation ($\phi_p = 0.57 \pm 0.06$ in aerated acetonitrile).^{10,11} All spectral data was processed with OriginPro 9.1 and Microsoft Office Excel 2016.

1.2.5 Photosubstitution followed by ¹H-NMR

An aliquot of compound (1.5 mg) was dissolved in acetone-d₆ and diluted further with D₂O to the desired ratio, with a total volume of 650 μ l. A portion (550 μ l) was transferred into an NMR tube and a “dark” ¹H-NMR spectrum was measured at 293 K. The NMR tube was then irradiated with a lamp of indicated (Figure I.3) outside of the NMR, and spectra were recorded intermittently at different time intervals to monitor the photoreaction.

1.3 Cell culture

General information

The human U-87 MG cells (glioblastoma cells) were purchased from ATCC (American Type Culture Collection, Manassas, Virginia, US). Human U251 (glioblastoma cells) cells were kindly provided by Rob C. Hoeben via Sabrina van der Zanden, LUMC, Leiden, the Netherlands. Human cancer cell line A549 (human lung carcinoma) and A375 (human epidormoid carcinoma) were distributed by the European Collection of Cell Cultures (ECACC) and purchased from Sigma Aldrich. Dulbecco's Modified Eagle Medium (DMEM, with phenol red, without glutamine), Glutamine-S (GM; 200 mM), MTT salt was purchased from Sigma Aldrich or Bio-connect. Fetal calf serum (FCS) was purchased from Hyclone. Penicillin and streptomycin were purchased from Duchefa and were diluted to a 100 mg/mL penicillin/streptomycin solution (P/S). Trypsin and OptiMEM (without phenol red) were purchased from Gibco Life Technologies. Trypan blue (0.4% in 0.81% sodium chloride and 0.06% potassium phosphate dibasic solution) was purchased from BioRad. Plastic disposable flasks and 96-well plates for cytotoxicity assays were purchased from Sarstedt. Cells were counted by using a BioRad TC20™ automated cell counter with BioRad cell-counting slides. Cells were inspected with an Olympus IX81 microscope. UV-vis measurements for analysis of 96-well plates were performed with a M1000 Tecan Reader, Tecan Trading AG, Switzerland).

Cell culture under normoxia and hypoxia

Cells were cultured in DMEM complete (Dulbecco's Modified Eagle Medium (DMEM) with phenol red) supplemented with 1% v/v GM, 0.1% v/v P/S and 10% v/v FCS. Cells were incubated at 37°C at 5% CO₂ atmosphere and subcultured upon reaching 80-90% confluency (approximately twice per week). Cells were converted into hypoxic phenotype by incubation in a hypoxic incubator at $t = 37^{\circ}\text{C}$ under atmosphere of >1% O₂ with 5% CO₂ for at least 10 days prior use. Cells were cultured for a maximum of 8 weeks for all biological experiments.

Cell-irradiation setup

96-well plates were irradiated using described in detail earlier.¹² In short, the 96-well plates were placed on Ditabis thermostate fitted with two flat-bottomed micro-plate thremoblocks and a 96-LED array was placed directly on top of the plates (with lid). For irradiation under hypoxic conditions, the 96-LED array was place on top of the plates inside the hypoxic incubator and irradiation was only started upon stabilization of the >1% O₂ atmosphere.

Cytotoxicity assay

For each photocytotoxicity experiment, three plates were prepared and treated identically. One to test the cytotoxicity in dark and green (520 ± 35 nm, 17.1 mW/cm² for 30 min, 30.78

J/cm²) and red (630 ± 24 nm, 31.3 mW/cm² for 60 min, 114.84 J/cm²) light. Cells were seeded at t = 0 h in 96-well plates in the respective density according to Table I.1 (100 µL), respectively in OptiMEM supplemented with 2.5% v/v FCS, 0.1% v/v P/S, and 1.0% v/v GM (OptiMEM complete) and incubated for 24 h at 37 °C and 5.0% CO₂.

Table I.1 Seeding density in 96-well plate for the respective cell lines given in cells/well cultured under normoxic (NX) or hypoxic (HX) conditions.

<i>Cell line</i>	<i>Condition</i>	<i>Density (cells/well)</i>
A375	NX	4.000
	HX	4.000
A549	NX	5.000
	HX	5.000
U87MG	NX	6.000
	HX	7.000
U251	NX	6.000

Only the inner 60 wells were used for seeding, the outer wells were equipped with 100 µL OptiMEM to prevent border effects during irradiation. At t = 24 h, aliquots (100 µL) of six different concentrations of freshly prepared stock solutions of the compounds in OptiMEM complete were added to the wells in triplicate and incubated for additional 24 h. Dimethylsulfoxide (DMSO) was used to dissolve the compounds in such amounts that the maximum v/v% of DMSO per well did not exceed 0.5%. At t = 48 h, medium was aspirated and exchanged against fresh OptiMEM medium and the plates were irradiated with the cell-irradiation setup while the control plate was kept in the dark. After irradiation, all the plates were incubated in the dark for further 48 h. After an overall incubation time of 72 h, cell viability was measured either using 10 µL of a MTT solution (5 mg/mL for A375 NX & HX and A549 NX & HX or 3 mg/mL for U-87 NX & HX in PBS) or via a modified MTT (EZ4U kit, Bio-Connect, BI-5000 for U251 cells) was added into each well. The mixture was incubated for 3 h under humanified conditions. The absorbance in each well was read at λ = 570 nm for MTT or 492 and 620 nm for EZ4U using M1000 Tecan reader.

The absorbance data per compound per concentration was averaged over three identical wells (technical replicates, n_t = 3) in Excel and was exported to GraphPad Prism. Relative cell populations were calculated by dividing the average absorbance of the treated wells by the average absorbance of the untreated wells. To ensure no light induced cytotoxicity occurred during the experiment, the maximum difference in cell viability between the untreated irradiated and non-irradiated control wells was 10%. The resulting data each biological replicate was fitted using the dose-response two parameter Hill slope equation (equation I.9), to obtain the half-maximal effective concentration (EC₅₀, defined as the drug concentration needed to reduced cell viability by 50% compared to the untreated control).

$$Y = 100 / (1 + 10^{\log(\text{EC}_{50}-X) \times \text{Hill Slope}}) \quad (I.9)$$

The reported EC₅₀ values (from at least three biological replicates) are expressed as the mean ± 95% confidence interval. Statistical significance between the irradiated groups and the dark control was evaluated by a two-way ANOVA test with the Dunnett's Multiple Comparison Test.

I.4 References

- (1) Calvert, J. G.; Pitts, J. N. *Photochemistry*; Wiley: New York, NY, 1966.
- (2) Demas, J. N.; Bowman, W. D.; Zalewski, E. F.; Velapoldi, R. A. *J. Phys. Chem.* **1981**, *85* (19), 2766–2771.
- (3) Snellenburg, J. J.; Laptinok, S. P.; Seger, R.; Mullen, K. M.; Stokkum, I. H. M. V. *J. Stat. Soft.* **2012**, *49* (3).
- (4) Meijer, M. S.; Bonnet, S. *Inorg. Chem.* **2019**, *58* (17), 11689–11698.
- (5) Attia, K. A. M.; Elabasawy, N. M.; Abolmagd, E. *Future Journal of Pharmaceutical Sciences* **2017**, *3* (2), 163–167.
- (6) Zhou, X.-Q.; Busemann, A.; Meijer, M. S.; Siegler, M. A.; Bonnet, S. *Chem. Commun.* **2019**, *55* (32), 4695–4698.
- (7) Partanen, S. B.; Erickson, P. R.; Latch, D. E.; Moor, K. J.; McNeill, K. *Environ. Sci. Technol.* **2020**, *54* (6), 3316–3324.
- (8) Ossola, R.; Jönsson, O. M.; Moor, K.; McNeill, K. *Chem. Rev.* **2021**, *121* (7), 4100–4146.
- (9) Suzuki, K.; Kobayashi, A.; Kaneko, S.; Takehira, K.; Yoshihara, T.; Ishida, H.; Shiina, Y.; Oishi, S.; Tobita, S. *Phys. Chem. Chem. Phys.* **2009**, *11* (42), 9850.
- (10) Schmidt, R.; Tanielian, C.; Dunsbach, R.; Wolff, C. *Journal of Photochemistry and Photobiology A: Chemistry* **1994**, *79* (1–2), 11–17.
- (11) Abdel-Shafi, A. A.; Beer, P. D.; Mortimer, R. J.; Wilkinson, F. *Phys. Chem. Chem. Phys.* **2000**, *2* (14), 3137–3144.
- (12) Hopkins, S. L.; Siewert, B.; Askes, S. H. C.; Veldhuizen, P.; Zwier, R.; Heger, M.; Bonnet, S. *Photochem Photobiol Sci* **2016**, *15* (5), 644–653.

Appendix II: Supporting Information for Chapter 2

II.1 Characterization of novel compounds

II.1.1 Amine-products

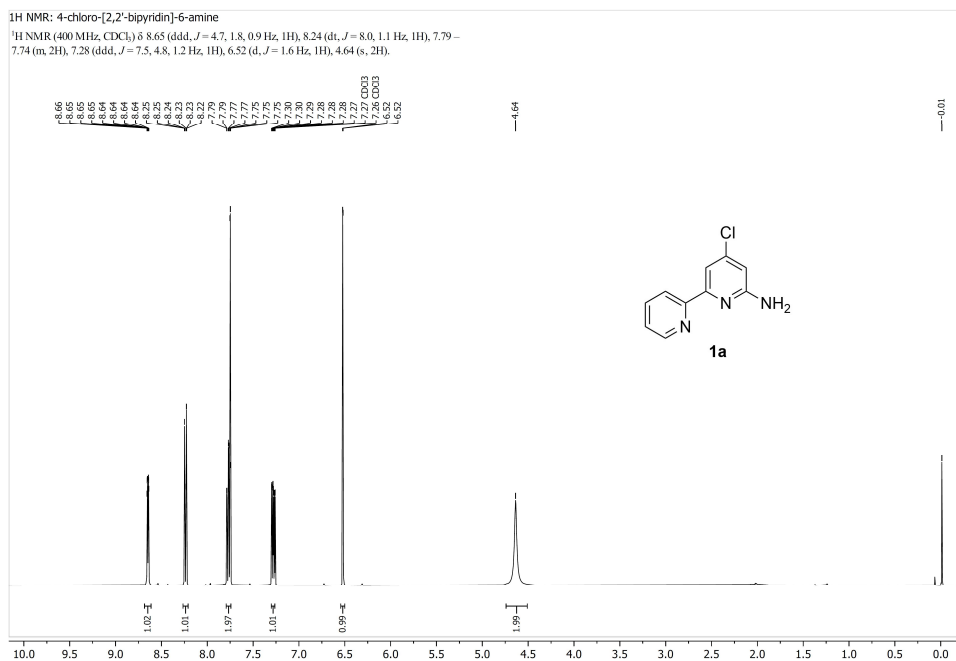
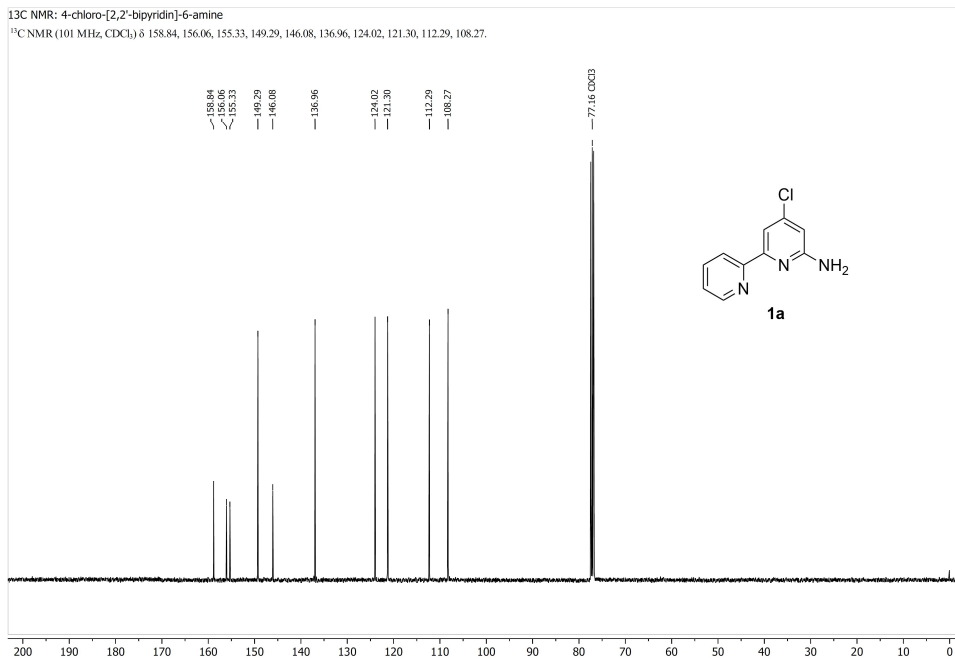
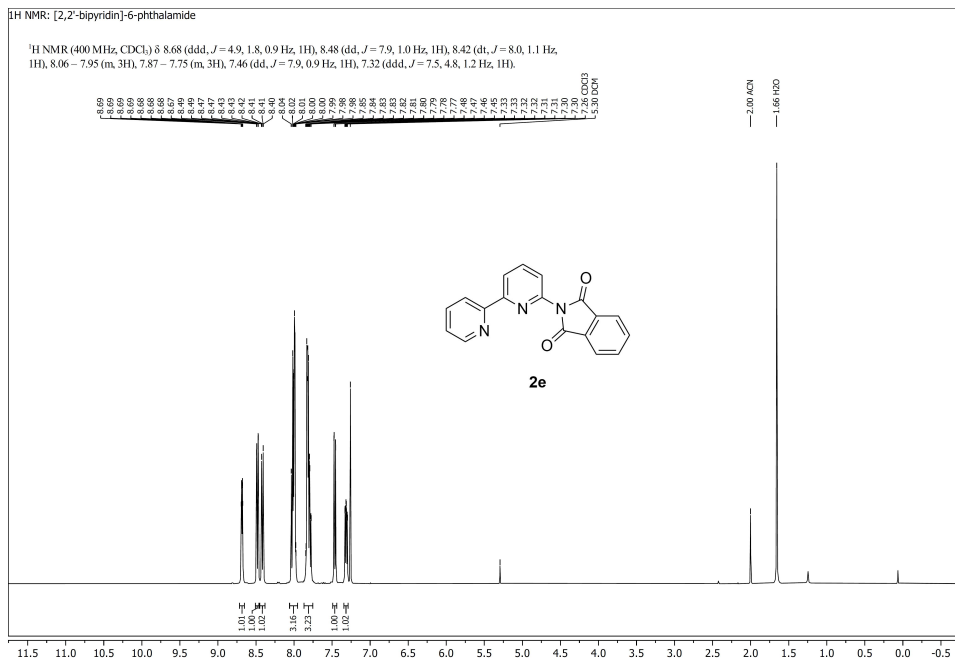
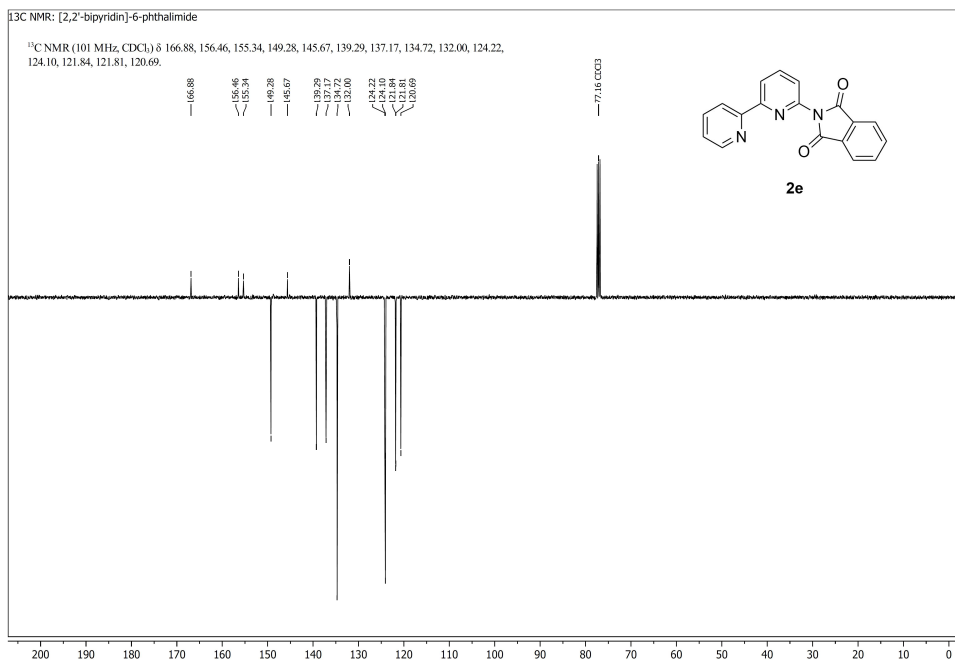
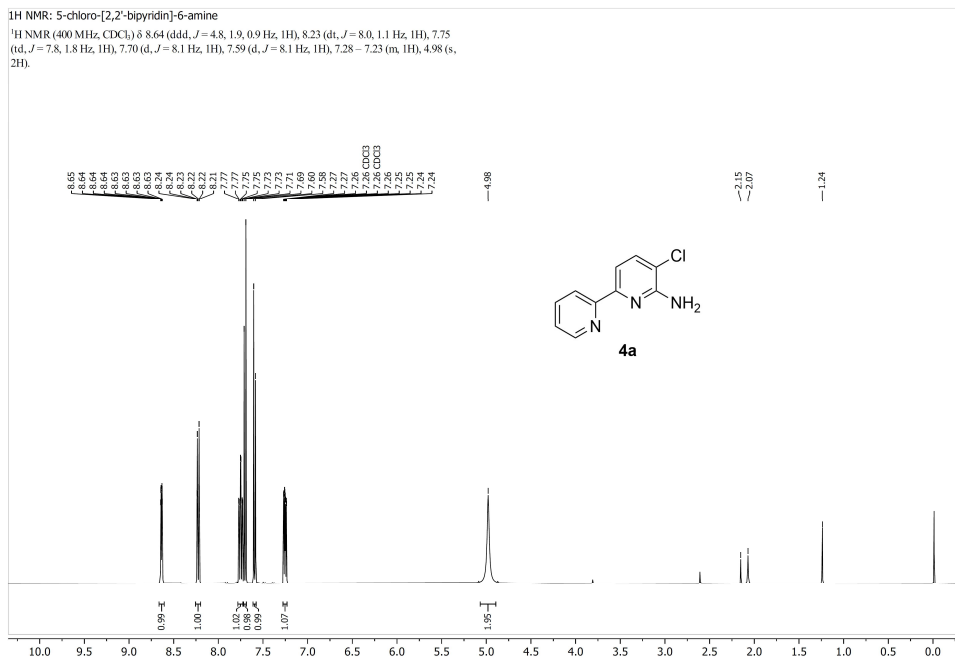
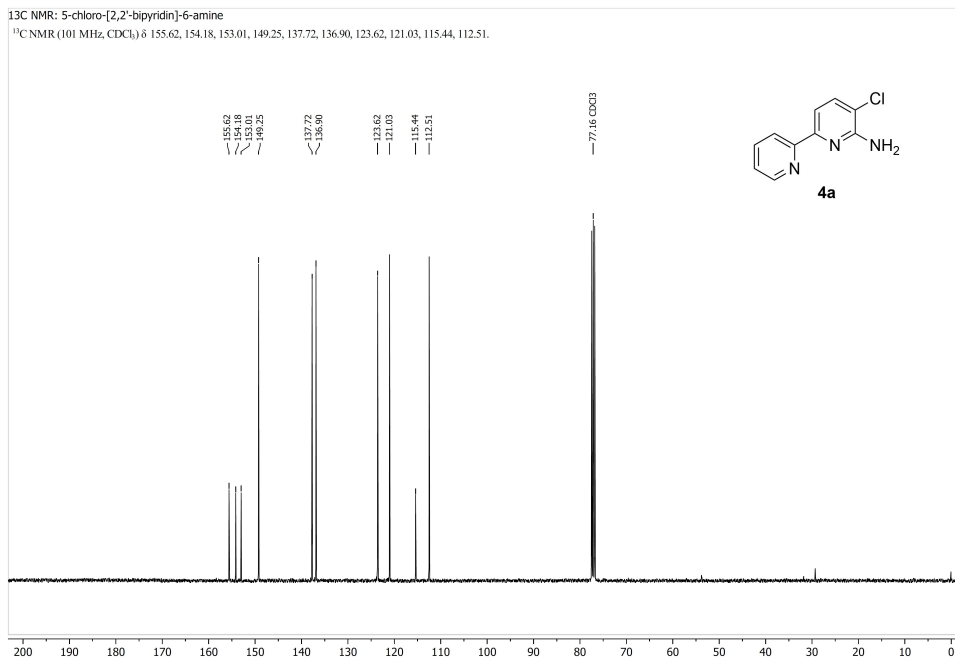
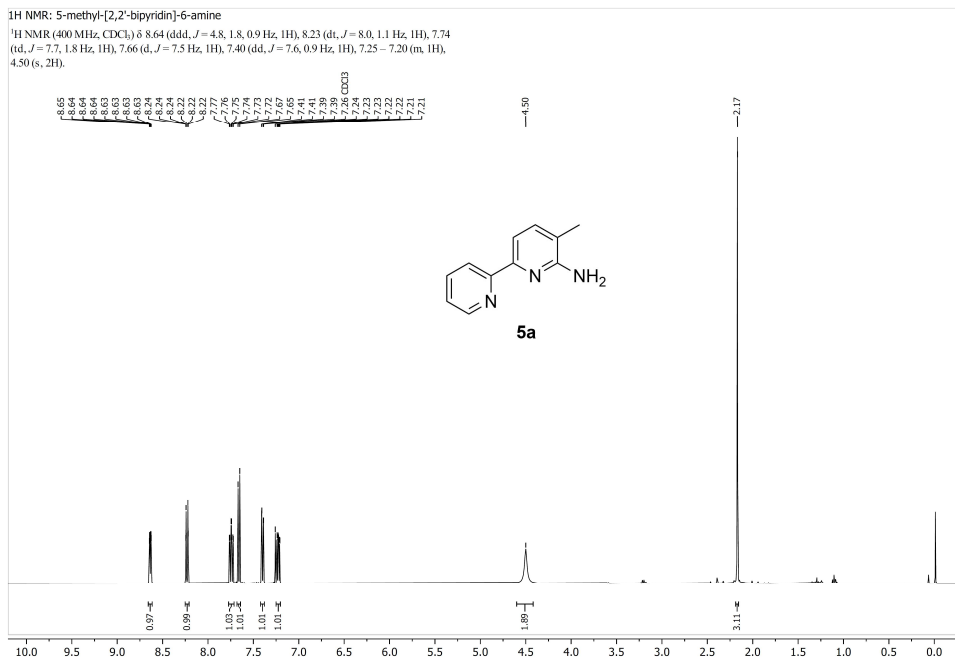
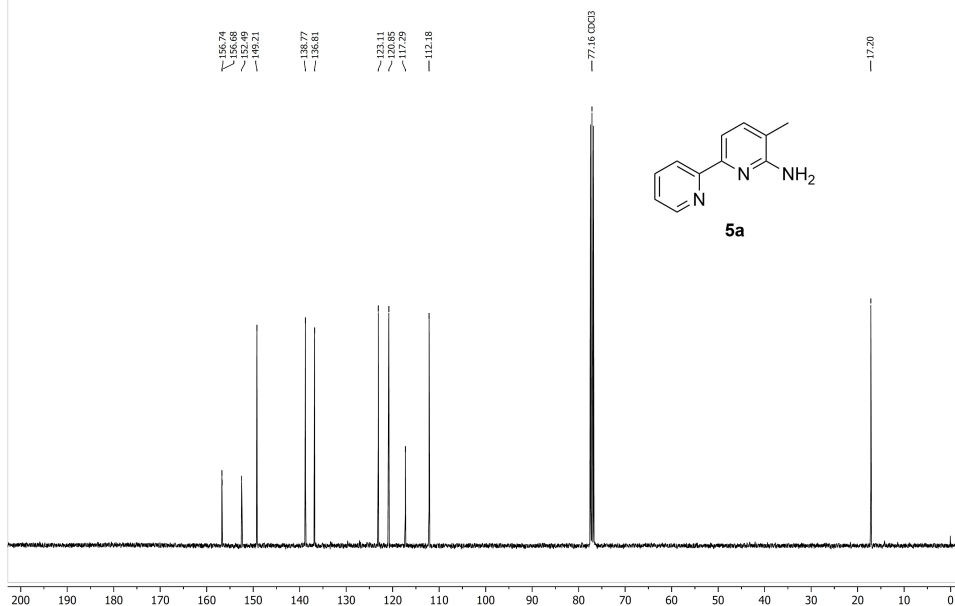
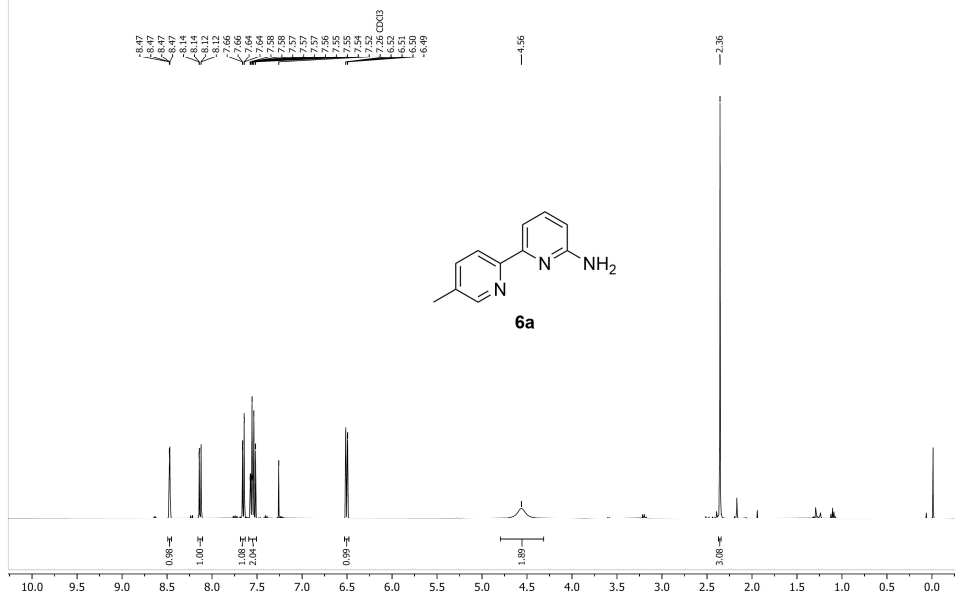


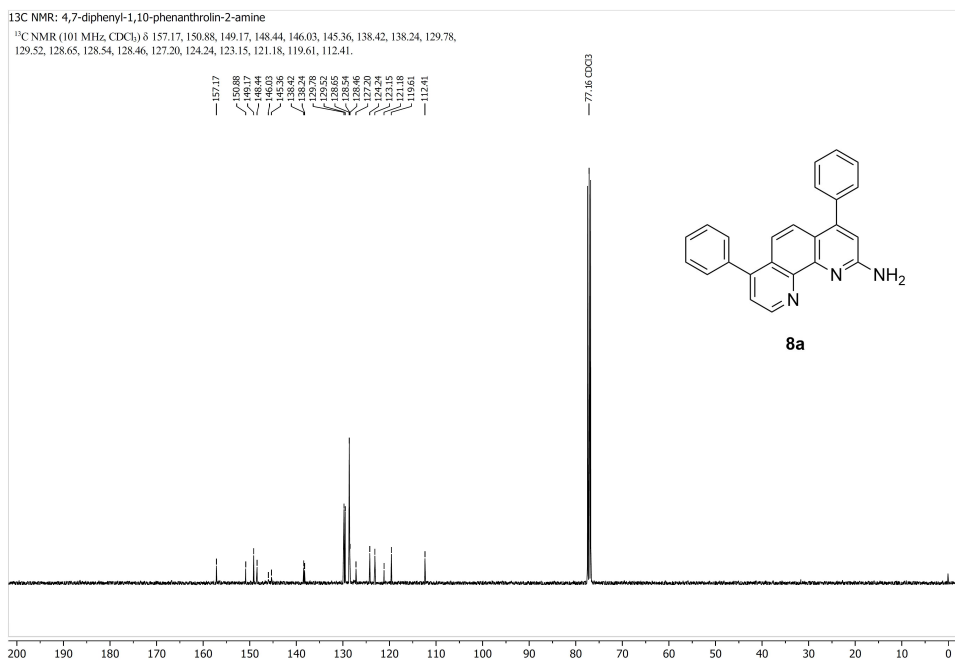
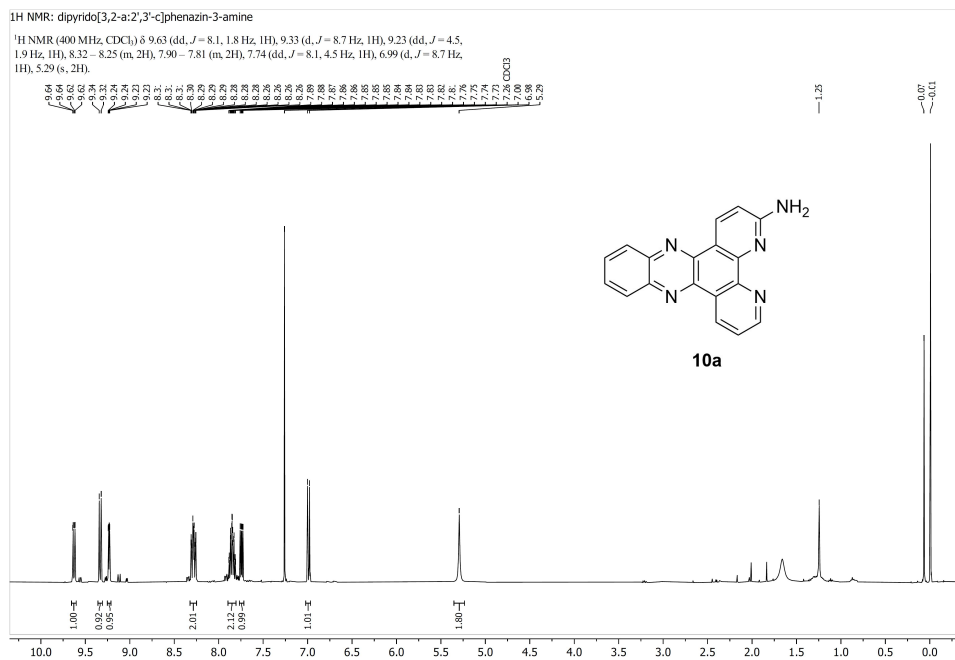
Figure II.1 ¹H-NMR of **1a** in CDCl₃.

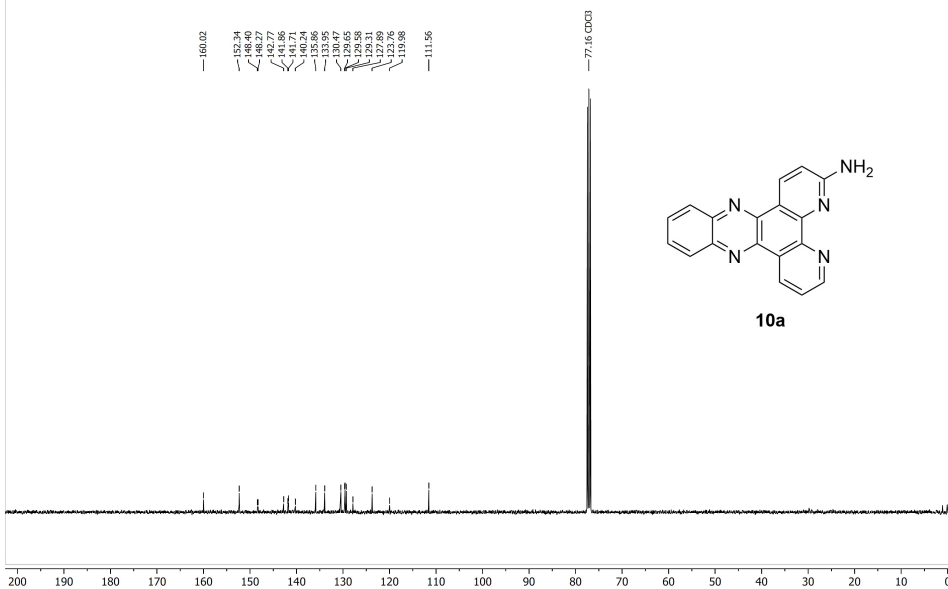
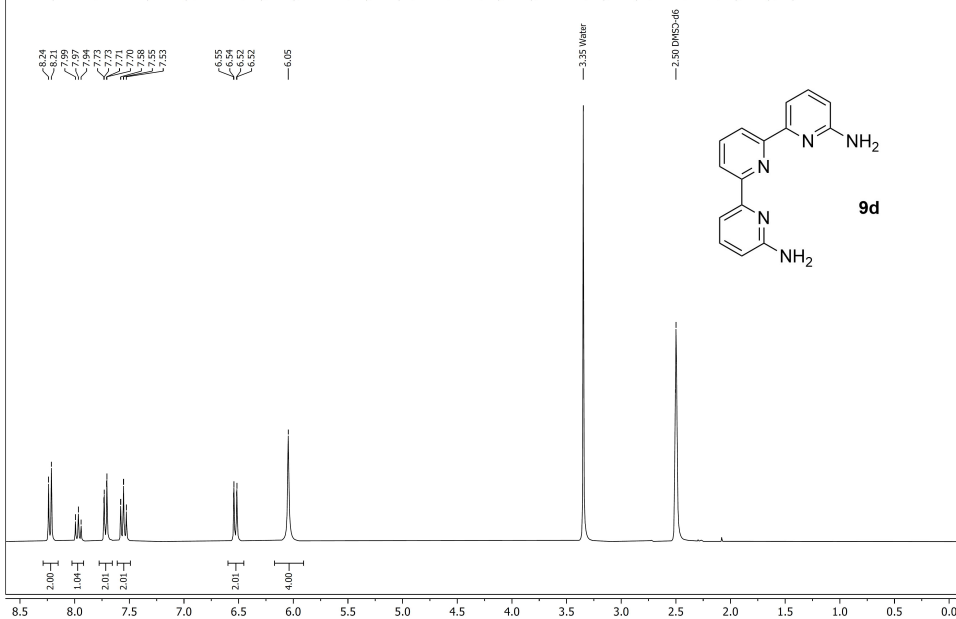
Figure II.2 ¹³C-NMR of **1a** in CDCl₃.Figure II.3 ¹H-NMR of **2e** in CDCl₃.

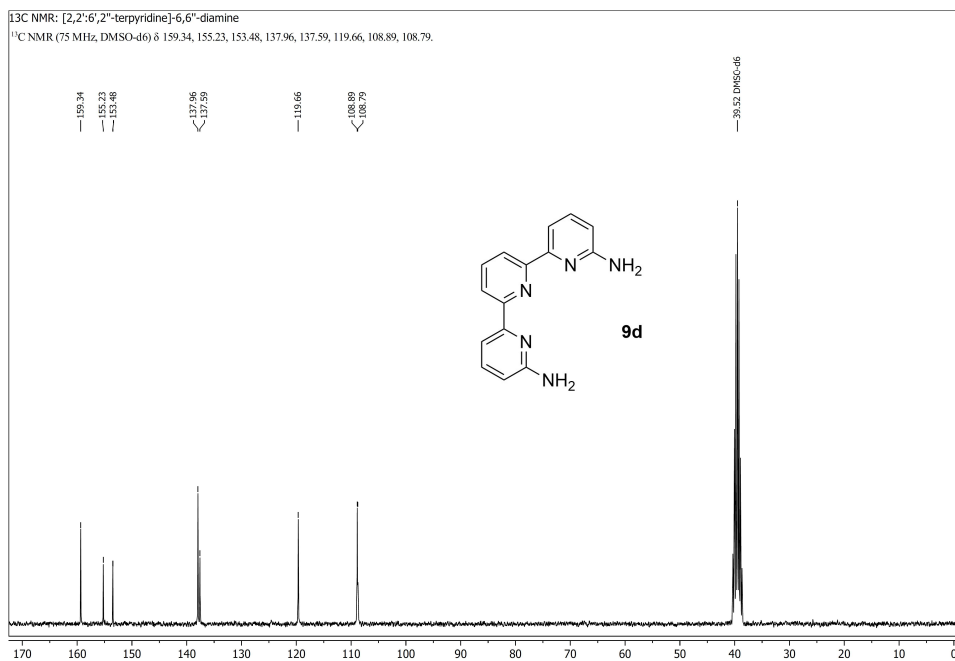
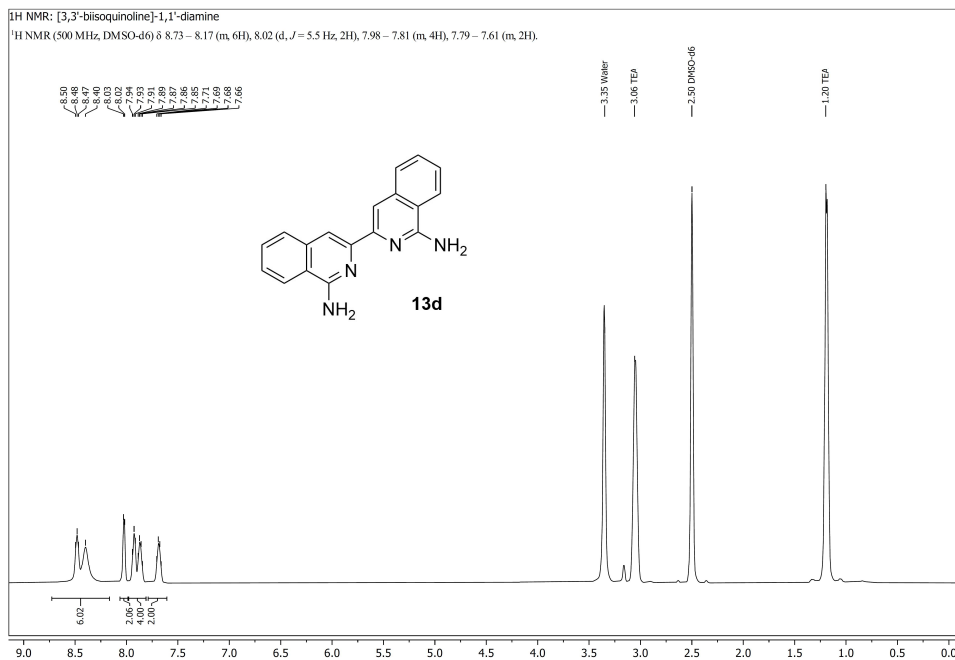
Figure II.4 ¹³C-NMR of **2e** in CDCl₃.Figure II.5 ¹H-NMR of **4a** in CDCl₃.

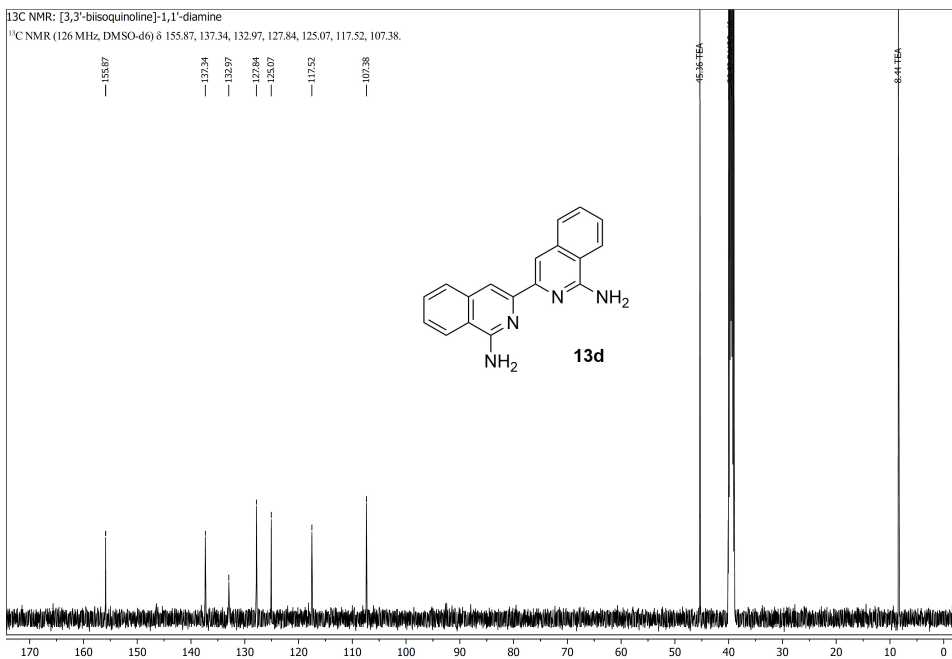
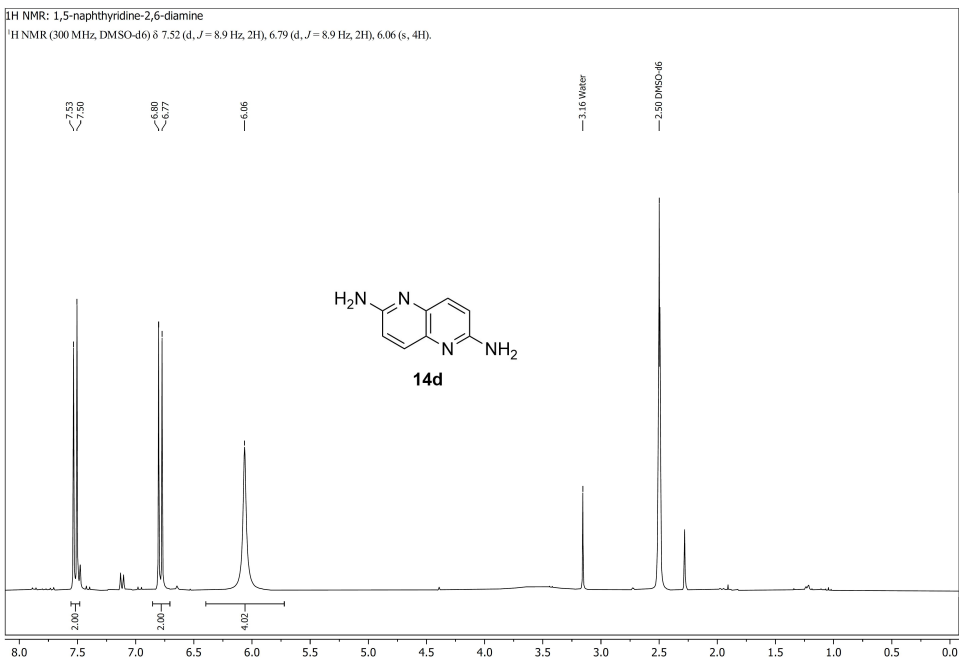
Figure II.6 ¹³C-NMR of **4a** in CDCl₃.Figure II.7 ¹H-NMR of **5a** in CDCl₃.

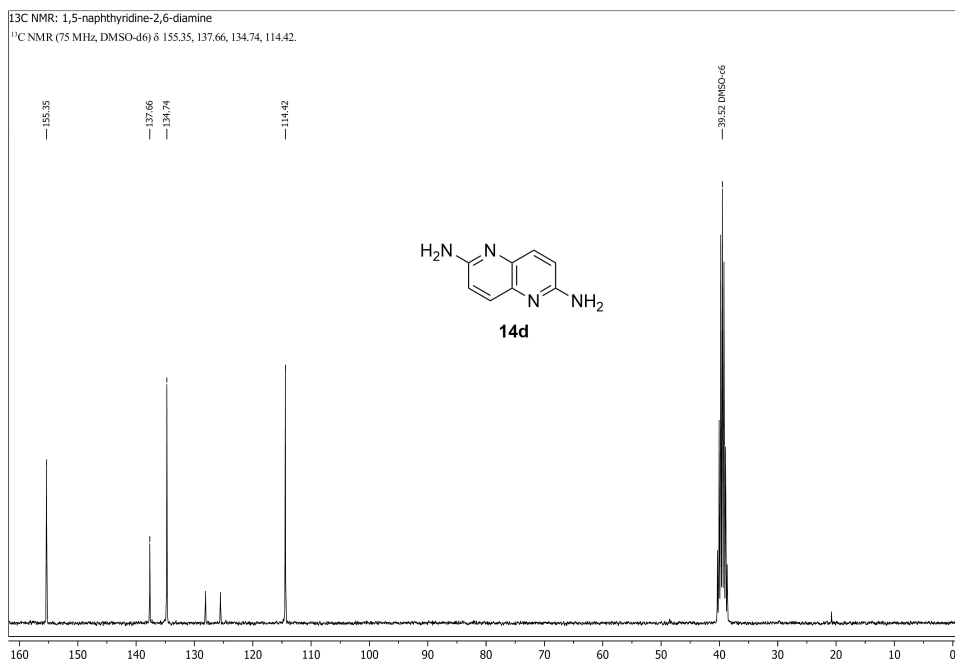
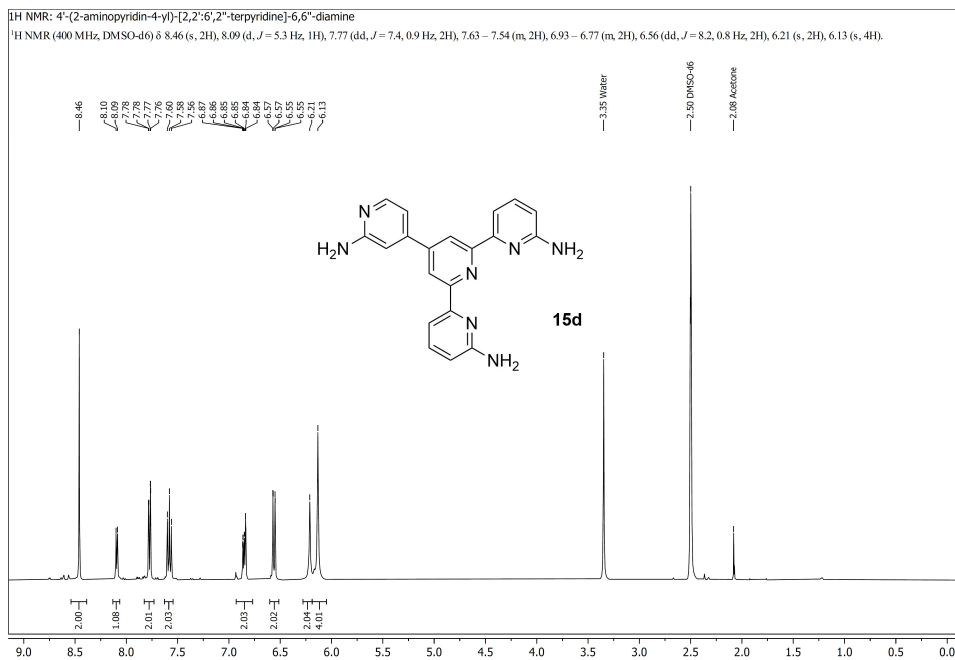
¹³C NMR: 5-methyl-[2,2'-bipyridin]-6-amine¹³C NMR (101 MHz, CDCl₃) δ 156.74, 156.68, 152.49, 149.21, 138.77, 136.81, 123.11, 120.85, 117.29, 112.18, 17.20.Figure II.8 ¹³C-NMR of 5a in CDCl₃.¹H NMR: 5'-methyl-[2,2'-bipyridin]-6-amine¹H NMR (400 MHz, CDCl₃) δ 8.49 – 8.45 (m, 1H), 8.13 (dd, *J* = 8.1, 0.8 Hz, 1H), 7.65 (dd, *J* = 7.6, 0.9 Hz, 1H), 7.59 – 7.51 (m, 2H), 6.51 (dd, *J* = 8.1, 0.9 Hz, 1H), 4.56 (s, 2H), 2.36 (s, 3H).Figure II.9 ¹H-NMR of 6a in CDCl₃.

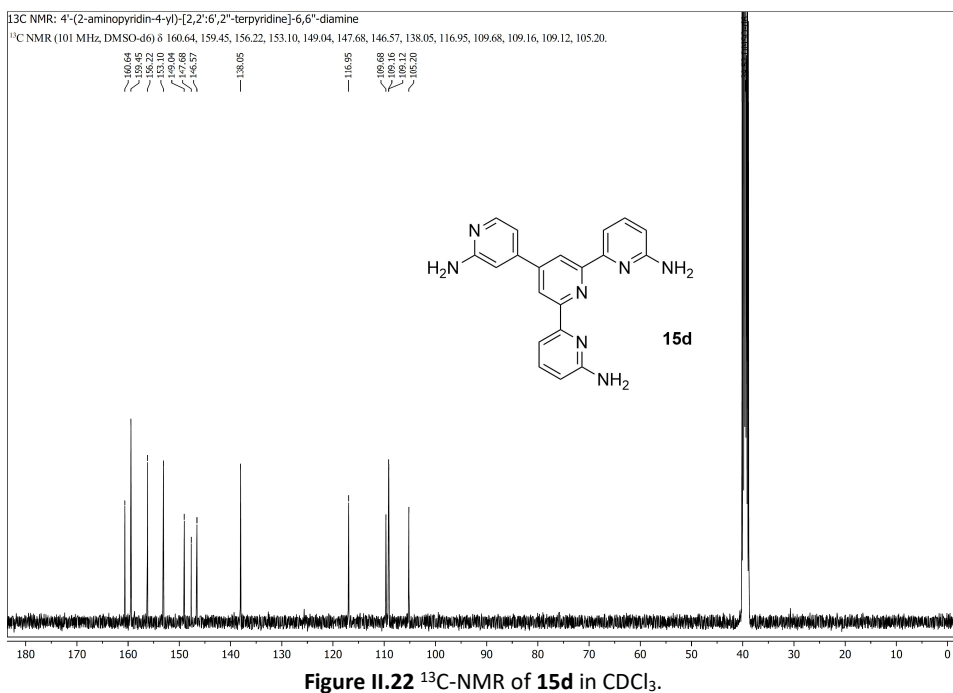
Figure II.12 ¹³C-NMR of **8a** in CDCl₃.Figure II.13 ¹H-NMR of **10a** in CDCl₃.

¹³C NMR: dipyrido[3,2-a:2',3'-c]phenazin-3-amine¹³C NMR (101 MHz, CDCl₃) δ 160.02, 152.34, 148.40, 148.27, 142.77, 141.86, 141.71, 140.24, 135.86, 133.95, 130.47, 129.65, 129.58, 129.31, 127.89, 123.76, 119.98, 111.56.Figure II.14 ¹³C-NMR of 10a in CDCl₃.¹H NMR: [2,2':6,2''-terpyridine]-6,6''-diamine¹H NMR (300 MHz, DMSO-d₆) δ 8.23 (d, *J* = 7.8 Hz, 2H), 7.97 (t, *J* = 7.8 Hz, 1H), 7.72 (dd, *J* = 7.4, 0.9 Hz, 2H), 7.55 (t, *J* = 7.8 Hz, 2H), 6.53 (dd, *J* = 8.1, 0.9 Hz, 2H), 6.05 (s, 4H).Figure II.15 ¹H-NMR of 9d in DMSO-d₆.

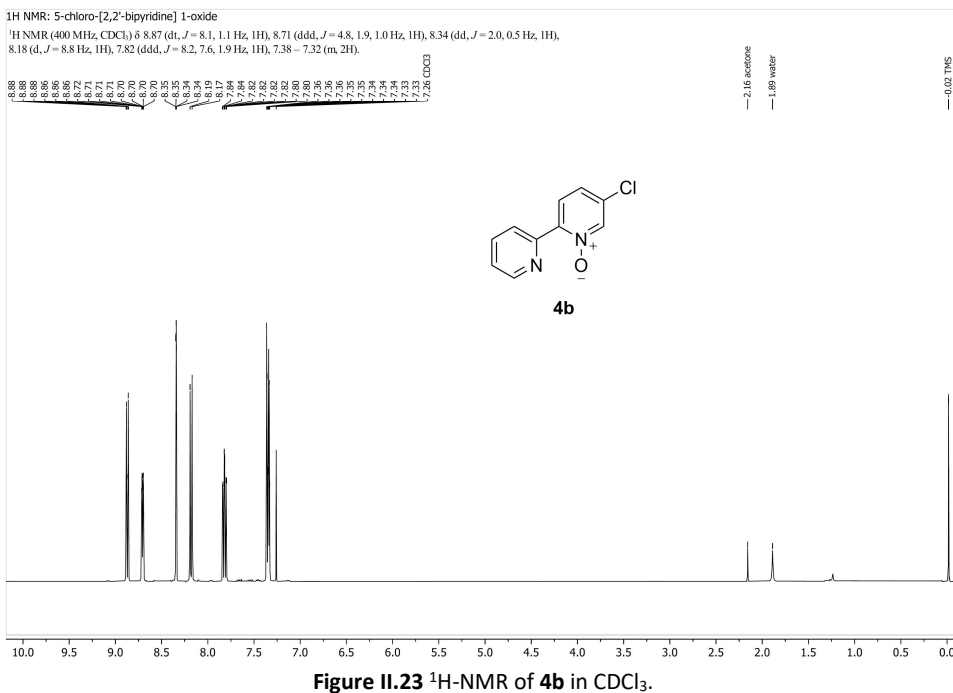
Figure II.16 ¹³C-NMR of **9d** in DMSO-*d*₆.Figure II.17 ¹H-NMR of **13d** in DMSO-*d*₆.

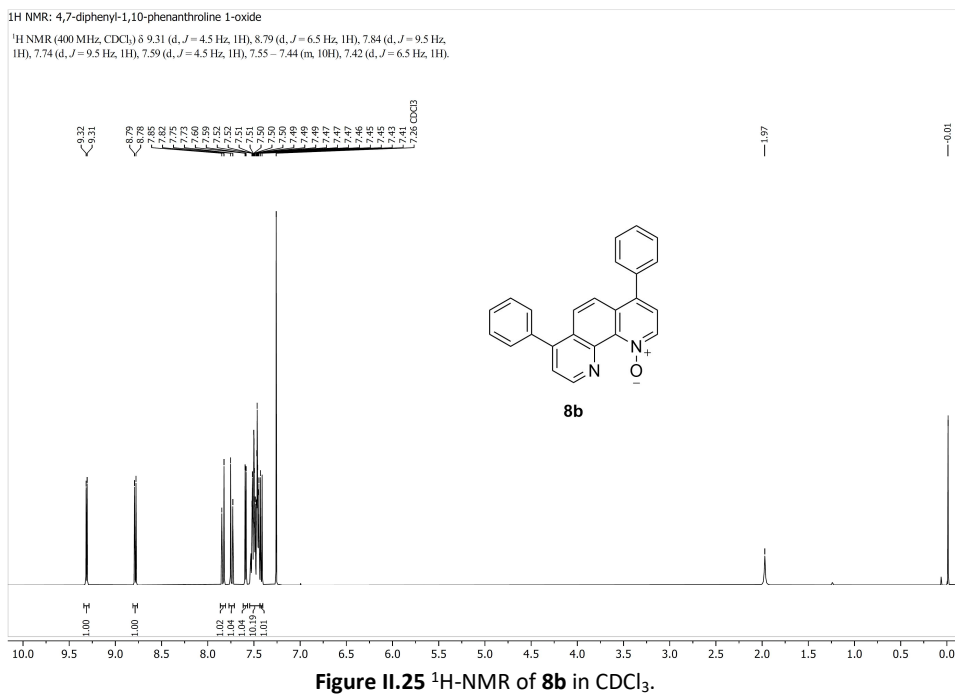
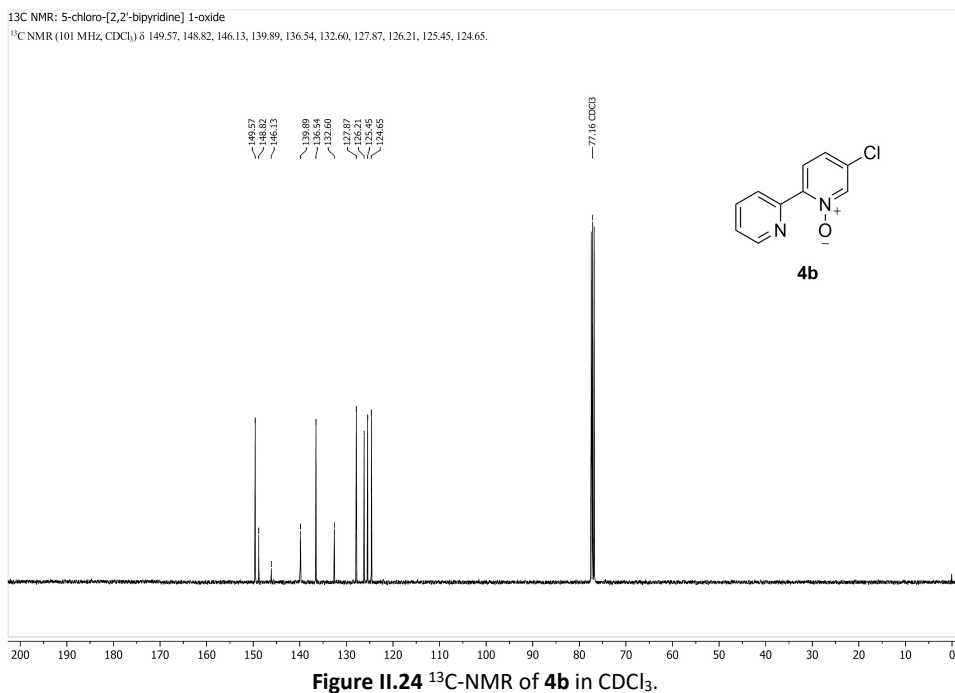
Figure II.18 ¹³C-NMR of **13d** in DMSO-d₆.Figure II.19 ¹H-NMR of **14d** in DMSO-d₆.

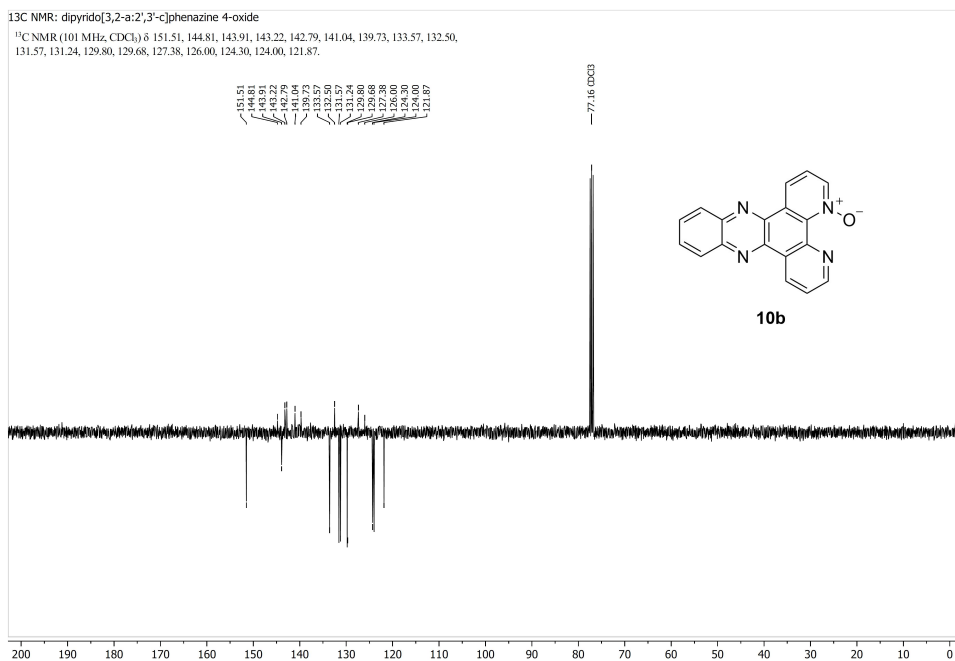
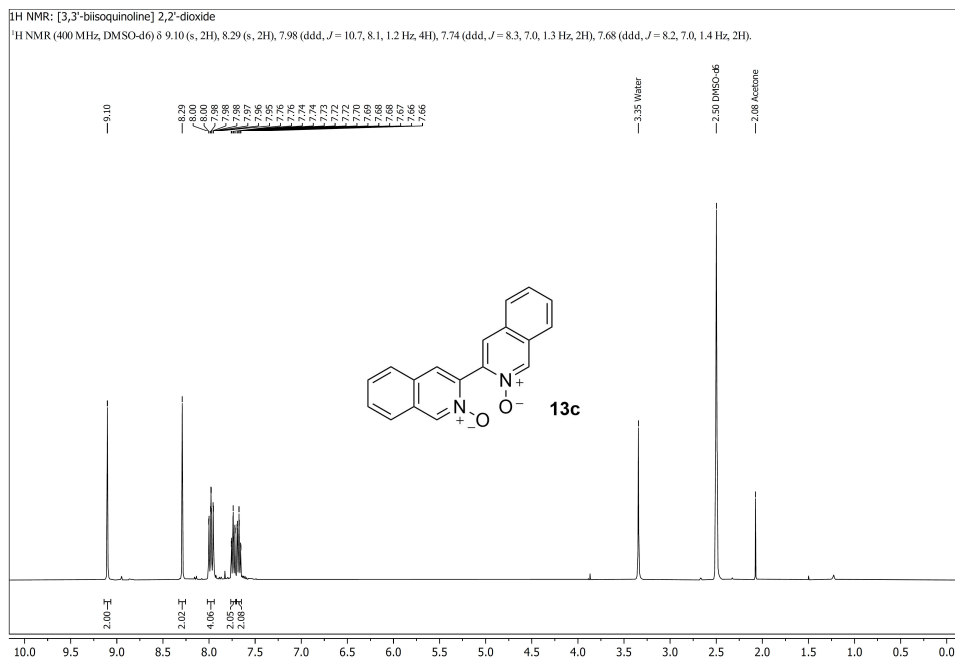
Figure II.20 ¹³C-NMR of **14d** in DMSO-*d*₆.Figure II.21 ¹H-NMR of **15d** in CDCl₃.

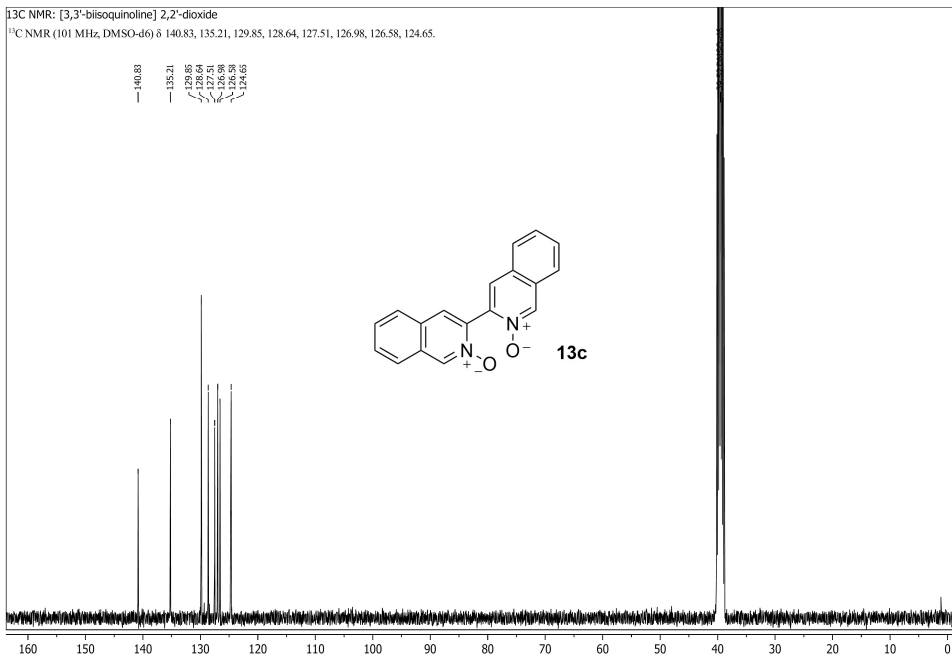
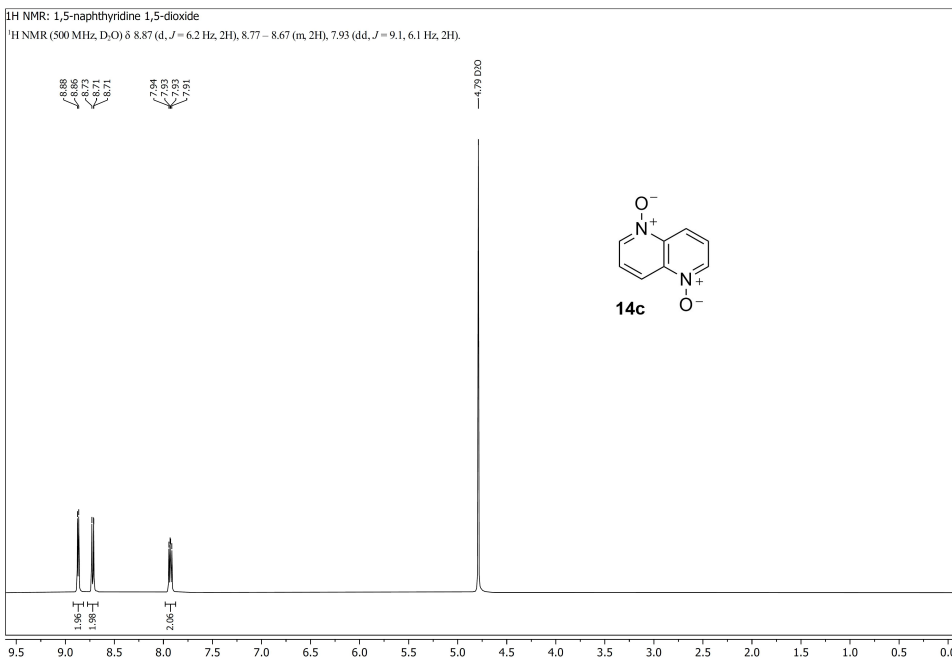


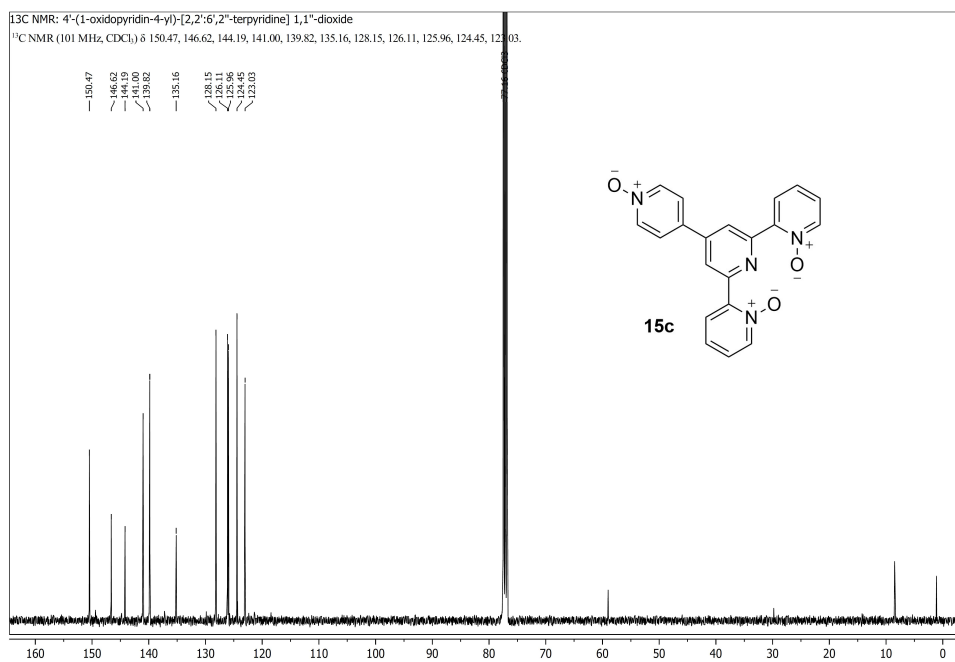
II.1.2 Precursors





Figure II.28 ¹³C-NMR of **10b** in CDCl₃.Figure II.29 ¹H-NMR of **13c** in DMSO-*d*₆.

Figure II.30 ¹³C-NMR of **13c** in DMSO-*d*₆.Figure II.31 ¹H-NMR of **14c** in DMSO-*d*₆.

Figure II.34 ¹³C-NMR of **15c** in CDCl₃.



Appendix III: Supporting information for Chapter 3

III.1 Single crystal X-ray crystallography

Experimental details

For **[2b]**(PF₆)₂ and **[3b]**(PF₆)₂, all reflection intensities were measured at 110(2) K using a SuperNova diffractometer (equipped with Atlas detector and the Cryojet system by Oxford Instruments for temperature control during data collection) with either Mo *K*α radiation ($\lambda = 0.71073 \text{ \AA}$) for **[2b]**(PF₆)₂ or Cu *K*α radiation ($\lambda = 1.54178 \text{ \AA}$) for **[3b]**(PF₆)₂ under the program CrysAlisPro (Version CrysAlisPro 1.171.42.49, Rigaku OD, 2022). All reflection intensities for **[1a]**(PF₆)₂, **[1b]**(PF₆)₂ and **[4b]**(PF₆)₂ were measured at 110.00(10) K using a Rigaku XtaLAB Synergy R (equipped with a rotating-anode X-ray source, HyPix-6000HE detector and the Cryostream 1000 system by Oxford Cryosystems for temperature control during data collection) with Cu *K*α radiation ($\lambda = 1.54178 \text{ \AA}$) under the program CrysAlisPro (Version CrysAlisPro 1.171.42.49, Rigaku OD, 2022). The same program was used to refine the cell dimensions and for data reduction. The structures were solved with the program SHELXS-2018/3 (Sheldrick, 2018) and was refined on F^2 with SHELXL-2018/3 (Sheldrick, 2018). Numerical absorption correction based on gaussian integration over a multifaceted crystal model was performed using CrysAlisPro for the data of **[2b]**(PF₆)₂. Analytical numeric absorption correction using a multifaceted crystal was applied using CrysAlisPro for the data of **[1a]**(PF₆)₂, **[1b]**(PF₆)₂, **[3b]**(PF₆)₂ and **[4b]**(PF₆)₂. The H atoms were placed at calculated positions using the instructions AFIX 23, AFIX 43, AFIX 83 or AFIX 137 with isotropic displacement parameters having values 1.2 or 1.5 U_{eq} of the attached C or O atoms.

The structure of **[1a]**(PF₆)₂ is disordered. The Ru complex is found at both sites of twofold axial and mirror symmetries, and thus must be disordered. Overall, the occupancy factor must be constrained to be 0.25. The PF₆⁻ counterion is found disordered over two orientations while also being located at one site of mirror symmetry, and thus the sum of the occupancy factors for both orientations must be constrained to 0.5. Since the target compound does not have the 2/m symmetry, the whole molecule had to be modelled with an occupancy factor of 0.25. Even though EADP constraints were used to minimize the number of parameters to refine, it was not sufficient enough to increase the data-to-parameter ratio.

The structure of **[1b]**(PF₆)₂ is partly disordered. One of the two coordinated Hmte ligands and both PF₆⁻ counterions are disordered over either two (counterions) or three (Hmte) orientations. All occupancy factors can be retrieved from the final .cif file.

For **[2b]**(PF₆)₂, the asymmetric unit contains ½ Ru complex (the Ru complex is found at one site of mirror symmetry, and only half is crystallographically independent) and two

disordered $\frac{1}{2}$ PF_6^- counterions (one counterion is found at one site of inversion symmetry and the other counterion is found at one site of mirror symmetry). The structure is pseudomerohedrally twinned. The twin relationship is given by the matrix M: 0 1 0 / 1 0 0 / 0 0 -1, and the BASF scale factor refines to 0.1054(8).

The structure of **[3b]**(PF_6)₂ is partially disordered. One of the two PF_6^- counterions is disordered over two orientations, and the occupancy factor of the major component of the disorder refines to 0.523(8). The structure was refined as an inversion twin, and the Flack and Hooft parameters refine to 0.088(9) and 0.088(1), respectively.

The structure of **[4b]**(PF_6)₂ is partly disordered. The axial pyridine and thioether ligands can be coordinated on both sides of the equatorial ligand, and the occupancy factor of the major component of the disorder refines to 0.775(5). One of the two PF_6^- counterions is also disordered over two orientations, and the occupancy factor of the major component of the disorder refines to 0.574(13). The crystal that was mounted on the diffractometer was non-merohedrally twinned, and the two twin components are related by a twofold rotation along [0.55 0.00 0.83]. The BASF scale factor refines to 0.4949(16).

Table III.1 Crystallographic data for the crystal structures presented in this work.

	[1a](PF ₆) ₂	[1b](PF ₆) ₂	[2b](PF ₆) ₂
Chemical formula	C ₂₆ H ₃₁ N ₅ O ₂ RuS ₂ ·2(F ₆ P)	C ₂₇ H ₃₃ N ₅ O ₂ RuS ₂ ·C ₁₈ H ₁₅ OP·2(F ₆ P)	C ₂₅ H ₂₃ N ₇ Ru·2(F ₆ P)
M _r	900.69	1192.98	812.51
Crystal system	Monoclinic	Triclinic	Orthorhombic
Space group	C2/m	P-1	Pnma
Cell lengths (<i>a</i> , <i>b</i> , <i>c</i>)(Å)	17.4981 (3), 11.4857 (3), 8.26232 (13)	8.50398 (15), 10.1685 (2), 28.0138 (4)	15.3570 (5), 15.3124 (4), 12.5014 (4)
Cell angles (α, β, γ)(°)	90, 98.1669 (17), 90	90.2939 (15), 92.6335 (14), 96.7146 (16)	90, 90, 90
Cell volume (Å ³)	1643.70 (6)	2403.14 (7)	2939.74 (15)
Z	2	2	4
μ (mm ⁻¹)	6.94	5.24	0.75
Crystal size (mm)	0.09 × 0.06 × 0.02	0.11 × 0.05 × 0.02	0.11 × 0.10 × 0.08
Temperature (K)	110(2)	110	110(2)
Diffractometer	XtaLAB Synergy R, HyPix	XtaLAB Synergy R, HyPix	SuperNova, Dual, Cu at zero, Atlas detector
Radiation type	Cu Kα	Cu Kα	Mo Kα
T _{min} , T _{max}	0.663, 0.875	0.629, 0.901	0.885, 1.000
No. of measured, independent and observed [<i>I</i> > 2σ(<i>I</i>)] reflections	19522, 1695, 1629	47520, 9445, 8464	28602, 3687, 3405
R _{int}	0.034	0.030	0.063
(sin θ/λ) _{max} (Å ⁻¹)	0.616	0.616	0.650
R[F ² > 2σ(F ²)], wR(F ²), S	0.040, 0.113, 1.06	0.034, 0.087, 1.04	0.036, 0.083, 1.09
No. of reflections	1695	9945	3687
No. of parameters	311	817	347
No. of restraints	729	842	542
H-atom treatment	H-atom parameters constrained	H-atom parameters constrained	H-atom parameters constrained
Δρ _{max} , Δρ _{min} (e Å ⁻³)	0.61, -0.60	0.81, -0.70	0.95, -0.53

	[3b](PF ₆) ₂	[4b](PF ₆) ₂
Chemical formula	C ₃₁ H ₂₇ N ₇ Ru·2(F ₆ P)	C ₂₉ H ₃₀ N ₆ ORuS·2(F ₆ P)
M _r	888.60	901.66
Crystal system	Orthorhombic	Monoclinic
Space group	<i>P</i> 2 ₁ 2 ₁ 2 ₁	<i>P</i> 2 ₁ / <i>c</i>
Cell lengths (<i>a</i> , <i>b</i> , <i>c</i>)(Å)	8.72848 (13), 9.82300 (13), 37.8019 (5)	18.8561 (8), 8.4130 (3), 20.9072 (11)
Cell angles (α, β, γ)(°)	90, 90, 90	90, 95.833 (4), 90
Cell volume (Å ³)	3241.13 (8)	3299.5 (3)
Z	4	4
μ (mm ⁻¹)	5.83	6.33
Crystal size (mm)	0.33 × 0.07 × 0.03	0.13 × 0.01 × 0.01
Temperature (K)	110(2)	110(2)
Diffractometer	SuperNova, Dual, Cu at zero, Atlas detector	XtaLAB Synergy R, HyPix
Radiation type	Cu Kα	Cu Kα
T _{min} , T _{max}	0.388, 0.879	0.697, 0.938
No. of measured, independent and observed [<i>I</i> > 2σ(<i>I</i>)] reflections	26948, 6263, 5958	24143, 6978, 4115
<i>R</i> _{int}	0.036	0.090
(sin θ/λ) _{max} (Å ⁻¹)	0.616	0.598
<i>R</i> [<i>F</i> ² > 2σ(<i>F</i> ²)], <i>wR</i> (<i>F</i> ²), <i>S</i>	0.026, 0.061, 1.04	0.057, 0.133, 0.88
No. of reflections	6263	6978
No. of parameters	538	589
No. of restraints	279	487
H-atom treatment	H-atom parameters constrained	H-atom parameters constrained
Δρ _{max} , Δρ _{min} (e Å ⁻³)	0.52, -0.47	1.112, -1.17

III.2 Photochemistry

III.2.1 Molar extinction coefficient determination

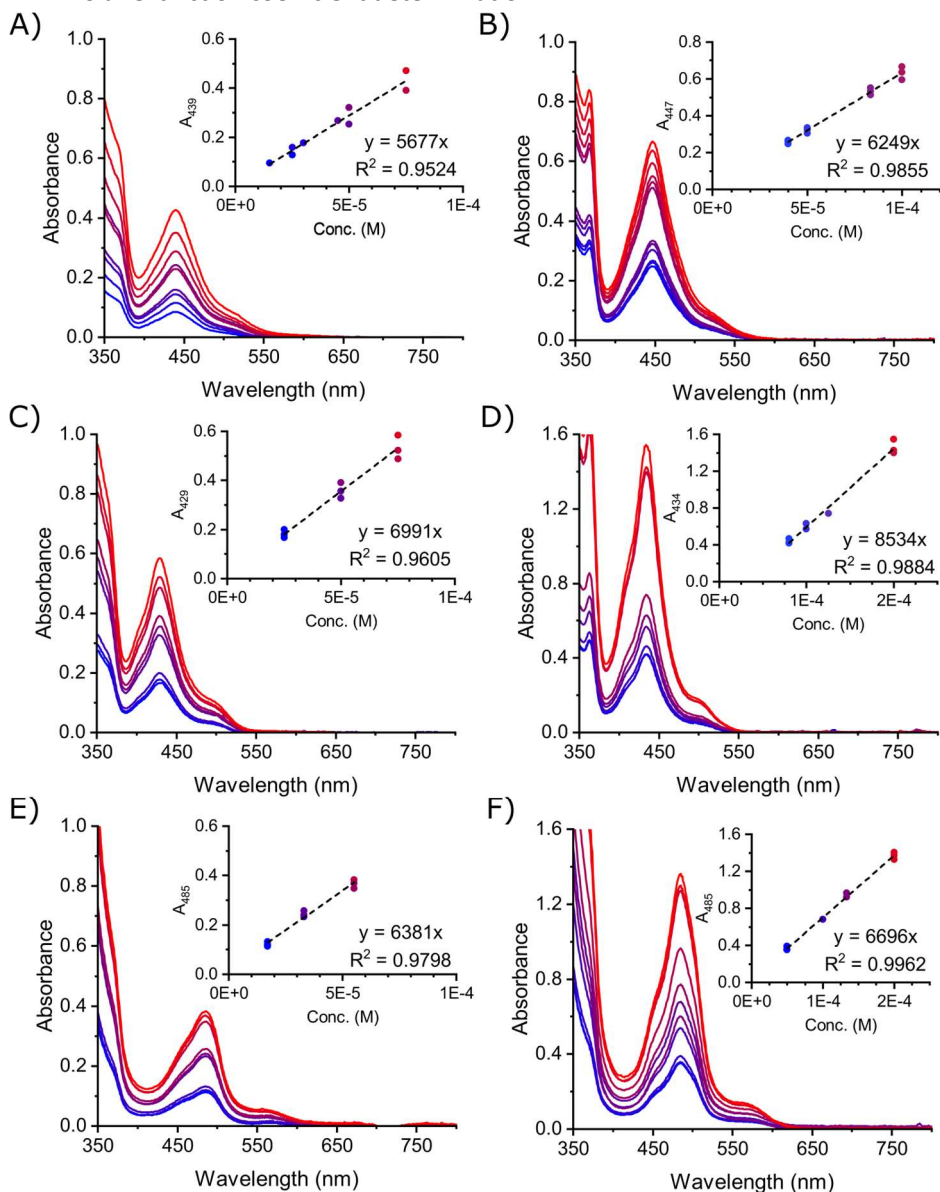


Figure III.1 UV-Vis absorbance spectra of complexes at different concentrations in 3 ml 20% acetone in H₂O at 298 K (l = 1 cm). Insets depict absorption at λ_{max} at different concentrations. A) [1a](PF₆)₂: $\epsilon = 5.68 \times 10^3 \text{ M}^{-1} \text{ cm}^{-1}$ at 439 nm. B) [1b](PF₆)₂: $\epsilon = 6.25 \times 10^3 \text{ M}^{-1} \text{ cm}^{-1}$ at 447 nm. C) [2a](PF₆)₂: $\epsilon = 6.99 \times 10^3 \text{ M}^{-1} \text{ cm}^{-1}$ at 429 nm. D) [2b](PF₆)₂: $\epsilon = 8.53 \times 10^3 \text{ M}^{-1} \text{ cm}^{-1}$ at 434 nm. E) [3a](PF₆)₂: $\epsilon = 6.38 \times 10^3 \text{ M}^{-1} \text{ cm}^{-1}$ at 485 nm. F) [3b](PF₆)₂: $\epsilon = 6.70 \times 10^3 \text{ M}^{-1} \text{ cm}^{-1}$ at 485 nm.

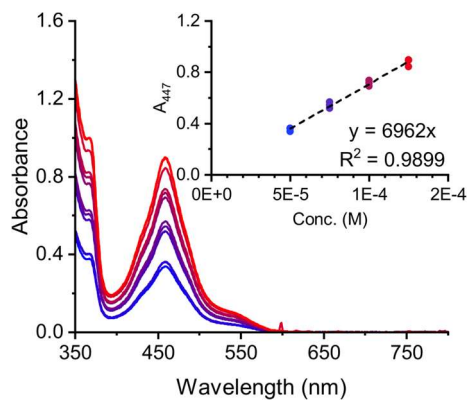


Figure III.2 UV-Vis absorbance spectra of [4b](PF₆)₂ at different concentrations in 3 ml 20% acetone in H₂O at 298 K (l = 1 cm). Insets depict absorption at λ_{max} at different concentrations; $\epsilon = 6.96 \times 10^3 \text{ M}^{-1} \text{ cm}^{-1}$ at 447 nm.

III.2.2 Photosubstitution quantum yield measurements

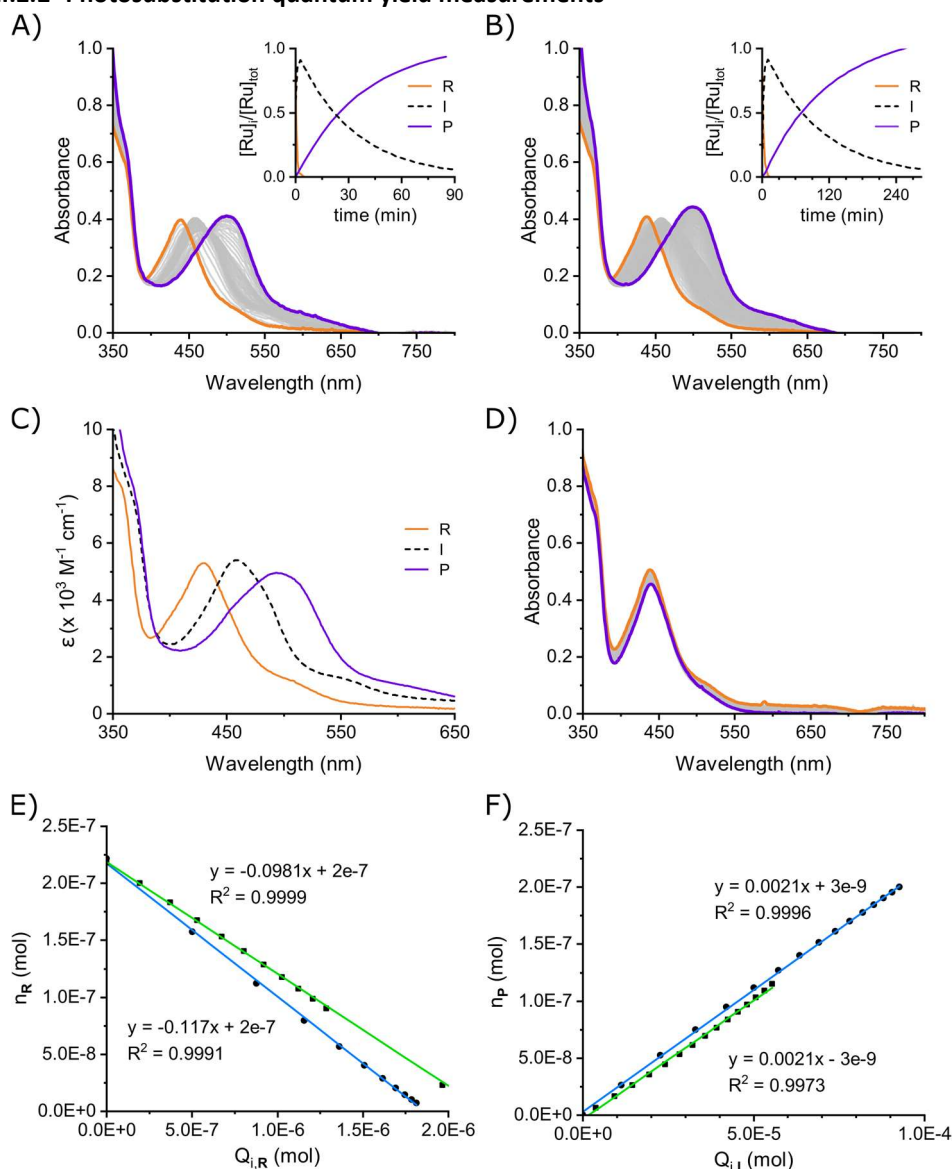


Figure III.3 Graphs for photosubstitution quantum yield for $[1a](PF_6)_2$ at 298 K in 20% acetone in H_2O . Time-evolution of UV-Vis absorbance upon irradiation with A) 435 nm (photon flux = 5.09×10^{-8} mol/s) for 85 min at $73.8 \mu M$ and B) 505 nm (photon flux = 2.95×10^{-8} mol/s) for 285 min at $72.8 \mu M$ (from orange to purple). C) Globally fitted UV-Vis absorption spectra of $[1a]^{2+}$ (R; orange line), the intermediate $[5a]^{2+}$ (I; black dashed) and the photoproduct $[8a]^{2+}$ (P; purple line). D) Absorption spectra of $[1a](PF_6)_2$ in the dark for 15 h (from orange to purple). E) Plot of n_R against $Q_{i,R}$ used to calculate the first step photosubstitution quantum yield. F) Plot of n_P against $Q_{i,I}$ used to calculate the second step photosubstitution quantum yield.

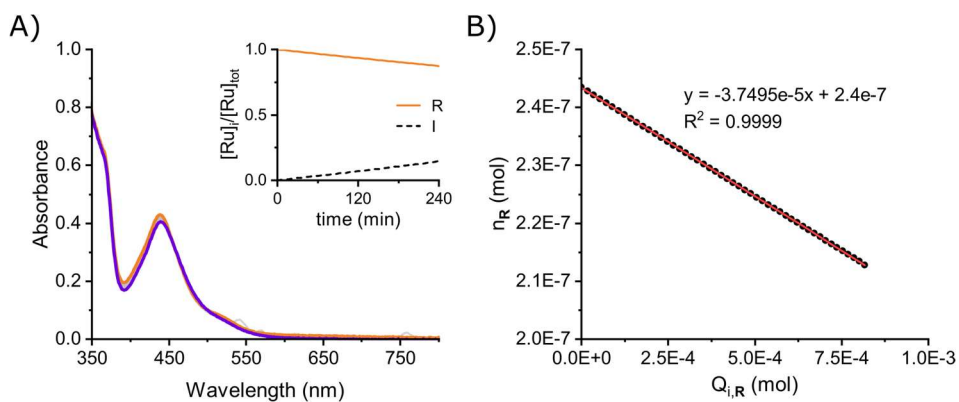


Figure III.4 Graphs for photosubstitution quantum yield for $[1a](PF_6)_2$ at 298 K in 20% acetone in H_2O . A) Time-evolution of UV-Vis absorbance upon irradiation with 625 nm (photon flux = 4.85×10^{-7} mol/s) for 4 h at 81.2 μM (from orange to purple). B) Plot of n_R against $Q_{i,R}$ used to calculate the first step photosubstitution quantum yield.

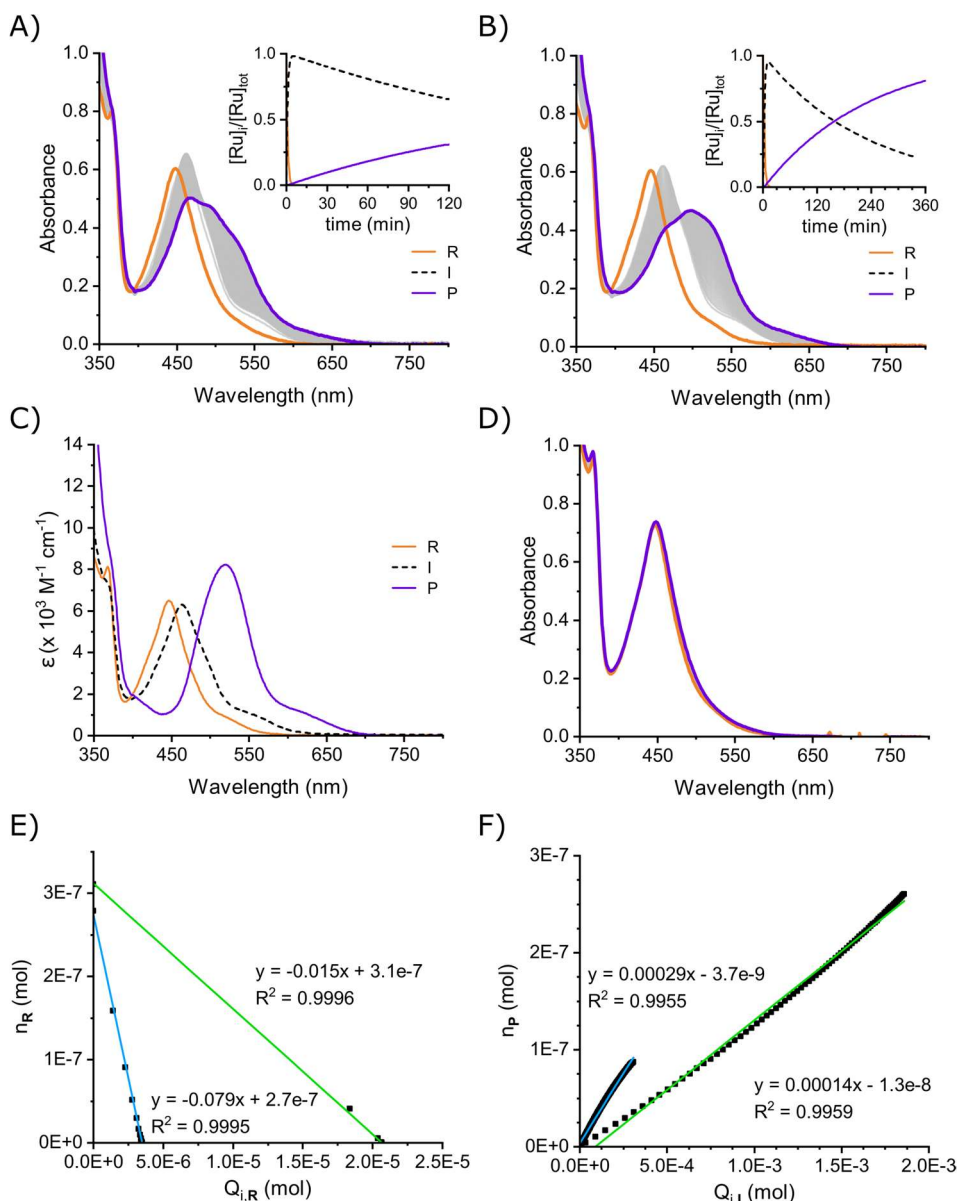


Figure III.5 Graphs for photosubstitution quantum yield for $[\mathbf{1b}](\text{PF}_6)_2$ at 298 K in 20% acetone in H_2O . Time-evolution of UV-Vis absorbance upon irradiation with A) 435 nm (photon flux = 5.70×10^{-8} mol/s) for 120 min at 90.7 μM and B) 505 nm (photon flux = 2.28×10^{-7} mol/s) for 360 min at 100.7 μM (from orange to purple). C) Globally fitted UV-Vis absorption spectra of $[\mathbf{1b}](\text{PF}_6)_2$ (R; orange line), the intermediate $[\mathbf{5b}]^{2+}$ (I; black dashed) and the photoproduct $[\mathbf{8b}]^{2+}$ (P; purple line). D) Absorption spectra of $[\mathbf{1b}](\text{PF}_6)_2$ in the dark for 12 h (from orange to purple). E) Plot of ϵ_R against $Q_{i,R}$ used to calculate the first step photosubstitution quantum yield. F) Plot of ϵ_P against $Q_{i,I}$ used to calculate the second step photosubstitution quantum yield.

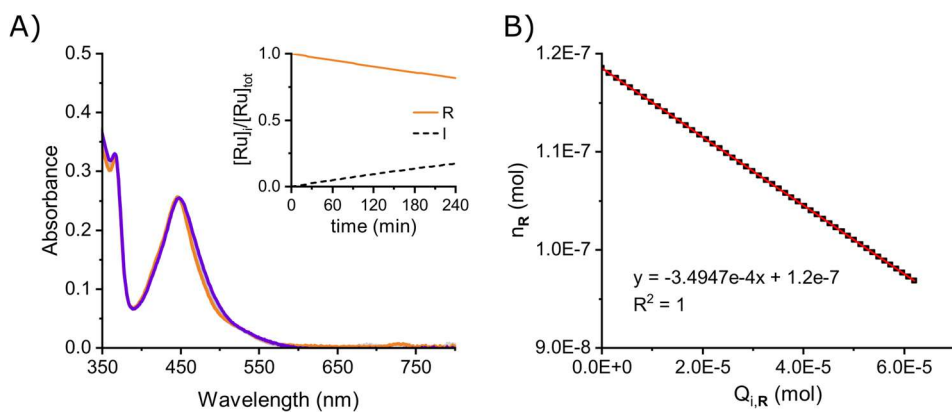


Figure III.6 Graphs for photosubstitution quantum yield for $[1b](PF_6)_2$ at 298 K in 20% acetone in H_2O . A) Time-evolution of UV-Vis absorbance upon irradiation with 625 nm (photon flux = 4.83×10^{-7} mol/s) for 4 h at $44.4 \mu M$ (from orange to purple). B) Plot of n_R against $Q_{i,R}$ used to calculate the first step photosubstitution quantum yield.

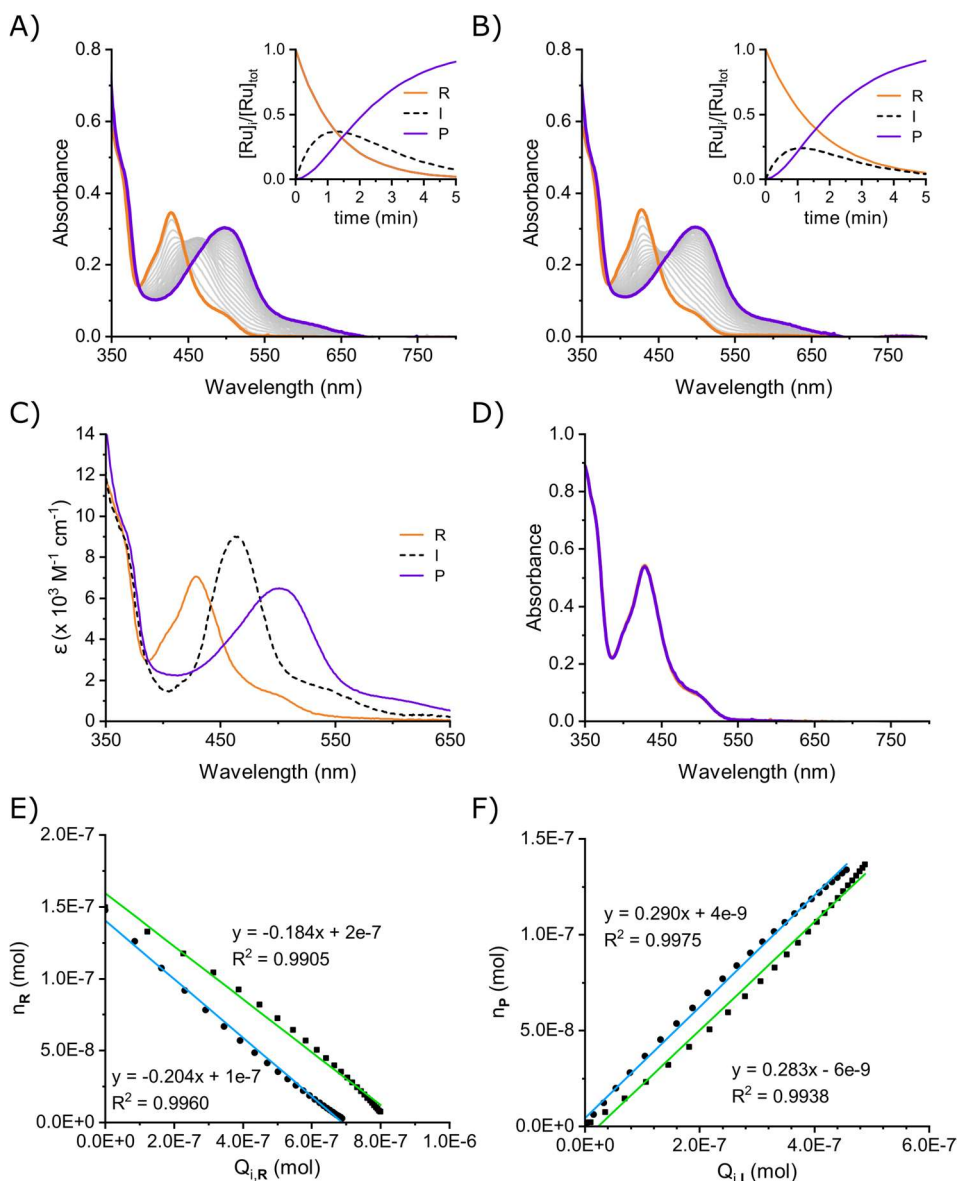


Figure III.7 Graphs for photosubstitution quantum yield for $[2a](PF_6)_2$ at 298 K in 20% acetone in H_2O . Time-evolution of UV-Vis absorbance upon irradiation with A) 435 nm (photon flux = 8.54×10^{-9} mol/s) for 5 min at 49.2 μM and B) 505 nm (photon flux = 2.92×10^{-8} mol/s) for 5 min at 49.9 μM (from orange to purple). C) Globally fitted UV-Vis absorption spectra of $[2a](PF_6)_2$ (R; orange line), the intermediate $[6a]^{2+}$ (I; black dashed) and the photoproduct $[8a]^{2+}$ (P; purple line). D) Absorption spectra of $[2a](PF_6)_2$ in the dark for 130 min (from orange to purple). E) Plot of n_R against $Q_{i,R}$ used to calculate the first step photosubstitution quantum yield. F) Plot of n_P against $Q_{i,I}$ used to calculate the second step photosubstitution quantum yield.

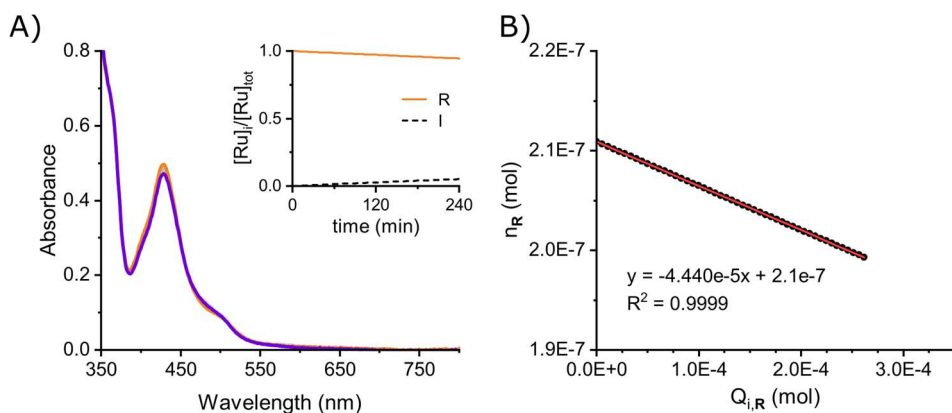


Figure III.8 Graphs for photosubstitution quantum yield for $[2a](PF_6)_2$ at 298 K in 20% acetone in H_2O . A) Time-evolution of UV-Vis absorbance upon irradiation with 625 nm (photon flux = 4.85×10^{-7} mol/s) for 4 h at 70.3 μM (from orange to purple). B) Plot of n_R against $Q_{i,R}$ used to calculate the first step photosubstitution quantum yield.

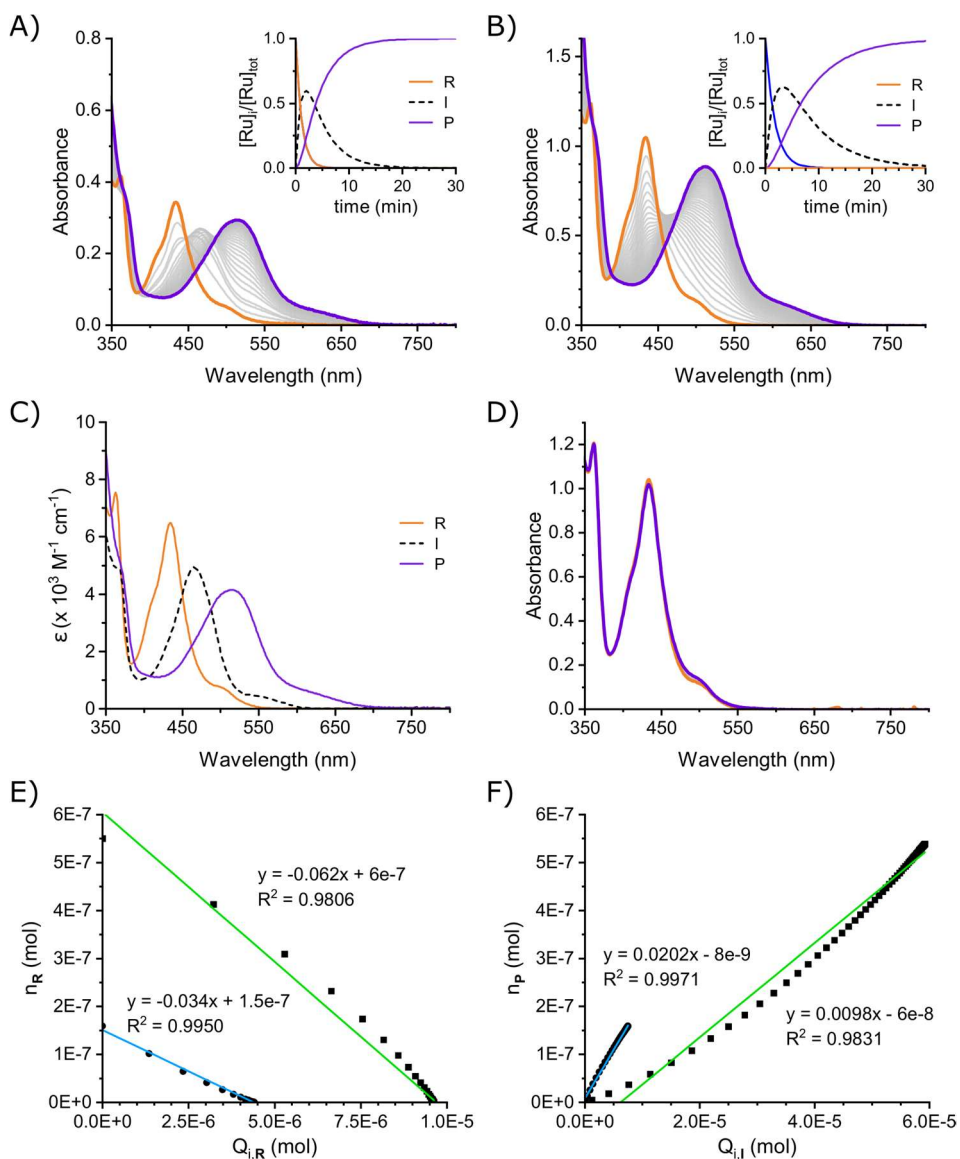


Figure III.9 Graphs for photosubstitution quantum yield for $[\mathbf{2b}](\text{PF}_6)_2$ at 298 K in 20% acetone in H_2O . Time-evolution of UV-Vis absorbance upon irradiation with A) 435 nm (photon flux = 5.70×10^{-8} mol/s) for 30 min at 53.0 μM and B) 505 nm (photon flux = 2.28×10^{-7} mol/s) for 30 min at 183 μM (from orange to purple). C) Globally fitted UV-Vis absorption spectra of $[\mathbf{2b}](\text{PF}_6)_2$ (R; orange line), the intermediate $[\mathbf{6b}]^{2+}$ (Int; black dashed) and the photoproduct $[\mathbf{8b}]^{2+}$ (P; purple line). D) Absorption spectra of $[\mathbf{2b}](\text{PF}_6)_2$ in the dark for 130 min (from orange to purple). E) Plot of n_R against $Q_{i,R}$ used to calculate the first step photosubstitution quantum yield. F) Plot of n_P against $Q_{i,I}$ used to calculate the second step photosubstitution quantum yield.

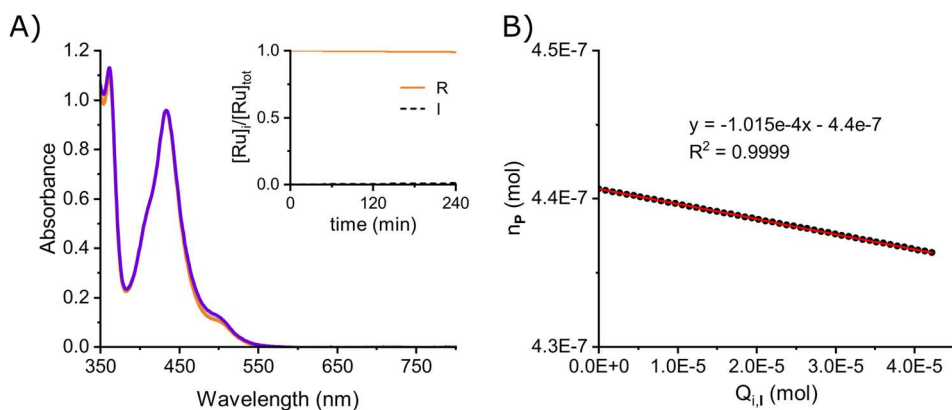


Figure III.10 Graphs for photosubstitution quantum yield for **[2b]**(PF₆)₂ at 298 K in 20% acetone in H₂O. A) Time-evolution of UV-Vis absorbance upon irradiation with 625 nm (photon flux = 4.84×10^{-7} mol/s) for 4 h at 147 μ M (from orange to purple). B) Plot of n_R against $Q_{i,R}$ used to calculate the first step photosubstitution quantum yield.

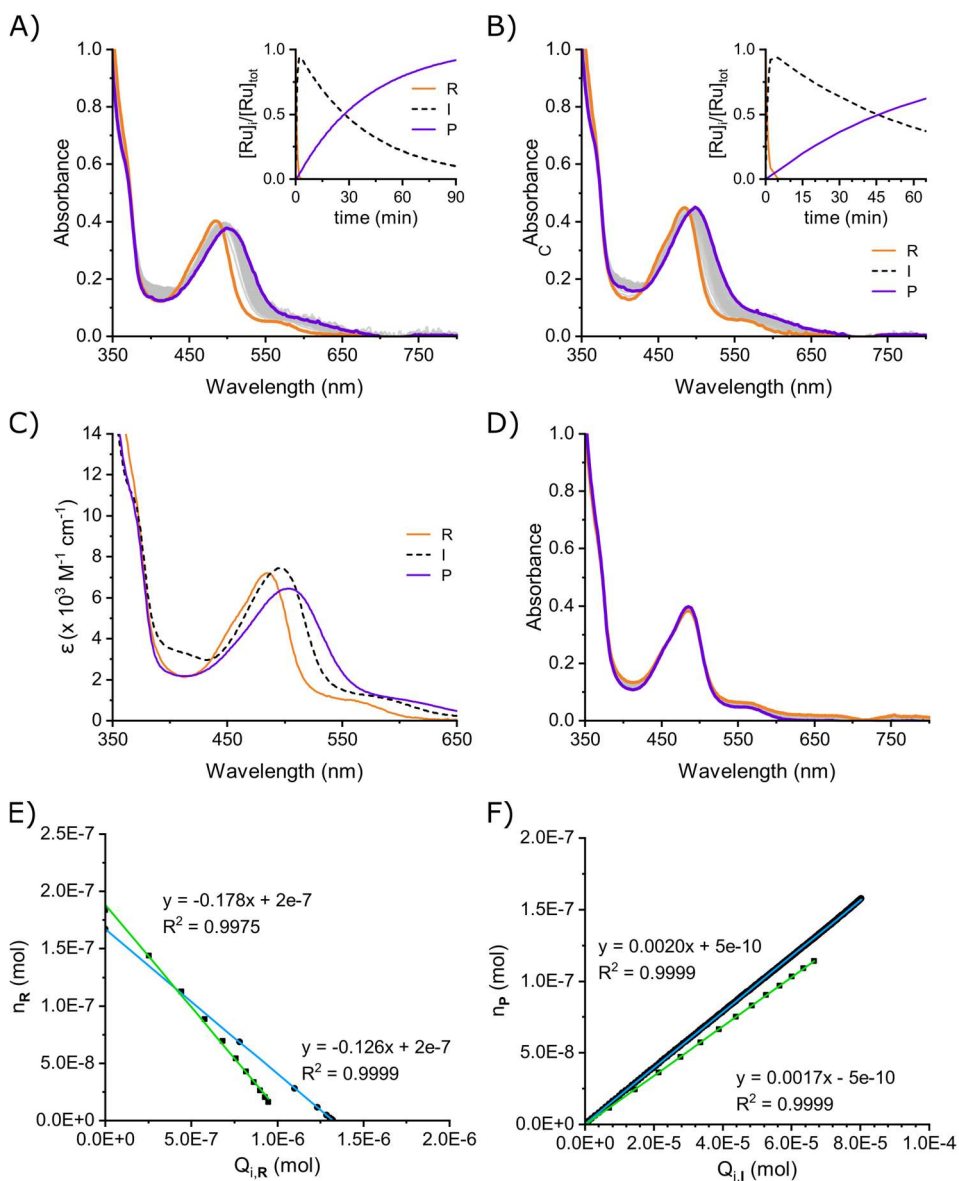


Figure III.11 Graphs for photosubstitution quantum yield for $[3a](PF_6)_2$ at 298 K in 20% acetone in H_2O . Time-evolution of UV-Vis absorbance upon irradiation with A) 435 nm (photon flux = 5.27×10^{-8} mol/s) for 100 min at $55.7 \mu M$ and B) 505 nm (photon flux = 2.95×10^{-8} mol/s) for 65 min at $61.1 \mu M$ (from orange to purple). C) Globally fitted UV-Vis absorption spectra of $[3a](PF_6)_2$ (R; orange line), the intermediate $[7a]^{2+}$ (I; black dashed) and the photoproduct $[8a]^{2+}$ (P; purple line). D) Absorption spectra of $[3a](PF_6)_2$ in the dark for 260 min (from orange to purple). E) Plot of n_R against $Q_{i,R}$ used to calculate the first step photosubstitution quantum yield. F) Plot of n_P against $Q_{i,I}$ used to calculate the second step photosubstitution quantum yield.

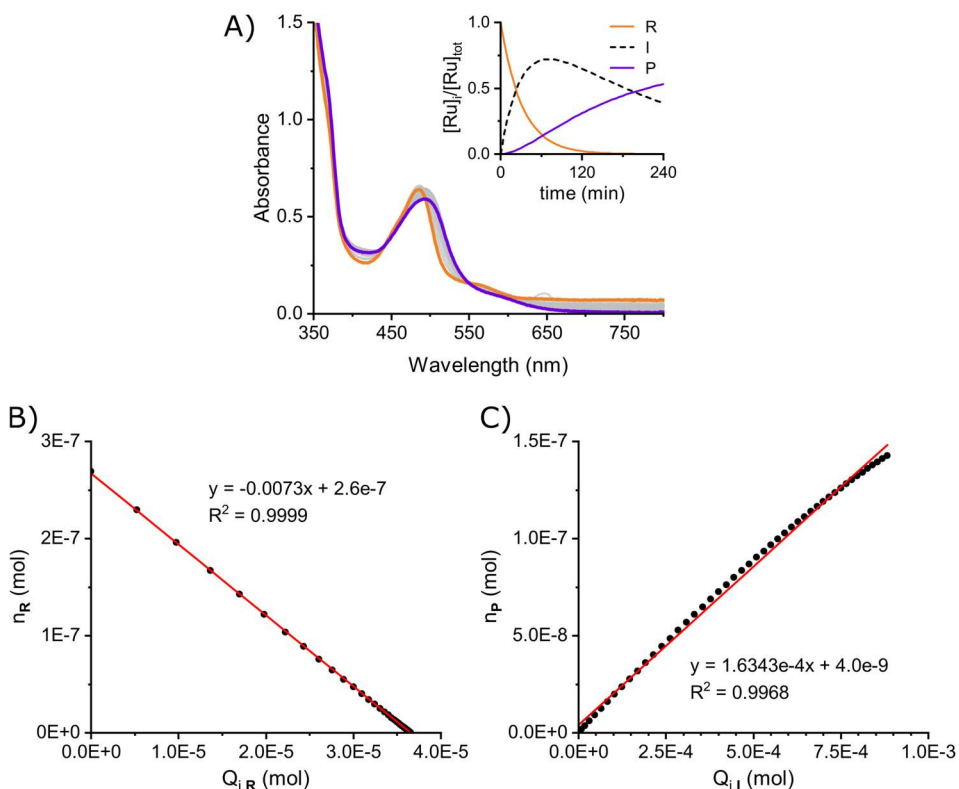


Figure III.12 Graphs for photosubstitution quantum yield for $[3a](PF_6)_2$ at 298 K in 20% acetone in H_2O . A) Time-evolution of UV-Vis absorbance upon irradiation with 625 nm (photon flux = 4.85×10^{-7} mol/s) for 4 h at 89.6 μM (from orange to purple). B) Plot of n_R against $Q_{i,R}$ used to calculate the first step photosubstitution quantum yield. C) Plot of n_P against $Q_{i,I}$ used to calculate the second step photosubstitution quantum yield.

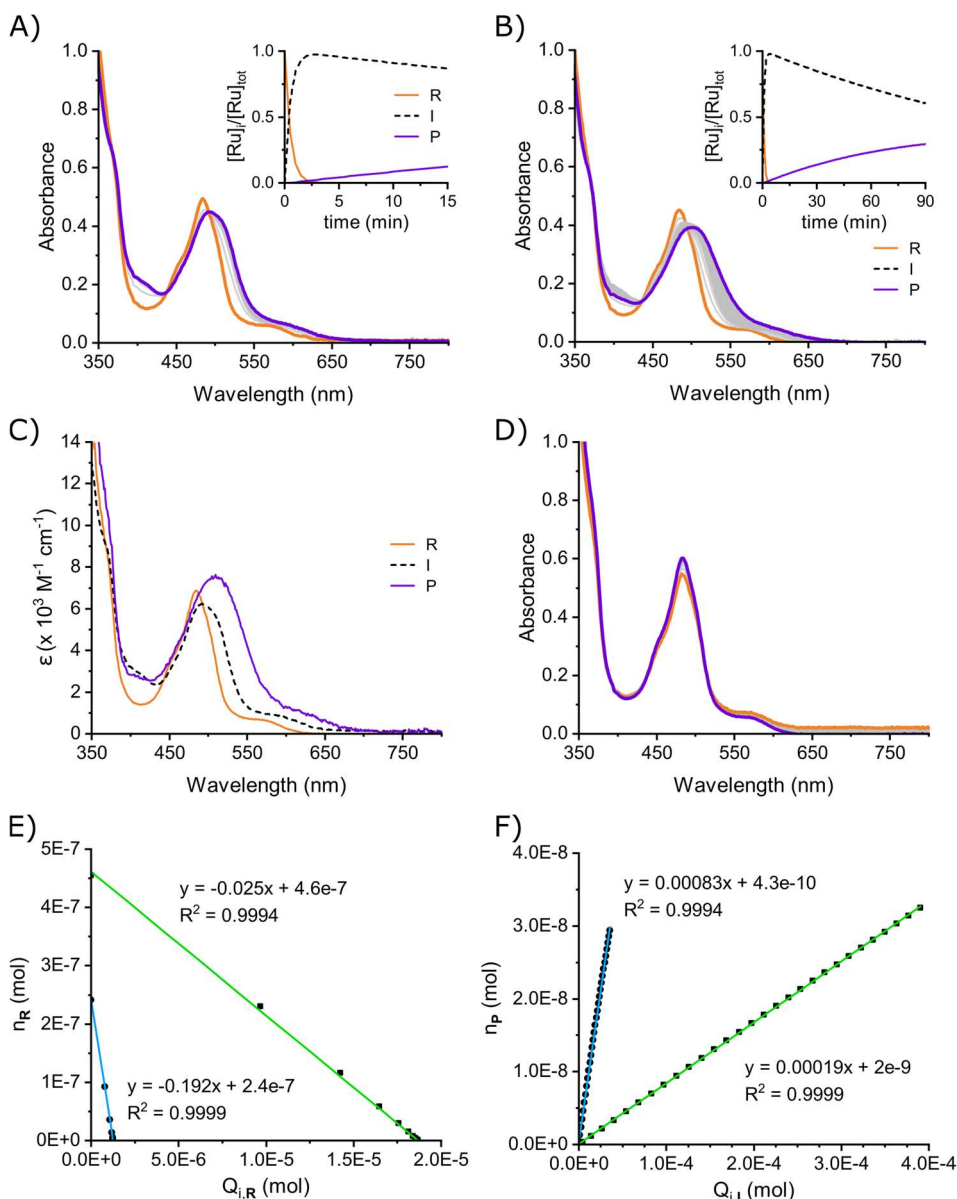


Figure III.13 Graphs for photosubstitution quantum yield for $[\mathbf{3b}](\text{PF}_6)_2$ at 298 K in 20% acetone in H_2O . Time-evolution of UV-Vis absorbance upon irradiation with A) 435 nm (photon flux = 5.70×10^{-8} mol/s) for 15 min at 72.9 μM and B) 505 nm (photon flux = 2.28×10^{-7} mol/s) for 90 min at 137.8 μM (from orange to purple). C) Globally fitted UV-Vis absorption spectra of $[\mathbf{3b}](\text{PF}_6)_2$ (R; orange line), the intermediate $[\mathbf{7b}]^{2+}$ (Int; black dashed) and the photoproduct $[\mathbf{8b}]^{2+}$ (P; purple line). D) Absorption spectra of $[\mathbf{3b}](\text{PF}_6)_2$ in the dark for 15 h (from orange to purple). E) Plot of n_R against $Q_{i,R}$ used to calculate the first step photosubstitution quantum yield. F) Plot of n_P against $Q_{i,I}$ used to calculate the second step photosubstitution quantum yield.

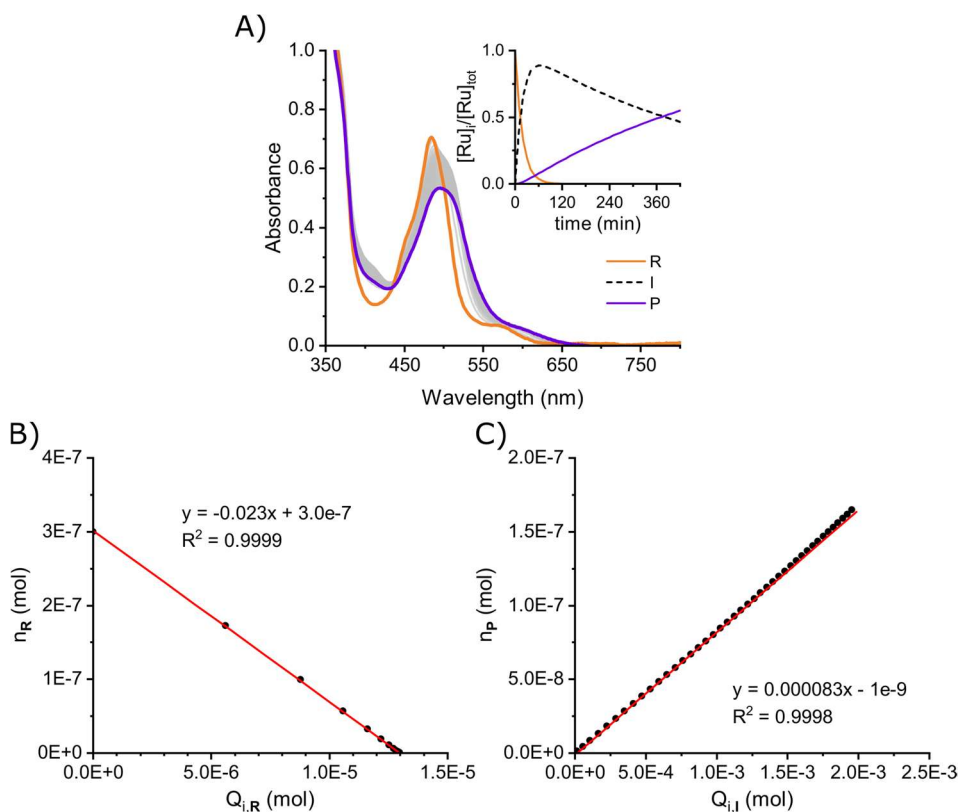


Figure III.14 Graphs for photosubstitution quantum yield for $[3b](PF_6)_2$ at 298 K in 20% acetone in H_2O . A) Time-evolution of UV-Vis absorbance upon irradiation with 625 nm (photon flux = 4.24×10^{-7} mol/s) for 7 h at 100.0 μM (from orange to purple). B) Plot of n_R against $Q_{i,R}$ used to calculate the first step photosubstitution quantum yield. C) Plot of n_P against $Q_{i,I}$ used to calculate the second step photosubstitution quantum yield.

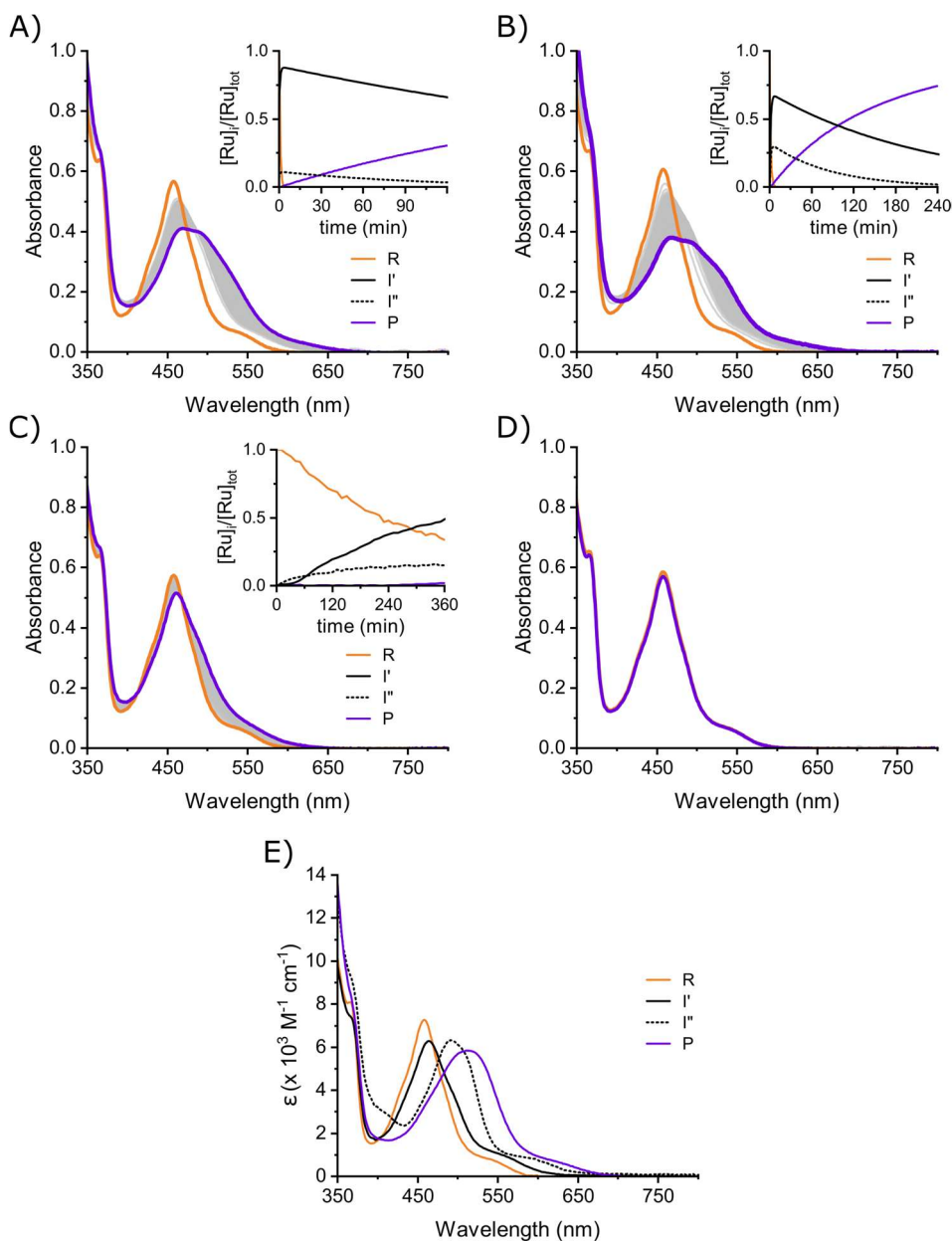


Figure III.15 Time-evolution of UV-Vis absorbance of $[4b](PF_6)_2$ at 298 K in 20% acetone in H_2O when irradiated with A) 435nm (photon flux = 3.29×10^{-7} mol/s; 84.1 μM ; 120 min), B) 505nm (photon flux = 2.00×10^{-7} mol/s; 83.3 μM ; 240 min), C) 625 nm (photon flux = 4.24×10^{-7} mol/s; 84.1 μM ; 360 min) and D) in the dark (84.1 μM ; 12 h) (from orange to purple). E) Globally fitted UV-Vis absorption spectra of $[4b](PF_6)_2$ (R; orange line), $[5b]^{2+}$ (I'; black solid), $[7b]^{2+}$ (I''; black dashed) and $[8b]^{2+}$ (P; purple line).

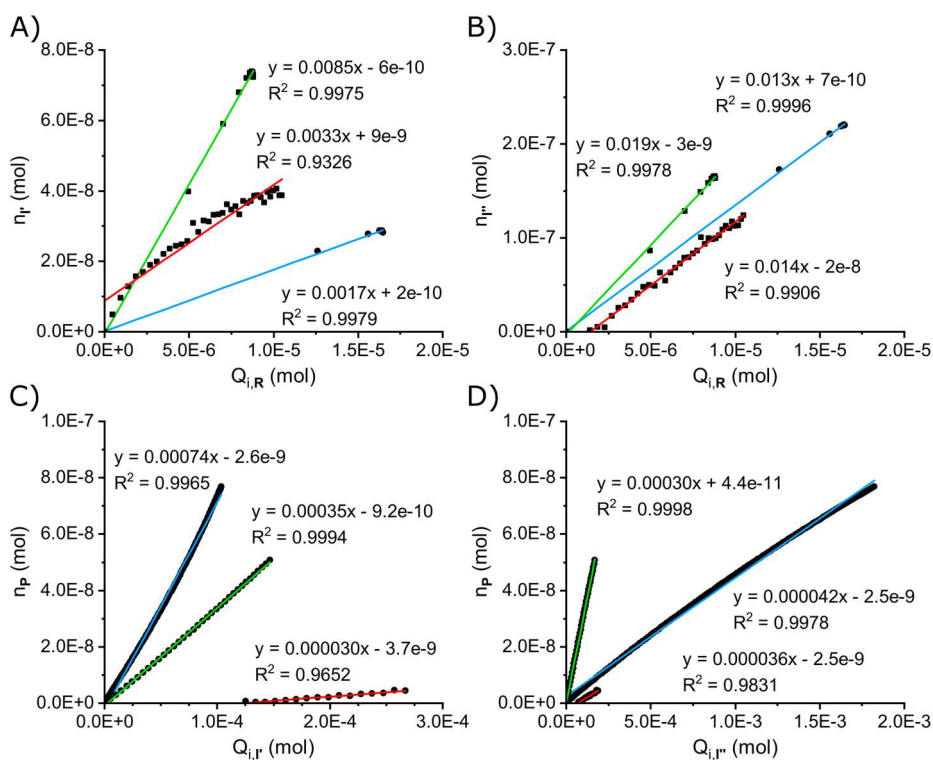


Figure III.16 Graphs for photosubstitution quantum yields for $[4b](PF_6)_2$ at 298 K in 20% acetone in H_2O upon irradiation with 435 nm, 505 nm or 625 nm. A) $[4b]^{2+} \rightarrow [7b]^{2+}$ ($\phi_{1,s}$). B) $[4b]^{2+} \rightarrow [5b]^{2+}$ ($\phi_{1,N}$). C) $[7b]^{2+} \rightarrow [8b]^{2+}$ ($\phi_{2,s}$). D) $[5b]^{2+} \rightarrow [8b]^{2+}$ ($\phi_{1,N}$).

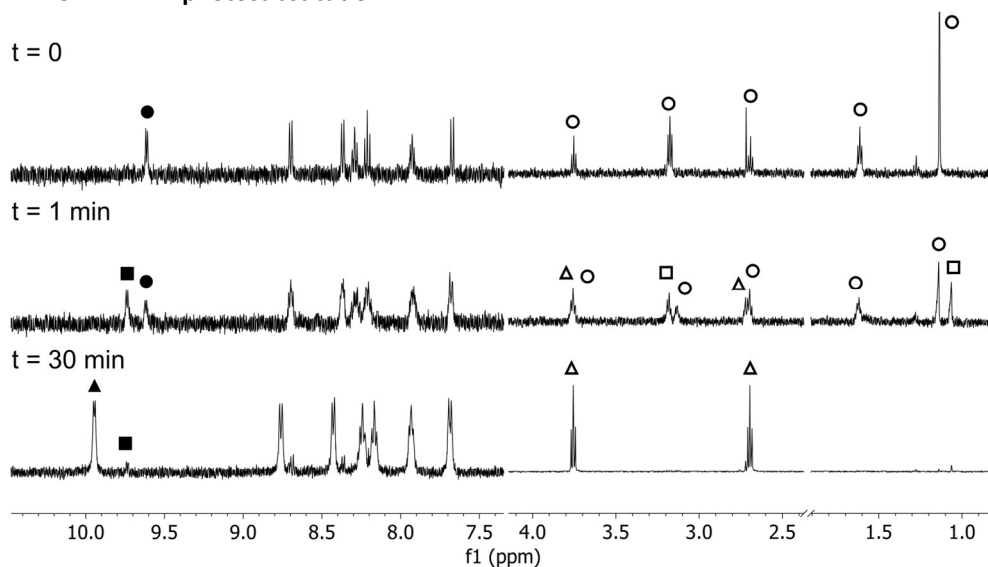
III.2.3 $^1\text{H-NMR}$ photosubstitution

Figure III.17 $^1\text{H-NMR}$ spectra evolution of $[\mathbf{1a}](\text{PF}_6)_2$ (● for complex, ○ for MTE) in 1/5 acetone- d_6 / D_2O at 298 K during irradiation with white light. Symbols indicate intermediate (■ for complex, □ for MTE), photoproduct (▲) and free MTE (Δ).

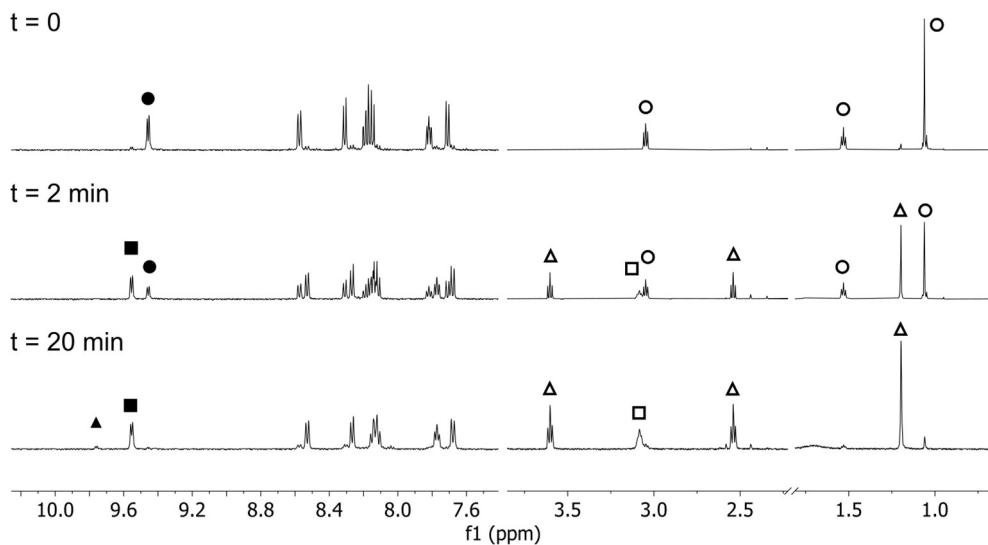


Figure III.18 $^1\text{H-NMR}$ spectra evolution of $[\mathbf{1b}](\text{PF}_6)_2$ (● for complex, ○ for MTE) in 1/5 acetone- d_6 / D_2O at 298 K during irradiation with 530 nm. Symbols indicate intermediate (■ for complex, □ for MTE), photoproduct (▲) and free MTE (Δ).

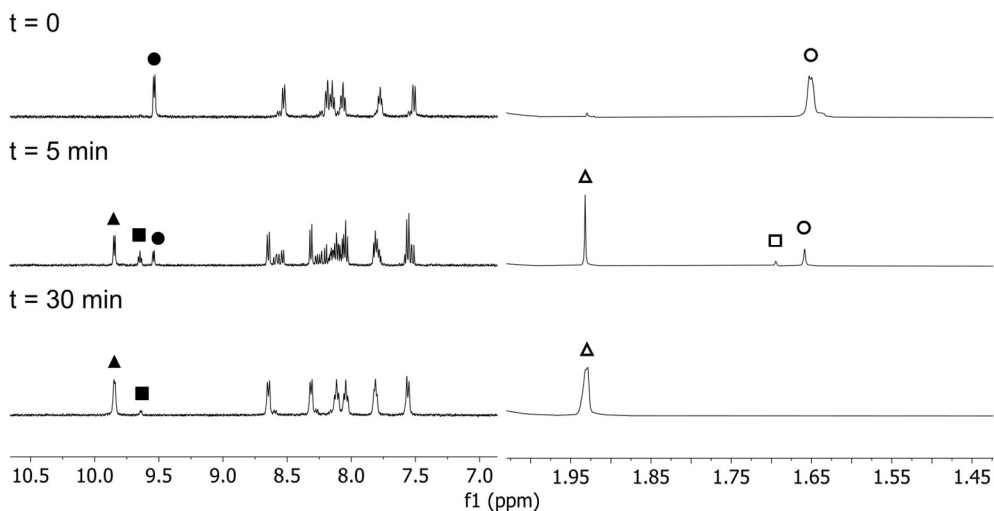


Figure III.19 ^1H -NMR spectra evolution of $[2\mathbf{a}](\text{PF}_6)_2$ (● for complex, ○ for ACN) in 1/5 acetone- d_6 / D_2O at 298 K during irradiation with white light. Symbols indicate intermediate (■ for complex, □ for ACN), photoproduct (▲) and free ACN (Δ).

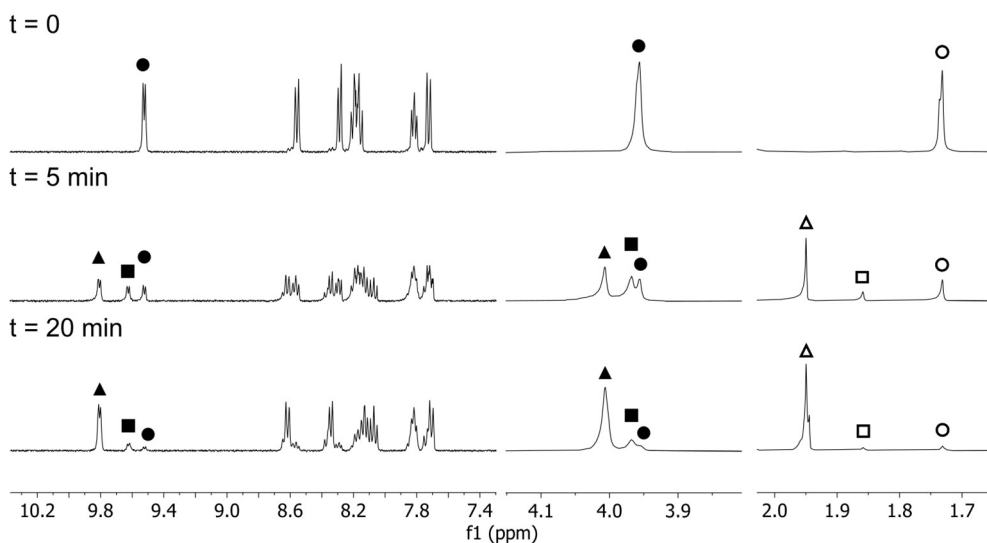


Figure III.20 ^1H -NMR spectra evolution of $[2\mathbf{b}](\text{PF}_6)_2$ (● for complex, ○ for ACN) in 1/3 acetone- d_6 / D_2O at 298 K during irradiation with 530 nm. Symbols indicate intermediate (■ for complex, □ for ACN), photoproduct (▲) and free ACN (Δ).

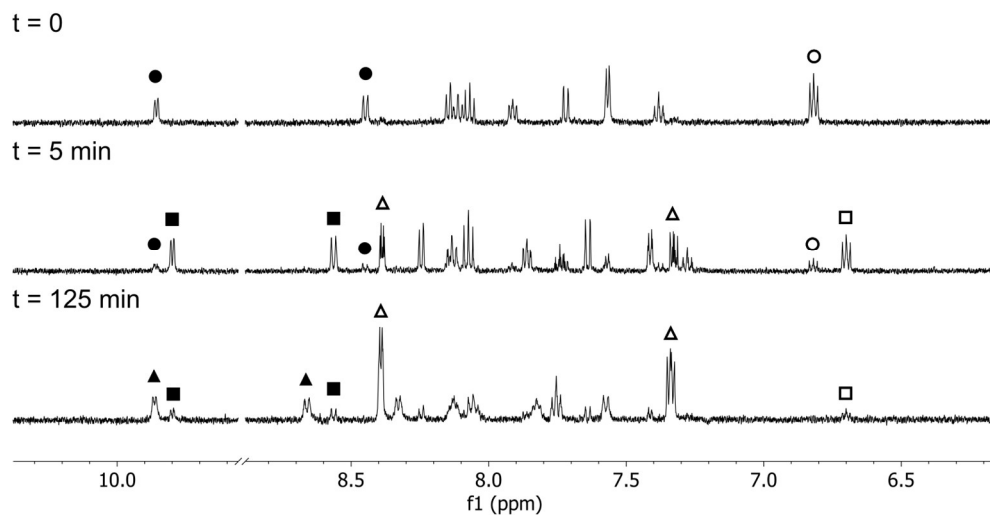
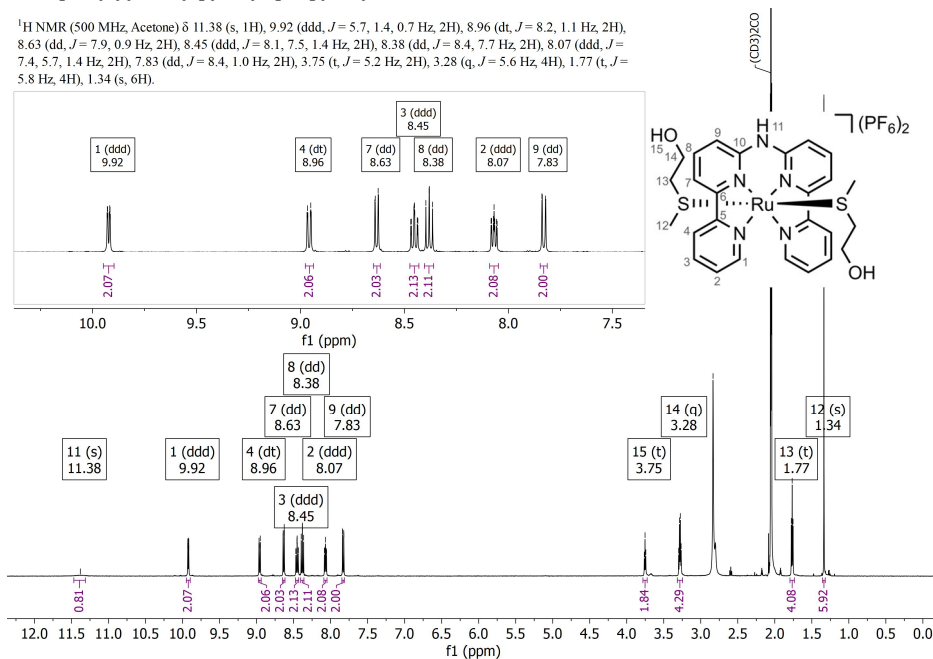
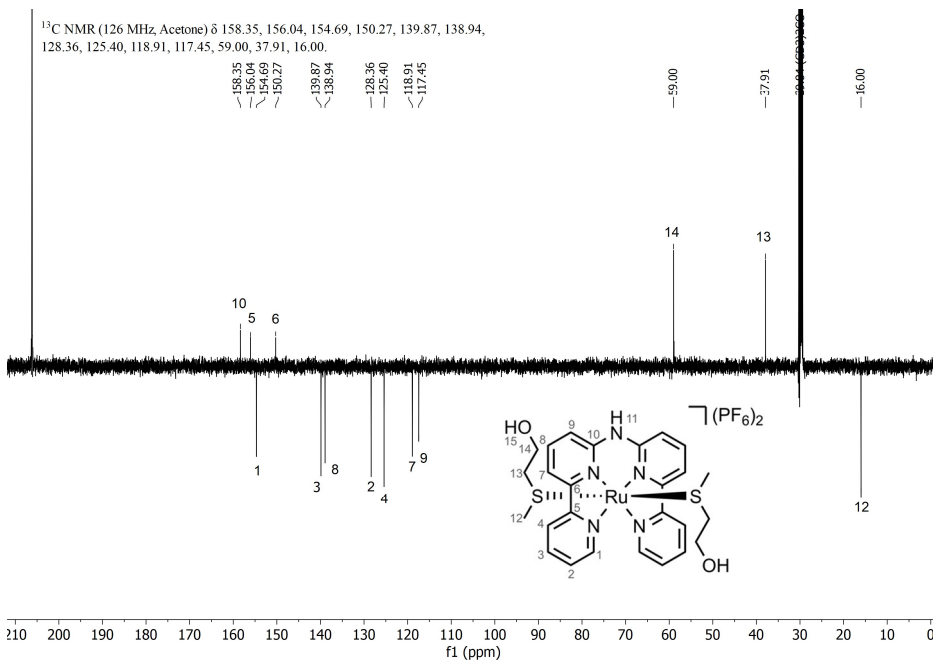


Figure III.21 ^1H -NMR spectra evolution of $[3\text{a}](\text{PF}_6)_2$ (● for complex, ○ for pyridine) in 1/5 acetone- $\text{d}_6/\text{D}_2\text{O}$ at 298 K during irradiation with white light. Symbols indicate intermediate (■ for complex, □ for pyridine), photoproduct (▲) and free pyridine (Δ).

III.3 Characterization of synthesized compounds

V.3.1 $[\text{Ru}(\text{L})(\text{MTE})_2](\text{PF}_6)_2$ [**1a**](PF_6)₂

¹H NMR (500 MHz, Acetone) δ 11.38 (s, 1H), 9.92 (ddd, $J = 5.7, 1.4, 0.7$ Hz, 2H), 8.96 (dt, $J = 8.2, 1.1$ Hz, 2H), 8.63 (dd, $J = 7.9, 0.9$ Hz, 2H), 8.45 (ddd, $J = 8.1, 7.5, 1.4$ Hz, 2H), 8.38 (dd, $J = 8.4, 7.7$ Hz, 2H), 8.07 (ddd, $J = 7.4, 5.7, 1.4$ Hz, 2H), 7.83 (dd, $J = 8.4, 1.0$ Hz, 2H), 3.75 (t, $J = 5.2$ Hz, 2H), 3.28 (q, $J = 5.6$ Hz, 4H), 1.77 (t, $J = 5.8$ Hz, 4H), 1.34 (s, 6H).

Figure III.22 ¹H-NMR of [**1a**](PF_6)₂ in Acetone-*d*₆.Figure III.23 ¹³C-APT-NMR of [**1a**](PF_6)₂ in Acetone-*d*₆.

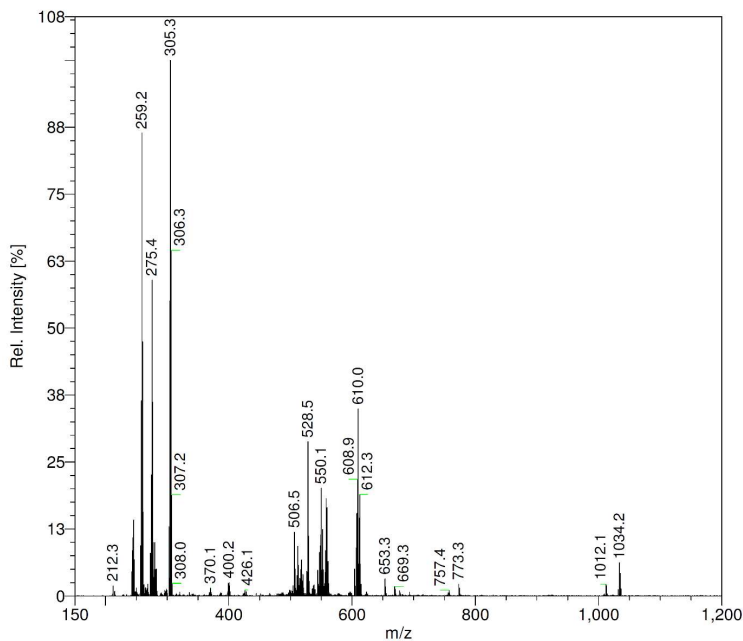


Figure III.24 ESI-MS of **[1a](PF₆)₂**. Calculated for $[\text{C}_{26}\text{H}_{31}\text{N}_5\text{O}_2\text{RuS}_2]^{2+}$: 305.6 m/z; $[\text{C}_{26}\text{H}_{31}\text{N}_5\text{O}_2\text{RuS}_2-\text{H}]^+$: 610.1 m/z; $[\text{C}_{26}\text{H}_{31}\text{N}_5\text{O}_2\text{RuS}_2-\text{C}_3\text{H}_8\text{OS}]^{2+}$: 259.5 m/z; $[\text{C}_{26}\text{H}_{31}\text{N}_5\text{O}_2\text{RuS}_2-\text{C}_3\text{H}_8\text{OS}+\text{C}_4\text{HO}]^{2+}$: 275.5 m/z.

V.3.2 **[Ru(L)(ACN)₂](PF₆)₂ [2a](PF₆)₂**

¹H NMR (500 MHz, Acetone) δ 11.30 (s, 1H), 9.88 (d, *J* = 5.6 Hz, 2H), 8.89 (d, *J* = 8.0 Hz, 2H), 8.55 (d, *J* = 8.0 Hz, 2H), 8.42 (td, *J* = 7.8, 1.4 Hz, 2H), 8.34 (t, *J* = 8.0 Hz, 2H), 8.02 (ddd, *J* = 7.3, 5.5, 1.4 Hz, 2H), 7.79 (dd, *J* = 8.4, 0.9 Hz, 2H), 1.98 (s, 6H).

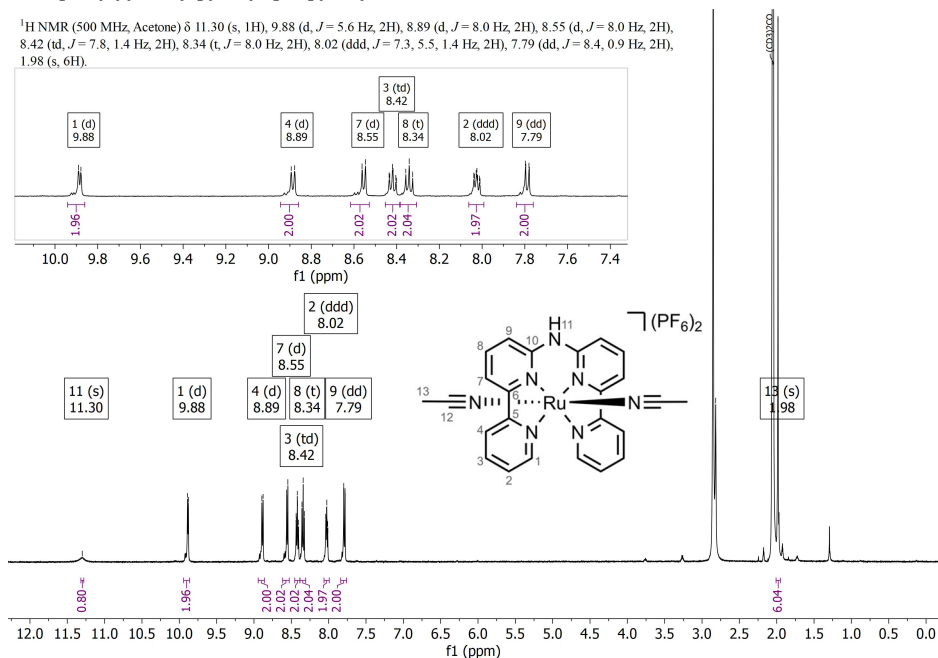


Figure III.25 ¹H-NMR of **[2a](PF₆)₂** in Acetone-*d*₆.

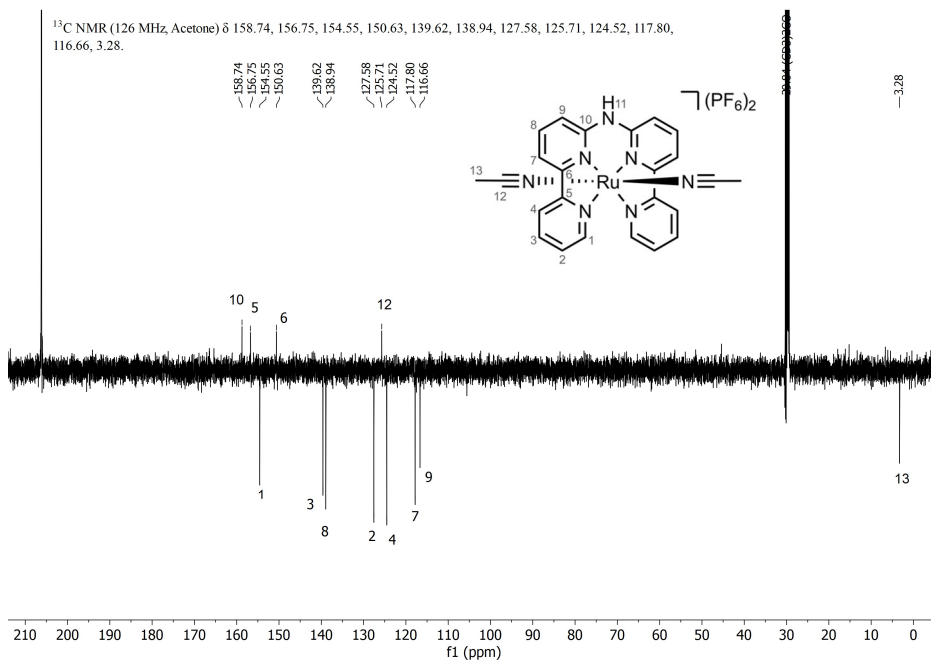


Figure III.26 ^{13}C -APT-NMR of $[\mathbf{2a}](\text{PF}_6)_2$ in Acetone- d_6 .

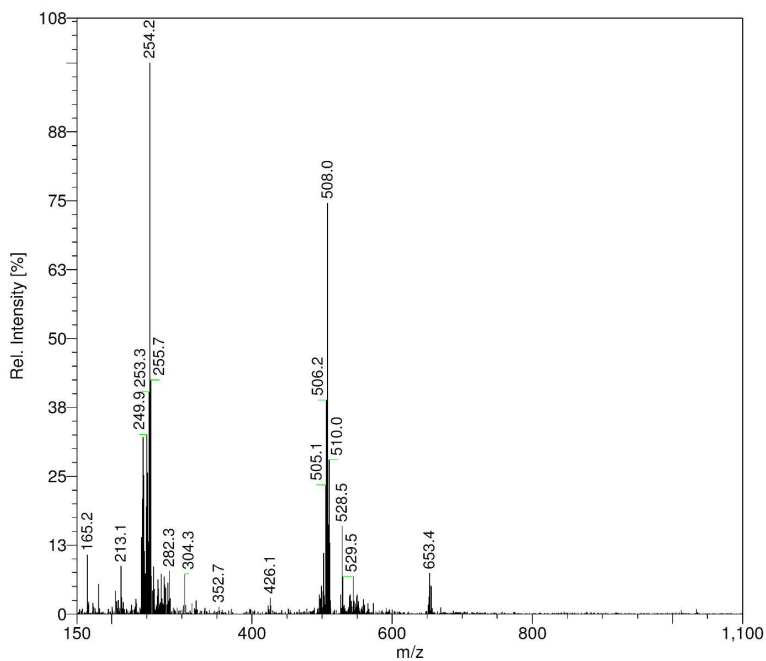
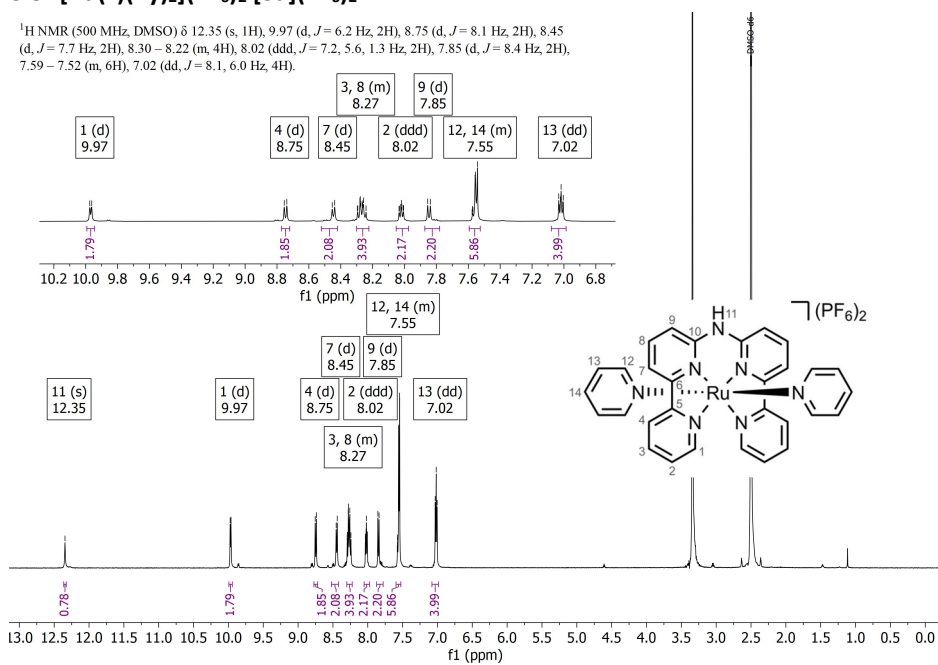


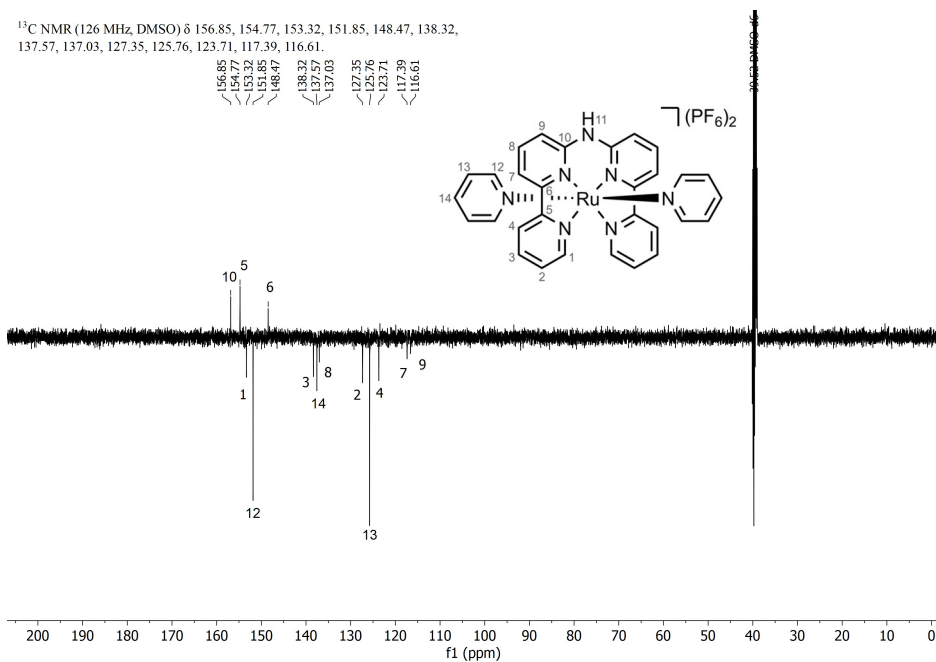
Figure III.27 ESI-MS of $[\mathbf{2a}](\text{PF}_6)_2$. Calculated for $[\text{C}_{24}\text{H}_{21}\text{N}_7\text{Ru}]^{2+}$: 254.5 m/z ; $[\text{C}_{24}\text{H}_{21}\text{N}_7\text{Ru}-\text{H}]^+$: 508.1 m/z .

V.3.3 [Ru(L)(Py)₂](PF₆)₂ [3a](PF₆)₂

¹H NMR (500 MHz, DMSO) δ 12.35 (s, 1H), 9.97 (d, *J* = 6.2 Hz, 2H), 8.75 (d, *J* = 8.1 Hz, 2H), 8.45 (d, *J* = 7.7 Hz, 2H), 8.30 – 8.22 (m, 4H), 8.02 (ddd, *J* = 7.2, 5.6, 1.3 Hz, 2H), 7.85 (d, *J* = 8.4 Hz, 2H), 7.59 – 7.52 (m, 6H), 7.02 (dd, *J* = 8.1, 6.0 Hz, 4H).

Figure III.28 ¹H-NMR of [3a](PF₆)₂ in Acetone-*d*₆.

¹³C NMR (126 MHz, DMSO) δ 156.85, 154.77, 153.32, 151.85, 148.47, 138.32, 137.57, 137.03, 127.35, 125.76, 123.71, 117.39, 116.61.

Figure III.29 ¹³C-APT-NMR of [3a](PF₆)₂ in Acetone-*d*₆.

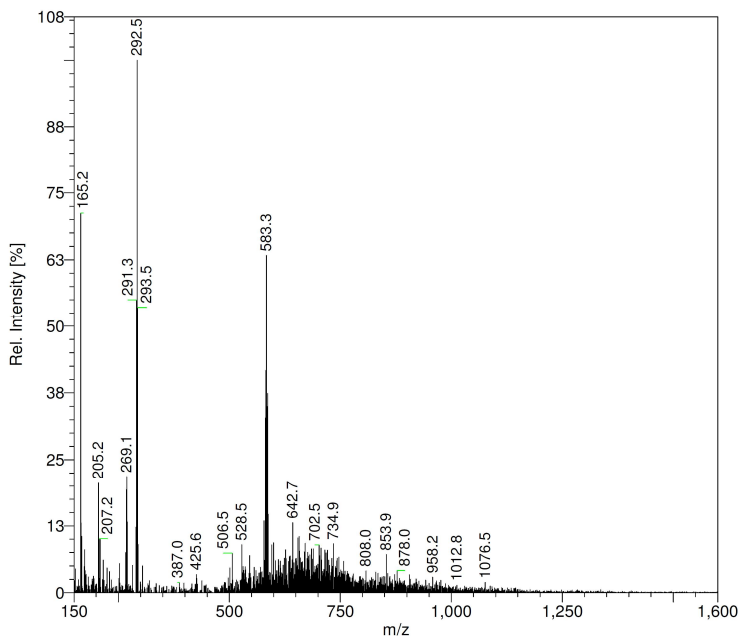


Figure II.30 ESI-MS of **[3a](PF₆)₂**. Calculated for **[C₃₀H₂₅N₇Ru]²⁺**: 292.6 m/z;
[C₃₀H₂₅N₇Ru-H]⁺: 584.3 m/z.

V.3.4 **[Ru(MeL)(MTE)₂](PF₆)₂ [1b](PF₆)₂**

¹H NMR (400 MHz, Acetone) δ 9.85 (ddd, *J* = 5.7, 1.6, 0.8 Hz, 2H), 8.92 (dt, *J* = 8.1, 1.1 Hz, 2H), 8.66 (dd, *J* = 7.9, 0.9 Hz, 2H), 8.47 – 8.37 (m, 5H), 8.08 – 7.99 (m, 5H), 4.22 (s, 3H), 3.75 (t, *J* = 5.2 Hz, 2H), 3.27 (q, *J* = 5.6 Hz, 4H), 1.80 (t, *J* = 5.8 Hz, 4H), 1.36 (s, 6H).

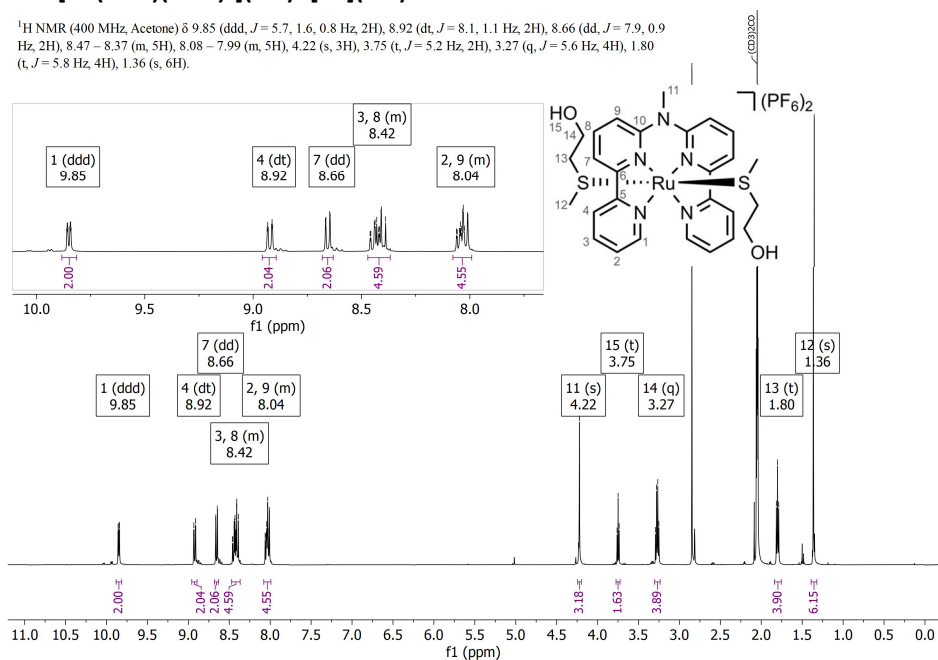
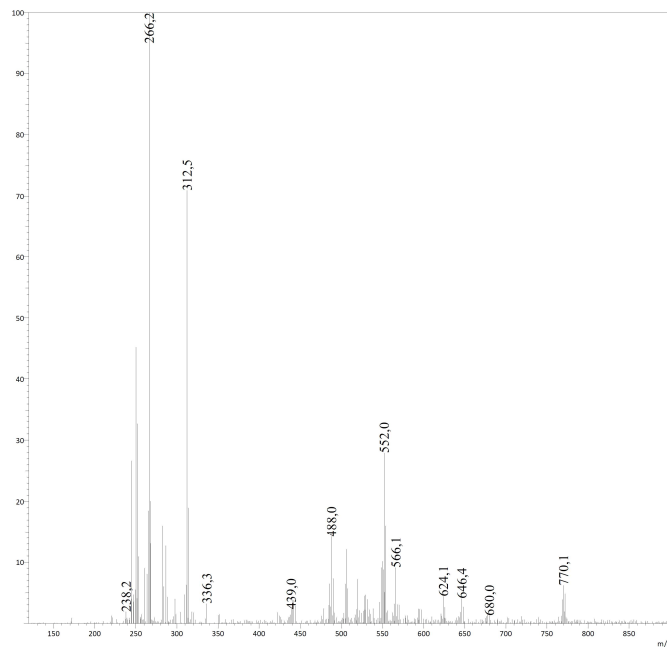
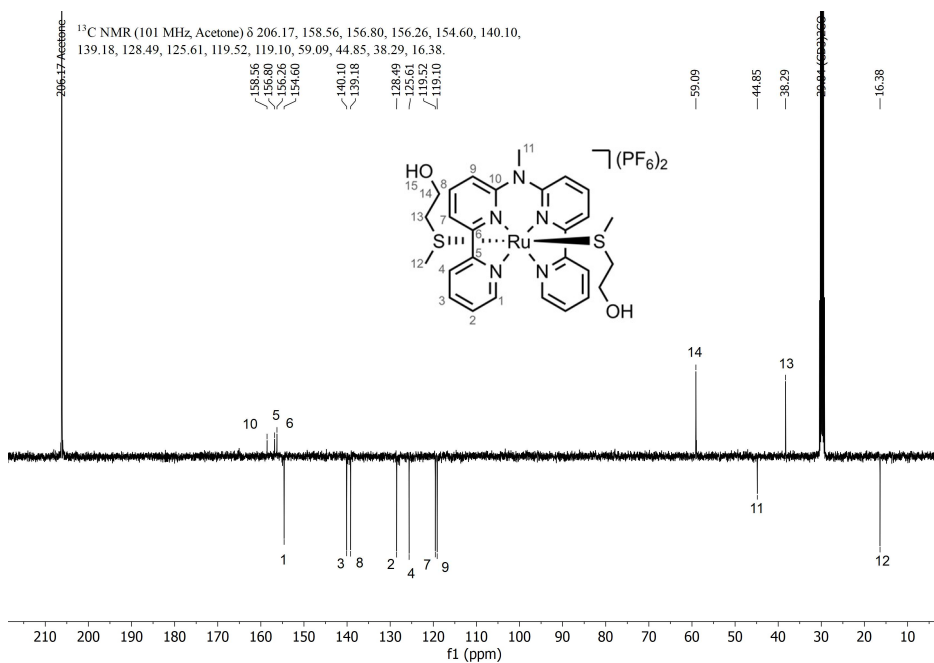
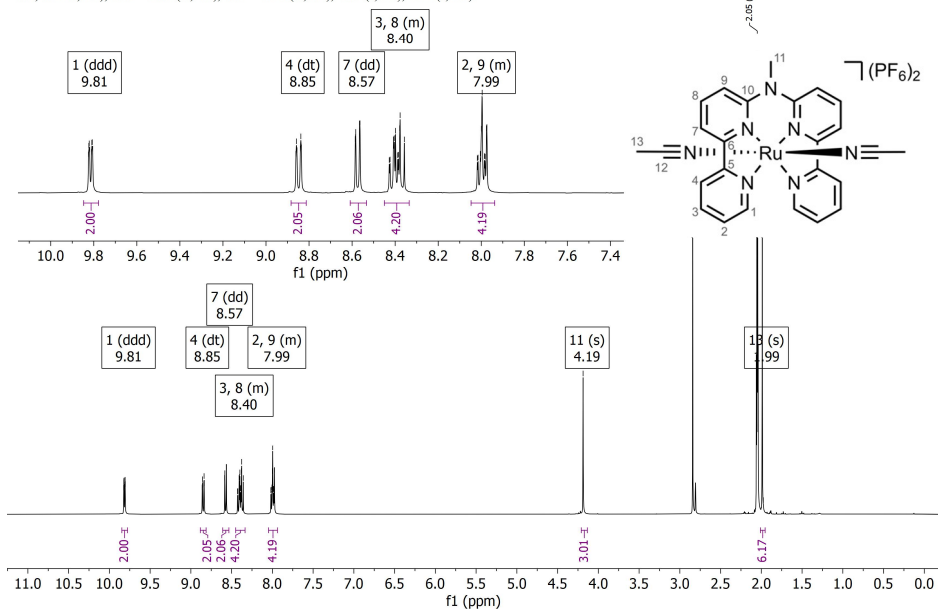
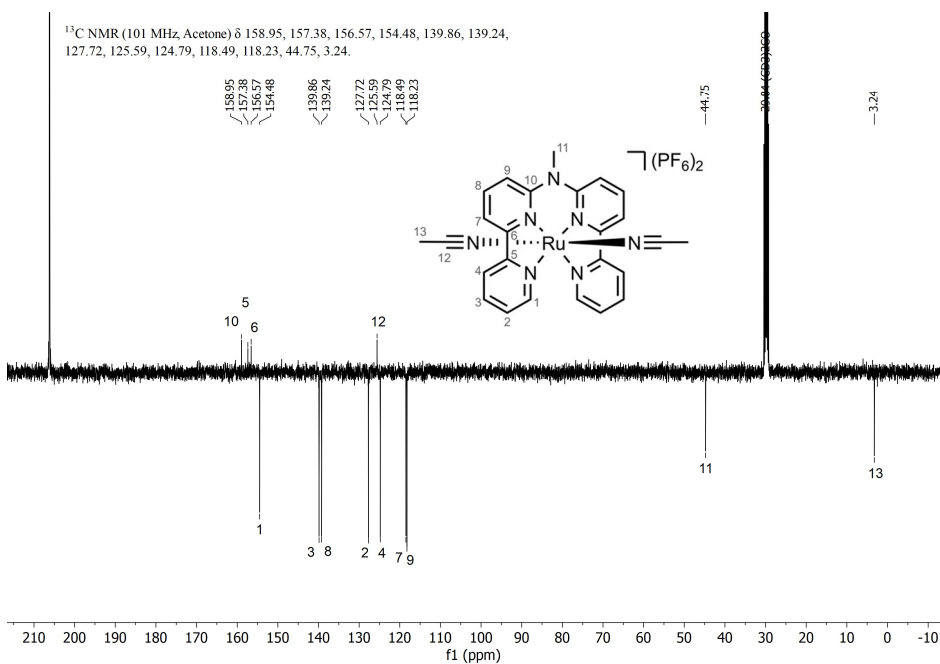


Figure III.31 ¹H-NMR of **[1b](PF₆)₂** in Acetone-*d*₆.



V.3.5 [Ru(MeL)(ACN)₂](PF₆)₂ [2b](PF₆)₂

¹H NMR (400 MHz, Acetone) δ 9.81 (ddd, *J* = 5.6, 1.5, 0.7 Hz, 2H), 8.85 (dt, *J* = 8.2, 1.0 Hz, 2H), 8.57 (dd, *J* = 7.9, 0.9 Hz, 2H), 8.45 – 8.33 (m, 4H), 8.05 – 7.94 (m, 4H), 4.19 (s, 3H), 1.99 (s, 6H).

Figure III.34 ¹H-NMR of [2b](PF₆)₂ in Acetone-*d*₆.Figure III.35 ¹³C-APT-NMR of [2b](PF₆)₂ in Acetone-*d*₆.

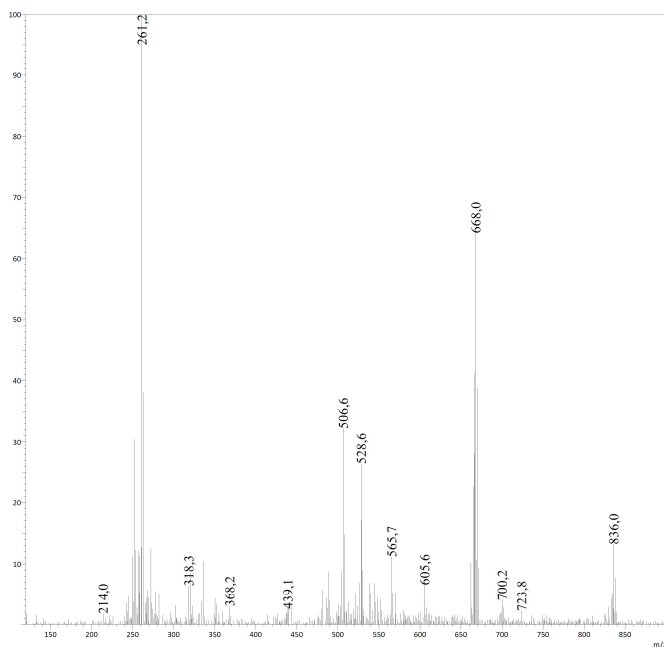


Figure III.36 ESI-MS of $[2b](PF_6)_2$. Calculated for $[C_{25}H_{23}N_7Ru]^{2+}$: 261.5 m/z; $[C_{25}H_{23}N_7Ru+PF_6]^+$: 668.1 m/z.

V.3.6 $[Ru(MeL)(Py)_2](PF_6)_2$ $[3b](PF_6)_2$

1H NMR (500 MHz, Acetone) δ 10.06 (d, $J = 5.6$ Hz, 2H), 8.73 (d, $J = 8.1$ Hz, 2H), 8.48 (d, $J = 7.7$ Hz, 2H), 8.32 (dt, $J = 10.6, 7.8$ Hz, 4H), 8.10 – 8.03 (m, 4H), 7.78 – 7.73 (m, 4H), 7.63 (dd, $J = 8.5, 7.0$ Hz, 2H), 7.02 (t, $J = 6.9$ Hz, 4H), 4.15 (s, 3H).

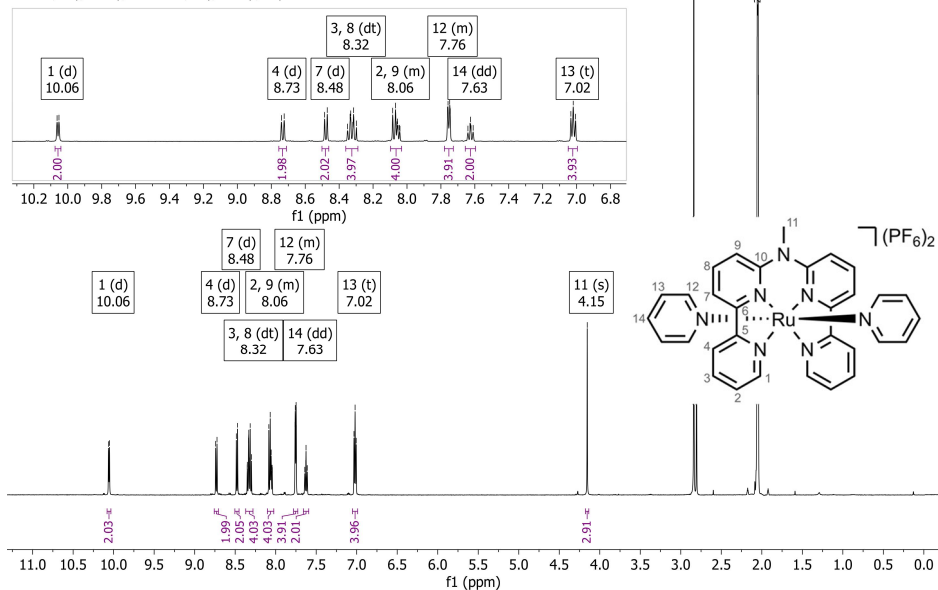
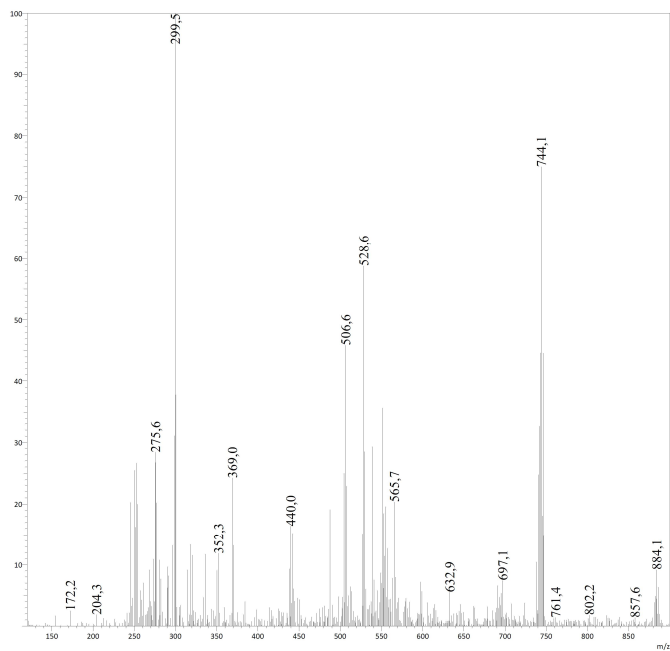
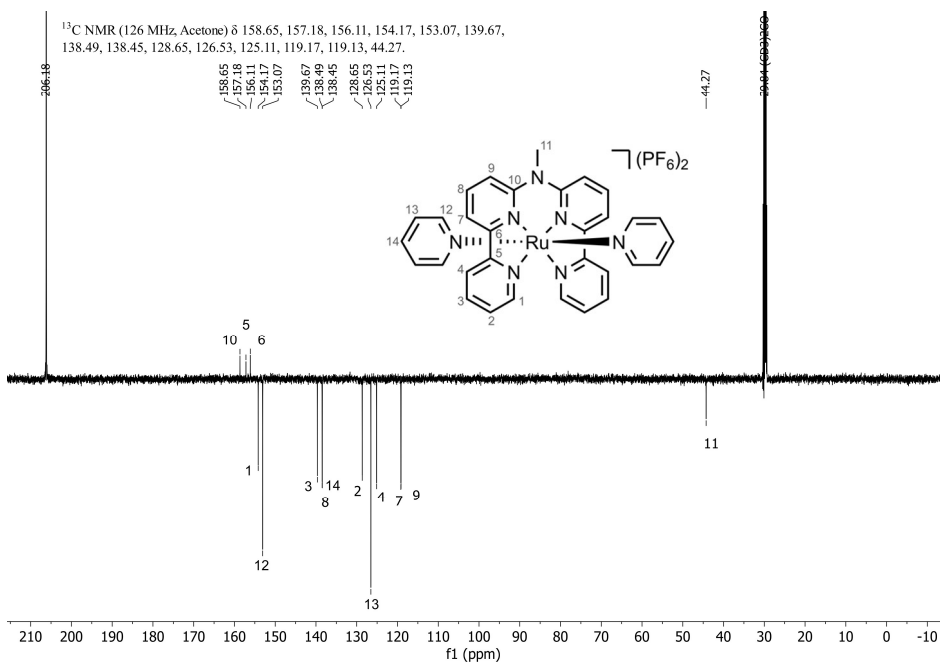
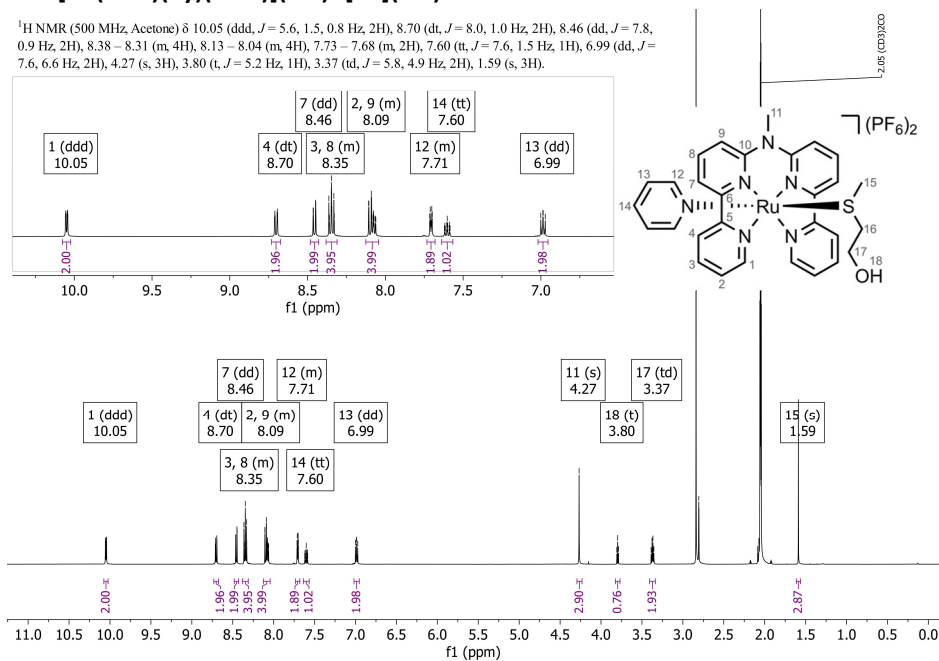
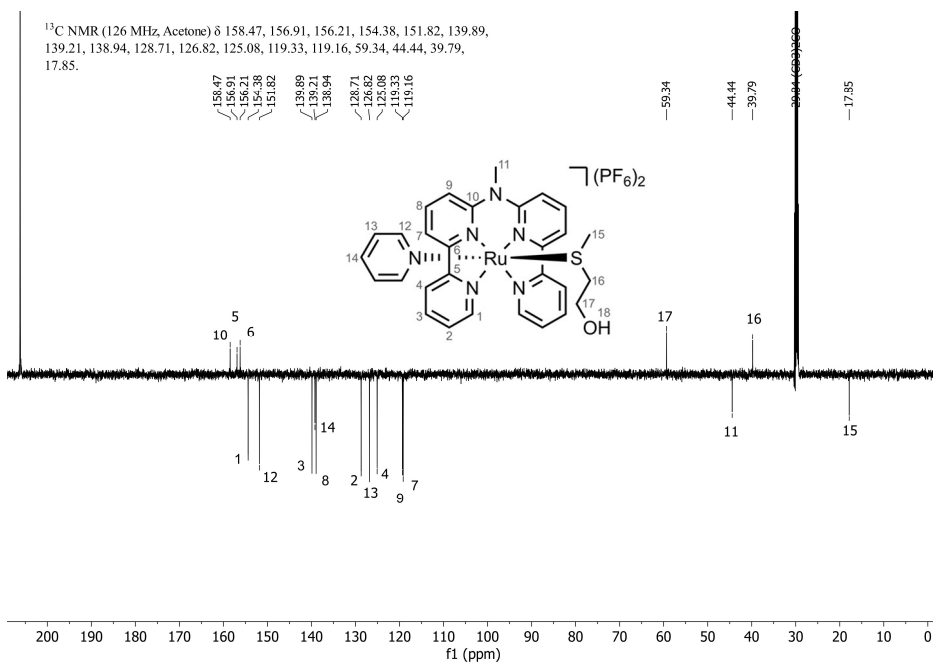


Figure III.37 1H -NMR of $[3b](PF_6)_2$ in $Acetone-d_6$.



V.3.7 [Ru(MeL)(Py)(MTE)](PF₆)₂ [4b](PF₆)₂

¹H NMR (500 MHz, Acetone) δ 10.05 (ddd, *J* = 5.6, 1.5, 0.8 Hz, 2H), 8.70 (dt, *J* = 8.0, 1.0 Hz, 2H), 8.46 (dd, *J* = 7.8, 0.9 Hz, 2H), 8.38 – 8.31 (m, 4H), 8.13 – 8.04 (m, 4H), 7.73 – 7.68 (m, 2H), 7.60 (tt, *J* = 7.6, 1.5 Hz, 1H), 6.99 (dd, *J* = 7.6, 6.6 Hz, 2H), 4.27 (s, 3H), 3.80 (t, *J* = 5.2 Hz, 1H), 3.37 (td, *J* = 5.8, 4.9 Hz, 2H), 1.59 (s, 3H).

Figure III.40 ¹H-NMR of [4b](PF₆)₂ in Acetone-*d*₆.Figure III.41 ¹³C-APT-NMR of [4b](PF₆)₂ in Acetone-*d*₆.

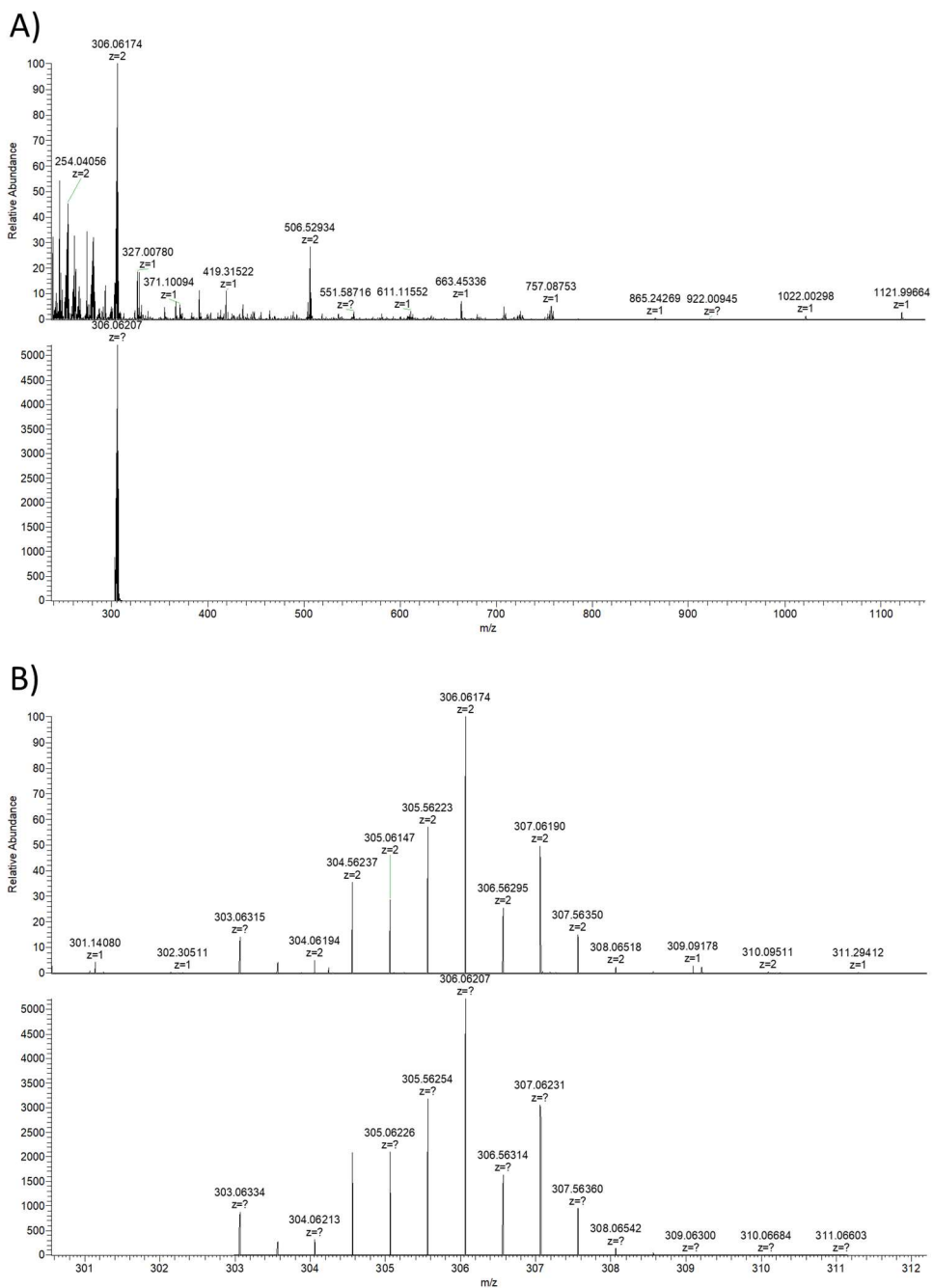


Figure III.42 HRMS of $[4b](PF_6)_2$. A) *Top* measured and *bottom* calculated for $[C_{29}H_{30}N_6ORuS]^{2+}$. B) Zoom between 301 and 312 m/z. *Top* measured and *bottom* calculated for $[C_{29}H_{30}N_6ORuS]^{2+}$.



Appendix IV: Supporting information for Chapter 4

IV.1 Photochemistry

IV.1.1 Molar extinction coefficient determination

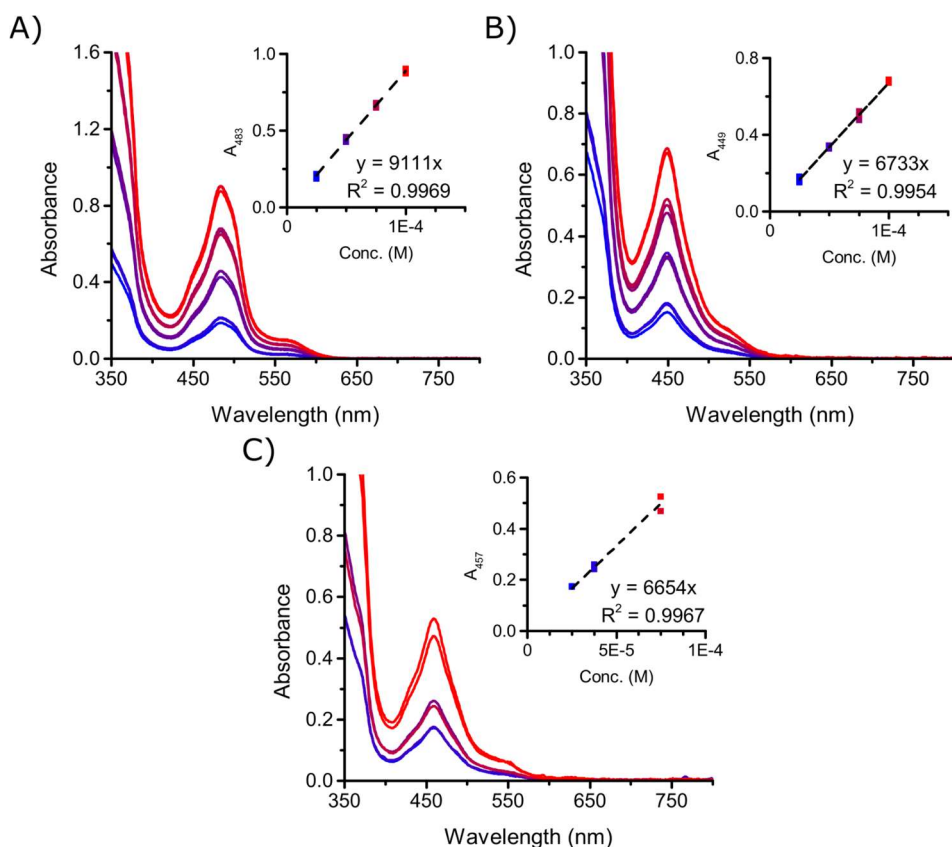


Figure IV.1 UV-Vis spectra of **[1](PF₆)₂**, **[2](PF₆)₂** and **[3](PF₆)₂** at different concentrations in 3 ml 50% acetone in H₂O at 298 K (l = 1 cm). Insets depicted absorption at λ_{\max} . A) **[1](PF₆)₂**: $\epsilon = 9.11 \times 10^3 \text{ M}^{-1}\text{cm}^{-1}$ at 483 nm. B) **[2](PF₆)₂**: $\epsilon = 67.3 \times 10^3 \text{ M}^{-1}\text{cm}^{-1}$ at 449 nm. C) **[3](PF₆)₂**: $\epsilon = 6.65 \times 10^3 \text{ M}^{-1}\text{cm}^{-1}$ at 457 nm.

IV.1.2 Photosubstitution quantum yield measurements

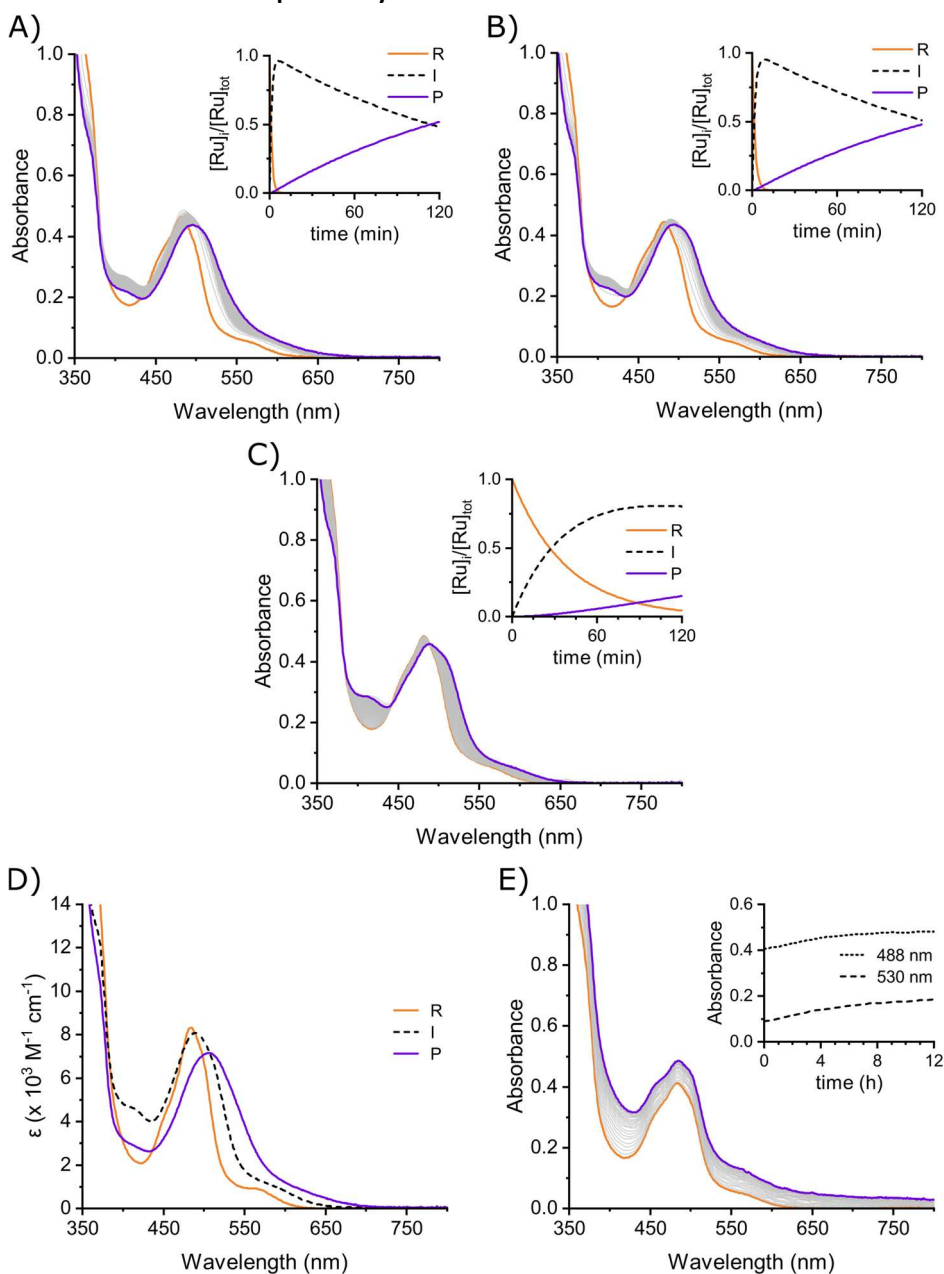


Figure IV.2 Absorbance measurements for $[\mathbf{1}](\text{PF}_6)_2$ at $59.4 \mu\text{M}$ in 50% acetone in H_2O at 298 K. Time-evolution of UV-Vis absorption upon irradiation for 120 min with A) 435 nm (photon flux = 3.26×10^{-7} mol/s), B) 505 nm (photon flux = 2.27×10^{-7} mol/s) and C) 625 nm (photon flux = 4.32×10^{-7} mol/s) (from orange to purple). D) Globally fitted UV-Vis absorption spectra of $[\mathbf{1}](\text{PF}_6)_2$ (R; orange), the mono-aqua intermediate $[\mathbf{6}]^{2+}$ (I; black dashed) and the bis-aqua photoproduct $[\mathbf{8}]^{2+}$ (P; purple). E) Absorption spectra of $[\mathbf{1}](\text{PF}_6)_2$ in the dark for 12 h (from orange to purple).

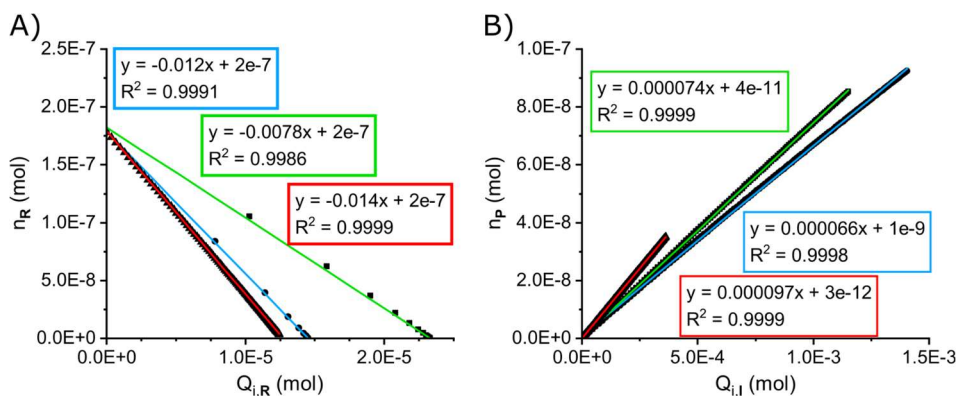


Figure IV.3 Plots for determination photosubstitution quantum yield of $\phi_{1,N}$ (A) and $\phi_{2,N}$ (B) for $[1](PF_6)_2$ at 59.4 μM in 50% acetone in H_2O at 298 K upon irradiation with 435 nm (blue), 505 nm (green) and 625 nm (red).

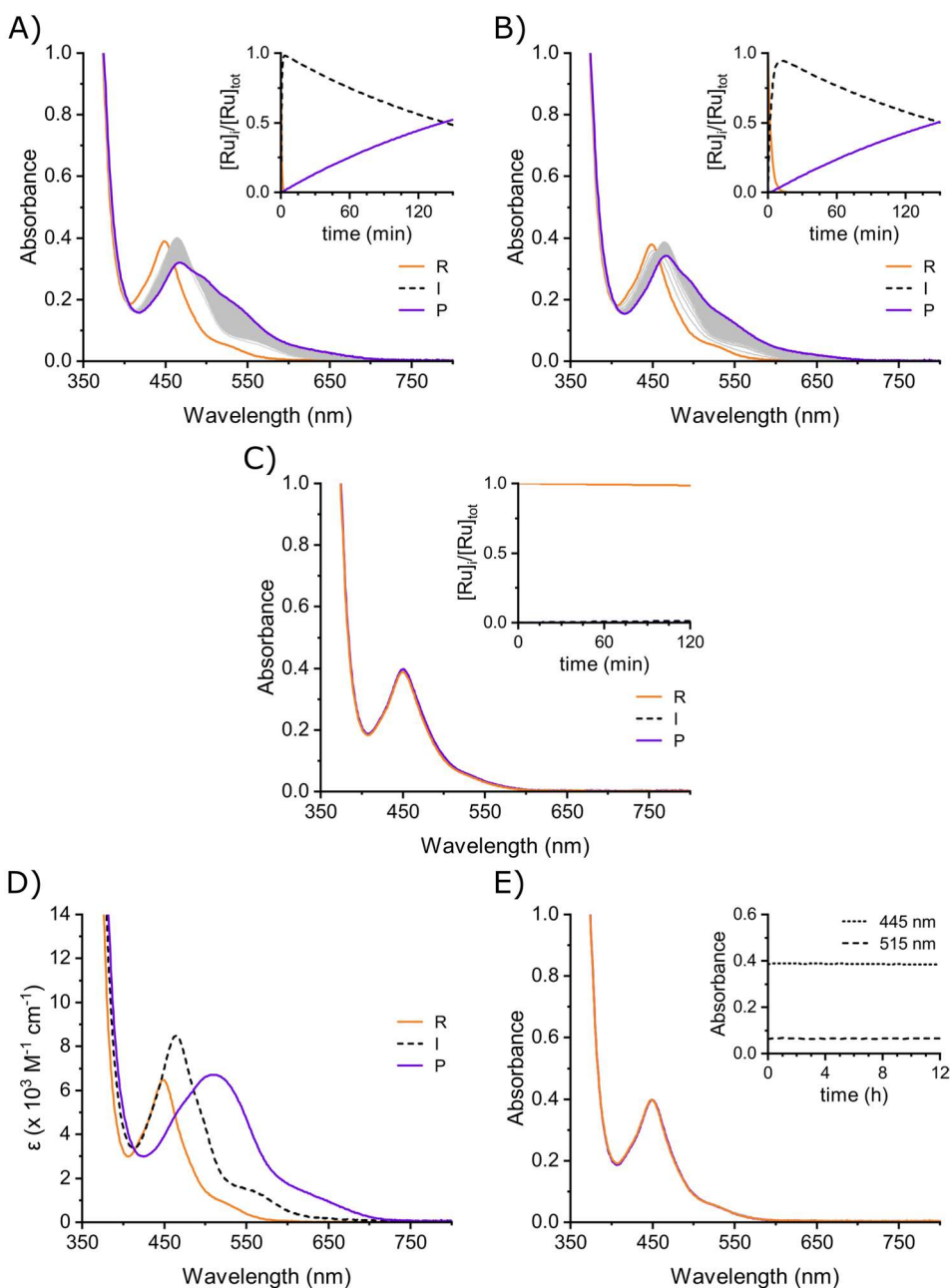


Figure IV.4 Absorbance measurements for $[\mathbf{2}](\text{PF}_6)_2$ at $61.0 \mu\text{M}$ in 50% acetone in H_2O at 298 K. Time-evolution of UV-Vis absorption upon irradiation for 150 min with A) 435 nm (photon flux = $3.26 \times 10^{-7} \text{ mol/s}$), B) 505 nm (photon flux = $2.27 \times 10^{-7} \text{ mol/s}$) and C) 625 nm (photon flux = $4.32 \times 10^{-7} \text{ mol/s}$) (from orange to purple). D) Globally fitted UV-Vis absorption spectra of $[\mathbf{2}](\text{PF}_6)_2$ (R; orange), the mono-aqua intermediate $[\mathbf{7}]^{2+}$ (I; black dashed) and the bis-aqua photoproduct $[\mathbf{8}]^{2+}$ (P; purple). E) Absorption spectra of $[\mathbf{2}](\text{PF}_6)_2$ in the dark for 12 h (from orange to purple).

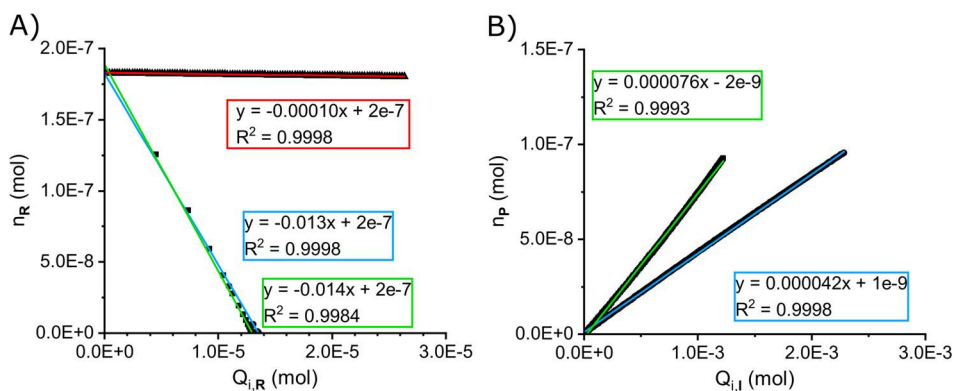


Figure IV.5 Plots for determination photosubstitution quantum yield $\phi_{1,s}$ (A) and $\phi_{2,s}$ (B) for $[2](PF_6)_2$ at $61.0 \mu\text{M}$ in 50% acetone in H_2O at 298 K upon irradiation with 435 nm (blue), 505 nm (green) and 625 nm (red).

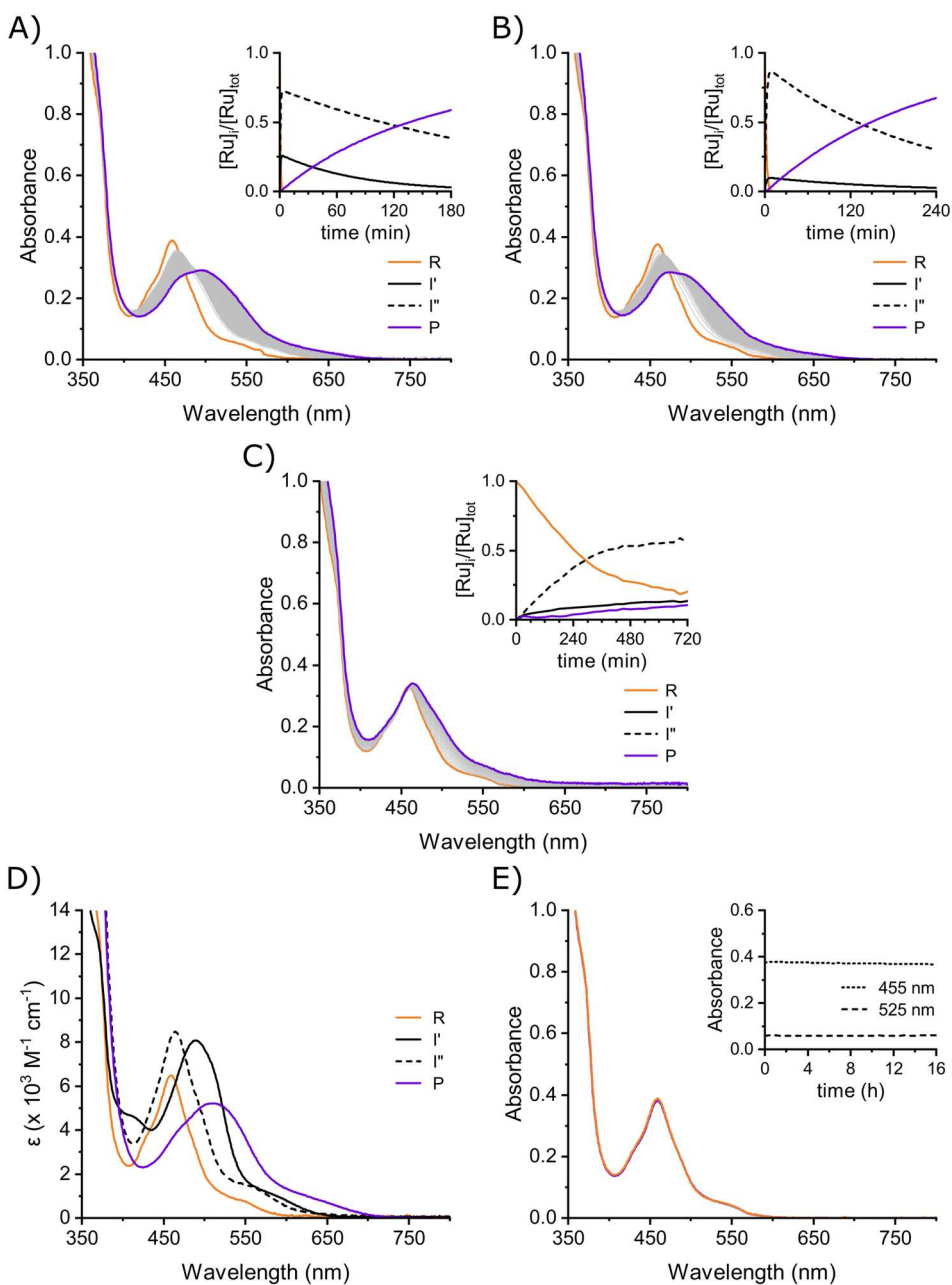


Figure IV.6 Absorbance measurements for $[3](PF_6)_2$ at 56.2 μM in 1:1 acetone:H₂O at 298 K. Time-evolution of UV-Vis absorption upon irradiation with A) 435 nm for 180 min (photon flux = 3.25×10^{-7} mol/s), B) 505 nm for 240 min (photon flux = 2.27×10^{-7} mol/s) and C) 625 nm for 720 min (photon flux = 4.24×10^{-7} mol/s) (from orange to purple). D) Globally fitted UV-Vis absorption spectra of $[1](PF_6)_2$ (R; orange line), the mono-aqua intermediates $[6]^{2+}$ (I' ; black dashed) and $[7]^{2+}$ (I'' ; solid black)

and the bis-aqua photoproduct $[8]^{2+}$ (P; purple line). E) Absorption spectra of $[3](PF_6)_2$ in the dark for 16 h (from orange to purple).

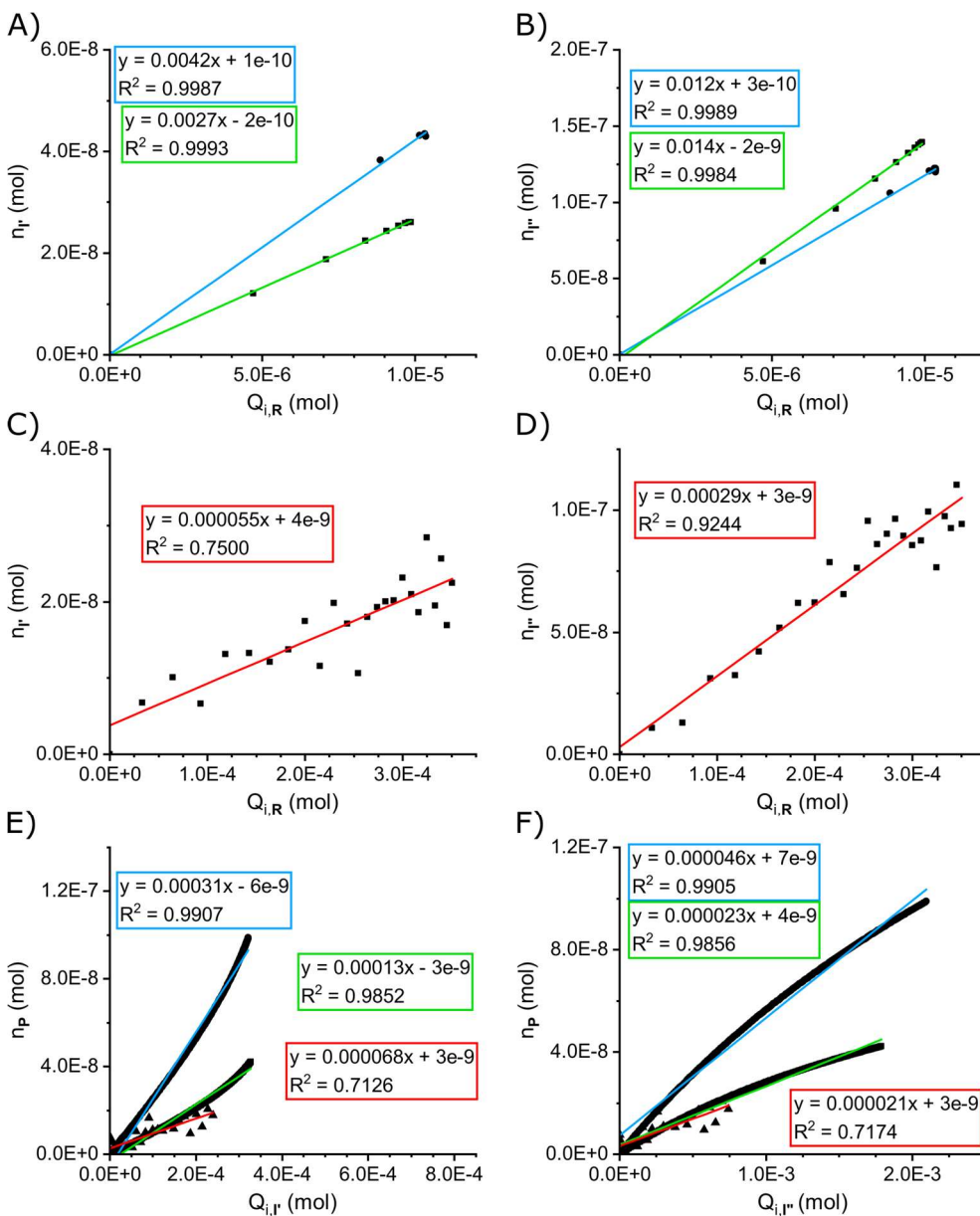


Figure IV.7 Plots for determination photosubstitution quantum yield $\phi_{1,s}$ (A, C), $\phi_{1,N}$ (B, D), $\phi_{2,N}$ (E) and $\phi_{2,s}$ (F) for $[3](PF_6)_2$ at 56.2 μ M in 50% acetone in H_2O at 298 K upon irradiation with 435 nm (blue), 505 nm (green) and 625 nm (red).

IV.1.3 Singlet oxygen generation quantum yield measurement

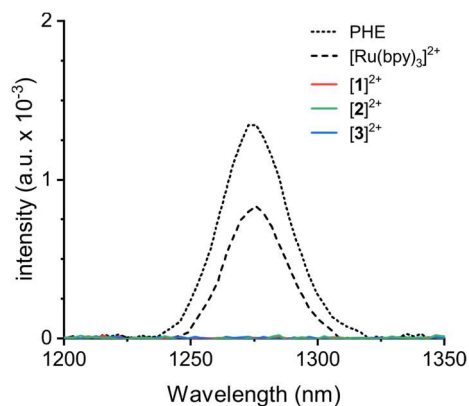


Figure IV.8 Near-infrared emission spectra of $^1\text{O}_2$ phosphorescence ($\lambda_{\text{em}} = 1275 \text{ nm}$) sensitized by $[\mathbf{1}](\text{PF}_6)_2 - [\mathbf{3}](\text{PF}_6)_2$, $[\text{Ru}(\text{bpy})_3]\text{Cl}_2$ and perinaphthenone (PHE) in aerated acetonitrile at 298 K under blue light irradiation (450 nm, 80 mW/cm²).

Table IV.1 Data for the determination of singlet oxygen generation quantum yields in aerated acetonitrile.

Compound	Abs. (450 nm)	Integrated intensity	$\phi_{\Delta} (^1\text{O}_2)$
Perinaphthenone	0.0960	0.0439	0.98
$[\text{Ru}(\text{bpy})_3]\text{Cl}_2$	0.1073	0.0266	0.53
$[\mathbf{1}](\text{PF}_6)_2$	0.1049	0.0004	<0.01
$[\mathbf{2}](\text{PF}_6)_2$	0.1127	0.0004	<0.01
$[\mathbf{3}](\text{PF}_6)_2$	0.1159	0.0001	<0.01

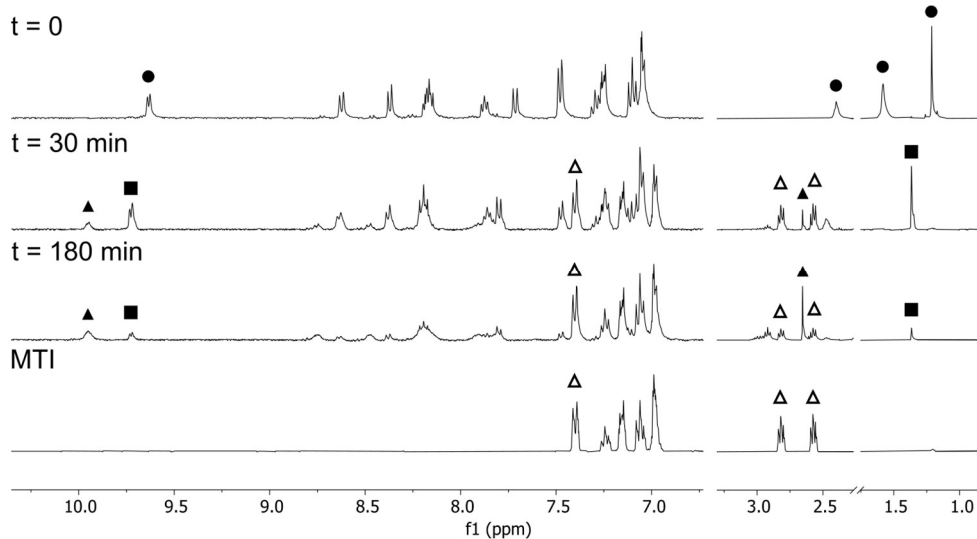
IV.1.4 Photosubstitution followed by $^1\text{H-NMR}$ 

Figure IV.9 Time-evolution of $^1\text{H-NMR}$ spectra of $[\mathbf{2}](\text{PF}_6)_2$ (\bullet) in 1:5 D_2O :Acetone- D_6 upon irradiation with 530 nm. Symbols indicate intermediate $[\mathbf{7}]^{2+}$ (\blacksquare), photoproduct $[\mathbf{8}]^{2+}$ (\blacktriangle) and MTI (\triangle).

IV.1.5 Photoactivation in biological media

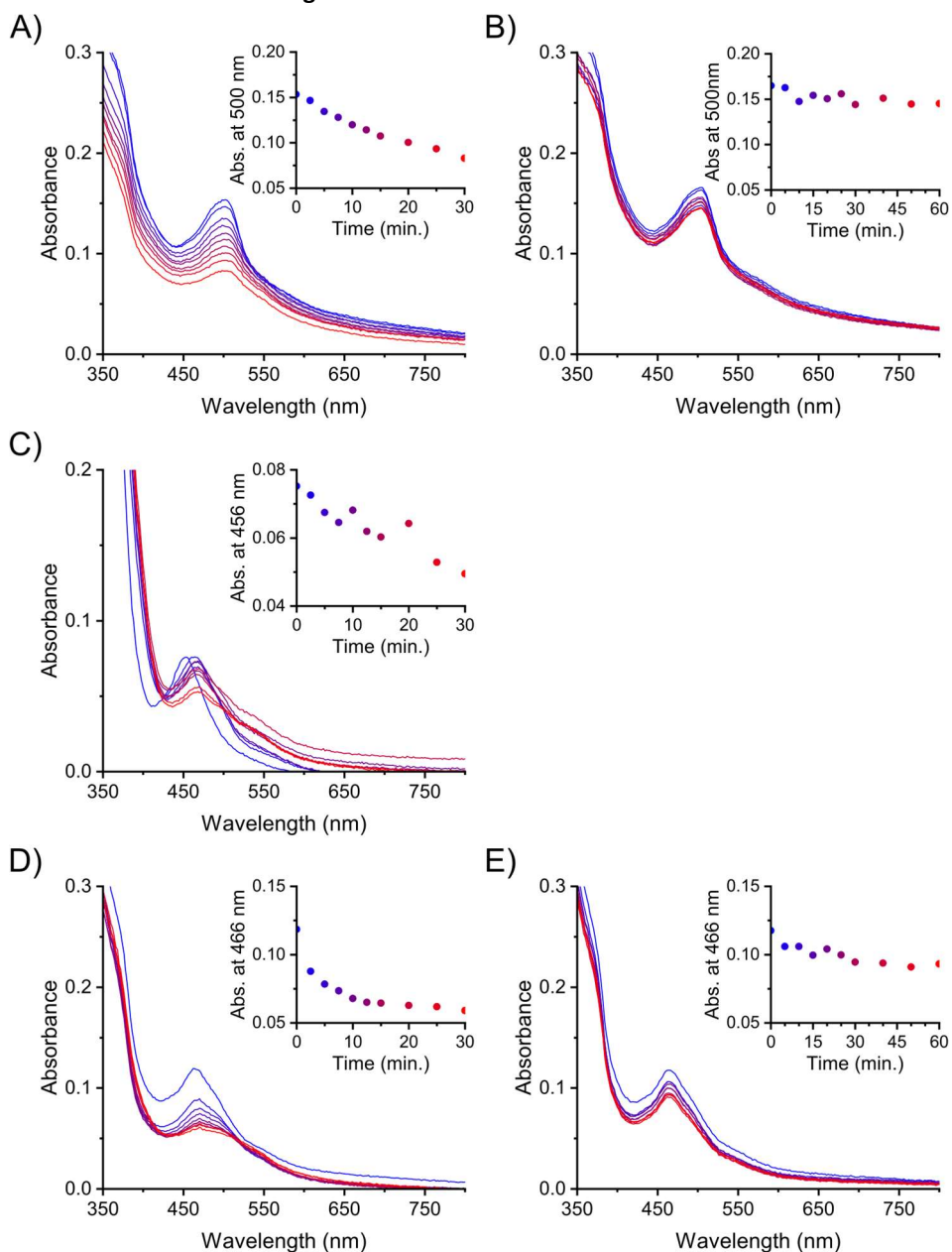


Figure IV.10 Time-evolution (blue to red) of UV-Vis absorbance spectra of [1]Cl₂ (A, B), [2]Cl₂ (C) and [3]Cl₂ (D, E) in OptiMEM complete media + 0.14% DMSO upon irradiation with green (A, C, D; 520 ± 35 nm; 17.1 mW · cm⁻²) and red (B, E; 630 ± 24 nm, 31.3 mW · cm⁻²) light array at 37 °C (conc. = 5 × 10⁻⁵ M; v = 200 μL).

IV.2 Cytotoxicity

Table IV.2 Cytotoxicity in the dark and under irradiation with green (520 nm) and red (630 nm) light in normoxic (21% O₂) and hypoxic (1% O₂) conditions.^a

Cell line	% O ₂	[1]Cl ₂			[2]Cl ₂			[3]Cl ₂		
		EC ₅₀ , dark Cl ₉₅ (μM)	EC ₅₀ , 520 Cl ₉₅ (μM)	EC ₅₀ , 630 Cl ₉₅ (μM)	EC ₅₀ , dark Cl ₉₅ (μM)	EC ₅₀ , 520 Cl ₉₅ (μM)	EC ₅₀ , 630 Cl ₉₅ (μM)	EC ₅₀ , dark Cl ₉₅ (μM)	EC ₅₀ , 520 Cl ₉₅ (μM)	EC ₅₀ , 630 Cl ₉₅ (μM)
A375	21%	6.38 ±3.29	0.53 ±0.38	1.38 ±0.61	0.95 ±0.18	0.74 ±0.17	1.03 ±0.32	2.35 ±1.62	0.27 ±0.12	1.20 ±0.49
	1%	19.7 ±4.26	0.93 ±0.49	1.99 ±1.68	0.84 ±1.29	1.10 ±0.65	0.78 ±1.77	3.47 ±2.03	0.22 ±0.15	2.17 ±0.86
A549	21%	9.81 ±5.90	0.45 ±0.19	1.80 ±0.78	6.63 ±2.67	2.55 ±1.43	4.21 ±1.30	3.66 ±0.61	1.10 ±0.36	3.15 ±0.96
	1%	19.5 ±4.39	0.60 ±0.43	1.43 ±1.15	0.65 ±1.50	1.10 ±0.93	0.66 ±0.28	2.98 ±0.70	0.37 ±0.18	2.04 ±1.08
U87MG	21%							>75	7.51 ±4.26	13.8 ±11.5
	1%							>75	3.13 ±2.70	8.44 ±7.86
U251	21%							14.4 ±3.16	7.39 ±2.29	12.3 ±5.87

^a Metabolic activity inhibition effective concentrations (EC₅₀ in μM) with 95% confidence interval (Cl₉₅ in μM) for [1]Cl₂, [2]Cl₂ and [3]Cl₂ on skin (A375), lung (A549) and glioblastoma (U87MG, U251) cancer cell lines. Irradiation was done with green light (520 ± 35 nm, dose = 30.78 J/cm²) and red light (630 ± 24 nm, dose = 114.84 J/cm²). Treatment-to-irradiation interval was 24 h. ^b Photo index (PI) = EC₅₀, dark/EC₅₀, light.

Table IV.3 Cytotoxicity in the dark and under irradiation with green (520 nm) and red (630 nm) light in normoxic (21% O₂) and hypoxic (1% O₂) conditions.^a

Cell line	% O ₂	[4]Cl ₂						STF	MTI	STF + MTI
		EC ₅₀ , dark Cl ₉₅ (μM)	EC ₅₀ , 520 Cl ₉₅ (μM)	EC ₅₀ , 630 Cl ₉₅ (μM)	PI ₅₂₀ ^b	PI ₆₃₀ ^b	EC ₅₀ , dark Cl ₉₅ (μM)			
A375	21%	>100	>100	-	-	-	0.84 ±0.55	0.26 ±0.18	0.29 ±0.06	
	1%	>100	>100	-	-	-	2.40 ±1.00	1.97 ±0.89	0.92 ±0.32	
A549	21%	>100	>100	-	-	-	2.30 ±1.52	6.21 ±2.63	1.01 ±0.47	
	1%	>100	>100	-	-	-	4.94 ±0.96	0.91 ±0.38	0.47 ±0.23	
U87MG	21%	>100	>100	-	-	-	18.4 ±0.46	1.79 ±1.27	1.25 ±0.57	
	1%	>100	>100	-	-	-	>25	2.95 ±1.89	1.25 ±0.57	
U251	21%	>100	>100	-	-	-	2.53 ±1.55	4.71 ±2.33	0.49 ±0.22	

^a Metabolic activity inhibition effective concentrations (EC₅₀ in μM) with 95% confidence interval (Cl₉₅ in μM) for [1]Cl₂, [2]Cl₂ and [3]Cl₂ on skin (A375), lung (A549) and glioblastoma (U87MG, U251) cancer cell lines. Irradiation was done with green light (520 ± 35 nm, dose = 30.78 J/cm²) and red light (630 ± 24 nm, dose = 114.84 J/cm²). Treatment-to-irradiation interval was 24 h. ^b Photo index (PI) = EC₅₀, dark/EC₅₀, light.

IV.3 Cellular uptake

Table IV.4 Cellular ruthenium uptake (in ng/ 10⁶ cells and % of administered dose per 10⁶ cells, both with standard deviation) determined by ICPMS in A375, U87MG and U251 incubated under normoxic (21% O₂) or hypoxic (1% O₂) conditions with [1]Cl₂ (2 μM), [2]Cl₂ (0.5 μM) and [3]Cl₂ (1 μM for A375, 5 μM for U87MG NX, 10 μM for U87MG HX and U251) for 24 hours in the dark.

Cell line	% O ₂	[1]Cl ₂		[2]Cl ₂		[3]Cl ₂	
		Ru content (ng/10 ⁶ cells)	% / 10 ⁶ cells	Ru content (ng/10 ⁶ cells)	% / 10 ⁶ cells	Ru content (ng/10 ⁶ cells)	% / 10 ⁶ cells
A375	21%	10.7 ± 2.75	19.3 ± 7.26	0.12 ± 0.02	0.99 ± 0.16	0.63 ± 0.08	2.73 ± 0.32
	1%	2.64 ± 1.47	5.89 ± 2.09	0.21 ± 0.01	1.37 ± 0.06	0.76 ± 0.34	2.50 ± 0.88
U87MG	21%	-	-	-	-	4.43 ± 1.05	7.86 ± 2.67
	1%	-	-	-	-	10.0 ± 3.53	7.03 ± 3.71
U251	21%	-	-	-	-	14.3 ± 6.61	11.3 ± 3.17

IV.4 Compound characterization

IV.4.1 [Ru(MeL)Cl₂] [5]

¹H NMR (400 MHz, DMSO) δ 9.64 (dd, *J* = 5.8, 1.5 Hz, 2H), 8.67 (dd, *J* = 8.2, 1.4 Hz, 2H), 8.38 (dd, *J* = 7.9, 0.9 Hz, 2H), 8.06 (td, *J* = 7.8, 1.4 Hz, 2H), 7.96 (t, *J* = 8.1 Hz, 2H), 7.73 (ddd, *J* = 7.2, 5.6, 1.3 Hz, 2H), 7.56 (dd, *J* = 8.5, 0.9 Hz, 2H), 3.96 (s, 3H).

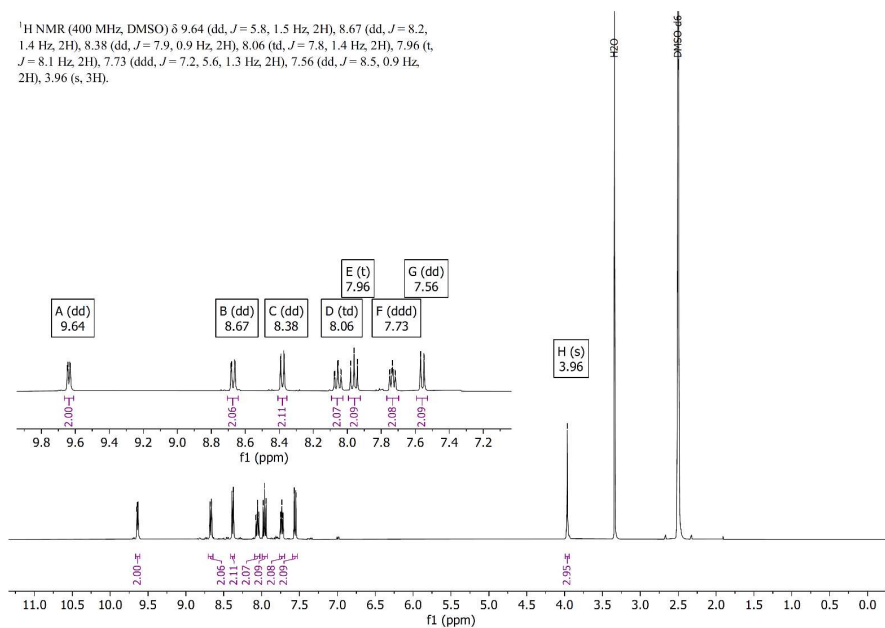


Figure IV.13 ¹H-NMR of [5] in DMSO-*d*₆.

^{13}C NMR (101 MHz, DMSO) δ 159.05, 158.33, 154.64, 153.54, 135.61, 133.21, 124.71, 122.11, 116.33, 114.25, 43.83.

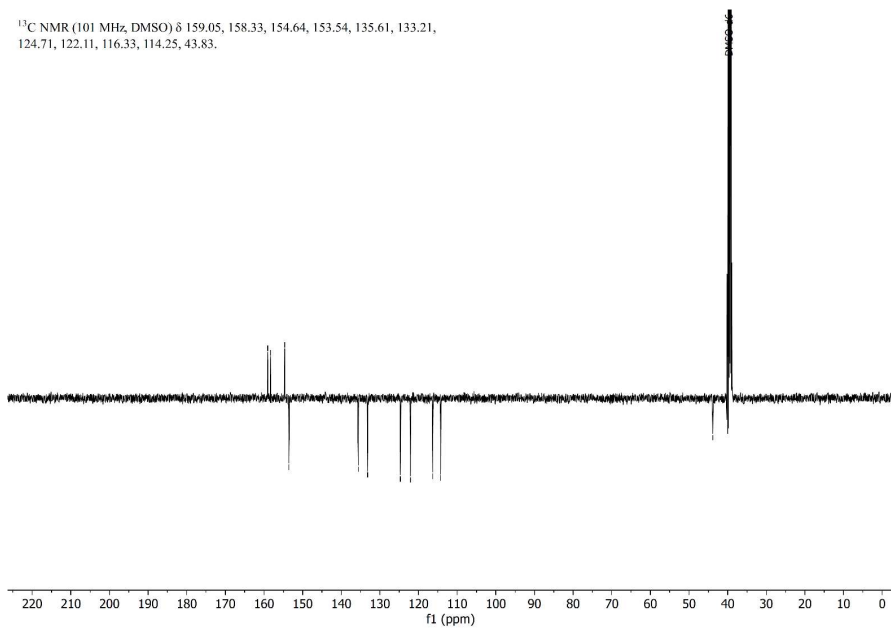


Figure IV.14 ^{13}C -APT-NMR of [5] in DMSO- d_6 .

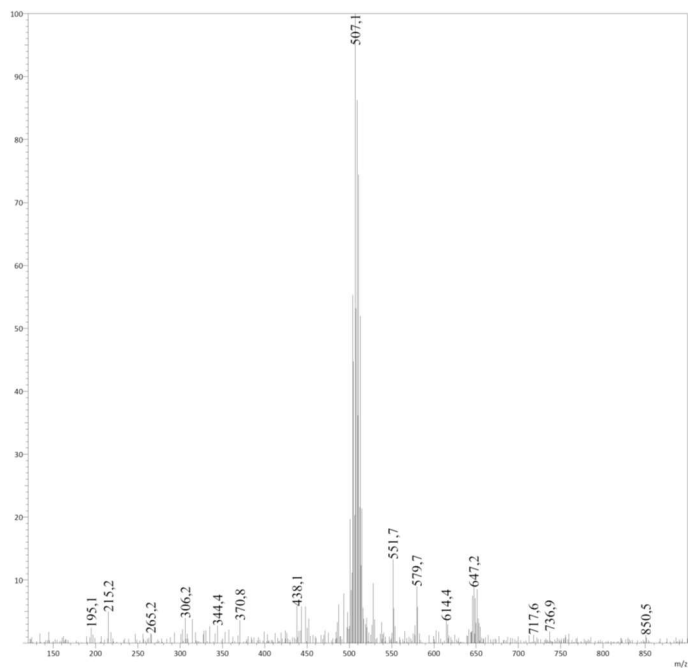
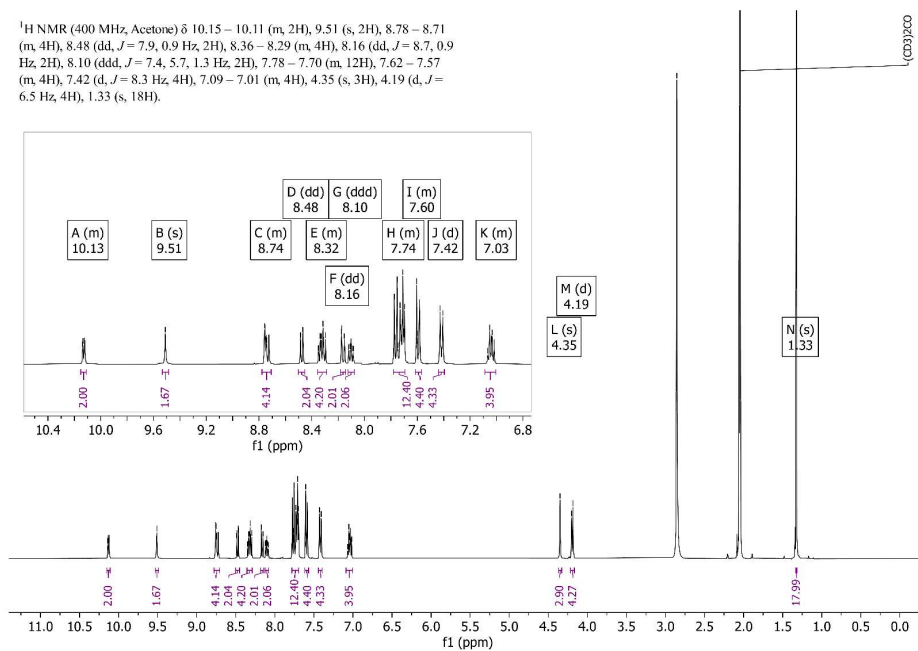
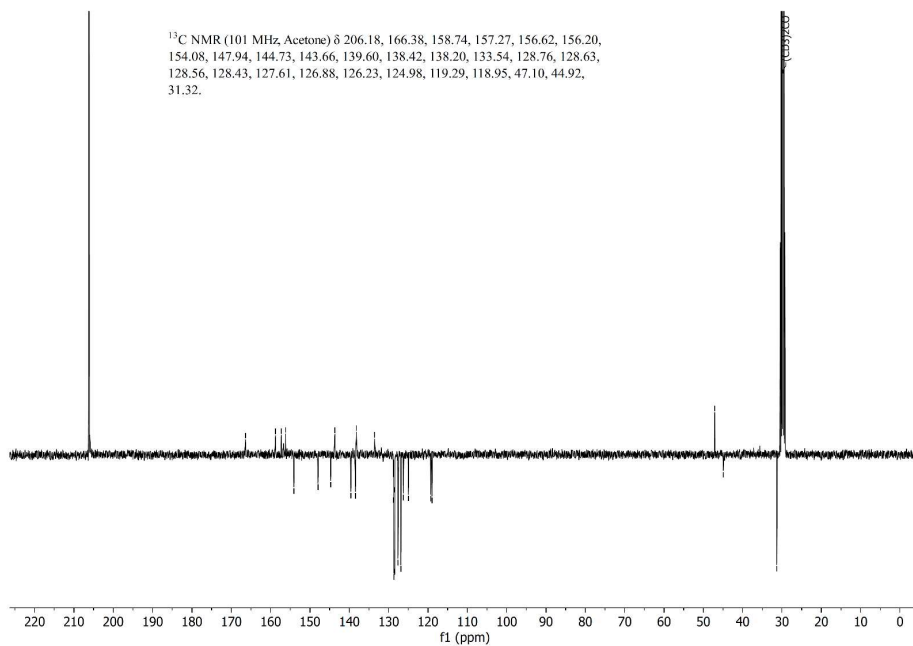


Figure IV.15 ESI-MS of [5]. Calculated for $[\text{C}_{21}\text{H}_{17}\text{N}_5\text{RuCl} + \text{CH}_3\text{OH}]^+$: 508.1 m/z.

IV.4.2 [Ru(MeL)(STF-31)₂]²⁺ [1]²⁺

¹H NMR (400 MHz, Acetone) δ 10.15 – 10.11 (m, 2H), 9.51 (s, 2H), 8.78 – 8.71 (m, 4H), 8.48 (dd, *J* = 7.9, 0.9 Hz, 2H), 8.36 – 8.29 (m, 4H), 8.16 (dd, *J* = 8.7, 0.9 Hz, 2H), 8.10 (ddd, *J* = 7.4, 5.7, 1.3 Hz, 2H), 7.78 – 7.70 (m, 12H), 7.62 – 7.57 (m, 4H), 7.42 (d, *J* = 8.3 Hz, 4H), 7.09 – 7.01 (m, 4H), 4.35 (s, 3H), 4.19 (d, *J* = 6.5 Hz, 4H), 1.33 (s, 18H).

Figure IV.16 ¹H-NMR of [1](PF₆)₂ in Acetone-*d*₆.Figure IV.17 ¹³C-APT-NMR of [1](PF₆)₂ in Acetone-*d*₆.

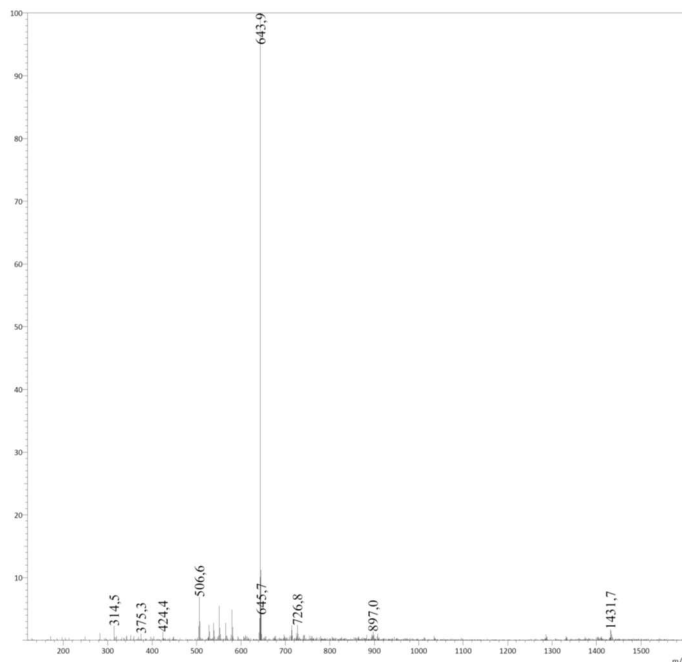


Figure IV.18 ESI-MS of $[1](PF_6)_2$. Calculated for $[C_{67}H_{67}N_{11}O_6S_2Ru]^{2+}$: 643.7 m/z.

1H NMR (400 MHz, MeOD) δ 9.90 (d, $J = 5.6$ Hz, 2H), 8.64 (d, $J = 8.1$ Hz, 2H), 8.50 (d, $J = 2.3$ Hz, 2H), 8.38 (d, $J = 7.8$ Hz, 2H), 8.24 (dt, $J = 11.2, 7.6$ Hz, 4H), 8.06 – 7.98 (m, 4H), 7.76 – 7.70 (m, 4H), 7.69 – 7.64 (m, 4H), 7.61 (ddd, $J = 8.5, 2.3, 1.2$ Hz, 2H), 7.57 – 7.53 (m, 4H), 7.40 (d, $J = 5.5$ Hz, 2H), 7.35 (d, $J = 8.1$ Hz, 4H), 6.95 (dd, $J = 8.4, 5.6$ Hz, 2H), 4.15 (s, 3H), 4.11 (s, 4H), 1.32 (s, 18H).

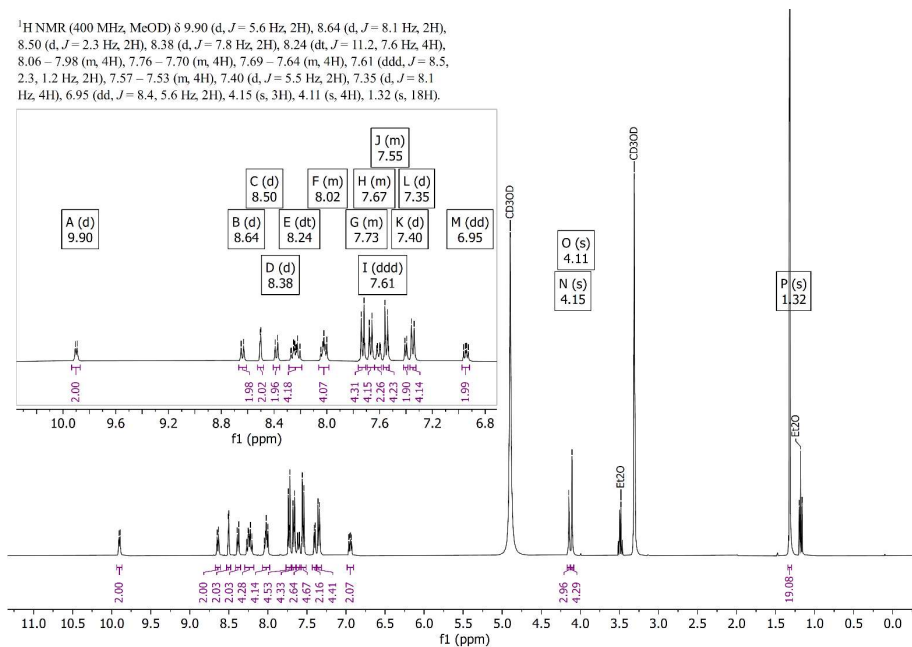


Figure IV.19 1H -NMR of $[1]Cl_2$ in MeOD.

^{13}C NMR (101 MHz, MeOD) δ 168.01, 159.17, 157.68, 157.47, 156.52, 154.23, 148.05, 144.83, 143.90, 139.87, 139.06, 138.80, 138.62, 133.90, 128.92, 128.76, 127.87, 127.16, 126.35, 125.37, 119.36, 119.27, 47.27, 44.49, 31.46.

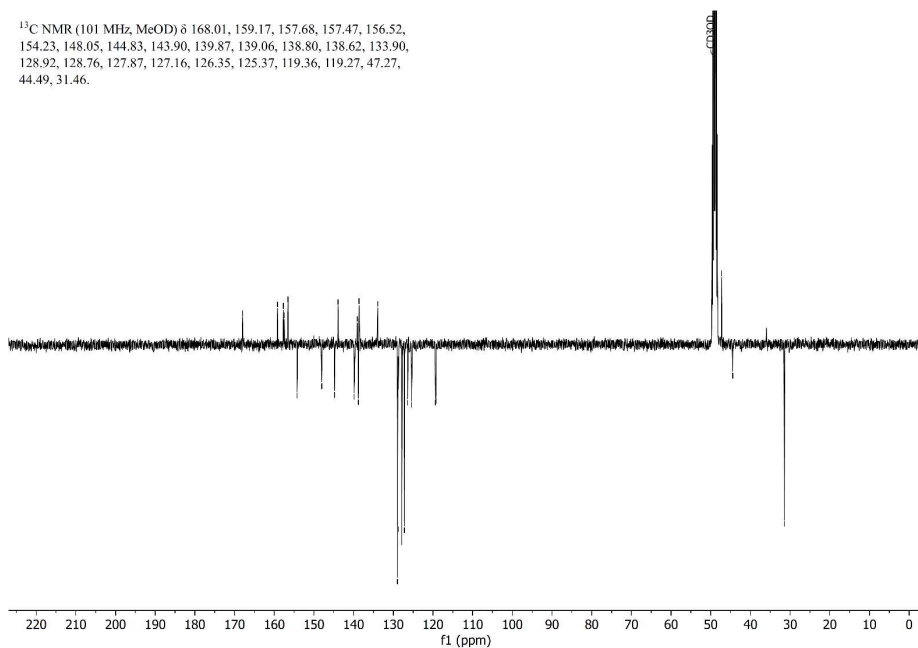


Figure IV.20 ^{13}C -APT-NMR of $[1]\text{Cl}_2$ in MeOD.

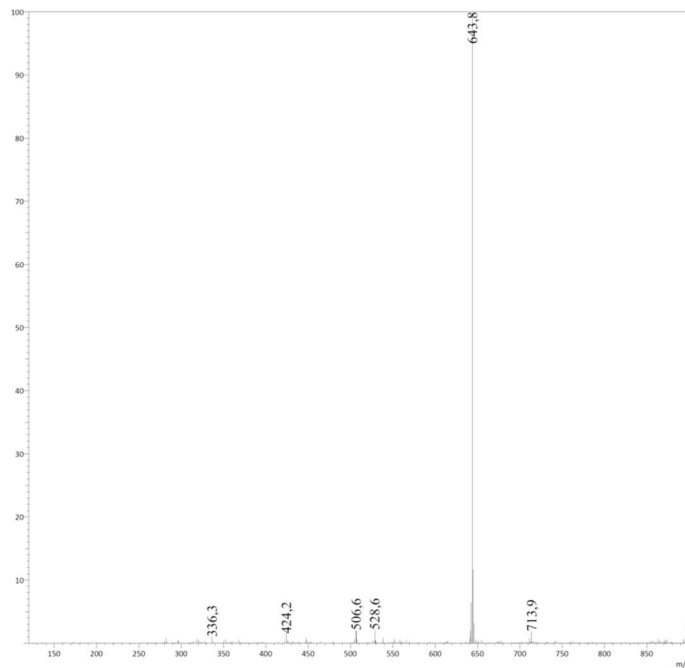
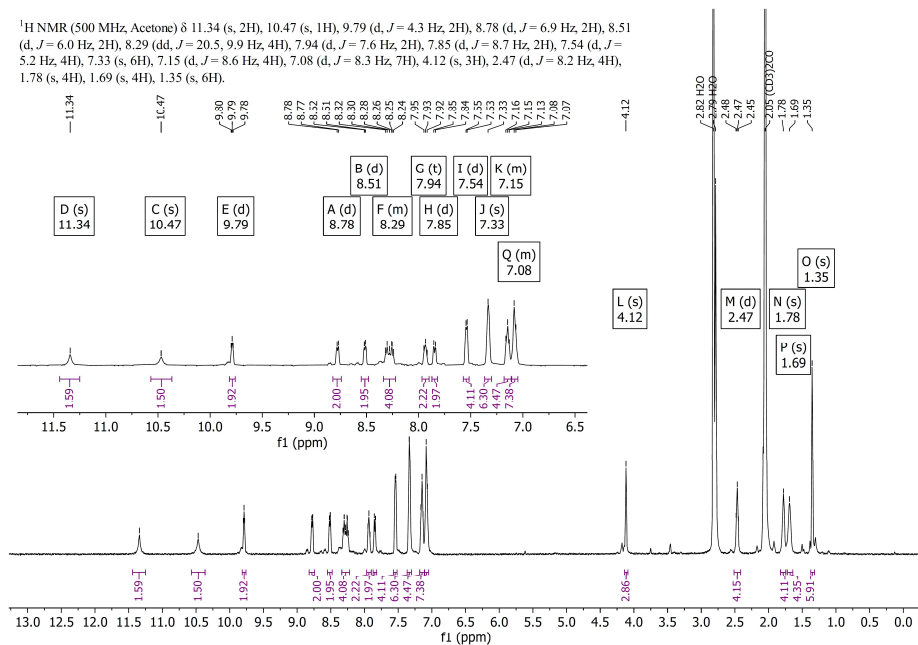
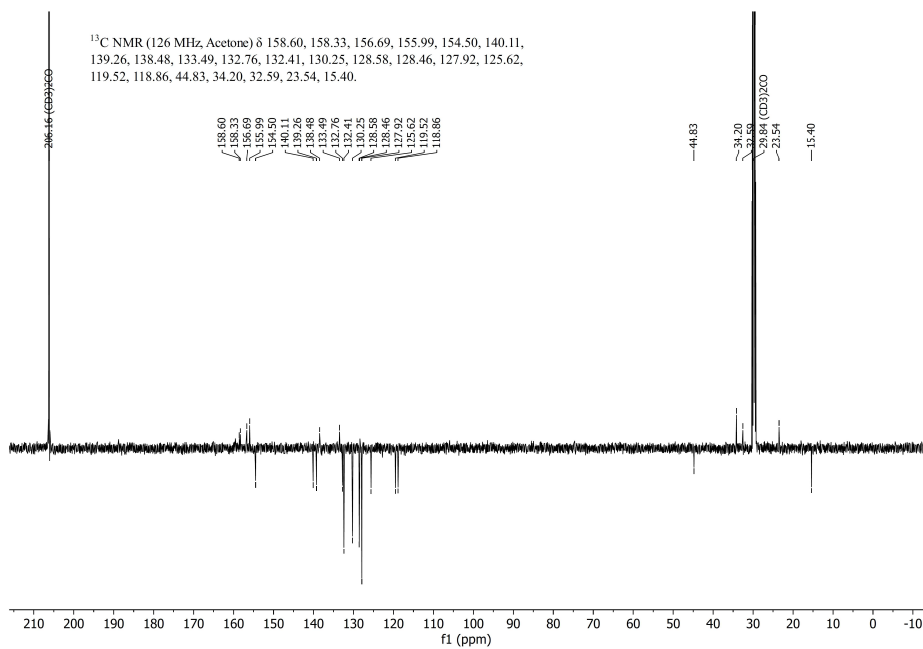


Figure IV.21 ESI-MS of $[1]\text{Cl}_2$. Calculated for $[\text{C}_{67}\text{H}_{67}\text{N}_{11}\text{O}_6\text{S}_2\text{Ru}]^{2+}$: 643.7 m/z .

IV.4.3 [Ru(MeL)(MTI)₂]²⁺ [2]²⁺

¹H NMR (500 MHz, Acetone) δ 11.34 (s, 2H), 10.47 (s, 1H), 9.79 (d, *J* = 4.3 Hz, 2H), 8.78 (d, *J* = 6.9 Hz, 2H), 8.51 (d, *J* = 6.0 Hz, 2H), 8.29 (dd, *J* = 20.5, 9.9 Hz, 4H), 7.94 (d, *J* = 7.6 Hz, 2H), 7.85 (d, *J* = 8.7 Hz, 2H), 7.54 (d, *J* = 5.2 Hz, 4H), 7.33 (s, 6H), 7.15 (d, *J* = 8.6 Hz, 4H), 7.08 (d, *J* = 8.3 Hz, 7H), 4.12 (s, 3H), 2.47 (d, *J* = 8.2 Hz, 4H), 1.78 (s, 4H), 1.69 (s, 4H), 1.35 (s, 6H).

Figure IV.22 ¹H-NMR of [2](PF₆)₂ in Acetone-*d*₆.Figure IV.23 ¹³C-APT-NMR of [2](PF₆)₂ in Acetone-*d*₆.

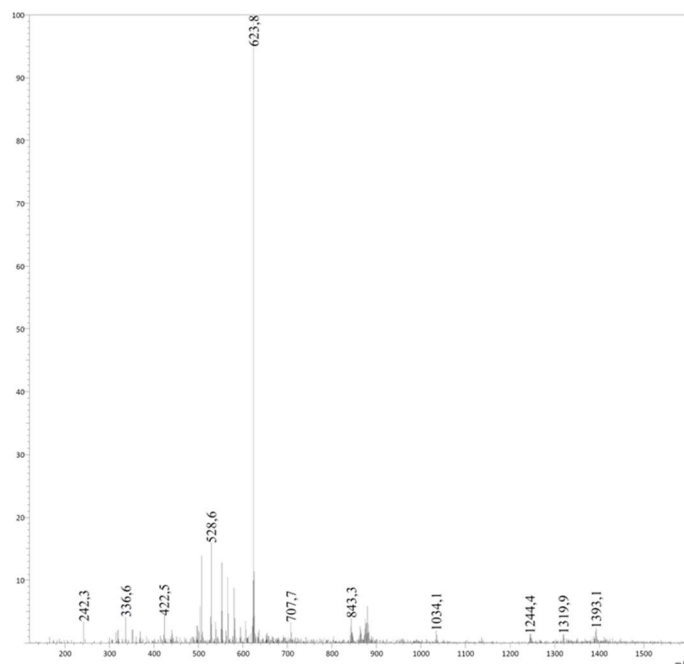


Figure IV.24 ESI-MS of $[2](PF_6)_2$. Calculated for $[C_{67}H_{59}N_{11}O_4S_2Ru]^{2+}$: 623.7 m/z.

1H NMR (600 MHz, MeOD) δ 9.54 (dt, $J = 5.7, 1.1$ Hz, 2H), 8.57 (dd, $J = 8.1, 1.3$ Hz, 2H), 8.32 – 8.28 (m, 2H), 8.17 (td, $J = 7.8, 1.3$ Hz, 2H), 8.12 – 8.08 (m, 2H), 7.84 (ddd, $J = 7.2, 5.5, 1.3$ Hz, 2H), 7.59 (d, $J = 8.5$ Hz, 2H), 7.57 – 7.55 (m, 4H), 7.36 – 7.31 (m, 6H), 7.16 – 7.10 (m, 10H), 3.90 (s, 3H), 2.44 – 2.37 (m, 4H), 1.69 – 1.61 (m, 4H), 1.54 (t, $J = 7.0$ Hz, 4H), 1.20 (s, 6H).

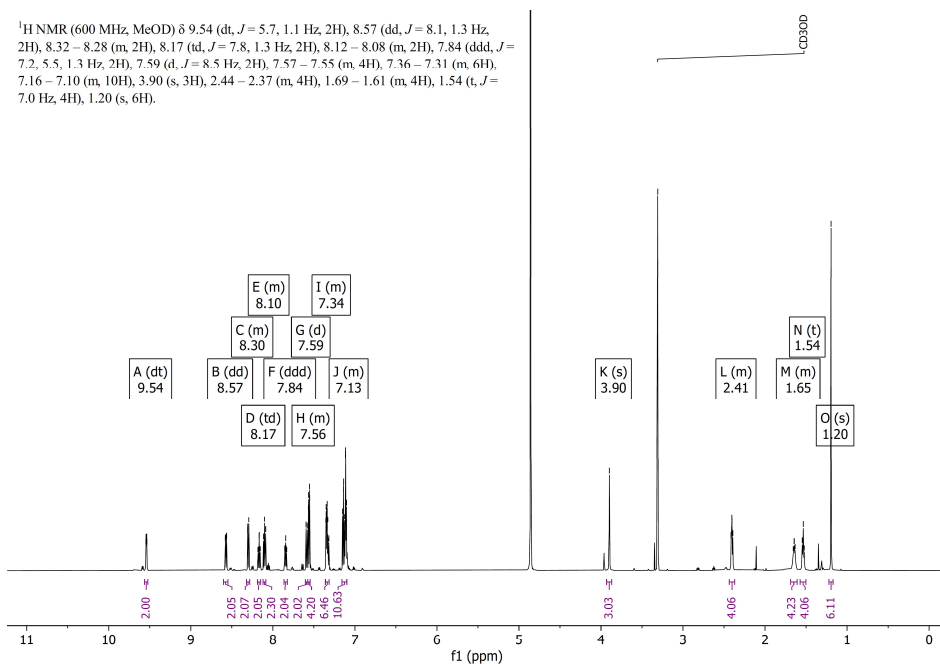


Figure IV.25 1H -NMR of $[2]Cl_2$ in MeOD.

^{13}C NMR (151 MHz, MeOD) δ 190.39, 161.54, 158.58, 158.53, 156.97, 156.08, 154.59, 151.01, 140.36, 139.66, 138.59, 133.72, 133.35, 132.63, 130.74, 129.42, 129.03, 128.93, 128.65, 128.53, 128.46, 125.80, 119.70, 118.71, 106.04, 44.67, 34.33, 32.06, 23.08, 15.37.

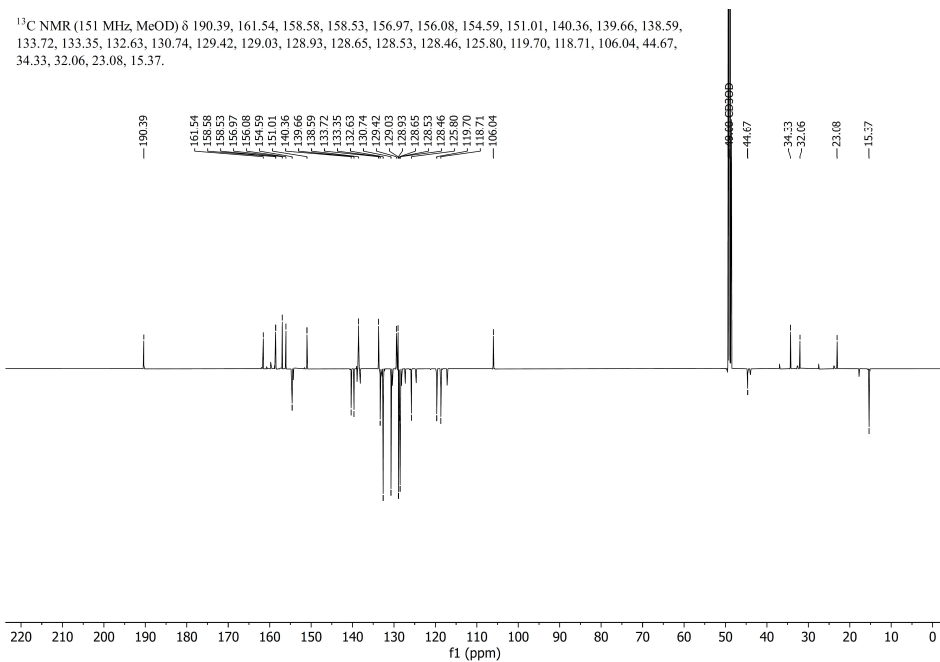


Figure IV.26 ^{13}C -APT-NMR of $[\mathbf{2}]\text{Cl}_2$ in MeOD.

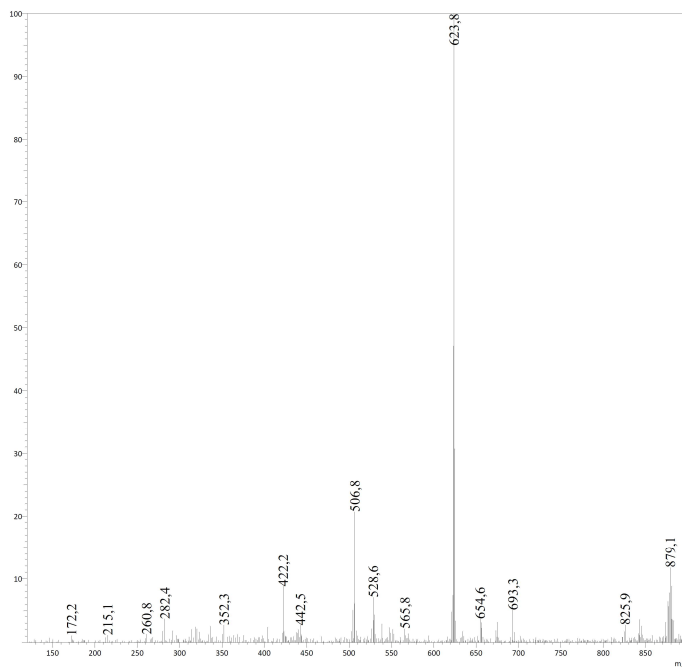
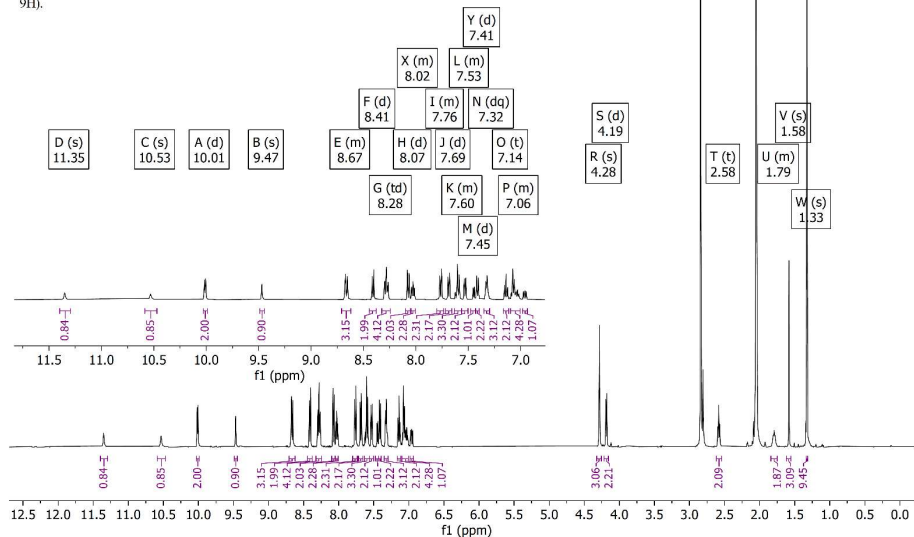
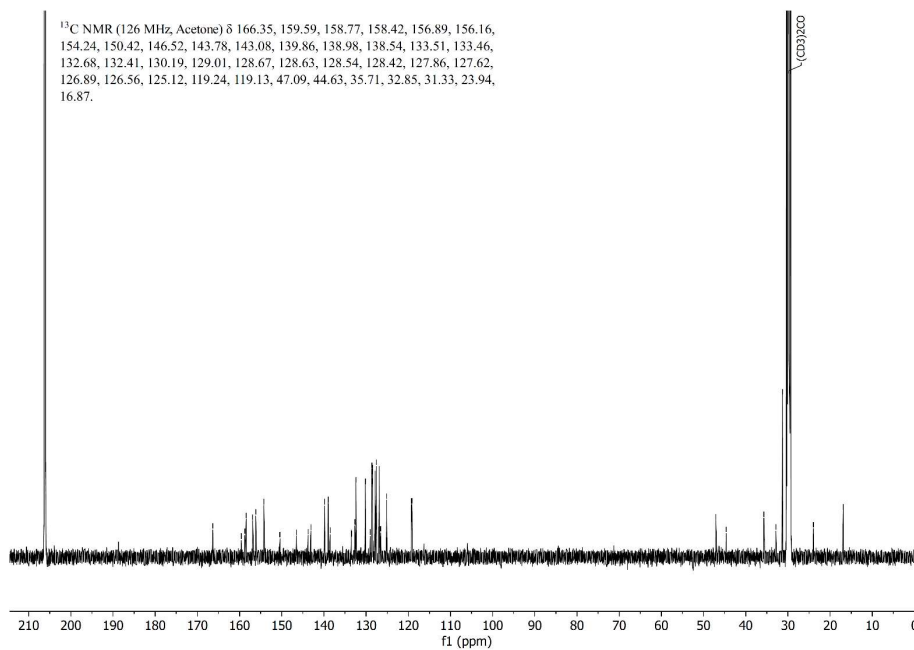


Figure IV.27 ESI-MS of $[\mathbf{2}]\text{Cl}_2$. Calculated for $[\text{C}_{67}\text{H}_{59}\text{N}_{11}\text{O}_4\text{S}_2\text{Ru}]^{2+}$: 623.7 m/z.

IV.4.4 [Ru(MeL)(STF-31)(MTI)]²⁺ [3]²⁺

¹H NMR (500 MHz, Acetone) δ 11.35 (s, 1H), 10.53 (s, 1H), 10.01 (d, *J* = 5.6 Hz, 2H), 9.47 (s, 1H), 8.71 – 8.62 (m, 3H), 8.41 (d, *J* = 7.8 Hz, 2H), 8.28 (td, *J* = 7.8, 2.7 Hz, 4H), 8.07 (d, *J* = 8.5 Hz, 2H), 8.05 – 8.01 (m, 2H), 7.80 – 7.73 (m, 2H), 7.69 (d, *J* = 8.1 Hz, 2H), 7.63 – 7.56 (m, 3H), 7.56 – 7.50 (m, 2H), 7.45 (d, *J* = 5.6 Hz, 1H), 7.41 (d, *J* = 8.3 Hz, 2H), 7.32 (dq, *J* = 5.9, 3.9, 2.9 Hz, 3H), 7.14 (t, *J* = 7.6 Hz, 2H), 7.10 – 7.01 (m, 4H), 6.96 (dd, *J* = 8.4, 5.7 Hz, 1H), 4.28 (s, 3H), 4.19 (d, *J* = 6.6 Hz, 2H), 2.58 (t, *J* = 6.7 Hz, 2H), 1.84 – 1.75 (m, 2H), 1.58 (s, 3H), 1.33 (s, 9H).

Figure IV.28 ¹H-NMR of [3](PF₆)₂ in Acetone-*d*₆.Figure IV.29 ¹³C-NMR of [3](PF₆)₂ in Acetone-*d*₆.

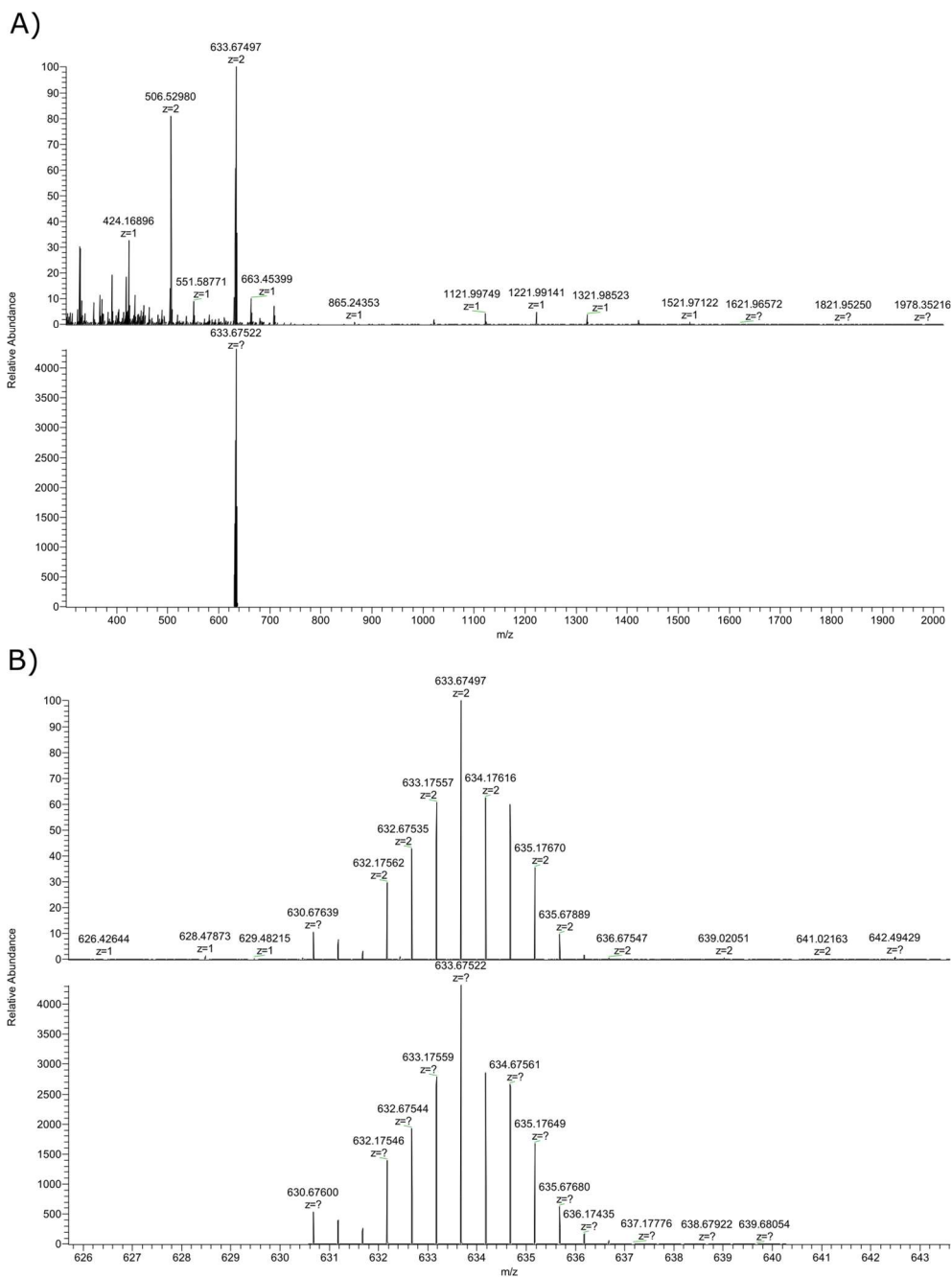


Figure IV.30 ESI-HRMS of **[3](PF₆)₂**. Calculated for $[C_{67}H_{63}N_{11}O_5S_2Ru]^{2+}$: 633.6752 m/z. A) full range between 200 and 2000 m/z. B) zoom between 625 and 645 m/z.

^1H NMR (500 MHz, MeOD) δ 9.78 (d, $J = 5.7$ Hz, 2H), 8.47 (d, $J = 8.1$ Hz, 2H), 8.42 (d, $J = 2.4$ Hz, 1H), 8.22 (d, $J = 7.8$ Hz, 2H), 8.16 (q, $J = 8.2$ Hz, 4H), 7.95 (t, $J = 6.7$ Hz, 2H), 7.89 (d, $J = 8.5$ Hz, 2H), 7.73 (d, $J = 8.3$ Hz, 2H), 7.64 (d, $J = 8.1$ Hz, 2H), 7.55 (dd, $J = 7.8, 4.4$ Hz, 5H), 7.49 (d, $J = 8.3$ Hz, 1H), 7.33 (dt, $J = 11.5, 7.8$ Hz, 5H), 7.22 (d, $J = 5.6$ Hz, 1H), 7.16–7.07 (m, 6H), 6.86 (dd, $J = 8.4, 5.6$ Hz, 1H), 4.11 (d, $J = 3.4$ Hz, 5H), 2.52 (t, $J = 6.2$ Hz, 2H), 1.84 (s, 2H), 1.75 (s, 2H), 1.45 (s, 3H), 1.32 (s, 10H).

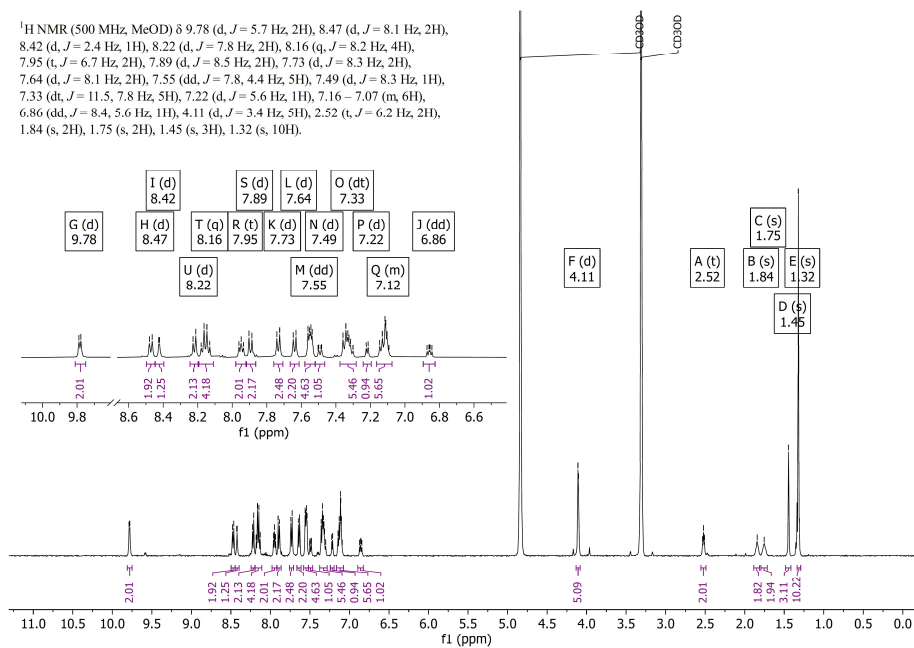


Figure IV.31 ^1H -NMR of $[\mathbf{3}]\text{Cl}_2$ in MeOD.

^{13}C NMR (126 MHz, MeOD) δ 168.06, 161.56, 158.76, 157.26, 156.47, 154.37, 146.72, 144.10, 143.22, 140.17, 139.40, 138.98, 138.68, 133.81, 133.75, 133.68, 133.31, 132.61, 130.63, 129.36, 128.93, 128.73, 128.50, 127.88, 127.17, 126.67, 125.33, 119.38, 119.21, 47.76, 44.39, 36.12, 32.47, 31.47, 17.03.

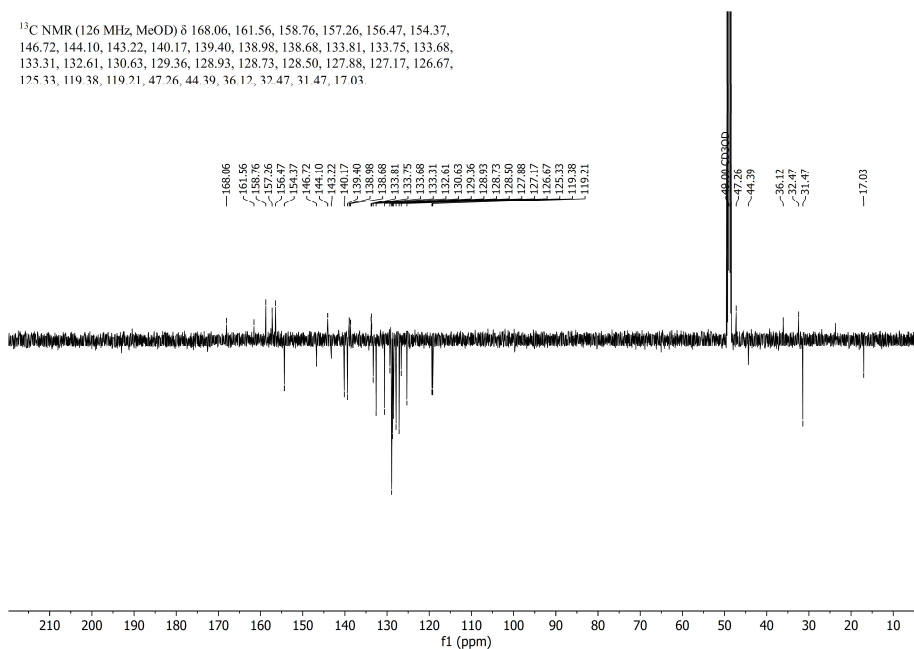


Figure IV.32 ^{13}C -APT-NMR of $[\mathbf{3}]\text{Cl}_2$ in MeOD.

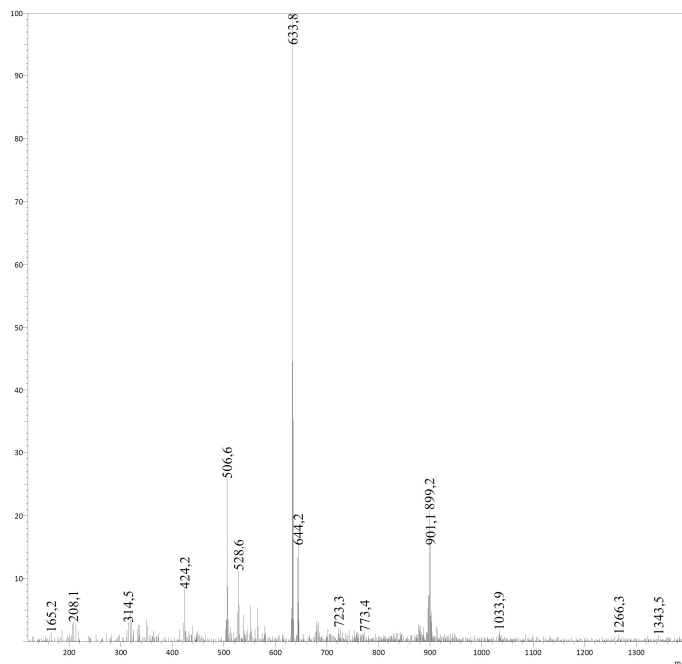


Figure IV.33 ESI-MS of **[3]**Cl₂. Calculated for [C₆₇H₆₃N₁₁O₅S₂Ru]²⁺: 633.7 m/z.

IV.4.5 [Ru(MeL)(Py)(MTE)]Cl₂ **[4]**Cl₂

¹H NMR (400 MHz, MeOD) δ 9.85 (dd, *J* = 6.1, 1.2 Hz, 2H), 8.58 (d, *J* = 7.8 Hz, 2H), 8.34 (dd, *J* = 7.9, 1.0 Hz, 2H), 8.29 – 8.22 (m, 4H), 8.02 (ddd, *J* = 7.3, 5.6, 1.4 Hz, 2H), 7.97 (dd, *J* = 8.5, 1.0 Hz, 2H), 7.53 (tt, *J* = 7.7, 1.5 Hz, 1H), 7.48 (dt, *J* = 5.1, 1.5 Hz, 2H), 6.95 – 6.87 (m, 2H), 4.14 (s, 3H), 1.90 (t, *J* = 5.7 Hz, 2H), 1.46 (s, 3H).

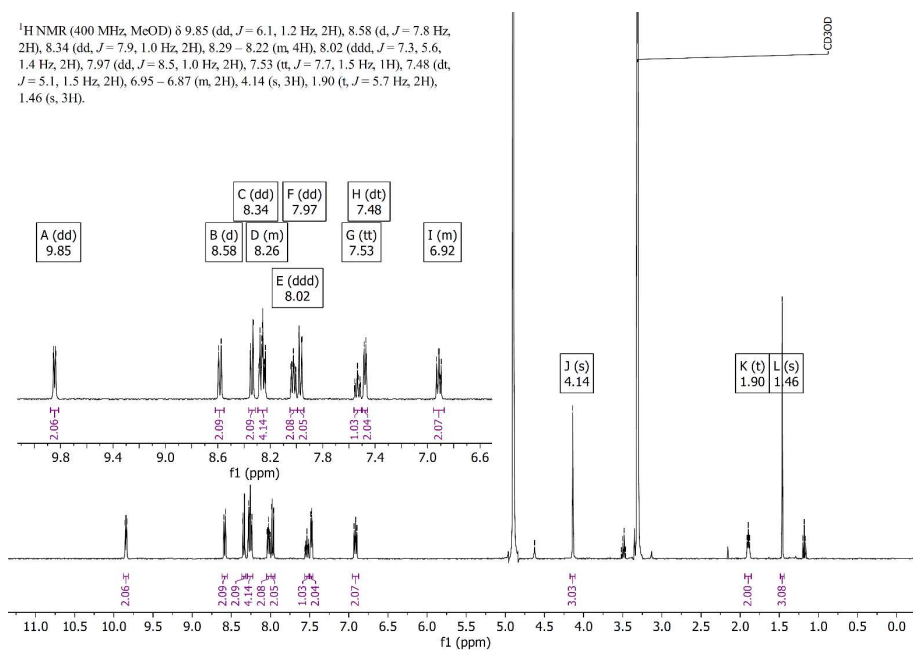


Figure IV.34 ¹H-NMR of **[4]**Cl₂ in MeOD.

^{13}C NMR (101 MHz MeOD) δ 158.91, 157.40, 156.56, 154.54, 151.90, 140.19,
139.36, 128.91, 127.07, 125.36, 119.44, 119.29, 58.98, 44.23, 40.29, 17.71.

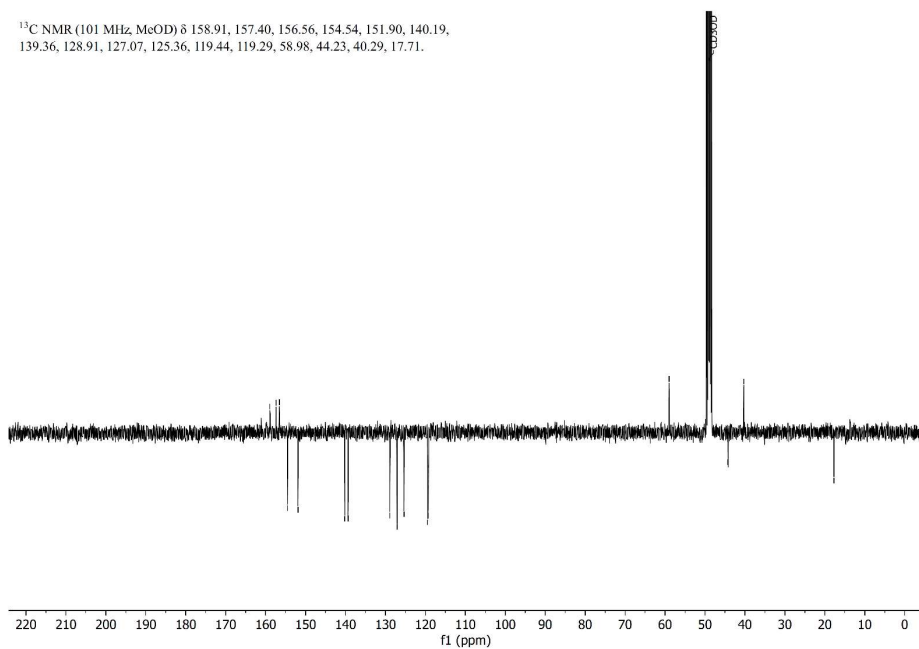


Figure IV.35 ^{13}C -APT-NMR of $[\mathbf{4}]\text{Cl}_2$ in MeOD.

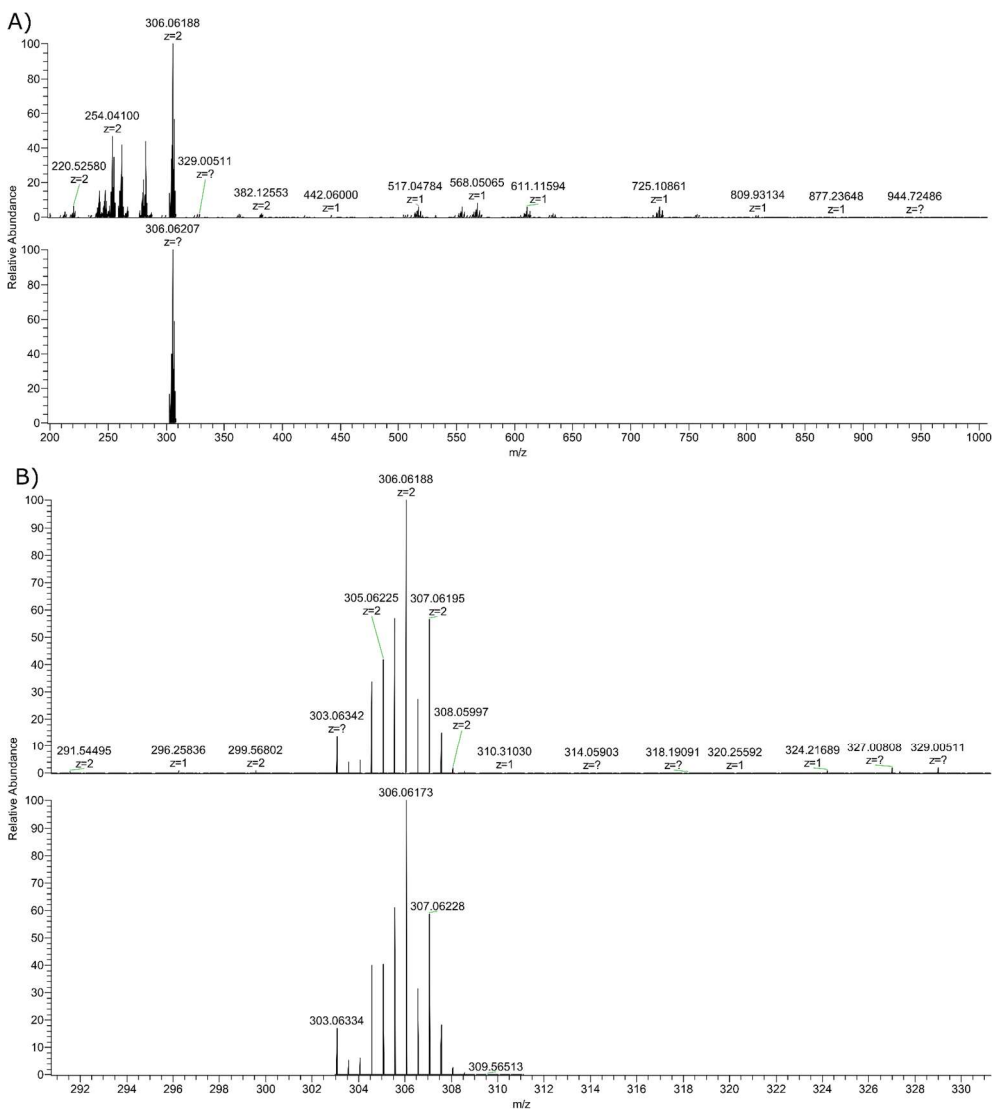


Figure IV.36 ESI-HRMS of $[4]Cl_2$. Calculated for $[C_{29}H_{30}N_6O_1S_1Ru]^{2+}$: 306.0617 m/z. A) full range between 200 and 1000 m/z. B) zoom between 291 and 331 m/z.

Appendix V: Supporting information for Chapter 5

V.1 Single crystal X-ray crystallography

Experimental details

For both [24]Cl₂ and [26](PF₆)₂, all reflection intensities were measured at 110.00(10) K using a Rigaku XtaLAB Synergy R (equipped with a rotating-anode X-ray source and HyPix-6000HE detector) with Cu K α radiation ($\lambda = 1.54178 \text{ \AA}$) under the program CrysAlisPro (Version CrysAlisPro 1.171.42.49, Rigaku OD, 2022). The same program was used to refine the cell dimensions and for data reduction. The structure was solved and refined on F^2 with the program SHELXL-2018/3.¹ Analytical numeric absorption correction using a multifaceted crystal was applied using CrysAlisPro. The temperature of the data collection was controlled using the system Cryostream 1000 from Oxford Cryosystems). The H atoms were placed at calculated positions using the instructions AFIX 13, AFIX 23, AFIX 43, AFIX 137 or AFIX 147 with isotropic displacement parameters having values 1.2 or 1.5 U_{eq} of the attached C or O atoms.

For [24]Cl₂, the structure is partly disordered. The adamantyl fragment of the N3' moiety and one of the two lattice MeOH solvent molecules are disordered over two orientations, and the occupancy factors of the major components of the disorder refine to 0.621(4) and 0.512(11), respectively. For [26](PF₆)₂, The structure is partly disordered. The coordinated pyridine, the adamantyl fragment, and the PF₆⁻ counterions are all disordered over two orientations. All occupancy factors of the major/minor components of the disorder can be retrieved from the final .cif file. The asymmetric unit contains three PF₆⁻ counterions located at three different sites: one site has one fully occupied counterion, another site has one half occupied counterion as it is found at one site of inversion symmetry, and the third site contains a heavily disordered and partly occupied counterion (the sum of the occupancies from the individual disordered components were constrained to be 0.5). The asymmetric unit also contains some amount of very disordered (and possibly partially occupied) lattice THF solvent molecules, and that contribution was removed from the final refinement using the SQUEEZE procedure in Platon.²

¹ Sheldrick, G.M., *Acta. Cryst.*, 2015, C71, 3-8, DOI: 10.1107/S2053229614024218

² Spek, A.L., *Acta. Cryst.*, 2009, D65, 148-155, DOI: 10.1107/S090744490804362X

Table V.1 Crystallographic data for the crystal structures presented in this work.

	[24](Cl) ₂	[26](PF ₆) ₂
Chemical formula	C ₅₁ H ₅₇ N ₉ O ₂ Ru·2(CH ₄ O)·2(Cl)	C ₄₁ H ₄₂ N ₈ ORu·2(F ₆ P)
M _r	1064.11	1053.83
Crystal system	Triclinic	Triclinic
Space group	<i>P</i> -1	<i>P</i> -1
Cell lengths (<i>a</i> , <i>b</i> , <i>c</i>)(Å)	11.32203 (18)	9.3424 (2)
	12.2551 (2)	13.8428 (6)
	18.558899 (18)	19.7677 (6)
Cell angles (α, β, γ)(°)	75.2897 (13)	99.089 (3)
	82.2838 (12)	94.080 (2)
	79.7078 (14)	95.336 (2)
Cell volume (Å ³)	2439.90 (6)	2503.82 (14)
Z	2	2
μ (mm ⁻¹)	4.06	3.89
Crystal size (mm)	0.17 × 0.03 × 0.03	0.28 × 0.04 × 0.04
Temperature (K)	110(10)	110(10)
Diffractometer	XtaLAB Synergy R, HyPix	XtaLAB Synergy R, HyPix
Radiation type	Cu Kα	Cu Kα
T _{min} , T _{max}	0.701, 0.914	0.603, 0.896
No. of measured, independent and observed [<i>I</i> > 2σ(<i>I</i>)] reflections	41896, 9545, 8928	36586, 9777, 8429
<i>R</i> _{int}	0.043	0.041
(sin θ/λ) _{max} (Å ⁻¹)	0.616	0.616
<i>R</i> [<i>F</i> ² > 2σ(<i>F</i> ²)], <i>wR</i> (<i>F</i> ²), <i>S</i>	0.038, 0.098, 1.07	0.056, 0.171, 1.03
No. of reflections	9545	9777
No. of parameters	730	920
No. of restraints	417	1212
H-atom treatment	H-atom parameters constrained	H-atom parameters constrained
Δρ _{max} , Δρ _{min} (e Å ⁻³)	1.02, -1.46	1.83, -1.05

V.2 Photochemistry

V.2.1 Molar extinction coefficient determination

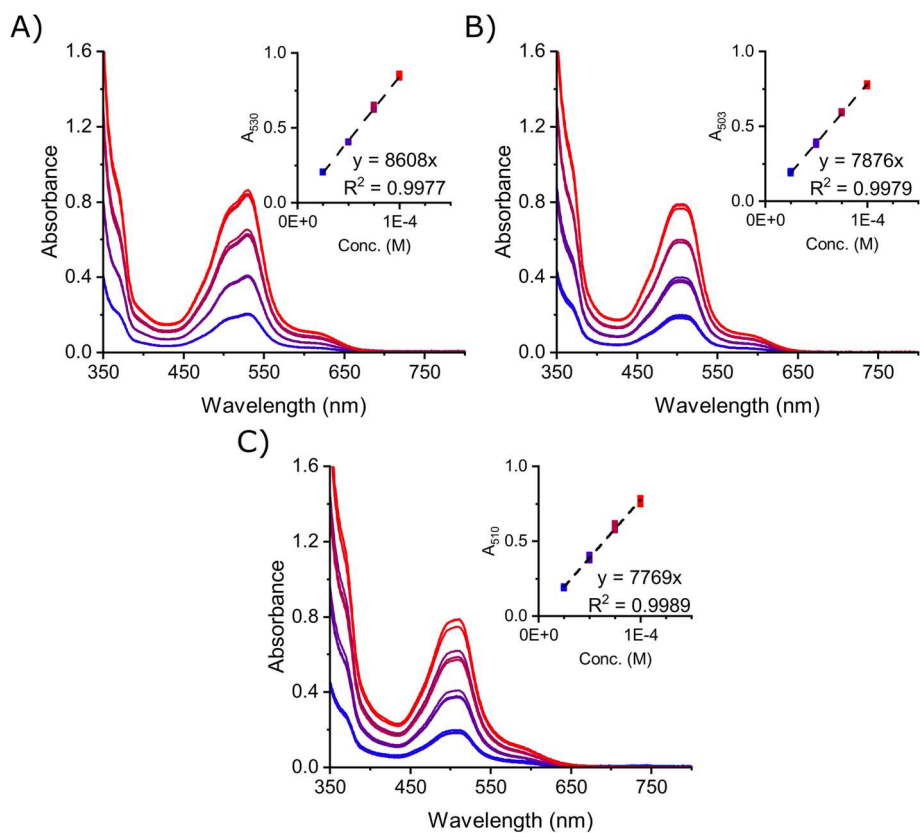


Figure V.1 UV-Vis spectra of $[24](PF_6)_2$ – $[26](PF_6)_2$ at different concentrations in 3 ml 50% acetone in H_2O at 298 K ($l = 1$ cm). Insets depict absorbance at λ_{max} at different concentrations. A) $[24](PF_6)_2$: $\epsilon = 8.61 \times 10^3 \text{ M}^{-1} \text{ cm}^{-1}$ at 530 nm. B) $[26](PF_6)_2$: $\epsilon = 7.88 \times 10^3 \text{ M}^{-1} \text{ cm}^{-1}$ at 503 nm. C) $[25](PF_6)_2$: $\epsilon = 7.77 \times 10^3 \text{ M}^{-1} \text{ cm}^{-1}$ at 510 nm.

V.2.2 Photosubstitution quantum yield measurements

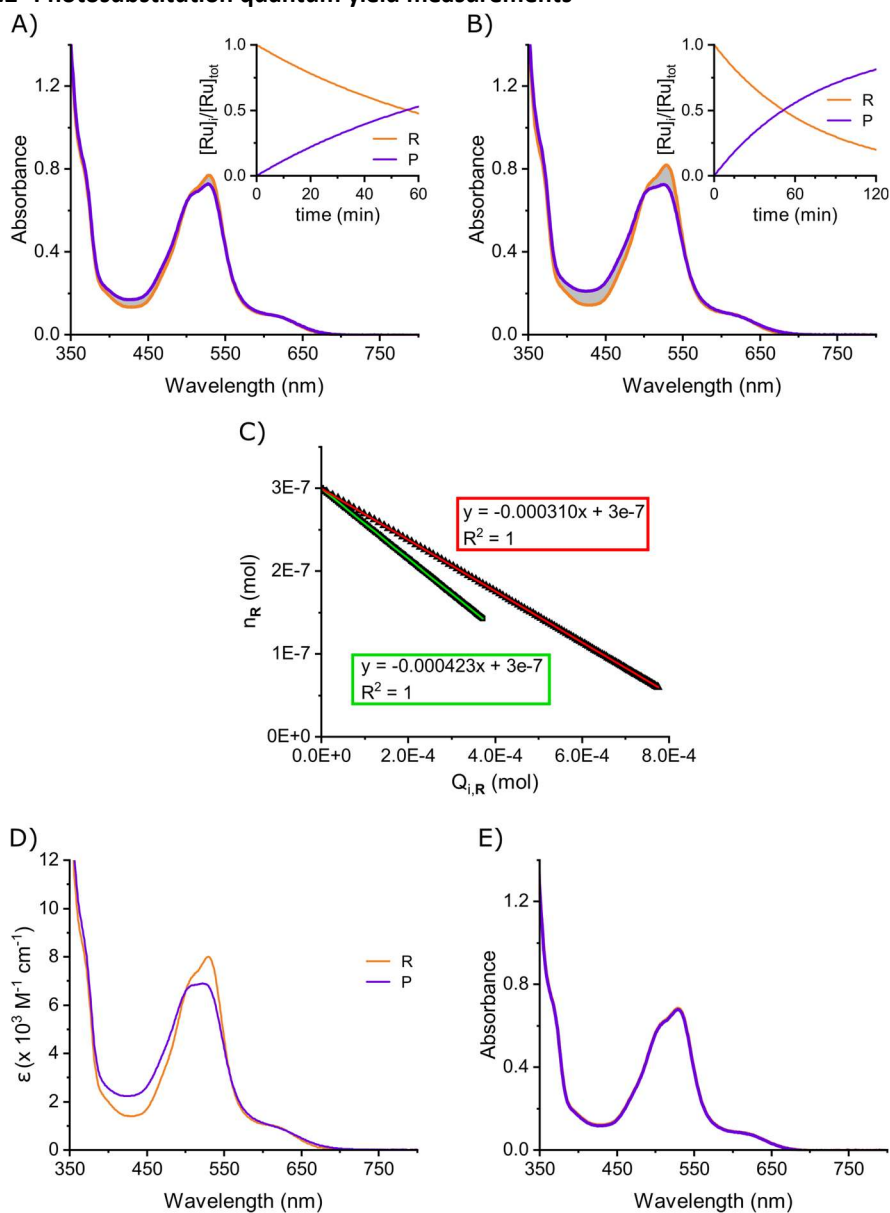


Figure V.2 Graphs for photosubstitution quantum yield for $[24](PF_6)_2$ at 298 K in 50% acetone in H_2O . Time-evolution of UV-Vis absorption upon irradiation with A) 505 nm (photon flux = 1.42×10^{-7} mol/s) for 60 min at 100 μM and B) 625 nm (photon flux = 4.76×10^{-7} mol/s) for 60 min at 100 μM (from orange to purple). C) Plot of n_R against $Q_{i,R}$ used to calculate the photosubstitution quantum yield. D) Globally fitted UV-Vis absorption spectra of $[24](PF_6)_2$ (R; orange line) and the photoproduct (P; purple line). E) Absorption spectra of $[24](PF_6)_2$ in the dark for 18 h (orange to purple).

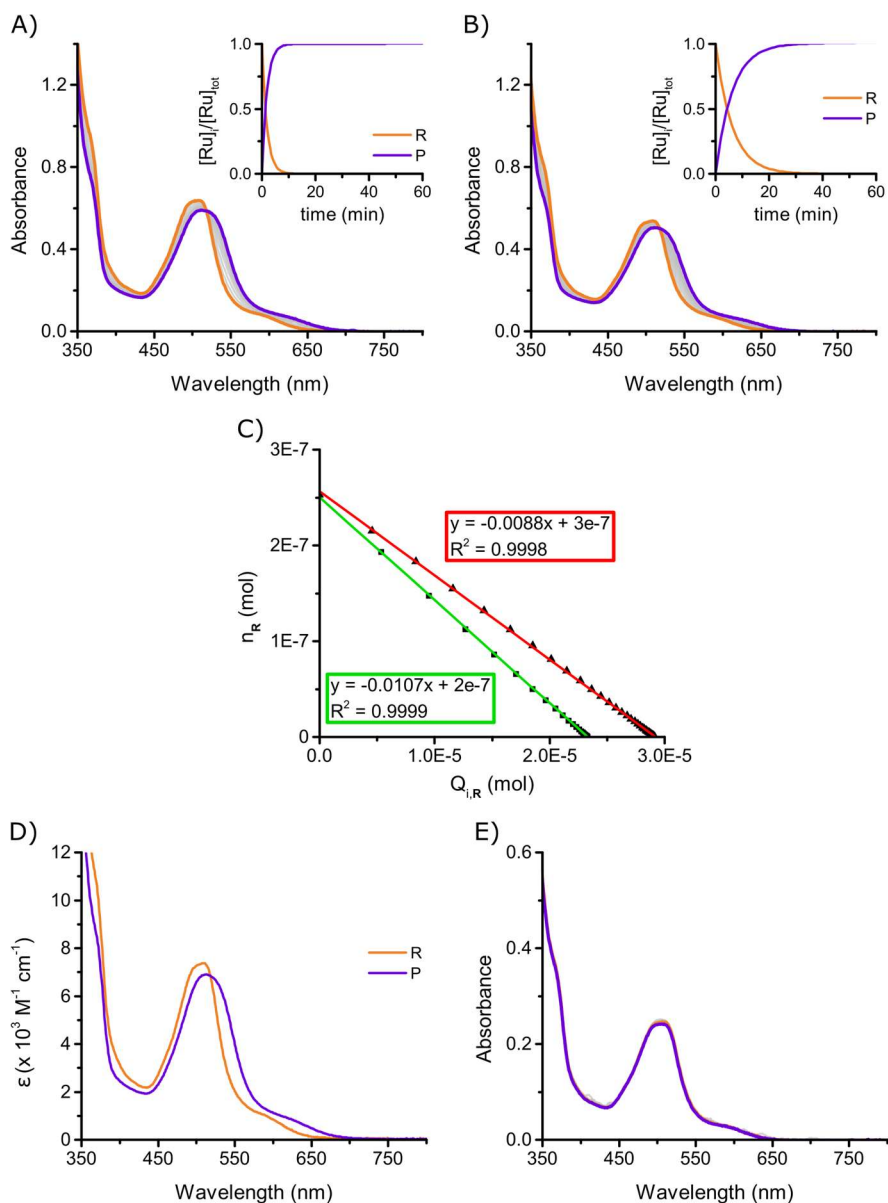


Figure V.3 Graphs for photosubstitution quantum yield for $[25](PF_6)_2$ at 298 K in 50% acetone in H_2O . Time-evolution of UV-Vis absorption upon irradiation with A) 505 nm (photon flux = 2.09×10^{-7} mol/s) for 60 min at 84.3 μM and B) 625 nm (photon flux = 4.14×10^{-7} mol/s) for 60 min at 84.3 μM (from orange to purple). C) Plot of n_R against $Q_{i,R}$ used to calculate the photosubstitution quantum yield. D) Globally fitted UV-Vis absorption spectra of $[25](PF_6)_2$ (R; orange line) and the photoproduct (P; purple line). E) Absorption spectra of $[25](PF_6)_2$ in the dark for 16 h (from orange to purple).

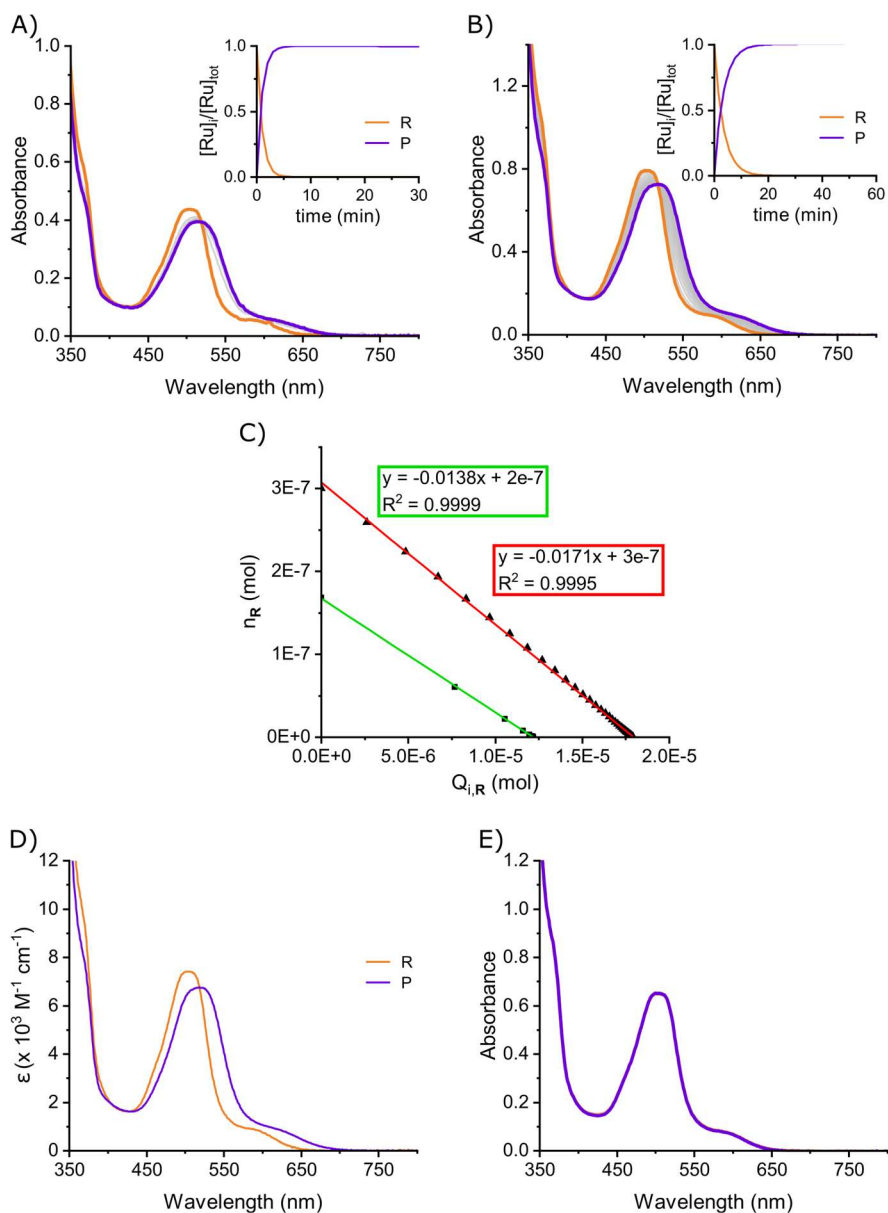


Figure V.4 Graphs for photosubstitution quantum yield for $[26](PF_6)_2$ at 298 K in 50% acetone in H_2O . Time-evolution of UV-Vis absorption upon irradiation with A) 505 nm (photon flux = 2.02×10^{-7} mol/s) for 30 min at 56.0 μM and B) 625 nm (photon flux = 4.76×10^{-7} mol/s) for 60 min at 100 μM (from orange to purple). C) Plot of n_R against $Q_{i,R}$ used to calculate the photosubstitution quantum yield. D) Globally fitted UV-Vis absorption spectra of $[26](PF_6)_2$ (R; orange line) and the photoproduct (P; purple line). E) Absorption spectra of $[26](PF_6)_2$ in the dark for 20 h (from orange to purple).

V.2.3 Phosphorescence and singlet oxygen generation quantum yield measurements

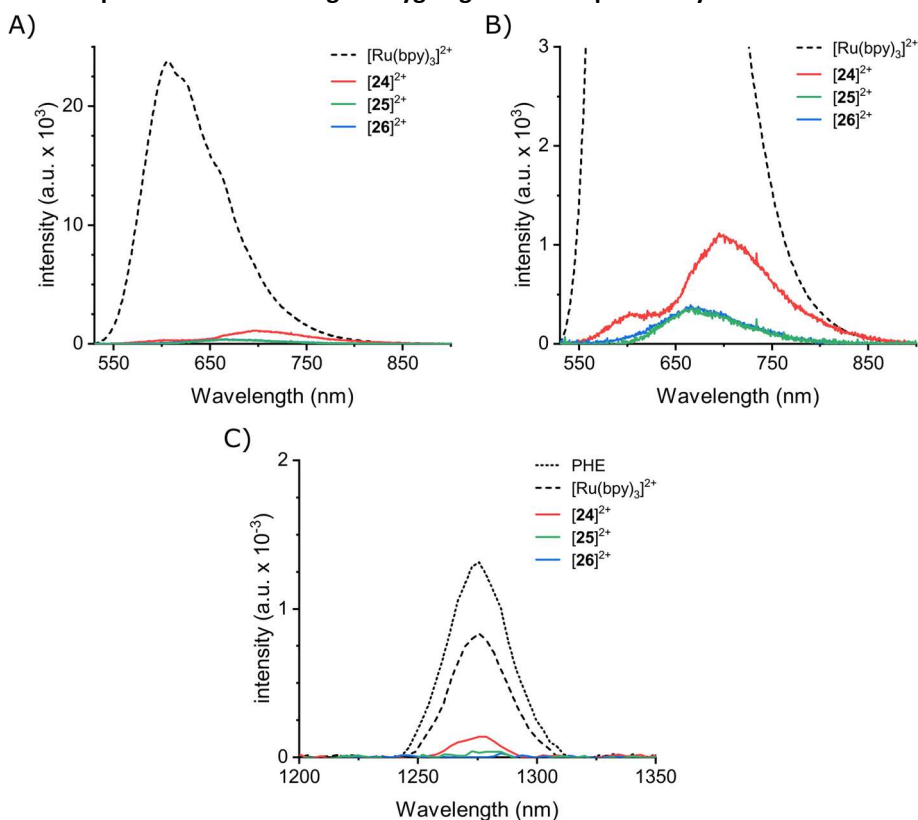


Figure V.5 A) Visible emission spectra of $[24](PF_6)_2$ – $[26](PF_6)_2$ and $[Ru(bpy)_3]Cl_2$ in aerated acetonitrile at 298 K under blue light irradiation (450 nm, 80 mW/cm²) with B) being a focused version of A). C) Near-infrared emission spectra of ¹O₂ phosphorescence ($\lambda_{em} = 1275$ nm) sensitized by $[24](PF_6)_2$ – $[26](PF_6)_2$, $[Ru(bpy)_3]Cl_2$ and perinaphthenone (PHE) in aerated acetonitrile at 298 K under blue light irradiation (450 nm, 80 mW/cm²).

Table V.2 Data for the determination of phosphorescence and singlet oxygen generation quantum yields in aerated acetonitrile.

Compound	Abs. (450 nm)	Integrated intensity	Φ_p	Abs. (450 nm)	Integrated intensity	$\Phi_{\Delta} (^1O_2)$
Perinaphthenone	-	-	-	0.0960	0.0403	0.980
$[Ru(bpy)_3]Cl_2$	0.1071	2.56×10^6	0.018	0.1073	0.0265	0.577
$[24](PF_6)_2$	0.1024	1.39×10^5	0.00102	0.1077	0.0034	0.073
$[25](PF_6)_2$	0.0973	3.29×10^4	0.00025	0.0992	0.0002	<0.01
$[26](PF_6)_2$	0.1041	3.95×10^4	0.00029	0.1010	0.0002	<0.01

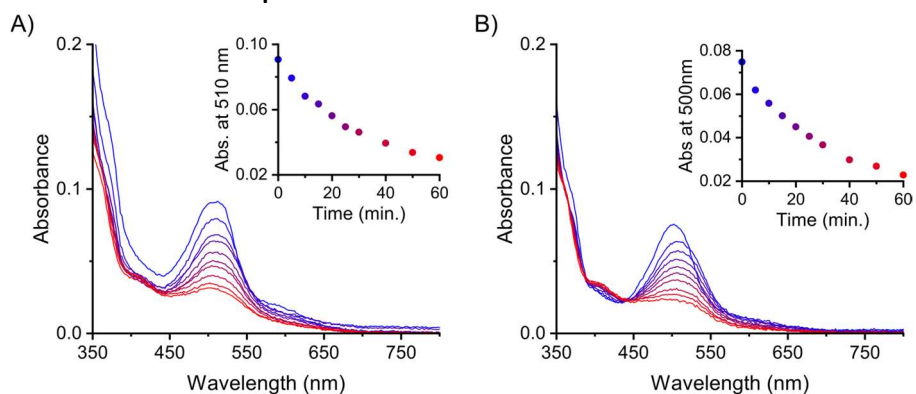
V.2.4 Mock irradiation experiment

Figure V.6 Time-evolution (blue to red) of UV-Vis absorbance spectra of [25]Cl₂ (A) and [26]Cl₂ (B) in OptiMEM complete media + 0.14% DMSO upon irradiation with red (630 ± 24 nm, 31.3 mW/cm²) light array at 37 °C (conc. = 5.0 × 10⁻⁵ M, v = 200 μL).

V.3 Cytotoxicity

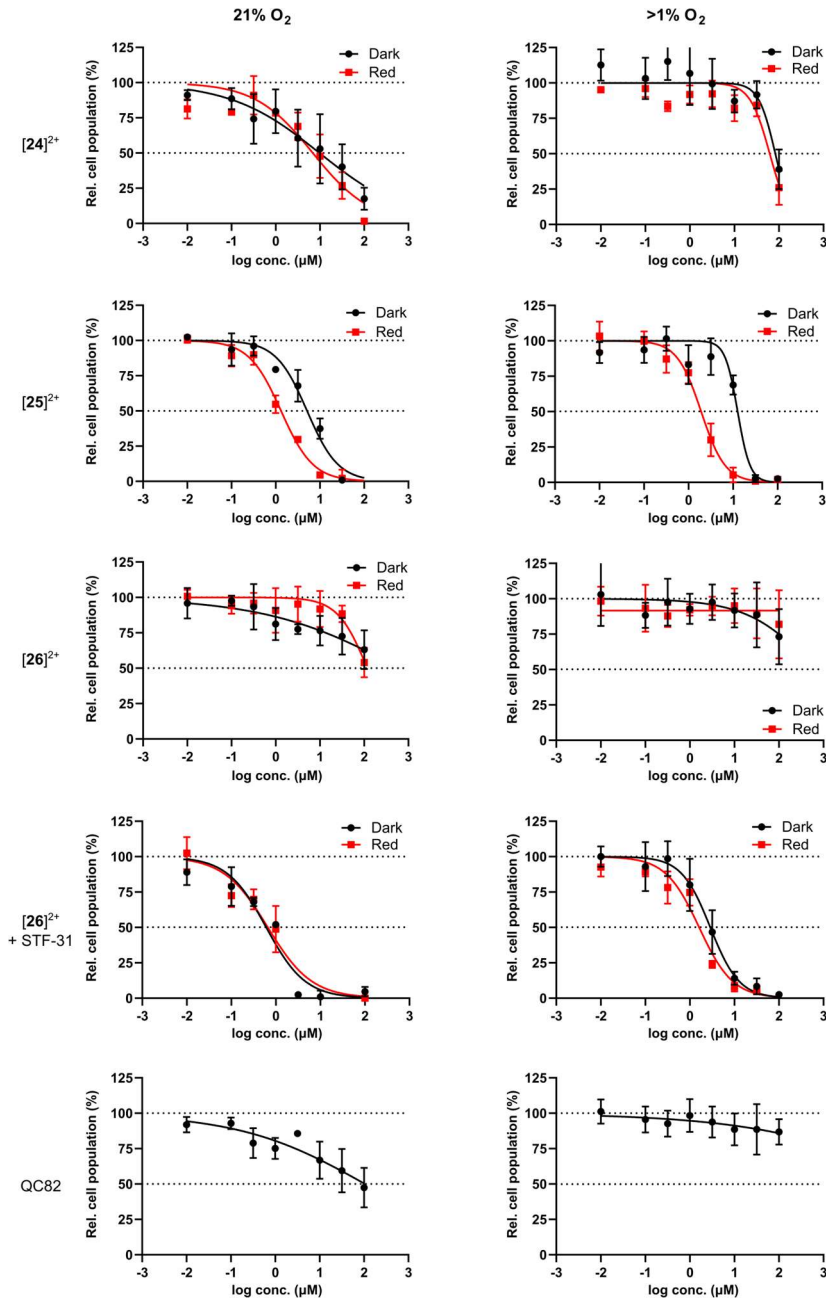
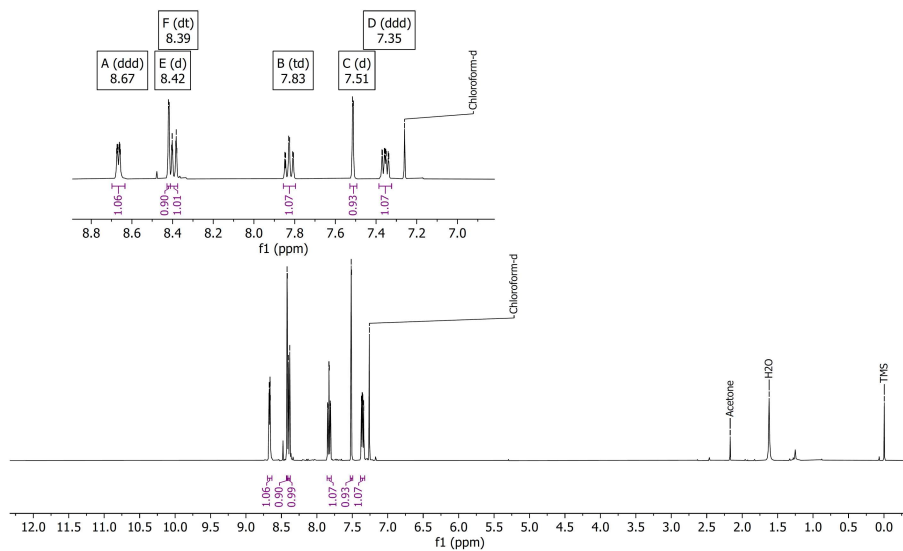


Figure V.7 Dose-response curves of [24] Cl_2 , [26] Cl_2 , [26] Cl_2 + STF31 (1:1 molar ratio), QC82 and STF31 in A375 cell line incubated in normoxic (21% O_2) and hypoxic (1% O_2) conditions in the dark (black curve) or with red light irradiation (630 nm, 58 J/cm^2 , 31.3 mW/cm^2 , 30 min). Data points are average of independent triplicate with error bars indicating 95% confidence intervals.

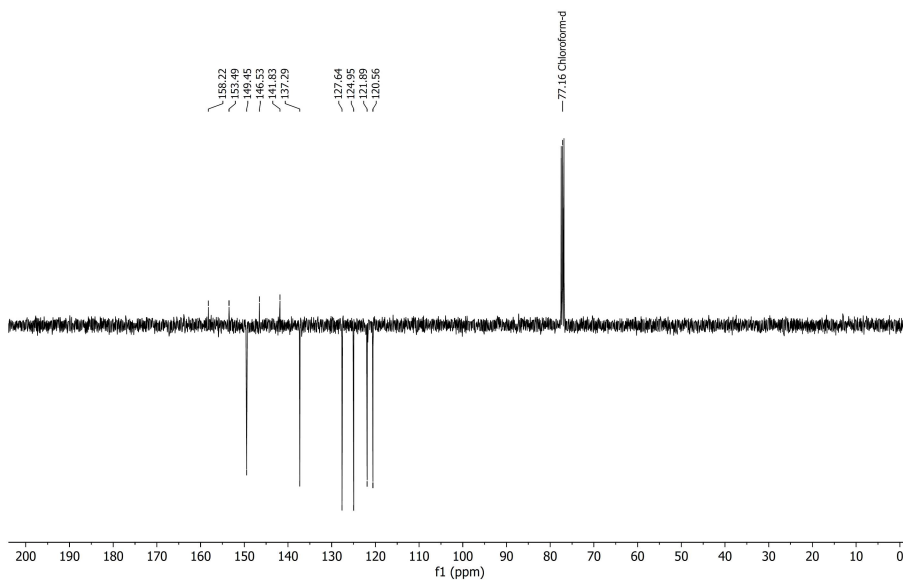
V.4 Characterization of synthesized compounds

V.4.1 6-bromo-4-chloro-2,2'-bipyridine, 2a

^1H NMR (400 MHz, CDCl_3) δ 8.67 (ddd, $J = 5.0, 1.8, 1.0$ Hz, 1H), 8.42 (d, $J = 1.7$ Hz, 1H), 8.39 (dt, $J = 8.0, 1.1$ Hz, 1H), 7.83 (td, $J = 7.8, 1.8$ Hz, 1H), 7.51 (d, $J = 1.7$ Hz, 1H), 7.35 (ddd, $J = 7.5, 4.8, 1.1$ Hz, 1H).



^{13}C NMR (101 MHz, CDCl_3) δ 158.22, 153.49, 149.45, 146.53, 141.83, 137.29, 127.64, 124.95, 121.89, 120.56.



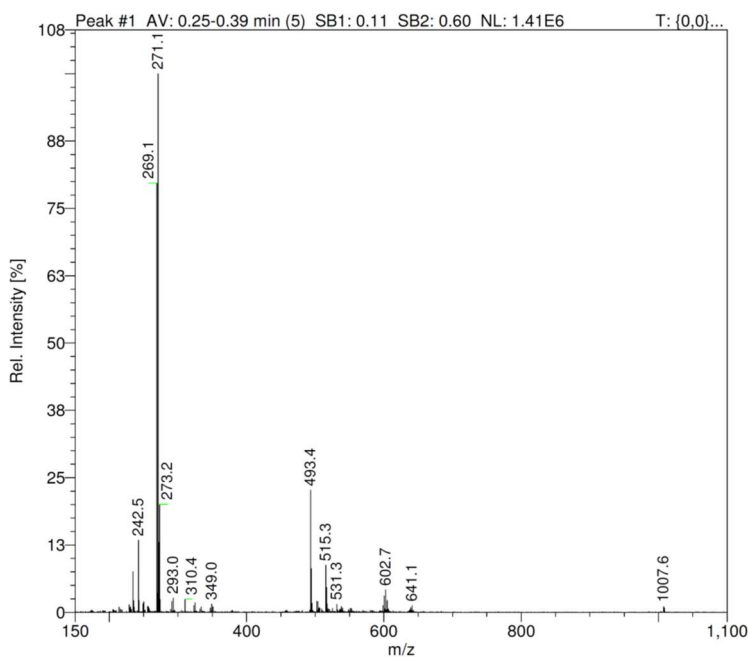


Figure V.10 ESI-MS of **2a**. Calculated for $[\text{C}_{10}\text{H}_6\text{BrClN}_2 + \text{H}^+]^{2+}$: 270.9 m/z.

V.4.2 6-bromo-5-chloro-2,2'-bipyridine, **2b**

^1H NMR (850 MHz, CDCl_3) δ 8.66 (ddd, $J = 4.7, 1.8, 1.0$ Hz, 1H), 8.38 (dt, $J = 7.9, 1.1$ Hz, 1H), 8.35 (d, $J = 8.2$ Hz, 1H), 7.84 (d, $J = 8.2$ Hz, 1H), 7.82 (ddd, $J = 7.9, 7.4, 1.8$ Hz, 1H), 7.34 (ddd, $J = 7.4, 4.7, 1.2$ Hz, 1H).

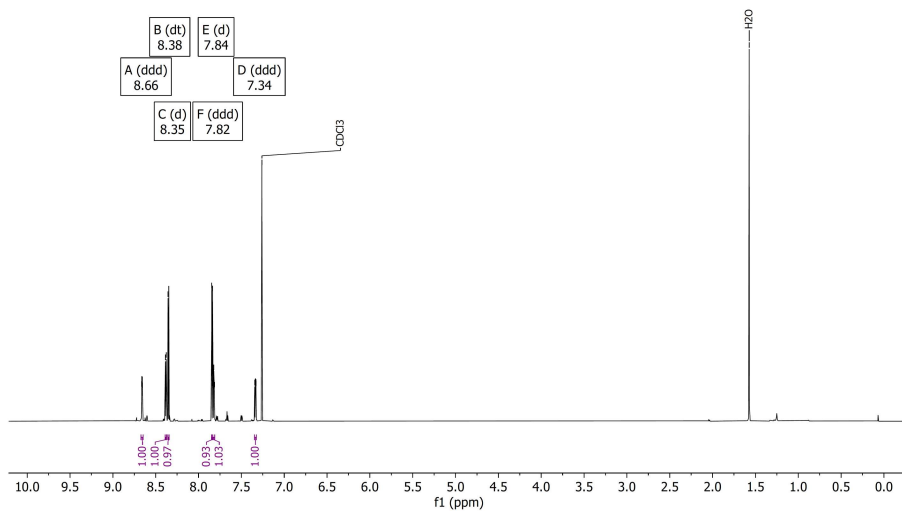


Figure V.11 ^1H -NMR of **2b** in CDCl_3 .

^{13}C NMR (214 MHz, CDCl_3) δ 155.06, 153.83, 149.44, 140.92, 137.25, 133.35, 124.58, 124.57, 121.59, 120.87, 120.86.

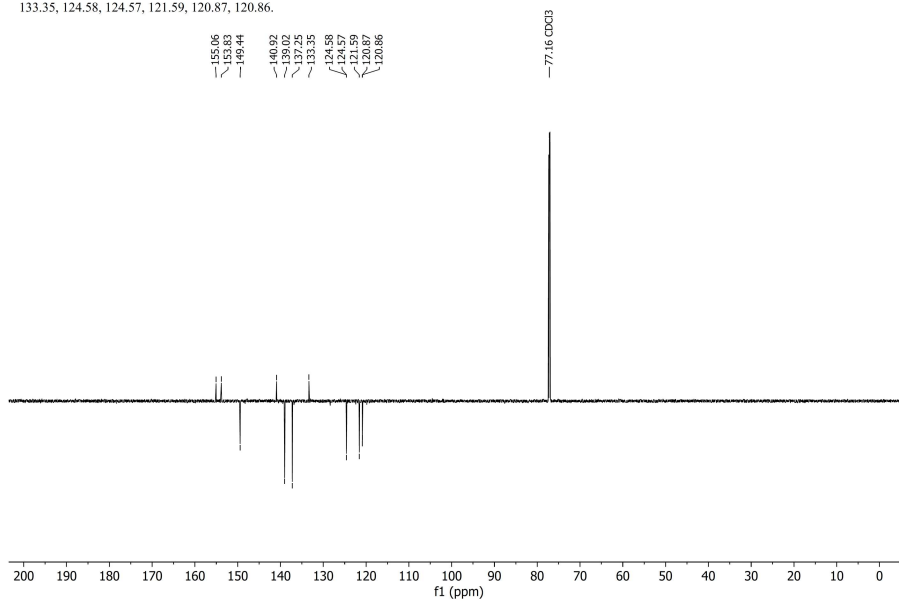


Figure V.12 ^{13}C -APT-NMR of **2b** in CDCl_3 .

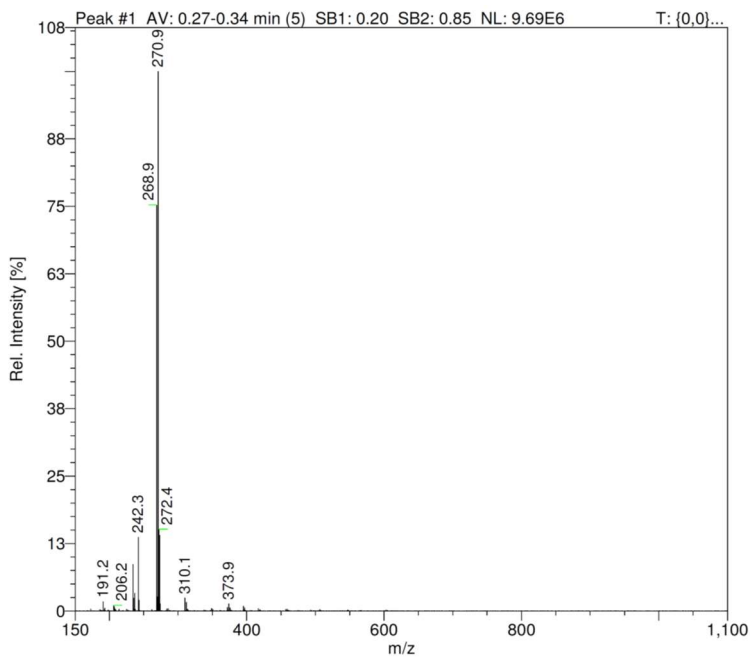


Figure V.13 ESI-MS of **2b**. Calculated for $[\text{C}_{10}\text{H}_6\text{BrClN}_2 + \text{H}^+]^+$: 270.9 m/z.

V.4.3 Bis(4-chloro-[2,2'-bipyridin]-6-yl)amine, 3a

^1H NMR (850 MHz, DMSO) δ 10.31 (s, 1H), 8.68 (d, $J = 4.6$ Hz, 2H), 8.27 (dt, $J = 7.9, 1.1$ Hz, 2H), 7.99 (td, $J = 7.6, 1.8$ Hz, 2H), 7.97 – 7.94 (m, 2H), 7.89 (d, $J = 1.8$ Hz, 2H), 7.48 (ddd, $J = 7.4, 4.6, 1.1$ Hz, 2H).

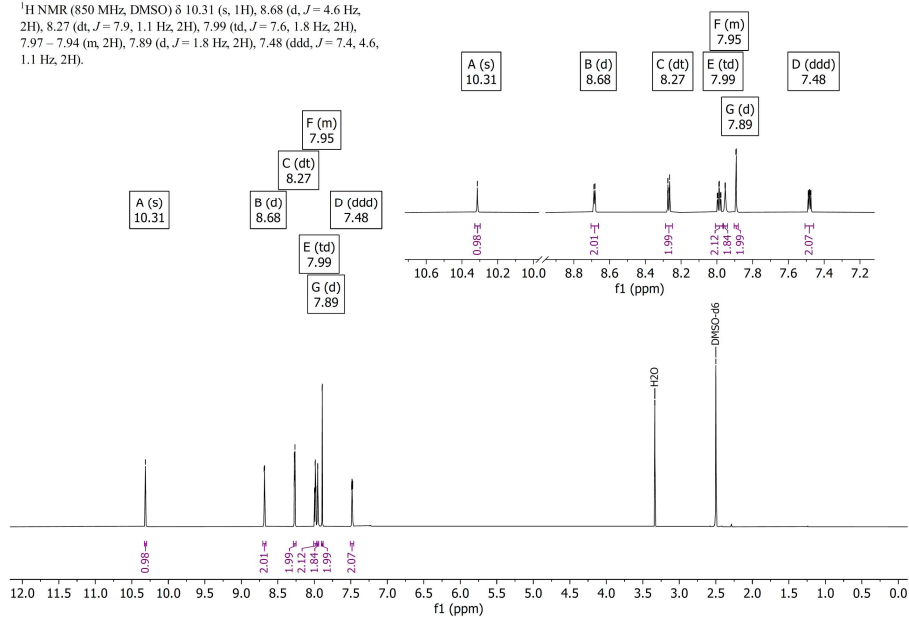


Figure V.14 ^1H -NMR of 3a in DMSO- d_6 .

^{13}C NMR (214 MHz, DMSO) δ 155.05, 154.29, 153.91, 149.44, 149.43, 144.51, 137.37, 124.73, 120.52, 113.05, 111.55.

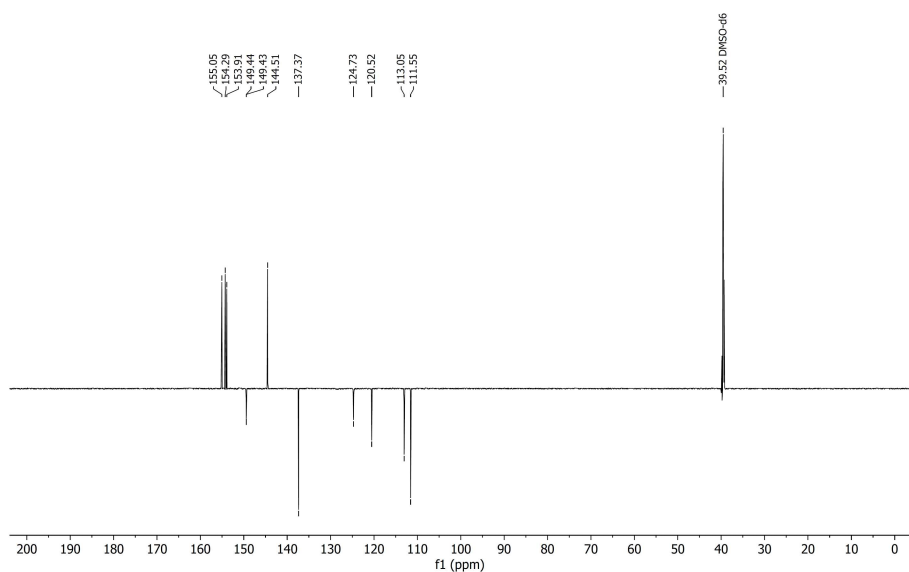


Figure V.15 ^{13}C -APT-NMR of 4a in DMSO- d_6 .

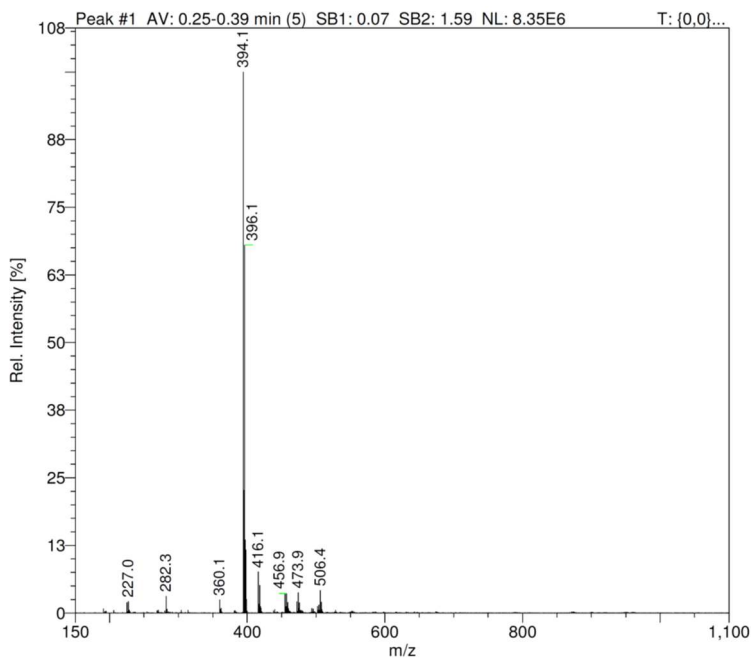


Figure V.16 ESI-MS of **3a**. Calculated for $[\text{C}_{20}\text{H}_{13}\text{Cl}_2\text{N}_5 + \text{H}^+]^+$: 394.1 m/z.

V.4.4 Bis(5-chloro-[2,2'-bipyridin]-6-yl)amine, **3b**

^1H NMR (500 MHz, DMSO) δ 9.12 (s, 1H), 8.66 (ddd, $J = 4.8, 1.8, 0.9$ Hz, 2H), 8.09 – 8.06 (m, 6H), 7.84 (ddd, $J = 8.0, 7.5, 1.8$ Hz, 2H), 7.41 (ddd, $J = 7.5, 4.8, 1.2$ Hz, 2H).

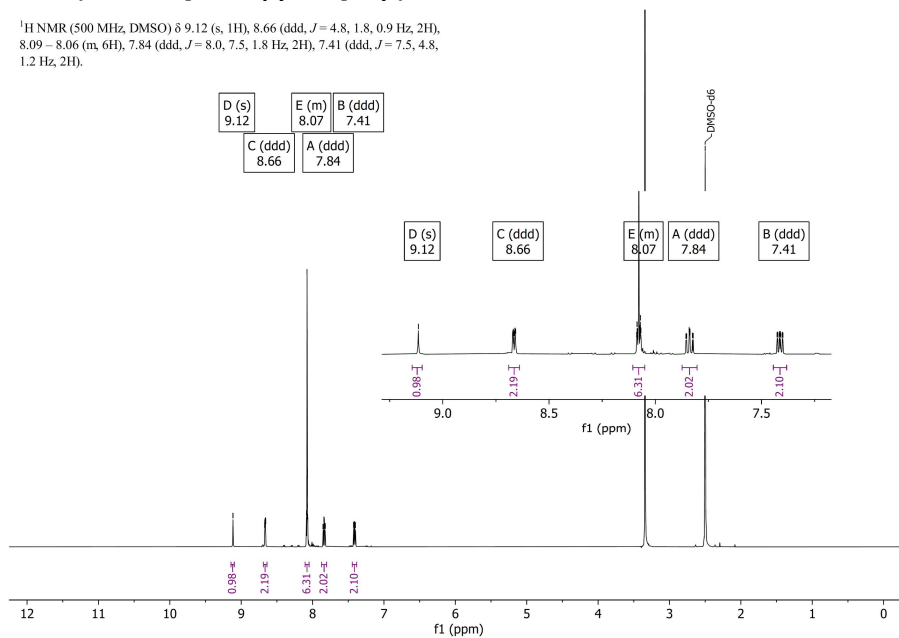


Figure V.17 ^1H -NMR of **3b** in DMSO- d_6 .

^{13}C NMR (126 MHz, DMSO) δ 154.27, 152.11, 150.15, 149.35, 139.06, 137.28, 124.28, 121.65, 120.39, 115.84.

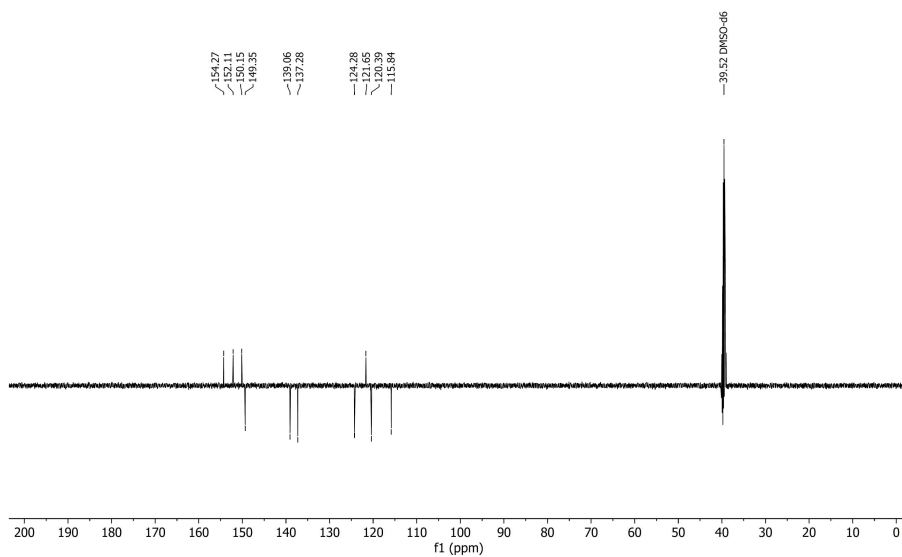


Figure V.18 ^{13}C -APT-NMR of **3b** in DMSO- d_6 .

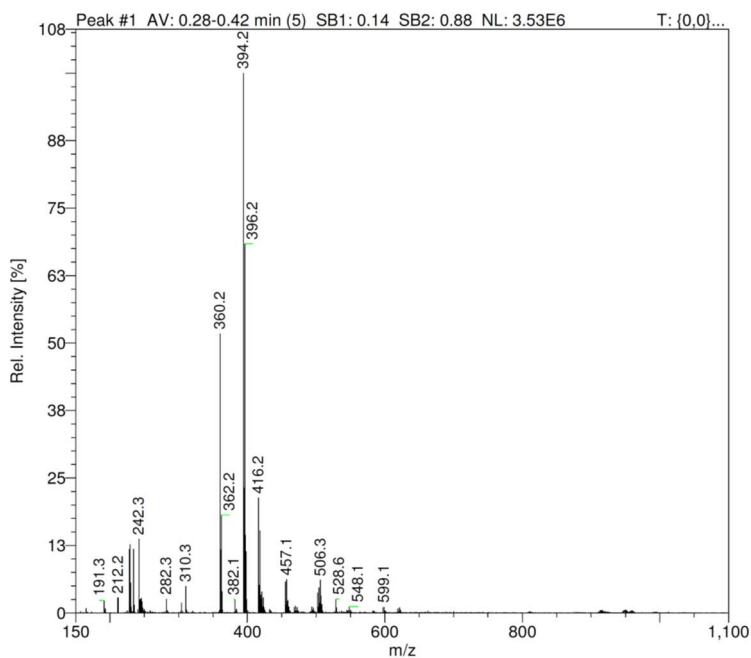
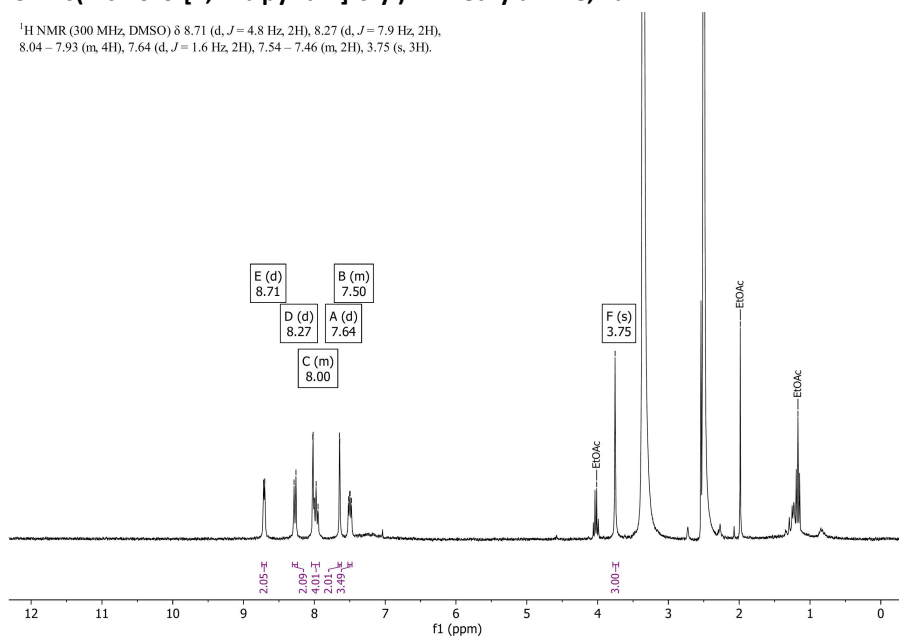


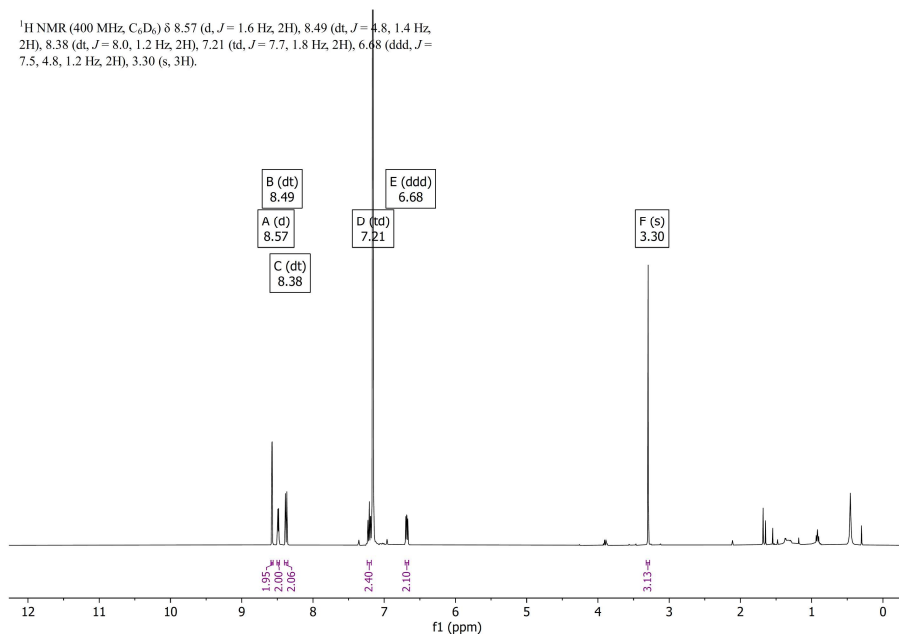
Figure V.19 ESI-MS of **3b**. Calculated for $[\text{C}_{20}\text{H}_{13}\text{Cl}_2\text{N}_5 + \text{H}^+]^+$: 394.1 m/z.

V.4.5 Bis(4-chloro-[2,2'-bipyridin]-6-yl)-*N*-methylamine, 4a

^1H NMR (300 MHz, DMSO) δ 8.71 (d, $J = 4.8$ Hz, 2H), 8.27 (d, $J = 7.9$ Hz, 2H), 8.04 – 7.93 (m, 4H), 7.64 (d, $J = 1.6$ Hz, 2H), 7.54 – 7.46 (m, 2H), 3.75 (s, 3H).

**Figure V.20** ^1H -NMR of **4a** in DMSO- d_6 .

^1H NMR (400 MHz, C_6D_6) δ 8.57 (d, $J = 1.6$ Hz, 2H), 8.49 (dt, $J = 4.8, 1.4$ Hz, 2H), 8.38 (dt, $J = 8.0, 1.2$ Hz, 2H), 7.21 (td, $J = 7.7, 1.8$ Hz, 2H), 6.68 (ddd, $J = 7.5, 4.8, 1.2$ Hz, 2H), 3.30 (s, 3H).

**Figure V.21** ^1H -NMR of **4a** in benzene- d_6 .

V.4.6 Bis(5-chloro-[2,2'-bipyridin]-6-yl)-*N*-methylamine, **4b**

^1H NMR (500 MHz, DMSO) δ 8.69 (ddd, $J = 4.8, 1.8, 0.9$ Hz, 2H), 8.16 – 8.10 (m, 4H), 8.04 (d, $J = 8.2$ Hz, 2H), 7.90 (td, $J = 7.7, 1.8$ Hz, 2H), 7.45 (ddd, $J = 7.5, 4.8, 1.2$ Hz, 2H), 3.60 (s, 3H).

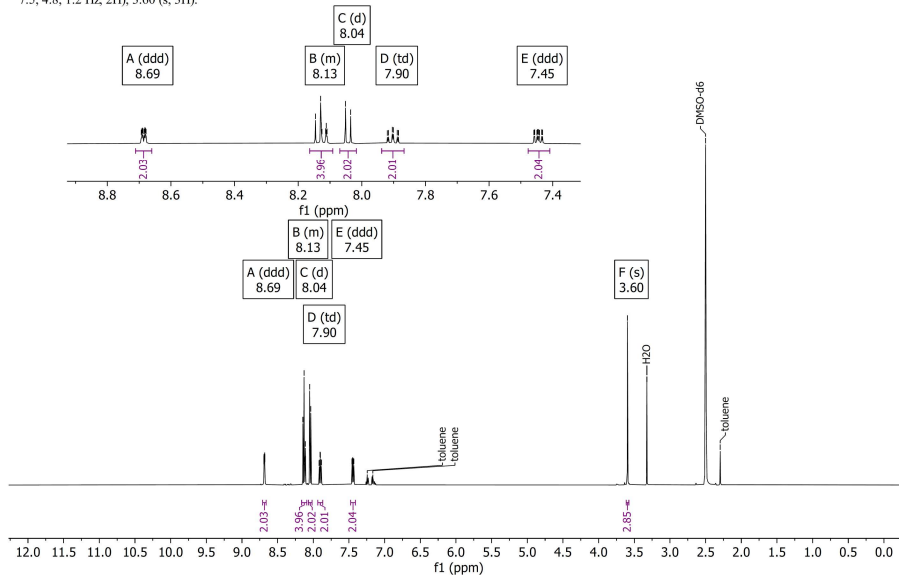


Figure V.24 ^1H -NMR of **4b** in DMSO- d_6 .

^{13}C NMR (126 MHz, DMSO) δ 154.55, 154.07, 152.07, 149.40, 140.19, 137.46, 124.39, 123.83, 120.45, 117.03, 37.73.

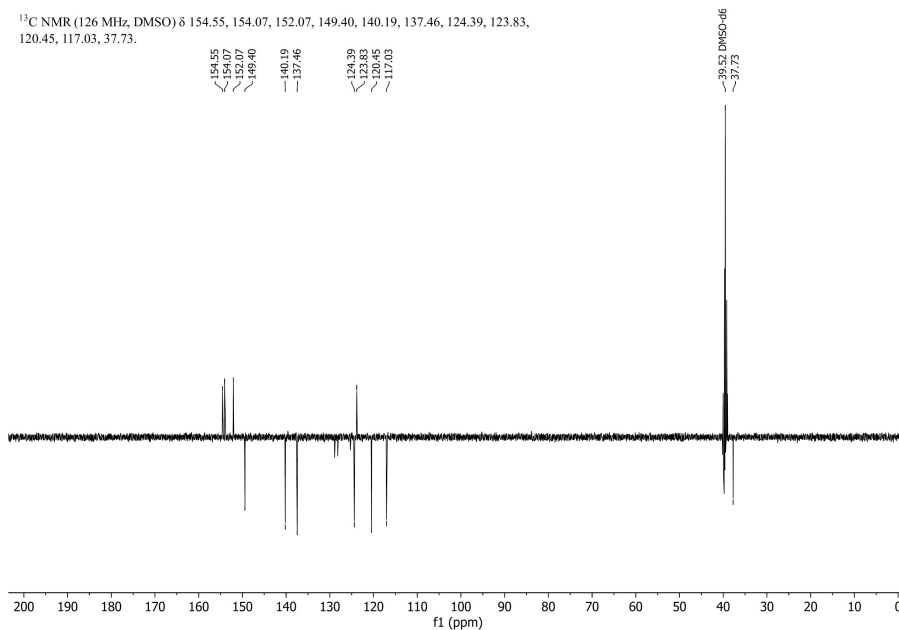


Figure V.25 ^{13}C -APT-NMR of **4b** in DMSO- d_6 .

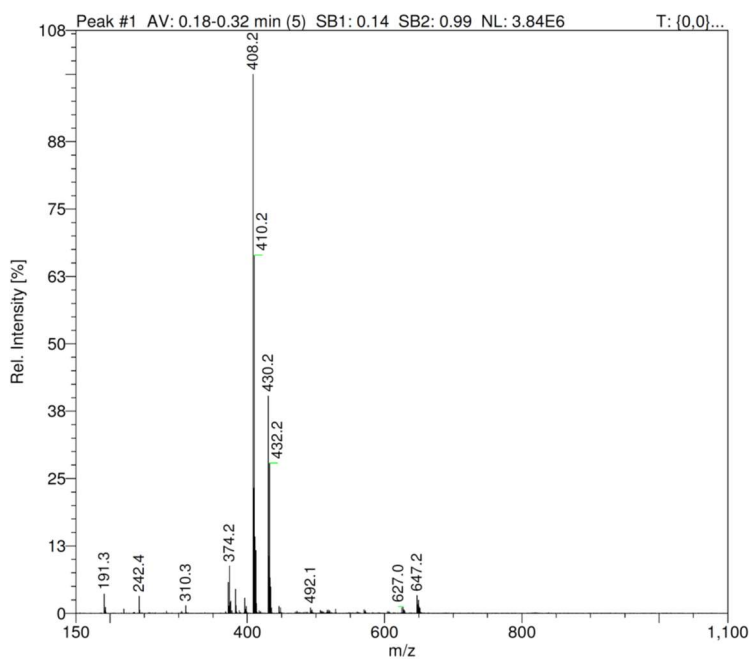


Figure V.26 ESI-MS of **4b**. Calculated for $[\text{C}_{21}\text{H}_{15}\text{Cl}_2\text{N}_5 + \text{H}^+]^+$: 408.1 m/z.

V.4.7 Bis(4-chloro-[2,2'-bipyridin]-6-yl)-N-(2,4-dimethoxybenzyl)amine, **5a**

^1H NMR (400 MHz, DMSO) δ 8.69 (ddd, $J = 4.8, 1.9, 0.9$ Hz, 2H), 8.24 (dt, $J = 8.0, 1.1$ Hz, 2H), 8.00 (d, $J = 1.6$ Hz, 2H), 7.95 (td, $J = 7.7, 1.8$ Hz, 2H), 7.59 (d, $J = 1.6$ Hz, 2H), 7.48 (ddd, $J = 7.5, 4.8, 1.2$ Hz, 2H), 7.18 (d, $J = 2.1$ Hz, 1H), 6.96 (dd, $J = 8.3, 2.0$ Hz, 1H), 6.85 (d, $J = 8.3$ Hz, 1H), 5.55 (s, 2H), 3.66 (s, 3H), 3.63 (s, 3H).

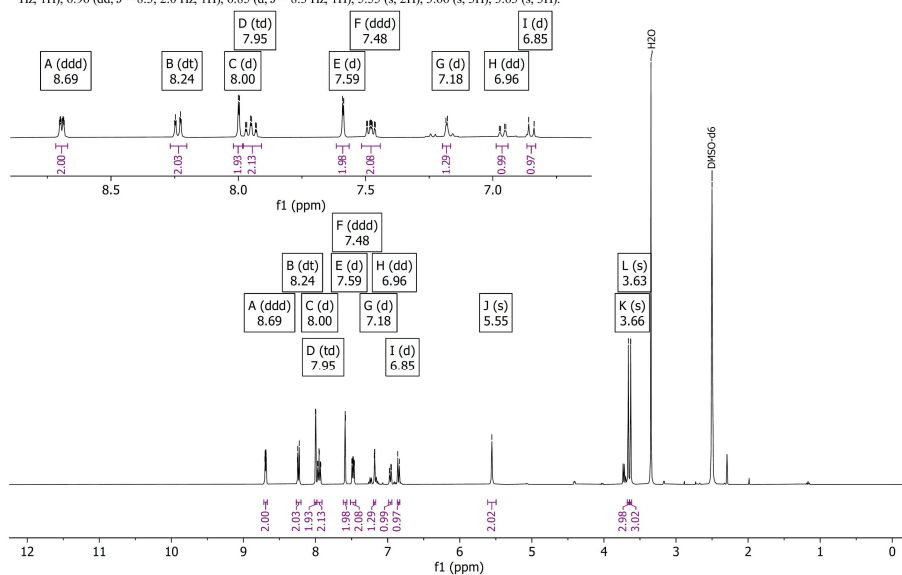


Figure V.27 ^1H -NMR of **5a** in DMSO- d_6 .

^{13}C NMR (101 MHz, DMSO) δ 156.58, 154.94, 153.78, 149.47, 148.63, 147.74, 144.73, 137.55, 130.71, 124.86, 120.64, 119.22, 114.55, 114.17, 111.73, 111.38, 55.36, 55.30, 50.62.

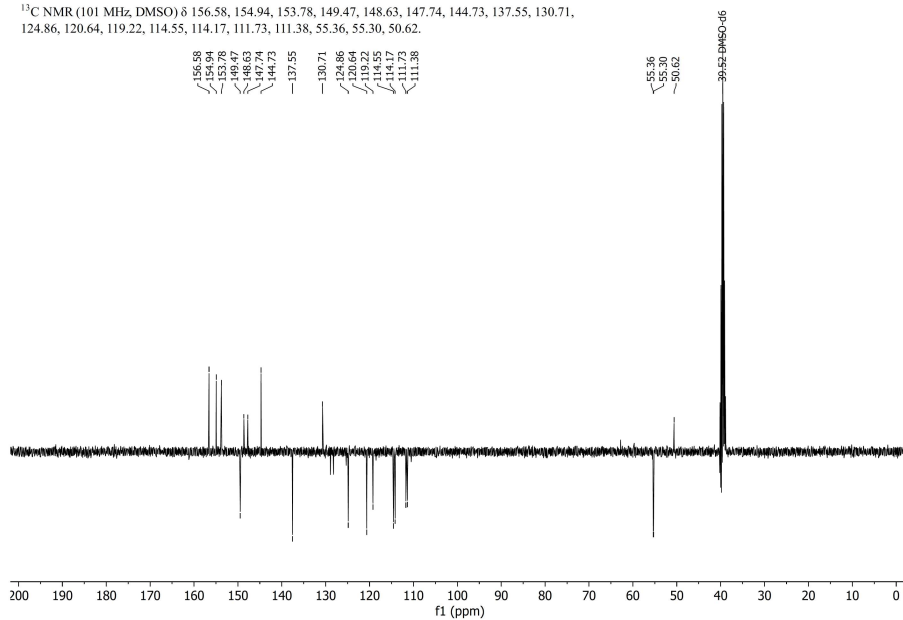


Figure V.28 ^{13}C -APT-NMR of **5a** in DMSO- d_6 .

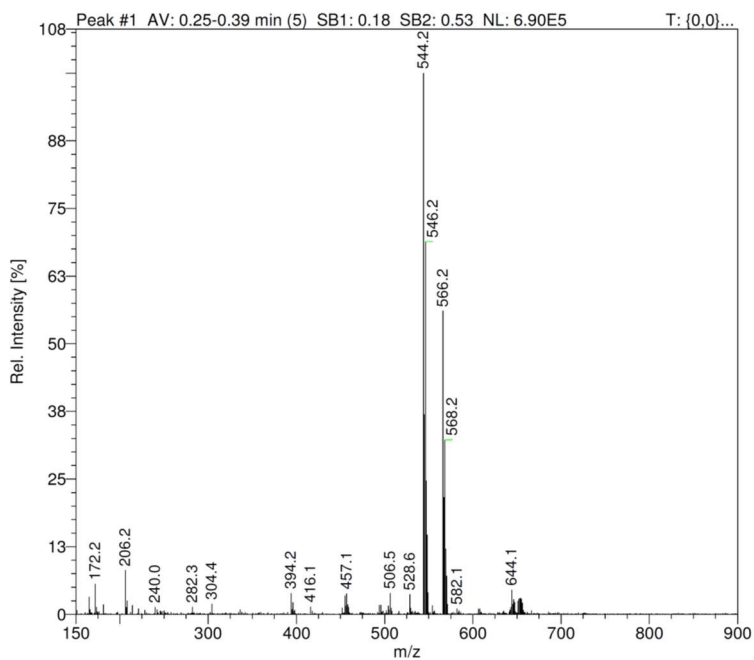
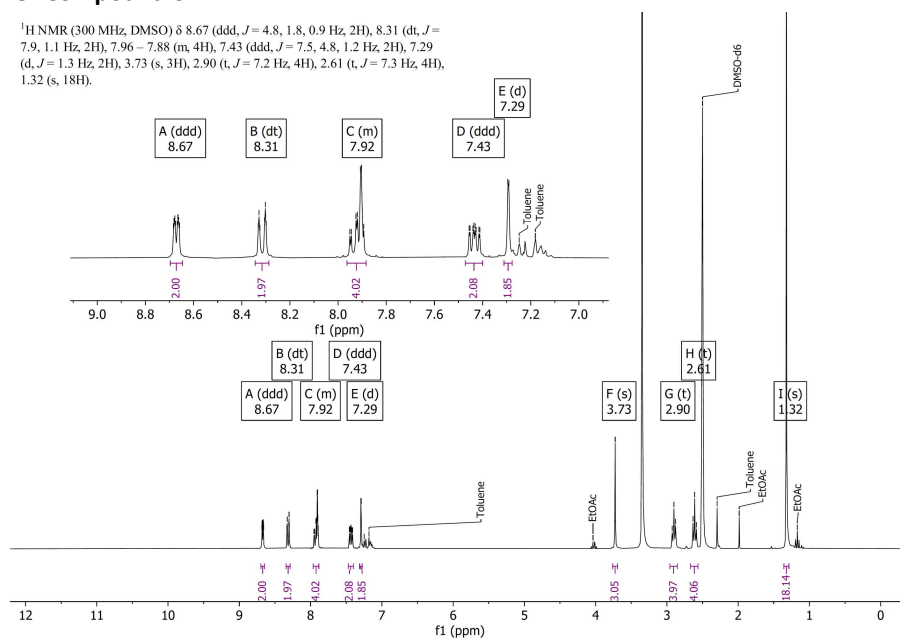


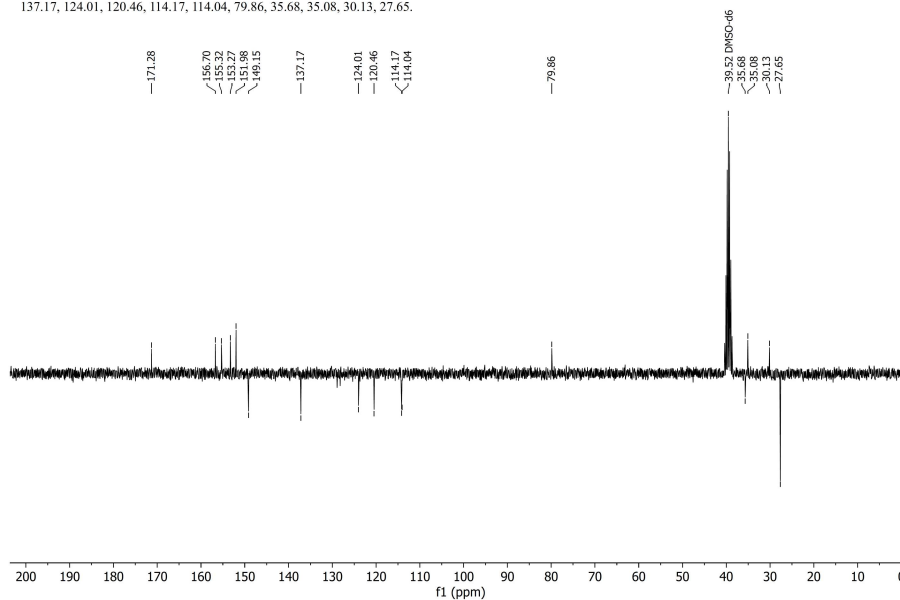
Figure V.29 ESI-MS of **5a**. Calculated for $[\text{C}_{29}\text{H}_{24}\text{Cl}_2\text{N}_5\text{O}_2 + \text{H}^+ + \text{MeOH}]^+$: 544.2 m/z.

V.4.8 Compound 6'

^1H NMR (300 MHz, DMSO) δ 8.67 (ddd, $J = 4.8, 1.8, 0.9$ Hz, 2H), 8.31 (dt, $J = 7.9, 1.1$ Hz, 2H), 7.96 – 7.88 (m, 4H), 7.43 (ddd, $J = 7.5, 4.8, 1.2$ Hz, 2H), 7.29 (d, $J = 1.3$ Hz, 2H), 3.73 (s, 3H), 2.90 (t, $J = 7.2$ Hz, 4H), 2.61 (t, $J = 7.3$ Hz, 4H), 1.32 (s, 18H).

Figure V.30 ^1H -NMR of 6' in DMSO- d_6 .

^{13}C NMR (75 MHz, DMSO) δ 171.28, 156.70, 155.32, 153.27, 151.98, 149.15, 137.17, 124.01, 120.46, 114.17, 114.04, 79.86, 35.68, 35.08, 30.13, 27.65.

Figure V.31 ^{13}C -APT-NMR of 6' in DMSO- d_6 .

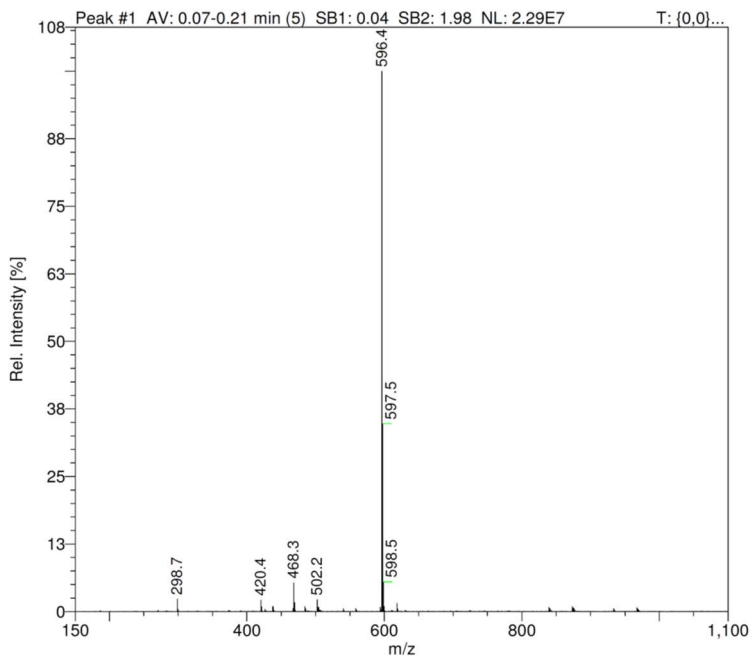


Figure V.32 ESI-MS of **6'**. Calculated for $[\text{C}_{35}\text{H}_{41}\text{N}_5\text{O}_4 + \text{H}^+]^+$: 596.3 m/z.

V.4.9 Compound **7'**

^1H NMR (400 MHz, DMSO) δ 8.66 (ddd, $J=4.8, 1.8, 0.9$ Hz, 2H), 8.30 (dt, $J=7.9, 1.1$ Hz, 2H), 7.95–7.87 (m, 4H), 7.42 (ddd, $J=7.6, 4.7, 1.2$ Hz, 2H), 7.26 (d, $J=1.2$ Hz, 2H), 7.25–7.13 (m, 6H), 6.98 (dd, $J=8.2, 2.0$ Hz, 1H), 6.80 (d, $J=8.3$ Hz, 1H), 5.55 (s, 2H), 3.62 (d, $J=18.5$ Hz, 6H), 2.87 (t, $J=7.2$ Hz, 4H), 2.58 (t, $J=7.2$ Hz, 4H), 1.30 (s, 17H).

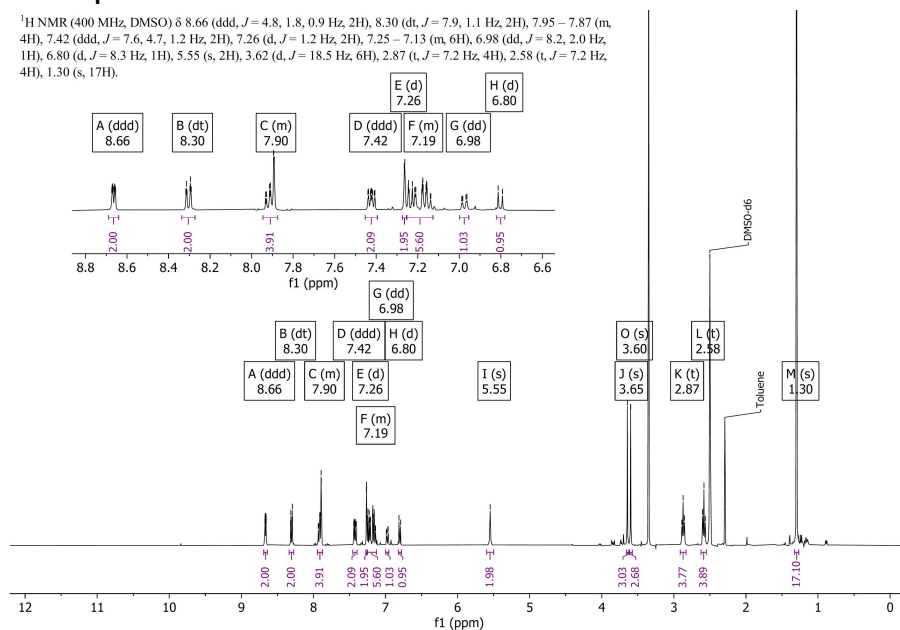
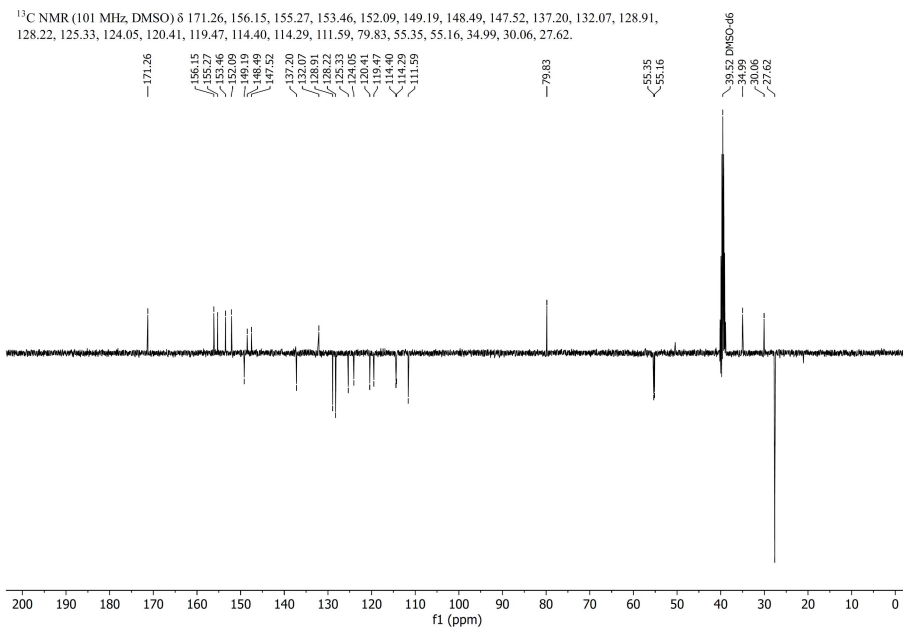
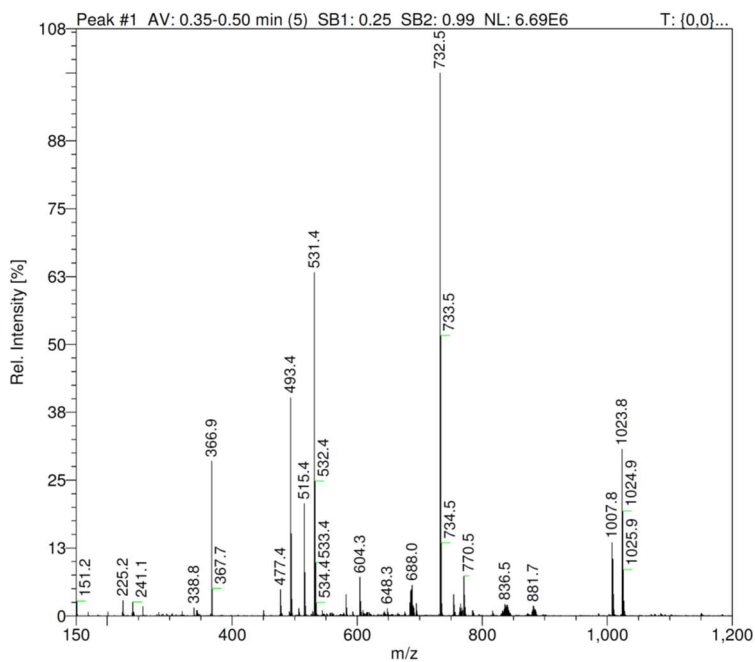
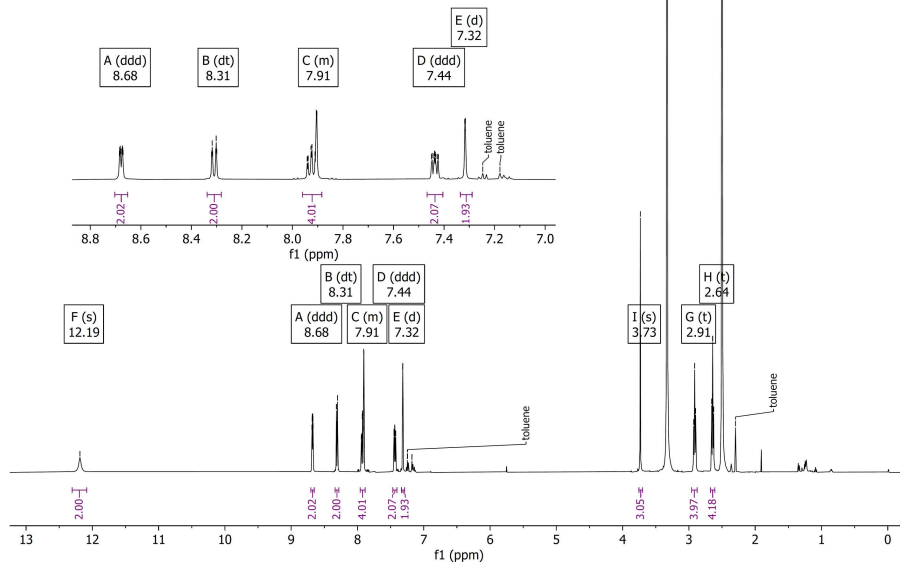


Figure V.33 ^1H -NMR of **7'** in DMSO- d_6 .

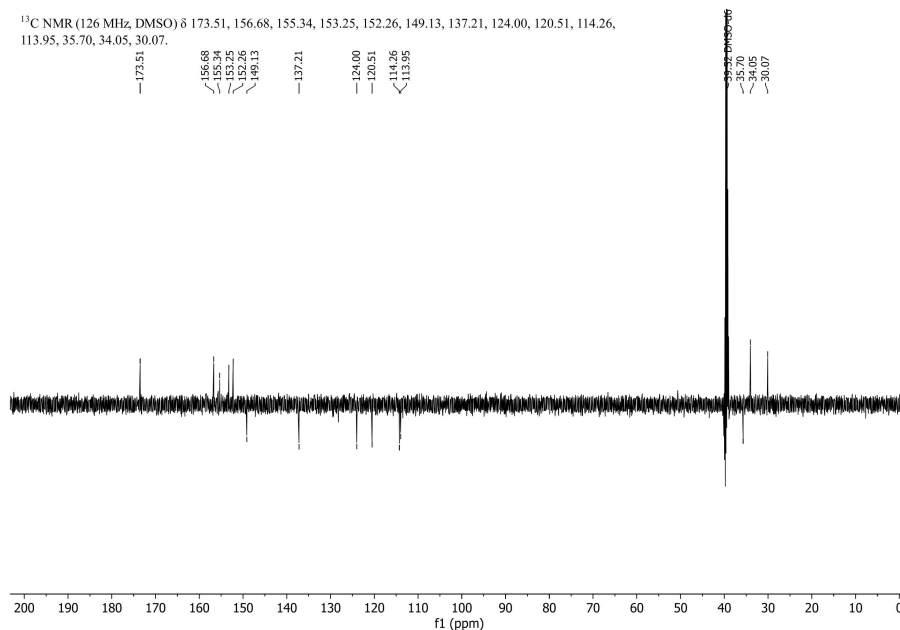
Figure V.34 ^{13}C -APT-NMR of **7'** in DMSO- d_6 .Figure V.35 ESI-MS of **7'**. Calculated for $[\text{C}_{43}\text{H}_{49}\text{N}_5\text{O}_6 + \text{H}^+]^+$: 735.4 m/z .

V.4.10 Compound 6

^1H NMR (500 MHz, DMSO) δ 12.19 (s, 2H), 8.68 (ddd, $J = 4.8, 1.8, 0.9$ Hz, 2H), 8.31 (dt, $J = 8.0, 1.1$ Hz, 2H), 7.95–7.88 (m, 4H), 7.44 (ddd, $J = 7.5, 4.8, 1.2$ Hz, 2H), 7.32 (d, $J = 1.3$ Hz, 2H), 3.73 (s, 3H), 2.91 (t, $J = 7.4$ Hz, 4H), 2.64 (t, $J = 7.5$ Hz, 4H).

Figure V.36 ^1H -NMR of 6 in DMSO- d_6 .

^{13}C NMR (126 MHz, DMSO) δ 173.51, 156.68, 155.34, 153.25, 152.26, 149.13, 137.21, 124.00, 120.51, 114.26, 113.95, 35.70, 34.05, 30.07.

Figure V.37 ^{13}C -APT-NMR of 6 in DMSO- d_6 .

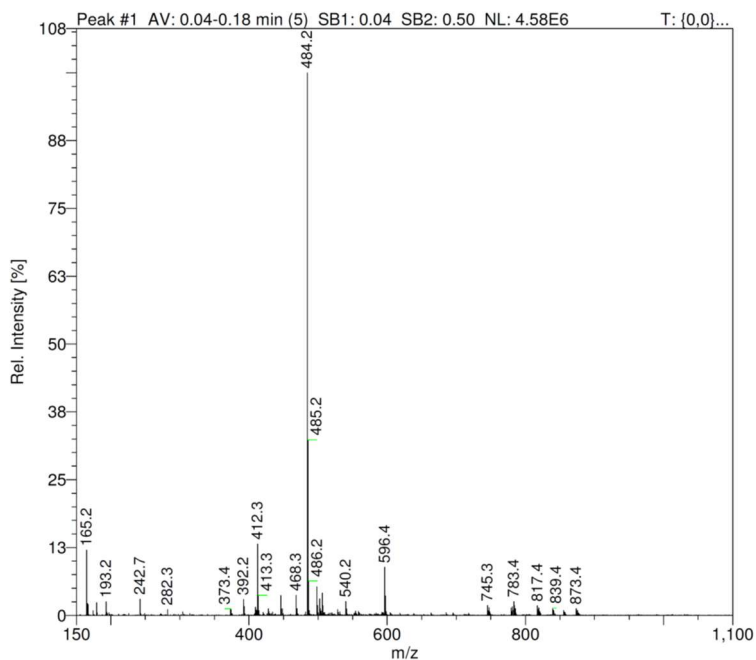


Figure V.38 ESI-MS of **6**. Calculated for $[\text{C}_{27}\text{H}_{25}\text{N}_5\text{O}_4 + \text{H}^+]^+$: 484.2 m/z.

V.4.11 Compound **7**

^1H NMR (400 MHz, DMSO) δ 12.35 (s, 2H), 8.61 (d, $J = 4.3$ Hz, 2H), 8.49 (d, $J = 8.0$ Hz, 2H), 8.03 (td, $J = 7.6, 2.2$ Hz, 4H), 7.61–7.48 (m, 4H), 3.00 (t, $J = 7.2$ Hz, 4H), 2.73 (t, $J = 7.3$ Hz, 4H).

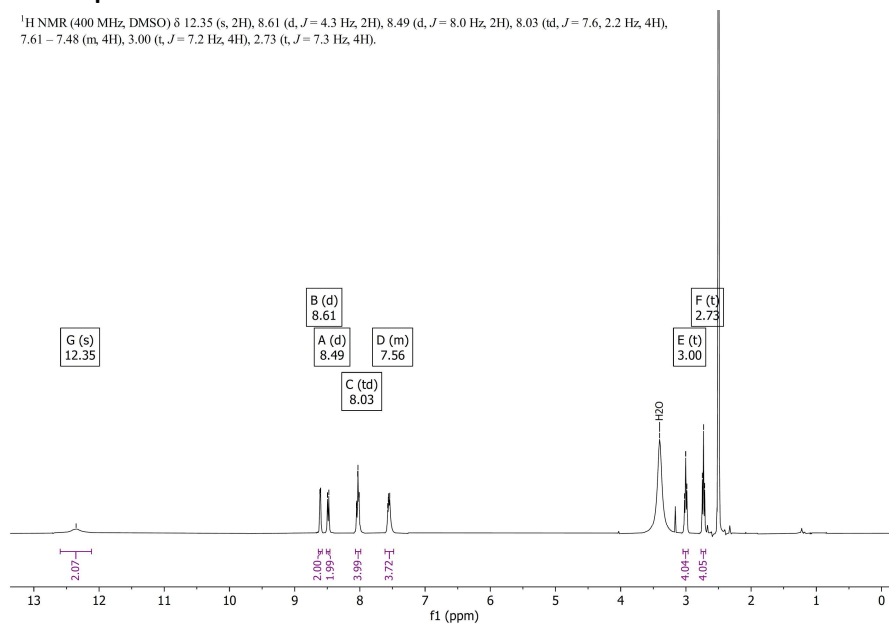


Figure V.39 ^1H -NMR of **7** in DMSO- d_6 .

^{13}C NMR (126 MHz, DMSO) δ 173.28, 158.44, 158.18, 149.27, 137.96, 125.23, 121.64, 118.02, 115.66, 113.51, 33.32, 30.20.

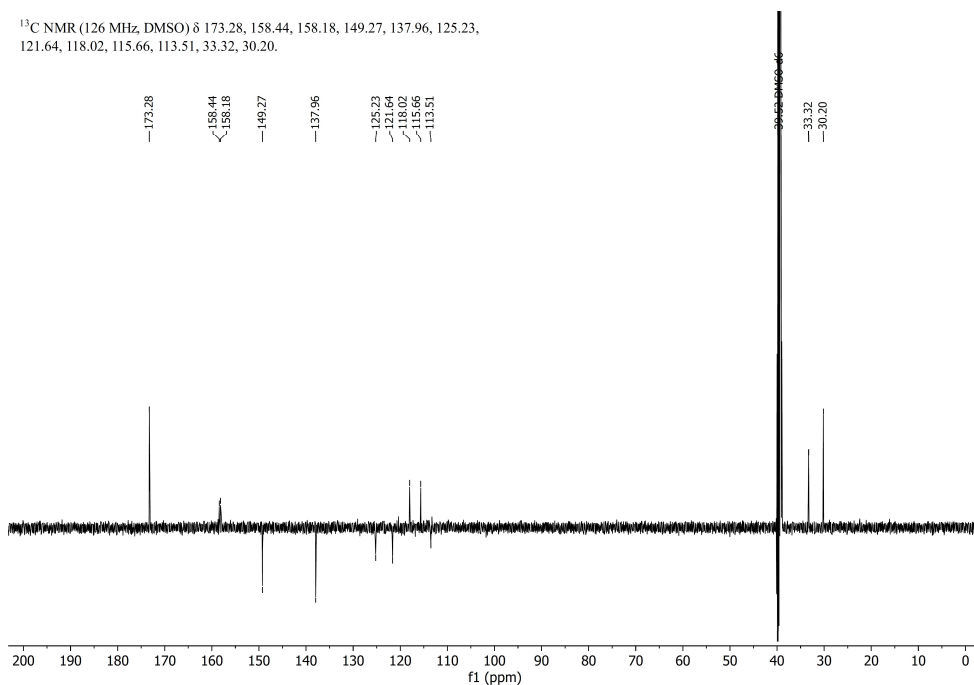


Figure V.40 ^{13}C -APT-NMR of **7** in $\text{DMSO-}d_6$.

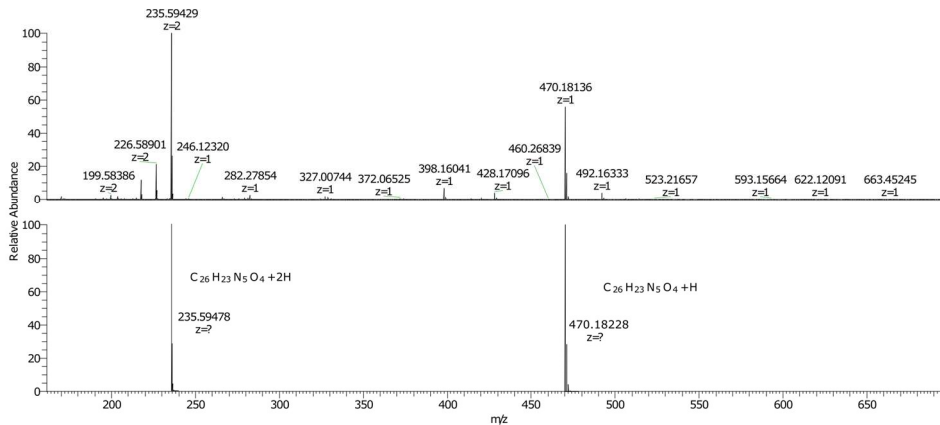
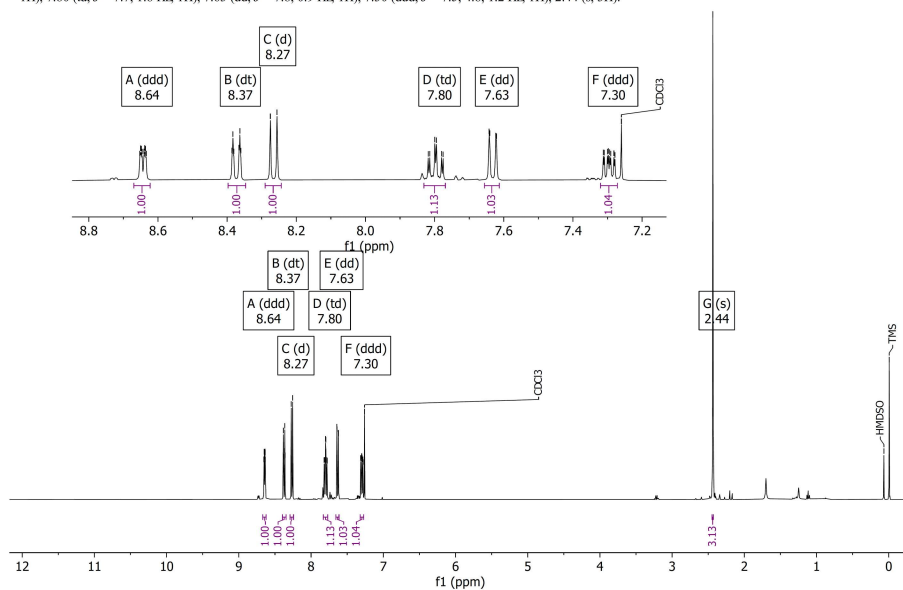


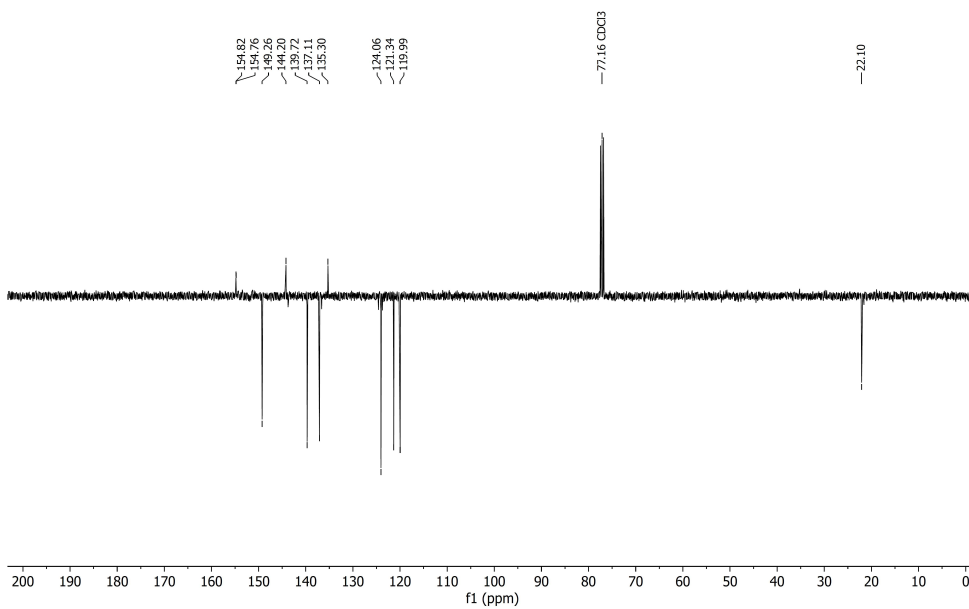
Figure V.41 ESI-HRMS of **7**. Calculated for $[\text{C}_{26}\text{H}_{23}\text{N}_5\text{O}_4 + \text{H}^+]^+$: 470.1823 m/z and $[\text{C}_{26}\text{H}_{23}\text{N}_5\text{O}_4 + 2\text{H}^+]^{2+}$: 235.5948 m/z.

V.4.12 6-bromide-5-methyl-2,2'-bipyridine, **17b**

^1H NMR (400 MHz, CDCl_3) δ 8.64 (ddd, $J = 4.8, 1.9, 1.0$ Hz, 1H), 8.37 (dt, $J = 8.0, 1.1$ Hz, 1H), 8.27 (d, $J = 7.7$ Hz, 1H), 7.80 (td, $J = 7.7, 1.8$ Hz, 1H), 7.63 (dd, $J = 7.8, 0.9$ Hz, 1H), 7.30 (ddd, $J = 7.5, 4.8, 1.2$ Hz, 1H), 2.44 (s, 3H).

Figure V.42 ^1H -NMR of **17b** in CDCl_3 .

^{13}C NMR (101 MHz, CDCl_3) δ 154.82, 154.76, 149.26, 144.20, 139.72, 137.11, 135.30, 124.06, 121.34, 119.99, 22.10.

Figure V.43 ^{13}C -APT-NMR of **17b** in CDCl_3 .

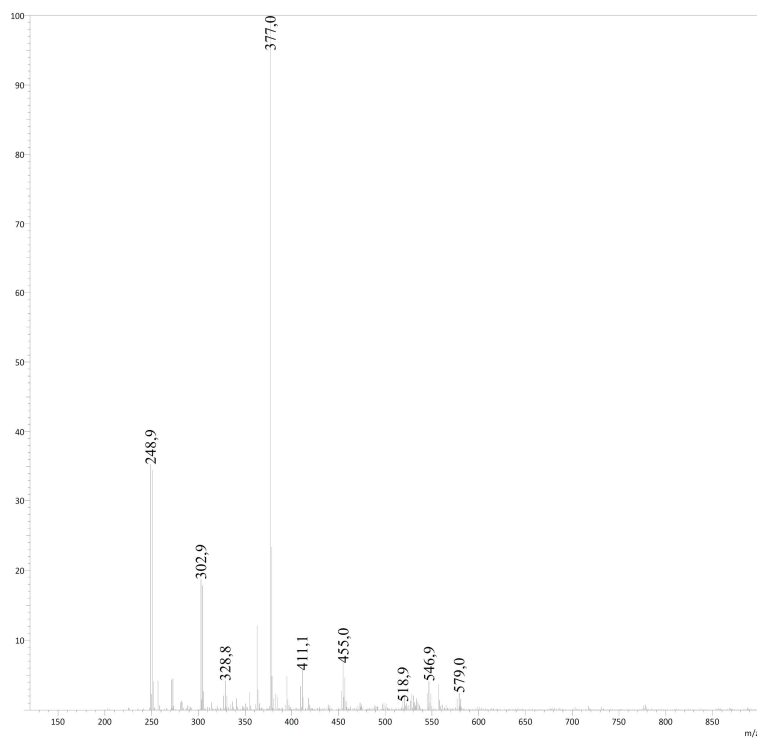


Figure V.44 ESI-MS of **17b**. Calculated for $[\text{C}_{11}\text{H}_9\text{BrN}_2 + \text{H}^+]$: 249.0 m/z.

V.4.13 Bis(5-methyl-[2,2'-bipyridin]-6-yl)amine, **18**

^1H NMR (400 MHz, DMSO- d_6) δ 8.63 (ddd, $J = 4.8, 1.8, 0.9$ Hz, 2H), 8.42 (s, 1H), 8.05 (dt, $J = 8.1, 1.1$ Hz, 2H), 7.98 (d, $J = 7.6$ Hz, 2H), 7.82 (td, $J = 7.7, 1.8$ Hz, 2H), 7.73 (dd, $J = 7.7, 0.9$ Hz, 2H), 7.35 (ddd, $J = 7.5, 4.7, 1.2$ Hz, 2H), 2.25 (s, 6H).

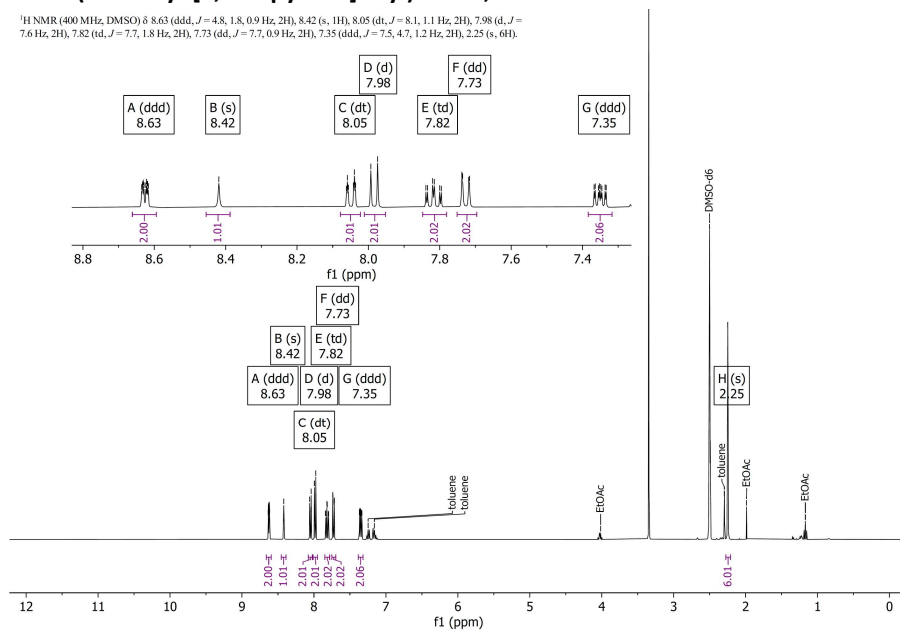


Figure V.45 ^1H -NMR of **18** in DMSO- d_6 .

^{13}C NMR (101 MHz, DMSO) δ 155.45, 153.60, 151.04, 149.15, 139.35, 137.04, 124.59, 123.57, 119.79, 114.29, 17.77.

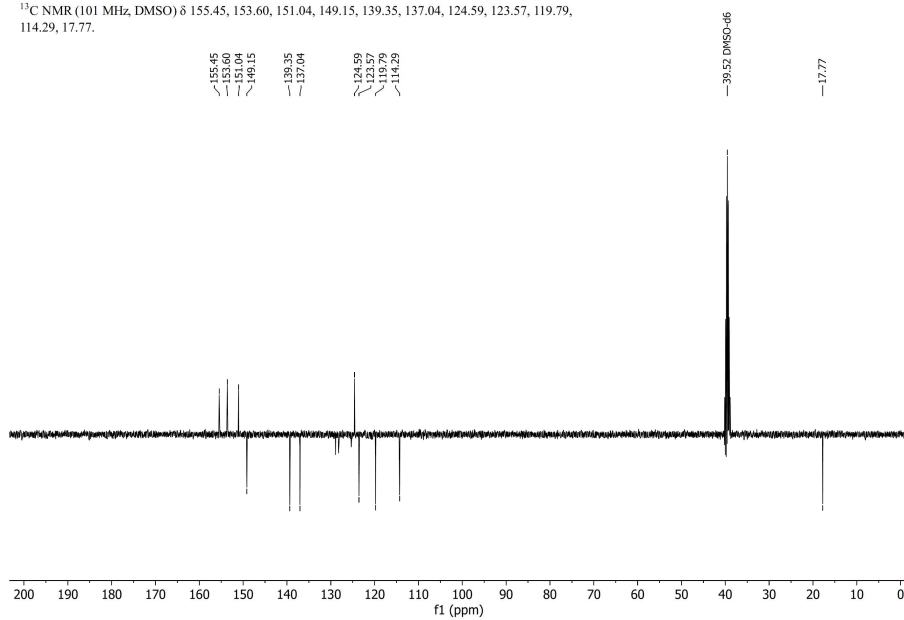


Figure V.46 ^{13}C -APT-NMR of **18** in DMSO- d_6 .

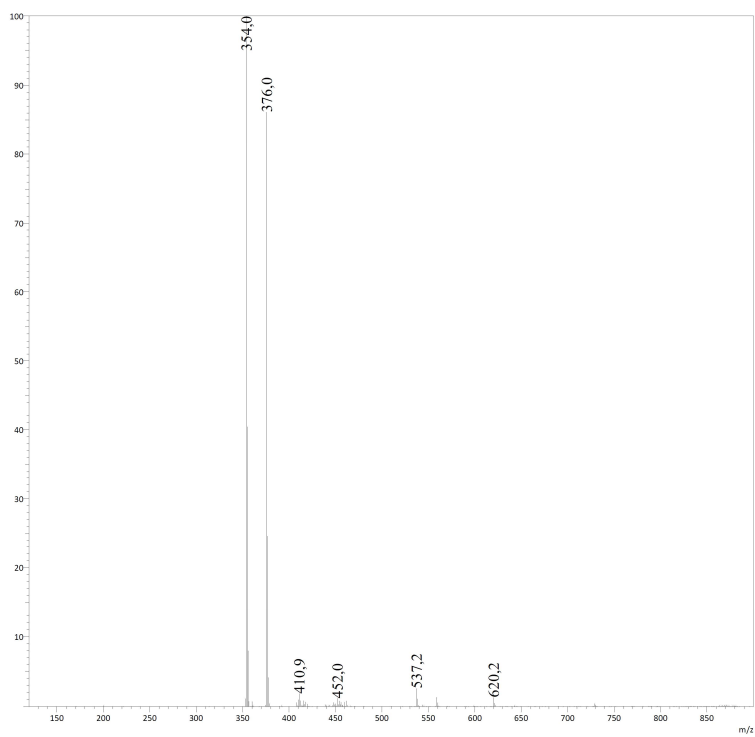
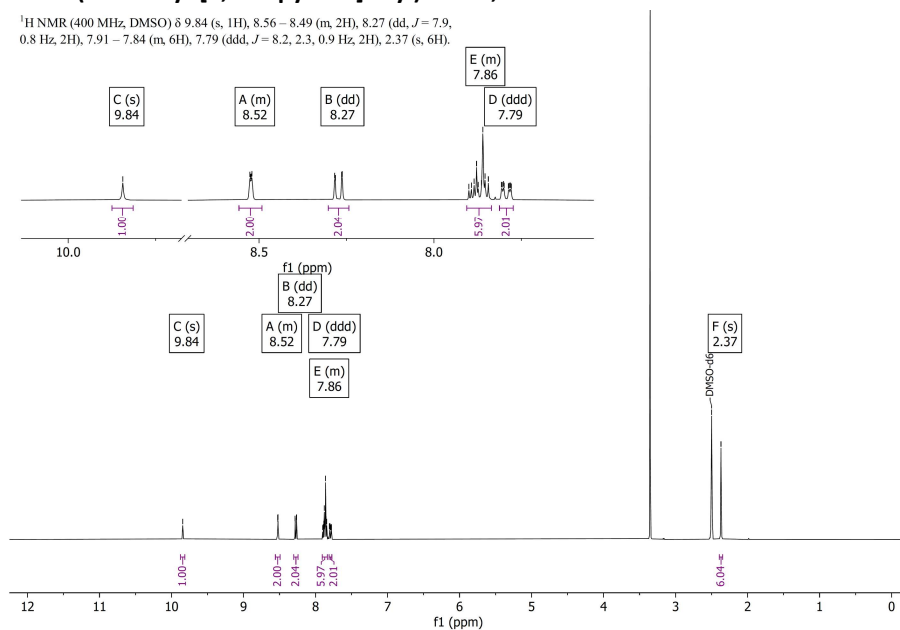


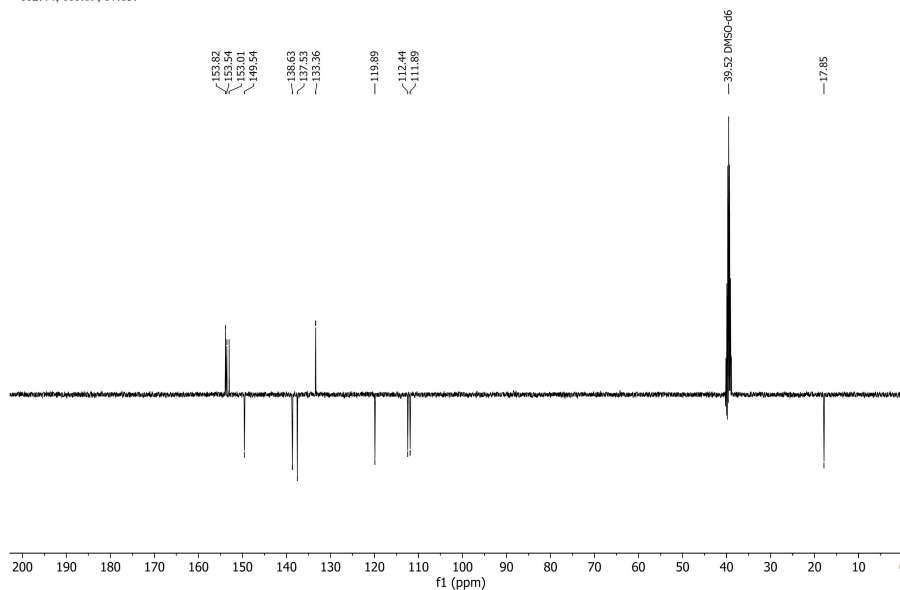
Figure V.47 ESI-MS of **18**. Calculated for $[\text{C}_{22}\text{H}_{19}\text{N}_5 + \text{H}^+]^+$: 354.2 m/z.

V.4.14 Bis(5'-methyl-[2,2'-bipyridin]-6-yl)amine, 19

^1H NMR (400 MHz, DMSO) δ 9.84 (s, 1H), 8.56 – 8.49 (m, 2H), 8.27 (dd, $J = 7.9$, 0.8 Hz, 2H), 7.91 – 7.84 (m, 6H), 7.79 (ddd, $J = 8.2, 2.3, 0.9$ Hz, 2H), 2.37 (s, 6H).

**Figure V.48** ^1H -NMR of **19** in DMSO- d_6 .

^{13}C NMR (101 MHz, DMSO) δ 153.82, 153.54, 153.01, 149.54, 138.63, 137.53, 133.36, 119.89, 112.44, 111.89, 17.85.

**Figure V.49** ^{13}C -APT-NMR of **19** in DMSO- d_6 .

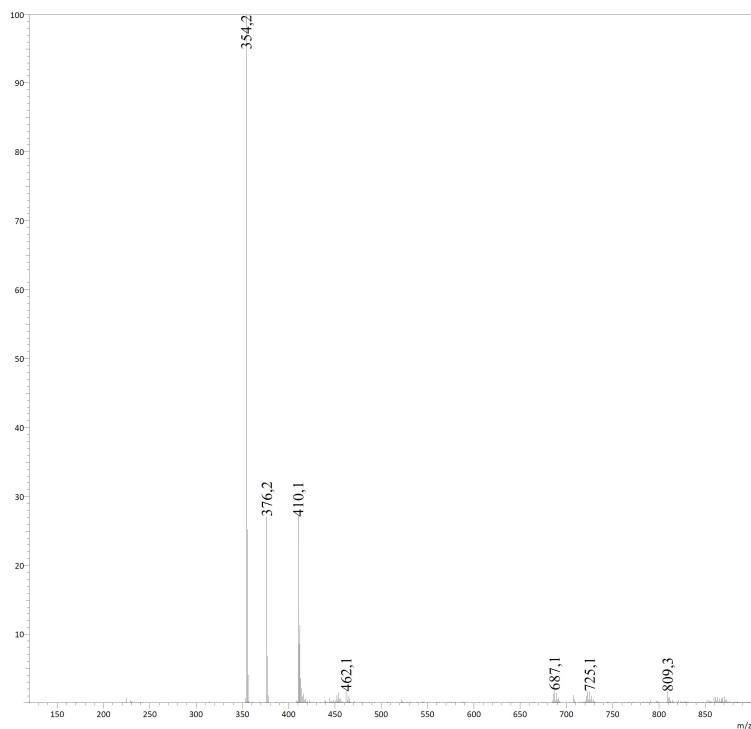


Figure V.50 ESI-MS of **19**. Calculated for $[\text{C}_{22}\text{H}_{19}\text{N}_5 + \text{H}^+]^+$: 354.2 m/z.

V.4.15 Bis(5'-methyl-[2,2'-bipyridin]-6-yl)-N-methylamine, **20**

^1H NMR (400 MHz, DMSO) δ 8.51 (dt, $J = 2.4, 0.9$ Hz, 2H), 8.20 (dd, $J = 7.9, 0.8$ Hz, 2H), 7.96 (dd, $J = 7.5, 0.8$ Hz, 2H), 7.82 (dd, $J = 8.2, 7.5$ Hz, 2H), 7.74 (ddd, $J = 8.1, 2.3, 0.8$ Hz, 2H), 7.37 (dd, $J = 8.2, 0.8$ Hz, 2H), 3.73 (s, 3H), 2.35 (s, 6H).

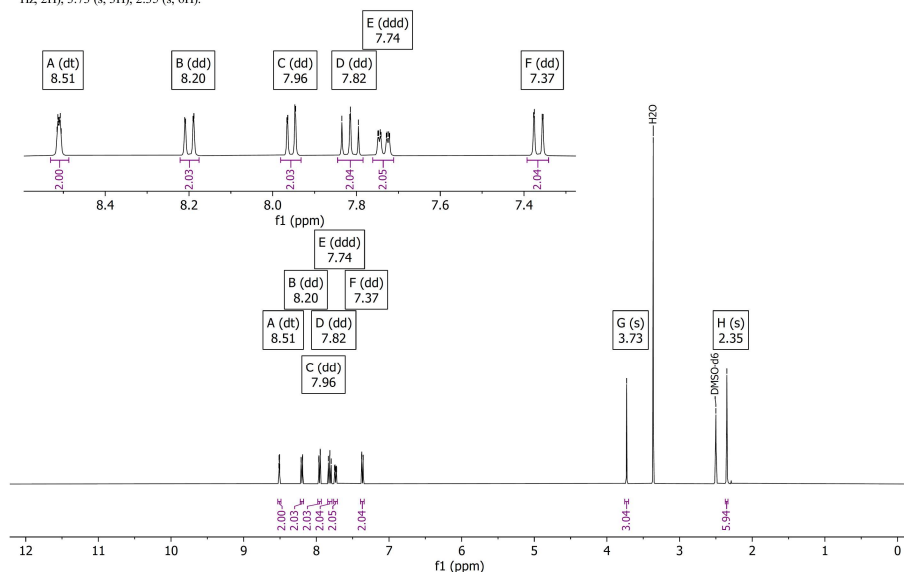


Figure V.51 ^1H -NMR of **20** in DMSO- d_6 .

^{13}C NMR (101 MHz, DMSO) δ 156.43, 153.62, 152.85, 149.51, 138.47, 137.55, 133.46, 119.89, 114.18, 113.29, 35.62, 17.86.

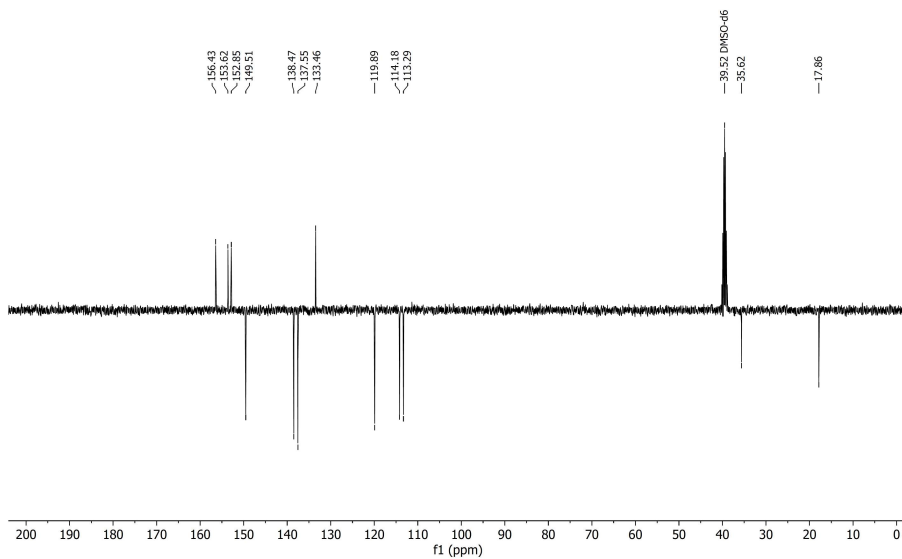


Figure V.52 ^{13}C -APT-NMR of **20** in DMSO- d_6 .

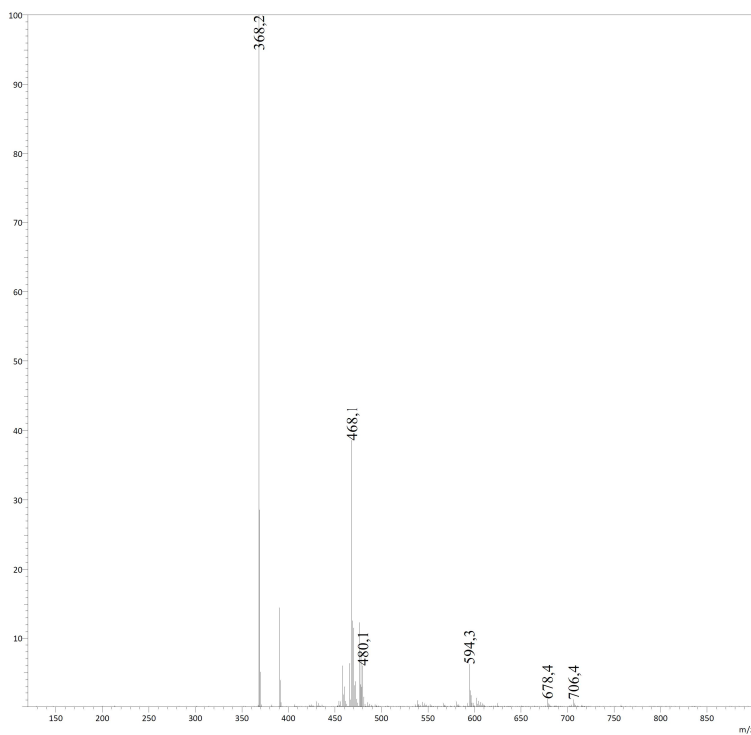
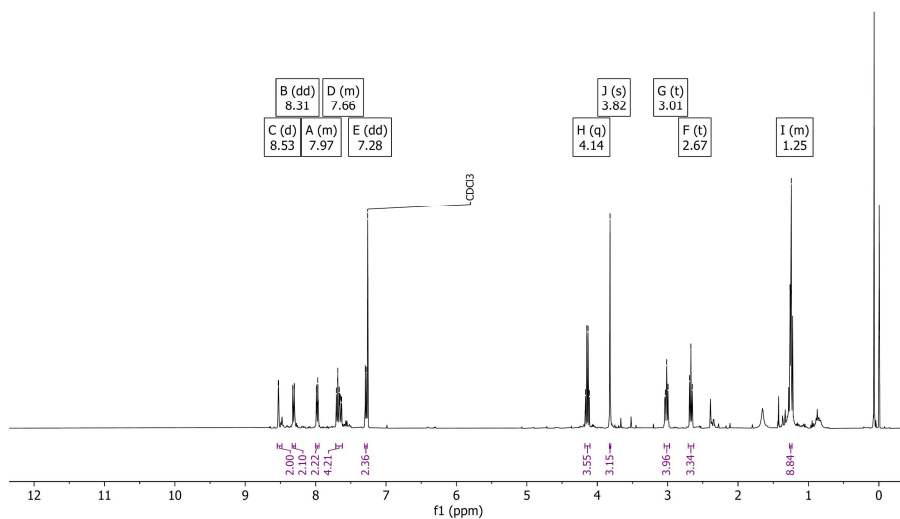


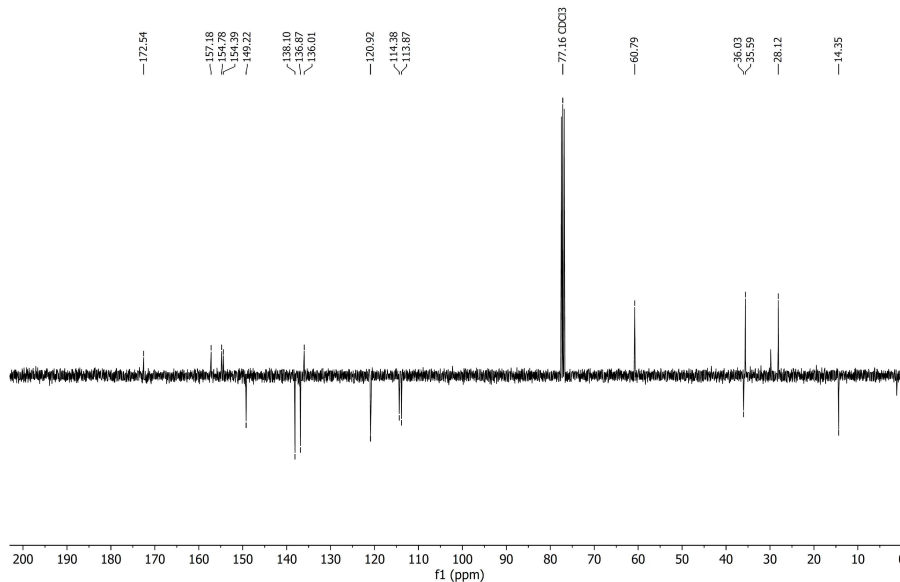
Figure V.53 ESI-MS of **20**. Calculated for $[\text{C}_{23}\text{H}_{21}\text{N}_5 + \text{H}]^+$: 368.2 m/z.

V.4.16 Compound 21

^1H NMR (400 MHz, CDCl_3) δ 8.53 (d, $J=1.5$ Hz, 2H), 8.31 (dd, $J=8.1, 0.8$ Hz, 2H), 8.00–7.95 (m, 2H), 7.71–7.62 (m, 4H), 7.28 (dd, $J=8.3, 0.8$ Hz, 2H), 4.14 (q, $J=7.1$ Hz, 4H), 3.82 (s, 3H), 3.01 (t, $J=7.6$ Hz, 4H), 2.67 (t, $J=7.6$ Hz, 3H), 1.27–1.23 (m, 9H).

Figure V.51 ^1H -NMR of 21 in $\text{DMSO}-d_6$.

^{13}C NMR (101 MHz, CDCl_3) δ 172.54, 157.18, 154.78, 154.39, 149.22, 138.10, 136.87, 136.01, 120.92, 114.38, 113.87, 60.79, 36.03, 35.59, 28.12, 14.35.

Figure V.52 ^{13}C -APT-NMR of 21 in $\text{DMSO}-d_6$.

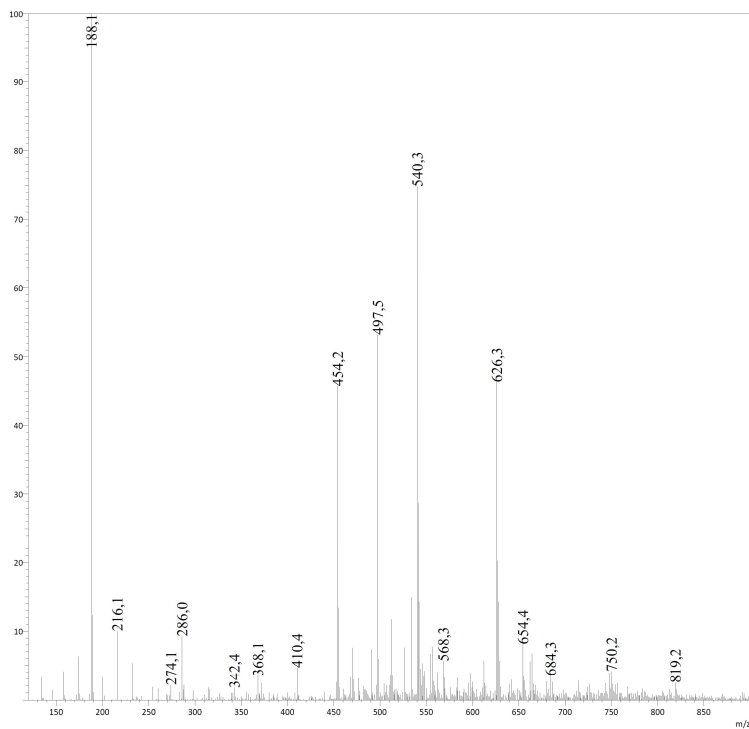


Figure V.53 ESI-MS of **21**. Calculated for $[\text{C}_{31}\text{H}_{33}\text{N}_5\text{O}_4 + \text{H}]^+$: 540.3 m/z

V.4.17 $[\text{Ru}(\text{Mebppy})(\text{QC82})_2]^{2+}$, $[\text{24}]^{2+}$:

^1H NMR (400 MHz Acetone) δ 9.98 (ddd, $J = 5.6, 1.5, 0.7$ Hz, 2H), 8.69 (dt, $J = 8.0, 1.1$ Hz, 2H), 8.41 (dd, $J = 7.9, 0.9$ Hz, 2H), 8.30 – 8.17 (m, 4H), 7.99 – 7.89 (m, 4H), 6.94 (t, $J = 1.4$ Hz, 2H), 6.69 (t, $J = 1.6$ Hz, 2H), 6.06 (t, $J = 1.5$ Hz, 2H), 4.89 (s, 4H), 4.18 (s, 3H), 1.93 (q, $J = 3.2$ Hz, 6H), 1.74 – 1.57 (m, 25H).

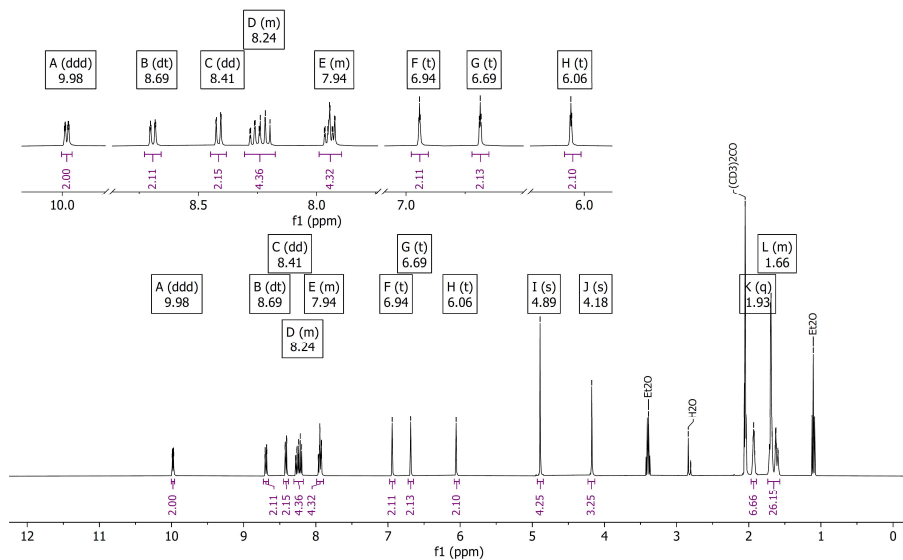
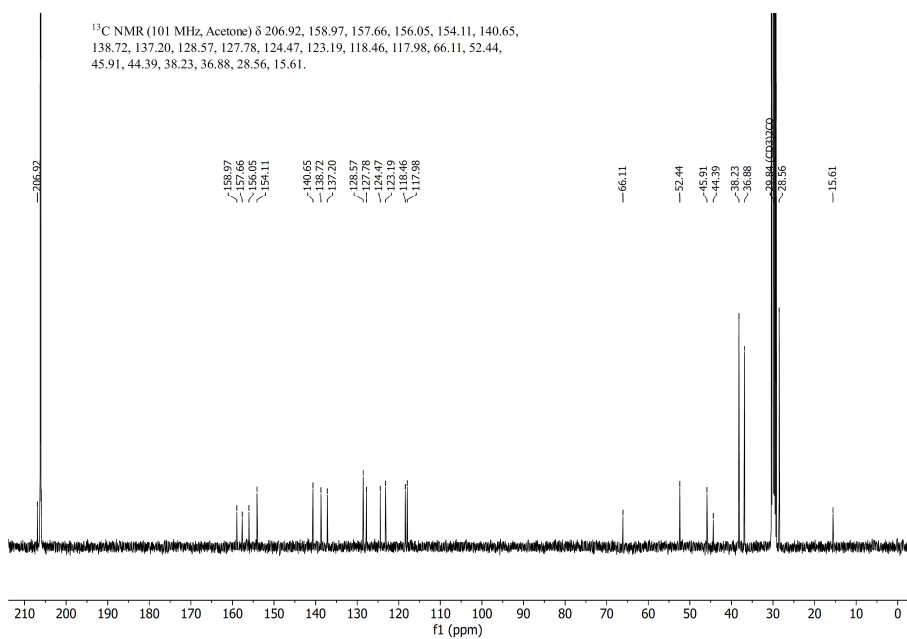
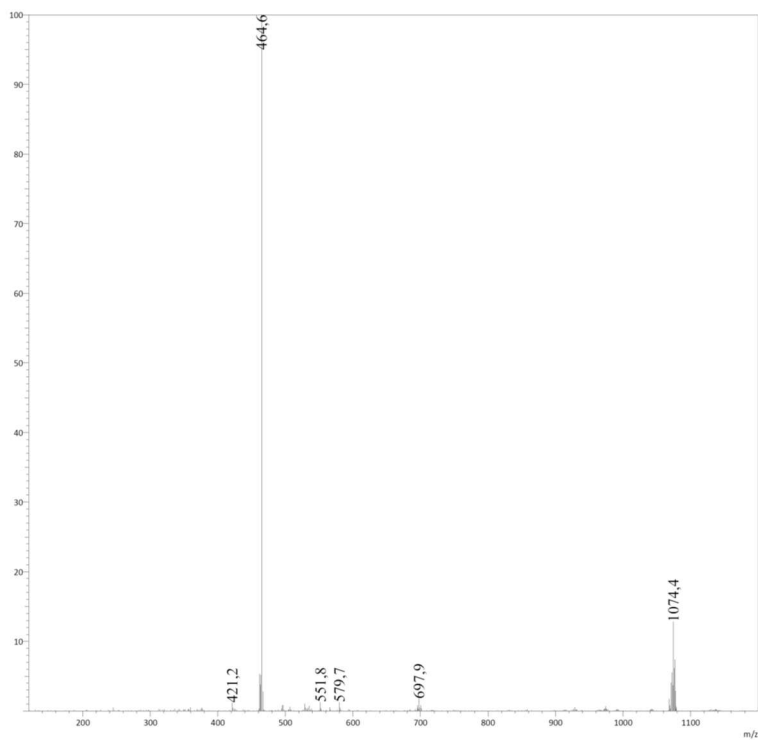


Figure V.54 ^1H -NMR of $[\text{24}](\text{PF}_6)_2$ in Acetone- d_6 .

Figure V.55 ^{13}C -NMR of $[\mathbf{24}](\text{PF}_6)_2$ in Acetone- d_6 .Figure V.56 ESI-MS of $[\mathbf{24}](\text{PF}_6)_2$. Calculated for $[\text{C}_{51}\text{H}_{57}\text{N}_9\text{O}_2\text{Ru}]^{2+}$: 464.7 m/z.

^1H NMR (400 MHz, MeOD) δ 9.78 (dt, $J = 5.4, 1.3$ Hz, 2H), 8.60 (dt, $J = 8.1, 1.1$ Hz, 2H), 8.32 (dd, $J = 7.9, 0.9$ Hz, 2H), 8.23–8.09 (m, 4H), 7.89 (ddd, $J = 7.3, 5.6, 1.3$ Hz, 2H), 7.81 (dd, $J = 8.5, 0.9$ Hz, 2H), 6.68 (t, $J = 1.4$ Hz, 2H), 6.56 (t, $J = 1.6$ Hz, 2H), 5.89 (t, $J = 1.5$ Hz, 2H), 4.05 (s, 3H), 1.97 (s, 6H), 1.79–1.64 (m, 24H).

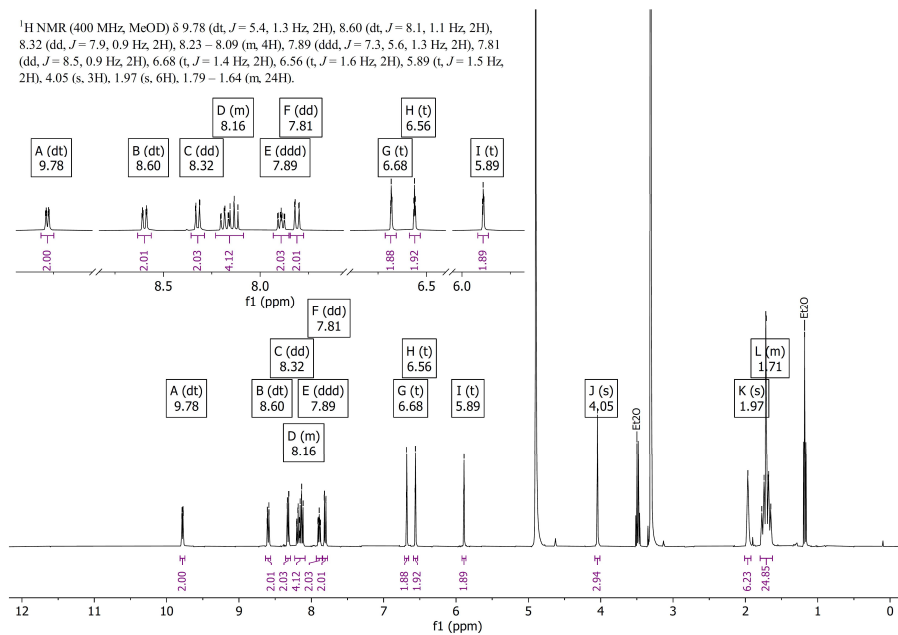


Figure V.57 ^1H -NMR of $[\text{24}]\text{Cl}_2$ in Methanol- d_4 .

^{13}C NMR (101 MHz, MeOD) δ 201.67, 159.57, 158.26, 156.42, 154.23, 140.86, 138.91, 137.49, 128.77, 127.86, 124.80, 123.23, 118.76, 117.86, 63.38, 38.71, 37.33, 29.18.

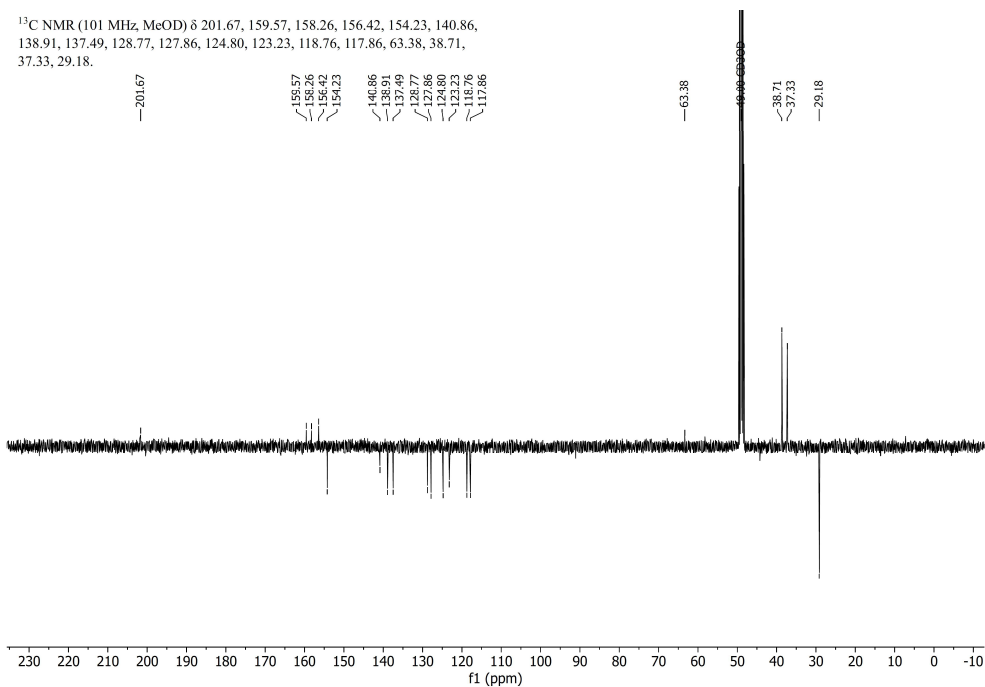


Figure V.58 ^{13}C -APT-NMR of $[\text{24}]\text{Cl}_2$ in Methanol- d_4 .

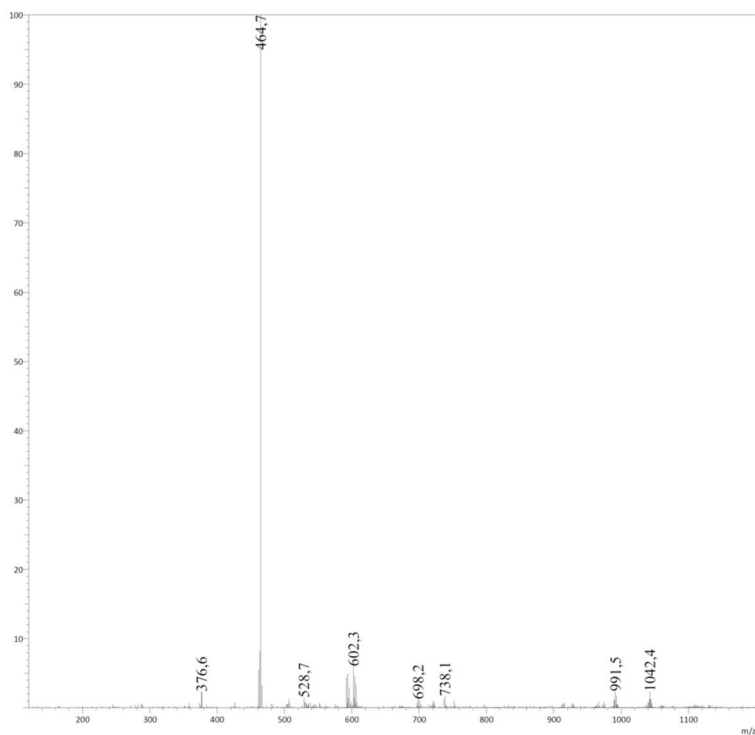


Figure V.59 ESI-MS of $[24]Cl_2$. Calculated for $[C_{51}H_{57}N_9O_2Ru]^{2+}$: 464.7 m/z.

V.4.18 $[Ru(\text{Mebppy})(\text{QC82})(\text{STF-31})]^{2+}$, $[25]^{2+}$:

1H NMR (850 MHz, Acetone) δ 10.04 (dd, $J = 5.0, 0.8$ Hz, 2H), 9.50 (s, 1H), 8.72 (td, $J = 7.0, 1.6$ Hz, 3H), 8.46 (d, $J = 7.3$ Hz, 2H), 8.30 (td, $J = 7.7, 1.4$ Hz, 2H), 8.27 (dd, $J = 8.5, 7.6$ Hz, 2H), 8.04 (dd, $J = 8.6, 0.9$ Hz, 2H), 8.02 (ddd, $J = 7.3, 5.5, 1.3$ Hz, 2H), 7.77–7.75 (m, 2H), 7.70 (d, $J = 7.7$ Hz, 4H), 7.59 (dd, $J = 8.5, 1.9$ Hz, 2H), 7.40 (d, $J = 8.4$ Hz, 2H), 7.05–7.00 (m, 2H), 6.93 (t, $J = 1.4$ Hz, 1H), 6.68 (t, $J = 1.6$ Hz, 1H), 6.03 (t, $J = 1.6$ Hz, 1H), 4.88 (s, 2H), 4.25 (s, 3H), 4.20–4.17 (m, 2H), 1.94 (d, $J = 3.2$ Hz, 3H), 1.73–1.68 (m, 9H), 1.64–1.60 (m, 4H), 1.33 (s, 9H).

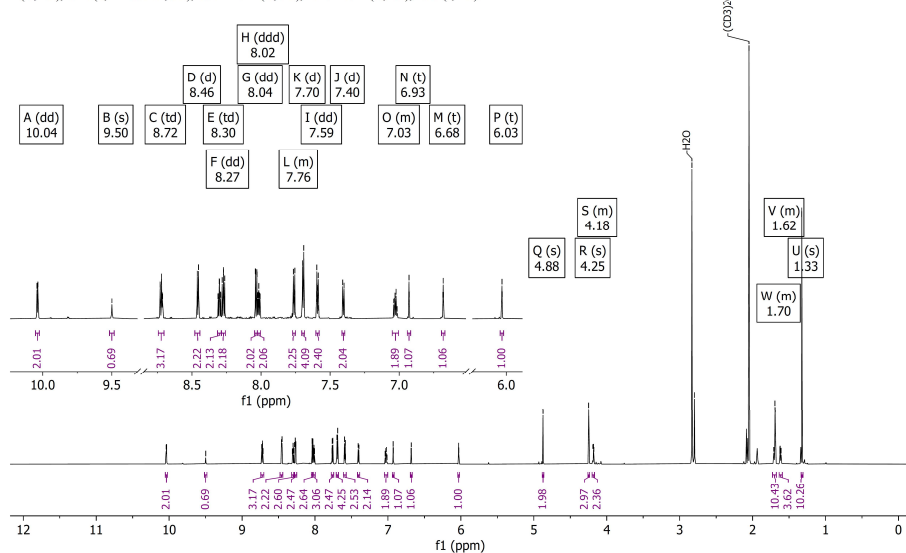


Figure V.60 1H -NMR of $[25](PF_6)_2$ in Acetone- d_6 .

^{13}C NMR (214 MHz, Acetone) δ 165.46, 165.39, 158.01, 156.61, 155.87, 155.85, 155.28, 153.21, 153.14, 147.12, 144.13, 144.05, 142.71, 139.82, 138.30, 138.23, 137.19, 136.98, 132.75, 127.73, 127.51, 127.34, 126.73, 125.99, 125.18, 123.90, 122.50, 117.89, 117.70, 51.63, 46.22, 46.12, 45.04, 43.78, 37.35, 36.00, 30.44, 27.69, 27.66.

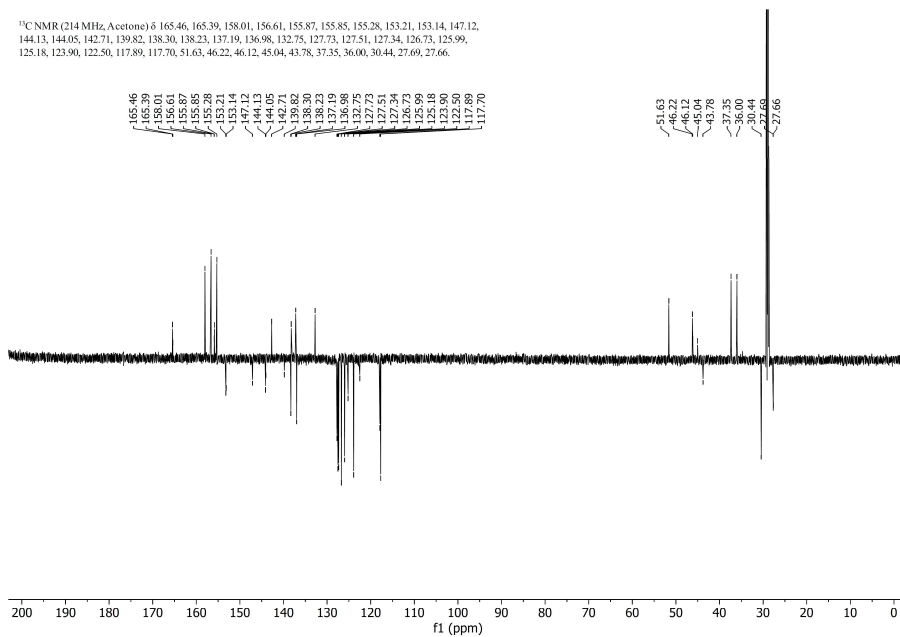


Figure V.61 ^{13}C -NMR of $[\mathbf{25}](\text{PF}_6)_2$ in Acetone- d_6 .

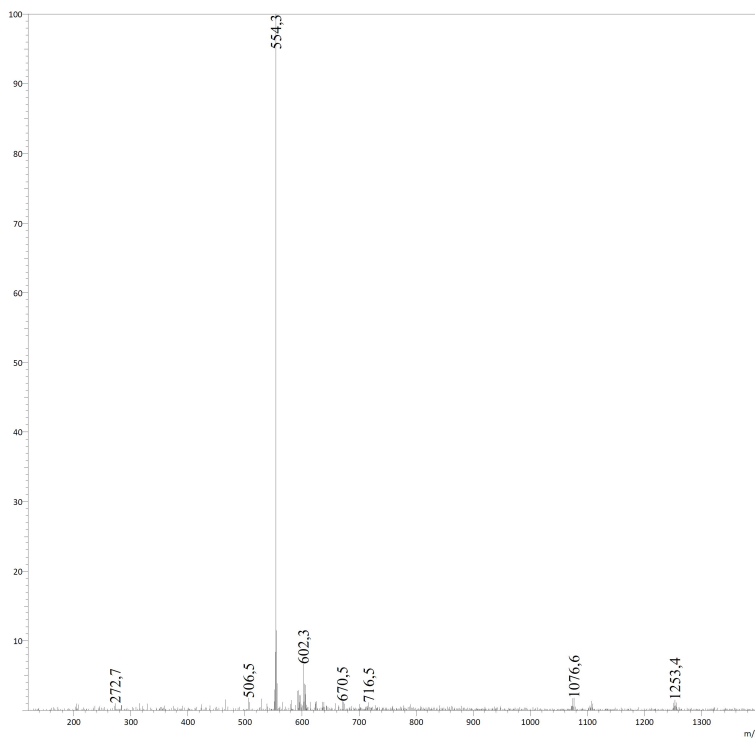


Figure V.62 ESI-MS of $[\mathbf{25}](\text{PF}_6)_2$. Calculated for $[\text{C}_{59}\text{H}_{62}\text{N}_{10}\text{O}_4\text{RuS}]^{2+}$: 554.2 m/z.

^1H NMR (400 MHz, MeOD) δ 9.83 (dd, $J = 5.8, 1.5$ Hz, 2H), 8.67 – 8.59 (m, 2H), 8.46 (d, $J = 2.3$ Hz, 1H), 8.37 (d, $J = 7.8$ Hz, 2H), 8.27 – 8.14 (m, 5H), 7.95 (ddd, $J = 7.3, 5.5, 1.3$ Hz, 2H), 7.90 (d, $J = 8.5$ Hz, 2H), 7.72 (d, $J = 8.6$ Hz, 2H), 7.67 – 7.63 (m, 2H), 7.61 (ddd, $J = 8.4, 2.3, 1.1$ Hz, 1H), 7.55 (d, $J = 8.5$ Hz, 2H), 7.39 (d, $J = 4.9$ Hz, 1H), 7.34 (d, $J = 8.1$ Hz, 2H), 6.94 (dd, $J = 8.4, 5.6$ Hz, 1H), 6.70 (d, $J = 1.4$ Hz, 1H), 6.56 (t, $J = 1.6$ Hz, 1H), 5.88 (t, $J = 1.5$ Hz, 1H), 4.79 (s, 2H), 4.10 (s, 2H), 4.08 (s, 3H), 3.35 (s, 3H), 1.97 (s, 3H), 1.81 – 1.63 (m, 12H), 1.32 (s, 9H).

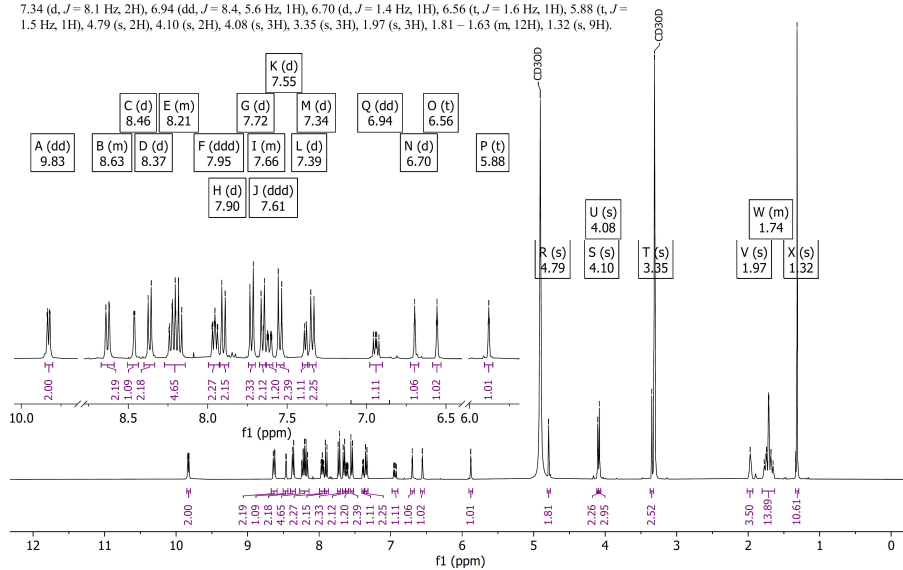


Figure V.63 ^1H -NMR of $[\mathbf{25}]\text{Cl}_2$ in Methanol- d_4 .

^{13}C NMR (101 MHz, MeOD) δ 208.22, 168.01, 159.38, 157.98, 157.47, 156.49, 154.19, 148.06, 145.05, 143.86, 141.02, 139.40, 139.07, 138.47, 138.19, 133.94, 128.92, 128.73, 128.65, 128.36, 127.87, 127.16, 126.18, 125.14, 123.44, 119.11, 118.51, 52.73, 47.27, 46.49, 44.34, 38.74, 37.32, 35.97, 31.46, 29.17.

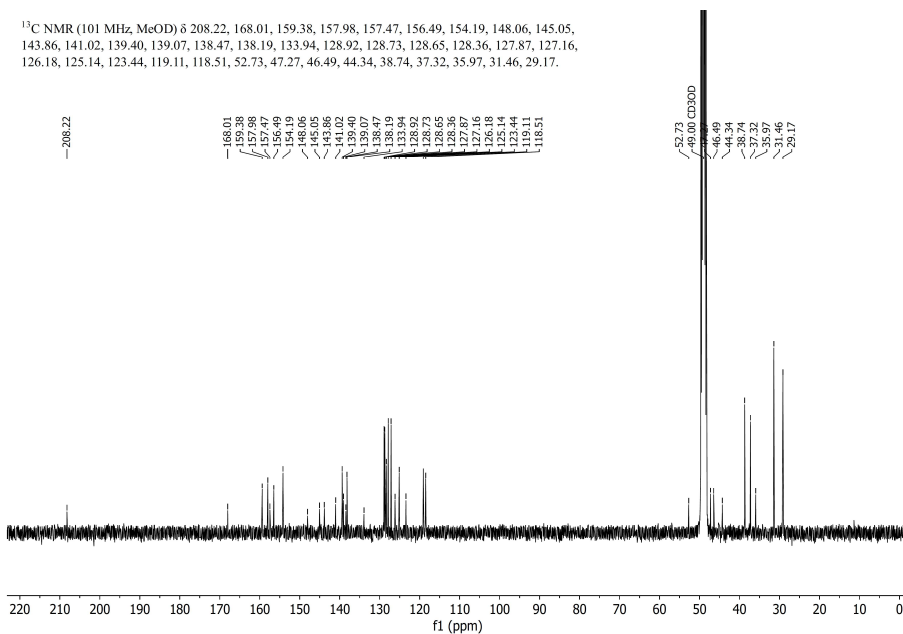


Figure V.64 ^{13}C -NMR of $[\mathbf{25}]\text{Cl}_2$ in Methanol- d_4 .

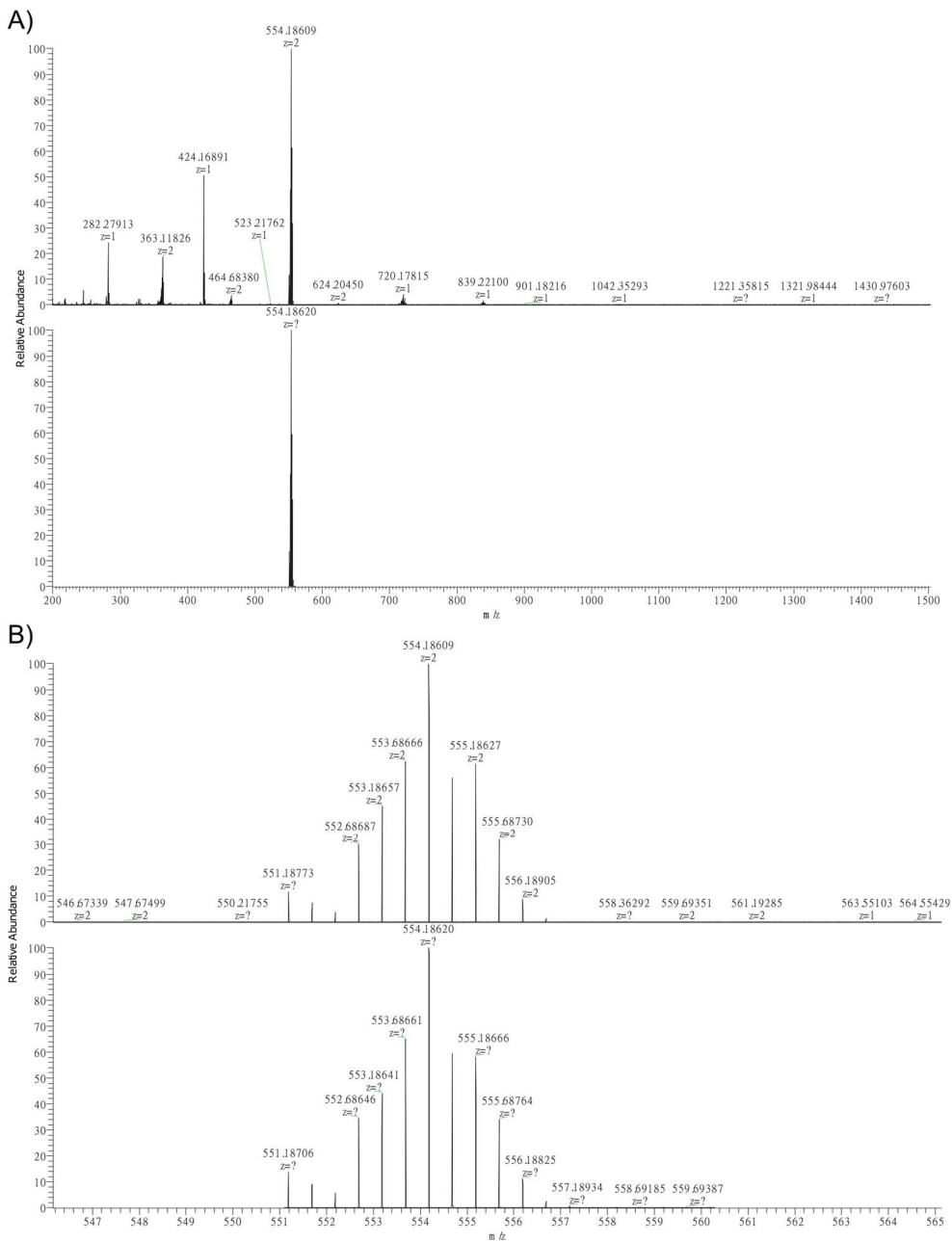
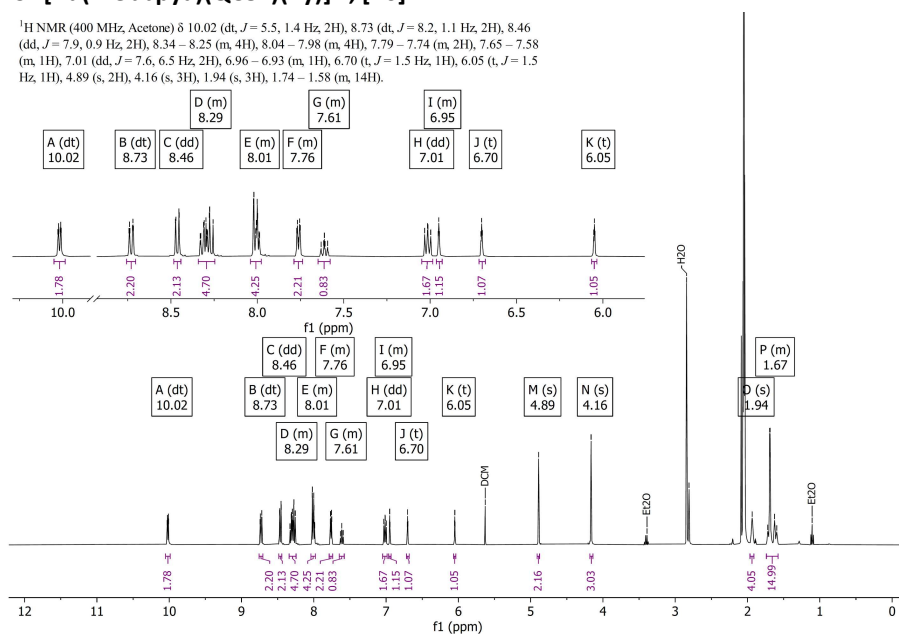
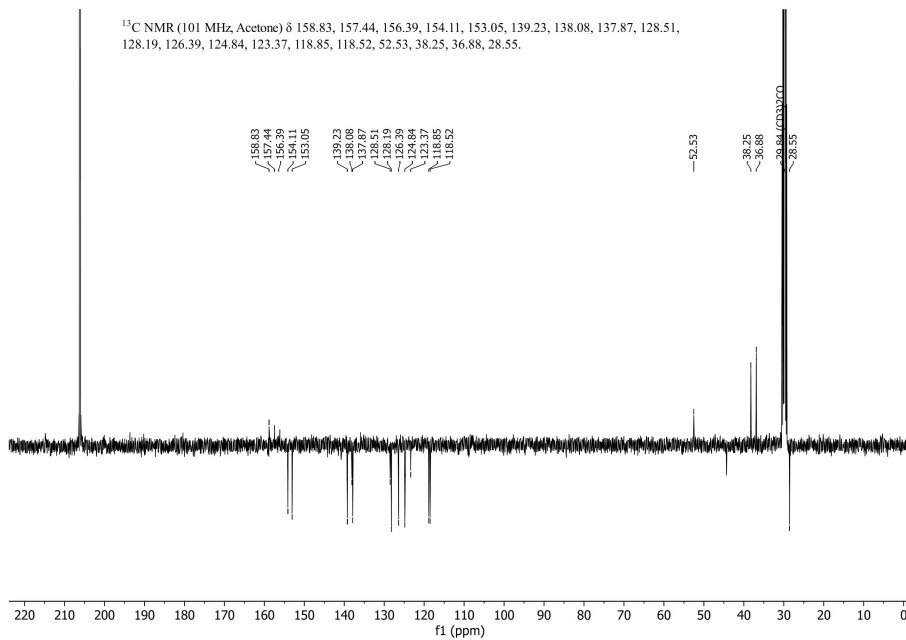


Figure V.65 ESI-HRMS of $[25]Cl_2$. Calculated for $[C_{59}H_{62}N_{10}O_4RuS]^{2+}$: 554.1862 m/z. Mass spectrum shown with range 200-1500 m/z (a) and 546-565 m/z (b).

V.4.19 [Ru(Mebppya)(QC82)(Py)]²⁺, [26]²⁺:

¹H NMR (400 MHz, Acetone) δ 10.02 (dt, *J* = 5.5, 1.4 Hz, 2H), 8.73 (dt, *J* = 8.2, 1.1 Hz, 2H), 8.46 (dd, *J* = 7.9, 0.9 Hz, 2H), 8.34–8.25 (m, 4H), 8.04–7.98 (m, 4H), 7.79–7.74 (m, 2H), 7.65–7.58 (m, 1H), 7.01 (dd, *J* = 7.6, 6.5 Hz, 2H), 6.96–6.93 (m, 1H), 6.70 (t, *J* = 1.5 Hz, 1H), 6.05 (t, *J* = 1.5 Hz, 1H), 4.89 (s, 2H), 4.16 (s, 3H), 1.94 (s, 3H), 1.74–1.58 (m, 14H).

Figure V.66 ¹H-NMR of [26](PF₆)₂ in Acetone-*d*₆.Figure V.67 ¹³C-NMR of [26](PF₆)₂ in Acetone-*d*₆.

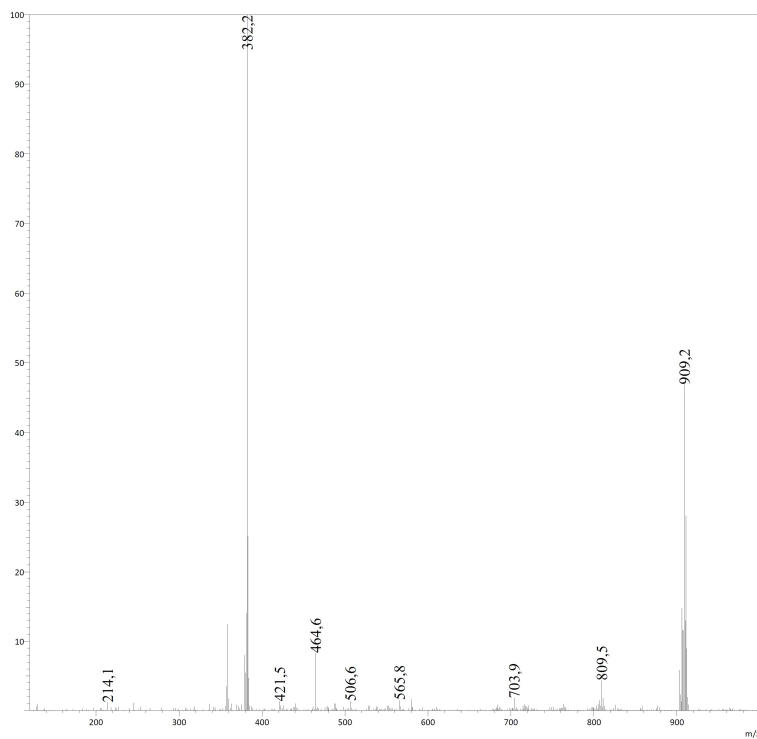


Figure V.68 ESI-MS of **[26](PF₆)₂**. Calculated for **[C₄₁H₄₂N₈ORu]²⁺**: 382.1 m/z

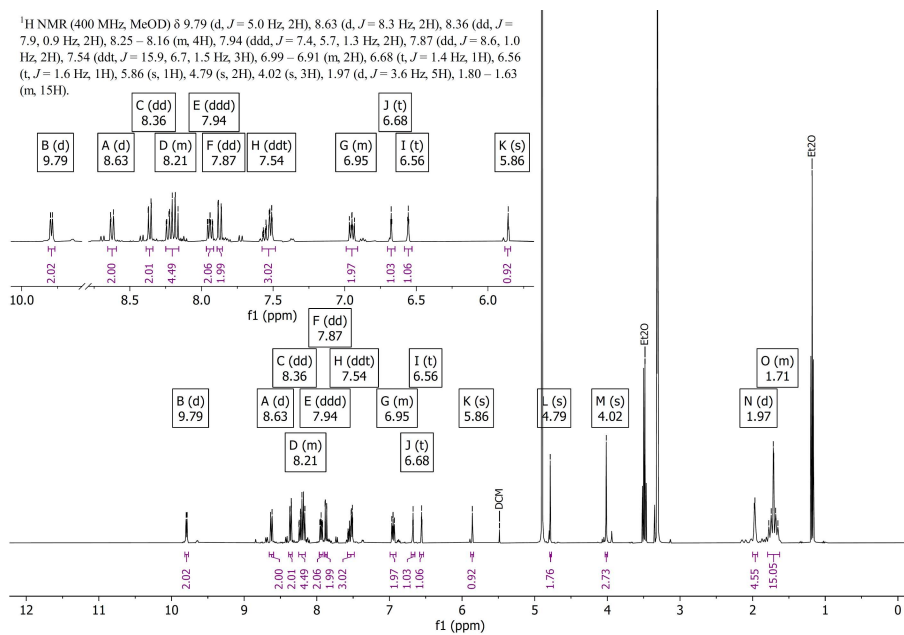


Figure V.69 ¹H-NMR of **[26]Cl₂** in Methanol-*d*₄.

Samenvatting

“*Trans*-Ruthenium(II)-Complexen voor Licht-Geactiveerde Chemotherapie – Van Ontwerp tot Anti-Kankeractiviteit”

Geneesmiddelen op basis van overgangsmetalen spelen een belangrijke rol in moderne kankerbehandeling; op platina(II) gebaseerde geneesmiddelen worden wereldwijd toegepast in ongeveer de helft van alle chemotherapeutische behandelregimes. Ondanks hun brede inzetbaarheid kennen Pt(II)-geneesmiddelen verschillende beperkingen, waaronder systemische toxiciteit en het optreden van resistentie. Deze nadelen hebben de zoektocht gestimuleerd naar chemotherapieën op basis van andere overgangsmetalen, waaronder goud, palladium, ijzer en ruthenium. **Hoofdstuk 1** geeft een overzicht van de klinische toepassing van op platina en ruthenium gebaseerde antikankergeneesmiddelen en bespreekt recente ontwikkelingen in licht-geactiveerde chemotherapie (PACT).

Polypyridyliganden vormen essentiële bouwstenen in vele therapieën gebaseerd op overgangsmetalen, waardoor er een grote behoefte is aan efficiënte en eenvoudige methoden voor de functionalisering van deze liganden. In **Hoofdstuk 2** wordt een nieuwe synthetische route naar *ortho*-amino-gesubstitueerde polypyridines beschreven. Uitgaande van pyridine-*N*-oxiden maakt deze methode introductie van één tot drie amine-substituenten mogelijk in diverse polypyridinederivaten, waaronder bipyridine, fenantroline, terpyridine, chinoline en isochinoline. De eenvoud, efficiëntie en selectiviteit van deze methode maken bovendien eenvoudige opschaling mogelijk, zoals geïllustreerd door de hoge opbrengst van 2,2'-bipyridine-6-amine op een schaal van meer dan 66 mmol.

Hoofdstuk 3 presenteert de ontwikkeling van een *trans*-ruthenium(II) polypyridinecomplex waarvan twee verschillende monodentate liganden sequentieel worden gesubstitueerd door bestraling met twee verschillende kleuren licht. Hiervoor is een reeks symmetrische complexen gesynthetiseerd op basis van $trans\text{-[Ru(RL)(X)(Y)]}^{2+}$, waarbij RL = HL (di([2,2'-bipyridin]-6-yl)amine) of MeL (di([2,2'-bipyridin]-6-yl)-*N*-methylamine) en X = Y = MTE (methyl(2-thioethanol)), ACN (acetonitril) of Py (pyridine). Hoewel alle complexen stabiel zijn in het donker, leidt bestraling met blauw (435 nm), groen (505 nm) of rood (625 nm) licht tot duidelijke verschillen in foto-substitutiekinetiek. Voor meerdere complexen is bovendien de kwantumopbrengst golflengte-afhankelijk, wat een zeldzaam voorbeeld vormt van anti-Kasha gedrag in fotosubstitutiereacties in ruthenium(II)-complexen. Deze bevindingen hebben geleid tot de synthese van de dissymmetrische verbinding $[\text{Ru}(\text{MeL})(\text{Py})(\text{MTE})]^{2+}$ via de bestraling met rood licht van $[\text{Ru}(\text{MeL})(\text{Py})_2]^{2+}$ in aanwezigheid van MTE. Onder bestraling met rood licht wordt van dit dissymmetrische complex selectief Py gesubstitueerd, waarna MTE met groen licht wordt vervangen. Dit vormt het eerste voorbeeld van selectieve, golflengte-afhankelijke fotosubstitutie in

ruthenium-polypyridylcomplexen en maakt tevens een eerste kwantitatieve analyse mogelijk van *trans*-effecten in tripletoestanden.

In **Hoofdstuk 4** wordt het concept “dual-targeting” PACT onderzocht waarbij twee biologisch-actieve liganden selectief vrijkomen vanuit één ruthenium(II)-complex na bestraling met licht. Daartoe zijn de pyridine-gebaseerde NAMPT-inhibitor STF31 en de thioether-gebaseerde inhibitor voor microtubulipolymerisatie MTI geïntegreerd in het dissymmetrische complex beschreven in **Hoofdstuk 3**. Dit heeft geleid tot de verbinding $[\text{Ru}(\text{MeL})(\text{STF31})(\text{MTI})]^{2+}$ en de symmetrische analogen $[\text{Ru}(\text{MeL})(\text{STF31})_2]^{2+}$ en $[\text{Ru}(\text{MeL})(\text{MTI})_2]^{2+}$. Deze complexen vertonen uiteenlopende fotoreactiviteit onder blauw, groen en rood licht in waterige oplossing. Belangrijk is dat de golflengte-afhankelijke, sequentiële activering behouden blijft in het dissymmetrische complex: substitutie van STF31 gebeurt door bestralen met rood licht, gevolgd door MTI als bestraald wordt met blauw licht. *In vitro* evaluatie van het bis-MTI complex in diverse menselijke kankercellijnen onder zowel normoxie en hypoxie heeft een sterke toxiciteit laten zien in het donker zonder duidelijke toename na belichting. Daarentegen neemt de toxiciteit van de bis-STF31 en STF31-MTI complexen tot 33-voudig toe na activering met groen licht. Gelijktijdige behandeling van tumorcellijnen met vrij STF31 en MTI leidt tot een synergistisch effect, dat eveneens wordt waargenomen na groen licht activering van $[\text{Ru}(\text{MeL})(\text{STF31})(\text{MTI})]^{2+}$, onafhankelijk van de zuurstofconcentratie. De uitzonderlijke fotochemische en biologische eigenschappen van dit dissymmetrische complex benadrukken het potentieel van dual-targeting PACT, met name voor de behandeling van hypoxische tumoren.

Voor veel van de PACT-verbindingen beschreven in de literatuur fungeert het ruthenium(II)-fragment voornamelijk als een lichtgevoelige beschermgroep die interactie tussen een organische cytotoxische inhibitor en zijn doeleiwit voorkomt. Hoewel deze benadering veelbelovend is gebleken voor het doden van kankercellen, blijft het potentieel van het ruthenium(II)-fragment dat vrijkomt door belichting als biologisch-actieve component grotendeels onbenut. Ondanks enkele observaties van interacties tussen rutheniumcomplexen en nucleïne-zuren, zijn er tot op heden geen rationeel ontworpen, licht-actieveerbare Ru(II)-gebaseerde proteïne-inhibitoren gerapporteerd. In **Hoofdstuk 5** worden twee strategieën beschreven voor het ontwerp en de ontwikkeling van nieuwe PACT-verbindingen als inhibitoren voor Heme Oxygenase 1 (HO-1). De eerste strategie betreft de functionalisering van het tetrapyridineligand di([2,2'-bipyridin]-6-yl)amine (HL) met propionzuurgroepen via kruiskoppeling- of C-H-functionaliseringsreacties. Na coördinatie vormt het resulterende ruthenium(II)-complex een nabootsing voor het natuurlijke HO-1 substraat, de heemgroep, en kan het na fotosubstitutie van de twee monodentate axiale liganden het enzym blokkeren.

Voor de tweede strategie is een reeks complexen ontwikkeld op basis van $[\text{Ru}(\text{MeL})(\text{QC82})(\text{X})]^{2+}$, waarbij QC82 een bekende HO-1 inhibitor is gebaseerd op imidazool

en X = QC82, pyridine of STF31. Alle complexen ondergaan fotosubstitutie onder groen of rood licht, waarbij steeds één QC82-ligand gecoördineerd blijft aan het Ru(II)-fotoproduct. Om het potentieel van dit Ru(II)-fotoproduct als HO-1 inhibitor te evalueren, zijn er *in silico*-dockingstudies uitgevoerd met $[\text{Ru}(\text{MeL})(\text{QC82})]^{2+}$ en HO-1, die wijzen op een bindingsmodus vergelijkbaar met die van heem. Hoewel $[\text{Ru}(\text{MeL})(\text{QC82})_2]^{2+}$ en $[\text{Ru}(\text{MeL})(\text{QC82})(\text{STF31})]^{2+}$ significante *in vitro* toxiciteit vertonen in menselijke melanoomcellen, kan op basis van de beschikbare data niet worden vastgesteld of deze toxiciteit het gevolg is van HO-1 inhibitie. De resultaten vormen echter een solide basis voor de verdere ontwikkeling van licht-geactiveerde HO-1 inhibitoren op basis van ruthenium(II).

In **Hoofdstuk 6** wordt het in dit proefschrift beschreven onderzoek samengevat en bediscussieerd, gevolgd door aanbevelingen voor toekomstig onderzoek.

Curriculum Vitae

Wessel Verbeet was born on November 14, 1992, in Vlaardingen, the Netherlands. After completing his secondary education (havo) at PENTA College Blaise Pascal in Spijkenisse in 2011, he started his bachelor's studies in Chemistry at Hogeschool Rotterdam. During this period, he conducted a research internship supervised by Prof. dr. Leonard J. Prins and under the daily supervision of Dr. Flavio della Salle at the University of Padova. His thesis, entitled "*Synthesis and Characterization of Novel Surfactants for the Creation of Life-like Supramolecular assemblies*", was awarded *Best Thesis of 2016 at Hogeschool Rotterdam* by Stichting Haags Laboratorium Onderwijs and received an honorable mention in the *Gouden Spatel 2016* competition organized by KNCV. Wessel obtained his BSc degree in Applied Sciences in 2016.

In the same year, he started his master's studies in Chemistry at Leiden University. His master's research internship was conducted in the group of Prof. dr. Alexander Kros, under the daily supervision of Dr. Niek S. A. Crone. His thesis, entitled "*Designing Intramolecular Cross-linked Peptides for Photoactivated Coiled-coil Mediated Membrane Fusion*", was completed in 2019, after which he obtained his MSc degree.

In September 2019, Wessel started his doctoral research studies in the Metals in Catalysis, Biomimetics & Inorganic Materials (MCBIM) group under the supervision of Prof. dr. Sylvestre Bonnet and Prof. dr. Elisabeth Bouwman at Leiden University. His doctoral research focused on the design and synthesis of *trans* ruthenium(II) complexes for applications in photoactivated chemotherapy. Parts of his doctoral research were presented at national and international conferences, including the *3rd Frontiers in Photochemistry* conference (2022 Cancun, Mexico), the *44th International Conference on Coordination Chemistry* (2022 Rimini, Italy) and the *16th International Symposium on Applied Bioinorganic Chemistry* (2023 Ioannina, Greece). As part of the PhD program, Wessel also followed several courses, namely, Scientific Conduct offered by the Graduate School of Leiden University and the Advanced Summer School on Photochemistry 2022 offered by the Holland Research School of Molecular Chemistry (HRSMC).

In October 2024, Wessel continued his academic career as a postdoctoral researcher in the group of Prof. dr. Alexander Kros as part of the *Cat4CanCenter Synergy* project, in collaboration with the University of Amsterdam and Netherlands Cancer institute (NKI).

List of Publications

Dual Targeting of NAMPT and Tubulin with *Trans*-Ruthenium(II)-based Photoactivated Chemotherapy Complexes

W. Verbeet, S. K. Götzfried, A. Kornienko, S. Bonnet*, *in preparation*

Building a *Trans* Dissymmetric Ruthenium(II) Complex for Sequential Ligand Photosubstitution

W. Verbeet, A. Jiao, M. A. Siegler, S. Bonnet*, *in preparation*

Simple and Efficient Method for Mono- and Di-Amination of Polypyridine *N*-Oxides

W. Verbeet‡, Y. Husiev‡, S. Bonnet*, *Eur. J. Org. Chem.* **2024**, 27, e202400054

Ruthenium-Peptide Conjugates for Photoactivated Chemotherapy

I. Regeni*, M. Puister, Y. Husiev, W. Verbeet, I. M. Nardella, M. L. A. Hakkennes, K. Kayastha, S. Brünle, S. Bonnet*, *in preparation*

Stepwise Hierarchical Self-Assembly of Supramolecular Amphiphiles into Higher-Order Three-Dimensional Nano Structure

F. della Salle, W. Verbeet, S. Silvestrini, I. Fortunati, C. Ferrante, L. J. Prins*, *ChemNanoMat* **2018**, 4, 821 - 830

* Corresponding author; ‡ Authors contributed equally

Acknowledgements

It goes without saying that the research presented in this thesis would have been impossible without the guidance, advice and overall support of others. Therefore, I would like to thank the people that have contributed in some way or form during these years.

Firstly, I would like to thank my promotor Prof. dr. *Sylvestre Bonnet* for giving me the opportunity to pursue a PhD under your supervision. After following your Photochemistry course during my master studies, I became fascinated by how light can be used for chemical and medicinal purposes. I want to thank you for the supportive and positive research environment you created, together with guidance and inspiration throughout the years. Even when times were tough, this kept me motivated and shaped me into the independent researcher I am today. Secondly, I want to thank my co-promotor Prof. dr. *Lies Bouwman* for her advice and insights on anything related to coordination chemistry, her meticulous corrections on my thesis chapters, and patiently reminding me to finish them.

I would also like to express my gratitude to all the collaborators that contributed to this thesis. Dr. *Sipeng Zheng* for the MS and ICPMS measurements. *Hans van den Elst* for the HRMS measurements. Dr. *Karthick Sai Sankar Gupta* and *Alfons Lefeber* for their help with the NMR experiments. For the X-ray crystal structures, thanks to Dr. *Maxime Sieglér* from Johns Hopkins University. Special thanks to Dr. *Yurii Husiev* for the collaboration on our amination paper (the first purely organic synthetic paper from an inorganic group) and all the discussions on metal chemistry/music. I also had the privilege to supervise several students during their graduation project. Many thanks to *Andy, Amanda, Jesse, Floris* and *Pieter* for your enthusiasm and motivation during the (sometimes challenging) projects which you managed to progress independently. I wish you all the best in your future careers.

A special thanks goes to all past and present members of the MCBIM group. Working in such a friendly and supportive environment made the past years productive and truly a lot of fun. Thanks to *Irene, Vasiliki, Maarten, Daria, Valeriia, Marleen, Dennis, Ashok, Aswin, Lan, Christian, Liyan, Corjan, Ehider, Erik, Sina, Agnese, Selda, Ludo, Yurii, Joeri, Matthijs, Sjoerd, Phebe* and all the others. For the helpful brainstorming sessions, shared frustrations, shenanigans and many coffee breaks/drinks that made the long days fly by. Also, to all the friends I met along the way: Thank you for the many moments of relaxation, laughter and distraction when it was needed most.

Finally, I would like to thank my *Mom, Boy, Annelies* and little *Guus* for their support, encouragement and patience throughout this journey. Last but certainly not least, I want to thank you *Elena* for your support, strength and understanding. The past years were challenging at times, but you are always there for me, and I am deeply grateful to have you by my side.

To everyone who contributed in one way or another, thank you.